frontiers | Research Topics

Pharmacokinetics of herbal medicines and herb-drug interactions

Edited by
Wei-Wei Jia, Ge Lin, Guangbo Ge and Chuang Lu

Published in
Frontiers in Pharmacology

ISSN 1664-8714
ISBN 978-2-83251-282-1
DOI 10.3389/978-2-83251-282-1

About Frontiers

Frontiers is more than just an open access publisher of scholarly articles: it is a pioneering approach to the world of academia, radically improving the way scholarly research is managed. The grand vision of Frontiers is a world where all people have an equal opportunity to seek, share and generate knowledge. Frontiers provides immediate and permanent online open access to all its publications, but this alone is not enough to realize our grand goals.

Frontiers journal series

The Frontiers journal series is a multi-tier and interdisciplinary set of open-access, online journals, promising a paradigm shift from the current review, selection and dissemination processes in academic publishing. All Frontiers journals are driven by researchers for researchers; therefore, they constitute a service to the scholarly community. At the same time, the *Frontiers journal series* operates on a revolutionary invention, the tiered publishing system, initially addressing specific communities of scholars, and gradually climbing up to broader public understanding, thus serving the interests of the lay society, too.

Dedication to quality

Each Frontiers article is a landmark of the highest quality, thanks to genuinely collaborative interactions between authors and review editors, who include some of the world's best academicians. Research must be certified by peers before entering a stream of knowledge that may eventually reach the public - and shape society; therefore, Frontiers only applies the most rigorous and unbiased reviews. Frontiers revolutionizes research publishing by freely delivering the most outstanding research, evaluated with no bias from both the academic and social point of view. By applying the most advanced information technologies, Frontiers is catapulting scholarly publishing into a new generation.

What are Frontiers Research Topics?

Frontiers Research Topics are very popular trademarks of the *Frontiers journals series*: they are collections of at least ten articles, all centered on a particular subject. With their unique mix of varied contributions from Original Research to Review Articles, Frontiers Research Topics unify the most influential researchers, the latest key findings and historical advances in a hot research area.

Find out more on how to host your own Frontiers Research Topic or contribute to one as an author by contacting the Frontiers editorial office: frontiersin.org/about/contact

Pharmacokinetics of herbal medicines and herb-drug interactions

Topic editors

Wei-Wei Jia — Shanghai Institute of Materia Medica, Chinese Academy of Sciences (CAS), China

Ge Lin — The Chinese University of Hong Kong, China

Guangbo Ge — Shanghai University of Traditional Chinese Medicine, China

Chuang Lu — Accent Therapeutics, Inc, United States

Citation

Jia, W.-W., Lin, G., Ge, G., Lu, C., eds. (2023). *Pharmacokinetics of herbal medicines and herb-drug interactions*. Lausanne: Frontiers Media SA.

doi: 10.3389/978-2-83251-282-1

Table of contents

frontiers | Frontiers in Pharmacology

TYPE Editorial
PUBLISHED 13 December 2022
DOI 10.3389/fphar.2022.1107777

OPEN ACCESS

EDITED AND REVIEWED BY
Michael Heinrich,
University College London,
United Kingdom

*CORRESPONDENCE
Wei-Wei Jia,
weiweijia@simm.ac.cn
Chuang Lu,
chuanglu7@gmail.com
Ge Lin,
linge@cuhk.edu.hk
Guang-Bo Ge,
geguangbo@dicp.ac.cn

SPECIALTY SECTION
This article was submitted to Ethnopharmacology, a section of the journal Frontiers in Pharmacology

RECEIVED 25 November 2022
ACCEPTED 29 November 2022
PUBLISHED 13 December 2022

CITATION
Jia W-W, Lu C, Lin G and Ge G-B (2022), Editorial: Pharmacokinetics of herbal medicines and herb-drug interactions. *Front. Pharmacol.* 13:1107777. doi: 10.3389/fphar.2022.1107777

Editorial: Pharmacokinetics of herbal medicines and herb-drug interactions

Wei-Wei Jia[1]*, Chuang Lu[2]*, Ge Lin[3]* and Guang-Bo Ge[4]*

[1]State Key Laboratory of Drug Research, Shanghai Institute of Materia Medica, Chinese Academy of Sciences, Shanghai, China, [2]Accent Therapeutics, Inc., Lexington, MA, United States, [3]School of Biomedical Sciences, Faculty of Medicine, The Chinese University of Hong Kong, Hong Kong SAR, China, [4]Shanghai Frontiers Science Center for Chinese Medicine Chemical Biology, Institute of Interdisciplinary Integrative Medicine Research, Shanghai University of Traditional Chinese Medicine, Shanghai, China

KEYWORDS

herbal medicine, pharmacokinetics, drug combination, drug interaction, molecular mechanism, drug transporter, drug-metabolizing enzyme

Editorial on the Research Topic
Pharmacokinetics of herbal medicines and herb-drug interactions

Herbal medicines have provided a basis for health management and disease prevention in many Asia countries, including China, India, and Japan. Several herbal medicines have been evidenced scientifically for their efficacy and safety in rigorous clinical trials (Wang et al., 2011; Li et al., 2013; Shang et al., 2013; Song et al., 2019). In the past few decades, therapeutic regimen combining synthetic drugs with herbal medicines represent a promising strategy for preventing and treating multifactorial diseases. Such combination probably exhibits different mechanisms of actions and improves the pharmacodynamic effects and safeties. The thorough knowledge of mechanisms of and chemical basis for herbal medicine actions on therapeutic targets may provide a better rationale for the understanding of combination of drugs with different mechanisms, which are preferable in the polytherapy of diseases. To support the drug combination, the impact of such combination on therapeutic outcome needs to be assessed, including pharmacokinetic interactions mediated by drug-metabolizing enzymes and drug transporters. Commonly, most of clinically used herbal medicines are prepared from multiple herbs that contain hundreds of chemically diverse constituents, which may interact with a variety of drug-metabolizing enzymes and drug transporters in extremely complex ways (Ge, 2019). The complex interactions make a great challenge for an investigator to quickly and accurately find the key compounds responsible for therapeutic actions of the herbal medicines. Pharmacokinetic research provides a practical approach to identifying potentially important compounds (bioavailable at the action loci with significant exposure levels after dosing an herbal medicine). Better understanding of the pharmacokinetic behaviors of the bioavailable compounds is vital in evaluating therapeutic and adverse effects of the

herbal medicine, as well as their pharmacokinetic interactions. This is of particular importance in cases where herbal medicine is added to conventional therapy.

Our Research Topic compiles 11 innovative original research contributions from prominent scientists in the field. This compilation covers a number of herbal medicines in pharmacokinetic-pharmacodynamic (PK-PD) relationships, herb-drug interactions, and the associated molecular mechanisms related to drug-metabolizing enzymes and drug transporters.

Multi-compound pharmacokinetic approach was used to identify potentially important compounds from single herb or herbal combinations and also characterize their pharmacokinetics and disposition (Lan et al., 2021; Li et al., 2022). Based on comprehensive and validated UPLC-MS/MS-bioanalytical assays, the study by Cheng et al. found that among ten main stilbene glycosides and anthraquinones, 2,3,5,4′-teterahydroxystilbene-2-*O*-β-D-glucoside, emodin, citreorosein, and emodin-8-*O*-β-D-glucoside exhibited higher levels of systemic exposure in rats orally dosed with an extract of the roots of *Polygonum multiflorum* Thunb. (Ploygoni multiglori radix in pharmacopeia of China). Besides these compounds, physcion-8-*O*-β-D-glucoside also significantly exposured to the liver and kidneys of rats. Chen et al. investigated that delicaflavone, robustaflavone, 2″,3″-dihydro-3′,3‴-biapigenin, 3′,3‴-binaringenin, and amentoflavone exhibited the highest levels of lung exposure in rats after receiving a flavonoid extract from the whole plants of *Selaginella doederleinii* Hieron, which is used to treat cancers. These five flavonoids were extensively cleared by fecal excretion. Huang et al. compared cellular pharmacokinetics of luteolin, chlorogenic acid, cryptochlorogenic acid, 3,4-dicaffeoylquinic acid, and 4,5-dicaffeoylquinic acid of the whole plants or roots of *Inula cappa* (Buch.-Ham. ex D. Don) DC. in normal RAW264.7 cells and the LPS-induced cells. WuJi pill, an herbal combination, is used for treating irritable bowel syndrome (IBS). Gong et al. reported the pharmacokinetic differences of five representative compounds (berberine, palmatine, evodiamine, rutaecarpine, and paeoniflorin) in normal rats and IBS-model rats after dosing the pill. The molecular mechanism underlying the pharmacokinetic differences was reported that the decreased expression of tight junction proteins resulted in the increased permeability of colon mucosa in the model rats. Another herbal combination TanReQing injection is used to treat respiratory diseases *via* off-label nebulization in China. Huang et al. demonstrated that lung exposure levels of baicalin and oroxyloside after aerosol inhalation were significantly higher than those after i.v. injection. The inhalation of TanReQing with lower dose could achieve the same effect against LPS-induced lung inflammation in mice. The investigation by Zhang et al. successfully established PK-PD correlation of Yangyin Tongnao granules in rats with cerebral ischemia-reperfusion injury.

Herb-drug interactions are widely recognized as an issue for many drug combinations. Zhang et al. efficiently identified that styrax (the medicinal balsam from the trunks of *Liquidambar orientalis* Mill.) exhibited the most potent inhibitory effects on human CYP3A4, following screening over 100 herbal medicines by a fluorescence-based high-throughput assay. Oral administration of this herbal medicine could elevate systemic exposure levels of midazolam and felodipine *via* oral, but not intravenous, administration of the CYP3A-substrate drugs to rats. Further investigations elucidated that seven styrax-derived pentacyclic triterpenoid acids with high inhibition potency toward CYP3A showed high intestinal exposure levels, while their systemic and hepatic exposure levels were extremely low. Kapelemera et al. found that Xiang-Sha-Liu-Jun-Zi Tang (XSLJZT) could significantly increase levels of systemic exposure to paclitaxel in rats when XSLJZT was pretreated for 3, 5, and 7 days. The results of mechanistic study indicated that XSLJZT could inhibit expression of CYP3A4 in Hep-G2 cells (Cyp3a1/2 in rat liver) and CYP3A4 enzymatic activity of human liver microsomes. Drug interaction was also found to have beneficial effects. For instance, liquorice (Glycyrrhizae radix et rhizome), the roots of *Glycyrrhiza uralensis* Fisch., *Glycyrrhiza glabra* L. or *Glycyrrhiza inflate* Bat., a hepato-protective herbal medicine, is used concurrently with pyrrolizidine alkaloid-containing herbs in many traditional Chinese medicine formulas, and no pyrrolizidine alkaloid poisoning cases have been reported with such combination. Wang et al. comprehensively demonstrated that both liquorice aqueous extract and 18β-glycyrrhetinic acid (the primary bioactive constituent of liquorice) exhibited significant hepato-protective effects against retrorsine (a representative pyrrolizidine alkaloid)-induced hepatotoxicity. The molecular mechanism was that 18β-glycyrrhetinic acid mainly and competitively inhibited the formation of metabolic activation-derived pyrrole-glutathione conjugate mediated by rat CYPs, especially Cyp3a1 (an ortholog of human CYP3A4).

Exploring molecular mechanism is critical for elucidation of pharmacokinetics of herbal medicines and drug interactions. Hepatic and/or renal uptake of phenolic acids, originating from the roots of *Salvia miltiorrhiza* Bge. (Salviae miltiorrhizae radix et rhizome) was the crucial steps in their systemic elimination. Lu et al. comprehensively investigated that several human uptake transporters were found to mediate hepatic and/or renal uptake of phenolic acids in a compound-molecular-mass-related manner. Lithospermic acid and salvianolic acid B (both >500 Da) underwent systemic elimination, initiated by OATP1B1/OATP1B3-mediated hepatic uptake. Rosmarinic acid and salvianolic acids D (350–450 Da) underwent systemic elimination, initiated by OATP1B1/OATP1B3/OAT2-mediated hepatic uptake and by OAT1/OAT2-mediated renal uptake. Protocatechuic acid and

tanshinol (both <200 Da) underwent systemic elimination, initiated by OAT1/OAT2-mediated renal uptake and OAT2-mediated hepatic uptake. Pang et al. utilized an ultra-sensitive and easy-to-use assay to assess the inhibitory activities of over 100 herbal products against UGT1A1 in living systems, and found that an extract from the leaves of *Ginkgo biloba* L. (Ginkgo folium) and its biflavones (bilobetin, isoginkgetin, sciadopitysin, and ginkgetin) exhibited the most inhibition potency toward UGT1A1.

We believe that the investigators of these articles have made great efforts to gain new insights into the key herbal constituents responsible for herbal medicine's therapeutic effects, adverse effects, and herb-drug interactions. We are confident that these innovative and important studies will be very useful for the researchers and clinical pharmacologists to better understand the complex interactions between herbal medicines and the human body, which will be very helpful for accurate medication of herbal medicines in clinical settings. Although great advances have been achieved in methodology, techniques, and applications of pharmacokinetic studies, complex chemical composition, chemical basis, and PK-PD correlation for most herbal medicines remain challenges in bringing herbal medicine from empirical medicine into evidence-based medicine and meeting regulatory requirements. With the advancement of *in vitro* and *in vivo* methodology and computational hardware and software, artificial intelligence represents a promising means to predict the pharmacokinetic properties of numerous constituents for an herbal medicine in a more high-throughput and cost-effective manner.

Author contributions

W-WJ wrote the manuscript. CL, GL, and G-BG read and revised the manuscript.

Funding

This work was funded by the National Natural Science Foundation of China (82274351) and Innovation Team and Talents Cultivation Program of National Administration of Traditional Chinese Medicine (ZYYCXTD-C-202009).

Conflict of interest

CL was employed by the Accent Therapeutics, Inc.

The remaining authors declare that the research was conducted in the absence of any commercial or financial relationships that could be construed as a potential conflict of interest.

Publisher's note

References

Ge, G. B. (2019). Deciphering the metabolic fates of herbal constituents and the interactions of herbs with human metabolic system. *Chin. J. Nat. Med.* 17, 801–802. doi:10.1016/S1875-5364(19)30098-6

Lan, X. F., Olaleye, O. E., Lu, J. L., Yang, W., Du, F. F., Yang, J. L., et al. (2021). Pharmacokinetics-based identification of pseudoaldosterogenic compounds originating from *Glycyrrhiza uralensis* roots (Gancao) after dosing LianhuaQingwen capsule. *Acta Pharmacol. Sin.* 42, 2155–2172. doi:10.1038/s41401-021-00651-2

Li, C., Jia, W. W., Yang, J. L., Cheng, C., and Olaleye, O. E. (2022). Multi-compound and drug-combination pharmacokinetic research on Chinese herbal medicines. *Acta Pharmacol. Sin.* 43 (12), 3080–3095. doi:10.1038/s41401-022-00983-7

Li, X., Zhang, J., Huang, J., Ma, A., Yang, J., Li, W., et al. (2013). A multicenter, randomized, double-blind, parallel-group, placebo-controlled study of the effects of qili qiangxin capsules in patients with chronic heart failure. *J. Am. Coll. Cardiol.* 62, 1065–1072. doi:10.1016/j.jacc.2013.05.035

Shang, H., Zhang, J., Yao, C., Liu, B., Gao, X., Ren, M., et al. (2013). Qi-shen-yi-qi dripping pills for the secondary prevention of myocardial infarction: A randomised clinical trial. *Evid. Based. Complement. Altern. Med.* 2013, 738391. doi:10.1155/2013/738391

Song, Y., Yao, C., Yao, Y., Han, H., Zhao, X., Yu, K., et al. (2019). Xuebijing injection versus placebo for critically ill patients with severe community-acquired pneumonia: A randomized controlled trial. *Crit. Care Med.* 47, e735–e743. doi:10.1097/CCM.0000000000003842

Wang, C., Cao, B., Liu, Q. Q., Zou, Z. Q., Liang, Z. A., Gu, L., et al. (2011). Oseltamivir compared with the Chinese traditional therapy maxingshigan-yinqiaosan in the treatment of H1n1 influenza: A randomized trial. *Ann. Intern. Med.* 155, 217–225. doi:10.7326/0003-4819-155-4-201108160-00005

frontiers in Pharmacology

ORIGINAL RESEARCH
published: 21 February 2022
doi: 10.3389/fphar.2022.815235

Discovery and Characterization of the Key Constituents in *Ginkgo biloba* Leaf Extract With Potent Inhibitory Effects on Human UDP-Glucuronosyltransferase 1A1

Hui-Lin Pang[1†], Guang-Hao Zhu[2†], Qi-Hang Zhou[2], Chun-Zhi Ai[3], Ya-Di Zhu[2], Ping Wang[2], Tong-Yi Dou[1], Yang-Liu Xia[1], Hong Ma[4]* and Guang-Bo Ge[2]**

[1]School of Life and Pharmaceutical Sciences, Dalian University of Technology, Panjin, China, [2]Shanghai Frontiers Science Center for Chinese Medicine Chemical Biology, Institute of Interdisciplinary Integrative Medicine Research, Shanghai University of Traditional Chinese Medicine, Shangha, China, [3]State Key Laboratory for Chemistry and Molecular Engineering of Medicinal Resources, School of Chemistry and Pharmacy, Guangxi Normal University, Guilin, China, [4]Shanghai Research Institute of Acupuncture and Meridian, Shanghai University of Traditional Chinese Medicine, Shanghai, China

Human UDP-glucuronosyltransferase 1A1 (hUGT1A1) is one of the most essential phase II enzymes in humans. Dysfunction or strong inhibition of hUGT1A1 may result in hyperbilirubinaemia and clinically relevant drug/herb-drug interactions (DDIs/HDIs). Recently, a high-throughput fluorescence-based assay was constructed by us to find the compounds/herbal extracts with strong inhibition against intracellular hUGT1A1. Following screening of over one hundred of herbal products, the extract of *Ginkgo biloba* leaves (GBL) displayed the most potent hUGT1A1 inhibition in HeLa-UGT1A1 cells (Hela cells overexpressed hUGT1A1). Further investigations demonstrated that four biflavones including bilobetin, isoginkgetin, sciadopitysin and ginkgetin, are key constituents responsible for hUGT1A1 inhibition in living cells. These biflavones potently inhibit hUGT1A1 in both human liver microsomes (HLM) and living cells, with the IC_{50} values ranging from 0.075 to 0.41 μM in living cells. Inhibition kinetic analyses and docking simulations suggested that four tested biflavones potently inhibit hUGT1A1-catalyzed NHPN-*O*-glucuronidation in HLM *via* a mixed inhibition manner, showing the K_i values ranging from 0.07 to 0.74 μM. Collectively, our findings uncover the key constituents in GBL responsible for hUGT1A1 inhibition and decipher their inhibitory mechanisms against hUGT1A1, which will be very helpful for guiding the rational use of GBL-related herbal products in clinical settings.

Keywords: human UDP-glucuronosyltransferase 1A1, cell-based fluorescence assay, *Ginkgo biloba* leaves, bioflavonoids, herb-drug interactions

OPEN ACCESS

Edited by:
Jianbo Xiao,
University of Vigo, Spain

Reviewed by:
Mona Abdel Tawab,
Central Laboratory of German Pharmacists, Germany
Danyi Lu,
Guangzhou University of Chinese Medicine, China
Zarko Kulic,
Dr. Willmar Schwabe GmbH & Co. KG, Germany
Sabariah Ismail,
Universiti Sains Malaysia (USM), Malaysia

****Correspondence:***
Guang-Bo Ge
geguangbo@dicp.ac.cn
Hong Ma
redlemononly@iCloud.com
Yang-Liu Xia
xiayl@dlut.edu.cn

[†]These authors have contributed equally to this work and share first authorship

Specialty section:
This article was submitted to Ethnopharmacology, a section of the journal Frontiers in Pharmacology

Received: *15 November 2021*
Accepted: *24 January 2022*
Published: *21 February 2022*

Citation:
Pang H-L, Zhu G-H, Zhou Q-H, Ai C-Z, Zhu Y-D, Wang P, Dou T-Y, Xia Y-L, Ma H and Ge G-B (2022) Discovery and Characterization of the Key Constituents in Ginkgo biloba Leaf Extract With Potent Inhibitory Effects on Human UDP-Glucuronosyltransferase 1A1. Front. Pharmacol. 13:815235. doi: 10.3389/fphar.2022.815235

INTRODUCTION

Human UDP-glucuronosyltransferases1A1 (hUGT1A1) is one of the most essential enzymes responsible for the biotransformation and detoxification of the endogenous toxins (e.g., bilirubin), and for the metabolic elimination of numerous therapeutic and diet-derived xenobiotics (Ouzzine et al., 2003; Kiang et al., 2005). In adults, hUGT1A1 is predominantly

expressed in the liver, while the conjugative enzyme is also distributed in the small intestine and kidney with relatively abundant levels (Drozdzik et al., 2018). Increasing evidence has illustrated that dysfunction or potent inhibition of hepatic UGT1A1 may trigger metabolic disorder of bilirubin, resulting in varying degrees of hyperbilirubinemia, liver disorders, and even death (Vítek and Ostrow, 2009; Bartlett and Gourley, 2011; Zhou et al., 2011; Ma et al., 2013). Furthermore, partial or complete loss of hepatic and intestinal UGT1A1 activity may affect the pharmacokinetic behaviours of the UGT1A1-substrate drugs, which in turn, enhance the *in vivo* effects of UGT1A1-substrate drugs or show clinically relevant drug/herb-drug interactions (Kadakol et al., 2000; Kiang et al., 2005) (DDI/HDI). Therefore, the major regulatory agencies including the US Food and Drug Administration (FDA) has recommended to assess the inhibition potency of new drug candidates or phytochemical products against hUGT1A1 before getting approval for marketing (US Food and Drug Administration, 2012). It also should be noted that in some cases, the UGT1A1 inhibitors with improved safety profiles can be used to increase the plasma exposure of phenolic drugs and to achieve desired *in vivo* therapeutic effects, by reducing the first pass metabolism mediated by intestinal UGT1A1 (Liu D. et al., 2019).

Over the past few decades, a wide range of hUGT1A1 inhibitors including therapeutic drugs (such as tyrosine kinase inhibitors) and herbal constituents (such as flavonoids and phenolic acids) have been reported (Zucker et al., 2001; Singer et al., 2007; Peer et al., 2012; Lv et al., 2019Liu et al., 2019). Notably, only a small part of the known hUGT1A1 inhibitors have been reported with the high risk to cause hyperbilirubinaemia or clinically relevant drug/herb-drug interactions. However, in most cases, the *in vitro* hUGT1A1 inhibition results do not match to the *in vivo* hUGT1A1 inhibition potency. Especially, many herbal constituents have been found with strong inhibition potentials against hUGT1A1, but in most cases, the inhibition potentials of these natural products in living systems are extremely weak (Goon et al., 2016). The primary cause of the false positives in hUGT1A1 inhibition assays is the enzyme sources. Currently almost all hUGT1A1 inhibition assays were performed by using recombinant hUGT1A1 or human liver preparations as enzyme sources. Under such incubation conditions, the small molecule inhibitors can directly bind on the target enzyme, lacking the physical barrier of cell membrane. It is well-known that hUGT1A1 is located within the lumen of endoplasmic reticulum. In this regard, the hUGT1A1 inhibitors should be able to penetrate the cell membrane to bind the target enzyme in the living cells. Thus, it is important to use a more practical and convenient approach for screening hUGT1A1 inhibitors to avoid the high false positive rate.

Recently, a high-throughput cell-based fluorescence assay was developed by using an artificial specific fluorescence substrate (termed N-butyl-4-(4-hydroxyphenyl)-1,8-naphthalimide (NHPN)) as the probe substrate and the hUGT1A1 overexpressed Hela cells (HeLa-UGT1A1 cells) as the enzyme sources (Zhu et al., 2020). With the help of this newly designed cell-based hUGT1A1 inhibition assay, we have screened the inhibition potentials of a number of commonly used herbal medicines against hUGT1A1 in living cells. The results clearly demonstrated that the used extract of *Ginkgo biloba* leaves (GBL) displayed the most potent hUGT1A1 inhibition potency, with the inhibition rate exceeding 95% at the dose of 100 μg/ml. This finding encouraged us to further investigate the inhibition potentials of GBL and its major constituents against hUGT1A1 in various enzyme sources including HeLa-UGT1A1 cells and human liver microsomes, as well as to identify the key constituents in GBL responsible for hUGT1A1 inhibition. Furthermore, the inhibition potential and the inhibitory mechanisms of the newly identified naturally occurring hUGT1A1 inhibitors from GBL were also investigated by performing an array of inhibition kinetic assays and docking simulations. All these studies are very helpful for researchers to understand the interactions between the used GBL and human drug-metabolizing enzymes, and also provide the key data to assess potential risks or beneficial effects of the used GBL by inhibition of hUGT1A1.

MATERIALS AND METHODS

Chemicals and Reagents

The standard *Ginkgo biloba* leaf extract (GBL) was obtained from Shanghai Sine Promod Pharmaceutical Co., Ltd. (Shanghai, China), and the chemical analysis of *Ginkgo biloba* leaf extract was analyzed by using ultra high performance liquid Chromatography-Q exactive hybrid quadrupole orbitrap high-resolution accurate mass spectrometric (UHPLC-Q-Orbitrap HRMS, Thermo Fisher Scientific Inc., Grand Island, NY, United States) (**Supplementary Figure S2** and **Supplementary Table S2**). Other 126 herbal products were provided by Tianjiang Pharmaceutical Co., Ltd (Jiangsu, China) (**Supplementary Table S1**). N-butyl-4-(4-hydroxyphenyl)-1,8-naphthalimide (NHPN) and NHPN-*O*-glucuronide (NHPNG) were chemically synthesized by one of the authors (Ping Wang) according to the previously reported scheme (Lv et al., 2017), with the purities ≥98%. Sixteen chemical constituents in GBL extract were purchased from Chengdu Gelipu Biotechnology Co., Ltd. (Chengdu, Sichuan, China), with the purities ≥96%. Human liver microsomes (HLMs) (from 50 donors, lot no. X008067) were obtained from Bioreclamation IVT (Baltimore, MD, United States). Recombinant UGT1A1 enzymes were purchased from BD Gentest Corp (Woburn, MA, United States). Tris and HCl were acquired from Sinopharm Chemical Reagent Co. Ltd. (Shanghai, China) and $MgCl_2$ was obtained from Meilunbio (Dalian, China). UDPGA trisodium salt and polyethylene glycol hexadecyl ether (Brij 58) were purchased from Sigma-Aldrich (St. Louis, MO, United States). Cell culture medium and fetal bovine serum were obtained from Hylcone (Logan, UK). Phosphate buffered saline (0.1 M, pH = 7.4), Millipore water and LC grade organic solvent (including acetonitrile, methanol and formic acid) were ordered from Tedia company (Tedia, United States) and used for all experiments.

Development and Validation of HeLa1A1 Cells

The UGT1A1-overexpressing HeLa cells were constructed according to the previous studies (Zhang et al., 2015; Zhang et al., 2019; Zhu et al., 2020). Briefly, UGT1A1 cDNA was synthesized and subsequently subcloned into the BamHI and MluI sites of the pLVXmCMV-ZsGreen-PGK-Puro vector. Next, lentiviral vectors were produced by transient transfection into 293T cells based on the third-generation packaging system. After that, wild-type HeLa cells were transfected following incubation with the lentivirus. The optimal value was obtained when the cells were best transfected as published previously (Zhang et al., 2015; Zhang et al., 2019; Zhu et al., 2020). The stably transfected HeLa cells were named as HeLa-UGT1A1 cells. The protein levels of hUGT1A1 in HeLa-UGT1A1 cells were assayed by Western blotting, while UGT1A1-catalyzed *O*-glucuronidation activity of HeLa-UGT1A1 cells were determined by using NHPN as the probe substrate (**Supplementary Figure S1**).

Determination of NHPN and NHPNG Using LC-FD

A RF-20A FD detector coupled UFLC system (Shimadzu, Kyoto, Japan), equipped with a DGU-20A5R vacuum degasser, two LC-20ADXR pumps, a SIL-20ACXR autosampler and a CTO-20A column oven, was used to quantify NHPN and NHPNG. Chromatographic separation of analytes was carried out on a shim-pack Acchrom HC-C18 analytical column (2.0 × 150 mm, 4.6 μm particle size), while the column temperature was kept at 40°C. The flow rate was kept at 0.5 ml/min. The mobile phase consisted of acetonitrile (A) and water containing 0.2% formic acid (B). The gradient of the mobile phase was as follows: 0–0.5 min, 80–60% B; 0.5–3.5 min, 60–5% B; 3.5–5 min, 5% B; 5–7.5 min, equilibration with 80% B. The excitation wavelength and the emission wavelength were set at 370 and 520 nm, respectively for detection.

UGT1A1 Inhibition Assays

UGT1A1 Inhibition Assay in HeLa-UGT1A1 Cells

The inhibitory effects of herbal products and chemical constituents of GBL extract on UGT1A1 were investigated in living HeLa-UGT1A1 cells by using a specific fluorescent substrate, NHPN, as a probe. HeLa-UGT1A1 cells were cultured at 37°C in 5% CO_2 in Modified Eagle's Medium (MEM) containing 0.1% antibiotic-antimycoticmix, supplemented with 10% fetal bovine serum (FBS). HeLa-UGT1A1 cells were seeded in 96-well plates and cultured for 24 h. The cells were incubated in the medium containing different kinds of herbal products (final concentration, 10 μg/ml) or chemical constituents of GBL extract (diluted to different concentration by DMSO with the final concentration of 1% DMSO in each incubation) for 60 min at 37°C under 5% CO_2, and co-incubated with NHPN (final concentration, 50 μM) for another 60 min. The reaction was terminated by adding an equal volume of ice-cold acetonitrile to each well, and then centrifuged at 20,000×*g* for 20 min at 4°C. After centrifugation, 5 μl aliquots of the supernatant was taken for LC-FD analysis. The validation data for this cell-based flourescence assay can be found in our previous publication (Zhu et al., 2020).

UGT1A1 Inhibition Assay in HLM and Recombinant UGT1A1

NHPN was used for evaluating the inhibitory effects of GBL extract on HLM. A typical incubation mixture with a total volume of 200 μl consisted of 50 mM Tris-HCl (pH = 7.4), 5 mM $MgCl_2$, 2 mM UDPGA, NHPN (diluted by DMSO, 5 μM) and the enzymes. Inhibitors (ginkgetin, bilobetin, isoginkgetin, sciadopitysin) were serially diluted to the required concentration by DMSO. The final concentration of DMSO in the incubation mixture was less than 1%. When HLM was used as the enzyme source, HLM (10 μg/ml) and Brij 58 (0.1 mg/mg microsomal protein) were pre-incubated for 20 min at 4°C to disrupt the ER membrane to remove the latency. A concentration of 5 μg/ml was used when recombinant UGT1A1 was the enzyme source. After pre-incubation for 3 min at 37°C, UDPGA was added to the incubation mixture to initiate the reaction. After 60 min incubation at 37°C, the reaction was terminated by adding 200 μl ice-cold acetonitrile, and the incubation mixture was kept on ice. After centrifugation at 20,000×*g* for 20 min at 4°C, 5 μl aliquots of the supernatant was taken for LC-FD analysis.

The residual activity of hUGT1A1 was determined as follows: Residual activity (%) = (the fluorescence intensity of NHPNG generated in the incubations with inhibitor)/(the fluorescence intensity of NHPNG generated in the incubations without inhibitor) × 100%. A set of incubations with the same fluorescent substrate concentration and different inhibitor concentrations were performed to determine the half maximal inhibition concentration (IC_{50}).

Inhibition Kinetic Analyses

A set of incubations by changing both the fluorescent substrate concentration and the inhibitor concentration were performed to determine the inhibition kinetic modes and the corresponding inhibition constant (K_i) values. The incubation and analytical sample preparation were conducted as described previously. Goodness-of-fit parameter and Akaike's Information Criterion (AIC) were employed to select the most appropriate inhibition kinetic modes from the following three inhibition modes including competitive inhibition **Eq. 1**, noncompetitive inhibition **Eq. 2**, or mixed inhibition **Eq. 3**,

$$V = \frac{V_{max} \times [S]}{K_m \times \left(1 + \frac{[I]}{K_i}\right) + [S]} \tag{1}$$

$$V = \frac{V_{max} \times [S]}{(K_m + [S]) \times \left(1 + \frac{[I]}{K_i}\right)} \tag{2}$$

$$V = \frac{V_{max} \times [S]}{K_m \times \left(1 + \frac{[I]}{K_i}\right) + [S] \times \left(1 + \frac{[I]}{\alpha K_i}\right)} \tag{3}$$

Here, V is the turnover of the glucuronidation reaction; V_{max} is the maximum velocity; S and I are the substrate and inhibitor concentrations, respectively; K_m is the Michaelis constant (substrate concentration at 0.5 V_{max}); K_i is the inhibition

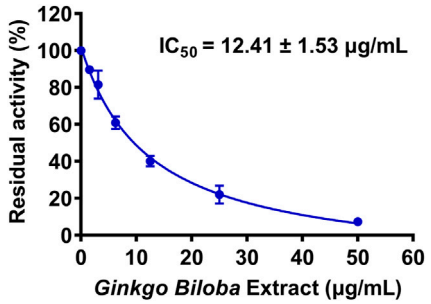

FIGURE 1 | Dose-inhibition curve of *Ginkgo biloba* leaf extract on UGT1A1-catalyzed NHPN-*O*-glucuronidation in HeLa-UGT1A1 cells. The data were expressed as the means of triplicate determinations.

constant that describes the affinity of the inhibitor towards hUGT1A1. The corresponding K_i value of each tested inhibitor is calculated by utilizing the slopes of second plot from Lineweaver-Burk plot versus inhibitor concentrations.

Molecular Docking Simulations

Docking simulations were used to explore the binding modes of each inhibitor into hUGT1A1 by using AutoDock Vina (1.1.2) (Luo et al., 2008). The 3D structure of hUGT1A1 was recently predicted by the AlphaFold (UniProt code: P22309) (Luo et al., 2008). Firstly, the structure of UDPGA was docked into the catalytic domain of hUGT1A1 by the alignment function of PyMOL (The PyMOL Molecular Graphics System 2.4.0a0 Open-Source, Schrödinger LLC., New York, United States) according to the structure of UGT74AC1 mutant (PDB code: 6L8Z) (Li et al., 2020). Secondly, the structures of target protein (hUGT1A1) and each ligand (including NHPN and each bioflavone-type inhibitor) were preprocessed by AutoDockTools 1.5.6, including adding polar hydrogen atoms, calculating atomic charges and defining atom types. Then, the druggable pockets of hUGT1A1 predicted by CavityPlus were defined as the ligand-binding sites (Xu et al., 2018; Li et al., 2020), which were used to dock each tested inhibitor. Meanwhile, the substrate NHPN was docked into the catalytic site of hUGT1A1 in the presence of UDPGA. Finally, receptor-ligand interactions analysis of the top docking poses was conducted by Discovery Studio Visualizer (BIOVIA Discovery Studio 2019; Dassault Systèmes, San Diego, United States).

Data Analysis

All assays were conducted in triplicate. Data was expressed as mean ± SD. IC_{50} and K_i values were determined by using GraphPad Prism 7.0 (GraphPad Software, Inc., La Jolla, United States).

RESULTS

Screening of the Herbal Products With Strong UGT1A1 Inhibition Potency

First, 127 herbal products were collected and their inhibitory effects on hUGT1A1 were assayed in HeLa-UGT1A1 cells at the final concentration of 10 μg/ml. As shown in **Supplementary Table S1**, among all tested herbal products, GBL displayed the most potent hUGT1A1 inhibition in living cells, with the residual activity of hUGT1A1 was less than 40%. To quantify the inhibition potency of GBL, the dose-dependent inhibition curve of GBL against hUGT1A1 were plotted by utilizing increasing concentrations of GBL. As depicted in **Figure 1**, the standard extract of GBL dose-dependently inhibits hUGT1A1-mediated NHPN-*O*-glucuronidation in HeLa-UGT1A1 cells, with an apparent IC_{50} value as low as 12.41 μg/ml.

Inhibition of hUGT1A1 by the Constituents in GBL in Living Cells

The chemical constituents in GBL were investigated by using ultra high performance liquid Chromatography-Q exactive hybrid quadrupole orbitrap high-resolution accurate mass spectrometric (UHPLC-Q-Orbitrap HRMS) (**Supplementary Figure S2**). A total of 51 chemicals were identified or tentatively characterized from GBL (**Supplementary Table S2**), including 32 flavonol glycosides, 5 terpene trilactones, 5 biflavones, 3 flavanols, 4 flavonols, and 2 organic acids, although some compounds which do not ionize in negative mode may not be detected. To discover the key constituents in GBL responsible for hUGT1A1 inhibition, sixteen representative constituents (including seven flavonoids, five bioflavones and four terpene lactones) present in GBL extract, were purchased for assaying their hUGT1A1 inhibition potentials in Hela-UGT1A1 cells. As shown in **Figure 2** and **Table 1**, the inhibition potency of 16 constituents in GBL varied significantly from each other. Four terpene lactones (bilobalide, ginkgolide A, ginkgolide B, and ginkgolide C) did not inhibit intracellular hUGT1A1 even at high concentration (100 μM). By contrast, seven tested flavonoids (myricetin, quercetin, apigenin, isorhamnetin, luteolin, genkwanin and kaempferol) displayed moderate to weak inhibition against intracellular hUGT1A1, with the IC_{50} values ranging from 1.38 μM (kaempferol) to 64.56 μM (myricetin) (**Supplementary Figure S3**). Notably, five tested bioflavones (amentoflavone, bilobetin, isoginkgetin, sciadopitysin and ginkgetin) displayed strong hUGT1A1 inhibition potency in living cells. In particular, bilobetin, isoginkgetin, sciadopitysin and ginkgetin dose-dependently inhibits hUGT1A1-catalyzed NHPN-*O*-glucuronidation in HeLa-UGT1A1 cells, with the apparent IC_{50} values ranging from 0.075 μM (ginkgetin) to 0.41 μM (bilobetin) (**Figure 3**). The five biflavones were quantified to be 5.89, 12.07, 7.06, 12.78, and 1.20 μg/g for amentoflavone, bilobetin, ginkgetin, isoginkgetin and sciadopitysin, respectively, in the used GBL using HPLC-UV (see **Supplementary Material**), which corresponds to a content in p.p.m. range.

Inhibition Kinetic Analyses of GBL and the Presented Biflavones Against hUGT1A1

To further explore the inhibitory mechanisms of the biflavones in GBL against hUGT1A1, a set of inhibition kinetic assays were performed by using HLM as enzyme source. As shown in **Figure 4** and **Table 2**, bilobetin, isoginkgetin, sciadopitysin

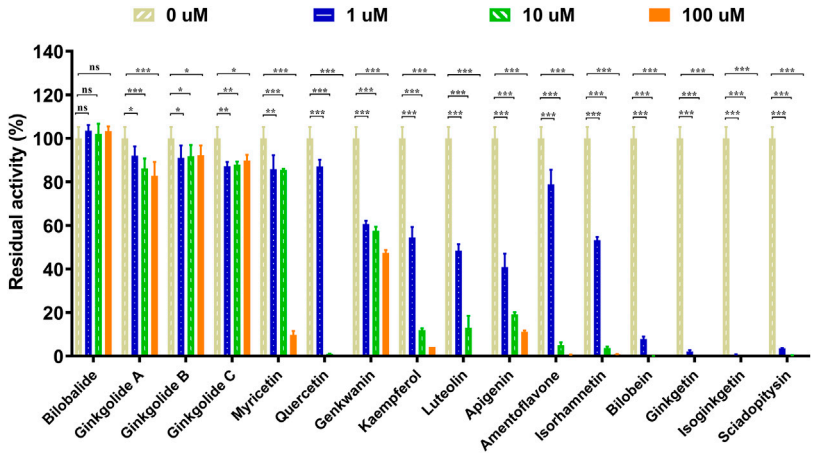

FIGURE 2 | Inhibitory effects of chemical constituents of *Ginkgo biloba* leaf extract (final concentration, 1, 10, 100 μM) on UGT1A1-catalyzed NHPN-O-glucuronidation in HeLa-UGT1A1 cells. The data were expressed as the means of triplicate determinations. ns, no significance; *$p < 0.05$; **$p < 0.01$; ***$p < 0.001$.

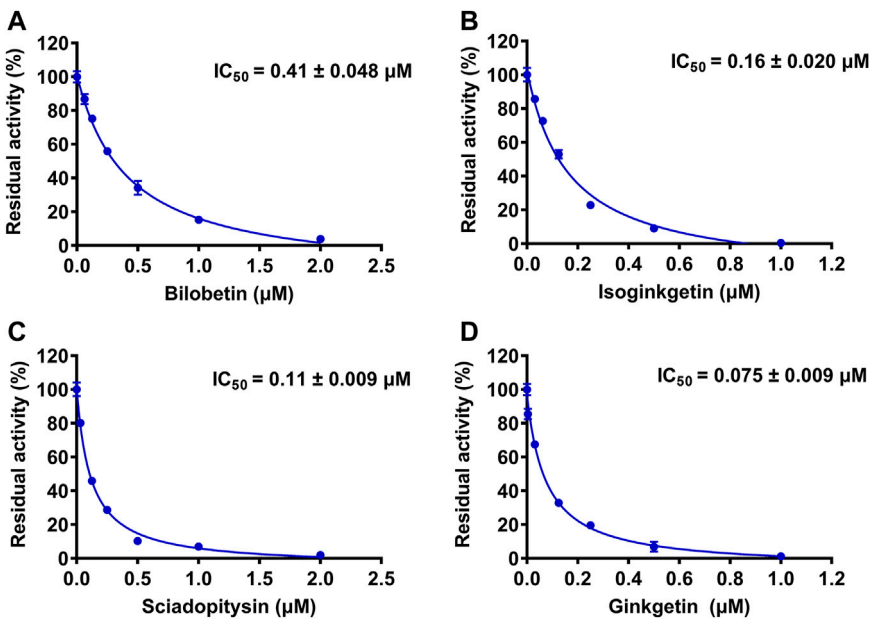

FIGURE 3 | The dose-dependent inhibition curves of bilobetin **(A)**, isoginkgetin **(B)**, sciadopitysin **(C)** and ginkfetin **(D)** on NHPN-*O*-glucuronidation in HeLa-UGT1A1 cells. The data were expressed as the means of triplicate determinations.

and ginkgetin also potently and dose-dependently inhibit hUGT1A1-catalzyed NHPN-*O*-glucuronidation in HLM, with the IC_{50} values ranging from 0.15 to 0.67 μM. Notably, the inhibition potentials of four tested bioflavones against hUGT1A1 in HLM are similar to that in Hela-UGT1A1 cells. However, the IC_{50} value of amentoflavone in HLM is much lower than that in living cells (0.41 vs. 3.29 μM) (**Supplementary Figure S5** and **Table 2**). For GBL, similar IC_{50} values are observed in HLM (16.91 μg/ml) and in Hela-UGT1A1 cells (12.41 μg/ml) (**Supplementary Figure S5** and **Supplementary Table S2**). In addition, comparable IC_{50} values are also obtained for bilobetin, isoginkgetin, sciadopitysin and ginkgetin in the recombinant UGT1A1 systems, ranging from 0.10 to 0.29 μM, to those derived from HLM (0.15–0.67 μM) (**Supplementary Figure S6**). The inhibition kinetic analyses of these four biflavones are further determined using HLM. As shown in **Figure 5** and **Table 2**, four biflavones isolated from GBL potently inhibit UGT1A1-catalyzed NHPN-*O*-glucuronidation in HLM *via* a mixed inhibition mode, with the K_i values of 0.07, 0.67, 0.18 and 0.74 μM, for ginkgetin, sciadopitysin, bilobetin and isoginkgetin, respectively. These findings clearly demonstrate that the biflavones in GBL are a class of naturally occurring

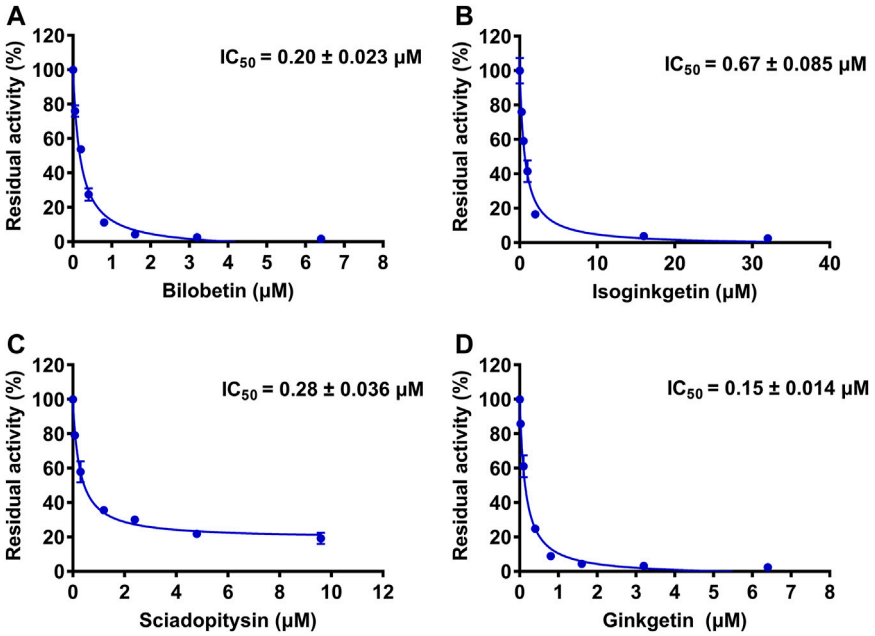

FIGURE 4 | The dose-dependent inhibition curves of isoginkgetin **(A)**, sciadopitysin **(B)**, bilobetin **(C)** and ginkfetin **(D)** on NHPN-O-glucuronidation in HLM. The data were expressed as the means of triplicate determinations.

TABLE 1 | The IC_{50} valuses of chemical constituents of *ginkgo biloba* extract on hUGT1A1-catalyzed NHPN-*O*-glucuronidation in HeLa-UGT1A1 cells.

No	Compound	CAS	MW	Enzyme source	IC_{50} (μM)
1	Myricetin	529-44–2	318.23	HeLa-UGT1A1	64.56 ± 12.24
2	Quercetin	117-39–5	302.24	HeLa-UGT1A1	2.05 ± 0.24
3	Apigenin	520-36–5	270.24	HeLa-UGT1A1	1.89 ± 0.24
4	Lsorhamnetin	480-19–3	316.26	HeLa-UGT1A1	1.68 ± 0.34
5	Luteolin	491-70–3	286.24	HeLa-UGT1A1	1.41 ± 0.17
6	Genkwanin	437-64–9	284.26	HeLa-UGT1A1	1.50 ± 0.46
7	Kaempferol	520-18–3	286.24	HeLa-UGT1A1	1.38 ± 0.19
8	Amentoflavone	1,617-53–4	538.46	HeLa-UGT1A1	3.29 ± 0.47
9	Bilobetin	521-32–4	552.50	HeLa-UGT1A1	0.41 ± 0.048
10	Isoginkgetin	548-19–6	566.51	HeLa-UGT1A1	0.16 ± 0.020
11	Sciadopitysin	521-34–6	580.55	HeLa-UGT1A1	0.11 ± 0.009
12	Ginkgetin	481-46–9	566.52	HeLa-UGT1A1	0.075 ± 0.009
13	Bilobalide	33,570-04–6	326.30	HeLa-UGT1A1	>100
14	Ginkgolide A	15,291-75–5	408.40	HeLa-UGT1A1	>100
15	Ginkgolide B	15,291-76–6	440.40	HeLa-UGT1A1	>100
16	Ginkgolide C	15,291-77–7	424.40	HeLa-UGT1A1	>100

TABLE 2 | The inhibition parameters and inhibition modes of bilobetin, isoginkgetin, sciadopitysin, ginkgetin, Amentoflavone and GBL extract against hUGT1A1-catalyzed NHPN-*O*-glucuronidation in HLM.

Inhibitor	Enzyme source	IC_{50} (μM)	K_i (μM)	Inhibition mode	Quality of fit (R^2)
Ginkgetin	HLM	0.15 ± 0.014 μM	0.07	Mixed	0.99
Sciadopitysin	HLM	0.28 ± 0.036 μM	0.67	Mixed	0.98
Bilobetin	HLM	0.20 ± 0.023 μM	0.18	Mixed	0.99
Isoginkgetin	HLM	0.67 ± 0.085 μM	0.74	Mixed	0.98
Amentoflavone	HLM	0.41 ± 0.034 μM	—	—	—
GBL extract	HLM	16.91 ± 1.599 μg/ml	—	—	—

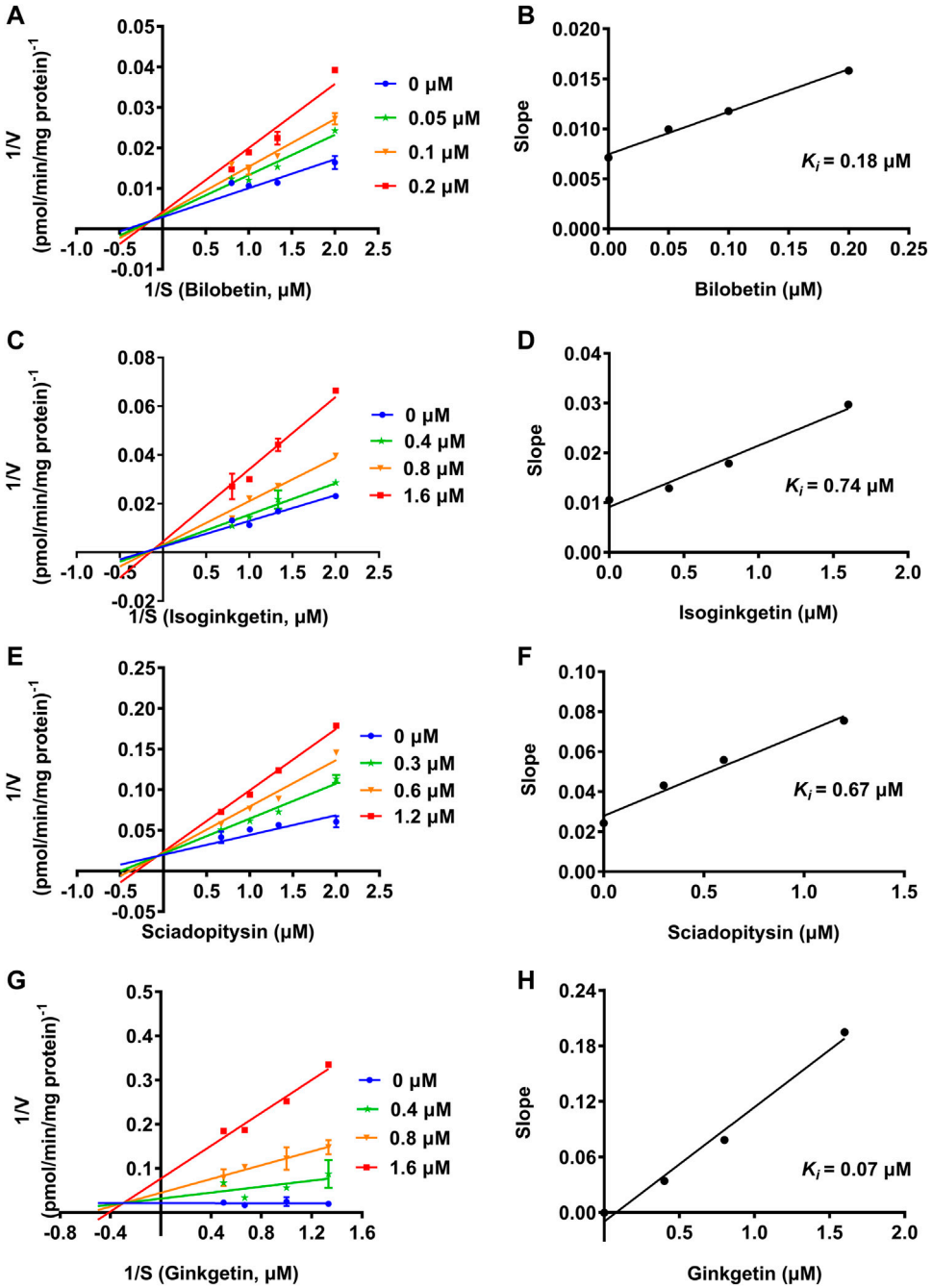

FIGURE 5 | Lineweaver-Burk plots **(A, C, E, G)** of bilobetin, isoginkgetin, sciadopitysin and ginkgetin against UGT1A1-catalyzed NHPN-*O*-glucuronidation in HLM, and the second plots **(B, D, F, H)** using the slopes obtained from the Lineweaver-Burk plots *VS* the concentrations of each inhibitor.

hUGT1A1 inhibitors, which act as mixed inhibitors against hUGT1A1.

Docking Simulations

Next, docking simulations were conducted to disclose the potential binding modes of NHPN and four biflavones on hUGT1A1. As depicted in **Supplementary Figure S8**, NHPN and UDPGA could simultaneously bind to the catalytic pocket of hUGT1A1 (Ciotti and Owens, 1996; Locuson and Tracy, 2007). The distance between the C-4 phenolic group of NHPN and the glycosyl group of UDPGA is 2.7 Å, suggesting that NHPN is a good substrate for hUGT1A1. As depicted in **Supplementary Figure S10**, four biflavones also can be well-fitted into the catalytic pocket of hUGT1A1, while their binding areas are

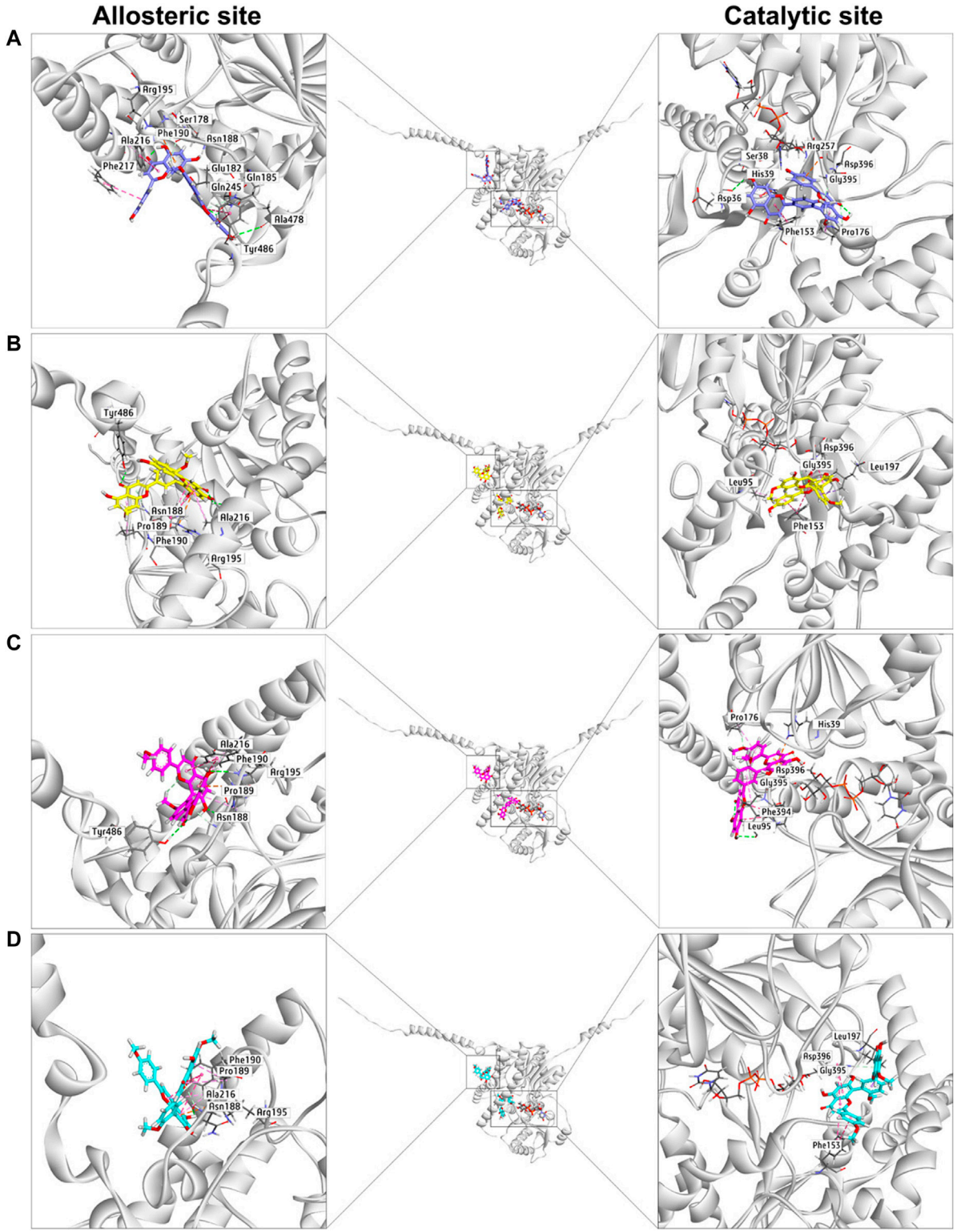

FIGURE 6 | The docking simulations of four biflavones **(A)**, bilobetin in purple, **(B)**, ginkgetin in yellow, **(C)**, isoginkgetin in magenta, **(D)**, sciadopitysin in cyan) in hUGT1A1 complexed with the sugar donor UDPGA (black).

highly overlapped with that of NHPN. 2D interaction analysis showed that bilobetin, ginkgetin, sciadopitysin and NHPN created strong hydrophobic interactions with Phe153 and Leu197 in the catalytic pocket of hUGT1A1 (**Supplementary Figures S6, S8, S11, S12, S14, and S15**). In addition, bilobetin, isoginkgetin and NHPN bound the same key residues including His39 and Asp396 *via* hydrophobic interactions (**Supplementary Figures S6, S8, S11, S13, and S15**). These four bioflavones were also found to dock into the allosteric pocket of hUGT1A1, which is adjacent to its transmembrane helix (**Figure 6**). 2D interaction analysis showed, that these four bioflavones formed strong hydrophobic interactions with the key residues surrounding the allosteric pocket including Tyr486, Ala216, Phe190, Arg195 and Pro189 (**Supplementary Figures S11, S12, S13, and S14**). These observations suggest that bilobetin, ginkgetin, sciadopitysin and isoginkgetin can tightly bind on hUGT1A1 at two distinct ligand-binding sites, which well-explained the mixed-inhibition mode of these newly identified hUGT1A1 inhibitors.

DISCUSSION

As one of the most important conjugative enzymes in the human body, hUGT1A1 plays a crucial role in the metabolic detoxification of endogenous toxicants (e.g., bilirubin) and a variety of clinical drugs (e.g., SN38) (Rowland et al., 2013). Inhibition of hUGT1A1 by xenobiotics may trigger both, metabolic disorders of endogenous substances and clinically relevant drug/herb-drug interactions. In the present study, to overcome the high false positive rate in the *in vitro* assays of hUGT1A1 inhibition, a high-throughput cell-based fluorescence assay was established and applied in hUGT1A1 inhibitors screening from commonly used herbal medicines. Our results demonstrated that GBL extract showed the most potent hUGT1A1 inhibition in Hela-UGT1A1 cells following screening 127 herbal products, and four biflavones including bilobetin, isoginkgetin, sciadopitysin and ginkgetin, were characterized as the key constituents responsible for hUGT1A1 inhibition of GBL in living cells. These four biflavones, which were cell-permeable and are active in living cells indicated by comparable IC_{50} values of hUGT1A1 inhibition between HeLa-UGT1A1 cells and HLM, were further revealed to inhibit hUGT1A1-catalyzed NHPN-*O*-glucuronidation through mixed-inhibition modes, which was consistent with the observations that these four compounds tightly bound on hUGT1A1 in both the catalytic pocket and an allosteric pocket of hUGT1A1 in docking simulations.

Ginkgo biloba is among the most widely consumed herbal supplements and phytopharmaceutical drugs used in the world. The primary active constituents of GBL are flavonoids and terpene lactones, which account for 26.8 and 9.8% of the tested GBL in the present study, respectively (**Supplementary materials**). Our current results showed that all 12 tested flavonoids except myricetin exerted potent inhibitory activities towards NHPN-*O*-glucuronidation with IC_{50} values less than 5 μM, while the four biflavones in GBL were found to be the strongest inhibitors of hUGT1A1 with IC_{50} values ranging from 0.075 to 0.41 μM, which are 10-fold lower than those for the flavones or flavanols (1.38–3.29 μM). It is worthy to be noted that, amentoflavone, also baring a biflavone structure, showed a relatively weak inhibition on hUGT1A1, with the IC_{50} value more than 10-fold higher than those of the other four biflavones. Although it only differs from the others in the number of the methoxy groups, a lower logP value (3.49), which indicates a poorer permeability compared to the other four with logP values of 5.23–5.38, could serve as an explanation for its decreased inhibition potency on hUGT1A1 observed in Hela-UGT1A1 cells. The much lower IC_{50} value in HLM (0.41 μM) than that in Hela-UGT1A1 cells (3.29 μM) for amentoflavone may further support the poor permeability of this compound (**Supplementary Figure S5** and **Table 2**). However, the sum effect of cell permeability of the other constituents in GBL may not be that significant, as quite similar IC_{50} values of GBL have been observed in HLM and in Hela-UGT1A1 cells (16.91 μg/ml vs 12.41 μg/ml) (**Supplementary Figure S5** and **Table 2**).

Although there is no available data in consideration of the maximal plasma concentration (C_{max}) of the specific four biflavones which were found to be the most potent hUGT1A1 inhibitors in the present study, the K_i values for these four compounds ranging from 0.15 to 0.67 μM were much higher than the measured plasma C_{max} of their bioflavone analogs orally administrated in rats (Chen et al., 2018). In addition, only trace amounts in the range of p.p.m. of biflavones have been determined in the used GBL extract (**Supplementary Figure S4** and **Supplementary Table S3**), therefore, GBL is unlikely to cause a clinically significant metabolic drug/herb-drug interaction *via* bioflavone mediated inhibition of hUGT1A1 involved in drug metabolism *in vivo*. It is also worth to be noted that the flavonoids are present as glycosides but not the free aglycones in GBL, and the hUGT1A1 inhibition of aglycones tested in the present study may not been straightforward for assessing DDI-potential at the gastrointestinal site *in vivo*. In addition, a previous study showed that *ginkgo biloba* leaf extract only slightly changed the pharmacokinetics of raltegravir (mainly eliminated through UGT1A1-mediated metabolism) in healthy volunteers (Blonk et al., 2012), indicating that the pharmacokinetic interactions between *ginkgo biloba* leaf extract and UGT1A1 substrates may be minor or negligible. Moreover, bioactive constitutes from *Ginkgo biloba* leaf extract have been reported to be able to induce the expression of hepatic drug-metabolizing enzymes including UGT1A1 (Li et al., 2008). Therefore, the real influence of GBL on the pharmacokinetics of UGT1A1 drug substrates in human warrants further investigation. On the other hand, for herbal medicines co-administrated with ginkgo preparations, which undergo extensive glucuronidation metabolism mediated by intestinal hUGT1A1, higher systemic exposure is expected through the inhibition of the intestinal UGT1A1-mediated glucuronidation by chemical constituents in ginkgo preparations. Furthermore, the four bioflavones with potent hUGT1A1 inhibitory activities contained in GBL could hold the potentials to be developed as hUGT1A1 inhibitors to exhibit broad-spectrum properties

through mediating a yet undefined potential drug/herb-drug interaction.

The docking simulations showed that the substrate-binding site of hUGT1A1 could be split into two embossed subdomains (**Supplementary Figure S7**). As shown in **Supplementary Figure S7**, the upper domain (UD) consists of a hydrophobic area (Pro176, Phe153, His39) and a H-bond acceptor from Asp36. The downward domain (DD) consists of a larger hydrophobic area (Leu197, Asp396, Gly395, Phe394, Leu95) and also Leu95 rendering a H-bond receptor from its back bone. Remarkably, the amide bond between Asp396 and Gly395 was greatly exposed to the surface of the substrate-binding site, which enabled an Amide-Pi stacked interaction with aromatic ring. More conspicuously, His39 and Asp396 seemed to be of great significance for the binding of flavoniod-like structures by forming electrostatic interactions. In summary, aromatic groups are highly preferred in the substrate-binding site of hUGT1A1. The binding poses of sciadopitysin and ginkgetin were highly overlapped, indicating that there is no difference in binding formation between methyl and methoxyl substitutions on R_2 (**Supplementary Figure S10**). Meanwhile, isoginkgetin, sciadopitysin and ginkgetin bonded to the substrate-binding site in a similar mode with R_2-side flavoniod structure binding to UD and R_1-side chromone group binding to DD (**Supplementary Figure S9**). The R_2-side flavoniod of isoginkgetin bonded to UD conversely as sciadopitysin and ginkgetin did to form a H-bond with Leu95, resulting in the tightest binding pose of isoginkgetin upon the substrate-binding site (**Figure 6**). Bilobetin, lacking of methyl on R_1 and R_2, bonded deeply inside into the polar internal cavity and formed a H-bond with Asp36 (**Figure 6**), which further immobilized bilobetin to the substrate-binding site. Furthermore, all four biflavones present in GBL, bilobetin, ginkgetin, sciadopitysin and isoginkgetin, occupied the overlapped binding area in the catalytic pocket of hUGT1A1 with NHPN, and also well fit into the allosteric pocket of hUGT1A1, by which the mixed inhibition modes of the four biflavones on NHPN-*O*-glucuronidation could be well explained (**Figure 6**, **Supplementary Figures S10 and S11**). Our previous study demonstrated that the ligand-binding site of NHPN on hUGT1A1was identical to that of bilirubin (Liu et al., 2019), thus, mixed inhibition types could be predicted in the condition where bilirubin is used as the substrate to evaluate the inhibitory effect of these biflavoneson hUGT1A1. However, how NHPN compares to the drug substrates of UGT1A1 such as belinostat or estrogens warrants further study.

CONCLUSION

In summary, with the help of a newly designed high-throughput cell-based fluorescence assay, the inhibitory potentials of a number of commonly used herbal medicines against hUGT1A1 were assayed in living cells. The results demonstrated that GBL extract used in the present study displayed the most potent hUGT1A1 inhibition potency, with the inhibition rate exceeding 95% at the dose of 100 μg/ml. Further investigations showed that four biflavones including bilobetin, isoginkgetin, sciadopitysin and ginkgetin, are key constituents responsible for hUGT1A1 inhibition in living cells, while the flavonoids in GBL contribute to a lesser extent for hUGT1A1 inhibition. Inhibition kinetic analyses suggested that the biflavones in GBL potently inhibit hUGT1A1-catalyzed NHPN-*O*-glucuronidation in HLM *via* a mixed-inhibition manner, with the K_i values ranging from 0.07 to 0.74 μM. Docking simulations suggested that bilobetin, ginkgetin, sciadopitysin and isoginkgetin could tightly bind on hUGT1A1 at two distinct ligand-binding sites (one is located at the catalytic pocket of hUGT1A1 and another one is an allosteric pocket which was adjacent to the transmembrane helix), which may be a plausible explanation for the mixed-inhibition mode of these newly identified hUGT1A1 inhibitors. In conclusion, our findings revealed that the biflavones in GBL are potent hUGT1A1 inhibitors, which can be very helpful for guiding the rational use of GBL-related herbal products in clinical settings.

DATA AVAILABILITY STATEMENT

The original contributions presented in the study are included in the article/**Supplementary Material**, further inquiries can be directed to the corresponding authors.

AUTHOR CONTRIBUTIONS

H-LP and G-HZ performed the experiments and analyzed the data; Q-HZ and Y-DZ contributed to the data analysis and worked on the manuscript; C-ZA and T-YD contributed to the interpretation of the computation results; PW synthesized the florescent probe substrate; Y-LX and HM helped supervise the project and drafted the manuscript; G-BG conceived the original idea, supervised the project and reviewed the manuscript.

FUNDING

This work was financially supported by the NSF of China (81773687, 81922070, 81603187), the National Key Research and Development Program of China (2017YFC1700200, 2017YFC1702000), Three-year Action Plan of Shanghai TCM Development (ZY-(2018-2020)-CCCX-5001), Shanghai Science and Technology Innovation Action Plans (20S21901500 and 21S21900600) supported by Shanghai Science and Technology Committee, Shanghai Talent Development Fund (2019093), Shuguang Program (18SG40) supported by Shanghai Education Development Foundation and Shanghai Municipal Education Commission, and the Fundamental Research Funds for the Central Universities (DUT20RC(4)013).

SUPPLEMENTARY MATERIAL

The Supplementary Material for this article can be found online at: https://www.frontiersin.org/articles/10.3389/fphar.2022.815235/full#supplementary-material

REFERENCES

Bartlett, M. G., and Gourley, G. R. (2011). Assessment of UGT Polymorphisms and Neonatal Jaundice. *Semin. Perinatol.* 35 (3), 127–133. doi:10.1053/j.semperi.2011.02.006

Blonk, M., Colbers, A., Poirters, A., Schouwenberg, B., and Burger, D. (2012). Effect of Ginkgo Biloba on the Pharmacokinetics of Raltegravir in Healthy Volunteers. *Antimicrob. Agents Chemother.* 56 (10), 5070–5075. doi:10.1128/AAC.00672-12

Chen, B., Wang, X., Zou, Y., Chen, W., Wang, G., Yao, W., et al. (2018). Simultaneous Quantification of Five Biflavonoids in Rat Plasma by LC-ESI-MS/MS and its Application to a Comparatively Pharmacokinetic Study of Selaginella Doederleinii Hieron Extract in Rats. *J. Pharm. Biomed. Anal.* 149, 80–88. doi:10.1016/j.jpba.2017.10.028

Ciotti, M., and Owens, I. S. (1996). Evidence for Overlapping Active Sites for 17 Alpha-Ethynlestradiol and Bilirubin in the Human Major Bilirubin UDPglucuronosyltransferase. *Biochemistry* 35 (31), 10119–10124. doi:10.1021/bi960584a

Liu, D., Zhang, L., Duan, L. X., Wu, J. J., Hu, M., Liu, Z. Q., et al. (2019). Potential of Herb-Drug/Herb Interactions between Substrates and Inhibitors of UGTs Derived from Herbal Medicines. *Pharmacol. Res.* 150, 104510. doi:10.1016/j.phrs.2019.104510

Drozdzik, M., Busch, D., Lapczuk, J., Müller, J., Ostrowski, M., Kurzawski, M., et al. (2018). Protein Abundance of Clinically Relevant Drug-Metabolizing Enzymes in the Human Liver and Intestine: A Comparative Analysis in Paired Tissue Specimens. *Clin. Pharmacol. Ther.* 104 (3), 515–524. doi:10.1002/cpt.967

Goon, C. P., Wang, L. Z., Wong, F. C., Thuya, W. L., Ho, P. C., and Goh, B. C. (2016). UGT1A1 Mediated Drug Interactions and its Clinical Relevance. *Curr. Drug Metab.* 17 (2), 100–106. doi:10.2174/1389200216666151103121253

Kadakol, A., Ghosh, S. S., Sappal, B. S., Sharma, G., Chowdhury, J. R., and Chowdhury, N. R. (2000). Genetic Lesions of Bilirubin Uridine-Diphosphoglucuronate Glucuronosyltransferase (UGT1A1) Causing Crigler-Najjar and Gilbert Syndromes: Correlation of Genotype to Phenotype. *Hum. Mutat.* 16 (4), 297–306. doi:10.1002/1098-1004(200010)16:4<297:AID-HUMU2>3.0.CO;2-Z

Kiang, T. K., Ensom, M. H., and Chang, T. K. (2005). UDP-glucuronosyltransferases and Clinical Drug-Drug Interactions. *Pharmacol. Ther.* 106 (1), 97–132. doi:10.1016/j.pharmthera.2004.10.013

Li, L., Stanton, J. D., Tolson, A. H., Luo, Y., and Wang, H. (2008). Bioactive Terpenoids and Flavonoids from Ginkgo Biloba Extract Induce the Expression of Hepatic Drug-Metabolizing Enzymes through Pregnane X Receptor, Constitutive Androstane Receptor, and Aryl Hydrocarbon Receptor-Mediated Pathways. *Pharm. Res.* 26 (4), 872–882. doi:10.1007/s11095-008-9788-8

Li, J., Yang, J., Mu, S., Shang, N., Liu, C., Zhu, Y., et al. (2020). Efficient O-Glycosylation of Triterpenes Enabled by Protein Engineering of Plant Glycosyltransferase UGT74AC1. *ACS Catal.* 10 (6), 3629–3639. doi:10.1021/acscatal.9b05232

Locuson, C. W., and Tracy, T. S. (2007). Comparative Modelling of the Human UDP-Glucuronosyltransferases: Insights into Structure and Mechanism. *Xenobiotica* 37 (2), 155–168. doi:10.1080/00498250601129109

Luo, X., Wang, C. Z., Chen, J., Song, W. X., Luo, J., Tang, N., et al. (2008). Characterization of Gene Expression Regulated by American Ginseng and Ginsenoside Rg3 in Human Colorectal Cancer Cells. *Int. J. Oncol.* 32 (5), 975–983. doi:10.3892/ijo.32.5.975

Lv, X., Feng, L., Ai, C. Z., Hou, J., Wang, P., Zou, L. W., et al. (2017). A Practical and High-Affinity Fluorescent Probe for Uridine Diphosphate Glucuronosyltransferase 1A1: A Good Surrogate for Bilirubin. *J. Med. Chem.* 60 (23), 9664–9675. doi:10.1021/acs.jmedchem.7b01097

Lv, X., Xia, Y., Finel, M., Wu, J., Ge, G., and Yang, L. (2019). Recent Progress and Challenges in Screening and Characterization of UGT1A1 Inhibitors. *Acta Pharm. Sin. B.* 9 (2), 258–278. doi:10.1016/j.apsb.2018.09.005

Ma, J. Y., Feng, R., Tan, X. S., Ma, C., Shou, J. W., Fu, J., et al. (2013). Excretion of Berberine and its Metabolites in Oral Administration in Rats. *J. Pharm. Sci.* 102 (11), 4181–4192. doi:10.1002/jps.23718

Ouzzine, M., Barré, L., Netter, P., Magdalou, J., and Fournel-Gigleux, S. (2003). The Human UDP-Glucuronosyltransferases: Structural Aspects and Drug Glucuronidation. *Drug Metab. Rev.* 35 (4), 287–303. doi:10.1081/dmr-120026397

Peer, C. J., Sissung, T. M., Kim, A., Jain, L., Woo, S., Gardner, E. R., et al. (2012). Sorafenib Is an Inhibitor of UGT1A1 but Is Metabolized by UGT1A9: Implications of Genetic Variants on Pharmacokinetics and Hyperbilirubinemia. *Clin. Cancer Res.* 18 (7), 2099–2107. doi:10.1158/1078-0432.CCR-11-2484

Rowland, A., Miners, J. O., and Mackenzie, P. I. (2013). The UDP-Glucuronosyltransferases: Their Role in Drug Metabolism and Detoxification. *Int. J. Biochem. Cel. Biol.* 45 (6), 1121–1132. doi:10.1016/j.biocel.2013.02.019

Singer, J. B., Shou, Y., Giles, F., Kantarjian, H. M., Hsu, Y., Robeva, A. S., et al. (2007). UGT1A1 Promoter Polymorphism Increases Risk of Nilotinib-Induced Hyperbilirubinemia. *Leukemia* 21 (11), 2311–2315. doi:10.1038/sj.leu.2404827

US Food and Drug Administration (2012). Guidance for Industry: Drug Interaction Studies—Study Design, Dataanalysis, Implications for Dosing and Labeling Recommendations, Draft Guidance. *Federal register* 77 (34), 9946–9947.

Vítek, L., and Ostrow, J. D. (2009). Bilirubin Chemistry and Metabolism; Harmful and Protective Aspects. *Curr. Pharm. Des.* 15 (25), 2869–2883. doi:10.2174/138161209789058237

Liu, X. Y., Lv, X., Wang, P., Ai, C. Z., Zhou, Q. H., Finel, M., et al. (2019). Inhibition of UGT1A1 by Natural and Synthetic Flavonoids. *Int. J. Biol. Macromol.* 126, 653–661. doi:10.1016/j.ijbiomac.2018.12.171

Xu, Y., Wang, S., Hu, Q., Gao, S., Ma, X., Zhang, W., et al. (2018). CavityPlus: a Web Server for Protein Cavity Detection with Pharmacophore Modelling, Allosteric Site Identification and Covalent Ligand Binding Ability Prediction. *Nucleic Acids Res.* 46 (W1), W374–W379. doi:10.1093/nar/gky380

Zhang, X., Dong, D., Wang, H., Ma, Z., Wang, Y., and Wu, B. (2015). Stable Knock-Down of Efflux Transporters Leads to Reduced Glucuronidation in UGT1A1-Overexpressing HeLa Cells: the Evidence for Glucuronidation-Transport Interplay. *Mol. Pharm.* 12 (4), 1268–1278. doi:10.1021/mp5008019

Zhang, B., Yang, J., Qin, Z., Li, S., Xu, J., Yao, Z., et al. (2019). Mechanism of the Efflux Transport of Demethoxycurcumin-O-Glucuronides in HeLa Cells Stably Transfected with UDP-Glucuronosyltransferase 1A1. *Plos. One.* 14 (5), e0217695. doi:10.1371/journal.pone.0217695

Zhou, J., Tracy, T. S., and Remmel, R. P. (2011). Correlation between Bilirubin Glucuronidation and Estradiol-3-Gluronidation in the Presence of Model UDP-Glucuronosyltransferase 1A1 Substrates/inhibitors. *Drug Metab. Dispos.* 39 (2), 322–329. doi:10.1124/dmd.110.035030

Zhu, Y. D., Pang, H. L., Zhou, Q. H., Qin, Z. F., Jin, Q., Finel, M., et al. (2020). An Ultra-sensitive and Easy-To-Use Assay for Sensing Human UGT1A1 Activities in Biological Systems. *J. Pharm. Anal.* 10 (3), 263–270. doi:10.1016/j.jpha.2020.05.005

Zucker, S. D., Qin, X., Rouster, S. D., Yu, F., Green, R. M., Keshavan, P., et al. (2001). Mechanism of Indinavir-Induced Hyperbilirubinemia. *Proc. Natl. Acad. Sci. U. S. A.* 98 (22), 12671–12676. doi:10.1073/pnas.231140698

Conflict of Interest: The authors declare that the research was conducted in the absence of any commercial or financial relationships that could be construed as a potential conflict of interest.

Publisher's Note: All claims expressed in this article are solely those of the authors and do not necessarily represent those of their affiliated organizations, or those of the publisher, the editors and the reviewers. Any product that may be evaluated in this article, or claim that may be made by its manufacturer, is not guaranteed or endorsed by the publisher.

frontiers in Pharmacology

ORIGINAL RESEARCH
published: 21 February 2022
doi: 10.3389/fphar.2022.827668

Pharmacokinetics, Tissue Distribution, and Excretion Characteristics of a Radix Polygoni Multiflori Extract in Rats

Wenhao Cheng[1,2†], Siyang Wu[2†], Zheng Yuan[2], Weiyu Hu[3], Xin Yu[2], Nianxin Kang[4], Qiutao Wang[5], Mingying Zhu[2], Kexin Xia[2], Wei Yang[2], Chen Kang[2], Shuofeng Zhang[1] and Yingfei Li[2]**

[1]School of Chinese Pharmacy, Beijing University of Chinese Medicine, Beijing, China, [2]Center for DMPK Research of Herbal Medicines, Institute of Chinese Materia Medica, China Academy of Chinese Medical Sciences, Beijing, China, [3]Department of Hepatobiliary Pancreatic Surgery, The Affiliated Hospital of Qingdao University, Qingdao, China, [4]School of Life Sciences, Beijing University of Chinese Medicine, Beijing, China, [5]School of Traditional Chinese Medicine, Shandong University of Traditional Chinese Medicine, Jinan, China

OPEN ACCESS

Edited by:
Weiwei Jia,
Shanghai Institute of Materia Medica (CAS), China

Reviewed by:
Washim Khan,
University of Mississippi, United States
Guang-Bo Ge,
Shanghai University of Traditional Chinese Medicine, China

***Correspondence:**
Shuofeng Zhang
shuofengzhang@sina.com
Yingfei Li
yfli@icmm.ac.cn

†These authors have contributed equally to this work

Specialty section:
This article was submitted to Ethnopharmacology, a section of the journal Frontiers in Pharmacology

Received: 02 December 2021
Accepted: 21 January 2022
Published: 21 February 2022

Citation:
Cheng W, Wu S, Yuan Z, Hu W, Yu X, Kang N, Wang Q, Zhu M, Xia K, Yang W, Kang C, Zhang S and Li Y (2022) Pharmacokinetics, Tissue Distribution, and Excretion Characteristics of a Radix Polygoni Multiflori Extract in Rats. Front. Pharmacol. 13:827668. doi: 10.3389/fphar.2022.827668

Although progress has been achieved in the pharmacological activity and toxicity of Radix Polygoni Multiflori (RPM), the chemical basis of its toxicity is still unclear. Here, we performed a multicompound pharmacokinetic analysis and investigated the tissue distribution and excretion characteristics of RPM components after oral administration in rats. The findings demonstrated that the active ingredients of the RPM extract were quickly absorbed after oral administration, with high exposure levels of emodin, 2,3,5,4′-teterahydroxystilbene-2-O-β-D-glucoside (TSG), citreorosein, torachrysone-8-O-glucoside (TG), emodin-8-O-β-D-glucoside (EG), and physcion-8-O-β-D-glucoside (PG). The tissue distributions of emodin, TSG, TG, EG, and PG were high in the liver and kidney. These components were the key contributors to the effectiveness and toxicity of RPM on the liver and kidney. Most of the active ingredients were mainly excreted through feces and bile, while a few were converted into other products in the body and excreted through urine and feces.

Keywords: Radix Polygoni Multiflori, pharmacokinetics, tissue distribution, excretion, UPLC-MS/MS

1 INTRODUCTION

Radix Polygoni Multiflori (RPM), the dried tuberous roots of *Reynoutria multiflora* (Thunb.) Moldenke (Polygonaceae), is a popular traditional Chinese medicine that has been used for hair darkening, prolonging life, and mitigating several dysfunctions (Tang et al., 2017). Modern pharmacological research and clinical practices have shown that RPM has several bioactive properties, including antioxidant (Liu X. et al., 2021; Wang et al., 2008), antiaging (Cheung et al., 2014; Fan et al., 2021), and antitumor activities (Ma et al., 2012; Hou et al., 2013; Way

Abbreviations: CE, collision energy; CG, chrysophanol-8-O-β-D-glucoside; CMC-Na, carboxymethyl cellulose; CXP, collision exit potential; DP, declustering potential; EG, emodin-8-O-β-D-glucoside; EP, entrance potential; ESI, electrospray ionization; IS, internal standard; PG, physcion-8-O-β-D-glucoside; PK, pharmacokinetic; RPM, radix polygoni multiflori; TG, torachrysone-8-O-glucoside; TSG, 2,3,5,4′-teterahydroxystilbene-2-O-β-D-glucoside; UPLC-MS/MS, ultra-performance liquid chromatography-tandem mass spectrometry.

et al., 2014; Lin et al., 2017; Xing et al., 2019), and it helps in regulating immunity (Chen et al., 2012), lowering blood lipids (Yao et al., 2013; Chang et al., 2016; Xie et al., 2012), and promoting neuroprotection (Sun et al., 2011; Yang X.-P. et al., 2014; Ruan et al., 2021). However, an increasing number of recently published studies have demonstrated the adverse effects of RPM. For instance, some studies have demonstrated that RPM exerts hepatotoxicity and shows possible drug interactions with warfarin, thus leading to bone marrow suppression (Lin et al., 2015; Liu et al., 2019).

To date, over 100 bioactive constituents of RPM have been isolated and identified, including stilbenes, anthraquinones, flavonoids, and phenolic acids. Of these, stilbene glycosides and anthraquinones are the main active or toxic components of RPM. Despite several reports on the toxicology of RPM, comprehensive information is not available on the chemical basis and mechanism of its toxicity. An herbal constituent can be defined as drug-like if it possesses the desired pharmacologic potency, a wide safety margin, appropriate pharmacokinetic (PK) properties, and adequate content in the prescribed dosage (Jia et al., 2015). TSG is one of the main active components in RPM, and it has strong antioxidant (Büchter et al., 2015) and antiatherosclerotic abilities (Yao et al., 2015; Qian et al., 2020), and can prevent thromboembolic diseases by inhibiting the proliferation of vascular smooth muscle (Xu et al., 2012; Xiang et al., 2014). Emodin can inhibit glutamate-induced apoptosis, and it has a significant neuroprotective effect (Ahn et al., 2016) and can also delay atherosclerotic plaque formation in gene knockout mice through the JAK2-STST3 pathway (Mei-Juan et al., 2018). Both physcion and questin can inhibit the growth of human colon cancer cells by inhibiting Cdc25B phosphatase (Choi et al., 2007). EG and PG can inhibit the activity of soluble epoxide hydrolase and thus have potential antitumor activity (Kwon et al., 2009; Sun et al., 2015), while TG can promote the proliferation of dermal papilla cells and significantly increase hair length (Wu et al., 2018). Rhein protects the liver and exerts antifibrotic effects, and its mechanism may be related to its anti-inflammatory and antioxidant effects and ability to inhibit transforming growth factor β1 and hepatic stellate cell activation (En-Ze et al., 2016). Chrysophanol can inhibit the growth of HeLa cervical cancer cells (Trybus et al., 2021). Citreorosein suppresses the gene expression of proinflammatory cytokines, including tumor necrosis factor (TNF)-α, interleukin (IL)-6 and IL-1β, in mouse bone marrow-derived mast cells (BMMCs) stimulated with phorbol 12-myristate 13-acetate (PMA) plus the calcium ionophore A23187 (Lu et al., 2012). Questinol can significantly inhibit NO production at the indicated concentrations and has also been found to inhibit the production of proinflammatory cytokines, including TNF-α and IL-1β (Yang X. et al., 2014), while CG at low concentrations (12 and 24 μM) significantly increase L-02 cell viability (Liu et al., 2018). These pharmacological effects are consistent with the pharmacological antioxidative, antiaging, neuroprotective, antitumor and anti-inflammatory effects of RPM and may all be effective components in RPM (Lin et al., 2015). RPM can cause liver injury and has certain hepatotoxicity, which is mostly believed to be caused by anthraquinone compounds. Studies have pointed out that rhein, emodin and PG in Polygonum multiflorum have certain cytotoxic effects on HepG2 cells, while rhein, emodin, chrysophanol, aloe emodin, EG and CG have inhibitory effects on HepG2 cells at high concentrations (Yang et al., 2016). TSG compounds may also be related to the hepatotoxicity of Polygonum multiflorum (Lin et al., 2015; Lv et al., 2015).

The pharmacokinetic characteristics of the active ingredients in traditional Chinese medicine have been used to predict the efficacy and potential toxicity of medicines and guide the rational clinical use of drugs (Wang et al., 2013; Zhang et al., 2018). Therefore, pharmacokinetic studies of the main bioactive components in RPM are essential for promoting their clinical application and may help clarify their pharmacological or toxicological action. However, pharmacokinetic studies of RPM mainly focus on its single component and single-dose components, and only a single study has analyzed the pharmacokinetics of seven components in RPM. In addition, although tissue distribution and excretion studies are important in understanding the mechanisms of action of a bioactive compound to the best of our knowledge, RPM has not been fully explored. Therefore, we hypothesized that a comprehensive knowledge of the absorption, distribution and excretion processes of RPM could provide insights on the pharmacodynamic and toxicological chemical basis of its toxicity.

This study aimed to investigate the pharmacokinetics, tissue distribution, and excretion of RPM in rats after oral administration. Using an established ultra-performance liquid chromatography-tandem mass spectrometry (UPLC-MS/MS) procedure (Cheng et al., 2020), several biological components in rat plasma were simultaneously measured, and the bioactive constituents of RPM in rat plasma were obtained. In addition, the tissue distribution and excretion routes of RPM ingredients in rats following an oral dose of RPM extract were also elucidated. This study provides helpful references for developing and utilizing the effective ingredients in RPM.

2 MATERIALS AND METHODS

2.1 Chemicals and Reagents

The dried herbal roots of *Reynoutria multiflora* (Thunb.) Moldenke (Polygonaceae) (RPM) were purchased from Beijing Tongrentang Pharmaceutical Co., Ltd. The raw materials were carefully authenticated by one of the authors, Prof. Shuofeng Zhang. The voucher specimen (lot no: YDZY-HSW-20180521) was deposited in a refrigerator at 4°C. Chrysophanol, emodin, aloe-emodin, rhein, physcion, questin, emodin-8-O-β-D-glucoside (EG), physcion-8-O-β-D-glucoside (PG), 2,3,5,4′-teterahydroxystilbene-2-O-β-D-glucoside (TSG), and puerarin (IS) were obtained from Chengdu Chroma-Biotechnology Co., Ltd. (Chengdu, China). Citreorosein, questinol, torachrysone-8-O-glucoside (TG), and chrysophanol-8-O-β-D-glucoside (CG) were purchased from Qingdao Advance Chem Technology Co., Ltd. (Qingdao, China). The purity of the various compounds was 98% (**Figure 1**). Sodium carboxymethyl cellulose (CMC-Na) was purchased from Sinopharm Chemical Reagent Co., Ltd (Shanghai, China). LC-grade acetonitrile and formic acid were purchased from Honeywell (Morristown, United States) and Roe Scientific Inc. (Newark, United States), respectively. Ultra-pure

water was prepared using a Millipore Milli-Q purification system (Bedford, United States).

2.2 Animals

Sprague–Dawley rats (200–240 g) were obtained from Beijing Vital River Laboratory Animal Technology Co., Ltd. (Beijing, China) [SCXK 2016 (jing)-0006]. The animals were maintained in a specific pathogen-free animal room maintained at 22 ± 2°C, 60 ± 5% humidity and a 12/12 h day/night cycle for at least 7 days prior to the study. The animals had free access to demineralized water and diets, with all nutrients at the standard levels. Before the experiment, the rats were fasted overnight for 12 h and were allowed free access to food 4 h after administration. Both before and during the experiment, water was provided *ad libitum*. The surgical rats were allowed to regain their preoperative body weight prior to the study, and they were euthanized with CO_2 gas after the study. The experimental protocol (2020B110) was approved by the experimental animal welfare ethics committee at the Institute of Chinese Materia Medica, China Academy of Chinese Medical Sciences (Beijing, China) and performed in accordance with the "Laboratory animal—Guideline for ethical review of animal welfare" (GB/T 35, 892–2018) issued by the General Administration of Quality Supervision, Inspection and Quarantine of the People's Republic of China (2018).

2.3 RPM Extract Preparation

Decoction pieces of RPM (1 kg) were refluxed with 10 volumes (10 L) of 70% (v/v) ethanol twice, for 3 h each time. The combined extract was concentrated under reduced pressure, freeze-dried to yield 162.2 g brown powder without residual ethanol and stored in a refrigerator at 4°C until use.

2.4 Dosing Solution Preparation

RPM lyophilized powder was prepared at different concentrations of the administration solutions using 0.5% CMC-Na solution. The dosages were 6, 18 and 36 g/kg for the low, middle, and high groups, respectively, which had RPM concentrations of 0.33, 1 and 2 g/ml, respectively. The administration volume was 18 ml/kg.

2.4.1 Pharmacokinetic Study

For the pharmacokinetic (PK) study, three groups (n = 6 each) of rats were orally administered RPM extract (6, 18, and 36 g/kg). In the plasma pharmacokinetics experiment, doses were 6, 18, and 36 g/kg for the single administration group and 18 g/kg for the continuous administration group. The doses were set at a subtoxic level (Zhang et al., 2013; Wang et al., 2015) to investigate the pharmacokinetic profiles of the constituents of RPM (36 g/kg group) and were approximately 60 times the upper dose (6 g/day) for humans recommended by the 2020 edition of Chinese Pharmacopoeia (Chinese Pharmacopoeia Commission, 2020), which was converted to a dose for rats based on body surface area conversion (Reagan-Shaw et al., 2008). In addition, the low and medium doses decreased in a certain proportion. Serial blood samples (~120 μL; before dosing and at 5, 15, and 30 min, and 1, 2, 4, 6, 8, 12, and 24 h after administration) were collected in heparinized tubes from the orbital sinus under light isoflurane. The blood samples were centrifuged at 12000 g for 2 min, and the plasma fractions were decanted and frozen at −70°C until analysis.

2.4.2 Tissue Distribution

For the tissue distribution study, 18 rats were randomly divided into three groups (n = 6, each) and orally administered 18 g/kg RPM extract. The rats under isoflurane anesthesia were sacrificed by bleeding from the abdominal aorta at 5, 15, and 60 min (six rats per time point) after gavage with 18 g/kg RPM extract. Subsequently, the heart, liver, spleen, lung, kidney, brain, stomach, small intestine, bladder, and gonads (testes of male rats, and uterus and ovaries of female rats) were immediately collected. An accurately weighed amount of fresh tissue sample (0.25 g) was individually homogenized with normal saline (1 ml) and transferred (50 μL) as a tissue homogenate to 1.5 ml centrifuge tubes for use as the tissue samples. All tissue samples were stored at −70°C until analysis.

2.4.3 Excretion Study

For the excretion study, the rats were housed singly in metabolic cages with urine collection tubes kept at 4 °C during sample collection. Urine and fecal samples were collected at time intervals of 0–4, 4–8, 8–24, 24–32, and 32–48 h after a single dose of RPM extract at 18 g/kg and then weighed. Another six rats were anesthetized with pentobarbital, fixed in the supine position and subjected to bile duct drainage surgery, and the abdominal wound was sutured. Blank bile samples were collected before the administration of RPM. The rats were weighed, and the state of the rats was observed. Subsequently, they were orally administered 18 g/kg RPM extract. The bile samples were collected at time intervals of 0–1, 1–2, 2–4, 4–6, 6–8, 8–24, 24–32 and 32–48 h. The urine, feces, and bile samples were stored at −70°C until use.

2.5 Standard Stock Solution and Sample Preparation

Standard stock solutions of chrysophanol, emodin, aloe-emodin, rhein, physcion, questin, citreorosein, questinol, TSG, TG, CG, EG, PG, and IS were prepared in methanol at 1 mg/ml. The calibration samples for the analytes were prepared by adding a series of different concentration working solution solutions (5 μL) to drug-free rat plasma (45 μL). All stock solutions and working solutions were stored at −70°C until use.

Samples were prepared using the protein precipitation process. Rat plasma (50 μL) spiked with 10 μL of IS (puerarin 100 ng/ml) was extracted with 150 μL acetonitrile. After vortex shaking for 5 min and centrifugation at 14,000 g for 5 min, 150 μL of the organic layer was transferred to a clean tube and evaporated to dryness at 25°C under a stream of nitrogen. The residue was reconstituted in 50 μL of the initial mobile phase and subjected to another round of centrifugation at 14,000 g for 5 min, and 5 μL of the supernatant was injected for LC–MS/MS analysis. The tissue samples were homogenized in four parts of ice-cold 0.9% saline solution and then centrifuged at 4°C and 12,000 × g for 10 min to obtain tissue homogenates. Urine and bile samples were centrifuged at 4°C and 12,000 × g for 15 min. Fecal samples were homogenized in 0.9% saline and then centrifuged at 4°C and

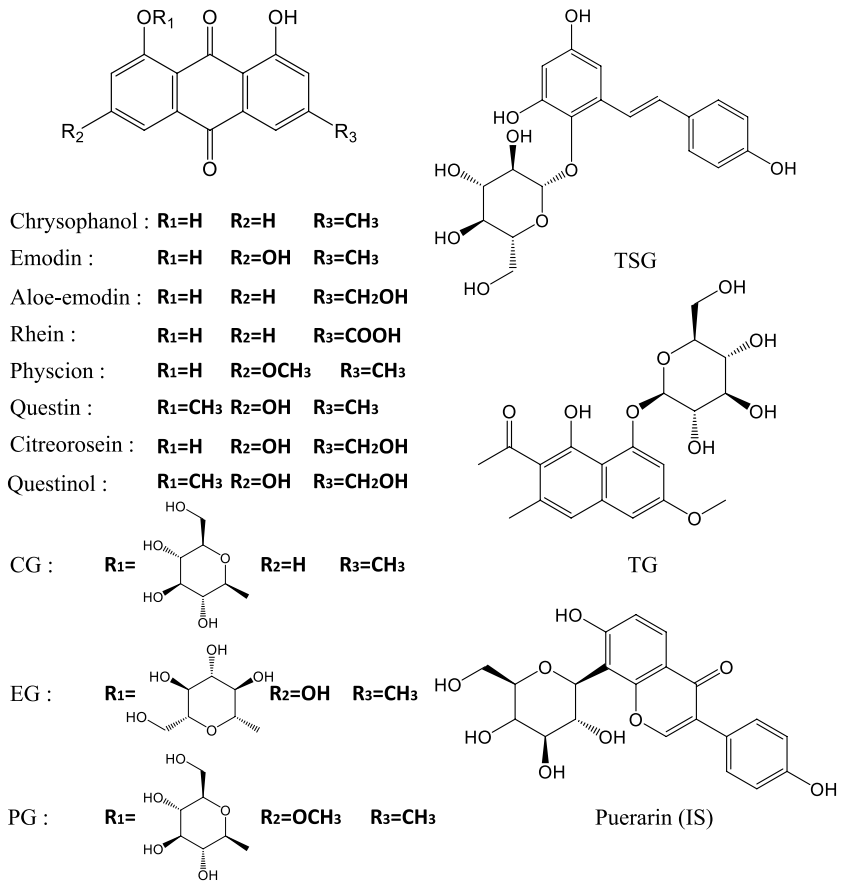

FIGURE 1 | The structures of the 13 constituents of RPM and intenal standard.

12,000 × g for 15 min to gather the fecal homogenates. Tissue homogenate, urine, bile and fecal samples were subjected to a similar process as the rat plasma samples.

2.6 LC–MS/MS Instrument and Analytical Conditions

Biological samples were analyzed using UPLC–MS/MS as described in a previous study (Cheng et al., 2020). The analysis was performed on an AB Sciex API 5500 Q Trap mass spectrometer (Toronto, Canada), interfaced with a Waters Acquity UPLC separation module.

Chromatographic separation was achieved on a Waters HSS-T3 C18 column (100 mm × 2.1 mm, 1.8 μm, kept at 40°C) using a mobile phase containing 0.025% formic acid that consisted of solvent A (water) and solvent B (acetonitrile). The mobile phase was delivered at 0.3 ml/min, and the gradient program shown in **Supplementary Table S1** was used (Cheng et al., 2020).

The electrospray ionization (ESI) source of the mass spectrometer was operated in negative ion mode. The ion source parameters were optimized as follows: turbo spray temperature, 500°C; nebulizer gas (gas 1), 45 psi; heater gas (gas 2), 50 psi; and curtain gas 45 psi. The dwell time was 50 ms for all analytes. The entrance potential (EP) and collision exit potential (CXP) were set at −10 and −16 V, respectively. The declustering potential (DP), collision energy (CE) and other detailed mass spectrometry conditions were applied according to Cheng et al. (2020).

2.7 Data Analysis

The pharmacokinetic parameters, including the area under the plasma concentration-time curve from time zero to time t (AUC_{0-t}) to time infinity ($AUC_{0-\infty}$), the time to reach the maximum plasma concentration (T_{max}), the elimination half-time ($t_{1/2}$), and the maximum plasma concentration (C_{max}), were calculated using the pharmacokinetic software Phoenix® WinNonlin®, version 7.0 (Scientific Consulting Inc., Apex, NC, United States). Data are expressed as the mean ± standard deviation (SD) for each group. The dose-exposure relationship was evaluated by the power function model combined with the confidence interval method (Smith et al., 2000; Sethuraman et al., 2007; Hummel et al., 2009). First, the administration dose, $AUC_{0-\infty}$ and C_{max} were logarithmically transformed, and then a linear regression was performed to obtain the curve correlation coefficient (R^2), slope and 90% confidence interval (90% CI).

3 RESULTS AND DISCUSSION

The LC–MS/MS method for the assay of 13 components from RPM in multiple biological samples was validated based on the Bioanalytical Method Validation Guidance for Industry issued by the Center for Drug Evaluation and Research and the Center for Veterinary Medicine of the US Food and Drug Administration (U.S. Department of Health and Human Services, Food and Drug Administration, Center for Drug Evaluation and Research, Center for Veterinary Medicine, 2018). For the method of validating rat plasma, see previously published articles (Cheng et al., 2020). The bioanalytical methods for validating rat tissue, bile, urine and feces are shown in **Supplementary Figures S1–S4** and **Supplementary Tables S2–S5**. After validation, the method was successfully applied to determine the pharmacokinetics, tissue distribution, and excretion characteristics study in rats following oral administration of the RPM extract.

3.1 Pharmacokinetics of the RPM Extract After Oral Administration in Rats

Previous studies reporting the pharmacokinetics of RPM have mainly focused on a single component. However, the constituents of RPM are complex, and there may be interactions and mutual transformations between them. Therefore, monomers can be used to study medicinal materials, and obvious differences will be observed in the overall pharmacokinetic studies. In this experiment, UPLC–MS/MS was used to analyze the pharmacokinetics of 13 active ingredients in the RPM extract orally administered at three different doses. The calculated doses of the components based on the contents in the extract were 7.38, 14.8, 13.7, 8.82, 15.5, 11.2, 55.8, 1.08, 1,170, 11.3, 25.7, 131.4, and 13.0 mg/kg for chrysophanol, emodin, aloe-emodin, rhein, physcion, questin, citreorosein, questinol, TSG, TG, CG, EG, and PG, respectively.

Increasing dosage is a useful way to facilitate uncovering the herbal compounds (unchanged and/or metabolized forms) with significant levels in general circulation and in target tissue. Therefore, we hope to set the dosage of the high-dose group as high enough to fully reveal the exposure of the target compounds in vivo in this study. However, after 28 days of continuous gavage of 40 g/kg ethanol extract of Polygonum multiflorum, the liver, kidney and lung of rats were damaged (Qi et al., 2013). In consideration of the welfare of experimental animals and the convenience of experimental operation, the concentration of the extract solution administered to rats should not be too high, and the administration volume should not be too large. In this way, the dose of 36 g/kg RPM extract was finally set as the high dose level with the concentration and volume of the administration solution 2 g/mL and 18 mL/kg, respectively, in this study.

The mean plasma concentration–time profiles are illustrated in **Figure 2**, and the pharmacokinetic parameters are presented in **Table 1**. The plasma concentrations of physcion, questin, and CG were too low to be detected, whereas rhein could not be detected in rats dosed with 6 g/kg RPM. Physcion has a moderate intestinal permeability with P_{eff} values of $(3.32 \pm 1.50) \times 10^{-3}$ $(2.30 \pm 1.57) \times 10^{-3}$ $(2.40 \pm 0.58) \times 10^{-3}$, and $(7.45 \pm 3.30) \times 10^{-3}$ cm/min in the duodenum, jejunum, ileum, and colon, respectively (Wang P. et al., 2011). Rhein is mostly administered orally due to its low solubility, although achieving a stable and effective blood concentration is difficult (Li et al., 2021). The components detected in the plasma gradually increased as the dose increased. Seven constituents detected in this study, namely, emodin, aloe-emodin, citreorosein, TSG, TG, EG and PG, exhibited C_{max} values within 20 min, thus demonstrating rapid gastrointestinal tract absorption. TSG had the highest C_{max} due to its good water solubility and a log*P* value of 0.10, and it content was highest among the 13 constituents in the RPM extract. Although emodin has poor water solubility with a high log*P* (5.03), it reached the second highest C_{max} due to its high content in the extract and fast absorption (Liu et al., 2010). The C_{max} values of the other ingredients, namely, chrysophanol, rhein, aloe-emodin, citreorosein, questinol, TG, EG, and PG, were relatively low. The low C_{max} of chrysophanol and rhein may be due to their low content in the RPM extract. Aloe-emodin is rapidly absorbed and quickly metabolized to rhein and other unknown metabolites in the body (Lang, 1993). In the Caco-2 cell model and the everted gut sac model, aloe-emodin was mainly absorbed in a glucuronidated or sulfated form, suggesting that a significant amount was transformed during absorption (Park et al., 2009). The index $AUC_{0-\infty}$, which reflects the degree of exposure to the drug in the body, also showed the same trend (**Supplementary Figure S6**), with the highest exposure observed for TSG and then emodin in a dose-dependent manner.

Subsequently, we performed a regression analysis using the log-transformed values of the dose, $AUC_{0-\infty}$ and C_{max} (**Supplementary Figure S6**, **Tables 2**, **3**). The $AUC_{0-\infty}$ and C_{max} of the active ingredient of the RPM extract were directly proportional to the dose except for rhein and chrysophanol. The $AUC_{0-\infty}$ of chrysophanol, emodin, questinol, TSG and PG were nonlinearly related to the dose (90% CI of the slope were beyond the critical interval of 0.88–1.12), whereas the $AUC_{0-\infty}$ and dose of aloe-emodin, citreorosein, TG, and EG showed an uncertain linear relationship (90% CI of the slope of some samples were within the critical interval of 0.88–1.12). Additionally, the C_{max} of emodin, TSG, TG, and PG was nonlinearly related to the dose (90% CI of the slope was beyond the critical interval of 0.80–1.20), whereas those of aloe-emodin, citreorosein, questinol, and EG could not be linearly correlated with the dose (90% CI of the slope of some samples was within the critical interval of 0.80–1.20). Understanding the pharmacokinetics of a drug, which affects drug availability at the target site is essential to eliciting the desired effects of a drug on its target.

For enhanced effects, drugs must enter the systemic circulation and reach the target site of action to interact with receptors. Therefore, pharmacokinetic analyses to determine a drug's significant systemic exposure after administration have gained increasing research interest (Li, 2017). This study showed that after the oral administration of RPM extract to SD rats, TSG, which has with a shorter half-life and faster elimination speed was absorbed into the blood in the form of a prototype component in the stomach. These observations are consistent with those reported in previous studies (Sun et al., 2005). In addition,

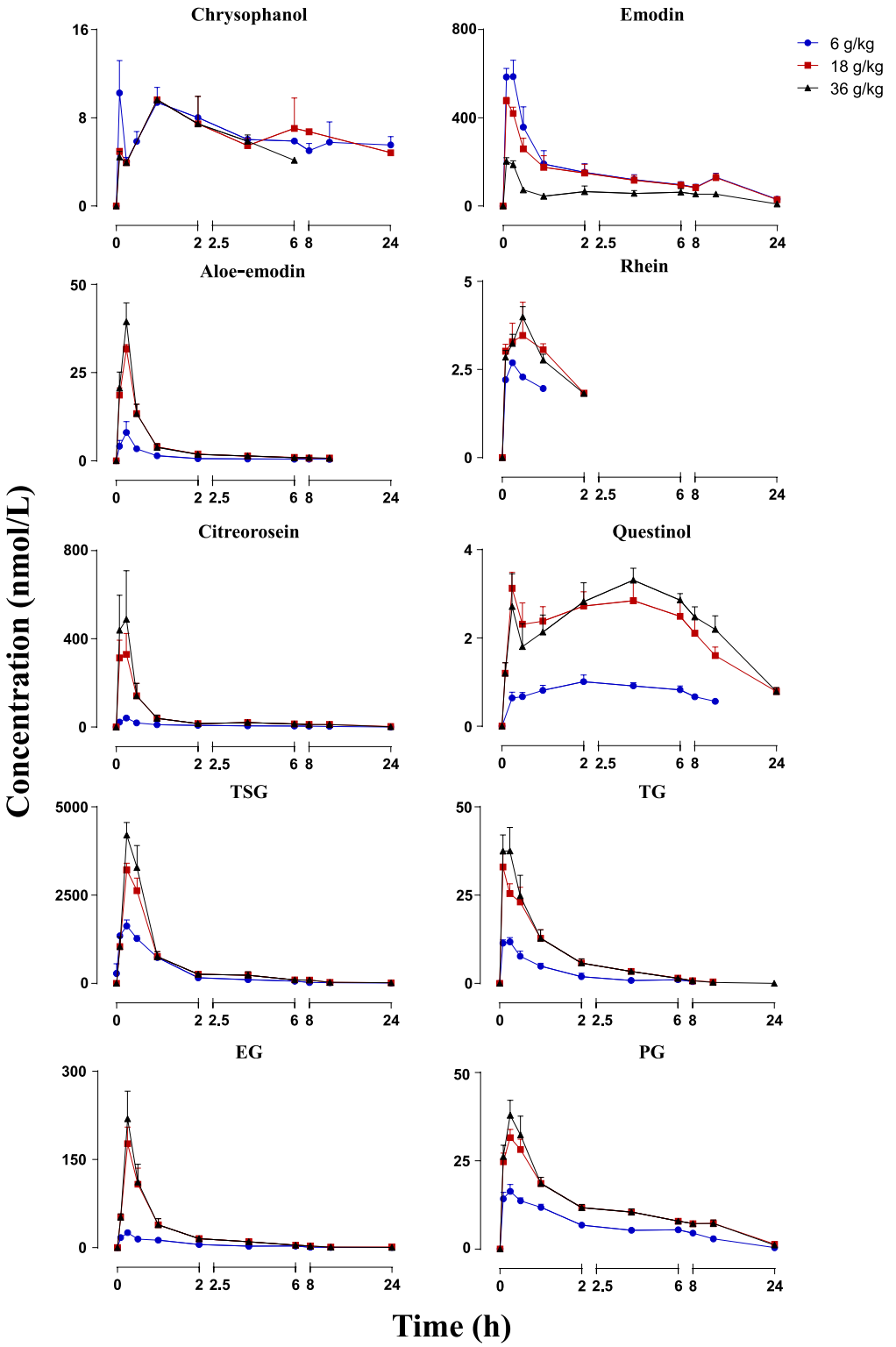

FIGURE 2 | Mean plasma concentration-time profiles of the 10 constituents after administration of RPM (6, 18 and 36 g/kg) to rats. The upper error bars represent the standard deviation obtained from six replicates.

TABLE 1 | Pharmacokinetics of the 10 constituents in rats after p.o. administration of RPM extract at dose of 6, 18, and 36 g/kg (Mean ± SD, n = 6).

Compound	Chrysophanol			Emodin			Aloe-emodin		
Dosing	**6 g/kg**	**18 g/kg**	**36 g/kg[a]**	**6 g/kg**	**18 g/kg**	**36 g/kg[a]**	**6 g/kg**	**18 g/kg**	**36 g/kg[a]**
C_{max} (nmol/L)	9.36 ± 3.26	7.87 ± 2.19	7.48 ± 2.21	205 ± 39.4	491 ± 35.8	648 ± 125	8.25 ± 7.47	31.7 ± 3.03	42.0 ± 11.5
T_{max}(h)	1.03 ± 0.96	3.51 ± 3.06	2.22 ± 1.76	0.12 ± 0.07	0.14 ± 0.09	0.19 ± 0.09	0.29 ± 0.10	0.25	0.22 ± 0.07
$t_{1/2}$ (h)	26.3 ± 14.4	–	3.18 ± 0.62	7.72 ± 3.67	9.44 ± 3.63	8.37 ± 4.17	8.46 ± 7.14	5.09 ± 3.38	3.44 ± 1.40
AUC_{0-t} (nmol·h/L)	74.8 ± 58.9	19.8 ± 9.41	16.9 ± 6.47	1,040 ± 133	2,480 ± 558	2,540 ± 694	8.32 ± 4.16	25.4 ± 9.70	27.0 ± 12.0
$AUC_{0-\infty}$ (nmol·h/L)	340 ± 195	–	40.4 ± 7.36	1,350 ± 504	2,910 ± 707	2,970 ± 863	12.4 ± 7.0	32.4 ± 14.4	31.3 ± 12.7
$MRT_{0-\infty}$ (h)	40.3 ± 23.3	–	6.76 ± 2.06	12.7 ± 4.65	13.0 ± 4.18	11.8 ± 5.27	9.61 ± 8.77	4.65 ± 3.53	3.17 ± 1.54

Compound	Rhein			Citreorosein			Questinol		
Dosing	**6 g/kg**	**18 g/kg**	**36 g/kg[a]**	**6 g/kg**	**18 g/kg**	**36 g/kg[a]**	**6 g/kg**	**18 g/kg**	**36 g/kg[a]**
C_{max} (nmol/L)	–	3.72 ± 1.25	3.74 ± 0.84	41.2 ± 8.80	349 ± 216	521 ± 512	1.09 ± 0.317	3.54 ± 0.652	4.00 ± 0.673
T_{max}(h)	–	0.42 ± 0.14	0.46 ± 0.10	0.25	0.19 ± 0.09	0.19 ± 0.09	3.50 ± 2.17	1.83 ± 1.80	4.38 ± 4.03
$t_{1/2}$ (h)	–	–	1.18 ± 0.39	5.07 ± 1.32	3.78 ± 0.75	3.97 ± 1.31	8.00 ± 2.01	14.4 ± 9.99	8.90 ± 2.70
AUC_{0-t} (nmol·h/L)	–	4.26 ± 2.99	3.91 ± 2.23	87.2 ± 21.5	416 ± 251	458 ± 338	8.61 ± 1.69	40.1 ± 8.98	47.3 ± 6.85
$AUC_{0-\infty}$ (nmol·h/L)	–	–	8.14 ± 1.78	96.1 ± 17.1	558 ± 499	468 ± 337	27.0 ± 22.8	58.3 ± 14.3	57.5 ± 9.45
$MRT_{0-\infty}$ (h)	–	–	1.83 ± 0.56	6.87 ± 1.42	5.69 ± 1.57	5.32 ± 1.85	12.2 ± 2.93	20.6 ± 13.5	13.6 ± 4.21

Compound	TSG			TG		
Dosing	**6 g/kg**	**18 g/kg**	**36 g/kg[a]**	**6 g/kg**	**18 g/kg**	**36 g/kg[a]**
C_{max} (nmol/L)	1,670 ± 403	3,260 ± 494	4,290 ± 986	12.4 ± 2.66	37.3 ± 4.57	45.8 ± 9.94
T_{max}(h)	0.24 ± 0.15	0.33 ± 0.13	0.33 ± 0.13	0.19 ± 0.09	0.11 ± 0.07	0.11 ± 0.07
$t_{1/2}$ (h)	6.53 ± 2.45	6.54 ± 2.02	5.98 ± 2.62	1.23 ± 0.58	1.90 ± 0.22	2.00 ± 0.63
AUC_{0-t} (nmol·h/L)	2,380 ± 280	4,040 ± 1,050	4,460 ± 1,360	15.8 ± 10.6	48.0 ± 17.2	51.9 ± 18.1
$AUC_{0-\infty}$ (nmol·h/L)	2,460 ± 273	4,200 ± 1,080	4,610 ± 1,430	16.6 ± 10.9	49.5 ± 17.1	53.0 ± 18.3
$MRT_{0-\infty}$ (h)	3.86 ± 1.17	4.37 ± 0.91	3.66 ± 0.97	1.58 ± 0.77	2.23 ± 0.30	2.10 ± 0.24

Compound	EG			PG		
Dosing	**6 g/kg**	**18 g/kg**	**36 g/kg[a]**	**6 g/kg**	**18 g/kg**	**36 g/kg[a]**
C_{max} (nmol/L)	25.7 ± 5.73	187 ± 68.5	233 ± 110	16.8 ± 4.10	34.2 ± 4.59	42.1 ± 10.9
T_{max}(h)	0.25	0.29 ± 0.10	0.29 ± 0.10	0.29 ± 0.10	0.26 ± 0.13	0.26 ± 0.13
$t_{1/2}$ (h)	3.54 ± 1.55	4.85 ± 1.99	3.92 ± 2.50	4.83 ± 0.99	7.09 ± 2.12	6.13 ± 1.06
AUC_{0-t} (nmol·h/L)	46.7 ± 24.6	186 ± 73.4	191 ± 74.3	77.7 ± 6.12	176 ± 16.8	178 ± 20.1
$AUC_{0-\infty}$ (nmol·h/L)	48.8 ± 24.4	194 ± 79.9	194 ± 74.7	91.9 ± 14.5	192 ± 12.6	188 ± 18.6
$MRT_{0-\infty}$ (h)	4.40 ± 1.79	3.87 ± 1.87	2.88 ± 1.41	7.55 ± 1.48	9.64 ± 2.05	8.58 ± 1.72

[a]*The pharmacokinetic parameters of the 36 g/kg dose have been published in Cheng et al., 2020.*

TABLE 2 | Relationships between system exposure level ($AUC_{0-\infty}$) of the 10 constituents and p.o. dose of RPM extract in rats.

Compound	R^2	*P*	Slope (90%CI)	Conclusion
Chrysophanol	0.288	2.63×10^{-2}	–0.667 (–1.14 to –0.193)	Nonlinear correlation
Emodin	0.573	2.77×10^{-4}	0.466 (0.290–0.642)	Nonlinear correlation
Aloe-emodin	0.430	4.29×10^{-3}	0.582 (0.278–0.885)	Uncertainty of linear relationship
Citreorosein	0.448	2.37×10^{-3}	0.818 (0.422–1.21)	Uncertainty of linear relationship
Questinol	0.491	3.64×10^{-3}	0.551 (0.275–0.827)	Nonlinear correlation
TSG	0.539	5.20×10^{-4}	0.342 (0.204–0.479)	Nonlinear correlation
TG	0.600	1.61×10^{-4}	0.720 (0.464–0.977)	Uncertainty of linear relationship
EG	0.592	1.90×10^{-4}	0.834 (0.520–1.11)	Uncertainty of linear relationship
PG	0.767	1.89×10^{-6}	0.429 (0.326–0.532)	Nonlinear correlation

P-glycoprotein and multidrug resistance-associated protein two are also involved in the absorption of TSG in the intestine (Lei et al., 2015; Liu et al., 2019; Wang et al., 2020). The absorption of emodin was also better, and its main absorption sites are the duodenum and jejunum (Liu et al., 2010). After emodin intragastric administration, emodin rapidly undergoes phase II metabolism to form its glucuronide. In addition, transporters, including Na^+/glucose cotransporter (SGLT1), MRP2, and P-glycoprotein, are also involved in the efflux transport of emodin (Liu et al., 2012). The exposure to emodin in RPM extract was also high, and the exposure level also gradually increased with an increase in the dose. TSG could further increase the hepatotoxicity of emodin by enhancing the absorption of emodin and inhibiting its metabolism (Li et al., 2020). Consistent with the findings of this study, a previous study comparing the absorption of various anthraquinone components using a Caco-2 cell model

TABLE 3 | Relationship between system exposure level (C_{max}) of the 10 constituents and p.o. dose of RPM extract in rats.

Compound	R^2	*P*	Slope (90%CI)	Conclusion
Chrysophanol	0.147	0.142	–0.158 (-0.337–0.021)	Nonlinear correlation
Emodin	0.887	5.37×10^{-9}	0.656 (0.554–0.758)	Nonlinear correlation
Aloe-emodin	0.740	4.73×10^{-6}	1.07 (0.795–1.35)	Uncertainty of linear relationship
Rhein	0.002	0.904	0.034 (-0.482–0.550)	Nonlinear correlation
Citreorosein	0.644	6.08×10^{-5}	1.27 (0.857–1.68)	Uncertainty of linear relationship
Questinol	0.810	3.71×10^{-7}	0.774 (0.610–0.938)	Uncertainty of linear relationship
TSG	0.810	3.67×10^{-7}	0.536 (0.422–0.649)	Nonlinear correlation
TG	0.868	1.91×10^{-8}	0.756 (0.627–0.884)	Nonlinear correlation
EG	0.766	2.02×10^{-6}	1.23 (0.931–1.52)	Uncertainty of linear relationship
PG	0.762	2.25×10^{-6}	0.524 (0.396–0.652)	Nonlinear correlation

demonstrated that the absorption of chrysophanol was the lowest (Wang and yang, 2008). Citreorosein and questinol ether are rarely reported; however, citreorosein presented a higher exposure with rapid and better absorption and faster elimination. In contrast, questinol ether presented a lower exposure level, poor absorption, and slower elimination. These results suggest that citreorosein could have a higher research value than questinol ether. These components are combination anthraquinones. Although several reports are available on EG, few studies have explored the pharmacokinetics of TG and PG. Here, we show that the exposure levels of the latter two in the body were not low and increased with an increase in the administered dose, and they also showed an accumulation effect. The cause of liver toxicity of Polygonum multiflorum is related to anthraquinones (Ruili et al., 2019). The possible mechanisms of anthraquinone-induced hepatotoxicity include inducement of lipid peroxidation in hepatocytes (Guoxin et al., 2019); inhibition of hepatocyte growth, which leads to hepatocyte apoptosis (Ronghua et al., 2016); and changes in the function and expression of bile acid transporters and metabolic enzymes, abnormal structure and metabolic function of liver cells (Pelkonen et al., 2015), and leads to oxidative stress damage of liver cells (Lei et al., 2015). Emodin, aloe emodin, chrysophanol and rhein exhibit cytotoxicity to normal human hepatocytes HepaRG and cause damage to hepatocyte DNA to different degrees (Lei et al., 2015). Research has shown that the hepatotoxic effect of these components on LO2 human hepatocytes was investigated, and EG, PG, emodin and physcion were finally confirmed to be at least partial hepatotoxic components (Lv et al., 2015). In this experiment, emodin and EG exposure was higher. Although citreorosein is less reported, it is also presents high exposure *in vivo*. These compounds easily accumulate *in vivo* with prolonged administration time, and they which may be the main factors that to induce hepatocellular toxicity; thus, they and deserve further study.

These findings revealed the exposure level, absorption, and elimination rate of the active components of RPM in rats. Of the several investigated components, TSG, emodin, TG and PG showed the most obvious results.

3.2 Tissue Distribution

The study of tissue distribution is one of the important areas of pharmacokinetics research because such distributions are closely related to the pharmacology, toxicity, and side effects of a drug. A drug must present pharmacological activity and effective concentrations of its chemical components at the target site to produce pharmacodynamic effects on the body. Therefore, the level of exposure to a compound in the tissue directly impacts its efficacy. The results showed that after 5, 15 and 60 min of oral administration of the RPM extract, each compound was distributed over various tissues throughout the body, suggesting that the body absorbs each active substance rapidly (**Figure 3**). Moreover, the distributions of TSG, emodin, and PG were relatively higher in each tissue compared with the other compounds (**Supplementary Table S11**), which could be related to their higher contents in the extract.

Drugs are distributed throughout various body tissues by systemic circulation after absorption into the blood, regardless of the administration method. Drugs enter tissues that receive high blood flow first, followed by those that receive low blood flow. Our study demonstrated that the nine key compounds in RPM were mainly distributed in the liver and kidney but presented a limited distribution in the bladder and gonads (**Supplementary Table S11**).

In addition to receiving higher blood flow, the liver is also an important metabolic organ, and drugs absorbed through the digestive tract enter the liver through the hepatic portal vein and are converted into other products under the action of liver drug enzymes. Modern pharmacological studies have shown that RPM can reduce hepatomegaly caused by CCL4, inhibit liver microsomal lipid peroxidation caused by ADP and ADP-reduced coenzymes, and reduce serum free fatty acid and lipid peroxide levels (Li et al., 2017). The liver injury caused by RPM was mostly hepatocellular injury, followed by mixed liver injury and cholestatic liver injury. Although RPM can cause varying degrees of liver injury and even death, most RPM-related liver injuries are reversible after stopping RPM products and conservative treatment (Zhu et al., 2015). Some *in vitro* studies have shown that anthraquinones from RPM, including emodin, chrysophanol, and physcion, can change the distribution of bile acids in sandwich-cultured rat hepatocytes (Kang et al., 2017). However, emodin in RPM can induce the expression of cytochrome P450 enzyme mRNA and damage normal human liver cells (Wang et al., 2016). Taken together, these results indicate that the liver is the target organ of RPM's medicinal and toxic effects. Furthermore, studies have shown that TSG, an effective RPM component, can inhibit the NO-ONOO renal oxidative stress pathway in early diabetic nephropathy and reduce the production of nitrotyrosine, thereby inhibiting kidney function damage caused by early

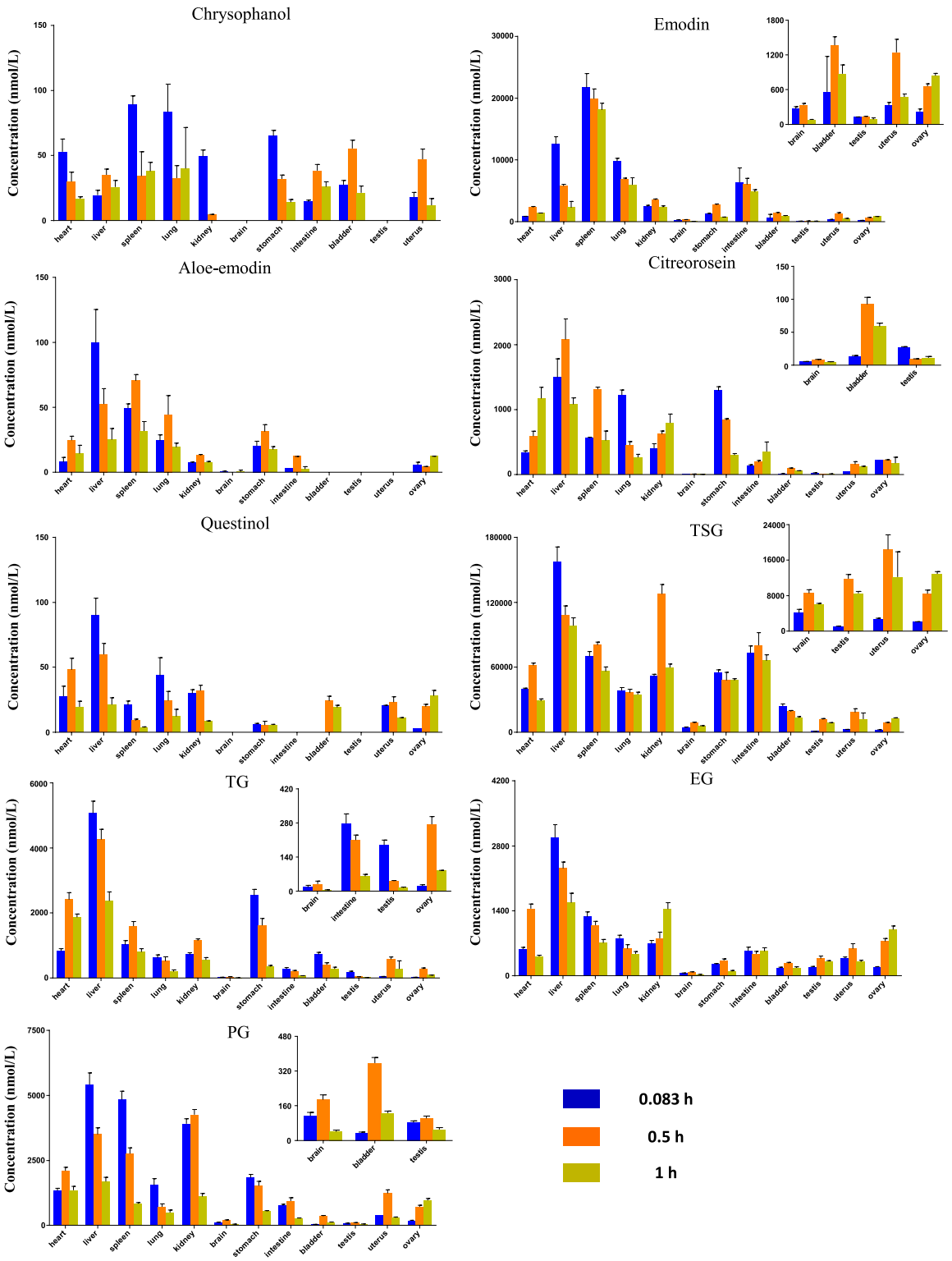

FIGURE 3 | Tissue distribution of the RPM constituents in different sampling time after rat orally administration of RPM extract (18 g/kg).

oxidative stress in diabetic nephropathy (Yuan and Liu, 2016). In contrast, another study showed that emodin and rhein could significantly inhibit the proliferation of HK-2 cells through the MAPK/ERK signaling pathway to inhibit the phosphorylation of ERK and change the proportion of its lipid part, which leads to damage to the outer mitochondrial membrane of renal tubular

epithelial cells (Wang et al., 2007), thus indicating that the kidney is also a prime target organ for the medicinal and toxic effects of RPM. Moreover, experimental studies have shown that the exposure of TSG in various tissues is higher than that of other compounds with a higher distribution in brain tissues (**Supplementary Table S11**), and pharmacokinetic studies have shown that TSG plays a role in improving learning and memory abilities (Wang T. et al., 2011). In addition to TSG, emodin, EG, and PG are also distributed in small amounts in the brain. Therefore, it would be worthwhile to study the pharmacological activities of these compounds on the central nervous system.

Compared with other organs, emodin and chrysophanol had the highest exposure in the spleen (AUC_{0-t} of 19,100 and 50.3 nmol h/L, respectively), whereas the remaining seven compounds had the highest exposure in the liver tissue (**Supplementary Table S11**). Chrysophanol, aloe-emodin, and questinol ether were rarely exposed in the liver, which could be related to their lower content in the extract. The AUC_{0-t} of TSG in the kidney was 86,400 nmol h/L, and the AUC_{0-t} of the other compounds varied from 9.77 to 3,210 nmol h/L. In addition, chrysophanol, aloe-emodin, and questinol ether were rarely exposed in the kidneys, which was also related to their lower content in the extract.

Preliminary studies have shown that the exposure of the active ingredients of RPM in the body is positively correlated with the RPM dose, and the current study further indicates that most of the active components of RPM are distributed in liver and kidney tissues. In addition, among the active components of RPM, emodin, TSG, and EG are exposed to higher levels and can cause liver or kidney damage (Wu et al., 2018), suggesting that long-term exposure to higher doses of RPM extract could cause the highest damage to the liver and kidney.

Collectively, these findings demonstrated that after orally administering RPM extract to rats, its active ingredients can be rapidly distributed to several tissues and organs, among which the liver and kidney are the main organs. In addition to TSG, emodin, EG and PG are distributed in the brain. The study also shows that the active ingredients of RPM are eliminated quickly from tissues.

3.3 Excretion Into Bile, Urine and Feces

Drugs and their metabolites are excreted from the body through excretory processes, such as through renal, bile, and intestinal excretions. With the continuous in-depth study of pharmacokinetics, research on drug excretion kinetics has also received increased attention. However, few reports have focused on the excretion kinetics of RPM extract. Therefore, this study determined the contents of the active ingredients of RPM extract in rat urine, feces, and bile using the UPLC–MS/MS method. Combined with a study of the plasma pharmacodynamics and tissue distribution, the excretion of multiple components of RPM in rats was analyzed (**Supplementary Table S7**, **Figures 4**, **5**). Although questinol and PG presented low recovery from the urine and feces at 4.12% and 16.40%, respectively, the remaining compounds, namely, chrysophanol, emodin, aloe-emodin, citreorosein, questinol, TSG, TG and EG, presented higher recovery from the urine and feces at 28.67%–45.50% (see **Supplementary Table S8** for specific data). The results demonstrated that most of the compounds could be detected in urine, feces, and bile after oral administration of RPM extract, with higher values observed in the fecal samples than the urine samples. This finding could be because the components in feces are obtained from several sources such as unabsorbed drug components, components secreted by bile into the intestinal lumen, resecretion in the intestines re-secretion, and metabolic transformations by gut flora.

The results showed that the excretion of citreorosein, TSG, TG, and EG in feces was higher than that in urine and bile. Tissue distribution studies have shown that citreorosein presents a greater distribution in the liver while its secretion from bile was 158 ± 13.2 nmol, indicating that this component is mainly metabolized by the liver. The average cumulative excretion of the components in feces increased slowly, even after 32 h of administration, which suggests that the prototype constituent in the feces is primarily associated with bile secretion or combined anthraquinone decomposition in the intestine and liver. Moreover, the tissue distribution study revealed a higher distribution of TSG in gastrointestinal tissues than the liver, and the amount excreted by bile secretion was far less than the cumulative amount excreted in feces. These results suggested that the high content of components in feces could be related to the excretion of components through the intestinal epithelium. TSG undergoes phase II metabolism in the liver, a few components are excreted through bile, and most components are excreted in feces (Wang et al., 2009). Additionally, consistent with the higher distribution of TSG in the kidneys the accumulated urine excretion was also higher, indicating that urine excretion is another key excretion method of TSG. In contrast, the cumulative bile excretion of TG and EG was much lower than the cumulative excretion in feces despite these components showing a relatively higher distribution in the liver than the kidney, indicating that the higher content of these components in feces could have been contributed by bile secretion through the intestinal epithelium. PG is mainly excreted by bile, but its cumulative excretion in feces was lower than that in bile, suggesting that PG might have entered the hepatoenteric circulation. Moreover, its excretion in urine was lower despite its higher distribution in the kidneys than in the other organs, suggesting that the compound could have an accumulation effect in the kidneys, thereby causing the nephrotoxicity of RPM. The excretion rate of emodin in bile was higher than that in urine but did not differ remarkably from that in feces. Emodin is mainly metabolized in the liver, which could be the reason for the high excretion rate of emodin in bile. However, the average cumulative excretion-time curve of the three excretion pathways revealed a slowly increasing trend of emodin, even after 32 h of administration, which could be due to a longer residence time of the compound in rats and its high content in various tissues. Rhein was mainly excreted by bile, whereas it was not detected in urine or feces, suggesting that rhein might have entered the hepato-intestinal circulation, which led to rendering its further metabolization and transformation after reabsorption through the intestine. However, there was no double peak in the blood concentration-time curve, which indicates that the component might have been converted into other products in the gastrointestinal tract and absorbed or excreted by the body.

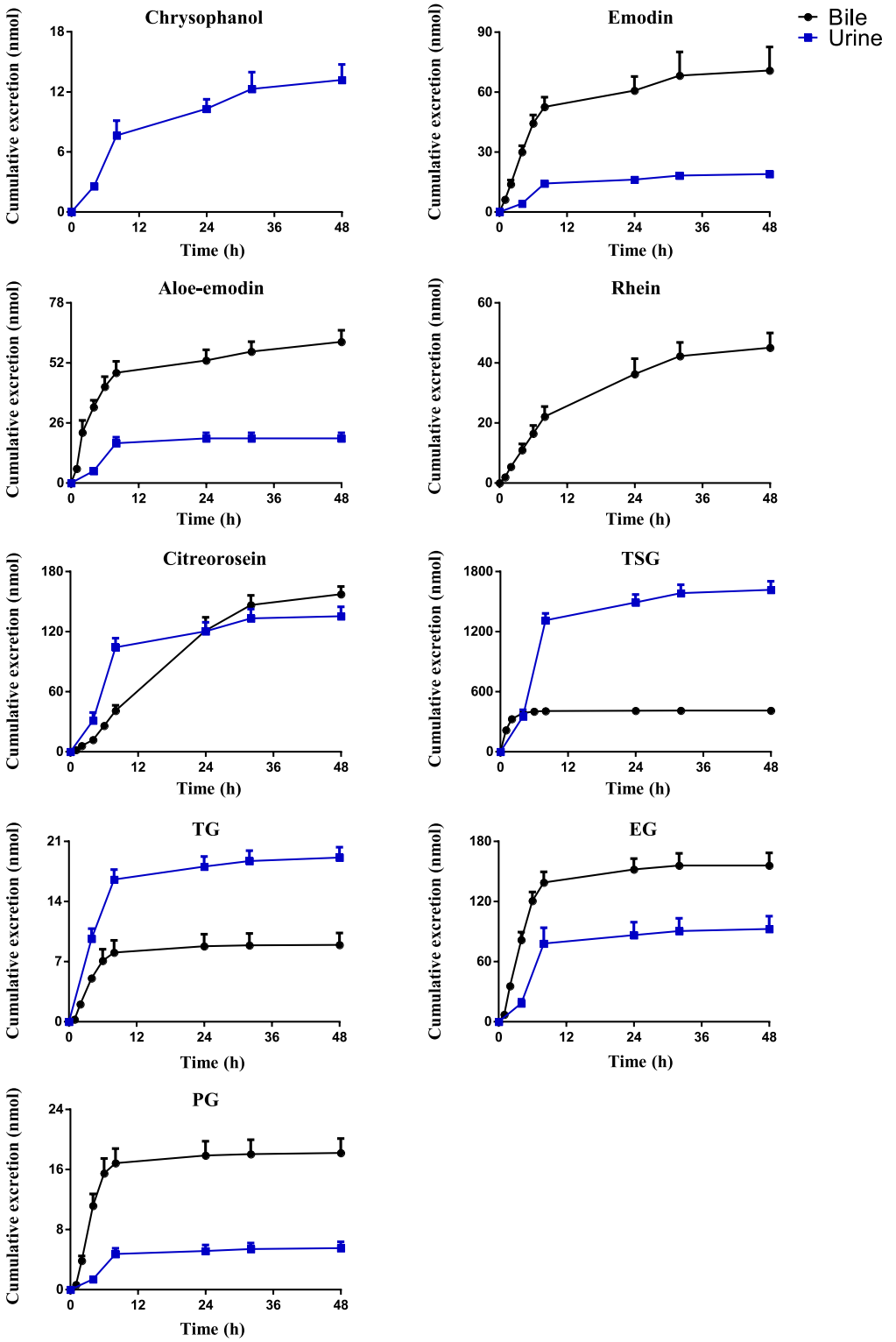

FIGURE 4 | The mean cumulative urinary and biliary excretion profile of the eight constituents in rat after single p.o. administration of RPM extract at 18 g/kg. The upper error bars represent the standard deviation obtained from six replicates.

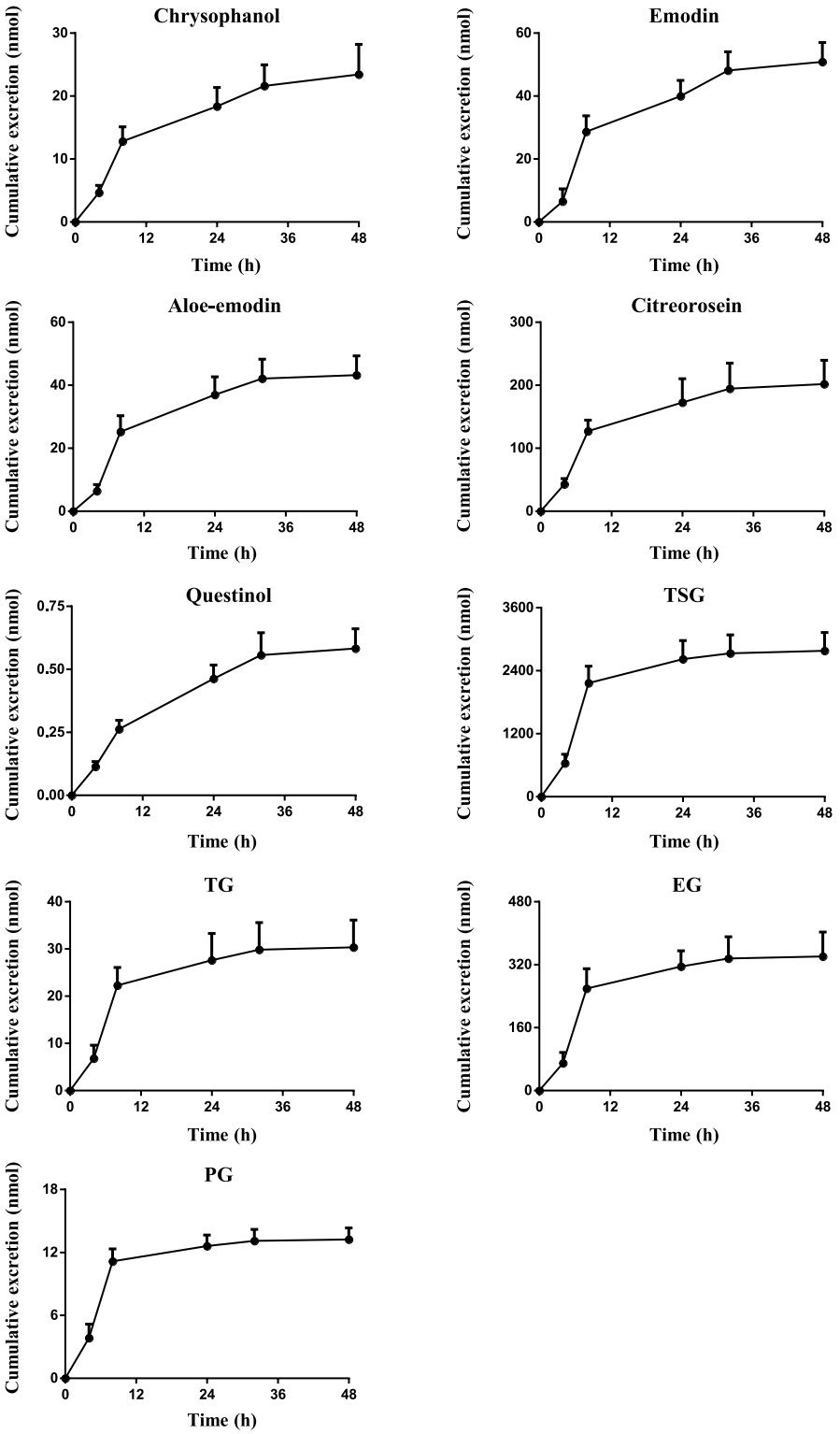

FIGURE 5 | The mean cumulative fecal excretion profile of the eight constituents in rat after single p.o. administration of RPM extract at 18 g/kg. The upper error bars represent the standard deviation obtained from six replicates.

Furthermore, the average cumulative excretion-time curve of chrysophanol and aloe-emodin slowly increased after administration, which may have been related to the slow elimination of each compound, the tissue hydrolysis of other compounds in the gastrointestinal tract or transformation by hepatic drug enzyme metabolism.

Chrysophanol and questinol ether were not detected in bile. Questinol ether may not have been detected in urine and bile because of its low content in the RPM extract, low absorption in the body, or conversion into other products to be excreted. The absence of chrysophanol in bile, but its presence in feces could be related to the low bioavailability of this component or the secretion of intestinal epithelial cells. Its absence in bile indicates that liver drug enzymes could have converted the component into other products with a faster conversion rate or that bile does not excrete the component.

In summary, most of the active ingredients of RPM can be excreted through urine excretion, bile secretion and intestinal epithelial cell secretion. Among them, PG, rhein, and emodin showed the possibility of entering the hepatointestinal circulation, wherein TSG, chrysophanol, TG, and EG are mainly excreted by intestinal epithelial cells and urine.

4 CONCLUSION

In conclusion, after oral administration of RPM extracts to SD rats, the active ingredients were quickly absorbed, including emodin, TSG, citreorosein, TG, EG and PG. These components were exposed at high levels in the body, and revealed a certain accumulation effect with increasing doses; thus, they are worthy of further in-depth study. Furthermore, the distributions of emodin, TSG, TG, EG, and PG in the liver and kidney were high, indicating that these components could be the main substances with pharmacodynamic and toxic effects on the liver and kidney. The excretion pathway of each active ingredient followed mainly fecal and bile excretion, whereas several were converted into other products and excreted through the urine and feces. Herbal medicines are complex mixturesthat may interact with a wide range of proteins in various metabolic organs in extremely complex ways (Ge, 2019; Liu W. et al., 2021). The interaction between drugs and herbs has received increasing attention. The interaction between the components of RPM will also become the focus of future research. Collectively, the results of this study would be helpful for developing new medicines related to RPM and identifying the safety of these medicines by providing insights on the pharmacokinetic characteristics of RPM.

DATA AVAILABILITY STATEMENT

The original contributions presented in the study are included in the article/**Supplementary Material**, further inquiries can be directed to the corresponding authors.

ETHICS STATEMENT

The animal study was reviewed and approved by Experimental animal welfare ethics committee, Institute of Chinese Materia Medica, China Academy of Chinese Medical Sciences.

AUTHOR CONTRIBUTIONS

YL and SZ conceived and designed the experiments: WC, SW, ZY, WH, XY, NK, QW, MZ, KX, WY, and CK performed the animal experiments; WC and SW developed and validated the analytical method; WC, ZY, XY, and NK analyzed the biological samples of rats; WC, SW, and WH carried on the statistical analysis to the data; WC and YL wrote paper; SZ proofread the manuscript.

FUNDING

This study has been financially supported by the National Natural Science Foundation of China (No. 81773990) and Fundamental Research Funds for the Central public welfare research institutes (ZXKT17059, L2020031, and Z2020045).

SUPPLEMENTARY MATERIAL

The Supplementary Material for this article can be found online at: https://www.frontiersin.org/articles/10.3389/fphar.2022.827668/full#supplementary-material

REFERENCES

Ahn, S. M., Kim, H. N., Kim, Y. R., Choi, Y. W., Kim, C. M., Shin, H. K., et al. (2016). Emodin from Polygonum Multiflorum Ameliorates Oxidative Toxicity in HT22 Cells and Deficits in Photothrombotic Ischemia. *J. Ethnopharmacol.* 188, 13–20. doi:10.1016/j.jep.2016.04.058

Büchter, C., Zhao, L., Havermann, S., Honnen, S., Fritz, G., Proksch, P., et al. (2015). TSG (2,3,5,4'-Tetrahydroxystilbene-2-O- β -D-Glucoside) from the Chinese Herb Polygonum Multiflorum Increases Life Span and Stress Resistance of *Caenorhabditis elegans*. *Oxid. Med. Cel. Longev.* 2015, 124357. doi:10.1155/2015/124357

Chang, Y. X., Ge, A. H., Jiang, Y., Teye Azietaku, J., Li, J., and Gao, X. M. (2016). A Bioactivity-Based Method for Screening, Identification of Lipase Inhibitors, and Clarifying the Effects of Processing Time on Lipase Inhibitory Activity of Polygonum Multiflorum. *Evid. Based Complement. Alternat Med.* 2016, 5965067. doi:10.1155/2016/5965067

Chen, Q., Zhang, S.-z., Ying, H.-z., Dai, X.-y., Li, X.-x., Yu, C.-h., et al. (2012). Chemical Characterization and Immunostimulatory Effects of a Polysaccharide from Polygoni Multiflori Radix Praeparata in Cyclophosphamide-Induced Anemic Mice. *Carbohydr. Polym.* 88 (4), 1476–1482. doi:10.1016/j.carbpol.2012.02.055

Cheng, W. H., Ye, H.-c., Yang, W., Wu, S. Y., Wei, M. M., Gao, Y., et al. (2020). Simultaneous Determination of 13 Constituents of Radix Polygoni Multiflori in

Rat Plasma and its Application in a Pharmacokinetic Study. *Int. J. Anal. Chem.* 2020, 1–10. doi:10.1155/2020/4508374

Cheung, F. W., Leung, A. W., Liu, W. K., and Che, C. T. (2014). Tyrosinase Inhibitory Activity of a Glucosylated Hydroxystilbene in Mouse Melan-A Melanocytes. *J. Nat. Prod.* 77 (6), 1270–1274. doi:10.1021/np4008798

Chinese Pharmacopoeia Commission (2020). *Pharmacopoeia of the People's Republic of China*. Beijing, China: China Medical Science Press.

Choi, S. G., Kim, J., Sung, N. D., Son, K. H., Cheon, H. G., Kim, K. R., et al. (2007). Anthraquinones, Cdc25B Phosphatase Inhibitors, Isolated from the Roots of Polygonum Multiflorum Thunb. *Nat. Prod. Res.* 21 (6), 487–493. doi:10.1080/14786410601012265

En-Ze, L. I., Yuan, Y., Shao, H., and Pharmacology, D. O. (2016). Study of the Analytical Method of Rhein and its Activated Metabolites in Liver Microsome Incubations. *J. Southeast Univ. (Med. ence Ed.)* 35 (6), 894–899. doi:10.3969/j.issn.1671-6264.2016.06.013

Fan, W., Guo, Y., Cao, S., Cao, S., Xie, Y., Liu, X., et al. (2021). Tetrahydroxystilbene Glucoside Alleviates Angiotensin II Induced HUVEC Senescence via SIRT1. *Can. J. Physiol. Pharmacol.* 99 (4), 389–394. doi:10.1139/cjpp-2020-0202

Ge, G. B. (2019). Deciphering the Metabolic Fates of Herbal Constituents and the Interactions of Herbs with Human Metabolic System. *Chin. J. Nat. Med.* 17 (11), 801–802. doi:10.1016/S1875-5364(19)30098-6

Guoxin, L., Zinan, L., and Junyu, N. (2019). General Situation of Studies on Anthraquinone Toxicity and its Mechanism. *Jounral Toxicol.* 33 (1), 70–74. doi:10.16421/j.cnki.1002-3127.2019.01.018

Hou, H., Li, D., Cheng, D., Li, L., Liu, Y., and Zhou, Y. (2013). Cellular Redox Status Regulates Emodin-Induced Radiosensitization of Nasopharyngeal Carcinoma Cells *In Vitro* and *In Vivo*. *J. Pharm. (Cairo)* 2013, 218297. doi:10.1155/2013/218297

Hummel, J., McKendrick, S., Brindley, C., and French, R. (2009). Exploratory Assessment of Dose Proportionality: Review of Current Approaches and Proposal for a Practical Criterion. *Pharm. Stat.* 8 (1), 38–49. doi:10.1002/PST.326

Jia, W., Du, F., Liu, X., Jiang, R., Xu, F., Yang, J., et al. (2015). Renal Tubular Secretion of Tanshinol: Molecular Mechanisms, Impact on its Systemic Exposure, and Propensity for Dose-Related Nephrotoxicity and for Renal Herb-Drug Interactions. *Drug Metab. Dispos* 43 (5), 669–678. doi:10.1124/dmd.114.062000

Kang, L., Si, L., Rao, J., Li, D., Wu, Y., Wu, S., et al. (2017). Polygoni Multiflori Radix Derived Anthraquinones Alter Bile Acid Disposition in sandwich-cultured Rat Hepatocytes. *Toxicol. Vitro* 40, 313–323. doi:10.1016/j.tiv.2017.01.022

Kwon, B. M., Kim, S. H., Baek, N. I., Lee, S. I., Kim, E. J., Yang, J. H., et al. (2009). Farnesyl Protein Transferase Inhibitory Components of Polygonum Multiflorum. *Arch. Pharm. Res.* 32 (4), 495–499. doi:10.1007/s12272-009-1403-y

Lang, W. (1993). Pharmacokinetic-metabolic Studies with 14C-Aloe Emodin after Oral Administration to Male and Female Rats. *Pharmacology* 47 Suppl 1 (Suppl. 1), 110–119. doi:10.1159/000139849

Lei, X., Chen, J., Ren, J., Li, Y., Zhai, J., Mu, W., et al. (2015). Liver Damage Associated withPolygonum multiflorumThunb.: A Systematic Review of Case Reports and Case Series. *Evid.-Based Complement. Altern. Med.* 2015, 459749. doi:10.1155/2015/459749

Li, H., Wang, X., Liu, Y., Pan, D., Wang, Y., Yang, N., et al. (2017). Hepatoprotection and Hepatotoxicity of Heshouwu, a Chinese Medicinal Herb: Context of the Paradoxical Effect. *Food Chem. Toxicol.* 108 (Pt B), 407–418. doi:10.1016/j.fct.2016.07.035

Li, D., Yang, M., and Zuo, Z. (2020). Overview of Pharmacokinetics and Liver Toxicities of Radix Polygoni Multiflori. *Toxins (Basel)* 12 (11), 729. doi:10.3390/toxins12110729

Li, G. M., Chen, J. R., Zhang, H. Q., Cao, X. Y., Sun, C., Peng, F., et al. (2021). Update on Pharmacological Activities, Security, and Pharmacokinetics of Rhein. *Evid. Based Complement. Alternat Med.* 2021, 4582412. doi:10.1155/2021/4582412

Li, C. (2017). Multi-compound Pharmacokinetic Research on Chinese Herbal Medicines: Approach and Methodology. *Zhongguo Zhong Yao Za Zhi* 42 (4), 607–617. doi:10.19540/j.cnki.cjcmm.2017.0016

Lin, L., Ni, B., Lin, H., Zhang, M., Li, X., Yin, X., et al. (2015). Traditional Usages, Botany, Phytochemistry, Pharmacology and Toxicology of Polygonum Multiflorum Thunb.: A Review. *J. Ethnopharmacol* 159, 158–183. doi:10.1016/j.jep.2014.11.009

Lin, C. L., Jeng, J. H., Wu, C. C., Hsieh, S. L., Huang, G. C., Leung, W., et al. (2017). Chemopreventive Potential of 2,3,5,4'-Tetrahydroxystilbene-2-O-β-D-Glucoside on the Formation of Aberrant Crypt Foci in Azoxymethane-Induced Colorectal Cancer in Rats. *Biomed. Res. Int.* 2017, 3634915. doi:10.1155/2017/3634915

Liu, W., Tang, L., Ye, L., Cai, Z., Xia, B., Zhang, J., et al. (2010). Species and Gender Differences Affect the Metabolism of Emodin via Glucuronidation. *AAPS J.* 12 (3), 424–436. doi:10.1208/s12248-010-9200-6

Liu, W., Feng, Q., Li, Y., Ye, L., Hu, M., and Liu, Z. (2012). Coupling of UDP-Glucuronosyltransferases and Multidrug Resistance-Associated Proteins Is Responsible for the Intestinal Disposition and Poor Bioavailability of Emodin. *Toxicol. Appl. Pharmacol.* 265 (3), 316–324. doi:10.1016/j.taap.2012.08.032

Liu, M., Gong, X., Quan, Y., Zhou, Y., Li, Y., and Peng, C. (2018). A Cell-Based Metabonomics Approach to Investigate the Varied Influences of Chrysophanol-8-O-β-D-Glucoside with Different Concentrations on L-02 Cells. *Front. Pharmacol.* 9, 1530. doi:10.3389/fphar.2018.01530

Liu, W., Huang, J., Zhang, F., Zhang, C.-C., Li, R.-S., Wang, Y.-L., et al. (2021). Comprehensive Profiling and Characterization of the Absorbed Components and Metabolites in Mice Serum and Tissues Following Oral Administration of Qing-Fei-Pai-Du Decoction by UHPLC-Q-Exactive-Orbitrap HRMS. *Chin. J. Nat. Medicines* 19 (4), 305–320. doi:10.1016/s1875-5364(21)60031-6

Liu, X., Yang, C., Deng, Y., Liu, P., Yang, H., Du, X., et al. (2021). Polygoni Multiflori Radix Preparat Delays Skin Aging by Inducing Mitophagy. *Biomed. Res. Int.* 2021, 5847153. doi:10.1155/2021/5847153

Liu, Y., Wang, W., Sun, M., Ma, B., Pang, L., Du, Y., et al. (2019). Polygonum Multiflorum-Induced Liver Injury: Clinical Characteristics, Risk Factors, Material Basis, Action Mechanism and Current Challenges. *Front. Pharmacol.* 10, 1–15. doi:10.3389/fphar.2019.01467

Lu, Y., Suh, S. J., Li, X., Liang, J. L., Chi, M., Hwangbo, K., et al. (2012). Citreorosein Inhibits Production of Proinflammatory Cytokines by Blocking Mitogen Activated Protein Kinases, Nuclear Factor-κB and Activator Protein-1 Activation in Mouse Bone Marrow-Derived Mast Cells. *Biol. Pharm. Bull.* 35 (6), 938–945. doi:10.1248/bpb.35.938

Lv, G. P., Meng, L. Z., Han, D. Q., Li, H. Y., Zhao, J., and Li, S. P. (2015). Effect of Sample Preparation on Components and Liver Toxicity of Polygonum Multiflorum. *J. Pharm. Biomed. Anal.* 109, 105–111. doi:10.1016/j.jpba.2015.02.029

Ma, Y. S., Weng, S. W., Lin, M. W., Lu, C. C., Chiang, J. H., Yang, J. S., et al. (2012). Antitumor Effects of Emodin on LS1034 Human colon Cancer Cells *In Vitro* and *In Vivo*: Roles of Apoptotic Cell Death and LS1034 Tumor Xenografts Model. *Food Chem. Toxicol.* 50 (5), 1271–1278. doi:10.1016/j.fct.2012.01.033

Mei-Juan, L. I., Wang, H. S., Wang, T. B., Lai, C., and Leng, C. L. (2018). Effect of Emodin from Polygonum Multiflori Radix Praeparata on JAK2/STAT3 Pathways in ApoE~(-/-) Mice Atherosclerosis Model. *Chin. J. Exp. Tradit. Med. Formulae* 24 (18). doi:10.13422/j.cnki.syfjx.20181823

Park, M. Y., Kwon, H. J., and Sung, M. K. (2009). Intestinal Absorption of Aloin, Aloe-Emodin, and Aloesin; A Comparative Study Using Two *In Vitro* Absorption Models. *Nutr. Res. Pract.* 3 (1), 9–14. doi:10.4162/nrp.2009.3.1.9

Pelkonen, O., Pasanen, M., Tolonen, A., Koskinen, M., Hakkola, J., Abass, K., et al. (2015). Reactive Metabolites in Early Drug Development: Predictive *In Vitro* Tools. *Curr. Med. Chem.* 22 (4), 538–550. doi:10.2174/0929867321666141012175543

Qian, J., Hou, M., Wu, X., Dai, C., Sun, J., and Dong, L. (2020). A Review on the Extraction, Purification, Detection, and Pharmacological Effects of 2,3,5,4'-Tetrahydroxystilbene-2-O-β-D-Glucoside from Polygonum Multiflorum. *Biomed. Pharmacother.* 124, 109923. doi:10.1016/j.biopha.2020.109923

Qi, L. I., Zhao, K. J., and Zhao, Y. L. (2013). High Dosage Administration of Polygonum multiflorum Alcohol Extract Caused the Multi-Organ Injury in Rats. *Global J. Tradit. Chin. Med.* 6 (1), 1–7. doi:10.3969/j.issn.1674-1749.2013.01.001

Reagan-Shaw, S., Nihal, M., and Ahmad, N. (2008). Dose Translation from Animal to Human Studies Revisited. *FASEB J.* 22 (3), 659–661. doi:10.1096/fj.07-9574LSF

Ronghua, Z., Song, M., Wang, W., Lin, P., and Zhao, R. (2016). Chronic Toxicity of Both Raw and Processed Polygoni Multiflori Radix on Rats. *J.Chin.Phram.Sci.* 25 (1), 46–56. doi:10.5246/jcps.2016.01.006

Ruan, L., Li, G., Zhao, W., Meng, H., Zheng, Q., and Wang, J. (2021). Activation of Adenosine A1 Receptor in Ischemic Stroke: Neuroprotection by Tetrahydroxy Stilbene Glycoside as an Agonist. *Antioxidants (Basel)* 10 (7), 1–27. doi:10.3390/ANTIOX10071112

Ruili, Y. U., Men, W., Zhou, K., and Yingli, Y. U. (2019). Research Progress on Toxic Material Basis and Hepatotoxicity Mechanism of Polygonum Multiflorum. *Chin. J. Pharmacovigilance* 16 (8), 496–503. doi:10.19803/j.1672-8629.2019.08.007

Sethuraman, V. S., Leonov, S., Squassante, L., Mitchell, T. R., and Hale, M. D. (2007). Sample Size Calculation for the Power Model for Dose Proportionality Studies. *Pharm. Stat.* 6 (1), 35–41. doi:10.1002/PST.241

Smith, B. P., Vandenhende, F. R., DeSante, K. A., Farid, N. A., Welch, P. A., Callaghan, J. T., et al. (2000). Confidence Interval Criteria for Assessment of Dose Proportionality. *Pharm. Res.* 17 (10), 1278–1283. doi:10.1023/A:1026451721686

Sun, J. H., Yuan, Z. F., Wang, C. Y., Hui-Jun, X. U., and Zhang, L. T. (2005). Pharmacokinetics of Stilbene Glycoside from Polygonum Multiflorum in Rats *In Vivo*. *Chin. Traditional Herbal Drugs* 36 (03), 405–408. doi:10.3321/j.issn:0253-2670.2005.03.034

Sun, F. L., Zhang, L., Zhang, R. Y., and Li, L. (2011). Tetrahydroxystilbene Glucoside Protects Human Neuroblastoma SH-SY5Y Cells against MPP+-induced Cytotoxicity. *Eur. J. Pharmacol.* 660 (2-3), 283–290. doi:10.1016/j.ejphar.2011.03.046

Sun, Y. N., Li, W., Kim, J. H., Yan, X. T., Kim, J. E., Yang, S. Y., et al. (2015). Chemical Constituents from the Root of Polygonum Multiflorum and Their Soluble Epoxide Hydrolase Inhibitory Activity. *Arch. Pharm. Res.* 38 (6), 998–1004. doi:10.1007/s12272-014-0520-4

Tang, W., Li, S., Liu, Y., Huang, M.-T., Ho, C.-T., and Ho, C. T. (2017). Anti-inflammatory Effects of Trans -2,3,5,4′-tetrahydroxystilbene 2- O - β -glucopyranoside (THSG) from Polygonum Multiflorum (PM) and Hypoglycemic Effect of Cis -THSG Enriched PM Extract. *J. Funct. Foods* 34, 1–6. doi:10.1016/j.jff.2017.04.014

Trybus, W., Krol, T., Trybus, E., Stachurska, A., and Krol, G. (2021). The Potential Antitumor Effect of Chrysophanol in Relation to Cervical Cancer Cells. *J. Cell Biochem.* 122 (6), 639–652. doi:10.1002/jcb.29891

U.S. Department of Health and Human Services, Food and Drug Administration, Center for Drug Evaluation and Research, Center for Veterinary Medicine (2018). *Bioanalytical Method Validation Guidance for Industry*. Office of Medical Products and Tobacco, Center for Drug Evaluation and Research Office of Foods and Veterinary Medicine, Center for Veterinary Medicine. Available at: https://www.fda.gov/media/70858/download (February 2, 2022).

Wang, Y., and Yang, X. W. (2008). Intestinal Transport of Free Anthraquinones in Caco-2 Cell Model. *Chin. J. Nat. Medicines* 6 (2), 141–145. doi:10.1016/S1875-5364(09)60012-110.3724/sp.j.1009.2008.00141

Wang, Q. X., Wu, C. Q., Yang, H. L., Jing, S. F., and Liao, M. Y. (2007). Cytotoxicity of free anthraquinone from Radix et Rhizoma Rheito HK-2 Cells. *Chin. J. New Drugs* 16 (03), 189–199. doi:10.3321/j.issn:1003-3734.2007.03.003

Wang, X., Zhao, L., Han, T., Chen, S., and Wang, J. (2008). Protective Effects of 2,3,5,4'-Tetrahydroxystilbene-2-O-Beta-D-Glucoside, an Active Component of Polygonum Multiflorum Thunb, on Experimental Colitis in Mice. *Eur. J. Pharmacol.* 578 (2-3), 339–348. doi:10.1016/j.ejphar.2007.09.013

Wang, C. Y., Guo, D., Yuan, Z. F., Feng, X., and Zhang, L. (2009). Metabolism of Stilbene Glycoside in Rats and *In Vitro*. *Chin. J. Pharm.* 40, 120–123. doi:10.3969/j.issn.1001-8255.2009.02.015

Wang, P., Meng, X. L., Wang, J. R., Liu, H., Yang, Y. M., and Liu, R. (2011). Intestinal Absorption Kinetics of Rhubarb Mixture Free Anthraquinones in Rats. *Lishizhen Med. Materia Med. Res.* 22 (4), 790–792. doi:10.1007/s10008-010-1224-4

Wang, T., Yang, Y. J., Wu, P. F., Wang, W., Hu, Z. L., Long, L. H., et al. (2011). Tetrahydroxystilbene Glucoside, a Plant-Derived Cognitive Enhancer, Promotes Hippocampal Synaptic Plasticity. *Eur. J. Pharmacol.* 650 (1), 206–214. doi:10.1016/j.ejphar.2010.10.002

Wang, Y., Xu, C., Wang, P., Lin, X., Yang, Y., Li, D., et al. (2013). Pharmacokinetic Comparisons of Different Combinations of Shaoyao-Gancao-Decoction in Rats: Simultaneous Determination of Ten Active Constituents by HPLC-MS/MS. *J. Chromatogr. B Analyt Technol. Biomed. Life Sci.* 932, 76–87. doi:10.1016/j.jchromb.2013.06.021

Wang, T., Wang, J. Y., Zhou, Z. X., Jiang, Z. Z., Li, Y. Y., Zhang, L., et al. (2015). Study on Hepatotoxicity of Aqueous Extracts of Polygonum Multiflorum in Rats after 28-day Oral Administration: Cholestasis-Related Mechanism. *Zhongguo Zhong Yao Za Zhi* 40 (11), 2163–2167. doi:10.4268/cjcmm20151118

Wang, M. X., Wang, Y. G., Huan-Hua, X. U., Zhang, Z. Y., Zeng-Chun, M. A., Xiao, C. R., et al. (2016). Effects of Emodin in Polygonum Multiflorum on Liver Cytotoxicity and CYP450 Isoenzymes Expression in L02 Cells. *Chin. Pharmacol. Bull.* 32 (11), 1543–1548. doi:10.3969/j.issn.1001-1978.2016.11.013

Wang, C., Zhou, Y., Gong, X., Zheng, L., and Li, Y. (2020). *In Vitro* and *In Situ* Study on Characterization and Mechanism of the Intestinal Absorption of 2,3,5,4'-Tetrahydroxy-Stilbene-2-O-β-D-Glucoside. *BMC Pharmacol. Toxicol.* 21 (1), 7. doi:10.1186/s40360-020-0384-9

Way, T. D., Huang, J. T., Chou, C. H., Huang, C. H., Yang, M. H., and Ho, C. T. (2014). Emodin Represses TWIST1-Induced Epithelial-Mesenchymal Transitions in Head and Neck Squamous Cell Carcinoma Cells by Inhibiting the β-catenin and Akt Pathways. *Eur. J. Cancer* 50 (2), 366–378. doi:10.1016/j.ejca.2013.09.025

Wu, L., Han, W., Chen, Y., Zhang, T., Liu, J., Zhong, S., et al. (2018). Gender Differences in the Hepatotoxicity and Toxicokinetics of Emodin: The Potential Mechanisms Mediated by UGT2B7 and MRP2. *Mol. Pharm.* 15 (9), 3931–3945. doi:10.1021/acs.molpharmaceut.8b00387

Xiang, K., Liu, G., Zhou, Y. J., Hao, H. Z., Yin, Z., He, A. D., et al. (2014). 2,3,5,4'-tetrahydroxystilbene-2-O-β-D-glucoside (THSG) Attenuates Human Platelet Aggregation, Secretion and Spreading *In Vitro*. *Thromb. Res.* 133 (2), 211–217. doi:10.1016/j.thromres.2013.11.006

Yang, X.-P., Liu, T. Y., Qin, X. Y., and Yu, L. C. (2014). Potential protection of 2,3,5,4'-Tetrahydroxystilbene-2-O-β-D-Glucoside against Staurosporine-Induced Toxicity on Cultured Rat hippocampus Neurons. *Neurosci. Lett.* 576, 79–83. doi:10.1016/j.neulet.2014.05.045

Xing, Y., Wang, L., Wang, C., Zhang, Y., Zhang, Y., Hu, L., et al. (2019). Pharmacokinetic Studies Unveiled the Drug-Drug Interaction between Trans-2,3,5,4'-tetrahydroxystilbene-2-O-β-d-glucopyranoside and Emodin that May Contribute to the Idiosyncratic Hepatotoxicity of Polygoni Multiflori Radix. *J. Pharm. Biomed. Anal.* 164, 672–680. doi:10.1016/j.jpba.2018.11.034

Yang, X., Kang, M. C., Li, Y., Kim, E. A., Kang, S. M., and Jeon, Y. J. (2014). Anti-inflammatory Activity of Questinol Isolated from marine-derived Fungus Eurotium amstelodami in Lipopolysaccharide-Stimulated RAW 264.7 Macrophages. *J. Microbiol. Biotechnol.* 24 (10), 1346–1353. doi:10.4014/jmb.1405.05035

Xie, W., Zhao, Y., and Du, L. (2012). Emerging Approaches of Traditional Chinese Medicine Formulas for the Treatment of Hyperlipidemia. *J. Ethnopharmacol.* 140 (2), 345–367. doi:10.1016/j.jep.2012.01.027

Xu, X. L., Huang, Y. J., Chen, X. F., Lin, D. Y., and Zhang, W. (2012). 2,3,4',5-tetrahydroxystilbene-2-O-β-D-glucoside Inhibits Proliferation of Vascular Smooth Muscle Cells: Involvement of NO/cGMP/PKG Pathway. *Phytother Res.* 26 (7), 1068–1074. doi:10.1002/ptr.3691

Yang, M., Liu, T., Feng, W. H., Hui, L. Q., Li, R. R., Liu, X. Q., et al. (2016). Exploration Research on Hepatotoxic Constituents from Polygonum Multiflorum Root. *Zhongguo Zhong Yao Za Zhi* 41 (7), 1289–1296. doi:10.4268/cjcmm20160721

Yao, W., Fan, W., Huang, C., Zhong, H., Chen, X., and Zhang, W. (2013). Proteomic Analysis for Anti-atherosclerotic Effect of Tetrahydroxystilbene Glucosi- Interaction between Trans-2,3,5,4'-tetrahydroxystilbene-2-O-β-d-glucopyranoside and Emodin that May Contribute to the Idiosyncratic Hepatotoxicity of Polygoni Multiflori Radix. *J. Pharm. Biomed. Anal.* 164, 672–680. doi:10.1016/j.jpba.2018.11.034

Yao, W., Gu, C., Shao, H., Meng, G., Wang, H., Jing, X., et al. (2015). Tetrahydroxystilbene Glucoside Improves TNF-α-Induced Endothelial Dysfunction: Involvement of TGFβ/Smad Pathway and Inhibition of Vimentin Expression. *Am. J. Chin. Med.* 43 (1), 183–198. doi:10.1142/s0192415x15500123

Yuan, T., and Liu, X. (2016). Fleece-Flower Root Extract Diphenylethylene Glycosides in Diabetic Renal Tubular Injury Protection Experimental Study. *Chin. J. Integr. Tradit. West. Nephrol.* 17 (2), 114–118. CNKI:SUN:JXSB.0.2016-02-009.

Zhang, C., Zhang, R. C., and Sun, Z. X. (2013). Study on the Hepatoxicity of Polygoni Multiflori Radix and Polygoni Multiflori Rodix Praeparata in Rats. *Zhong Yao Cai* 36 (9), 1416–1419. doi:10.13863/j.issn1001-4454.2013.09.017

Zhang, M., Lin, L., Lin, H., Qu, C., Yan, L., and Ni, J. (2018). Interpretation the Hepatotoxicity Based on Pharmacokinetics Investigated through Oral Administrated Different Extraction Parts of Polygonum Multiflorum on Rats. *Front. Pharmacol.* 9 (505), 505–513. doi:10.3389/fphar.2018.00505

Zhu, Y., Liu, S. H., Wang, J. B., Song, H. B., Li, Y. G., He, T. T., et al. (2015). Clinical Analysis of Drug-Induced Liver Injury Caused by Polygonum Multiflorum and its Preparations. *Zhongguo Zhong Xi Yi Jie He Za Zhi* 35 (12), 1442–1447. doi:10.7661/CJIM.2015.12.1442

Conflict of Interest: The authors declare that the research was conducted in the absence of any commercial or financial relationships that could be construed as a potential conflict of interest.

Publisher's Note: All claims expressed in this article are solely those of the authors and do not necessarily represent those of their affiliated organizations, or those of the publisher, the editors, and the reviewers. Any product that may be evaluated in this article, or claim that may be made by its manufacturer, is not guaranteed or endorsed by the publisher.

frontiers in Pharmacology

ORIGINAL RESEARCH
published: 16 March 2022
doi: 10.3389/fphar.2022.850859

Liquorice Extract and 18β-Glycyrrhetinic Acid Protect Against Experimental Pyrrolizidine Alkaloid-Induced Hepatotoxicity in Rats Through Inhibiting Cytochrome P450-Mediated Metabolic Activation

*Zhangting Wang[1], Jiang Ma[1], Sheng Yao[2], Yisheng He[1], Kai-Kei Miu[1], Qingsu Xia[3], Peter P. Fu[3], Yang Ye[2] and Ge Lin[1]**

[1]School of Biomedical Sciences, Faculty of Medicine, The Chinese University of Hong Kong, Hong Kong SAR, China, [2]State Key Laboratory of Drug Research and Natural Products Chemistry Department, Shanghai Institute of Materia Medica, Chinese Academy of Sciences, Shanghai, China, [3]National Center for Toxicological Research, U.S. Food and Drug Administration, Jefferson, AR, United States

OPEN ACCESS

Edited by:
Michael Heinrich,
University College London,
United Kingdom

Reviewed by:
Rolf Teschke,
Hospital Hanau, Germany
Mona Abdel Tawab,
Central Laboratory of German Pharmacists, Germany
Dieter Schrenk,
University of Kaiserslautern, Germany

***Correspondence:**
Ge Lin
linge@cuhk.edu.hk

Specialty section:
This article was submitted to Ethnopharmacology, a section of the journal Frontiers in Pharmacology

Received: 08 January 2022
Accepted: 25 February 2022
Published: 16 March 2022

Citation:
Wang Z, Ma J, Yao S, He Y, Miu K-K, Xia Q, Fu PP, Ye Y and Lin G (2022) Liquorice Extract and 18β-Glycyrrhetinic Acid Protect Against Experimental Pyrrolizidine Alkaloid-Induced Hepatotoxicity in Rats Through Inhibiting Cytochrome P450-Mediated Metabolic Activation. Front. Pharmacol. 13:850859. doi: 10.3389/fphar.2022.850859

Misuse of pyrrolizidine alkaloid (PA)-containing plants or consumption of PA-contaminated foodstuffs causes numerous poisoning cases in humans yearly, while effective therapeutic strategies are still limited. PA-induced liver injury was initiated by cytochrome P450 (CYP)-mediated metabolic activation and subsequent formation of adducts with cellular proteins. Liquorice, a hepato-protective herbal medicine, is commonly used concurrently with PA-containing herbs in many compound traditional Chinese medicine formulas, and no PA-poisoning cases have been reported with this combination. The present study aimed to investigate hepato-protective effects of liquorice aqueous extract (EX) and 18β-glycyrrhetinic acid (GA, the primary bioactive constituent of liquorice) against PA-induced hepatotoxicity and the underlying mechanism. Histopathological and biochemical analysis demonstrated that both single- and multiple-treatment of EX (500 mg/kg) or GA (50 mg/kg) significantly attenuated liver damage caused by retrorsine (RTS, a representative hepatotoxic PA). The formation of pyrrole-protein adducts was significantly reduced by single- (30.3% reduction in liver; 50.8% reduction in plasma) and multiple- (32.5% reduction in liver; 56.5% reduction in plasma) treatment of GA in rats. Single- and multiple-treatment of EX also decreased the formation of pyrrole-protein adducts, with 30.2 and 31.1% reduction in rat liver and 51.8 and 53.1% reduction in rat plasma, respectively. In addition, *in vitro* metabolism assay with rat liver microsomes demonstrated that GA reduced the formation of metabolic activation-derived pyrrole-glutathione conjugate in a dose-dependent manner with the estimated IC_{50} value of 5.07 μM. Further mechanism study showed that GA inhibited activities of CYPs, especially CYP3A1, the major CYP isoform responsible for the metabolic activation of RTS in rats. Enzymatic kinetic study revealed a competitive inhibition of rat CYP3A1 by GA. In conclusion, our findings demonstrated that both EX and GA exhibited significant hepato-protective effects against RTS-induced hepatotoxicity, mainly through the competitive inhibition of CYP-mediated metabolic activation of RTS.

Keywords: 18β-glycyrrhetinic acid, pyrrolizidine alkaloid, cytochrome P450, metabolic activation, competitive inhibition

INTRODUCTION

Pyrrolizidine alkaloids (PAs) are one of the most significant groups of phytotoxins widely presented in various plant species (He et al., 2021a). More than 660 PAs and their *N*-oxides have been identified in over 6,000 plants, which account for 3% of flowering plants (Dusemund et al., 2018; Schrenk et al., 2020). In addition, more than half of the identified PAs and their *N*-oxides have been reported to be hepatotoxic, carcinogenic, pneumotoxic, neurotoxic, and embryotoxic (Fu, 2017). PAs require metabolic activation in the liver to exert toxicity. Mediated by hepatic cytochrome P450 (CYPs), three toxic types (retronecine-type, heliotridine-type, and otonecine-type) of PAs generate reactive metabolites, dehydropyrrolizidine alkaloids (DHPAs), which form adducts with proteins (pyrrole-protein adducts) and cause dysfunction of critical proteins, thus damaging hepatic sinusoidal endothelial cells and leading to hepatotoxicity (**Figure 1**) (Ruan et al., 2014; Yang et al., 2016; Geburek et al., 2020; He et al., 2021b; Geburek et al., 2021). Among all CYP subfamilies, CYP3A and CYP2B isoforms have been identified as the major subfamily responsible for the metabolic activation of toxic PAs (Ruan et al., 2014). Alteration of activity of CYP3A subfamily, especially CYP3A4 isoenzyme, was reported to significantly affect the outcome of PA intoxication. For instance, phenobarbital, a CYP3A isozymes inducer, enhanced metabolic activation of riddelliine (a retronecine-type PA) and then increased the riddelliine-induced liver toxicity (Kasahara et al., 1997). In addition, the human CYP3A4-overexpressed Madin Darby Canine Kidney (MDCK) cells were more susceptible to monocrotaline (a retronecine-type PA) compared to mock MDCK cells, due to the increased metabolic activation of monocrotaline (Tu et al., 2014).

PA-poisoning cases have been constantly reported across the world (Willmot and Robertson, 1920; Tandon et al., 1976; Zhuge et al., 2019; Ma et al., 2021; Zhu et al., 2021). Humans are exposed to PAs through misuse of PA-containing herbs (Dai et al., 2007; Yang et al., 2017) or PA-contaminated foodstuffs such as grains, honey, milk, and eggs (Mohabbat et al., 1976; Dussourd et al., 1989; Kakar et al., 2010; Bodi et al., 2014). Intake of high amounts of toxic PAs injured the protein membranes of hepatocytes, particularly liver sinusoidal endothelia cell (SECs), leading to life-threatening hepatic sinusoidal obstruction syndrome (HSOS), which presented with clinical manifestations such as tender hepatomegaly, hyperbilirubinemia, and ascites (Deleve et al., 2002; Gao et al., 2012; Teschke et al., 2021). This injury is confirmatively diagnosed by blood pyrrole-protein adducts, which are specific diagnostic biomarkers, supporting the causality evaluation using the updated Roussel Uclaf Causality Assessment Method (RUCAM) (Danan and Teschke, 2016; Teschke and Danan, 2020). Furthermore, our recent study discovered an unexpectedly extensive implication of PA exposure in patients with liver cancer, providing a clinical indication of PA-associated liver cancer (He et al., 2021c).

Liquorice (Glycyrrhizae radix et rhizome), the roots of *Glycyrrhiza uralensis* Fisch., *Glycyrrhiza glabra* L. or *Glycyrrhiza inflate* Bat., has long been used as a tonic herbal medicine in traditional Chinese medicine (TCM) due to its ability to harmonize unpleasant characteristics of other herbs or reduce the toxicities of certain herbs when used together in the herbal formulas (Wang et al., 2013; Wahab et al., 2021). In China, although there are no reports on the scientific rationale, liquorice is presented with PA-containing herbs in TCM compound formulas, yet no PA-poisoning cases have been reported with this combinational use. For example, Nin Jiom Pei Pa Koa, a very popular herbal formula used in Chinese communities worldwide for relief of minor discomfort in sore mouth/throat, contains both coltsfoot (a PA-containing herb) and liquorice. In addition, in Pharmacopeia of P.R. China (ChP 2020 Edition) six PA-containing herbs are listed and used in the preparation of many Chinese proprietary herbal products, and among them, 16 out of 35 are found to contain liquorice (**Table 1**). Furthermore, in the medical encyclopedia database, 68 compound TCM formulas and 12 TCM proprietary products were found to contain PA-containing herbs, and ~53% of compounded TCM formulas and ~25% of the TCM proprietary products contained liquorice, respectively (**Table 1**), suggesting the potential role of liquorice in detoxifying/harmonizing PA intoxication.

Liquorice extract contains sugar, starch, resins, low levels of protein, and individual amino acids. Triterpene saponins and flavonoids are the main constituents isolated from *Glycyrrhiza* species. Glycyrrhizin (GL) is the predominant constituent of liquorice and biotransformed to its aglycone 18β-glycyrrhetinic acid (GA) in the body, and thus, GA has been confirmed as the primary bioactive form *in vivo* (Öztürk et al., 2017). Both GL and GA were reported to protect the livers from damages caused by carbon tetrachloride (Lee et al., 2007) and acetaminophen (Yan et al., 2016). Therefore, it is highly possible that liquorice may antagonize the toxic effects of PAs and relieve any potential liver damage caused by PAs. In the present study, we investigated the hepato-protective effect of liquorice extract (EX) and its primary bioactive ingredient GA on liver damage caused by retrorsine (RTS, a representative toxic PA) and delineated the underlying mechanism, in order to provide a scientific basis for the use of liquorice and/or GA as the antidote(s) for the prevention/detoxification of PA-induced liver injury.

MATERIALS AND METHODS

Chemical and Reagents

RTS and GA (G10105, 97%) were purchased from Sigma-Aldrich Chemical Co. (St. Louis, MO, United States). Cocktail substrate and metabolite standards, NADPH tetrasodium salt, glucose-6-phosphate dehydrogenase (G-6-PD), glutathione (GSH), and all other chemicals, unless indicated, were purchased from Sigma-Aldrich Chemical Co. (St. Louis, MO, United States). Pyrrole-GSH conjugate, 7,9-diGSH-(±)-6,7-dihydro-7-hydroxy-1-

hydroxymethyl-5*H*-pyrrolizine (7,9-diGS-DHP), was prepared as previously reported (Lin et al., 2000; Ma et al., 2015). HPLC-grade ethanol, acetone, formic acid, and acetonitrile were purchased from Merck (Darmstadt, Germany). Anti-CYP3A1 antibody was purchased from Santa Cruz Biotechnology (sc-53246, Santa Cruz, CA, United States). Horseradish peroxidase-conjugated goat anti-rabbit and goat anti-mouse were purchased from Cell Signaling Technology Inc. (Danvers, MA, United States). Anti-RECA-1 antibody (ab197727) and Alexa Fluor 488-conjugated goat anti-mouse IgG (ab150117) were supplied by Abcam (Cambridge, MA, United States).

Preparation of Liquorice Aqueous Extract

Liquorice aqueous extract prepared from the root of *Glycyrrhizae glabra* L. (No. LC151018) was collected from Kazakhstan in Oct. 2015 and dried at 55°C for 12 h, and then authenticated by the co-author Prof. Yang YE's group. The dried root of liquorice was extracted three times by refluxing with water (1:5 w/v) for 2 h per time. The water extract was then combined and lyophilized to provide liquorice extract (EX). EX was accurately weighed, completely dissolved in distilled water, and analyzed by HPLC-UV. The HPLC-UV analysis was performed on an Agilent 1100 liquid chromatograph system (Agilent Technologies, Inc., Palo Alto, United States). The chromatographic separation was performed on an Agilent C18 (4.6 × 250 mm, Shodex, Tokyo, Japan) column. The mobile phase was a mixture of water containing 1% formic acid (A) and acetonitrile (B), with a gradient elution as follows: 0–15 min, 75% A; 15–25 min, 25% A; 25–35 min, 75% A. The flow rate was set at 1 ml/min. The detection wavelength was 254 nm, and the injection volume was 20 μL. A representative HPLC-UV chromatogram of EX is shown in **Supplementary Figure S1**. The obtained EX was stored at -20°C before use.

Animals and Treatments

Male Sprague Dawley rats (about 200–220 g) were supplied by the Laboratory Animal Service Centre at the Chinese University of Hong Kong. The animal room was maintained at 25 ± 1°C with a 12-h light-dark cycle and 55 ± 5% humidity. The rats had free access to standard rodent chow and water. All procedures were approved by the Animal Experimental Ethics Committee, the Chinese University of Hong Kong under the regulations of Hong Kong SAR government.

Rats were randomly divided into the following twelve groups: 1 and 2) Single- or Multiple-dose of distilled water groups (Vehicle), 3 and 4) Single-dose of RTS groups (RTS), 5 and 6) Single- or Multiple-dose of EX groups (SD-EX and MD-EX), 7 and 8) Single- or Multiple-dose of GA groups (SD-GA and MD-GA), 9) Single-dose of EX + RTS group (RTS-SD-EX), 10) Multiple-dose of EX + RTS group (RTS-MD-EX), 11) Single-dose of GA + RTS group (RTS-SD-GA), and 12) Multiple-dose of GA + RTS group (RTS-MD-GA). EX and GA were dissolved in distilled water at 37°C for oral administration with the dosage of EX and GA as 500 mg/kg and 50 mg/kg. RTS was dissolved in distilled water at room temperature to make the final concentration of 40 mg/kg. RTS was given following the last dose of distilled water/GA/EX. Detailed dosage regimens are described in **Supplementary Figure S2**. All rats were sacrificed at 48 h after the last dosing. Serum and liver samples were collected and stored at −80°C until use. The dose of RTS chosen for this study was based on our previous findings in that 40 mg/kg of RTS caused significant acute liver injury with moderate to severe SECs damage in male SD rats (Chen et al.,

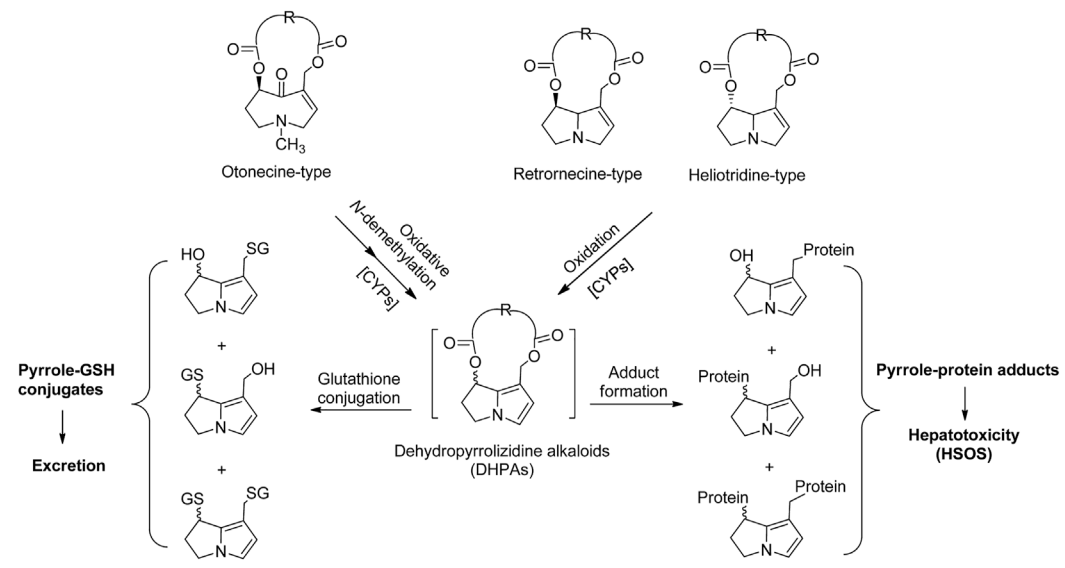

FIGURE 1 | The scheme of hepatic metabolic activation of retronecine-, heliotridine-, and otonecine-type PAs to form dehydropyrrolizidine alkaloids (DHPAs), which either bind with glutathione as a detoxification pathway, or interact with proteins to generate pyrrole-protein adducts, leading to liver damage.

TABLE 1 | Percentage of liquorice in PA-containing TCM proprietary products and Compound TCM formulas.

PA-containing botanical drug	TCM proprietary products in ChP 2020			TCM proprietary products in medical encyclopedia database			Compound TCM formulas in medical encyclopedia database		
	Liquorice		Percentage[a]	Liquorice		Percentage[a]	Liquorice		Percentage[a]
	−	+		−	+		−	+	
Senecionis scandentis hebra	4	0	0	7	1	14.3%	11	3	27.3%
Farfarae flos	14	12	85.7%	4	2	50.0%	19	14	73.7%
Eupatorii herba	2	0	0	1	0	0	16	3	18.8%
Arnebiae radix	8	3	37.5%	/	/	/	22	16	72.7%
Arnebiae radix[b]	7	1	14.3%	/	/	/	/	/	/
Total	35	16	45.7%	12	3	25.0%	68	36	52.9%

[a]*The percentage of liquorice present in TCM, proprietary products/Compound TCM, formulas having PA-containing herbs.*
[b]*The herb is for external use.*

2021). According to the intake of the Compound Glycyrrhizin Tablets (containing 25 mg GL/per tablet), the suggested daily intake of GL is 225 mg/day for humans, which is approximately 20 mg/kg/day GA for rats. In our experiments, we used 50 mg/kg/day GA and 500 mg/kg/day EX (suggested daily intake of 5–20 g of liquorice root) for 5 consecutive days, which is close to the normal dose and has also been reported in many publications (Lin et al., 1999; Zhang et al., 2019; Yan et al., 2021).

For the toxicokinetic study, jugular vein cannulation was performed on rats on the day before drug administration. The right jugular vein was cannulated with a polyethylene tube (0.4 mm i.d. × 0.8 mm o.d., SIMS Portex, United Kingdom) for blood sampling. The rats were maintained in individual metabolic cages and fasted overnight with free access to water. Rats were orally dosed with GA (50 mg/kg) or distilled water (<5 ml/kg) 2 hours prior to RTS (30 mg/kg). After RTS dosing, blood samples (about 0.2 ml/sample) were collected at 5, 10, 20, 40, 60, 120, 240, 360, 480, 720, and 1440 min and placed in heparinized tubes. Saline (0.2 ml) containing 25 units of heparin/mL was injected after each blood sampling for compensation of blood withdrawal. The blood samples were then centrifuged at 3,000 x g for 30 min, and plasma samples were harvested and stored at −20°C until use.

Histological and Biochemical Analysis

The largest lobe of the liver was sliced, fixed in 10% buffered-neutral formalin for 24 h, and embedded in wax. Sections of 5 μm in thickness were subjected to hematoxylin and eosin staining before being examined. Liver injury (necrosis, endothelial cell damage, and hemorrhage) was evaluated with a LEICA DM5000B Microscope (Leica, Heidelberg, Germany).

The serum alanine transaminase (ALT) level was measured by a kit obtained from Sigma-Aldrich Chemical Co. (St. Louis, MO, United States). The total bilirubin level was measured by the QuantiChromTM Bilirubin Assay kit according to the manufacturer's instructions (BioAssay Systems, Hayward, CA, United States). Hepatic malondialdehyde (MDA) level was measured using a kit obtained from Nanjing Jiancheng Bioengineering Institute (Nanjing, China). Total GSH content in the liver was measured following a standard spectrophotometric method using Ellaman's reagent.

Immunofluorescence of Rat Endothelial Cell Antigen-1

The largest lobe of the rat liver was sliced, cold-embedded in Tissue-Tek OCT compound, and processed for immunohistochemistry according to the Abcam IHC frozen sections staining protocol. The tissue slices were incubated with rat endothelial cell antigen (RECA)-1 antibody and Alexa Fluor 488-conjugated goat anti-mouse IgG, and then stained with DAPI and observed under Olympus FluoViewTM FV1000 confocal microscope.

Quantification of Pyrrole-Protein Adducts, 7,9-diGS-DHP, and RTS

The pyrrole-protein adducts were measured according to our previously developed method (Lin et al., 2011; Ruan et al., 2014). Briefly, 50 mg liver or 100 μL serum/plasma was mixed with acetone and centrifuged at 900 x g for 10 min. The precipitated protein was treated with silver nitrate (20 mg/ml) in ethanol containing 5% trifluoroacetic acid to release pyrrole moiety from the pyrrole-protein adducts. After centrifugation, an aliquot of the supernatant was incubated with 4-dimethylaminobenzaldehyde (20 mg/ml) at 56°C for 10 min. The mixture was filtered and subjected to LC-MS/MS analysis. 7,9-diGS-DHP was used as a standard with a concentration ranging from 0.2 to 2000 nM and underwent the same preparation process to construct a calibration curve. To measure the concentration of RTS and 7,9-diGS-DHP, liver, serum, plasma samples, or the incubation mixture were mixed with five volumes of acetone (for liver samples) or three volumes of acetonitrile (for serum and plasma samples) to precipitate the proteins. After centrifuging at 20,000 x g for 30 min, the supernatants were collected and analyzed by LC-MS/MS according to our previously developed methods (Ma et al., 2019; He et al., 2021a; Ma et al., 2021).

Effects of GA on the Formation of 7,9-diGS-DHP and Different CYP Activities

To determine the effect of GA on the formation of pyrrole-GSH conjugate (7,9-diGS-DHP), GA (0, 2.5, 5, 10, 30, 50, and 80 μM, prepared in DMSO) or ketoconazole (KCZ, 25 μM, prepared in DMSO) was incubated with 200 μM RTS in the incubation mixture containing 1 mg/ml rat liver microsomes, 1 mM $NADP^+$, 10 mM G-6-P, 5 mM $MgCl_2$, 2 mM GSH, 1 U/ml G-6-PD and potassium phosphate buffer (0.1 M, pH 7.4). The reaction was initiated by adding RTS and stopped with the addition of ice-cold acetonitrile after 120 min incubation at 37°C. The mixtures were centrifuged, and supernatants were analyzed by LC-MS/MS.

A reported cocktail assay (Otten et al., 2011) was used for evaluating the effect of GA on different CYP activities by LC-MS/MS with high sensitivity and selectivity. The concentrations of probe substrates were listed in **Supplementary Table S1**. Various concentrations of GA (0, 2.5, 5, 10, 30, 50, and 80 μM) were added to the reaction mixture containing mixed CYPs probe substrates, NAPDH-regenerating system (5 mM $MgCl_2$, 1 mM $NADP^+$, 1 mM G-6-PD), and 1 mg/ml rat liver microsomes.

Enzymatic Kinetic Study

The kinetic study was performed to determine the inhibitory mechanism of GA on rat CYP3A1. Briefly, GA (0, 10, 25 and 50 μM) was incubated in 200 μL incubation system containing 1 mg/ml rat liver microsomes, 5 mM $MgCl_2$, 1 mM $NADP^+$, 1 mM G-6-PD, and nifedipine (0.1, 0.5, 1, 2, 5, 10, 20, 50, 100, and 200 μM). The mixture was pre-incubated at 37°C for 15 min. The reaction was initiated by adding nifedipine for 45 min incubation at 37°C, and then quenched with ice-cold acetonitrile and centrifuged at 15,000 x g for 20 min. The supernatant was filtered through a 0.22 μm membrane filter before the LC-MS/MS analysis.

LC-MS/MS Analysis

The LC-MS/MS analysis was performed on an Agilent 6460 Triple Quadrupole LC/MS System using a Waters Acquity BEH C18 column (2.1 × 100 mm, 1.7 mm). For the detection of pyrrole-protein adducts, the mobile phase of water containing 0.1% formic acid (A) and acetonitrile containing 0.1% formic acid (B) was used with a gradient elution as follows: 0–5 min, 35–95% B; 5.5–6 min, 95–35% B. The flow rate was 0.3 ml/min. The injection volume was 3 μL. For the detection of pyrrole-GSH conjugates and RTS, a gradient elution was used as follows: 0–1 min, 2% B; 1–7 min, 2–25% B, 7–7.5 min, 25–95% B. 7.5–10 min, 95% B. The flow rate was 0.3 ml/min. The injection volume was 5 μL. The mass spectrometer was operated in multiple reactions monitoring for data acquisition. The multiple reaction monitoring (MRM) transitions, fragmentor, and collision energy for 7,9-diGS-RTS, RTS, and pyrrole-protein adducts are listed in **Supplementary Table S1**.

For the cocktail assay, a gradient elution was used as follows: 20% A (0–1 min), 20–95% A (1–4 min), 95% A (4–6 min). The MRM transitions and linearity information for each substrate are indicated in **Supplementary Table S2**. The calibration curves of individual CYP substrates and their corresponding metabolites were constructed by plotting the peak area versus the spiked concentration.

Immunoblot Analysis

Proteins were separated by gel electrophoresis and electrophoretically transferred to nitrocellulose paper. The nitrocellulose paper was then incubated with rat CYP3A1 antibody (1:1000) overnight and then reacted with horseradish peroxidase-conjugated secondary antibody. Bands were developed using an ECL chemiluminescence detection kit. Equal loading of proteins was verified by GAPDH. The semi-quantification of each band was measured by ImageJ software.

Statistical Analysis

Data are expressed as mean ± SD. The Student's *t* test was used for the comparison between two groups. The one-way ANOVA followed with a post hoc Bonferroni's multiple comparison test was used for the comparison among multiple groups. Toxicokinetic parameters were calculated by noncompartmental methods using WinNonlin version 4.0 (Pharsight, Mountain View, CA, United States). The enzyme kinetic parameters were estimated from the best fit line using least-squares linear regression of the inverse substrate concentration versus the inverse velocity (Lineweaver-Burk plots), and the mean values were used to calculate the K_m and V_{max}. The inhibition constant (K_i) value of GA was determined by the secondary Lineweaver-Burk plots. The statistical significance was set as $^*p < 0.05$, $^{**}p < 0.01$ or $^{***}p < 0.001$.

RESULTS

EX and GA Protected Rats From RTS-Induced Liver Injury

Compared with the vehicle groups, serum ALT and hepatic MDA levels were unchanged after both single and multiple administrations of EX and GA but elevated significantly at 48 h after RTS treatment. While a single dose of GA significantly reduced RTS-induced ALT and MDA elevations (**Figures 2A,C**), the multiple doses of both EX and GA also significantly attenuated these RTS-induced elevations (**Figures 2B,D**). In addition, hepatic GSH level increased significantly (2.82-fold, $p < 0.001$) at 48 h after RTS dosing as a feedback response to the activation of the antioxidant system, while this elevation was attenuated by the treatment of both EX and GA, especially their multiple dosage regimens (**Figures 2E,F**).

Protective effects of EX and GA on RTS-induced hepatotoxicity were also evaluated by histopathological examination. No obvious liver damage was observed in rats treated with EX or GA alone (**Figures 3A,B**). A single dose of RTS caused severe hepatotoxicity in rats, as demonstrated by

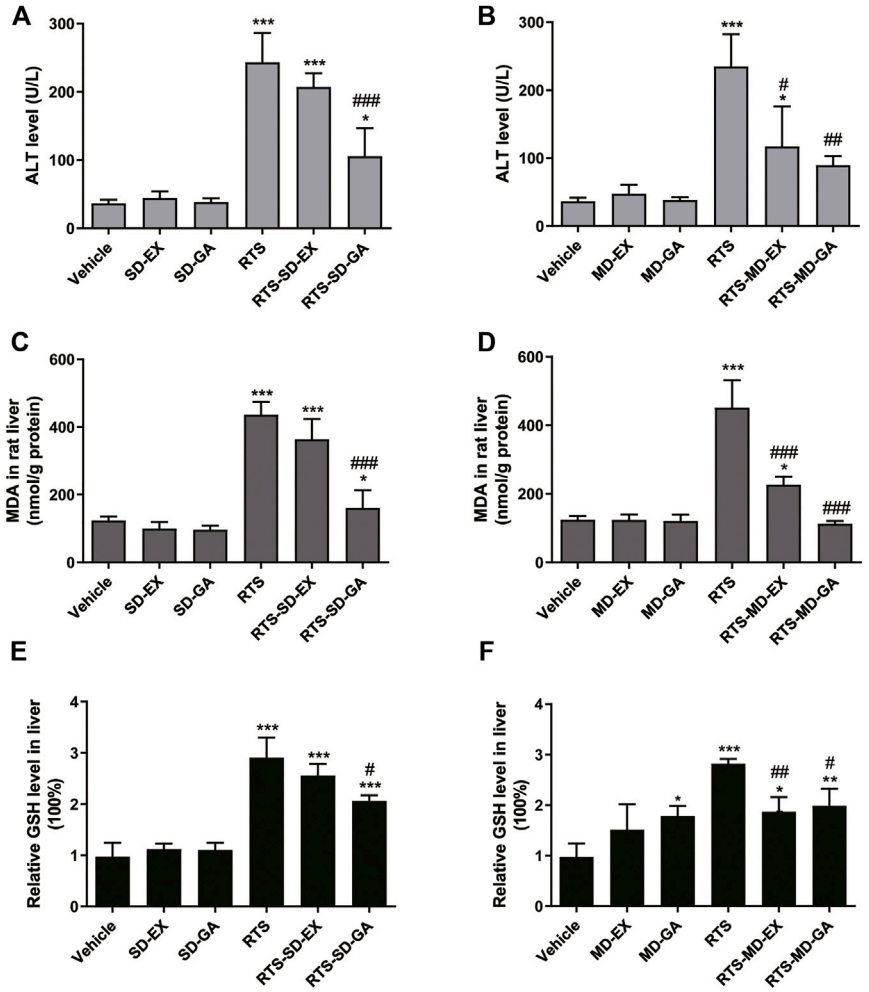

FIGURE 2 | Single-dose (SD) and multiple-dose (MD) of EX or GA protected against RTS-induced liver injury. The activity/levels of serum ALT **(A,B)**, hepatic MDA **(C,D)**, and GSH **(E,F)** were measured in each group. ALT, alanine aminotransferase; MDA, malondialdehyde; GSH, glutathione. $^{*}p < 0.05$, $^{**}p < 0.01$, and $^{***}p < 0.001$ versus vehicle group. $^{\#}p < 0.05$, $^{\#\#}p < 0.01$, and $^{\#\#\#}p < 0.001$ *vs*. the corresponding RTS group.

massive hemorrhage and hepatocytes necrosis observed in the liver sections, whereas both single and multiple doses of EX or GA significantly ameliorated RTS-induced hemorrhage and necrosis (**Figure 3A**). The damage of sinusoidal endothelial cells was further measured by the immunofluorescence of RECA-1. Sinusoids, tightly distributed around central veins, were markedly damaged by RTS, and the injured sinusoids merged to form a large space with wide gaps among individual sinusoids, while this damage was significantly less in EX or GA treated groups (**Figure 3B**). The degrees of hemorrhage, sinusoidal dilation, and necrosis were assessed and scored (**Table 2**) according to a modified DeLeve's system (Deleve et al., 1999) as summarized in **Supplementary Table S3**. All these biochemical and histopathological results clearly demonstrated that both EX and GA produced similar hepato-protective effects against PA-induced liver toxicity. Considering the individual hepato-protective effect of EX or GA multiple treatments exhibited a better protective effect than the single treatment scenario.

EX and GA Inhibited the Formation of Pyrrole-Protein Adducts

The formation of pyrrole-protein adducts is a critical initiating event of RTS-induced hepatotoxicity. As shown in **Figure 4**, the formation of pyrrole-protein adducts in the liver was significantly reduced by both single (**Figure 4A**) and multiple (**Figure 4B**) treatments with GA and EX to similar levels. Similarly, the serum pyrrole-protein adducts levels were also significantly reduced with the treatment of EX and GA in both single and multiple treatments to the same extent (**Figures 4C,D**). The following studies to delineate the mechanism underlying protective effect on RTS-induced hepatotoxicity were carried out with GA that is reported as the primary bioactive form *in vivo* (Öztürk et al., 2017).

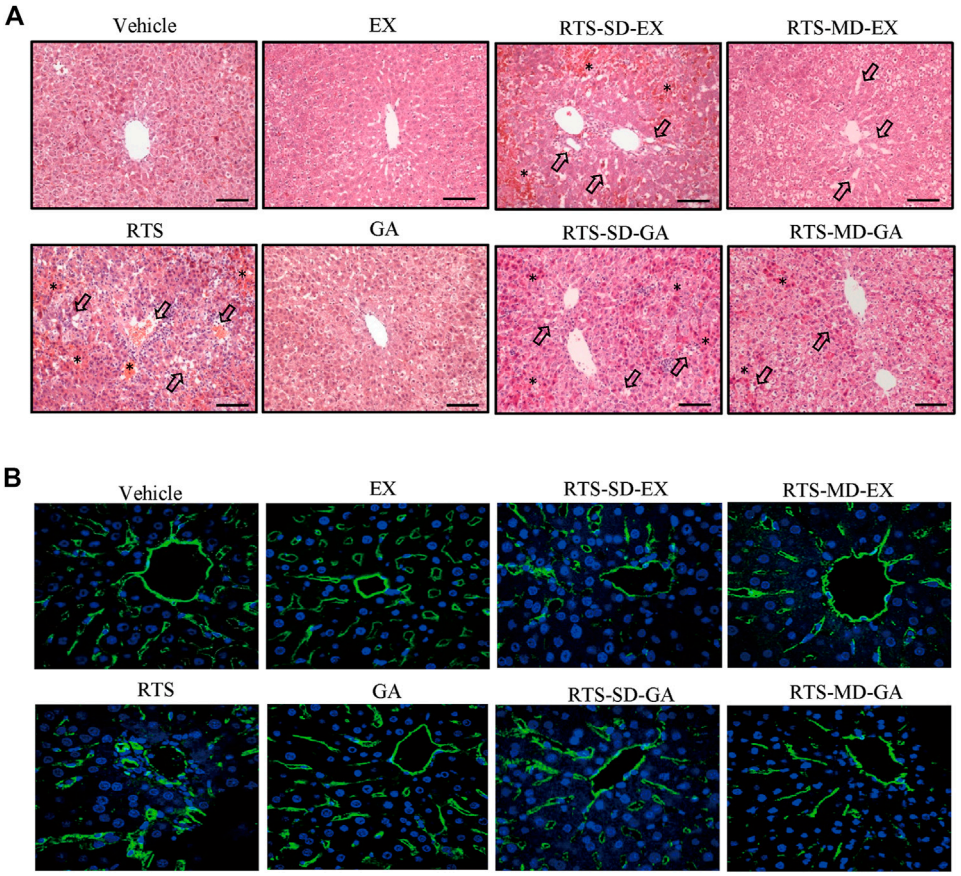

FIGURE 3 | Single-dose and multiple-dose of EX or GA protected against RTS-induced liver damage. **(A)** Hematoxylin and eosin staining of liver. Arrows indicate the necrosis of hepatocytes. *, hemorrhage; black scale bar, 100 μm. **(B)** Immunostaining of RECA-1 in liver sections. Sinusoidal endothelial cells (SECs) in central vein and pericentral area were immunostained with anti-endothelial cell antibody (green), nucleus stained with DAPI (blue).RECA-1, rat endothelial cell antigen-1.

TABLE 2 | Histological scoring of liver damage in the study of protective effect of EX and GA against RTS intoxication.

Group	Scoring parametersa								Overallb
	Central vein endothelial damage	Subendothelial hemorrhage	Sinusoidal hemorrhage	Sinusoidal dilation	Coagulative necrosis	Apoptotic bodies	Subendothelial fibrosis	Sinusoid fibrosis	
Vehicle	0	0	0	0	0	0	0	0	0
EX	0	0	0	0	0	0	0	0	0
GA	0	0	0	0	0	0	0	0	0
RTS	2-3	2-3	2	2-3	2	1	0	0	11-14
RTS-SD-EX	2-3	2	2	2	1-2	0	0	0	9-11
RTS-MD-EX	2	2	1	2	1	0	0	0	8
RTS-SD-GA	1	1-2	1	2	1	0	0	0	6-7
RTS-MD-GA	1	0-1	0-1	1-2	0	0	0	0	2-5

[a]*Each parameter is graded on a four-point system: 0-absent, 1-mild, 2-moderate, and 3-severe.*
[b]*Overall represents the sum of the scores from all individual parameters.*

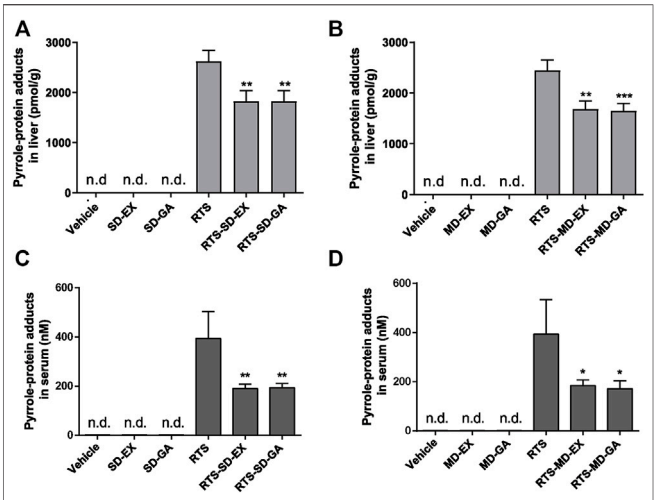

FIGURE 4 | Single-dose and multiple-dose of EX or GA inhibited metabolic activation of RTS both *in vivo* and *in vitro*. Formation of pyrrole-protein adducts in the liver **(A,B)** and serum **(C,D)** in rats. Data are expressed as mean ± SD ($n = 4$). *$p < 0.05$, **$p < 0.01$, and ***$p < 0.001$ versus the corresponding RTS group.

For the study of the effect of GA on the toxicokinetic profile of RTS, rats treated with a single dose of GA and RTS exhibited significantly higher plasma C_{max} (4806.31 ± 133.74 ng/ml *vs*. 3188.07 ± 144.65 ng/ml, $p < 0.001$) and $AUC_{0-1440min}$ (341.52 ± 7.57 min×μg/mL *vs*. 234.49 ± 34.07 min×μg/mL, $p < 0.05$) of RTS compared to the group treated with RTS alone (**Figure 5A**). In addition, the kinetic profile of pyrrole-protein adducts revealed an inhibitory effect of GA on the formation of pyrrole-protein adducts (**Supplementary Table S4**). In RTS + GA group, GA significantly reduced $AUC_{0-1440min}$ of pyrrole-protein adducts to 856.49 ± 11.05 min × μM (16.2% reduction) compared to that (1022.49 ± 11.05 min × μM) in RTS group (**Figure 5B**). The results indicated that GA significantly inhibited the metabolic activation of RTS, leading to the reduced formation of pyrrole-protein adducts in rats.

Furthermore, the *in vitro* incubation with rat liver microsomes was also performed to confirm the inhibitory effect of GA on the metabolic activation of RTS. The dehydro-RTS, produced from metabolic activation of RTS by rat liver microsomes, was trapped by GSH to form pyrrole-GSH conjugate (7,9-diGS-DHP), since our previous study demonstrated that pyrrole mono-GSH adducts could not be detected in the blood of rats dosed with RTS (Lian W. and Lin G. 2017). The formation of 7,9-diGS-DHP after co-incubation with GA or ketoconazole (KCZ, CYP3A1 inhibitor) was then detected. GA significantly inhibited the formation of 7,9-diGS-DHP in a concentration-dependent manner with the estimated IC_{50} value of 5.07 μM, while in parallel, the concentration of intact RTS increased along with the concentration of GA (**Figure 5C**). In addition, the formation of 7,9-diGS-DHP was significantly reduced by 62% with the co-incubation of KCZ (25 μM) (**Figure 5C**). All the results confirmed that GA significantly inhibited metabolic activation of RTS, and thus reduced the production of toxic metabolite dehydro-RTS evidenced by the decreased formation of 7,9-diGS-DHP.

GA Inhibited Activity Rather than Expression of CYPs

It is well-known that metabolic activation of PAs is mediated by hepatic CYPs, thus the effects of GA on the activity and protein expression of CYPs were determined by the cocktail assay. The results showed that GA inhibited the activities of rat CYPs, in particular CYP3A1, CYP2A2, and CYP2B2 (**Figure 6**). CYP3A1 (homologue to human CYP3A4), the predominant CYP isoform responsible for the metabolic activation of RTS, was inhibited by GA in a concentration-dependent manner with 68.5% inhibition at the highest concentration (80 μM) of GA tested (**Figure 6A**). For other tested CYPs which play minor roles in the metabolism of RTS (Ruan et al., 2014), the activities of CYP2A2 and CYP2B2 were also reduced by GA (**Figures 6B,C**), while the activities of CYP2C11 and CYP2D1 were not altered by GA (**Figures 6D,E**). Furthermore, the effect of GA on protein expression of CYP3A1 was tested in rats, and the results revealed that multiple oral administration of GA once a day for 5 consecutive days did not affect the protein expression level of rat hepatic CYP3A1 (**Figure 6F**), further confirming that only the activity but not expression of CYP3A1 could be inhibited by GA.

GA Competitively Inhibited Enzyme Activity of CYP3A1

To further explore the inhibitory mechanism of GA towards CYP3A1, an enzyme kinetic study was performed using nifedipine as the probe substrate for rat CYP3A1. The results from the Michaelis-Menten curve (**Figure 7A**) demonstrated that GA inhibited CYP3A1-mediated nifedipine metabolism with K_m value increased along with the increase in GA concentrations (**Figure 7C**). Furthermore, the Lineweaver-Burk plot (**Figure 7B**) indicated that GA concentration-dependently altered the slope but did not affect the *Y*-intercept, and the slope of each curve correlated well with the concentration of GA ($R^2 = 0.9952$) with K_i value of 8.52 μM (**Figure 7B**). All the results demonstrated that GA competitively inhibited the enzyme activity of CYP3A1.

DISCUSSION

Liquorice has been widely used in TCM for thousands of years to ameliorate liver damage associated with a number of clinical disorders. One of the most important known components of liquorice extract is GL, which has been explicitly recommended as a hepatoprotective drug by several guides (Wu et al., 2021; Wu et al., 2008). When GL is hydrolyzed, almost 100% of GL is irreversibly transformed into 18β-GA in the gastrointestinal tract by bacterial *β-D*-glucuronidase after it is orally administrated (Takeda et al., 1996). Therefore, GA is the main metabolite of GL and the main active component of liquorice after oral administration. In the present study, we found that both single and multiple doses of EX or GA exerted protective effects against

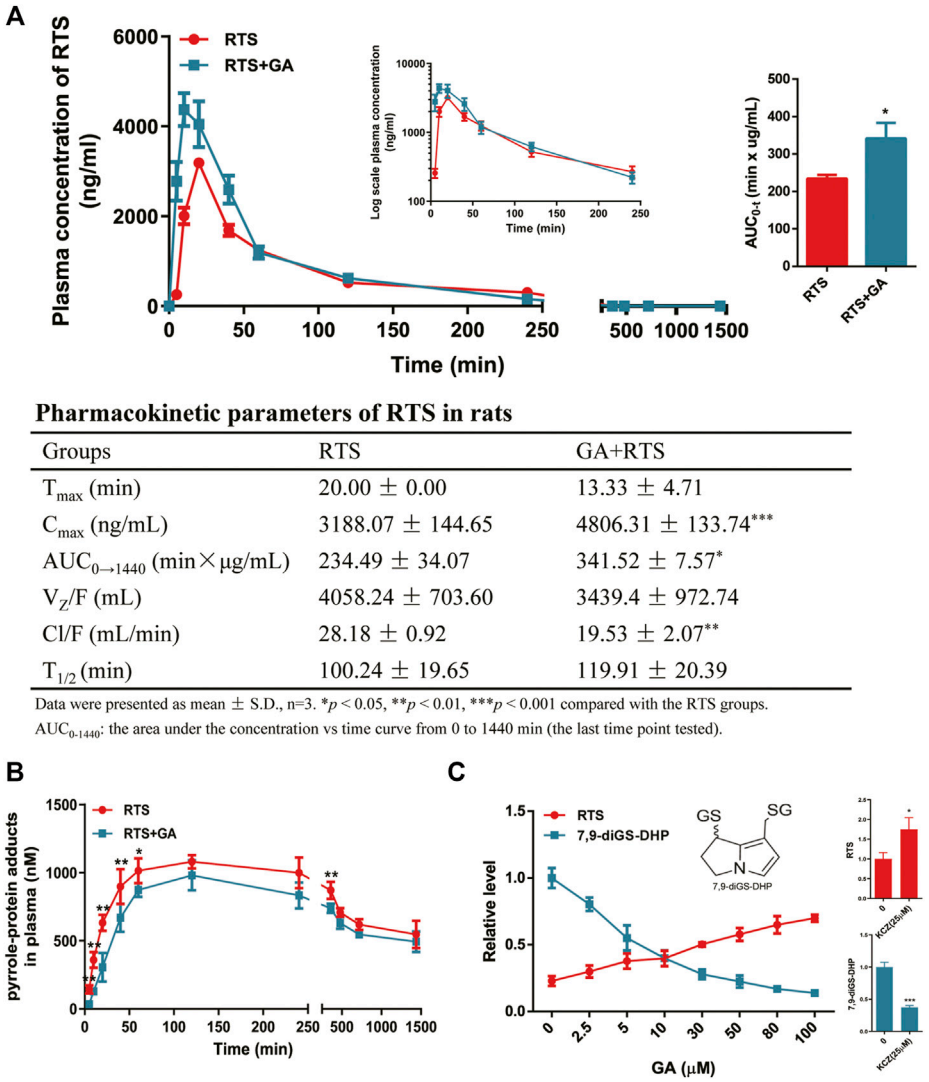

Pharmacokinetic parameters of RTS in rats

Groups	RTS	GA+RTS
T_{max} (min)	20.00 ± 0.00	13.33 ± 4.71
C_{max} (ng/mL)	3188.07 ± 144.65	4806.31 ± 133.74***
$AUC_{0\rightarrow1440}$ (min×μg/mL)	234.49 ± 34.07	341.52 ± 7.57*
V_Z/F (mL)	4058.24 ± 703.60	3439.4 ± 972.74
Cl/F (mL/min)	28.18 ± 0.92	19.53 ± 2.07**
$T_{1/2}$ (min)	100.24 ± 19.65	119.91 ± 20.39

Data were presented as mean ± S.D., n=3. *$p < 0.05$, **$p < 0.01$, ***$p < 0.001$ compared with the RTS groups.
$AUC_{0\text{-}1440}$: the area under the concentration vs time curve from 0 to 1440 min (the last time point tested).

FIGURE 5 | GA inhibited metabolic activation of RTS both *in vivo* and *in vitro*. Plasma kinetic profiles, AUC, and pharmacokinetic parameter of RTS **(A)** and plasma kinetic profiles of pyrrole-protein adducts **(B)** in RTS-treated rats orally dosed with vehicle or GA. Concentration changes of RTS and 7,9-diGS-DHP in the rat liver microsome incubation of RTS with GA (0–100 μM) or ketoconazole (KCZ, 25 μM) **(C)**. Data are expressed as mean ± SD ($n = 3$). *$p < 0.05$, **$p < 0.01$, and ***$p < 0.001$ versus the corresponding RTS group.

RTS-induced liver damage, as evidenced by ameliorated liver hemorrhage and hepatocytes necrosis, and lowered ALT levels (**Figure 2** and **Figure 3**). Moreover, rats treated with EX or GA with both single and multiple treatments exhibited reduced oxidative stress with lower hepatic MDA levels when compared to those treated with RTS alone (**Figures 2C,D**), demonstrating the hepato-protective effect of both EX and GA against RTS-induced liver toxicity.

Pathogenetic studies of drug-induced liver injury (DILI) and herb-induced liver injury (HILI) have substantially increased within the past years. However, the clinical diagnosis of DILI/HILI remains a challenge. The updated RUCAM provides a robust quantitative diagnosis approach to assess the causality of suspected DILI and HILI cases (Danan and Teschke, 2016). Among the recent comprehensive review applied the RUCAM for causality assessment in 95885 cases of liver injury including 81856 DILI and 14029 HILI cases, 28 HSOS cases were demonstrated to be caused by PAs (Teschke and Danan, 2020). In China, the RUCAM is also recommended in the Chinese Society of Hepatology guidelines for the diagnosis and treatment of DILI. In addition, PA exposure biomarkers such as pyrrole-protein adducts, pyrrole-DNA adducts, and pyrrole-amino acid adducts have also been demonstrated to be specific and diagnostic biomarkers for the clinical diagnosis of suspected PA-induced HSOS cases (Ruan et al., 2015; Ma et al., 2019; He et al., 2021d; Ma et al., 2021). In our study, RTS caused typical HSOS with the disarray and necrosis of SECs around portal areas and central veins in rats (**Figure 3B**). Both single and multiple doses of EX or GA significantly attenuated the SEC damage, and multiple doses showed a stronger protective effect than the single

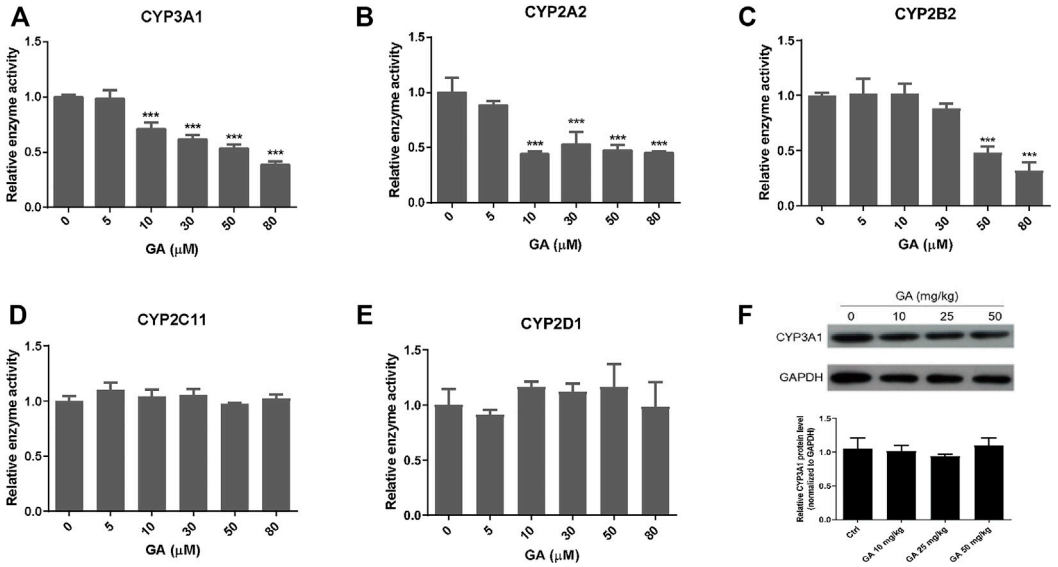

FIGURE 6 | The effect of GA on the activity and expression of CYPs. **(A–E)** Inhibitory effects of GA on the activities of CYP3A1, CYP2A2, CYP2B2, CYP2C11, and CYP2D1 measured by cocktail assay *in vitro*. **(F)** Protein expression of CYP3A1 in the liver measured by western blot. Specific band intensity was quantified and normalized to GAPDH. Rats were orally administrated with different doses of GA (0, 10, 25, 50 mg/kg) for 5 consecutive days and sacrificed at 24 h after the last dose. Data are expressed as mean ± SD (n = 3). ***p < 0.001 versus the corresponding GA (0 μM) group.

dose (**Figure 3B**), In addition, both single- and multiple-dose of GA significantly inhibited the formation of pyrrole-protein adducts in the liver, providing firm evidence for the protective effect of EX and GA against RTS intoxication, especially reducing the risk of HSOS.

It has been reported that GL has poor oral bioavailability in both humans and rats, with very low levels after a single oral dose in the range of 100–1600 mg/kg (Gunnarsdóttir and Jóhannesson, 1997). However, GA is readily detected in plasma following the ingestion of GL or liquorice extract by rats and humans. In addition, the plasma peak of GA are lower and occur later when GL is administrated in liquorice extract than an equivalent dose of GL as a pure compound, suggesting a potential different hepatoprotective effect of EX and GL at the same dosage (Hou et al., 2005; Isbrucker and Burdock, 2006). Interestingly, results produced by EX or GA demonstrated very similar degrees of detoxification effect on RTS-induced hepatotoxicity with higher potencies via their multiple treatments than the single dosing (**Figures 2–4**). Apparently, these observations indicated that 1) almost all GL in EX was biotransformed to GA in the body, with the consideration of the doses of EX (500 mg/kg containing 10.82% of glycyrrhizin) and GA (50 mg/kg); 2) GA played a key role in detoxification; and 3) multiple treatments of GA exhibited a better hepato-protective effect than the single dose, suggesting a repeated/continuous treatment regimen of GA for better detoxification of PAs. Therefore, GA was then used in our following studies to delineate its underlying mechanism.

The cytochrome P450 (CYP) plays a vital role in the metabolism of toxic PAs. Dehydro-PAs, generated by CYP-mediated oxidation, are either detoxified by forming pyrrole-GSH conjugates followed by degradation and urinary/biliary excretion, or covalently bind to macromolecules, such as proteins, and cause massive hepatic necrosis. The clinical focus is on the most active CYP isoforms such as CYP3A4, CYP3A5, and CYP2A6 which show a striking difference in their substrate specificities, with the possible consequence that the degree of liver toxicity may be variable depending on the PA types and the specific CYP isoforms involved (Teschke et al., 2021). In general, most toxic PA types including retrorsine, riddelliine, senecionine, senkirkine, and lasiocarine are mainly metabolized by CYP3A4, which account for 30–50% of the hepatic CYP isoforms (Teschke et al., 2021). While PAs such as monocrotaline are mainly metabolized by the CYP2A6 (Suparmi et al., 2020). In the present study, because CYP3A4 is the predominant CYP isoform accounting for the RTS intoxication, we, therefore, focus on the study of the interaction between GA and CYP3A4 in our animal and cell models.

Previously, liquorice extract and its constituents have been reported to inhibit the activity of certain CYP isoforms (Kent et al., 2002; Tsukamoto et al., 2005; Pandit et al., 2011). For example, the methanol extract of liquorice was shown to inhibit CYP3A4 recombinant enzyme activity (Tsukamoto et al., 2005). A study using midazolam as a probe substrate revealed that GA decreased CYP3A4 activity in the human liver microsomes (Lv et al., 2015). In our toxicokinetic study, GA was found to significantly inhibit the metabolic activation of RTS and the formation of pyrrole-protein adducts (**Figures 5A,B**). Further *in vitro* cocktail assay revealed that GA significantly inhibited rat CYP3A1 (ortholog to human CYP3A4) activity in a concentration-dependent manner with 68.5% inhibition at the highest concentration (80 μM) tested (**Figure 6**). In addition, a

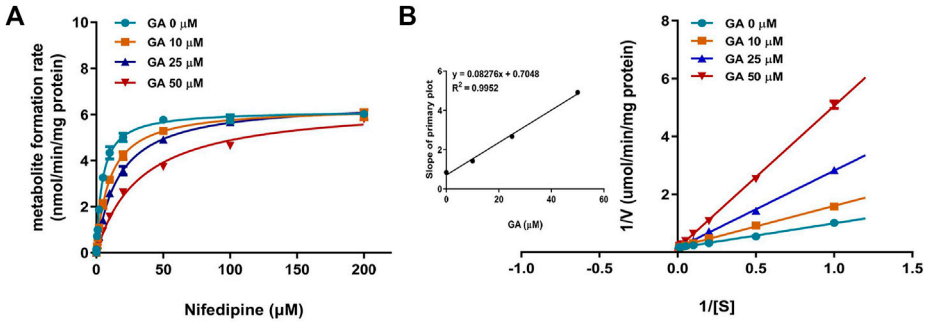

C

Kinetic parameters of Michaelis-Menten plots

GA (μM)	Vmax (nmol/min/mg protein)	Km (μM)	R^2
0	6.175±0.077	4.490±0.249	0.9925
10	6.326±0.079	9.922±0.484**	0.9947
25	6.586±0.083	16.74±0.735***	0.9961
50	6.473±0.146	32.61±2.204***	0.9921

Parameters of Lineweaver-Burk plot of each group

GA (μM)	Slope	Y-intercept when X=0.0	R^2
0	0.843±0.032	0.150±0.014	0.9729
10	1.424±0.040***	0.174±0.017	0.9850
25	2.671±0.041***	0.144±0.018	0.9955
50	4.916±0.064***	0.137±0.028	0.9968

FIGURE 7 | Michaelis-Menten kinetic plot **(A)** and Lineweaver-Burk plot **(B)** for K_i in the inhibition of rat CYP3A1-mediated metabolism of probe substrate (nifedipine, 0.1–200 μM) by GA (0, 10, 25, 50 μM) in rat liver microsomes. The kinetic parameters of Michaelis-Menten plot and Lineweaver-Burk plot **(C)**. Data are expressed as mean ± SD (n = 3). **p < 0.01 and ***p < 0.001 versus the corresponding GA (0 μM) group.

competitive inhibitory mechanism of GA towards rat CYP3A1 was delineated by using standard Michaelis-Menten and Lineweaver-Burk plots (**Figure 7**). Therefore, our findings demonstrated that direct and competitive inhibition of rat CYP3A1 by GA was the predominant reason accounting for its protection against PA intoxication. On the other hand, with the observation of a better detoxification effect produced by the repeated doses of GA (**Figure 6**; **Table 2**), other mechanism contributed by the multiple treatments of GA is unknown and encouraged for further investigation.

Furthermore, it was found that K_m of nifedipine for rat CYP3A1 decreased along with the increasing concentration of GA (**Figure 7C**), revealing that GA and nifedipine competitively occupied the same active site of rat CYP3A1. We then used a computational docking model to investigate the molecular binding mode of GA with human CYP3A4 (Grosdidier et al., 2011). The results obtained from the SwissDock website showed that the energy of full fitness and estimated free energy of GA (-2468.20 kcal/mol, −6.7 kcal/mol) was comparable to those of KCZ (-2432.84 kcal/mol, −8.21 kcal/mol), a well-characterized CYP3A4 inhibitor causing a type II spectrum upon binding and indicating a direct heme binding and complex formation (Ekroos and Sjögren, 2006). The findings suggested that these two molecules might exhibit a similar distance towards the heme group of CYP3A4 and form potential interaction with this site. In addition, results obtained from AUTODOCK software further demonstrated that the keto group of GA located in the polar pocket of CYP3A4 through forming hydrogen bonds with the amino acid Arg-106 and Arg-372 on the side chain of CYP3A4 (**Supplementary Figure S3**). The data suggest that GA may interact with the CYP3A4 binding domain similar to that of KCZ, which interacts with the side chains of Arg-372, Arg-106, and Glu-374 by hydrophobic interactions such as π-stacking (Ekroos and Sjögren, 2006). Further studies are warranted to confirm the interaction pattern and binding domain of GA towards human CYP3A4.

Modern and traditional herbal medicines commonly used some PA-containing herbal products as medicinal plants to treat patients with less serious ailments, although the efficacy for most indications is insufficiently reported due to their traditional usage with the lack of randomized controlled trials in modern medical practice. Medical plants containing PAs are widely described in Europe, United States, Canada, China, etc.

PA-producing medical pants belong to the plant families such as Boraginaceae, Asteraceae, Apiaceae, and Leguminosae, and their plants produce a high variability of PA profiles (Roeder, 2000). In the normal practice of TCM, these PA-containing herbs are commonly combined with other herbs in a single prescription in TCM. Liquorice, as a widely used herbal medicine applied in both medicinal and confectionery sectors, is regarded as a unique 'guide drug' to enhance the effectiveness of other ingredients, to reduce toxicity, or improve flavor in almost half of Chinese herbal formulas/prescriptions (Wang et al., 2013). Based on our study, we found that liquorice is present in almost half of the formulas which contain PA-containing herbs (**Table 1**), and no PA-poisoning cases have been reported under such combinational use, which may suggest the effect of liquorice against potential PA poisoning, and is warranted for future in-depth investigations.

In conclusion, the present study demonstrated that EX, especially its major bioactive ingredient GA, protected the liver from RTS, a representative toxic PA, induced toxicity. Furthermore, our results also delineated the underlying mechanism of such detoxification via competitive inhibition of GA on rat CYP3A1 (ortholog to human CYP3A4), resulting in the inhibition of CYP3A1/3A4-catalyzed metabolic activation of PAs followed by the toxic metabolites-mediated hepatotoxicity. All the findings provided a scientific rationale for the current practice of combining liquorice with PA-containing herbs, and also for the recommendation of future use of liquorice or GA for prevention of PA intoxication.

DATA AVAILABILITY STATEMENT

The original contributions presented in the study are included in the article/**Supplementary Material**, further inquiries can be directed to the corresponding author.

ETHICS STATEMENT

The animal study was reviewed and approved by AEEC committee of The Chinese University of Hong Kong.

AUTHOR CONTRIBUTIONS

ZW contributed to the research design, conduction of experiments, data collection, interpretation, and manuscript preparation. JM, YH, and K-KM contributed to research design and data interpretation. SY and YY prepared the herbal extraction and contributed to manuscript revision. QX and PF contributed to the data interpretation and manuscript revision. GL contributed to the research design, study supervision, data interpretation, manuscript revision and funding support.

FUNDING

This study was supported by Research Grant Council of Hong Kong SAR (GRF Grant No. 14106120) and The Chinese University of Hong Kong Direct Grant (Grant No. 4054577). This article is not an official U.S. Food and Drug Administration (FDA) guidance or policy statement. No official support or endorsement by the U.S. FDA is intended or should be inferred.

SUPPLEMENTARY MATERIAL

The Supplementary Material for this article can be found online at: https://www.frontiersin.org/articles/10.3389/fphar.2022.850859/full#supplementary-material

REFERENCES

Bodi, D., Ronczka, S., Gottschalk, C., Behr, N., Skibba, A., Wagner, M., et al. (2014). Determination of Pyrrolizidine Alkaloids in Tea, Herbal Drugs and Honey. *Food Addit Contam. Part. A. Chem. Anal. Control. Expo. Risk Assess.* 31, 1886–1895. doi:10.1080/19440049.2014.964337

Chen, X., Ma, J., He, Y., Xue, J., Song, Z., Xu, Q., et al. (2021). Characterization of Liver Injury Induced by a Pyrrolizidine Alkaloid in Rats. *Phytomedicine* 89, 153595. doi:10.1016/j.phymed.2021.153595

Dai, N., Yu, Y. C., Ren, T. H., Wu, J. G., Jiang, Y., Shen, L. G., et al. (2007). Gynura Root Induces Hepatic Veno-Occlusive Disease: A Case Report and Review of the Literature. *World J. Gastroenterol.* 13, 1628–1631. doi:10.3748/wjg.v13.i10.1628

Danan, G., and Teschke, R. (2016). RUCAM in Drug and Herb Induced Liver Injury: The Update. *Int. J. Mol. Sci.* 17 (1), 14. doi:10.3390/ijms17010014

Deleve, L. D., Mccuskey, R. S., Wang, X., Hu, L., Mccuskey, M. K., Epstein, R. B., et al. (1999). Characterization of A Reproducible Rat Model of Hepatic Veno-Occlusive Disease. *Hepatology* 29, 1779–1791. doi:10.1002/hep.510290615

Deleve, L. D., Shulman, H. M., and Mcdonald, G. B. (2002). Toxic Injury to Hepatic Sinusoids: Sinusoidal Obstruction Syndrome (Veno-Occlusive Disease). *Semin. Liver Dis.* 22, 27–42. doi:10.1055/s-2002-23204

Dusemund, B., Nowak, N., Sommerfeld, C., Lindtner, O., Schäfer, B., and Lampen, A. (2018). Risk Assessment of Pyrrolizidine Alkaloids in Food of Plant and Animal Origin. *Food Chem. Toxicol.* 115, 63–72. doi:10.1016/j.fct.2018.03.005

Dussourd, D. E., Harvis, C. A., Meinwald, J., and Eisner, T. (1989). Paternal Allocation of Sequestered Plant Pyrrolizidine Alkaloid to Eggs in the Danaine Butterfly, *Danaus Gilippus*. *Experientia* 45, 896–898. doi:10.1007/BF01954068

Ekroos, M., and Sjögren, T. (2006). Structural Basis for Ligand Promiscuity in Cytochrome P450 3A4. *Proc. Natl. Acad. Sci. U S A.* 103 (37), 13682–13687. doi:10.1073/pnas.0603236103

Fu, P. P. (2017). Pyrrolizidine Alkaloids: Metabolic Activation Pathways Leading to Liver Tumor Initiation. *Chem. Res. Toxicol.* 30, 81–93. doi:10.1021/acs.chemrestox.6b00297

Gao, H., Li, N., Wang, J. Y., Zhang, S. C., and Lin, G. (2012). Definitive Diagnosis of Hepatic Sinusoidal Obstruction Syndrome Induced by Pyrrolizidine Alkaloids. *J. Dig. Dis.* 13, 33–39. doi:10.1111/j.1751-2980.2011.00552.x

Geburek, I., Preiss-Weigert, A., Lahrssen-Wiederholt, M., Schrenk, D., and These, A. (2020). *In Vitro* Metabolism of Pyrrolizidine Alkaloids - Metabolic Degradation and GSH Conjugate Formation of Different Structure Types. *Food Chem. Toxicol.* 135, 110868. doi:10.1016/j.fct.2019.110868

Geburek, I., Rutz, L., Gao, L., Küpper, J. H., These, A., and Schrenk, D. (2021). Metabolic Pattern of Hepatotoxic Pyrrolizidine Alkaloids in Liver Cells. *Chem. Res. Toxicol.* 34, 1101–1113. doi:10.1021/acs.chemrestox.0c00507

Grosdidier, A., Zoete, V., and Michielin, O. (2011). SwissDock, a Protein-Small Molecule Docking Web Service Based on EADock DSS. *Nucleic Acids Res.* 39, W270–W277. doi:10.1093/nar/gkr366

Gunnarsdóttir, S., and Jóhannesson, T. (1997). Glycyrrhetic Acid in Human Blood after Ingestion of Glycyrrhizic Acid in Licorice. *Pharmacol. Toxicol.* 81, 300–302.

He, Y., Lian, W., Ding, L., Fan, X., Ma, J., Zhang, Q. Y., et al. (2021a). Lung Injury Induced by Pyrrolizidine Alkaloids Depends on Metabolism by Hepatic Cytochrome P450s and Blood Transport of Reactive Metabolites. *Arch. Toxicol.* 95, 103–116. doi:10.1007/s00204-020-02921-0

He, Y., Shi, M., Wu, X., Ma, J., Ng, K. T., Xia, Q., et al. (2021b). Mutational Signature Analysis Reveals Widespread Contribution of Pyrrolizidine Alkaloid Exposure to Human Liver Cancer. *Hepatology* 74, 264–280. doi:10.1002/hep.31723

He, Y., Zhu, L., Ma, J., and Lin, G. (2021d). Metabolism-mediated Cytotoxicity and Genotoxicity of Pyrrolizidine Alkaloids. *Arch. Toxicol.* 95, 1917–1942. doi:10.1007/s00204-021-03060-w

He, Y., Zhang, W., Ma, J., Xia, Q., Song, Z., Zhu, L., et al. (2021c). Blood Pyrrole-DNA Adducts Define the Early Tumorigenic Risk in Patients with Pyrrolizidine Alkaloid-Induced Liver Injury. *Environ. Sci. Technol. Lett.* 8, 551–557. doi:10.1021/acs.estlett.1c00359

Hou, Y. C., Hsiu, S. L., Ching, H., Lin, Y. T., Tsai, S. Y., Wen, K. C., et al. (2005). Profound Difference of Metabolic Pharmacokinetics between Pure Glycyrrhizin and Glycyrrhizin in Licorice Decoction. *Life Sci.* 76, 1167–1176. doi:10.1016/j.lfs.2004.10.020

Isbrucker, R. A., and Burdock, G. A. (2006). Risk and Safety Assessment on the Consumption of Licorice Root (Glycyrrhiza sp.), its Extract and Powder as a Food Ingredient, with Emphasis on the Pharmacology and Toxicology of Glycyrrhizin. *Regul. Toxicol. Pharmacol.* 46, 167–192. doi:10.1016/j.yrtph.2006.06.002

Kakar, F., Akbarian, Z., Leslie, T., Mustafa, M. L., Watson, J., Van Egmond, H. P., et al. (2010). An Outbreak of Hepatic Veno-Occlusive Disease in Western Afghanistan Associated with Exposure to Wheat Flour Contaminated with Pyrrolizidine Alkaloids. *J. Toxicol.* 2010, 313280. doi:10.1155/2010/313280

Kasahara, Y., Kiyatake, K., Tatsumi, K., Sugito, K., Kakusaka, I., Yamagata, S., et al. (1997). Bioactivation of Monocrotaline by P-450 3A in Rat Liver. *J. Cardiovasc. Pharmacol.* 30, 124–129. doi:10.1097/00005344-199707000-00018

Kent, U. M., Aviram, M., Rosenblat, M., and Hollenberg, P. F. (2002). The Licorice Root Derived Isoflavan Glabridin Inhibits the Activities of Human Cytochrome P450S 3A4, 2B6, and 2C9. *Drug Metab. Dispos* 30, 709–715. doi:10.1124/dmd.30.6.709

Lee, C. H., Park, S. W., Kim, Y. S., Kang, S. S., Kim, J. A., Lee, S. H., et al. (2007). Protective Mechanism of Glycyrrhizin on Acute Liver Injury Induced by Carbon Tetrachloride in Mice. *Biol. Pharm. Bull.* 30, 1898–1904. doi:10.1155/2014/87213910.1248/bpb.30.1898

Lian, W., and Lin, G. (2017). *Investigation of Pyrrolizidine Alkaloid-Induced Pulmonary Toxicity and its Underlying Biochemical Mechanism*. Hong Kong SAR, China: The Chinese University of Hong Kong Graduate School, 35–37.

Lin, G., Cui, Y. Y., and Hawes, E. M. (2000). Characterization of Rat Liver Microsomal Metabolites of Clivorine, an Hepatotoxic Otonecine-type Pyrrolizidine Alkaloid. *Drug Metab. Dispos* 28, 1475–1483.

Lin, G., Nnane, I. P., and Cheng, T. Y. (1999). The Effects of Pretreatment with Glycyrrhizin and Glycyrrhetinic Acid on the Retrorsine-Induced Hepatotoxicity in Rats. *Toxicon* 37, 1259–1270. doi:10.1016/s0041-0101(98)00263-3

Lin, G., Wang, J. Y., Li, N., Li, M., Gao, H., Ji, Y., et al. (2011). Hepatic Sinusoidal Obstruction Syndrome Associated with Consumption of Gynura Segetum. *J. Hepatol.* 54, 666–673. doi:10.1016/j.jhep.2010.07.031

Lv, Q. L., Wang, G. H., Chen, S. H., Hu, L., Zhang, X., Ying, G., et al. (2015). *In Vitro* and *In Vivo* Inhibitory Effects of Glycyrrhetinic Acid in Mice and Human Cytochrome P450 3A4. *Int. J. Environ. Res. Public Health* 13, 84. doi:10.3390/ijerph13010084

Ma, J., Ruan, J., Chen, X., Li, D., Yao, S., Fu, P. P., et al. (2019). Pyrrole-Hemoglobin Adducts, a More Feasible Potential Biomarker of Pyrrolizidine Alkaloid Exposure. *Chem. Res. Toxicol.* 32 (6), 1027–1039. doi:10.1021/acs.chemrestox.8b00369

Ma, J., Zhang, W., He, Y., Zhu, L., Zhang, C., Liu, J., et al. (2021). Clinical Application of Pyrrole-Hemoglobin Adducts as a Biomarker of Pyrrolizidine Alkaloid Exposure in Humans. *Arch. Toxicol.* 95 (2), 759–765. doi:10.1007/s00204-020-02947-4

Ma, L., Zhao, H., Xia, Q., Cai, L., and Fu, P. P. (2015). Synthesis and Phototoxicity of Isomeric 7,9-Diglutathione Pyrrole Adducts: Formation of Reactive Oxygen Species and Induction of Lipid Peroxidation. *J. Food Drug Anal.* 23, 577–586. doi:10.1016/j.jfda.2015.06.001

Mohabbat, O., Younos, M. S., Merzad, A. A., Srivastava, R. N., Sediq, G. G., and Aram, G. N. (1976). An Outbreak of Hepatic Veno-Occlusive Disease in North-Western Afghanistan. *Lancet* 2, 269–271. doi:10.1016/s0140-6736(76)90726-1

Otten, J. N., Hingorani, G. P., Hartley, D. P., Kragerud, S. D., and Franklin, R. B. (2011). An *In Vitro*, High Throughput, Seven CYP Cocktail Inhibition Assay for the Evaluation of New Chemical Entities Using LC-MS/MS. *Drug Metab. Lett.* 5 (1), 17–24. doi:10.2174/187231211794455235

Öztürk, M., Altay, V., Hakeem, K. R., and Akçiçek, E. (2017). "Pharmacological Activities and Phytochemical Constituents," in *Liquorice. SpringerBriefs in Plant Science* (Cham: Springer). doi:10.1007/978-3-319-74240-3_7

Pandit, S., Ponnusankar, S., Bandyopadhyay, A., Ota, S., and Mukherjee, P. K. (2011). Exploring the Possible Metabolism Mediated Interaction of Glycyrrhiza Glabra Extract with CYP3A4 and CYP2D6. *Phytother Res.* 25, 1429–1434. doi:10.1002/ptr.3426

Roeder, E. (2000). Medicinal Plants in China Containing Pyrrolizidine Alkaloids. *Pharmazie* 55, 711–726.

Ruan, J., Gao, H., Li, N., Xue, J., Chen, J., Ke, C., et al. (2015). Blood Pyrrole-Protein Adducts--A Biomarker of Pyrrolizidine Alkaloid-Induced Liver Injury in Humans. *J. Environ. Sci. Health C Environ. Carcinog Ecotoxicol Rev.* 33, 404–421. doi:10.1080/10590501.2015.1096882

Ruan, J., Yang, M., Fu, P., Ye, Y., and Lin, G. (2014). Metabolic Activation of Pyrrolizidine Alkaloids: Insights into the Structural and Enzymatic Basis. *Chem. Res. Toxicol.* 27, 1030–1039. doi:10.1021/tx500071q

Schrenk, D., Gao, L., Lin, G., Mahony, C., Mulder, P. P. J., Peijnenburg, A., et al. (2020). Pyrrolizidine Alkaloids in Food and Phytomedicine: Occurrence, Exposure, Toxicity, Mechanisms, and Risk Assessment - A Review. *Food Chem. Toxicol.* 136, 111107. doi:10.1016/j.fct.2019.111107

Suparmi, S., Wesseling, S., and Rietjens, I. M. C. M. (2020). Monocrotaline-induced Liver Toxicity in Rat Predicted by a Combined *In Vitro* Physiologically Based Kinetic Modeling Approach. *Arch. Toxicol.* 94, 3281–3295. doi:10.1007/s00204-020-02798-z

Takeda, S., Ishthara, K., Wakui, Y., Amagaya, S., Maruno, M., Akao, T., et al. (1996). Bioavailability Study of Glycyrrhetic Acid after Oral Administration of Glycyrrhizin in Rats; Relevance to the Intestinal Bacterial Hydrolysis. *J. Pharm. Pharmacol.* 48, 902–905. doi:10.1111/j.2042-7158.1996.tb05998.x

Tandon, B. N., Tandon, H. D., Tandon, R. K., Narndranathan, M., and Joshi, Y. K. (1976). An Epidemic of Veno-Occlusive Disease of Liver in Central India. *Lancet* 2, 271–272. doi:10.1016/s0140-6736(76)90727-3

Teschke, R., and Danan, G. (20202020). Worldwide Use of RUCAM for Causality Assessment in 81,856 Idiosyncratic DILI and 14,029 HILI Cases Published 1993-Mid 2020: A Comprehensive Analysis. *Medicines (Basel)* 7 (10), 62. doi:10.3390/medicines7100062

Teschke, R., Vongdala, N., Quan, N. V., Quy, T. N., and Xuan, T. D. (2021). Metabolic Toxification of 1,2-Unsaturated Pyrrolizidine Alkaloids Causes Human Hepatic Sinusoidal Obstruction Syndrome: The Update. *Int. J. Mol. Sci.* 22, 10419. doi:10.3390/ijms221910419

Tsukamoto, S., Aburatani, M., Yoshida, T., Yamashita, Y., El-Beih, A. A., and Ohta, T. (2005). CYP3A4 Inhibitors Isolated from Licorice. *Biol. Pharm. Bull.* 28, 2000–2002. doi:10.1248/bpb.28.2000

Tu, M., Li, L., Lei, H., Ma, Z., Chen, Z., Sun, S., et al. (2014). Involvement of Organic Cation Transporter 1 and CYP3A4 in Retrorsine-Induced Toxicity. *Toxicology* 322, 34–42. doi:10.1016/j.tox.2014.04.007

Wahab, S., Annadurai, S., Abullais, S. S., Das, G., Ahmad, W., Ahmad, M. F., et al. (2021). Glycyrrhiza Glabra (Licorice): A Comprehensive Review on its Phytochemistry, Biological Activities, Clinical Evidence and Toxicology. *Plants (Basel)* 10 (12), 2751. doi:10.3390/plants10122751

Wang, X., Zhang, H., Chen, L., Shan, L., Fan, G., and Gao, X. (2013). Liquorice, a Unique "guide Drug" of Traditional Chinese Medicine: a Review of its Role in Drug Interactions. *J. Ethnopharmacol* 150, 781–790. doi:10.1016/j.jep.2013.09.055

Willmot, F. C., and Robertson, G. W. (1920). Senecio Disease, or Cirrhosis of the Liver Due to Senecio Poisoning. *The Lancet* 196, 848–849. doi:10.1016/s0140-6736(01)00020-4

Wu, S. Y., Wang, W. J., Dou, J. H., and Gong, L. K. (2021). Research Progress on the Protective Effects of Licorice-Derived 18β-Glycyrrhetinic Acid against Liver Injury. *Acta Pharmacol. Sin* 42 (1), 18–26. doi:10.1038/s41401-020-0383-9

Wu, X., Zhang, L., Gurley, E., Studer, E., Shang, J., Wang, T., et al. (2008). Prevention of Free Fatty Acid-Induced Hepatic Lipotoxicity by 18beta-

Glycyrrhetinic Acid through Lysosomal and Mitochondrial Pathways. *Hepatology* 47, 1905–1915. doi:10.1002/hep.22239

Yan, M., Guo, L., Yang, Y., Zhang, B., Hou, Z., Gao, Y., et al. (2021). Glycyrrhetinic Acid Protects α-Naphthylisothiocyanate- Induced Cholestasis through Regulating Transporters, Inflammation and Apoptosis. *Front. Pharmacol.* 12. doi:10.3389/fphar.2021.701240

Yan, T., Wang, H., Zhao, M., Yagai, T., Chai, Y., Krausz, K. W., et al. (2016). Glycyrrhizin Protects against Acetaminophen-Induced Acute Liver Injury via Alleviating Tumor Necrosis Factor α-Mediated Apoptosis. *Drug Metab. Dispos* 44, 720–731. doi:10.1124/dmd.116.069419

Yang, M., Ruan, J., Fu, P. P., and Lin, G. (2016). Cytotoxicity of Pyrrolizidine Alkaloid in Human Hepatic Parenchymal and Sinusoidal Endothelial Cells: Firm Evidence for the Reactive Metabolites Mediated Pyrrolizidine Alkaloid-Induced Hepatotoxicity. *Chem. Biol. Interact* 243, 119–126. doi:10.1016/j.cbi.2015.09.011

Yang, M., Ruan, J., Gao, H., Li, N., Ma, J., Xue, J., et al. (2017). First Evidence of Pyrrolizidine Alkaloid N-Oxide-Induced Hepatic Sinusoidal Obstruction Syndrome in Humans. *Arch. Toxicol.* 91, 3913–3925. doi:10.1007/s00204-017-2013-y

Zhang, M., Chang, Z., Zhao, F., Zhang, P., Hao, Y. J., Yan, L., et al. (2019). Protective Effects of 18β-Glycyrrhetinic Acid on Monocrotaline-Induced Pulmonary Arterial Hypertension in Rats. *Front. Pharmacol.* 10, 13. doi:10.3389/fphar.2019.00013

Zhu, L., Zhang, C. Y., Li, D. P., Chen, H. B., Ma, J., Gao, H., et al. (2021). Tu-San-Qi (*Gynura Japonica*): the Culprit behind Pyrrolizidine Alkaloid-Induced Liver Injury in China. *Acta Pharmacol. Sin* 42, 1212–1222. doi:10.1038/s41401-020-00553-9

Zhuge, Y., Liu, Y., Xie, W., Zou, X., Xu, J., and Wang, J. (2019). Expert Consensus on the Clinical Management of Pyrrolizidine Alkaloid-Induced Hepatic Sinusoidal Obstruction Syndrome. *J. Gastroenterol. Hepatol.* 34, 634–642. doi:10.1111/jgh.14612

Conflict of Interest: The authors declare that the research was conducted in the absence of any commercial or financial relationships that could be construed as a potential conflict of interest.

Publisher's Note: All claims expressed in this article are solely those of the authors and do not necessarily represent those of their affiliated organizations, or those of the publisher, the editors and the reviewers. Any product that may be evaluated in this article, or claim that may be made by its manufacturer, is not guaranteed or endorsed by the publisher.

frontiers | Frontiers in Pharmacology

ORIGINAL RESEARCH
published: 05 April 2022
doi: 10.3389/fphar.2022.858007

Pharmacokinetic Herb-Drug Interactions of *Xiang-Sha-Liu-Jun-Zi-Tang* and Paclitaxel in Male Sprague Dawley Rats and Its Influence on Enzyme Kinetics in Human Liver Microsomes

Alinafe Magret Kapelemera[1], *Yow-Shieng Uang*[2,3], *Li-Hsuan Wang*[4], *Tien-Yuan Wu*[5], *Fang-Yu Lee*[2], *Li Tai*[3], *Ching-Chiung Wang*[1,2,4,6*†] and *Chia-Jung Lee*[1,2,6*†]

[1]PhD Program in Clinical Drug Development of Herbal Medicine, Taipei Medical University, Taipei, Taiwan, [2]Graduate Institute of Pharmacognosy, Taipei Medical University, Taipei, Taiwan, [3]Rosetta Pharmamate Co., Ltd, New Taipei City, Taiwan, [4]School of Pharmacy, Taipei Medical University, Taipei, Taiwan, [5]Department of Pharmacology, School of Medicine, College of Medicine, Tzu Chi University, Hualien, Taiwan, [6]Traditional Herbal Medicine Research Center, Taipei Medical University Hospital, Taipei, Taiwan

OPEN ACCESS

Edited by:
Guangbo Ge,
Shanghai University of Traditional Chinese Medicine, China

Reviewed by:
Ping Du,
Capital Medical University, China
Xin Wang,
East China Normal University, China

***Correspondence:**
Ching-Chiung Wang
crystal@tmu.edu.tw
Chia-Jung Lee
cjlee@tmu.edu.tw

[†]These authors have contributed equally to the work

Specialty section:
This article was submitted to Ethnopharmacology, a section of the journal Frontiers in Pharmacology

Received: 19 January 2022
Accepted: 28 February 2022
Published: 05 April 2022

Citation:
Kapelemera AM, Uang Y-S, Wang L-H, Wu T-Y, Lee F-Y, Tai L, Wang C-C and Lee C-J (2022) Pharmacokinetic Herb-Drug Interactions of Xiang-Sha-Liu-Jun-Zi-Tang and Paclitaxel in Male Sprague Dawley Rats and Its Influence on Enzyme Kinetics in Human Liver Microsomes. Front. Pharmacol. 13:858007. doi: 10.3389/fphar.2022.858007

Paclitaxel is a prescribed anticancer drug used to treat various cancers. It is a substrate of cytochrome P-450 (CYP-450) enzymes. Despite its efficacy, paclitaxel has severe side effects. Herbal medicines are commonly used to treat the side effects of chemotherapy. They can be administered before, during, and after chemotherapy. Xiang-Sha-Liu-Jun-Zi Tang (XSLJZT) is a herbal formula commonly used in breast cancer patients. The main purpose of this study was to assess the pharmacokinetic (PK) influence of XSLJZT on paclitaxel PK parameters, determine its effect on CYP-450 enzyme expression, and evaluate its effect on enzyme activity. Sprague Dawley rats were classified into pretreatment and co-treatment groups, where XSLJZT was pre-administered for 3, 5, and 7 days and co-administered 2 h before paclitaxel administration. The rat liver tissues and Hep-G2 cells were used to determine the effects of XSLJZT on CYP3A1/2 and CYP3A4 enzymes respectively. Western blot analysis was used to detect changes in the CYP3A1/2 and CYP3A4 enzymes expression. The influence of XSLJZT on enzyme activity was evaluated using human liver microsomes, and a liquid chromatography-tandem mass spectrometric system was developed to monitor paclitaxel levels in rat plasma. Results demonstrated that XSLJZT increased the area under the concentration versus time curve (AUC) for paclitaxel in pretreatment groups by 2-, 3-, and 4-fold after 3, 5, and 7 days, respectively. In contrast, no significant change in the AUC was observed in the co-treatment group. However, the half-life was prolonged in all groups from 17.11 min to a maximum of 37.56 min. XSLJZT inhibited CYP3A1/2 expression in the rat liver tissues and CYP3A4 enzymes in Hep-G2 cells in a time-dependent manner, with the highest inhibition observed after 7 days of pretreatment in rat liver tissues. In the enzyme kinetics study, XSLJZT inhibited enzyme activity in a competitive dose-dependent manner. In conclusion,

there is a potential interaction between XSLJZT and paclitaxel at different co-treatment and pretreatment time points.

Keywords: traditional Chinese medicine formula, Xiang-Sha-Liu-Jun-Zi tang, paclitaxel, pharmacokinetics, enzyme kinetics

1 INTRODUCTION

Paclitaxel is an antineoplastic drug used for the first-line treatment of both early-stage and metastatic cancers. It has excellent anticancer activity against a wide range of solid tumors, including breast, ovarian, lung, and colorectal cancers (Gallego-Jara et al., 2020). It inhibits the depolarization of microtubules and arrests cell division during the metaphase. Despite its efficacy, paclitaxel has a low bioavailability. It is classified as a class IV drug according to the biopharmaceutical classification, with poor aqueous solubility (<1 μg/ml) and low oral bioavailability (<2%). To improve bioavailability, paclitaxel is administered intravenously, which, unfortunately, is associated with several side effects including gastrointestinal (GI) toxicities such as nausea, vomiting, diarrhea, and stomatitis (Boussios et al., 2012; Tekade et al., 2013; Bernabeu et al., 2017).

In order to reduce the side effects of chemotherapy, most cancer patients opt to use herbal medicines. In Taiwan, over 80% of cancer patients use herbal medicines as adjuvants for chemotherapy (Lo et al., 2012; Cheng et al., 2018), to improve their quality of life and general health, prevent recurrence, and reduce the side effects of chemotherapy (Koçaşlı and Demircan, 2017). Herbal medicines can be used before, during, and after chemotherapy. Koçaşlı et al. reported that 38.9% of cancer patients used herbal medicines before surgery and chemotherapy to fight cancer and 54.1% used herbal medicines during chemotherapy to improve their quality of life and reduce the side effects. Some cancer patients use herbal medicines before and during chemotherapy for reasons that are not related to chemotherapy (Smith et al., 2014; Koçaşlı and Demircan, 2017; Lee et al., 2021).

Xiang-Sha-Liu-Jun-Zi Tang (XSLJZT) is a herbal formula commonly prescribed with chemotherapy. It is the second most commonly prescribed herbal formula after Jia-Wei-Xiao-Yao-San (JWXYS) in breast cancer patients (Lai et al., 2012; Lee et al., 2014). It consists of eight herbal constituents and originates from the herbal formula Liu-Jun-Zi Tang (LJZT) with the addition of *Amomum villosum* and *Aucklandia lappa*. The addition of these two herbs to the LJZT herbal formula promotes Qi circulation and improves GI motility and gastric emptying (Xiao et al., 2012; Shih et al., 2019). Clinically, XSLJZT is used for the treatment of spleen deficiency and Qi stagnation syndrome according to the Chinese Society of Digestive Diseases. Thus, it is one of the herbal medicines commonly prescribed in cancer patients to reduce chemotherapy-induced GI disturbances, including nausea, vomiting, abdominal distension, and diarrhea (Huang et al., 2017; Xiao et al., 2021).

Although herbal medicines are beneficial for cancer patients, their use should be closely monitored (Ohnishi and Takeda, 2015). The use of herbal medicines before and during chemotherapy can result in toxic, allergic, and carcinogenic effects due to herb-drug interactions (Koçaşlı and Demircan, 2017). Herb-drug interactions occur when some phytochemicals inhibit or induce the drug-metabolizing enzymes, which can in turn affect the dose-effect relationship of the co-administered drugs (Fasinu and Rapp, 2019). Cytochrome P-450 (CYP-450) enzymes include different subfamilies depending on the gene sequences (McDonnell and Dang, 2013; Zanger and Schwab, 2013). Paclitaxel is a substrate of CYP-450 enzymes, specifically CYP3A4 and CYP2C8 subfamilies in humans. Some studies have reported that the major metabolite of paclitaxel in the human liver is 6α-hydroxypaclitaxel (6α-OHP), which is formed by CYP2C8 and is seconded by C3′-hydroxypaclitaxel (C3′α-OHP) formed by CYP3A4. In contrast to humans, C3′α-OHP is the major metabolite in the rat liver, while 6α-OHP, the major metabolite in the human liver, is not formed in the rat liver (Václavíková et al., 2003; Vaclavikova, et al., 2004). The inhibition or induction of CYP2C8 or CYP3A4 can affect the metabolism of paclitaxel, which may in turn affect the dose-effect relationship (Hendrikx et al., 2013). XSLJZT contains phytochemicals that can potentially induce or inhibit CYP-450 enzymes (Liu et al., 2018).

The potential influence of XSLJZT on co-administered chemotherapeutics has not been extensively studied. In this study, a liquid chromatographic tandem mass spectroscopic (LC/MS/MS) detection system was used to assess the presence of paclitaxel in biological samples. Using Sprague Dawley (SD) rats, we assessed the potential herb-drug pharmacokinetic interactions of XSLJZT with paclitaxel. XSLJZT was pretreated for several days before paclitaxel administration and co-treated with paclitaxel on the same day. The effect of XSLJZT on CYP-450 enzymes was evaluated using western blot, where CYP 3A1/2 enzymes were detected in the rat liver tissues and CYP3A4 enzymes in Hep-G2 cells. Since different species metabolize paclitaxel differently, human liver microsomes were used to assess the effects of XSLZJT on the metabolism of paclitaxel in humans (Vaclavikova, et al., 2004).

2 MATERIALS AND METHODS

2.1 Chemicals and Reagents

DMSO, MTT, trypan blue, and other chemicals were purchased from Sigma. Paclitaxel (Phyxol®), purity >99%, was obtained from Sinphar Pharmaceutical (Yilan County, Taiwan). Dulbecco's modified minimal essential medium (DMEM), streptomycin, penicillin, and fetal bovine serum (FBS) were

obtained from Gibco BRL. Trifluoroacetic acid, methanol, and acetonitrile were used as LC/MS/MS grade reagents (Merck, Darmstadt, Germany). Anhydrous ethyl ether (AEE) was used for sample preparation (Merck, Darmstadt, Germany).

2.2 XSLJZT Sample Preparation

The XSLJZT prescription was based on the unified formula announced by the Committee on Chinese Medicine and Pharmacy of the Department of Health (Taipei, Taiwan). It consists of Ginseng radix (*Panax ginseng* C. A. Mey. (2.5 g), Ren She), Atractylodis macrocephalae rhizoma (*Atractylodes macrocephala* Koidz. (5 g), Bai zhu); Hoelen (*Wolfiporia cocos* (Schw.) Wolf (5 g); Fu ling), and Glycyrrhizae Radix et Rhizoma. (*Glycyrrhiza uralensis* Fisch. ex DC. (2 g) Gan cao), Citri Reticulatae Pericarpium (*Citrus reticulata* Blanco, (2 g), Chen pi), Pinelliae Rhizoma (*Pinellia ternata* (Thunb.) Makino, (2.5 g), Ban xia), Amomi Fructus (*Amomum villosum* Lour. (2 g), Sha ren), and Aucklandiae Radix (*Aucklandia costus* Falc. (2 g), Mu xiang) (Liu et al., 2017). All materials were purchased from Sun Ten Pharmaceutical (New Taipei City, Taiwan) and authenticated by a non-profit organization, Brion Research Institute of Taiwan (New Taipei City, Taiwan). Voucher specimens (No. GR-20180001 for Ginseng radix, No. AMR-20180001 for Atractylodis macrocephalae rhizoma, No. H-20180001 for Hoelen, No. GLR-20180001 for Glycyrrhizae Radix et Rhizoma, No. CR-20180001 for Citri reticulatae pericarpium, No. PR-20180001 for Pinellia rhizoma, No. AF-20180001 for Amomi Fructus and No. AR-20180001 for Aucklandiae Radix was deposited at the College of Pharmacy, Taipei Medical University. XSLJZT was prepared using the following method: total drug weight of 112 g was placed in an extractor, distilled water (10-fold) was added and boiled for 30 min until half the volume was left. This procedure was repeated once. The two extracts were combined and filtered through gauze layers. The residue was discarded, and the filtrate was lyophilized at −20°C to yield a drug powder, which was stored at 4°C. The yield of XSLJZT was 25.6%.

2.3 High-Performance Liquid Chromatography Analysis of Marker Substances in XSLJZT

The XSLJZT sample (0.5 g) was extracted using 20 ml of 70% methanol through ultrasonic oscillation at 25°C for 15 min and then vortexed at 160 rpm at 40°C for 40 min. The sample was then filtered through a 0.45 μm syringe filter, and a 20 μl sample was directly injected into the Waters HPLC system (Milford, MA, United States), which comprised a Waters 600 pump system, Waters 2996 Photodiode array detector, Waters 717 plus autosampler, and Sugai U-620 column oven (Wakayama City, Japan). A Cosmosil 5C18-MS-II reversed-phase column (5 μm, 4.6 mm × 250 mm, Nacalai Tesque, Japan) equipped with a Lichrospher RP-18 end-capped guard column (5 μm, 4.0 mm × 10 mm, Merck, Germany) was used as the stationary phase. The gradient elution was performed using the eluents A and B (A: acetonitrile; B: 0.1 % H_3PO_4) according to the following profile: 0–25 min, 19%–20% A and 81%–80% B; 25–60 min, 20%–40% A and 80%–60% B; 60–90 min, 40%–55% A and 60%–45% B; 90–100 min, 55%–60% A and 45%–40% B; 100–125 min, 19% A and 81% B. The flow rate was 1 ml/min, and the column temperature was maintained at 35°C. The following marker substances in XSLJZT were chosen according to the regulations of the Taiwan Herbal Pharmacopoeia and Pharmacopoeia of the People's Republic of China: glycyrrhizin and liquiritin for *Glycyrrhiza uralensis*, costunolide and dehydrocostus lactone for *Aucklandia lappa*; and hesperidin for *Citrus reticulata*. We used an ultraviolet detection wavelength of 225 nm for costunolide and dehydrocostus lactone, 250 nm for glycyrrhizin, and 280 nm for liquiritin and hesperidin.

2.4 LC/MS/MS Conditions and Reagent Preparation for Paclitaxel Analysis

An LC/MS/MS system was used for analytical separation. It consisted of a Quattro Ultima mass spectrometer (Micromass, Manchester, United Kingdom), a Waters Alliance 2795 pump and autosampler (Waters, MA, United States), Biosil ODS 4.6 × 250 mm, 5-μm column (Biotic Chemical, Taipei, Taiwan). Data acquisition was performed using MassLynx vers. 4.0, (Micromass). The mobile phase consisted of 70% CH_3CN and 0.1% formic acid. The flow rate was 1.00 ml/min with a post column split of 1/10 to tandem MS. The ionization mode was electrospray/positive ionization, and mass scanning was conducted in the multiple reaction monitor (MRM) mode. The paclitaxel precursor ion was detected at *m/z* 854.36, and the product ion at *m/z* 286.04. The capillary voltage was 3.2 kV, cone voltage was 35 eV, source temperature was 80°C, desolation temperature was 400°C, and collision voltage was 25 eV. A primary standard stock solution of paclitaxel (1,000 μg/ml) was prepared by dissolving 1 mg of pure paclitaxel in 1 ml methanol to prepare a standard stock solution of 1 mg/ml. A working solution was prepared by diluting the stock solution in 50% (v/v) methanol to obtain the following concentrations: three standard solutions of 10, 100, and 1,000 ng/ml, representing low-, intermediate-, and high-strength stock solutions prepared using serial dilution.

2.5 Method Validation

All method validation experiments were performed according to the Food and Drug Administration (FDA) guidelines (Health, U.D.o. and H. Services, 2001). The matrix effect, recovery rate, accuracy, and precision were evaluated. The liquid–liquid extraction method was used for the preparation of all biological samples.

2.5.1 Matrix Effect and Recovery Rate

To determine the matrix effect and recovery rate, samples were classified into sets 1, 2, and 3. Three different concentrations (10, 100, and 1,000 ng/ml) of paclitaxel were used in each set to represent high, middle, and low concentrations. In set 1, paclitaxel was prepared in the mobile phase, while in set 2, three lots of blank plasmas were extracted and spiked with paclitaxel after the extraction. Set 3 consisted of three lots of

blank plasma spiked with paclitaxel before extraction. Anhydrous ethyl ether was used for extraction, and all samples were evaporated to dryness after extraction, which was later reconstituted with 100 µl methanol for LC-MS/MS detection. The matrix effect was established by comparing the paclitaxel peak areas of set 2 samples to peak areas of equivalent concentrations in set 1, and the recovery rate was established by comparing the peak areas of set 3 to the corresponding peak areas in set 2.

2.5.2 Calibration Curve

A calibration curve was prepared by spiking 90 µl of rat plasma with different concentrations (5–1,000 ng/ml) of paclitaxel (10 µl). Linearity was achieved at a regression coefficient of $r^2 > 0.995$. The limit of detection (LOD) and lower limit of quantification (LLOQ) were defined as the signal-to-noise (S/N) ratios of 3 and 10, respectively.

2.5.3 Evaluation of Accuracy and Precision Using Inter-day and Intra-day Assay

The accuracy and precision were determined by quantitating three replicates of plasma samples spiked with paclitaxel at concentrations of 10, 100, and 1,000 ng/ml. The samples were prepared on the same day and on three consecutive days to represent the intra-day and inter-day samples, respectively. The accuracy was estimated using the equation: bias (%) = [(observed concentration—nominal concentration)/nominal concentration] × 100. The precision was calculated using the formula: relative standard deviation (RSD %) = [standard deviation/observed concentration] × 100.

2.6 Herb-Drug Pharmacokinetic Interactions

Male SD rats, provided by the Laboratory Animal Center of Taipei Medical University, were used to determine the effects of XSLJZT on the pharmacokinetics of paclitaxel. All animal experiments were done in accordance with regulations of the animal experimentation committee of Taipei Medical University (IACUC, approval no. LAC-2015-0105). The animals had a 12 h light/dark cycle and had free access to food and water. Each group consisted of six rats, and paclitaxel (2 mg/kg, i. v.) was administered to the control group, while other animals were divided into four groups according to the different treatments they received. The first treatment group (which represented co-treatment) received XSLJZT (250 mg/kg, p. o.) 2 h prior to paclitaxel (2 mg/kg, i. v.) administration, while in the second, third, and fourth groups (pretreatment), XSLJZT (250 mg/kg, p. o.) was administered for 3, 5, and 7 days prior to paclitaxel administration, respectively. Blood samples (220 µl) were collected from the jugular vein at the following time intervals: 1, 5, 10, 15, 30, 60, 120, 180, 240, 300, and 360 min following paclitaxel administration, and centrifuged at 1800 rpm for 10 min to collect the plasma. Samples were prepared using a liquid-liquid extraction method, and LC/MS/MS was used to detect paclitaxel.

2.7 Western Blot Analysis for Metabolic Enzymes Expression

2.7.1 Preparation of Animals for Rat Liver Tissue

Male SD rats were used for liver tissue protein collection and were randomly divided into seven groups. The first group served as control group and was administered distilled water. The second, third and fourth groups were treated with XSLJZT (250 mg/kg, p. o.) only for the different treatment days (3,5, and 7 days, respectively), whereas the sixth, seventh and eighth groups received XSLJZT (250 mg/kg, p. o.) for three different pre-treatment days (3, 5, and 7 days, respectively), in addition to paclitaxel (2 mg/kg, i. v.). Liver tissues were collected, and RIPA lysis buffer was used to extract the protein from the liver tissues. The samples were then centrifuged, and the supernatants were collected for protein quantification.

2.7.2 Hep-G2 Cells Preparation

Hep-G2 cells were cultured in Dulbecco's modified Eagle's medium (DMEM) supplemented with 10% fetal bovine serum (FBS), 1% penicillin-streptomycin, and 1% L-glutamine at 37°C in a 5% CO_2 atmosphere. The cells were seeded in 6-well plates at a concentration of 1×10^5/ml. Medium (0.2 ml) was added to each well, and the cells were incubated for 24 h. Then, the medium was discarded, and the cells were treated with different concentrations of XSLJZT for 24 h. Time dependency was evaluated by treating the cells with 800 µg/ml XSLJZT for 1, 2, 4, 6 and 24 h. After cell collection using trypsin, the protein was extracted using RIPA lysis buffer and stored at −20°C for western blot analysis (Cui et al., 2014).

2.7.3 Western Blot Analysis

To determine the influence of XSLJZT on CYP3A4 enzymes in Hep-G2 cells and CYP3A1/2 in rat liver tissues, a bicinchoninic acid (BCA) assay kit was used to quantify the protein concentration. Protein samples (50 µg) were used for western blot analysis. Sodium dodecyl sulfate-polyacrylamide gels (10%) were used for protein separation and transferred onto polyvinylidene difluoride (PVDF) membranes. Non-fat milk (5%) was used to block the samples at room temperature for 1 h before adding the primary antibodies (GAPDH and CYP3A4 antibodies). This was followed by incubating the membranes overnight at 4°C. The next day, the membranes were washed with Tris buffer at room temperature for 30 min. Mouse and goat anti-rabbit IgG were used as secondary antibodies at room temperature for 1 h before visualizing the protein bands with ECL prime detection reagent, using the Chemi Doc MP imaging system (Li et al., 2021).

2.8 Enzyme Kinetics Using Human Liver Microsomes

To determine the influence of XSLJZT on the metabolism of paclitaxel, human liver microsomes were used (HLMs). The HLMs (0.5 mg/ml) were added with phosphate buffered saline (0.1 M, pH = 7.4) (PBS) and XSLJZT (0.5, 5, and 10 mg/ml) and paclitaxel (1, 4, 8, and 16 µM) and). The reaction was initiated by the addition of an NADPH generating system (1 mM NADP, 10 mM glucose 6-phosphate, 2 IU/ml glucose 6-phosphate dehydrogenase, and 5 mM MgCl2), and the samples were

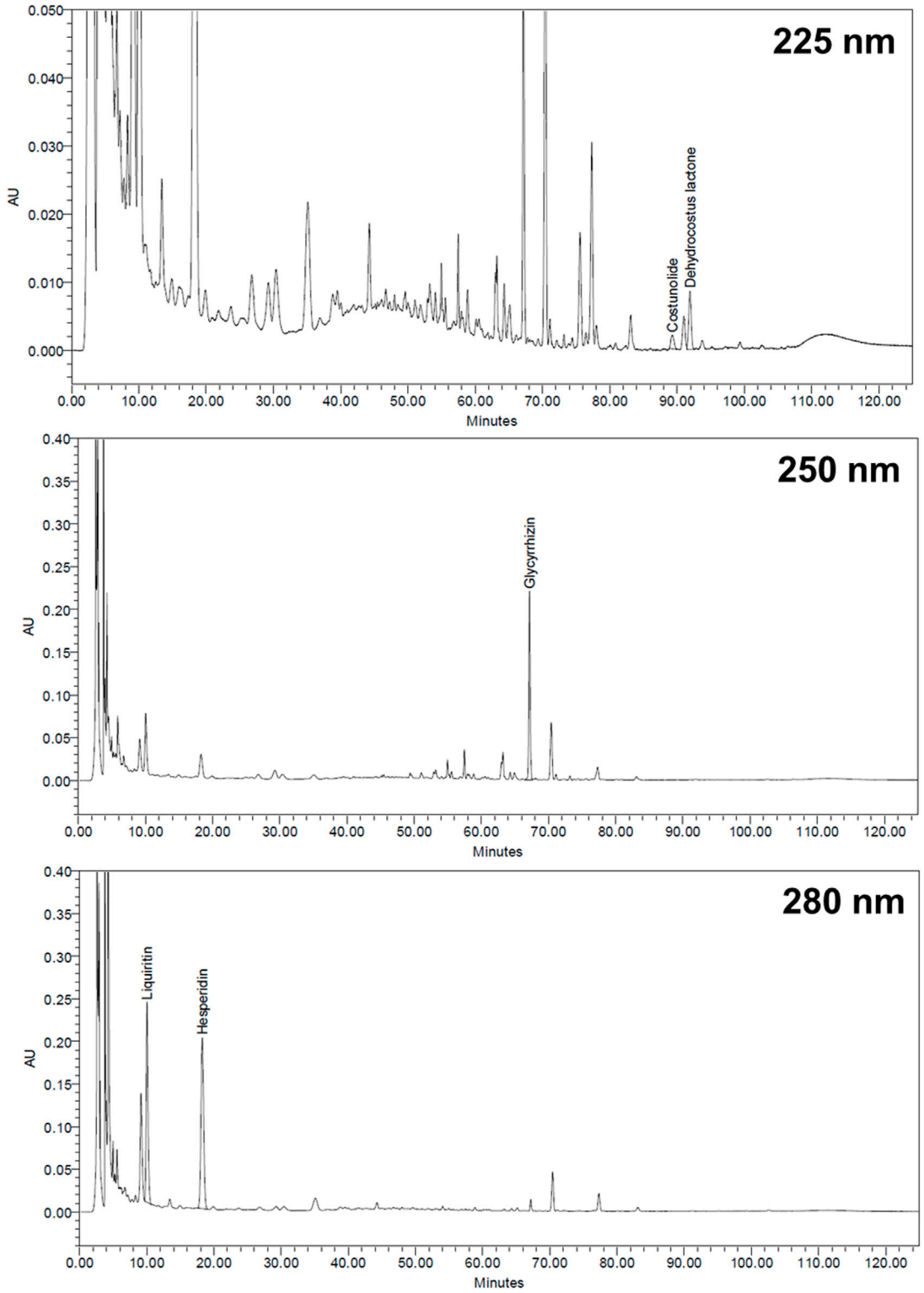

FIGURE 1 | HPLC chromatogram of Xiang-Sha-Liu-Jun-Zi Tang (XSLJZT).

incubated for 30 min at 37°C in a shaking water bath. The reaction was terminated by the addition of acetonitrile (200 μL) and centrifugation at 18,000 × *g* for 10 min. The supernatant was extracted into new Eppendorf tubes and evaporated to dryness. The residues were then reconstituted for the analysis. Time dependency was evaluated by pre-incubating the HLMs with

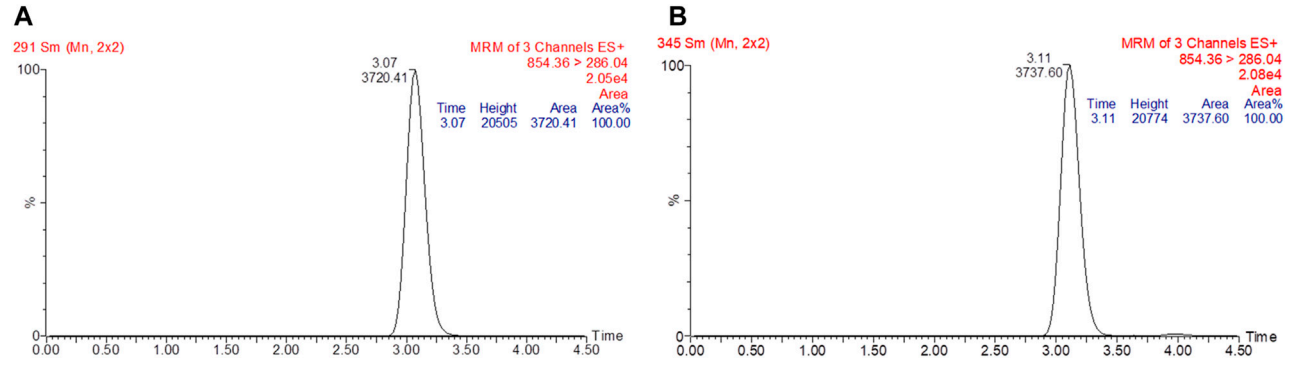

FIGURE 2 | Chromatogram of standard paclitaxel prepared in methanol **(A)**. The retention time for paclitaxel was at 3.07 min with a peak area of 3720.41. Chromatogram of paclitaxel spiked in rat plasma **(B)**. The retention time for paclitaxel was at 3.11 min with a peak area of 3737.60.

XSLJZT (0.5, 5, and 10 mg) for different pre-incubation times (0, 10, and 30 min). After each pre-incubation period, paclitaxel (16 μM) was added, and the samples were incubated for 30 min (Wattanachai et al., 2011; Cheng et al., 2017).

2.9 Data Analysis

WinNonlin standard edition version 1.1 software was used to analyze the PK parameters. Each dataset was analyzed using a two-compartment model. The PK parameters observed included the drug concentration at zero time (C_0), the area under the concentration versus time curve (AUC), half-life ($T_{1/2}$), clearance (CL), and mean residence time (MRT). For the statistical analysis, two groups were compared with an unpaired Student's t-test using Sigma Plot 10.0 software. Statistical significance was set to $p < 0.05$. Data were summarized as the mean ± standard deviation.

3 RESULTS

3.1 HPLC Analysis of Marker Substances in XSLJZT

The retention times for liquiritin, hesperidin, glycyrrhizin, costunolide, and dehydrocostus lactone were 10.04, 18.27, 67.17, 89.25, and 91.92 min, respectively (**Figure 1**). Each Gram of XSLJZT contained liquiritin, hesperidin, glycyrrhizin,

TABLE 1 | Intra-day and inter-day accuracy (%bias) and precision (%RSD) values for quantifying paclitaxel in plasma using an LC/MS/MS method.

Cnormal (ng/ml)	Intra-day (*n* = 6)			Inter-day (*n* = 6)		
	Cobs (ng/ml)	Precision (%)	Accuracy (%)	Cobs (ng/ml)	Precision (%)	Accuracy (%)
5	5.03 ± 0.1	0.9	0.6	4.9 ± 0.1	2.1	−2.0
10	10.67 ± 1.2	10.8	6.7	10.6 ± 0.7	6.1	6.0
50	47.31 ± 4.0	8.5	−5.4	48.1 ± 2.7	5.5	−3.8
100	96.41 ± 5.2	5.4	−3.6	98.9 ± 2.7	2.7	−1.1
500	527.78 ± 24.4	4.6	5.6	493.8 ± 26.5	5.4	−1.2
1,000	1,026.90 ± 121.9	11.9	2.7	998.2 ± 22.9	2.3	−0.2

C normal: Normal concentration.
Cobs: Observed concentration.
Data expressed as the mean ± standard deviation.
Accuracy = (Cobs-Cnormal)/Cnormal × 100; precision = standard deviation/Cobs × 100.

TABLE 2 | Recovery rate and matrix effect of paclitaxel.

Cnormal (ng/ml)	Spiked in mobile phase (set 1)	Spiked after extraction (set 2)	Spiked before extraction (set 3)	Matrix effect (%)	Recovery rate (%)
10	44 ± 5	38 ± 3	34 ± 2	85	91
100	313 ± 118	275 ± 95	244 ± 0.8	88	89
1,000	2642 ± 600	2341 ± 926	2006 ± 342	89	86

C normal: Normal concentration.
Data are expressed as the mean ± standard deviation (n = 3).
Matrix effect = (Set 2/Set 1) × 100, and recovery rate = (Set 3/Set 2) × 100.

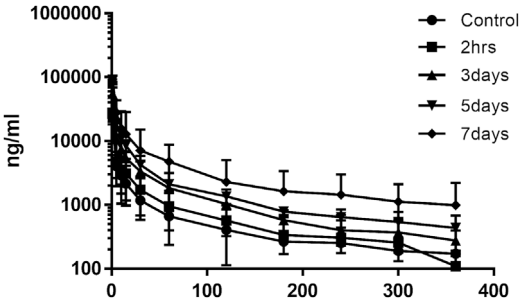

FIGURE 3 | Mean time-concentration curve of paclitaxel in rat blood samples. $n = 6$. The curve shows the change in plasma concentration of paclitaxel in the groups that were pre-treated with XSLJZT for 3, 5, and 7 days.

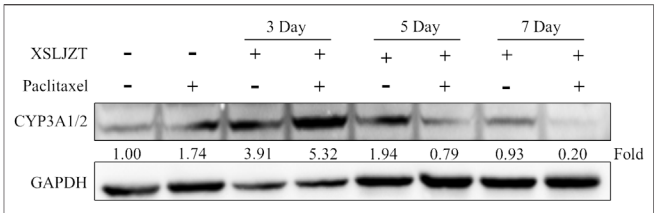

FIGURE 4 | Results showing the inhibitory effect of XSLJZT on CYP3A4 expression in SD rat liver tissues. XSLJZT inhibited the expression of CYP3A4 enzymes with highest effect observed in the 7-days-pretreatment group.

costunolide, and dehydrocostus lactone at 3.13, 16.86, 3.84, 0.04, and 0.15 mg, respectively.

3.2 LC/MS/MS Method Validation

The linearity of the calibration curve was established by plotting the peak ratio of paclitaxel. Good linearity was achieved over the concentration range of 5–1,000 ng/ml with a coefficient of estimation (r^2) of 0.9998. Chromatograms of the standard and paclitaxel-spiked rat plasma are shown in **Figures 2A,B**. The LOD of paclitaxel was 2 ng/ml with an S/N ratio of 5.3, and the LOQ was 5 ng/ml with an S/N ratio of 33.9. The values of both precision and accuracy were within 15% (**Table 1**), which is an acceptable criterion. Both the extraction efficiency and matrix effect were within the acceptable limits of >80% (**Table 2**). These results proved that the LC/MS/MS method was reliable and reproducible; thus, it was used for sample analysis.

3.3 Effect of XSLJZT on the Pharmacokinetics of Paclitaxel in Rats

The effects of XSLJZT on paclitaxel plasma concentrations were evaluated by comparing the changes in PK parameters between the treatment groups and the control group. The time-concentration curve is displayed in **Figure 3**, and the PK parameters are summarized in **Table 3**. The results indicated that XSLJZT significantly increased the AUC in the pretreated groups. The highest increase was observed in the 7-days-pretreated group with an AUC of 786.44 ± 193.14 min μg/ml as compared to the control group which had an AUC of 186.19 ± 64.42 min μg/ml. No significant change in the AUC (212.36 ± 138.92 min μg/ml) was observed in the co-treatment group. XSLJZT significantly prolonged the half-life ($T_{1/2}$) from 17.11 ± 2.48 min to 22.77 ± 2.08, 30.75 ± 8.81, 34.74 ± 7.97, and 37.56 ± 4.75 in the co-treatment groups and in the pretreatment groups of 3, 5, and 7 days, respectively. However, the MRT was significantly prolonged only in the pretreatment groups of 5 and 7 days.

3.4 Influence of XSLJZT on CYP3A4 Expression

SD rat liver tissues and Hep-G2 cells were used to evaluate the influence of XSLJZT on CYP 3A4 enzymes. XSLJZT inhibited the enzyme expression in both the rat liver tissues and Hep-G2 cells. In the rat liver tissue, XSLJZT inhibited CYP3A1/2 expression starting from 5 days pretreatment. However, the highest effect was observed in the 7 days pretreatment group (**Figure 4**). In Hep G2 cells, XSLJZT inhibited the expression of CYP3A4 in a dose-and time-dependent manner. The highest inhibition was observed at a concentration of 800 μg/ml XSLJZT (**Figures 5**, **6**).

3.5 Inhibitory Effect of XSLJZT on Enzyme Activity in HLMs

HLMs were incubated with paclitaxel (16, 8, 4, and 1 μM) with or without XSLJZT (0.5, 5, and 10 mg/ml) for 30 min. The residual paclitaxel concentration significantly increased in the groups where HLMs were incubated with both paclitaxel and XSLJZT as compared to the control group, which was incubated

TABLE 3 | Pharmacokinetic properties of paclitaxel (2 mg/kg i.v) with or without XSLJZT (250 mg/kg).

Parameters	Units	Paclitaxel (2 mg/kg)	Pretreatment groups			Co-treatment group
			3 Days	5 Days	7 Days	2 h
AUC	Min μg/mL	186.2 ± 64.4	439.2 ± 89.9*	631.7 ± 190.6*	786.4 ± 193.1**	212.4 ± 138.9
Co	μg/mL	87.9 ± 67.3	111.3 ± 116.1	116.3 ± 74.3	134.7 ± 16.0	65.8 ± 6.5
$T_{1/2}$	Min	17.1 ± 2.5	32.7 ± 7.1*	34.7 ± 8.0*	37.6 ± 4.8*	22.8 ± 2.1*
MRT	Min	21.5 ± 9.3	35.5 ± 8.7	38.8 ± 10.4*	45.9 ± 11.7*	21.4 + 8.3
K10		0.4 ± 0.3	0.3 ± 0.4	0.27 ± 0.04	0.2 ± 0.07	0.4 ± 0.2

*Abbreviations: AUC, area under the concentration versus time curve; C0, drug concentration at zero time; T1/2, terminal half-life; K10, elimination constant. (*p < 0.05, **p < 0.001).*

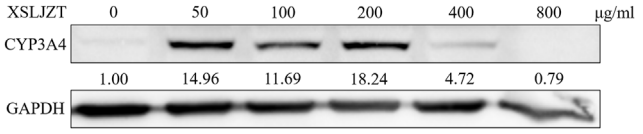

FIGURE 5 | Results showing the inhibitory effect of XSLJZT on CYP3A4 enzyme expression in Hep G2 cells after 24 h incubation period. XSLJZT inhibited CYP3A6 enzyme expression in a dose-dependant manner with the highest effect observed at 800 μg/ml.

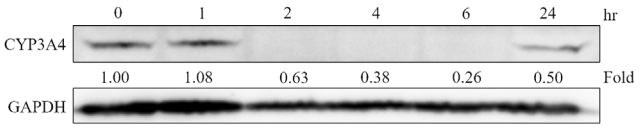

FIGURE 6 | Cells were treated with 800 μg/ml XSLJZT and incubated for different incubation times. The results indicated that XSLJZT inhibited CYP3A4 enzyme expression in a time-dependant manner.

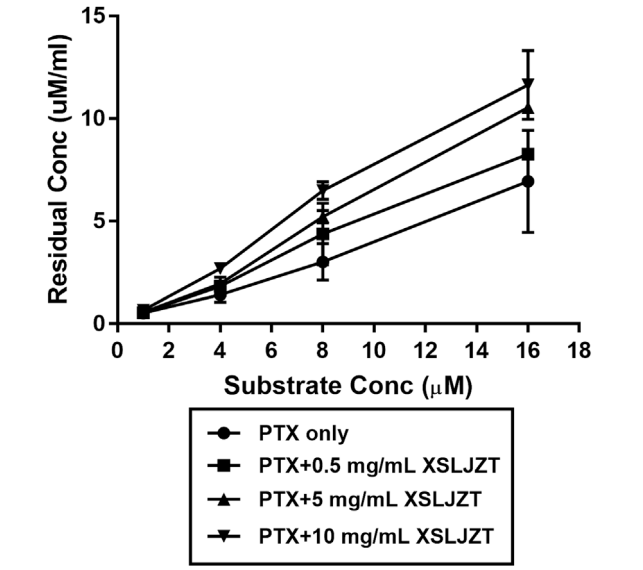

FIGURE 7 | The inhibitory effect of XSLJZT on paclitaxel metabolism in HLMs. Data were expressed at mean ± standard deviation. XLJZT inhibited paclitaxel metabolism in a dose-dependent manner with the highest effect observed in the groups co-incubated with XSLJZT 10 mg/ml.

with paclitaxel only. This indicated that XSLJZT inhibited paclitaxel metabolism, which in turn increased its concentration (**Figure 7**). To determine the influence of XSLJT on enzyme activity at different incubation times, the HLMs were pre-incubated with different concentrations of XSLJZT (0.5, 5, and 10 mg/ml) for 0, 10, and 30 min. No significant difference was observed with the different pre-incubation times, indicating that XSLJZT did not significantly inhibit XSLJZT in a time-dependent manner (**Figure 8**). To understand the inhibition kinetics, different concentrations of

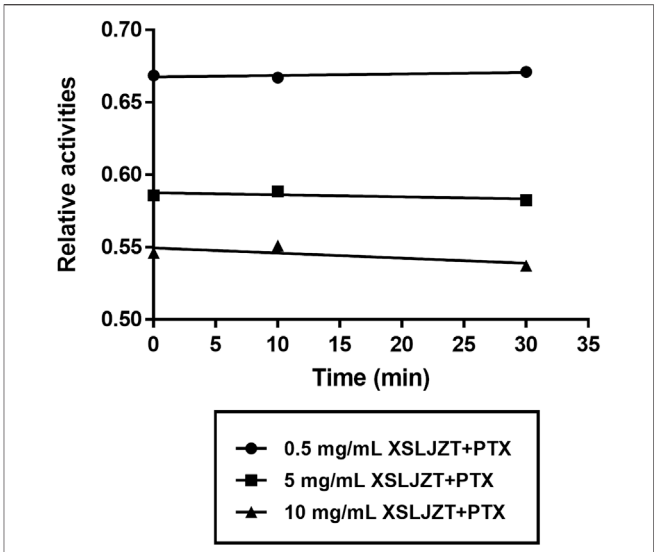

FIGURE 8 | Time-course inhibition of XSLZJT on enzyme activity in HLMs. HLMs were pre-incubated with XSLJZT for 0, 10, and 30 min before the addition of 16 μM paclitaxel. XSLJZT inhibited the enzyme activity in a dose-dependent manner but no time-dependence was observed.

XSLJZT (5 and 10 mg/ml) were incubated with different concentrations of paclitaxel (4, 8, and 16 μM). A Lineweaver-Burk plot and a secondary plot indicated that XSLJZT inhibited the enzyme activity in HLMs by competitive inhibition with a Ki value of 6.4 mg/ml (**Figures 9A,B**).

4 DISCUSSION

Different species metabolize paclitaxel differently. 6α-OHP is the major paclitaxel metabolite formulated in humans which is seconded by C3′α-OHP. 6α-OHP is formulated by CYP2C8 enzymes in humans which is not available in rats. In both rats and humans, paclitaxel is metabolized to C3′α-OHP by CYP3A enzymes. In humans C3′α-OHP is formulated by isoform CYP3A4 and in rats it is formulated by isoform CYP3A2/1. The rats CYP3A1/2 enzymes are orthologous to the human CYP3A4 enzymes (Václavíková et al., 2003; Vaclavikova et al., 2004; Sun et al., 2016). The influence of XSLJZT on CYP3A enzymes was evaluated in both Hep-G2 cells and rat liver tissues. In the rat liver tissue, the animals were pre-treated with XSLJZT prior to the experiment. XSLJZT inhibited CYP3A1/2 enzymes expression differently with variations in pre-treatment periods. In the Hep-G2 cells, XSLJZT inhibited CYP3A4 enzymes expression in a dose and time dependent manner.

In the rat blood plasma, XSLJZT increased paclitaxel AUC differently with variation in co-treatment and pre-treatment periods. In line with the animal study, western blot results indicated a variation in the reduction of CYP3A1/2 enzyme expression with differences in pre-treatment days. Similar results were observed in the HLM, where XSLJZT inhibited enzymes activities which in turn decrease paclitaxel metabolism and increased its residual concentration. In line

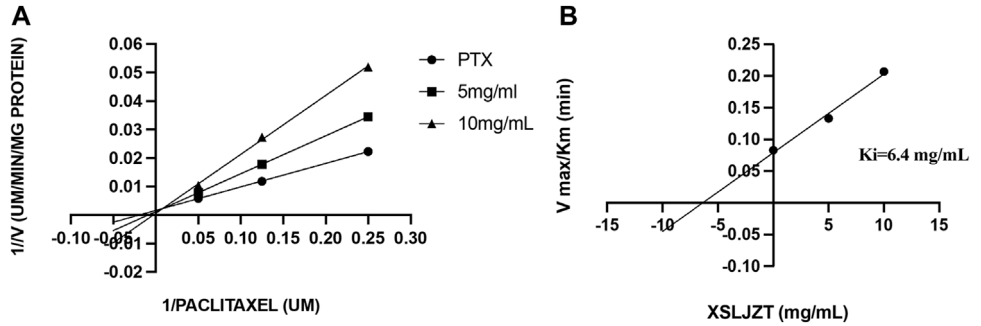

FIGURE 9 | The Lineweaver-Burk plot **(A)** was obtained after different concentrations of paclitaxel (1, 8, and 16 μM) were incubated with different concentrations of XSLJT (5 and 10 mg/ml) for 30 min. XSLJZT inhibited the enzyme activity by a competitive inhibition method. The second plot of slope from Lineweaver-Burk plots **(B)** was obtained and XSLJZT competitively inhibited XSLJZT with a Ki value of 15 μM.

with the enzyme activity study, XSLJZT inhibited the expression on CYP3A4 enzymes in Hep-G2 cells.

XSLJZT is a herbal formula that contains a high polyphenol content. Liu *et al.* reported that glycyrrhizin and liquiritin from *Glycyrrhiza uralensis* (*Gan Cao*), quercetrin, and hesperidin from *Citrus reticulata* (*Chen Pi*), ginsenoside Rg1, ginsenoside Re, ginsenoside Rb1 from *Panax ginseng* (*Ren Shen*), 6-gingerol and 6-shogaol from *Zingiber officinale*, and costunolide and dehydrocostus lactone from *Aucklandia lappa* (*Mu Xiang*) could be detected in XSLJZT using HPLC-MS (Liu et al., 2017). Polyphenols can potentially influence the cytotoxicity of chemotherapeutic drugs either by additive or synergistic effects, which can result in toxicity (Mahbub et al., 2015; Klimaszewska-Wisniewska et al., 2016). They can also affect the metabolizing enzymes either by direct polyphenol enzyme binding or by affecting the protein expression of the enzymes. In previous reports, it was observed that most polyphenols inhibit the expression of the major metabolizing enzymes in the body (CYP-450 enzymes), which can affect the metabolism of co-administered substrate drugs (Korobkova, 2015; Yang et al., 2019).

Studies have reported an increase in the use of herbal medicines among cancer patients in order to minimize the side effects of chemotherapy and improve the general health (Yin et al., 2013). Although herbal medicines can minimize the side effects of chemotherapy, it is important to assess the potential herb-drug PK interactions. In a clinical setting, cancer patients can take herbal medicines before, during, and or after chemotherapy. The combination of herbal medicines and chemotherapy can potentially result in herb-drug interactions. Therefore, in order to understand the potential influence of XSLJZT on paclitaxel pharmacokinetics in clinics, SD rats were classified into control, pretreatment, and co-treatment groups (Koçaşlı and Demircan, 2017; Li et al., 2020). XSLJZT differently influenced paclitaxel PK parameters, with variation in pretreatment days. It increased paclitaxel AUC for 2-, 3-, and 4-fold after 3, 5, and 7 days of pretreatment, respectively. However, it did not significantly influence the AUC of paclitaxel in the co-treatment group. XSLJZT significantly prolonged the half-life of paclitaxel in both pre-and co-treatment groups, with the highest increase in the 7-days pretreatment group.

To investigate the influence of XSLJZT on paclitaxel metabolism in humans, an enzyme kinetic study was conducted using HLMs. Human liver microsomes are the dominant systems used *in vitro* to understand drug metabolism and can be used to easily understand the effect of herbal medicines on chemotherapeutic metabolism in the clinic (Zhang et al., 2015). XSLJZT increased the residual paclitaxel concentration in a dose-dependent manner, with the highest increase observed in the group co-incubated with 10 mg/ml XSLJZT. It competitively inhibited enzyme activity in a dose-dependent manner. However, no significant time-dependency was observed.

XSLJZT is a herb commonly used by breast cancer patients. It contains a high content of polyphenols, which could possibly result in herb-drug PK interactions (Kaspera and Croteau, 2006). *Panax ginseng* (Ren Shen) in XSLJZT contains ginsenosides that specifically inhibit metabolism and decrease CYP3A4 enzyme activity, gene, and protein expression, and *Glycyrrhiza uralensis* (Gan Cao) can inhibit CYP2C8 (Yu et al., 2011; Li et al., 2017). In this study, XSLJZT increased paclitaxel AUC in rat blood samples, inhibited CYP 3A enzymes expression and inhibited paclitaxel metabolism in human liver microsomes but the effects of individual XSLJZT herbs on paclitaxel were not evaluated.

5 CONCLUSION

In this study, the influence of XSLJZT on paclitaxel was assessed. XSLJZT increased paclitaxel AUC by 2-, 3-, and 4-fold in the groups pretreated for 3, 5, and 7 days, respectively. However, no significant influence was observed in the co-treated groups. In line with the animal study, XSLJZT inhibited paclitaxel metabolism in HLM which resulted in the increase in paclitaxel residual concentration. Western blot results indicated a reduction in CYP3A1/2 enzyme expression in rat liver tissues and CYP3A4 enzymes in Hep-G2 cells. The inhibitory effects of XSLJZT on CYP3A enzymes can potentially result in paclitaxel herb-drug interactions. In the pharmacokinetic results, it was observed that XSLJZT influenced paclitaxel parameters differently with variations in pre-treatment days and in the rat

liver tissue, XSLJZT inhibited CYP3A1/2 enzymes expression differently with variations in pre-treatment days. This indicates that XSLJZT can clinically affect paclitaxel differently with differences in pretreatment and co-treatment regimens.

Although XSLJZT significantly increased paclitaxel AUC and inhibited CYP3A1/2 enzymes in the pretreatment groups, no significant difference was detected in the co-treatment group. This could indicate that XSLJZT can be safely co-administered with paclitaxel on the same treatment day but should be monitored in longer pre-treatment durations. This study serves as a foundation for guidance when XSLJZT is co-administered with paclitaxel and other chemotherapeutics metabolized via a similar pathway. Different species metabolize paclitaxel differently therefore to fully establish the effects of XSLJZT on paclitaxel in clinic, further studies should be carried out with human experiments.

DATA AVAILABILITY STATEMENT

The original contributions presented in the study are included in the article/Supplementary Material, further inquiries can be directed to the corresponding authors.

ETHICS STATEMENT

The animal study was reviewed and approved by the Laboratory Animal Center of Taipei Medical University.

AUTHOR CONTRIBUTIONS

Conceptualization, C-CW and C-JL; Investigation, AK, Y-SU, F-YL, LT, and C-JL; Methodology, AK, Y-SU, L-HW, T-YW, F-YL, LT, C-CW, and C-JL; Supervision, C-CW; Writing—original draft, AK; Writing—review and editing, C-JL.

FUNDING

This work was financially supported by the by Taipei Medical University (Grant Number: TMU103-AE1-B38).

ACKNOWLEDGMENTS

Authors would thanks for the HPLC analysis technical support from HERBIOTEK Co., Ltd.

REFERENCES

Bernabeu, E., Cagel, M., Lagomarsino, E., Moretton, M., and Chiappetta, D. A. (2017). Paclitaxel: what Has Been Done and the Challenges Remain Ahead. *Int. J. Pharm.* 526 (1-2), 474–495. doi:10.1016/j.ijpharm.2017.05.016

Boussios, S., Pentheroudakis, G., Katsanos, K., and Pavlidis, N. (2012). Systemic Treatment-Induced Gastrointestinal Toxicity: Incidence, Clinical Presentation and Management. *Ann. Gastroenterol.* 25 (2), 106–118.

Cheng, X., Lv, X., Qu, H., Li, D., Hu, M., Guo, W., et al. (2017). Comparison of the Inhibition Potentials of Icotinib and Erlotinib against Human UDP-Glucuronosyltransferase 1A1. *Acta Pharm. Sin. B.* 7 (6), 657–664. doi:10.1016/j.apsb.2017.07.004

Cheng, Y. Y., Hsieh, C. H., and Tsai, T. H. (2018). Concurrent Administration of Anticancer Chemotherapy Drug and Herbal Medicine on the Perspective of Pharmacokinetics. *J. Food Drug Anal.* 26 (2S), S88–S95. doi:10.1016/j.jfda.2018.01.003

Cui, H. M., Zhang, Q. Y., Wang, J. L., Chen, J. L., Zhang, Y. L., and Tong, X. L. (2014). *In Vitro* studies of Berberine Metabolism and its Effect of Enzyme Induction on HepG2 Cells. *J. Ethnopharmacol.* 158 Pt A, 388–396. doi:10.1016/j.jep.2014.10.018

Fasinu, P. S., and Rapp, G. K. (2019). Herbal Interaction with Chemotherapeutic Drugs-A Focus on Clinically Significant Findings. *Front. Oncol.* 9, 1356. doi:10.3389/fonc.2019.01356

Gallego-Jara, J., Lozano-Terol, G., Sola-Martínez, R. A., Cánovas-Díaz, M., and de Diego Puente, T. (2020). A Compressive Review about Taxol: History and Future Challenges. *Molecules* 25 (24), 5986. doi:10.3390/molecules25245986

Health, U.D.o., H. Services (2001). Bioanalytical Method Validation, Guidance for Industry. Available at: http://www.fda.gov./cder/guidance/4252fnl.Htm.

Hendrikx, J. J., Lagas, J. S., Rosing, H., Schellens, J. H., Beijnen, J. H., and Schinkel, A. H. (2013). P-glycoprotein and Cytochrome P450 3A Act Together in Restricting the Oral Bioavailability of Paclitaxel. *Int. J. Cancer* 132 (10), 2439–2447. doi:10.1002/ijc.27912

Huang, K. C., Yen, H. R., Chiang, J. H., Su, Y. C., Sun, M. F., Chang, H. H., et al. (20172017). Chinese Herbal Medicine as an Adjunctive Therapy Ameliorated the Incidence of Chronic Hepatitis in Patients with Breast Cancer: A Nationwide Population-Based Cohort Study. *Evid. Based Complement. Alternat. Med.* 2017, 1052976. doi:10.1155/2017/1052976

Kaspera, R., and Croteau, R. (2006). Cytochrome P450 Oxygenases of Taxol Biosynthesis. *Phytochem. Rev.* 5 (2-3), 433–444. doi:10.1007/s11101-006-9006-4

Klimaszewska-Wisniewska, A., Halas-Wisniewska, M., Tadrowski, T., Gagat, M., Grzanka, D., and Grzanka, A. (2016). Paclitaxel and the Dietary Flavonoid Fisetin: a Synergistic Combination that Induces Mitotic Catastrophe and Autophagic Cell Death in A549 Non-small Cell Lung Cancer Cells. *Cancer Cel. Int.* 16, 10. doi:10.1186/s12935-016-0288-3

Kocasli, S., and Demircan, Z. (2017). Herbal Product Use by the Cancer Patients in Both the Pre and post Surgery Periods and during Chemotherapy. *Ajtcam* 14 (2), 325–333. doi:10.21010/ajtcam.v14i2.34

Korobkova, E. A. (2015). Effect of Natural Polyphenols on CYP Metabolism: Implications for Diseases. *Chem. Res. Toxicol.* 28 (7), 1359–1390. doi:10.1021/acs.chemrestox.5b00121

Lai, J. N., Wu, C. T., and Wang, J. D. (2012). Prescription Pattern of Chinese Herbal Products for Breast Cancer in Taiwan: a Population-Based Study. *Evid. Based Complement. Alternat. Med.* 2012, 891893. doi:10.1155/2012/891893

Lee, R. T., Kwon, N., Wu, J., To, C., To, S., Szmulewitz, R., et al. (2021). Prevalence of Potential Interactions of Medications, Including Herbs and Supplements, before, during, and after Chemotherapy in Patients with Breast and Prostate Cancer. *Cancer* 127 (11), 1827–1835. doi:10.1002/cncr.33324

Lee, Y. W., Chen, T. L., Shih, Y. R., Tsai, C. L., Chang, C. C., Liang, H. H., et al. (2014). Adjunctive Traditional Chinese Medicine Therapy Improves Survival in Patients with Advanced Breast Cancer: a Population-Based Study. *Cancer* 120 (9), 1338–1344. doi:10.1002/cncr.28579

Li, G., Simmler, C., Chen, L., Nikolic, D., Chen, S. N., Pauli, G. F., et al. (2017). Cytochrome P450 Inhibition by Three Licorice Species and Fourteen Licorice Constituents. *Eur. J. Pharm. Sci.* 109, 182–190. doi:10.1016/j.ejps.2017.07.034

Li, H., Tang, Y., Wei, W., Yin, C., and Tang, F. (2021). Effects of Xiaochaihu Decoction on the Expression of Cytochrome P450s in Rats. *Exp. Ther. Med.* 21 (6), 588. doi:10.3892/etm.2021.10020

Li, S., So, T. H., Tang, G., Tan, H. Y., Wang, N., Ng, B. F. L., et al. (2020). Chinese Herbal Medicine for Reducing Chemotherapy-Associated Side-Effects in Breast Cancer Patients: a Systematic Review and Meta-Analysis. *Front. Oncol.* 10, 599073. doi:10.3389/fonc.2020.599073

Liu, J. H., Cheng, Y. Y., Hsieh, C. H., and Tsai, T. H. (2017). Identification of a Multicomponent Traditional Herbal Medicine by HPLC-MS and Electron and Light Microscopy. *Molecules* 22 (12), 2242. doi:10.3390/molecules22122242

Liu, J. H., Cheng, Y. Y., Hsieh, C. H., and Tsai, T. H. (2018). The Herb-Drug Pharmacokinetic Interaction of 5-Fluorouracil and its Metabolite 5-Fluoro-5,6-Dihydrouracil with a Traditional Chinese Medicine in Rats. *Int. J. Mol. Sci.* 19 (1), 25. doi:10.3390/ijms19010025

Lo, L. C., Chen, C. Y., Chen, S. T., Chen, H. C., Lee, T. C., and Chang, C. S. (2012). Therapeutic Efficacy of Traditional Chinese Medicine, Shen-Mai San, in Cancer Patients Undergoing Chemotherapy or Radiotherapy: Study Protocol for a Randomized, Double-Blind, Placebo-Controlled Trial. *Trials* 13, 232. doi:10.1186/1745-6215-13-232

Mahbub, A. A., Le Maitre, C. L., Haywood-Small, S. L., Cross, N. A., and Jordan-Mahy, N. (2015). Polyphenols Act Synergistically with Doxorubicin and Etoposide in Leukaemia Cell Lines. *Cell Death Discov.* 1, 15043. doi:10.1038/cddiscovery.2015.43

McDonnell, A. M., and Dang, C. H. (2013). Basic Review of the Cytochrome P450 System. *J. Adv. Pract. Oncol.* 4 (4), 263–268. doi:10.6004/jadpro.2013.4.4.7

Ohnishi, S., and Takeda, H. (2015). Herbal Medicines for the Treatment of Cancer Chemotherapy-Induced Side Effects. *Front. Pharmacol.* 6, 14. doi:10.3389/fphar.2015.00014

Shih, Y. S., Tsai, C. H., Li, T. C., Lai, H. C., Wang, K. T., Liao, W. L., et al. (2019). The Effect of Xiang-Sha-Liu-Jun-Zi Tang (XSLJZT) on Irritable Bowel Syndrome: a Randomized, Double-Blind, Placebo-Controlled Trial. *J. Ethnopharmacol.* 238, 111889. doi:10.1016/j.jep.2019.111889

Smith, P. J., Clavarino, A., Long, J., and Steadman, K. J. (2014). Why Do Some Cancer Patients Receiving Chemotherapy Choose to Take Complementary and Alternative Medicines and what Are the Risks? *Asia Pac. J. Clin. Oncol.* 10 (1), 1–10. doi:10.1111/ajco.12115

Sun, Z., Zhang, Z., Ji, M., Yang, H., Cromie, M., Gu, J., et al. (2016). BDE47 Induces Rat CYP3A1 by Targeting the Transcriptional Regulation of miR-23b. *Sci. Rep.* 6, 31958. doi:10.1038/srep31958

Tekade, R. K., D'Emanuele, A., Elhissi, A., Agrawal, A., Jain, A., Arafat, B. T., et al. (2013). Extraction and RP-HPLC Determination of Taxol in Rat Plasma, Cell Culture and Quality Control Samples. *J. Biomed. Res.* 27 (5), 394–405. doi:10.7555/JBR.27.20120123

Vaclavikova, R., Soucek, P., Svobodova, L., Anzenbacher, P., Simek, P., Guengerich, F. P., et al. (2004). Different *In Vitro* Metabolism of Paclitaxel and Docetaxel in Humans, Rats, Pigs, and Minipigs. *Drug Metab. Dispos.* 32 (6), 666–674. doi:10.1124/dmd.32.6.666

Václavíková, R., Horský, S., Šimek, P., and Gut, I. (2003). Paclitaxel Metabolism in Rat and Human Liver Microsomes Is Inhibited by Phenolic Antioxidants. *Naunyn-schmiedeberg's Arch. Pharmacol.* 368 (3), 200–209. doi:10.1007/s00210-003-0781-9

Wattanachai, N., Polasek, T. M., Heath, T. M., Uchaipichat, V., Tassaneeyakul, W., Tassaneeyakul, W., et al. (2011). In Vitro-In Vivo Extrapolation of CYP2C8-Catalyzed Paclitaxel 6α-Hydroxylation: Effects of Albumin on *In Vitro* Kinetic Parameters and Assessment of Interindividual Variability in Predicted Clearance. *Eur. J. Clin. Pharmacol.* 67 (8), 815–824. doi:10.1007/s00228-011-1001-z

Xiao, H., Liu, L., Ke, S., Zhang, Y., Zhang, W., Xiong, S., et al. (2021). Efficacy of Xiang-Sha-Liu-Jun-Zi on Chemotherapy-Induced Nausea and Vomiting. *Medicine (Baltimore)* 100 (19), e25848. doi:10.1097/MD.0000000000025848

Xiao, Y., Liu, Y. Y., Yu, K. Q., Ouyang, M. Z., Luo, R., and Zhao, X. S. (2012). Chinese Herbal Medicine Liu Jun Zi Tang and Xiang Sha Liu Jun Zi Tang for Functional Dyspepsia: Meta-Analysis of Randomized Controlled Trials. *Evid. Based Complement. Alternat. Med.* 2012, 936459. doi:10.1155/2012/936459

Yang, L., Wang, Y., Xu, H., Huang, G., Zhang, Z., Ma, Z., et al. (20192019). *Panax Ginseng* Inhibits Metabolism of Diester Alkaloids by Downregulating CYP3A4 Enzyme Activity via the Pregnane X Receptor. *Evid. Based Complement. Alternat. Med.* 2019, 3508658. doi:10.1155/2019/3508658

Yin, S. Y., Wei, W. C., Jian, F. Y., and Yang, N. S. (2013). Therapeutic Applications of Herbal Medicines for Cancer Patients. *Evid. Based Complement. Alternat. Med.* 2013, 302426. doi:10.1155/2013/302426

Yu, C., Chai, X., Yu, L., Chen, S., and Zeng, S. (2011). Identification of Novel Pregnane X Receptor Activators from Traditional Chinese Medicines. *J. Ethnopharmacol.* 136 (1), 137–143. doi:10.1016/j.jep.2011.04.022

Zanger, U. M., and Schwab, M. (2013). Cytochrome P450 Enzymes in Drug Metabolism: Regulation of Gene Expression, Enzyme Activities, and Impact of Genetic Variation. *Pharmacol. Ther.* 138 (1), 103–141. doi:10.1016/j.pharmthera.2012.12.007

Zhang, H., Gao, N., Tian, X., Liu, T., Fang, Y., Zhou, J., et al. (2015). Content and Activity of Human Liver Microsomal Protein and Prediction of Individual Hepatic Clearance *In Vivo*. *Sci. Rep.* 5, 17671. doi:10.1038/srep17671

Conflict of Interest: Author LT is employed by Rosetta Pharmamate Co., Ltd.

The remaining authors declare that the research was conducted in the absence of any commercial or financial relationships that could be construed as a potential conflict of interest.

Publisher's Note: All claims expressed in this article are solely those of the authors and do not necessarily represent those of their affiliated organizations, or those of the publisher, the editors and the reviewers. Any product that may be evaluated in this article, or claim that may be made by its manufacturer, is not guaranteed or endorsed by the publisher.

frontiers | Frontiers in Pharmacology

ORIGINAL RESEARCH
published: 29 April 2022
doi: 10.3389/fphar.2022.849110

Tissue Distribution, Excretion, and Interaction With Human Serum Albumin of Total Bioflavonoid Extract From *Selaginella doederleinii*

Bing Chen[1,2†], Dafen Xu[1,2†], Zhijun Li[3], Yafei Jing[2], Luping Lin[2], Shaoguang Li[2], Liying Huang[2], Xiuwang Huang[4], Ailin Liu[2], Xinhua Lin[1,2]* and Hong Yao[2,5]**

[1]Key Laboratory of Nanomedical Technology (Education Department of Fujian Province), School of Pharmacy, Nano Medical Technology Research Institute, Fujian Medical University, Fuzhou, China, [2]Department of Pharmaceutical Analysis, School of Pharmacy, Fujian Medical University, Fuzhou, China, [3]Department of Orthopedic, The First Affiliated Hospital, Fujian Medical University, Fuzhou, China, [4]Department of Pharmacy, Xiamen Humanity Hospital, Fujian Medical University, Xiamen, China, [5]Fujian Key Laboratory of Drug Target Discovery and Structural and Functional Research, Fujian Medical University, Fuzhou, China

OPEN ACCESS

Edited by:
Guangbo Ge,
Shanghai University of Traditional Chinese Medicine, China

Reviewed by:
Aihua Zhang,
Heilongjiang University of Chinese Medicine, China
Xianchun Duan,
First Affiliated Hospital of Anhui University of Traditional Chinese Medicine, China
Yangliu Xia,
Dalian University of Technology, China

***Correspondence:**
Ailin Liu
ailinliu@fjmu.edu.cn
Xinhua Lin
13906909638@163.com
Hong Yao
yauhung@126.com

[†]These authors have contributed equally to this work and share first authorship

Specialty section:
This article was submitted to Ethnopharmacology, a section of the journal Frontiers in Pharmacology

Received: 05 January 2022
Accepted: 28 March 2022
Published: 29 April 2022

Citation:
Chen B, Xu D, Li Z, Jing Y, Lin L, Li S, Huang L, Huang X, Liu A, Lin X and Yao H (2022) Tissue Distribution, Excretion, and Interaction With Human Serum Albumin of Total Bioflavonoid Extract From Selaginella doederleinii. Front. Pharmacol. 13:849110. doi: 10.3389/fphar.2022.849110

Selaginella doederleinii Hieron is a traditional Chinese medicinal herb widely used to treat different cancers. Previously, we showed that the total bioflavonoid extract of *S. doederleinii* (TBESD) exhibits anti-carcinogenic activities both *in vitro* and *in vivo*. However, the plasma protein binding and pharmacokinetics parameters of TBESD remain unclear. To investigate plasma protein binding, tissue distribution, and excretion of TBESD, rats were administered a single dose of TBESD (600 mg/kg) intragastrically and tissue distribution and excretion of TBESD components were determined by rapid high-performance liquid chromatography and tandem mass spectrometry. TBESD binding to human serum albumin (HSA) was assessed by fluorescence spectroscopy. TBESD components amentoflavone, delicaflavone, robustaflavone, 2″,3″-dihydro-3′,3‴-biapigenin, and 3′,3‴-binaringenin were rapidly absorbed and distributed in various tissues, mostly in the lungs, kidneys, and ovaries, without long-term accumulation. The excretion of bioflavonoids occurred mostly via the intestinal tract and constituted 30% of the administered dose up to 48 h. Spectral analysis indicated that TBESD had a dynamic quenching effect on HSA by binding to one HSA site through hydrophobic interactions and hydrogen bond formation. This is the first comprehensive report on the tissue distribution, excretion, and plasma protein binding of TBESD. This study provides important information on TBESD pharmacokinetics necessary for its further development into a therapeutic form for clinical applications.

Keywords: selaginella doederleinii, bioflavonoid, tissue distribution, excretion, human serum albumin

INTRODUCTION

Selaginella doederleinii Hieron, a perennial herb with medicinal properties in southern China, has been traditionally used in folk medicine to treat inflammation, cardiovascular disease, and malignant tumors (Sui et al., 2016; Zou et al., 2017a; Zou et al., 2017b). The antitumor effect of *S. doederleinii* has garnered attention because its extract has been shown to considerably inhibit tumor growth *in vivo*

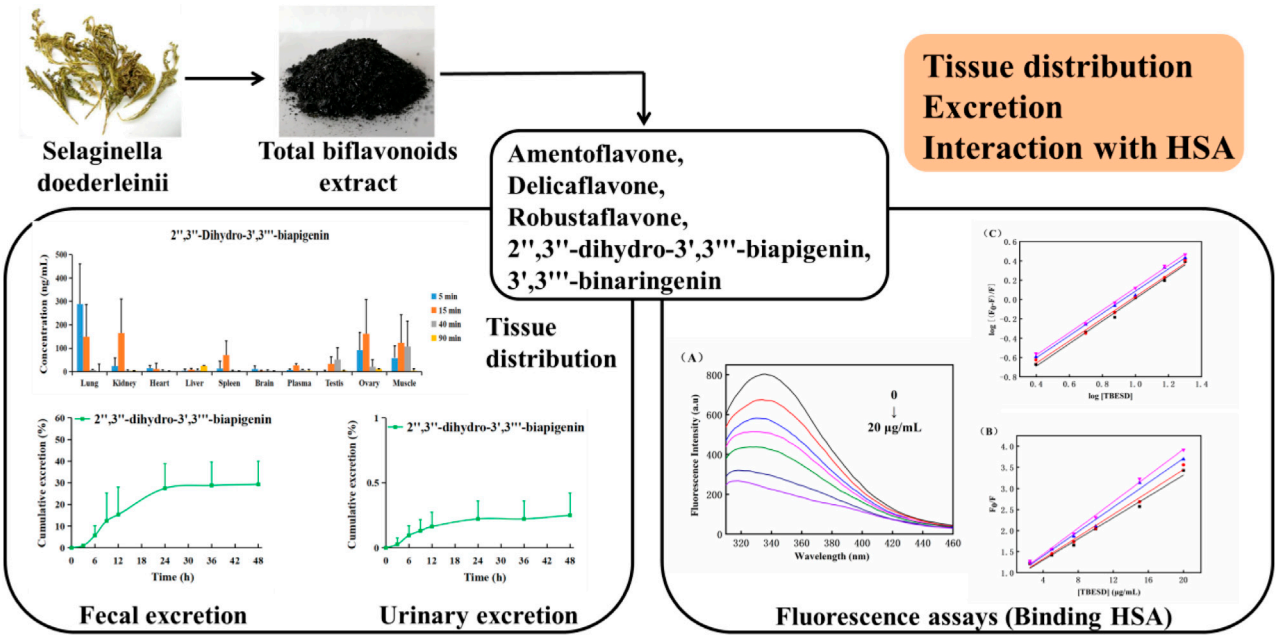

GRAPHICAL ABSTRACT |

(Yao et al., 2017; Li et al., 2020). Previous phytochemical studies have indicated that the main biologically active ingredients in *S. doederleinii* are flavonoids. Among the flavonoids, amentoflavone, delicaflavone, robustaflavone, 2″,3″-dihydro-3′,3‴-biapigenin, and 3′,3‴-binaringenin are considered to be mostly responsible for the antitumor effects of *S. doederleinii* (Chen et al., 2020; Kang et al., 2021; Liu et al., 2021). Functional pharmacological analysis revealed that the total bioflavonoid extract of *S. doederleinii* (TBESD), especially delicaflavone, can induce ROS-mediated apoptosis via caspase-dependent pathway accompanying with cell cycle arrest and inhibition of MAPK signaling cascades (Yao et al., 2019; Yao et al., 2020). In addition, delicaflavone can induce autophagy cell death by inhibiting the Akt/mTOR/p70S6K signaling pathway (Sui et al., 2016; Li et al., 2020). Overall, these studies suggest that TBESD is a promising anti-cancer candidate that deserves further investigation.

Previous pharmacokinetics studies on delicaflavone and TBESD have indicated that when administered as single oral (30–60 and 300–600 mg/kg, respectively) or intravenous (4 and 5–15 mg/kg, respectively) doses, amentoflavone, delicaflavone, robustaflavone, 2″,3″-dihydro-3′,3‴-biapigenin, and 3′,3‴-binaringenin have a short *in vivo* half-life and oral bioavailability below 3.5% (Chen et al., 2018). Analysis of tissue distribution of delicaflavone after intravenous administration has illustrated distribution predominantly in the livers, lungs, and kidneys, followed by rapid elimination. However, to the best of our knowledge, there are no specific reports on the tissue distribution, excretion, and plasma protein binding of TBESD (Chen et al., 2021).

Pharmacokinetic analysis of TBESD would reveal the absorption, distribution, metabolism, and excretion of its ingredients *in vivo* (Li et al., 2019). Furthermore, it may help elucidate their functional mechanisms, pharmacodynamics, and clinical efficacy, providing valuable information for the rational use of this herbal medicine and its further development (Zhu et al., 2020; Matsumoto et al., 2021). Therefore, pharmacokinetic investigation of TBESD is critical for understanding its safety and pharmacological and clinical effectiveness (Liao et al., 2021).

The pharmacokinetic parameters of drugs, such as absorption, metabolism, tissue distribution, and excretion, strongly depend on drug affinity to serum proteins, especially serum albumins, which are extensively used in drug-binding studies (Rabbani and Ahn, 2019). Human serum albumin (HSA), a primary protein in human blood, is known for its high drug affinity and the consequent effects on drug solubility, stability, and toxicity reduction (Cao et al., 2019; Qiu et al., 2020). Therefore, HSA is one of the main targets in the prediction of pharmacokinetic profiles of candidate therapeutic agents, and it is important to study TBESD binding to HSA in order to fully characterize the reactions of an organism to TBESD.

High-performance liquid chromatography-electrospray ionization-tandem mass spectrometry (HPLC-ESI-MS/MS) is an analytical method that has been widely applied in the pharmacokinetic analysis of multiple components in traditional Chinese medicines because of its high sensitivity and selectivity (Romański et al., 2017; Wang et al., 2021). In the

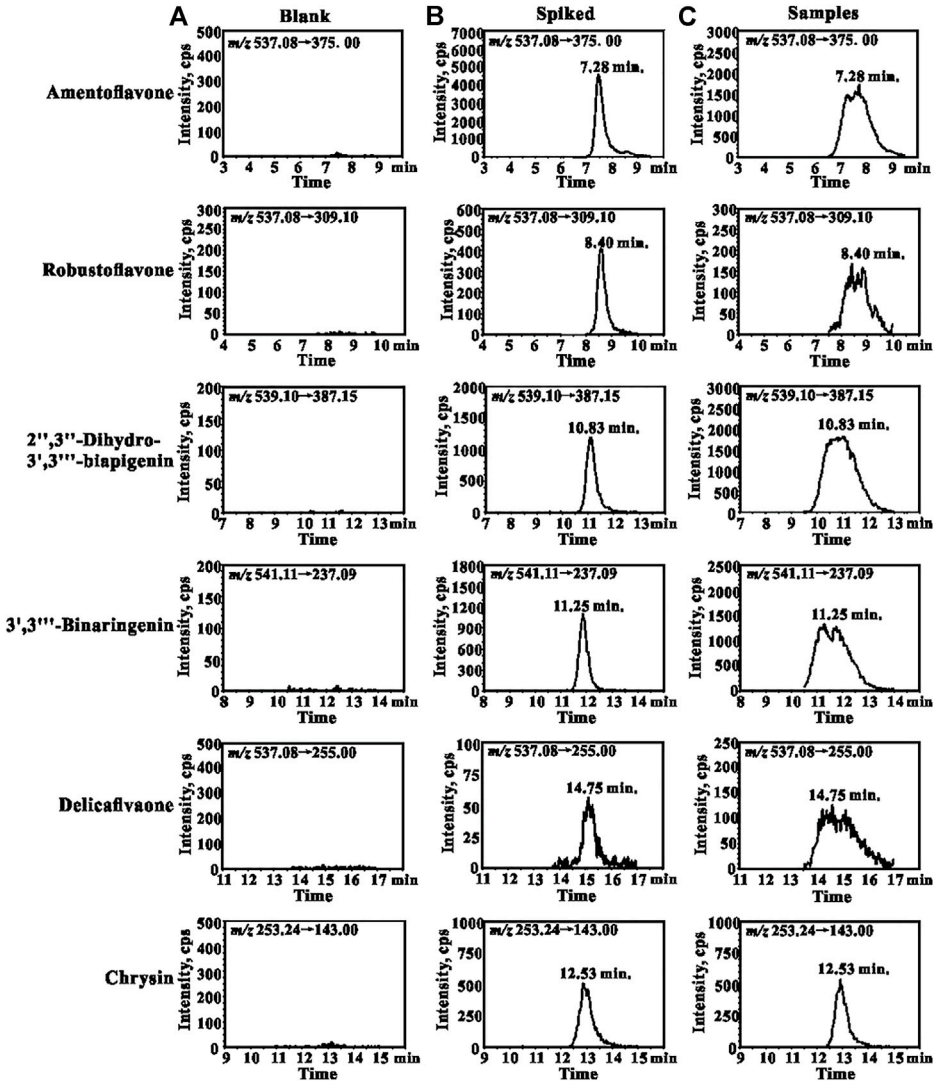

FIGURE 1 | Representative MRM chromatograms for amentoflavone, robustaflavone, 2″,3″-dihydro-3′,3‴-biapigenin, 3′,3‴-binaringenin, delicaflavone, and chrysin (IS): **(A)** blank lungs sample; **(B)** blank lungs spiked with QCM and IS (50 ng/ml); **(C)** lungs sample collected from the rat 5 min after oral administration of TBESD at a dose of 600 mg/kg.

present study, we analyzed TBESD tissue distribution and excretion by HPLC-ESI-MS/MS and its binding to HSA by fluorescence spectroscopy. The results provide not only reliable pharmacokinetic profiles of TBESD ingredients but also more information about the quality and functional mechanisms of TBESD.

TABLE 1 | Linear regression data of biflavonoids in lungs.

Analyte	Linear Range (ng/ml)	LLOQ (ng/ml)	Regression Equation (w = $1/X^2$)
Amentoflavone	4–1,000	0.37	y = 1.261x+0.056 (R^2 = 0.999)
Robustaflavone	2–500	0.26	y = 0.218x+0.004 (R^2 = 0.999)
2″,3″-Dihydro-3′,3‴-biapigenin	2–500	0.48	y = 0.671x+0.003 (R^2 = 0.999)
3′,3‴-Binaringenin	2–500	1.29	y = 0.585x+0.010 (R^2 = 0.998)
Delicaflavone	2–500	1.63	y = 0.035x+0.021 (R^2 = 0.997)

METHODS

Chemicals and Reagents

HPLC-grade acetonitrile and HPLC-grade methanol used in the study were purchased from Merck (Darmstadt, Germany). HPLC-grade acetic acid was purchased from Aladdin (Shanghai, China) and analytical-grade ethanol was obtained from Sinopharm Chemical Reagents (Shanghai, China). Free-fatty acid HSA (lyophilized powder) was acquired from Sigma-Aldrich (St. Louis, MO, United States). Reference standards of amentoflavone (batch number: 160,529) and chrysin (150,204) were purchased from Winherb (Shanghai, China). Delicaflavone, robustaflavone, 2″,3″-dihydro-3′,3‴-biapigenin, and 3′,3‴-binaringenin (purity ≥98%) were isolated from *S. doederleinii* and their molecular structures were fully characterized by FT-IR, UV, MS, ^{1}H-NMR, and ^{13}C-NMR (Chen et al., 2019). Ultrapure water was purified using a Milli-Q system (MA, United States).

Plant Material

Dried *S. doederleinii* Hieron was obtained from a local traditional Chinese medicine store in Fuzhou, and identified by Pro. Yao (Fujian Medical University, Fuzhou, China). A voucher specimen (batch number: 201,909) has been deposited at the Phytochemistry Laboratory, Fujian Medical University (Fuzhou, China).

Preparation of Herb Extracts

The process of obtaining TBESD and characterization of its main components were performed as previously described (Li et al., 2014). The contents of amentoflavone, delicaflavone, robustaflavone, 2″,3″-dihydro-3′,3‴-biapigenin, and 3′,3‴-binaringenin in TBESD, quantified by our previous HPLC method (**Supplementary Figure S1**), was 103.82, 35.12, 37.52, 44.40, and 53.36 mg/g, respectively.

Animals

Thirty healthy Sprague–Dawley rats (weighing 250 ± 20 g) were obtained from the Laboratory Animal Center of Fujian Medical University (Fuzhou, China). All rats were maintained in an environmentally controlled breeding room (temperature: 25 ± 2°C and relative humidity: 55 ± 5%) at a 12-/12-h light/dark cycle and were observed for 1 week before the experiment. The rats were provided rat feed and water *ad libitum*; before drug administration, they were fasted for 12 h but were allowed free access to water. All experiments were conducted in accordance with the Guidelines for the Care and Use of Laboratory Animals approved by the Animal Ethics Committee of Fujian Medical University.

TABLE 2 | Method validation of amentoflavone in rat tissue homogenates (n = 5).

Sample matrix	Con	Intra-day		Inter-day	
	ng/mL	Precision (RSD, %)	Accuracy (RE, %)	Precision (RSD, %)	Accuracy (RE, %)
Lungs	12	2.46	3.54	3.81	0.88
	160	2.70	4.68	3.69	2.64
	800	3.18	6.68	2.88	4.65
Liver	12	3.45	-5.55	4.22	-1.83
	160	1.83	-0.79	2.01	1.13
	800	1.29	1.00	1.20	0.60
Heart	12	2.20	2.70	3.26	3.65
	160	1.68	1.25	2.09	2.34
	800	3.21	-3.02	1.52	0.55
Spleen	12	0.40	0.60	0.86	0.16
	160	0.66	0.06	1.53	0.82
	800	0.82	-0.42	1.34	0.06
Kidney	12	2.92	-1.57	2.01	-2.72
	160	1.44	-0.79	2.25	0.85
	800	0.25	0.25	0.75	-0.14
Brain	12	1.29	3.71	1.48	2.44
	160	1.27	-0.32	3.55	1.09
	800	3.47	1.69	1.73	2.14
Testis	12	4.29	2.83	2.51	4.02
	160	3.77	0.54	2.38	1.06
	800	1.58	-0.60	1.30	0.71
Ovary	12	3.46	1.49	2.95	2.05
	160	4.63	-0.21	4.35	-0.90
	800	1.52	1.25	1.15	-0.29
Plasma	12	4.08	-0.71	0.93	0.66
	160	3.59	1.39	1.63	0.46
	800	3.61	0.83	0.81	0.62
Muscle	12	3.18	0.95	2.57	1.49
	160	3.17	1.75	3.12	2.40
	800	6.21	-1.26	5.22	0.03

Conc., concentration. RSD, relative S.D. (calculated from S.D., divided by mean and multiplied by 100).

TABLE 3 | Matrix effect and extraction recovery of amentoflavone in rat tissue homogenates (n = 5).

Sample matrix	Spiked con	Matrix Effect		Extraction Recovery	
	(ng/ml)	Mean ± SD (%)	RSD (%)	Mean ± SD (%)	RSD (%)
Lungs	12	102.56 ± 3.10	3.02	98.17 ± 2.36	2.40
	160	104.80 ± 4.08	3.90	97.57 ± 0.66	0.67
	800	101.54 ± 1.85	1.82	101.73 ± 3.10	3.05
Liver	12	101.38 ± 3.94	3.89	83.29 ± 8.74	10.49
	160	103.18 ± 2.38	2.30	97.94 ± 0.61	0.62
	800	98.44 ± 1.14	1.15	101.64 ± 5.03	4.95
Heart	12	97.29 ± 2.26	2.32	106.40 ± 6.93	6.52
	160	102.37 ± 0.33	0.33	98.84 ± 2.27	2.29
	800	101.24 ± 0.30	0.30	96.16 ± 1.55	1.62
Spleen	12	98.67 ± 1.87	1.89	99.09 ± 6.52	6.58
	160	101.97 ± 3.19	3.13	98.61 ± 3.74	3.79
	800	97.93 ± 1.25	1.27	100.98 ± 0.30	0.30
Kidney	12	101.50 ± 5.55	5.47	93.13 ± 6.32	6.79
	160	99.45 ± 3.40	3.42	102.63 ± 5.00	4.88
	800	93.00 ± 1.78	1.91	103.79 ± 2.09	2.01
Brain	12	100.41 ± 3.80	3.78	98.00 ± 1.96	2.00
	160	103.11 ± 1.84	1.78	95.56 ± 1.20	1.25
	800	98.37 ± 1.86	1.89	101.09 ± 3.16	3.13
Testis	12	99.92 ± 3.88	3.88	99.10 ± 4.05	4.09
	160	103.17 ± 5.11	4.95	98.18 ± 1.47	1.50
	800	99.36 ± 1.09	1.10	98.82 ± 3.23	3.27
Ovary	12	98.85 ± 2.12	2.14	94.09 ± 6.69	7.11
	160	103.17 ± 0.91	0.88	97.04 ± 0.73	0.75
	800	96.70 ± 1.36	1.41	100.26 ± 3.21	3.20
Plasma	12	100.41 ± 0.93	0.93	96.49 ± 1.53	0.02
	160	100.65 ± 1.84	1.83	100.02 ± 0.13	0.01
	800	101.61 ± 0.91	0.90	96.55 ± 1.36	0.01
Muscle	12	95.60 ± 2.29	2.39	103.98 ± 7.36	7.08
	160	100.45 ± 2.62	2.61	101.80 ± 8.61	8.45
	800	100.12 ± 2.53	2.53	101.71 ± 6.44	6.33

HPLC-ESI-MS/MS

HPLC-ESI-MS/MS was conducted on a Shimadzu LC-20AD HPLC system with a Shimadzu LC/MS-8040 instrument (Shimadzu, Kyoto, Japan) using an Ultimate® XB-C18 column (50 mm × 4.6 mm, 3.5 μm; Welch Materials, Inc., Ellicott, MD, United States). The sample injection volume was 5 μL. Gradient elution was performed at 30°C with 0.5% glacial acetic acid in water (solvent A) and acetonitrile (solvent B) at a flow rate of 0.2 ml/min. The gradient elution was set as follows, 0–1 min (40–44% B); 1–14 min (44–49.5% B); 14–15 min (49.5–95% B); 15–16 min (95% B); 16–18 min (40% B) for equilibration. The sample injection volume was 5 μL.

Triple-quadrupole MS/MS detection was carried out on a Shimadzu LC/MS-8040 system with electrospray ionization (ESI). Multiple reaction monitoring analysis in the negative ion mode was conducted based on ion transitions of amentoflavone, delicaflavone, robustaflavone, 2″,3″-dihydro-3′,3‴-biapigenin, 3′,3‴-binaringenin, and chrysin (internal standard, IS) at m/z 537.08→375.00 (CE = 35 V), *m/z* 537.08→255.00 (CE = 55 V), m/z 537.08→309.10 (CE = 40 V), *m/z* 541.11→237.09 (CE = 30 V), *m/z* 539.10→387.15 (CE = 45 V), and *m/z* 253.24 → 143.00 (CE = 28 V), respectively.[11] The optimized MS parameters were set as follows: ion spray voltage, 6.0 kV; heat block temperature, 400°C; DL temperature, 250°C; drying gas flow, 12 L/min; nebulizer gas flow, 3 L/min. Data acquisition and processing were performed using LabSolutions LCMS Ver. 5.5 software.

Preparation of Standard Solutions and Quality Control (QC) Samples

Standard stock solutions of amentoflavone, delicaflavone, robustaflavone, 2″,3″-dihydro-3′,3‴-biapigenin, 3′,3‴-binaringenin, and chrysin were prepared by dissolving them individually in methanol to a final concentration of 1 mg/ml; standard working and QC solutions were obtained by further dilution in methanol. For tissue distribution and excretion analyses, standard working solutions were prepared by serial dilution to obtain a linear concentration gradient. Calibration standards of delicaflavone, robustaflavone, 2″,3″-dihydro-3′,3‴-biapigenin, and 3′,3‴-binaringenin were prepared by spiking drug-free blank biological samples with the working solutions to obtain concentrations of 2, 5, 10, 25, 50, 125, 250, and 500 ng/ml and QC samples of 6, 80, and 400 ng/ml; for amentoflavone, standards of 4, 10, 20, 50, 100, 250, 500, and 1,000 ng/ml, and QC samples of 12, 160, and 800 ng/ml were prepared. The chrysin stock solution was diluted to a final concentration of 50 ng/ml. All stock solutions were stored at 4°C until use.

TABLE 4 | The stability of amentoflavone in rat tissue homogenates (n = 5).

Sample matrix	Spiked con	Bench-top stability (37°C, 8 h)		Short-term stability (4°C, 12 h)		Freeze-thaw stability (Three cycles)		Long-term stability (–80°C, 60 days)	
	(ng/ml)	Bias (%)	RSD (%)	Bias (%)	RSD (%)	Bias (%)	RSD (%)	Bias (%)	RSD (%)
Lungs	12	2.19	7.74	4.32	5.93	0.40	3.86	4.79	4.21
	160	2.06	3.12	3.32	1.75	0.74	5.17	0.30	1.60
	800	–0.35	2.07	0.68	4.54	1.28	2.22	2.60	2.24
Liver	12	1.28	2.78	4.33	3.64	–1.13	2.95	–2.41	1.93
	160	–0.66	3.82	–1.86	2.96	–1.92	2.24	0.74	1.39
	800	–1.86	1.25	0.75	0.64	0.67	1.49	–1.13	2.04
Heart	12	0.27	2.45	–0.29	1.16	0.32	1.95	–4.76	3.53
	160	2.11	2.10	0.03	1.97	2.13	3.01	–1.35	2.86
	800	1.56	3.60	2.42	2.94	–4.90	3.35	–1.52	4.06
Spleen	12	–0.53	1.85	3.35	4.28	–2.27	3.98	4.04	2.19
	160	3.56	2.00	2.80	3.22	–4.11	1.82	2.02	1.99
	800	0.78	1.85	–1.09	3.25	–4.41	6.84	3.80	2.46
Kidney	12	–1.53	3.12	2.88	3.21	–4.01	5.30	–5.62	3.63
	160	2.02	1.01	2.39	1.42	–3.13	2.03	–3.88	1.47
	800	–2.50	4.56	–0.50	3.76	–4.85	2.39	–2.47	3.12
Brain	12	–0.37	1.08	1.42	3.83	0.96	2.04	4.09	2.81
	160	3.01	1.16	–3.82	4.38	2.87	2.74	–2.14	3.08
	800	–1.54	3.45	–2.72	5.21	-0.50	2.64	–0.55	2.06
Testis	12	0.23	1.78	–1.25	7.18	2.92	2.85	2.24	2.35
	160	1.00	0.99	1.52	2.18	1.40	1.43	2.34	2.31
	800	–2.24	1.10	–0.85	1.94	0.91	2.52	–0.63	2.10
Ovary	12	1.87	4.26	3.64	3.36	–0.93	6.65	2.89	1.72
	160	–0.52	2.99	2.48	2.91	3.71	6.85	0.52	1.51
	800	–0.79	2.44	1.61	1.40	1.81	2.47	–0.40	4.87
Plasma	12	3.58	1.73	0.26	1.55	–0.02	2.97	3.81	2.56
	160	–0.56	4.76	1.05	2.58	–0.93	4.25	0.70	3.98
	800	0.59	0.59	0.12	2.75	–2.13	3.33	–1.20	1.96
Muscle	12	0.03	0.78	–0.32	4.90	–0.01	3.18	2.01	1.27
	160	2.26	4.25	–0.81	3.98	–6.18	2.30	–2.14	3.59
	800	0.13	3.03	–0.22	3.42	2.02	2.90	0.76	3.74

Sample Preparation

To obtain tissue samples for analysis, each organ was weighed, diced into small pieces, and homogenized in three volumes of ice-cold physiological saline. Thereafter, 100 μL of the tissue homogenate was spiked with 10 μL of IS working solution, mixed by vortexing with 300 μL of methanol for 2 min, centrifuged at 15,000 × *g* for 20 min at 4°C to precipitate proteins, and the resultant supernatant (5 μL) was used for HPLC-MS/MS.

The feces were dried at 50°C to a constant weight and homogenized in three volumes of physiological saline-methanol (1:1, v/v). Thereafter, 100 μL of fecal and urine samples were processed as described above for tissue samples. The HPLC-ESI-MS/MS method developed and validated previously was only used for rat plasma samples. In the present study, the method was further verified for specificity, linearity, accuracy, precision, recovery, and stability of tissue, urine, and fecal samples.

Tissue Distribution and Excretion

To assess the tissue distribution of orally administered TBESD, 24 Sprague–Dawley rats (12 females and 12 males, weight 200 ± 20 g) were randomly divided into four groups (3 females and 3 males per group) and intragastrically administered a single dose of TBESD (600 mg/kg) dissolved in a mixture of ethanol (2%) and propylene glycol (3.5%) in physiological saline (pH adjusted to 7.5 with 0.5 M NaOH). The rats were sacrificed by cervical dislocation at 5, 15, 40, and 90 min after TBESD administration; the time points for tissue collection were determined based on the concentration–time curves. The brain, heart, kidney, liver, lung, ovary, spleen, testes, and muscle tissues were immediately harvested, thoroughly rinsed in ice-cold physiological saline, dried with filter paper, and stored at −80°C until analysis.

To investigate urinary and fecal excretion, 3 female and 3 male rats housed in individual stainless-steel metabolic cages were orally administered a single dose of TBESD (600 mg/kg), and urine and fecal samples were collected after 0–3, 3–6, 6–9, 9–12, 12–24, 24–36, and 36–48 h. After drying the fecal samples to a constant weight at 50°C and measuring urine sample volumes, the specimens were stored at −80°C.

Binding to HSA

The interactions of TBESD with HSA were analyzed by fluorescence spectroscopy. HSA (10 μM in phosphate buffer, pH 7.4) was incubated in the presence and absence of various TBESD concentrations (2.5, 5, 7.5, 10, and 20 μg/ml), and HSA

intrinsic fluorescence spectra were recorded at 37°C. Fluorescence measurements were performed using a Cary Eclipse spectrofluorometer (CA, United States) with a thermostat bath using a 1.0-cm quartz cuvette. The width of the excitation and emission slits was set to 5 nm. An excitation wavelength of 295 nm was used in the experiments to avoid interference from tryptophan and/or tyrosine residues (Strugała et al., 2018). To avoid the inner filter effect, the fluorescence intensities were corrected using the following formula:

$$F_{corr} = F_{obs} \times antilog\left[\frac{(A_{em} + A_{ex})}{2}\right] \quad (1)$$

where, A_{em} and A_{ex} are the absorbance of the test sample at the excitation and emission wavelengths, respectively; F_{obs} and F_{corr}

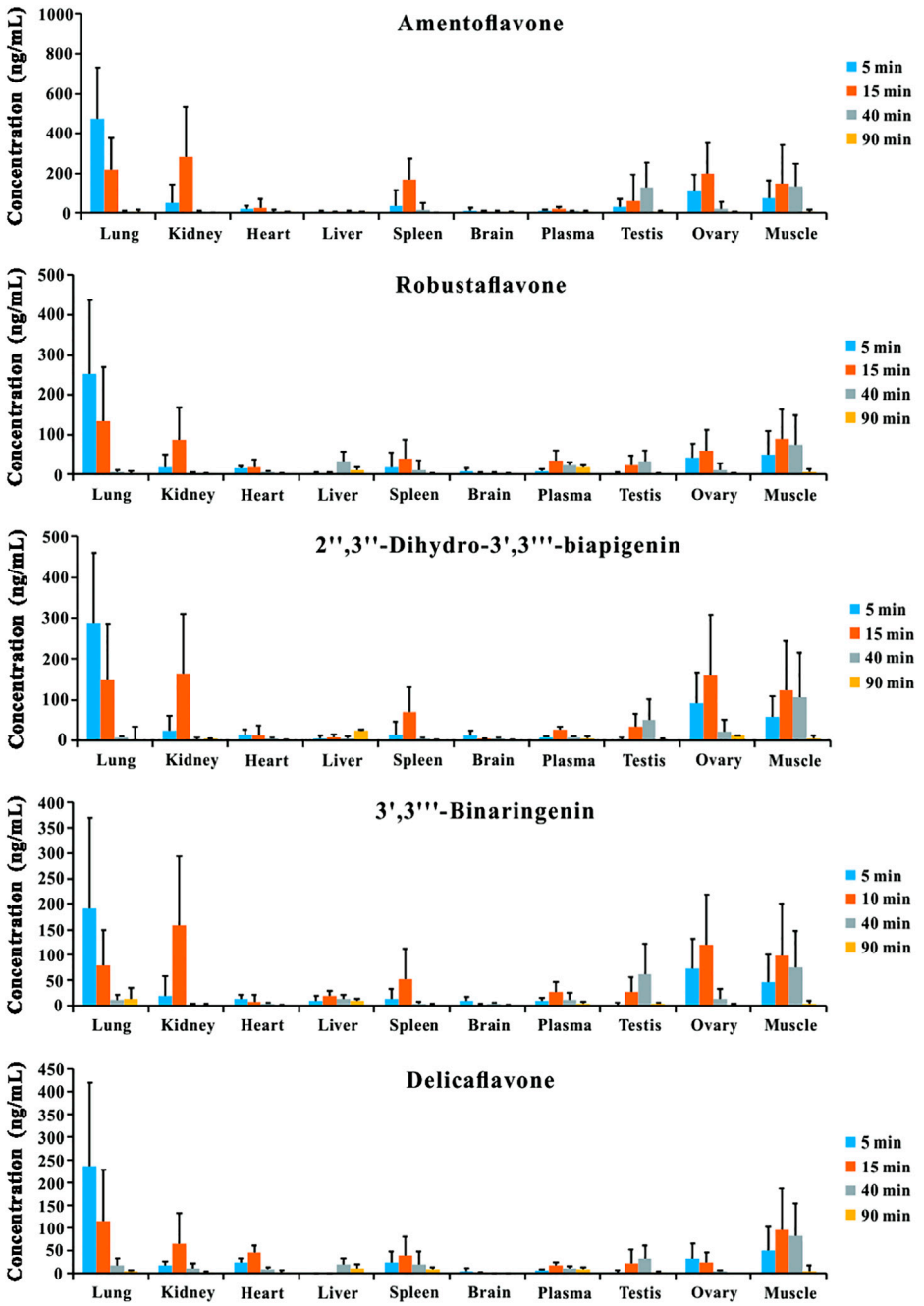

FIGURE 2 | Tissue distribution profiles of amentoflavone, robustaflavone, 2″,3″-dihydro-3′,3‴-biapigenin, 3′,3‴-binaringenin, and delicaflavone in rat after oral administration of TBESD at a dose of 600 mg/kg (Mean ± SD, n = 6).

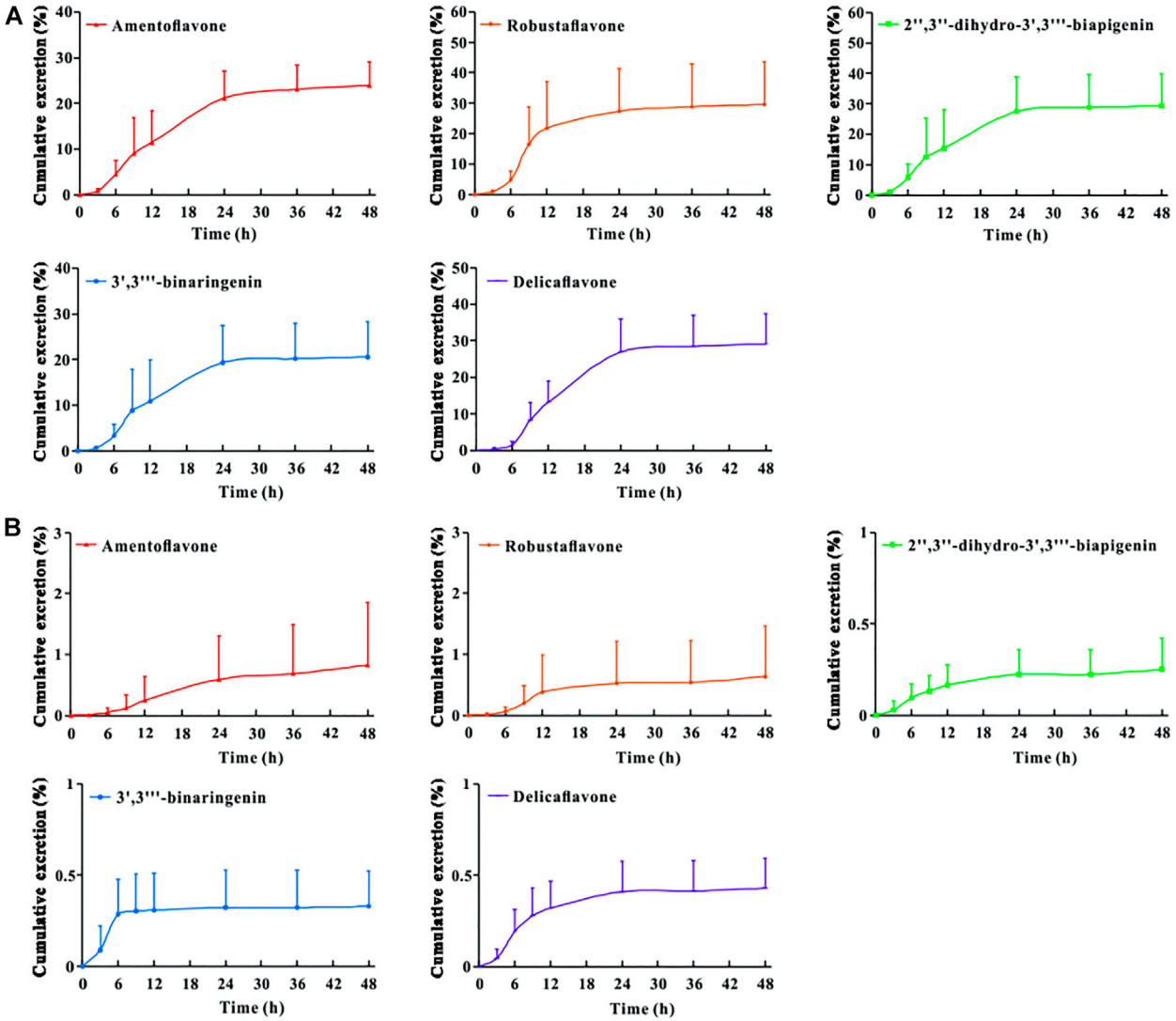

FIGURE 3 | Cumulative excretion-time profiles of amentoflavone, robustaflavone, 2″,3″-dihydro-3′,3‴-biapigenin, 3′,3‴-binaringenin, and delicaflavone in rat feces **(A)** and urine **(B)** after oral administration of TBESD at a dose of 600 mg/kg (Mean ± SD, n = 6).

are the observed and corrected fluorescence intensities, respectively.

Fluorescence quenching experiments were performed at different concentrations of TBESD (2.5, 5, 7.5, 10, and 20 μg/ml) to HSA (10 μM) at different temperatures (298, 303, 308, and 313 K). The emission spectra were recorded in the range of 300–480 nm and then calculated using the Stern–Volmer equation:

$$\frac{F_0}{F} = 1 + K_{SV}[Q] = 1 + k_q\tau_0[Q] \quad (2)$$

where, F and F_0 are HSA fluorescence intensities in the presence and absence, respectively, of the quencher (TBESD); [Q] is the concentration of TBESD; K_{SV} is the dynamic quenching constant; K_q is the apparent bimolecular quenching rate constant; and τ_0 is the fluorophore lifetime without TBESD (10^{-8} s).

The apparent binding constant (K_b) and number of binding sites (n) per macromolecule at the corresponding temperature were analyzed using the modified Stern–Volmer equation:

$$\log\left\{\frac{F_0 - F}{F}\right\} = \log K_b + n\log[Q] \quad (3)$$

The thermodynamic parameters of the TBESD-HSA binding were used to determine the binding mode. The thermal dependency of the binding constant was investigated at 298, 303, 308, and 313 K, and enthalpy and entropy changes (ΔH° and ΔS°, respectively) were analyzed based on the van't Hoff plot to determine the binding forces between TBESD and HSA:

$$\ln K_b = -\left(\frac{\Delta H^\circ}{RT}\right) + \left(\frac{\Delta S^\circ}{R}\right) \quad (4)$$

where, R is the universal gas constant and T is the absolute temperature.

Assuming that ΔH° is nearly constant in the studied temperature range, the free energy change (ΔG°) can be calculated from the Gibbs equation:

$$\Delta G^\circ = \Delta H^\circ - \Delta S^\circ \quad (5)$$

Data Analysis

Data acquisition and processing were conducted using LabSolutions LCMS Ver.5.5 software. The concentrations of bioflavonoids in tissues, urine, and feces were determined using the calibration curve of each analysis batch. The pharmacokinetic parameters of bioflavonoids were calculated using a non-compartmental approach with DAS 3.0 Version (Shanghai, China).

All data are expressed as mean ± standard deviation (SD). Independent *t*-tests were performed to assess the differences between the groups; $p < 0.05$ was considered to indicate statistical significance.

RESULTS

Method Validation

A sensitive and reliable HPLC-ESI-MS/MS method for the simultaneous quantification of five bioflavonoids (amentoflavone, delicaflavone, robustaflavone, 2″,3″-dihydro-3′,3‴-biapigenin, and 3′,3‴-binaringenin) in rat tissue, urine, and fecal samples was successfully developed and validated according to the Food and Drug Administration guidelines (Kamble et al., 2021; Shen et al., 2021). The representative chromatograms of blank rat lung homogenate, blank lung homogenate spiked with QC and IS samples, and lung homogenate samples collected 5 min after TBESD (600 mg/kg) administration are shown in **Figure 1**. Amentoflavone, robustaflavone, 2″,3″-dihydro-3′,3‴-biapigenin, 3′,3‴-binaringenin, IS, and delicaflavone were eluted at approximately 7.2, 8.4, 10.8, 11.2, 12.5, and 14.7 min, respectively. No detectable interfering peaks were observed in tissue, urine, or fecal samples at the retention time close to that of the five bioflavonoids and IS. The detailed method validation parameters are summarized in **Tables 1–4** and **Supplementary Tables S1–S12**. The linearity of all calibration curves was characterized with regression coefficients (R^2) of 0.99 or higher. The intra- and inter-day precision (RSD, %) and accuracy (RE, %) of the method for each bioflavonoid were within the acceptable limit of 15%, and the matrix effect and extraction recovery of each bioflavonoid were consistent among the three different concentrations (n = 5 at high, medium, and low) and constituted >80% of the response. The five bioflavonoids were stable on the bench for up to 8 h, in the autosampler for up to 12 h, at −80°C for up to 2 months at three different concentrations, and after up to three cycles of freezing and thawing (Du et al., 2020).

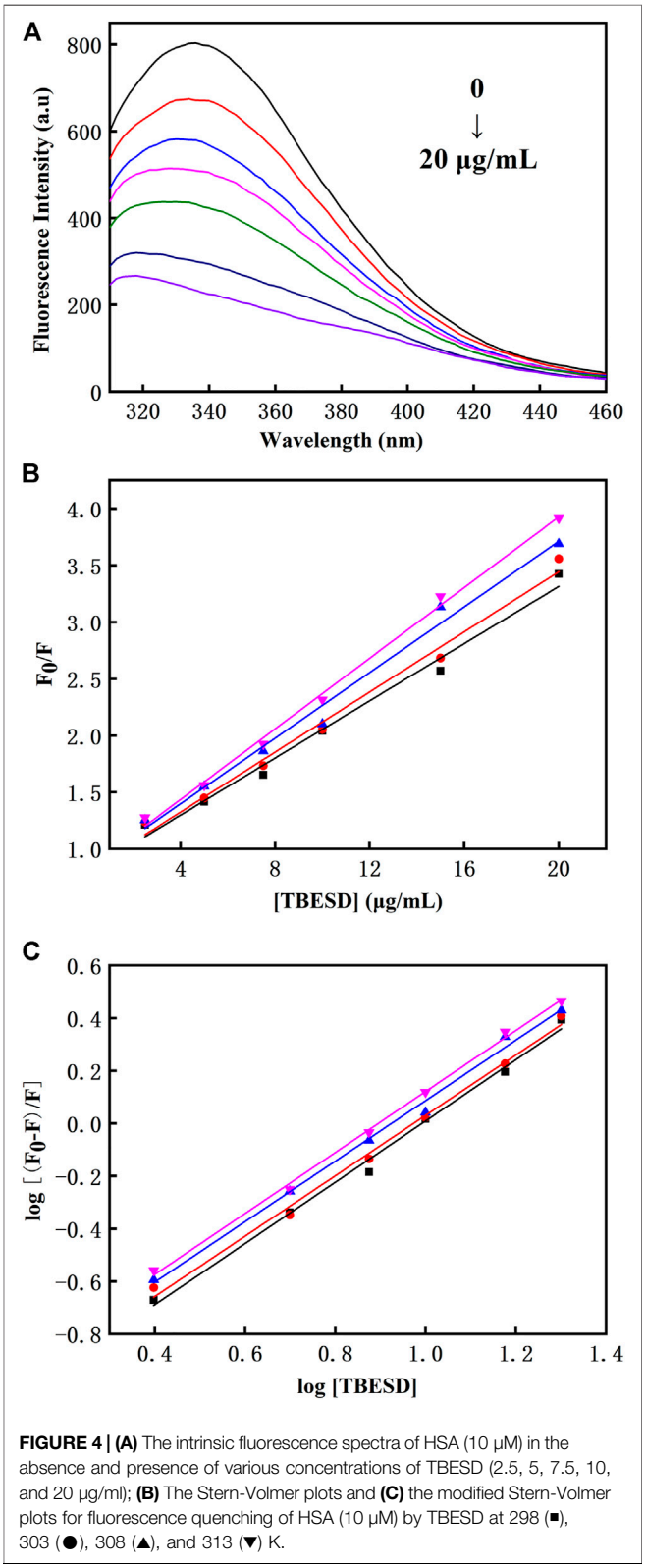

FIGURE 4 | (A) The intrinsic fluorescence spectra of HSA (10 μM) in the absence and presence of various concentrations of TBESD (2.5, 5, 7.5, 10, and 20 μg/ml); **(B)** The Stern-Volmer plots and **(C)** the modified Stern-Volmer plots for fluorescence quenching of HSA (10 μM) by TBESD at 298 (■), 303 (●), 308 (▲), and 313 (▼) K.

TABLE 5 | The Stern-Volmer quenching constant (K_{SV}), quenching rate constant (Kq), binding constant (K_b) and number of binding site (n) of the interaction between HSA and TBESD at different temperatures (Mean ± SD, n = 3).

T (K)	$K_{SV} \times 10^4$ (ml g^{-1})	$K_q \times 10^{12}$ (ml g^{-1} s^{-1})	$K_b \times 10^4$ (ml g^{-1})	n
298	12.60 ± 0.60	12.60 ± 0.60	7.02 ± 0.26	1.16
303	13.24 ± 0.11	13.24 ± 0.11	7.65 ± 0.05	1.15
308	14.47 ± 0.28	14.47 ± 0.28	8.66 ± 0.17	1.15
313	15.57 ± 0.26	15.57 ± 0.26	9.18 ± 0.07	1.16

Tissue Distribution

The tissue distribution profiles of the five bioactive ingredients in the rats after the oral administration of TBESD (600 mg/kg) are depicted in **Figure 2**. The highest concentration of the five bioflavonoids was observed in the lungs at 5 min, followed by the kidneys, muscle, ovary, spleen, and testes, suggesting that amentoflavone, delicaflavone, robustaflavone, 2″,3″-dihydro-3′,3‴-biapigenin, and 3′,3‴-binaringenin distributed rapidly in various tissues. The peak levels in the lungs, kidneys, muscle, ovary, spleen, and testes were significantly higher than those in the plasma. However, the content of the five bioflavonoids in the lungs significantly decreased, whereas that in the kidneys, ovary, and spleen initially increased and then significantly decreased. Only a small amount of the five bioflavonoids was detected in the brain, indicating that amentoflavone, delicaflavone, robustaflavone, 2″,3″-dihydro-3′,3‴-biapigenin, and 3′,3‴-binaringenin could not easily cross the blood–brain barrier. The highest content of the five bioflavonoids in the lungs after oral TBESD administration suggests that TBESD can be used to treat lung-related diseases (Sui et al., 2017). Clearly, the pharmacological effects of TBESD are results from multi-ingredients and multi-targets synergistic integration, thus, the integrated pharmacokinetic studies have carried out to reveal the overall *in vivo* process of TBESD. The half maximal inhibitory concentration (IC_{50}) of an ingredient against human lung cancer cell line (take A549 cell line for example) curve was used to the integrated pharmacokinetic studies of TBESD (Shi et al., 2018). The IC_{50} of amentoflavone, delicaflavone, robustaflavone, 2″,3″-dihydro-3′,3‴-biapigenin, and 3′,3‴-binaringenin were 36.3, 13.2, 50.0, 40.2, and 19.3 μg/ml, respectively (Li et al., 2014; Sui et al., 2016). The tissue distribution profiles of multiple ingredients of TBESD are shown in **Supplementary Figure S2**. The weighting coefficient and integrated concentrations are calculated by following equations:

$$\omega j = \frac{1/IC_{50j}}{\sum_1^n 1/IC_{50n}} \quad (6)$$

$$\sum_1^n {}^1/_{IC_{50_n}} = {}^1/_{IC_{50_1}} + {}^1/_{IC_{50_2}} + {}^1/_{IC_{50_3}} + \cdots + {}^1/_{IC_{50_n}} \quad (7)$$

$$C_T = \omega_1 C_1 + \omega_2 C_2 + \omega_3 C_3 + \cdots + \omega_n C_n \quad (8)$$

Where j represents ingredient j, ω_j represents the weighting coefficient of the ingredient j, n represents the number of ingredients studied, C_n represents the concentration of each ingredients at time point T, and C_T represented the integrated concentration, respectively.

Excretion Analysis

The urinary and fecal excretion profiles of the five bioflavonoids after a single oral administration of TBESD are shown in **Figure 3**. The cumulative concentration of amentoflavone, delicaflavone, robustaflavone, 2″,3″-dihydro-3′,3‴-biapigenin, and 3′,3‴-binaringenin excreted in feces and urine was 23.93 and 0.82%, 29.11 and 0.43%, 29.58 and 0.63%, 29.31 and 0.25%, and 20.51 and 0.32%, respectively, up to 48 h, indicating a considerably higher excretion rate in feces than in urine. These results suggest fecal excretion as the main excretion route for the five bioflavonoids of TBESD, and this is consistent with the findings of a previous study on flavonoids (Zheng et al., 2019).

To the best of our knowledge, this is the first study to report that TBESD is excreted mainly through feces. In addition, the cumulative excretion of the five bioflavonoids in feces after the oral administration of TBESD was considerable, which may have contributed to their low bioavailability and could be attributed to the abundant expression of organic anion transporters and multidrug resistance-related proteins in the membrane of intestinal epithelial cells (Barreca et al., 2017).

Binding to HSA and Characterization of the Bioflavonoid-HSA Complex

The tryptophan residues in HSA are highly sensitive to polarity changes, making fluorescence spectroscopy a valuable method for studying HSA conformational shifts after binding to different ligands (Balaei and Ghobadi, 2019). TBESD exhibited very low fluorescence under the present experimental conditions. Quenching of intrinsic HSA fluorescence was measured in the presence and absence of different concentrations of TBESD at 298 K (**Figure 4A**). The results indicated that the fluorescence intensity of HSA decreased with the increase in TBESD concentration, suggesting the presence of tryptophan residues at or near the HSA-TBESD binding site.

There are two types of fluorescence quenching mechanisms: dynamic and static. The dynamic quenching occurs in the presence of high quencher concentrations, and the effective number of collisions increases at higher temperatures; therefore, the increase in temperature should cause an increase in the quenching constant (K_{SV}). In contrast, in static quenching, the stability of the formed complex decreases with the increase in

TABLE 6 | Thermodynamic parameters of the interaction between HSA and TBESD at different temperatures (Mean ± SD, n = 3).

T (K)	ΔS° (J mol^{-1} K^{-1})	ΔH° (kJ mol^{-1})	ΔG° (kJ mol^{-1})
298	0.27 ± 0.01	29.10 ± 2.86	−51.26 ± 0.13
303			−52.61 ± 0.09
308			−53.96 ± 0.05
313			−55.30 ± 0.03

temperature, which results in the decrease in K_{SV} (Strugała et al., 2021). To elucidate the mechanism underlying TBESD quenching of HSA fluorescence, we analyzed HSA fluorescence at four different temperatures (**Figure 4** and **Table 5**). The Stern–Volmer plots for the TBESD-HSA complexes were linear, showing a directly proportional relationship between the examined concentration range and the temperature. The number of binding sites (n) for TBESD in HSA at different temperatures is shown in **Table 5**. The results indicated that there was one binding site, that is, only one interaction point between the TBESD components and HSA. According to the obtained results, the most probable mechanism of HSA fluorescence quenching by TBESD should be dynamic quenching, in which higher temperatures increase the stability of the TBESD-HSA complex as indicated by higher K_{SV} and K_b values.

To characterize the energy changes during the interaction between TBESD and HSA, the thermodynamic binding parameters ΔH°, ΔS°, and ΔG° were calculated from the van't Hoff plot and Gibbs equation (**Table 6**). The ΔH° and ΔS° values were 29.10 ± 2.86 kJ $(g\,ml\text{-}1)^{-1}$ and 0.27 ± 0.01 J $(g\,mL\text{-}1\ K)^{-1}$, respectively. The high negative ΔG° value accompanied by positive ΔS° is indicative of a spontaneous process. The positive ΔS° value signifies hydrophobic interactions, whereas the variations in ΔH° indicate that the binding process is enthalpy-driven and probably depends on the formation of hydrogen bonds between the TBESD components and HSA. Thus, thermodynamic analysis of the binding between TBESD and HSA revealed the role of hydrophobic interactions and hydrogen bonds in complex formation.

DISSCUSION

Multiple studies have established that TBESD with an excellent antitumor effect and low toxicity *in vivo*, and deserved to be further developed as a novel anti-cancer agent (Wang et al., 2019; Xu et al., 2021). An understanding of the pharmacokinetic properties of TBESD is an essential prerequisite to the drug discovery and preclinical development. Especially pharmacokinetic studies of natural products, since they typically involve the administration of complex mixtures of substances. In this study, we revealed how the body affects the five biological activity of TBESD after administration through the mechanisms of absorption and distribution, and the effects and routes of excretion.

As our previous reported, five bioflavonoids were retained in the intestinal tract for a long time and maintained lower levels plasma concentration after a single dose oral administration of TBESD (Chen et al., 2018). In the tissue distribution study, the content of amentoflavone, delicaflavone, robustaflavone, 2″,3″-dihydro-3′,3‴-biapigenin, 3′,3‴-binaringenin and integrated TBESD in the lungs was the highest among these organs, followed by kindeys, ovary, and spleen, suggesting that the application of TBESD in the treatment of lungs, kindeys, and ovary related diseases. However, only a small amount of five bioflavonoids was detected in the brain, indicating that most flavonoids from TBESD had difficulty passing the blood-brain barrier.

To investigate the elimination of TBESD in rats, 5 major bioflavonoids were measured in the fecal and urine samples within 48 h after a single dose oral administration. The cumulative amount of amentoflavone, delicaflavone, robustaflavone, 2″,3″-dihydro-3′,3‴-biapigenin, and 3′,3‴-binaringenin was detected mainly in feces with 23.93, 29.11, 29.58, 29.31 and 20.51%, respectively, while the ratios were 0.82, 0.43, 0.63, 0.25%, and 0.32 in urine. Fecal excretion was proven to be the main excretion route for the TBESD, which may account for their poor bioavailability and membrane transporters (Čvorović et al., 2018). In addition, the absorbed flavonoids of TBESD undergo further metabolism of glucuronide, sulfation, and methylation in the epithelium of intestine and liver (Zheng et al., 2019). From the above results, the high excretion rate may be related to its incomplete absorption and metabolic way under the oral administration route, which we will share the research advances in more detail in an upcoming installment.

Fluorescence spectroscopy studies were conducted to investigate the interaction between TBESD and HSA. It is recognized that the bioavailability of many active compounds is related to the interaction and successful binding with HSA (Poureshghi et al., 2017). Forming stable binding complexes could be considered a suitable model for gaining various information of protein binding (Wang et al., 2015). Our previous study verified that the fluorescence intensity of HSA decreased regularly with increasing active ingredient concentration, due to an increased hydrophobicity of the region surrounding the tryptophan amino acid residue after binding with TBESD's component. In the present study, the binding constant of the whole ingredients of TBESD to HSA was determined by the intrinsic fluorescence quenching of HSA. These results indicate that the strong and spontaneous binding of the whole ingredients of TBESD to HSA is responsible for poor pharmacokinetic profiles.

CONCLUSION

We developed a sensitive and reliable LC-MS/MS method to simultaneously determine the concentration of five main TBESD bioflavonoids, amentoflavone, robustaflavone, 2″,3″-dihydro-3′,3‴-biapigenin, 3′,3‴-binaringenin, and delicaflavone, in rat tissues, urine, and feces after the oral administration of TBESD. We successfully applied the method to assess TBESD tissue distribution and excretion in rats. The concentration of the five bioflavonoids was the highest in the lungs, and they were mostly excreted through the feces. TBESD had a dynamic quenching effect on HSA by binding to a single HSA site through hydrophobic interactions and hydrogen bond formation. To the best of our knowledge, this is the first comprehensive study on the tissue distribution and excretion of TBESD components in rats and their interaction with HSA. Further research on the pharmacokinetics and

pharmacodynamics of TBESD is needed to provide a solid foundation for the application of TBESD in clinical practice.

DATA AVAILABILITY STATEMENT

The original contributions presented in the study are included in the article/**Supplementary Materials**, further inquiries can be directed to the corresponding authors.

ETHICS STATEMENT

The animal study was reviewed and approved by the Animal Ethics Committee of Fujian Medical University.

AUTHOR CONTRIBUTIONS

HY, XL, AL and BC contributed to conception and design of the study. BC, DX, ZL, YJ and LL contributed to the experimental procedures. SL, XH and LH analyzed the data and prepared all the figures and wrote the manuscript. All authors contributed to article revision, read and approved the submitted version.

FUNDING

The authors gratefully acknowledge the financial supports of the National Natural Science Foundation of China (81973558 and 22074017), Natural Science Foundation of Fujian province (2020J01631, 2021J02033, and 2021J02034), Joint Funds for the innovation of science and Technology of Fujian province (2017Y9123 and 2018Y9076) and Health and Youth Research Project of Fujian province (2019-1-60).

ACKNOWLEDGMENTS

We acknowledge the Fujian Medical University Ethics Committee for their kind guidance in the animal experiments and the Public Technology Service Center of Fujian Medical University.

SUPPLEMENTARY MATERIAL

The Supplementary Material for this article can be found online at: https://www.frontiersin.org/articles/10.3389/fphar.2022.849110/full#supplementary-material

REFERENCES

Balaei, F., and Ghobadi, S. (2019). Hydrochlorothiazide Binding to Human Serum Albumin Induces Some Compactness in the Molecular Structure of the Protein: A Multi-Spectroscopic and Computational Study. *J. Pharm. Biomed. Anal.* 162, 1–8. doi:10.1016/j.jpba.2018.09.009

Barreca, D., Laganà, G., Toscano, G., Calandra, P., Kiselev, M. A., Lombardo, D., et al. (2017). The Interaction and Binding of Flavonoids to Human Serum Albumin Modify its Conformation, Stability and Resistance against Aggregation and Oxidative Injuries. *Biochim. Biophys. Acta Gen. Subj* 1861, 3531–3539. doi:10.1016/j.bbagen.2016.03.014

Cao, H., Liu, X., Ulrih, N. P., Sengupta, P. K., and Xiao, J. (2019). Plasma Protein Binding of Dietary Polyphenols to Human Serum Albumin: A High Performance Affinity Chromatography Approach. *Food Chem.* 270, 257–263. doi:10.1016/j.foodchem.2018.07.111

Chen, B., Luo, H., Chen, W., Huang, Q., Zheng, K., Xu, D., et al. (2021). Pharmacokinetics, Tissue Distribution, and Human Serum Albumin Binding Properties of Delicaflavone, a Novel Anti-tumor Candidate. *Front. Pharmacol.* 12, 761884. doi:10.3389/fphar.2021.761884

Chen, B., Wang, X., Lin, D., Xu, D., Li, S., Huang, J., et al. (2019). Proliposomes for Oral Delivery of Total Biflavonoids Extract from Selaginella Doederleinii: Formulation Development, Optimization, and In Vitro-In Vivo Characterization. *Int. J. Nanomedicine* 14, 6691–6706. doi:10.2147/IJN.S214686

Chen, B., Wang, X., Zhang, Y., Huang, K., Liu, H., Xu, D., et al. (2020). Improved Solubility, Dissolution Rate, and Oral Bioavailability of Main Biflavonoids from Selaginella Doederleinii Extract by Amorphous Solid Dispersion. *Drug Deliv.* 27, 309–322. doi:10.1080/10717544.2020.1716876

Chen, B., Wang, X., Zou, Y., Chen, W., Wang, G., Yao, W., et al. (2018). Simultaneous Quantification of Five Biflavonoids in Rat Plasma by LC-ESI-MS/MS and its Application to a Comparatively Pharmacokinetic Study of Selaginella Doederleinii Hieron Extract in Rats. *J. Pharm. Biomed. Anal.* 149, 80–88. doi:10.1016/j.jpba.2017.10.028

Čvorović, J., Ziberna, L., Fornasaro, S., Tramer, F., and Passamonti, S. (2018). "Chapter 22 - Bioavailability of Flavonoids: The Role of Cell Membrane Transporters," in *Polyphenols: Mechanisms of Action in Human Health and Disease*. Editors R. R. Watson, V. R. Preedy, and S. Zibadi. Second Edition (Academic Press), 295–320.

Du, C., Yan, Y., Shen, C., Cui, X., Pei, X., and Qin, X. (2020). Comparative Pharmacokinetics of Six Major Compounds in normal and Insomnia Rats after Oral Administration of Ziziphi Spinosae Semen Aqueous Extract. *J. Pharm. Anal.* 10, 385–395. doi:10.1016/j.jpha.2020.03.003

Kamble, S. H., Berthold, E. C., King, T. I., Raju Kanumuri, S. R., Popa, R., Herting, J. R., et al. (2021). Pharmacokinetics of Eleven Kratom Alkaloids Following an Oral Dose of Either Traditional or Commercial Kratom Products in Rats. *J. Nat. Prod.* 84, 1104–1112. doi:10.1021/acs.jnatprod.0c01163

Kang, F., Zhang, S., Chen, D., Tan, J., Kuang, M., Zhang, J., et al. (2021). Biflavonoids from Selaginella Doederleinii as Potential Antitumor Agents for Intervention of Non-small Cell Lung Cancer. *Molecules* 26, 5401. doi:10.3390/molecules26175401

Li, C., Liu, B., Chang, J., Groessl, T., Zimmerman, M., He, Y. Q., et al. (2013). A Modern *In Vivo* Pharmacokinetic Paradigm: Combining Snapshot, Rapid and Full PK Approaches to Optimize and Expedite Early Drug Discovery. *Drug Discov. Today* 18, 71–78. doi:10.1016/j.drudis.2012.09.004

Li, S., Wang, X., Wang, G., Shi, P., Lin, S., Xu, D., et al. (2020). Ethyl Acetate Extract of Selaginella Doederleinii Hieron Induces Cell Autophagic Death and Apoptosis in Colorectal Cancer via PI3K-Akt-mTOR and AMPKα-Signaling Pathways. *Front. Pharmacol.* 11, 565090. doi:10.3389/fphar.2020.565090

Li, S., Zhao, M., Li, Y., Sui, Y., Yao, H., Huang, L., et al. (2014). Preparative Isolation of Six Anti-tumour Biflavonoids from Selaginella Doederleinii Hieron by High-Speed Counter-current Chromatography. *Phytochem. Anal.* 25, 127–133. doi:10.1002/pca.2478

Li, Y., Meng, Q., Yang, M., Liu, D., Hou, X., Tang, L., et al. (2019). Current Trends in Drug Metabolism and Pharmacokinetics. *Acta Pharm. Sin B* 9, 1113–1144. doi:10.1016/j.apsb.2019.10.001

Liao, X., Hong, Y., and Chen, Z. (2021). Identification and Quantification of the Bioactive Components in Osmanthus Fragrans Roots by HPLC-MS/MS. *J. Pharm. Anal.* 11, 299–307. doi:10.1016/j.jpha.2020.06.010

Liu, L. F., Sun, H. H., Tan, J. B., Huang, Q., Cheng, F., Xu, K. P., et al. (2021). New Cytotoxic Biflavones from Selaginella Doederleinii. *Nat. Prod. Res.* 35, 930–936. doi:10.1080/14786419.2019.1611813

Matsumoto, T., Takiyama, M., Sakamoto, T., Kaifuchi, N., Watanabe, J., Takahashi, Y., et al. (2021). Pharmacokinetic Study of Ninjin'yoeito: Absorption and Brain

Distribution of Ninjin'yoeito Ingredients in Mice. *J. Ethnopharmacol* 279, 114332. doi:10.1016/j.jep.2021.114332

Poureshghi, F., Ghandforoushan, P., Safarnejad, A., and Soltani, S. (2017). Interaction of an Antiepileptic Drug, Lamotrigine with Human Serum Albumin (HSA): Application of Spectroscopic Techniques and Molecular Modeling Methods. *J. Photochem. Photobiol. B* 166, 187–192. doi:10.1016/j.jphotobiol.2016.09.046

Qiu, H., Jin, L., Chen, J., Shi, M., Shi, F., Wang, M., et al. (2020). Comprehensive Glycomic Analysis Reveals that Human Serum Albumin Glycation Specifically Affects the Pharmacokinetics and Efficacy of Different Anticoagulant Drugs in Diabetes. *Diabetes* 69, 760–770. doi:10.2337/db19-0738

Rabbani, G., and Ahn, S. N. (2019). Structure, Enzymatic Activities, Glycation and Therapeutic Potential of Human Serum Albumin: A Natural Cargo. *Int. J. Biol. Macromol* 123, 979–990. doi:10.1016/j.ijbiomac.2018.11.053

Romański, M., Kasprzyk, A., Teżyk, A., Widerowska, A., Żaba, C., and Główka, F. (2017). Determination of Prodrug Treosulfan and its Biologically Active Monoepoxide in Rat Plasma, Liver, Lungs, Kidneys, Muscle, and Brain by HPLC-ESI-MS/MS Method. *J. Pharm. Biomed. Anal.* 140, 122–129. doi:10.1016/j.jpba.2017.03.023

Shen, M. R., He, Y., and Shi, S. M. (2021). Development of Chromatographic Technologies for the Quality Control of Traditional Chinese Medicine in the Chinese Pharmacopoeia. *J. Pharm. Anal.* 11, 155–162. doi:10.1016/j.jpha.2020.11.008

Shi, P., Lin, X., and Yao, H. (2018). A Comprehensive Review of Recent Studies on Pharmacokinetics of Traditional Chinese Medicines (2014-2017) and Perspectives. *Drug Metab. Rev.* 50 (2), 161–192. doi:10.1080/03602532.2017.1417424

Strugała, P., Urbaniak, A., Kuryś, P., Włoch, A., Kral, T., Ugorski, M., et al. (2021). Antitumor and Antioxidant Activities of Purple Potato Ethanolic Extract and its Interaction with Liposomes, Albumin and Plasmid DNA. *Food Funct.* 12, 1271–1290. doi:10.1039/d0fo01667e

Strugała, P., Loi, S., Bażanów, B., Kuropka, P., Kucharska, A. Z., Włoch, A., et al. (2018). A Comprehensive Study on the Biological Activity of Elderberry Extract and Cyanidin 3-O-Glucoside and Their Interactions with Membranes and Human Serum Albumin. *Molecules* 23, 2566.

Sui, Y., Li, S., Shi, P., Wu, Y., Li, Y., Chen, W., et al. (2016). Ethyl Acetate Extract from Selaginella Doederleinii Hieron Inhibits the Growth of Human Lung Cancer Cells A549 via Caspase-dependent Apoptosis Pathway. *J. Ethnopharmacol* 190, 261–271. doi:10.1016/j.jep.2016.06.029

Sui, Y., Yao, H., Li, S., Jin, L., Shi, P., Li, Z., et al. (2017). Delicaflavone Induces Autophagic Cell Death in Lung Cancer via Akt/mTOR/p70S6K Signaling Pathway. *J. Mol. Med. (Berl)* 95, 311–322. doi:10.1007/s00109-016-1487-z

Wang, L., Shen, X., Mi, L., Jing, J., Gai, S., Liu, X., et al. (2019). Simultaneous Determinations of Four Major Bioactive Components in Acacia Catechu (L.f.) Willd and Scutellaria Baicalensis Georgi Extracts by LC-MS/MS: Application to its Herb-Herb Interactions Based on Pharmacokinetic, Tissue Distribution and Excretion Studies in Rats. *Phytomedicine* 56, 64–73. doi:10.1016/j.phymed.2018.09.239

Wang, X., Chen, B., Xu, D., Li, Z., Liu, H., Huang, Z., et al. (2021). Molecular Mechanism and Pharmacokinetics of Flavonoids in the Treatment of Resistant EGF Receptor-Mutated Non-small-cell Lung Cancer: A Narrative Review. *Br. J. Pharmacol.* 178, 1388–1406. doi:10.1111/bph.15360

Wang, X., Liu, Y., He, L. L., Liu, B., Zhang, S. Y., Ye, X., et al. (2015). Spectroscopic Investigation on the Food Components-Drug Interaction: The Influence of Flavonoids on the Affinity of Nifedipine to Human Serum Albumin. *Food Chem. Toxicol.* 78, 42–51. doi:10.1016/j.fct.2015.01.026

Xu, D., Wang, X., Huang, D., Chen, B., Lin, X., Liu, A., et al. (2022). Disclosing Targets and Pharmacological Mechanisms of Total Bioflavonoids Extracted from Selaginella Doederleinii against Non-small Cell Lung Cancer by Combination of Network Pharmacology and Proteomics. *J. Ethnopharmacol* 286, 114836. doi:10.1016/j.jep.2021.114836

Yao, H., Chen, B., Zhang, Y., Ou, H., Li, Y., Li, S., et al. (2017). Analysis of the Total Biflavonoids Extract from Selaginella Doederleinii by HPLC-QTOF-MS and its *In Vitro* and *In Vivo* Anticancer Effects. *Molecules* 22, 325. doi:10.3390/molecules22020325

Yao, W., Lin, Z., Shi, P., Chen, B., Wang, G., Huang, J., et al. (2020). Delicaflavone Induces ROS-Mediated Apoptosis and Inhibits PI3K/AKT/mTOR and Ras/MEK/Erk Signaling Pathways in Colorectal Cancer Cells. *Biochem. Pharmacol.* 171, 113680. doi:10.1016/j.bcp.2019.113680

Yao, W., Lin, Z., Wang, G., Li, S., Chen, B., Sui, Y., et al. (2019). Delicaflavone Induces Apoptosis via Mitochondrial Pathway Accompanying G2/M Cycle Arrest and Inhibition of MAPK Signaling Cascades in Cervical Cancer HeLa Cells. *Phytomedicine* 62, 152973. doi:10.1016/j.phymed.2019.152973

Zheng, D., Sun, C. C., Su, H., and Zhang, Q. F. (2019). Metabolism, Excretion, and Tissue Distribution of Astilbin-Zein Nanoparticles in Rats. *J. Agric. Food Chem.* 67, 8332–8338. doi:10.1021/acs.jafc.9b02569

Zhu, L. J., Chen, L., Bai, C. F., Wu, A. G., Liang, S. C., Huang, F. H., et al. (2020). A Rapid and Sensitive UHPLC-MS/MS Method for the Determination of Ziyuglycoside I and its Application in a Preliminary Pharmacokinetic Study in Healthy and Leukopenic Rats. *Biomed. Pharmacother.* 123, 109756. doi:10.1016/j.biopha.2019.109756

Zou, Z., Xu, K., Xu, P., Li, X., Cheng, F., Li, J., et al. (2017a). Seladoeflavones A-F, Six Novel Flavonoids from Selaginella Doederleinii. *Fitoterapia* 116, 66–71. doi:10.1016/j.fitote.2016.11.014

Zou, Z., Xu, P., Zhang, G., Cheng, F., Chen, K., Li, J., et al. (2017b). Selagintriflavonoids with BACE1 Inhibitory Activity from the Fern Selaginella Doederleinii. *Phytochemistry* 134, 114–121. doi:10.1016/j.phytochem.2016.11.011

Conflict of Interest: The authors declare that the research was conducted in the absence of any commercial or financial relationships that could be construed as a potential conflict of interest.

Publisher's Note: All claims expressed in this article are solely those of the authors and do not necessarily represent those of their affiliated organizations, or those of the publisher, the editors and the reviewers. Any product that may be evaluated in this article, or claim that may be made by its manufacturer, is not guaranteed or endorsed by the publisher.

frontiers | Frontiers in Pharmacology

ORIGINAL RESEARCH
published: 10 May 2022
doi: 10.3389/fphar.2022.911982

Molecular Basis Underlying Hepatobiliary and Renal Excretion of Phenolic Acids of *Salvia miltiorrhiza* Roots (Danshen)

Jun-Lan Lu[1,2], *Xue-Shan Zeng*[1,2], *Xin Zhou*[1,2], *Jun-Ling Yang*[1,2,3], *Ling-Ling Ren*[2,3], *Xin-Yu Long*[2,3], *Feng-Qing Wang*[2], *Olajide E. Olaleye*[2], *Nan-Nan Tian*[1,2], *Ya-Xuan Zhu*[1,2], *Jia-Jia Dong*[4]*, *Wei-Wei Jia*[2]* and *Chuan Li*[1,2,3]*

[1]Graduate School, Tianjin University of Traditional Chinese Medicine, Tianjin, China, [2]State Key Laboratory of Drug Research, Shanghai Institute of Materia Medica, Chinese Academy of Sciences, Shanghai, China, [3]School of Pharmacy, University of Chinese Academy of Sciences, Beijing, China, [4]College of Pharmacy, Nanjing University of Chinese Medicine, Nanjing, China

OPEN ACCESS

Edited by:
Toshiaki Makino,
Nagoya City University, Japan

Reviewed by:
Dengke Yin,
Anhui University of Chinese Medicine, China
Tomoya Yasujima,
Nagoya City University, Japan

***Correspondence:**
Jia-Jia Dong
dongjiajia300512@njucm.edu.cn
Wei-Wei Jia
weiweijia@simm.ac.cn
Chuan Li
chli@simm.ac.cn

Specialty section:
This article was submitted to Ethnopharmacology, a section of the journal Frontiers in Pharmacology

Received: 03 April 2022
Accepted: 22 April 2022
Published: 10 May 2022

Citation:
Lu J-L, Zeng X-S, Zhou X, Yang J-L, Ren L-L, Long X-Y, Wang F-Q, Olaleye OE, Tian N-N, Zhu Y-X, Dong J-J, Jia W-W and Li C (2022) Molecular Basis Underlying Hepatobiliary and Renal Excretion of Phenolic Acids of Salvia miltiorrhiza Roots (Danshen). Front. Pharmacol. 13:911982. doi: 10.3389/fphar.2022.911982

Phenolic acids are cardiovascular constituents (originating from the Chinese medicinal herb *Salvia miltiorrhiza* root/Danshen) of DanHong and many other Danshen-containing injections. Our earlier pharmacokinetic investigation of DanHong suggested that hepatic and/or renal uptake of the Danshen compounds was the crucial steps in their systemic elimination. This investigation was designed to survey the molecular basis underlying hepatobiliary and renal excretion of the Danshen compounds, i.e., protocatechuic acid, tanshinol, rosmarinic acid, salvianolic acid D, salvianolic acid A, lithospermic acid, and salvianolic acid B. A large battery of human hepatic and renal transporters were screened for transporting the Danshen compounds and then characterized for the uptake kinetics and also compared with associated rat transporters. The samples were analyzed by liquid chromatography/mass spectrometry. Because the Danshen phenolic acids are of poor or fairly good membrane permeability, their elimination *via* the liver or kidneys necessitates transporter-mediated hepatic or renal uptake from blood. Several human transporters were found to mediate hepatic and/or renal uptake of the Danshen compounds in a compound-molecular-mass-related manner. Lithospermic acid and salvianolic acid B (both >500 Da) underwent systemic elimination, initiated by organic anion-transporting polypeptide (OATP)1B1/OATP1B3-mediated hepatic uptake. Rosmarinic acid and salvianolic acids D (350–450 Da) underwent systemic elimination, initiated by OATP1B1/OATP1B3/organic anion transporter (OAT)2-mediated hepatic uptake and by OAT1/OAT2-mediated renal uptake. Protocatechuic acid and tanshinol (both <200 Da) underwent systemic elimination, initiated by OAT1/OAT2-mediated renal

Abbreviations: ABC, ATP-binding cassette; BCRP/Bcrp, breast cancer resistance protein; BSEP/Bsep, bile salt export pump; CL_{int}, intrinsic clearance; DDI, drug-drug interaction; E_1S, estrone-3-sulfate; $E_2$17βG, estradiol-17β-D-glucuronide; $f_{u\text{-}plasma}$, unbound fraction in plasma; K_m, Michaelis constant; GL, glycyrrhizin; GS, glycylsarcosine; MDR, multidrug resistance protein; MRP/Mrp, multidrug resistance-associated protein; MTX, methotrexate; NTCP/Ntcp, Na^+/taurocholate cotransporting polypeptide; OAT/Oat, organic anion transporter; OATP/Oatp, organic anion-transporting polypeptide; OCT/Oct, organic cation transporter; Octn, carnitine/organic cation transporter; PAH, para-aminohippuric acid; PEPT/Pept, peptide transporter; $PGF_{2\alpha}$, prostaglandin $F_{2\alpha}$; SLC, solute carrier; TCA, taurocholic acid; TEA, tetraethylammonium; V_{max}, maximum transport velocity.

uptake and OAT2-mediated hepatic uptake. A similar scenario was observed with the rat orthologs. The investigation findings advance our understanding of the disposition of the Danshen phenolic acids and could facilitate pharmacokinetic research on other Danshen-containing injections.

Keywords: Danshen, Salvia miltiorrhiza, phenolic acid, hepatic transporter, renal transporter

INTRODUCTION

Salvia miltiorrhiza roots (Danshen in Chinese) are a commonly used Chinese cardiovascular herb which, alone or in combination with other medicinal herbs, is formulated for oral or intravenous administration. Hydrophilic phenolic acids and lipophilic diterpene quinones are believed to be responsible for most of the cardiovascular effects of Danshen (Li et al., 2018; Ren et al., 2019). DanHong injection is prepared from a 3:1 mixture of Danshen and *Carthamus tinctorius* flowers (Honghua) (Feng et al., 2019). It is an injectable solution available as a sterile, nonpyrogenic parenteral dosage form for intravenous administration. DanHong is approved by the Chinese National Medical Products Administration (NMPA) for the treatment of atherosclerotic coronary artery disease and acute ischemic stroke. In a recent adaptive, 31-center, double-blind, randomized controlled trial in 920 patients with stable angina, treatment with 14-days DanHong significantly reduced the number of angina episodes and improved angina-specific health status for at least 90 days, particularly for patients with severe angina, faster heart rate, or diabetes (Liu et al., 2021). It is reassuring that no substantial harm was observed in the clinical trial.

Due to the aqueous extraction for preparing DanHong, the constituents originating from Danshen were the hydrophilic acids, rather than the lipophilic diterpene quinones. The major Danshen hydrophilic phenolic acids present in DanHong are caffeic acid derivatives, occurring as monomers (tanshinol), dimers (rosmarinic acid and salvianolic acid D), trimers (salvianolic acid A and lithospermic acid), and tetramers (salvianolic acid B). In addition, these compounds contain one or more catechol moieties and have one or more carboxylic acid groups (Jiang et al., 2005). Protocatechuic aldehyde is also a major Danshen hydrophilic compound in DanHong; it is a catechol compound but has no carboxy group. In our earlier multi-compound pharmacokinetic investigation of DanHong, these Danshen compounds were evaluated for systemic exposure in humans (who intravenously received the herbal injection) and for elimination from the systemic circulation (Li et al., 2015). After dosing DanHong, metabolism of the Danshen phenolic acids occurs mainly in the liver and comprises methylation, glucuronidation, and sulfation. Given that all these phenolic acids have poor or fairly good membrane permeability, hepatic uptake, which is the prerequisite for their metabolism, needs to be mediated by some transporters. Meanwhile, the kidneys can also compete with the liver for elimination of some Danshen phenolic acids. Renal excretion of these Danshen compounds appears to involve tubular secretion, which needs transporter(s) to mediate the renal uptake. After dosing DanHong, protocatechuic aldehyde is extensively transformed into protocatechuic acid by hepatic aldehyde dehydrogenase, and this metabolite is a phenolic acid, which is eliminated as unchanged and metabolized forms by renal excretion. This investigation was designed to survey the molecular basis of the preceding hepatobiliary and renal excretion of the compounds (**Figure 1**). The investigation findings advance our understanding of disposition of Danshen phenolic acids. Given that these Danshen phenolic acids are also major active compounds of many other Danshen-containing herbal injections (**Supplementary Table S1**), the results of the current investigation could facilitate pharmacokinetic research on these herbal injections.

MATERIALS AND METHODS

Chemicals and Reagents

The test Danshen compounds protocatechuic acid, tanshinol, rosmarinic acid, salvianolic acid D, salvianolic acid A, lithospermic acid, and salvianolic acid B were obtained from the Tongtian Biotechnology (Shanghai, China) and their purity exceeded 98%. The positive substrates for testing validity of transporter systems, i.e., estradiol-17β-D-glucuronide ($E_2$17βG), estrone-3-sulfate (E_1S), prostaglandin $F_{2\alpha}$ ($PGF_{2\alpha}$), tetraethylammonium (TEA), taurocholic acid (TCA), para-aminohippuric acid (PAH), glycylsarcosine (GS), methotrexate (MTX), and glycyrrhizin (GL) were obtained from Sigma-Aldrich (St. Louis, MO, United States). Adenosine 5′-triphosphate (ATP; disodium salt hydrate) and other reagents were obtained from Sinopharm Chemical Reagent Co., Ltd. (Shanghai, China).

Human embryonic kidney 293 (HEK-293) cells were obtained from the American Type Culture Collection (Manassas, VA, United States). Full open reading frames of cDNA for human organic anion-transporting polypeptide (OATP) 1B1, OATP1B3, OATP2B1, organic anion transporter (OAT) 1, OAT2, OAT3, OAT4, organic cation transporter (OCT) 1, OCT2, OCT3, Na^+/taurocholate cotransporting polypeptide (NTCP), peptide transporter (PEPT) 1, and PEPT2 and rat Oatp1a1, Oatp1b2, Oat1, Oat2, Oat3, Oct1, Oct2, Oct3, carnitine/organic cation transporter (Octn) 2, Ntcp, Pept1, and Pept2 were synthesized and subcloned into pcDNA 3.1 (+) expression vectors by Invitrogen Life Technologies (Shanghai, China). Prior to the study, all expression plasmids were sequence-verified according to their GeneBank accession numbers, i.e., NM_006446 (human OATP1B1), NM_019844 (human OATP1B3), NM_007256 (OATP2B1), NM_004790 (OAT1), NM_006672 (OAT2), NM_004254 (OAT3), NM_018484 (OAT4), NM_003057 (OCT1), NM_003058 (OCT2),

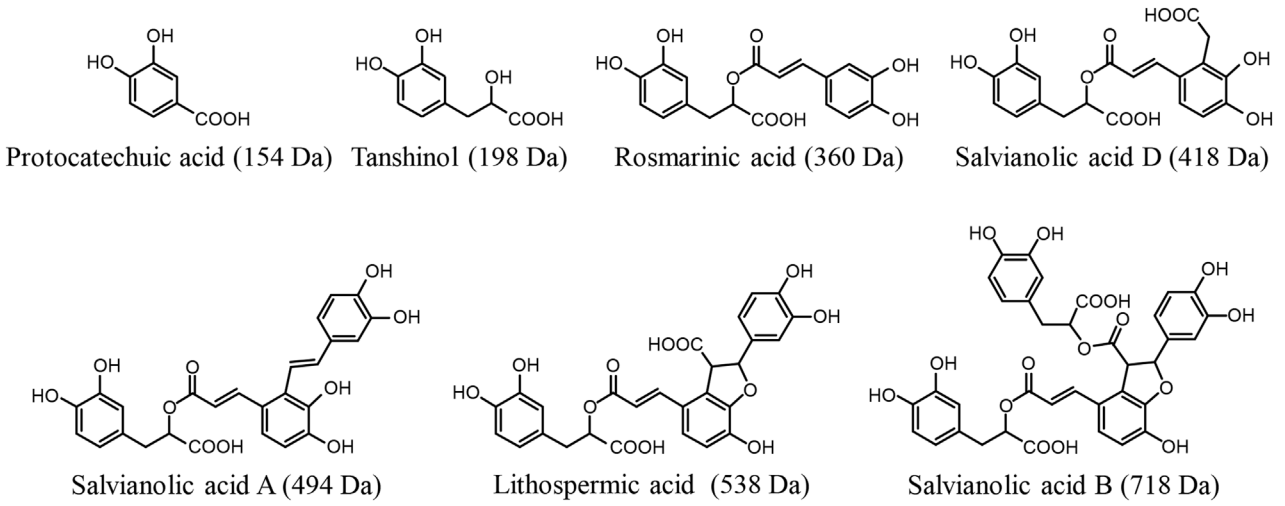

FIGURE 1 | Chemical structures of Danshen phenolic acids.

NM_021977 (OCT3), and NM_003049 (NTCP) and NM_017111 (Oatp1a1), NM_031650 (Oatp1b2), NM_017224 (Oat1), NM_053537 (Oat2), NM_031332 (Oat3), NM_012697 (Oct1), NM_031584 (Oct2), NM_019230 (Oct3), NM_019269 (Octn2), and NM_017047 (Ntcp).

Inside-out membrane vesicles (5 mg protein/mL), prepared from insect cells expressing human multidrug resistance-associated protein (MRP) 2, MRP3, MRP4, breast cancer resistance protein (BCRP), bile salt export pump (BSEP), and multidrug resistance protein (MDR) one and rat Mrp2, Mrp4, Bcrp, and Bsep, and vesicles (5 mg protein/mL; prepared from the insect cells expressing no ABC transporter; serving as negative control) were obtained from Genomembrane (Kanazawa, Japan).

Cell Culture and Transfection

Cell cultures and transfection were performed as described previously (Jia et al., 2015; Dong et al., 2018). Briefly, HEK-293 cells were grown, at 37°C and 5% CO_2, in Dulbecco's modified Eagle's medium, which was fortified with 10% fetal bovine serum, 1% minimal essential medium nonessential amino acids, and 1% antibiotic-antimycotic solution. A day before transfection, cells were seeded onto 24-well poly-D-lysine-coated plates at a density of 2×10^5 cells per well. After incubation at 37°C and 5% CO_2 for 24 h, the expression plasmid and the empty vector were introduced separately into the HEK293 cells with Lipofectamine 2000 transfection reagent (Invitrogen, Carlsbad, CA, United States), according to the manufacturer's protocol to yield transporter-expressing cells and mock cells, respectively. Before use, the transfected cells were validated functionally using the positive substrate GL (OATP1B1, OATP1B3, and Oatp1b2), $E_2$17βG (for Oatp1a1), PAH (OAT1 and Oat1), $PGF_{2\alpha}$ (OAT2 and Oat2), E_1S (OATP2B1, OAT3, OAT4, and Oat3), TEA (OCT1, OCT2, OCT3, Oct1, Oct2, Oct3, and Octn2), TCA (NTCP and Ntcp), and GS (PEPT1, PEPT2, Pept1, and Pept2) (Jia et al., 2015; Jiang et al., 2015; Dong et al., 2018).

Cellular Transport Assays

Transport studies were performed 48 h after the transfection. The test Danshen compounds, i.e., protocatechuic acid, tanshinol, rosmarinic acid, salvianolic acid D, salvianolic acid A, lithospermic acid, and salvianolic acid B at 100 μM final concentration each, were separately incubated with the transfected cells for 10 min. Krebs-Henseleit buffer was used for preincubation, incubation, and cell washing, except for the transporters PEPT1, PEPT2, Pept1, and Pept2 using buffer A (containing 145 mM NaCl, 3 mM KCl, 1 mM $CaCl_2$, 0.5 mM $MgCl_2$, 5 mM glucose, and 5 mM HEPES, pH 7.4) for preincubation and cell washing and buffer B (containing 145 mM NaCl, 3 mM KCl, 1 mM $CaCl_2$, 0.5 mM $MgCl_2$, 5 mM glucose, and 5 mM MES, pH 6.0) for incubation. The transport rate (pmol/mg protein/min) of the test Danshen phenolic acids was calculated using **Equation (1)**:

$$\text{Transport} = (C_L \times V_L)/T/W_L \quad (1)$$

where C_L, V_L, T, and W_L are the concentration of the test Danshen compound in the cellular lysate (μM), the volume of the lysate (μL), the incubation time (10 min), and the protein amounts measured in the lysate (mg), respectively. Differential uptake between the transfected cells and mock cells was defined as net transport ratio ($Transport_{TC}/Transport_{MC}$ ratio), where $Transport_{TC}$ and $Transport_{MC}$ are the transport rates of a test Danshen compound into transfected and mock cells, respectively. A net transport ratio >3, with a statistically significant difference between $Transport_{TC}$ and $Transport_{MC}$, demonstrated enough substrate activity in the screen to warrant determination of the compound for the Michaelis constant (K_m), maximum velocity (V_{max}), and intrinsic clearance (CL_{int}). The determination was performed under linear uptake conditions by incubation for

TABLE 1 | Final concentrations of Danshen phenolic acids used in the cellular uptake kinetic study.

Danshen phenolic compound	SLC transporter	Final concentration (μM)
Protocatechuic acid	Human OAT1	7.81–500
	Human OAT2	15.6–1,000
	Rat Oat1	25.0–600
	Rat Oat2	15.6–1,000
	Rat Oat3	25.0–600
Tanshinol	Human OAT1	15.6–1,000
	Human OAT2	312–10,000
	Human OAT3	156–5,000
	Human OAT4	312–10,000
	Rat Oat1	25.0–600
	Rat Oat2	100–3,200
	Rat Oat3	312–10,000
Rosmarinic acid	Human OATP1B1	62.5–4,000
	Human OATP1B3	62.5–4,000
	Human OAT1	6.25–400
	Human OAT2	12.5–600
	Human OAT4	31.2–2,000
	Rat Oatp1b2	100–6,400
	Rat Oat1	12.5–400
	Rat Oat2	25.0–600
	Rat Oat3	12.5–400
Salvianolic acid D	Human OATP1B1	50.0–1,600
	Human OATP1B3	50.0–3,200
	Human OAT1	6.25–400
	Human OAT2	25.0–600
	Rat Oatp1b2	50.0–3,200
	Rat Oat1	6.25–400
	Rat Oat2	25.0–600
Salvianolic acid A	Rat Oatp1b2	12.5–400
Lithospermic acid	Human OATP1B1	12.5–800
	Human OATP1B3	12.5–800
	Rat Oatp1b2	6.25–600
Salvianolic acid B	Human OATP1B1	3.13–200
	Human OATP1B3	3.13–200
	Rat Oatp1b2	3.13–200

5 min. **Table 1** summarizes the final concentrations of the test Danshen compounds for different transporters. All the incubation samples were analyzed by liquid chromatography/mass spectrometry.

Vesicular Transport Assays

Inside-out membrane vesicles expressing one of the ABC transporters MRP2, MRP3, MRP4, BCRP, BSEP, MDR1, Mrp2, Mrp4, Bcrp, and Bsep were used to assess the transport of the test Danshen compound, i.e., protocatechuic acid, tanshinol, rosmarinic acid, salvianolic acid D, salvianolic acid A, lithospermic acid, and salvianolic acid B, using a rapid filtration method (Jiang et al., 2015; Dong et al., 2018). Before use, membrane vesicles expressing MRP2, MRP3, MRP4, Mrp2, or Mrp4 were functionally validated using $E_2$17βG, those expressing BCRP or Bcrp using MTX, those expressing BSEP or Bsep using TCA, and those expressing MDR1 using GL. The test Danshen compounds at 100 μM final concentration were separately incubated with the membrane vesicles for 10 min. Buffer C (50 mM MOPS-tris, 70 mM KCl, 7.5 mM $MgCl_2$, pH 7.0) was used for preincubation and incubation, while buffer D (40 mM MOPS-tris, 70 mM KCl, pH 7.0) was used for vesicle washing. The transport rate (pmol/mg protein/min) of the test Danshen compound was calculated using **Equation (2)**:

$$\text{Transport} = (C_V \times V_V)/T/W_V \quad (2)$$

where C_V, V_V, T, and W_V represent concentration of the compound in vesicular lysates supernatant (μM), volume of the lysates (μL), incubation time (10 min), and amount of vesicle protein amount per well (0.05 mg), respectively. Differential transport of the test Danshen compound between ATP-containing vesicles and AMP-containing vesicles was defined as net transport ratio ($\text{Transport}_{ATP}/\text{Transport}_{AMP}$ ratio). Based on the experience in our laboratory, a net transport ratio >3, with a statistically significant difference between Transport_{ATP} and Transport_{AMP}, often suggests a positive result. All the incubation samples were analyzed by liquid chromatography/mass spectrometry.

Liquid Chromatography/Mass Spectrometry-Based Bioanalytical Assays

Validated bioanalytical assays were used to measure the test Danshen compounds in cell- and vesicle-based biomatrices.

Analyses were performed on a TSQ Vantage mass spectrometer (Thermo Fisher, San Jose, CA, United States) interfaced *via* a HESI source with an Agilent 1290 infinity LC system (Waldbronn, Germany). The chromatographic separation was achieved on Phenomenex Gemini 5-μm C_{18} column (50 mm × 2.0 mm i.d, Torrance, CA, United States). The mobile phases, which consisted of solvent A (water/methanol, 99:1, v/v, containing 0.15% formic acid) and solvent B (water/methanol, 1:99, v/v, containing 0.15% formic acid), was delivered at 0.3 ml/min. A 6-min gradient elution method was used as follows: 0–3.5 min, from 1% solvent B to 40% solvent B; 3.5–4.5 min, at 98% solvent B; and 4.6–6 min, at 1% solvent B. The mass spectrometry measurement was performed in the negative ion mode with precursor-product ion pairs for selected-reaction-monitoring of protocatechuic acid, tanshinol, rosmarinic acid, salvianolic acid D, salvianolic acid A, lithospermic acid, and salvianolic acid B at *m/z* 153→108, 197→123, 359→133, 417→197, 493→185, 537→185, and 717→321, respectively. Matrix-matched calibration curves for quantification of these test Danshen compounds (4.1, 12.3, 37, 111, 333, and 500 nM) were constructed using weighted (1/*X*) linear regression of the peak area (*Y*) against the corresponding nominal analyte concentration (*X*, nM). The sample preparation was performed using methanol-based protein precipitation and centrifugation; the supernatant was analyzed by liquid chromatography/mass spectrometry. Although no internal standard was used, assay validation, implemented according to the European Medicines Agency Guideline on bioanalytical method validation (2012; www.ema.europa.eu), demonstrated that the developed assays were reliable and reproducible for the intended use. The assays' lower limit of quantification was 4.1 nM for all the test Danshen compounds. The intra-batch accuracy and precision were within 94.1–105% and 2.41–10.1%, respectively, while associated inter-batch values were within 86.6–104% and 2.91–11.3%, respectively. The coefficients of variation reflecting matrix effects on assays were 2.23–10.7%. The analyte stability under conditions mimicking the analytical process was also evaluated, including storage at 24°C for 3 h, storage at 8°C for 24 h, and three freeze-and-thaw cycles. The analytes were stable under the test conditions, as indicated by the measured mean concentrations fluctuating within 86.9–113% of the nominal concentrations. All the preceding validation results were within the acceptable ranges.

Measurement of $E_2$17βG, E_1S, $PGF_{2\alpha}$, TEA, TCA, PAH, GS, MTX, and GL was achieved using liquid chromatography/mass spectrometry-based methods described previously (Jia et al., 2015; Dong et al., 2018).

Data Processing

GraFit software (version 5.0; *Erithacus* Software Ltd, Surrey, United Kingdom) was used to determine the K_m and V_{max} values by nonlinear regression analysis of initial transport rates as a function of substrate concentration. K_m and V_{max} values of the test Danshen compound were calculated using the following **Equation (3)**:

$$V = V_{max} \cdot S / (K_m + S) + P_{dif} \cdot S \quad (3)$$

where V is the initial transport of the test Danshen compound in transfected cells (pmol/min/mg protein), V_{max} is the maximal transport rate (pmol/min/mg protein), S is the concentration of the test Danshen compound (μM) and P_{dif} is the clearance of the test Danshen compound *via* passive diffusion in mock cells.

All data are expressed as the mean ± standard deviation. Statistical analysis was performed using SPSS Statistics Software (version 19.0; IBM, Chicago, IL, United States). A value of $p < 0.05$ was considered to be the minimum level of statistical significance.

RESULTS AND DISCUSSION

Transport of Danshen Phenolic Acids by Human and Rat Hepatic Transporters

Rosmarinic acid (molecular mass: 360 Da), salvianolic acid D (418 Da), lithospermic acid (538 Da), and salvianolic acid B (718 Da) were found to be substrates of the human hepatic sinusoidal uptake solute carrier (SLC) transporters OATP1B1 and OATP1B3; their net transport ratios are summarized in **Table 2**. **Figure 2** shows their saturable cellular uptake with K_m, V_{max}, and CL_{int} values summarized in **Table 3**. Meanwhile, protocatechuic acid (154 Da), tanshinol (198 Da), rosmarinic acid, and salvianolic acid D were substrates of OAT2 (another human hepatic sinusoidal uptake SLC transporter), with their net transport ratios shown in **Table 2** and associated K_m, V_{max}, and CL_{int} values in **Figure 2** and **Table 3**. The Danshen phenolic acids were not substrates of other human hepatic sinusoidal uptake SLC transporters. Recently, Cao et al. (2019) reported salvianolic acid B as a substrate of human OATP1B1. In the current investigation, we found this Danshen phenolic acid to be also a substrate of human OATP1B3. In addition, salvianolic acid B and lithospermic acid were substrates of human MRP2, a hepatic canalicular efflux ABC transporter, while salvianolic acid D was a substrate of human MRP4, a hepatic sinusoidal efflux ABC transporter. No other human hepatic ABC transporter was found to mediate transport of the Danshen compounds. Despite being closely structure-related to the other Danshen phenolic acids, salvianolic acid A (494 Da) was not a substrate of OATP1B1, OATP1B3, OAT2, or any other test hepatic sinusoidal uptake SLC transporter; it was also not a substrate of hepatic canalicular or sinusoidal efflux ABC transporter. Regarding protocatechuic acid (154 Da) and tanshinol (198 Da), these Danshen phenolic acids had little substrate activity at human hepatic SLC or ABC transporters when screened at 100 μM final concentration (**Table 2**).

Similar to the situation for human hepatic transporters, rosmarinic acid, salvianolic acid D, lithospermic acid, and salvianolic acid B were substrates of the rat hepatic sinusoidal uptake SLC transporter Oatp1b2 (the closest ortholog of both human hepatic OATP1B1 and OATP1B3) (**Table 2**); **Figure 2** shows their saturable cellular uptake, with K_m, V_{max}, and CL_{int} values summarized in **Table 3**. Although neither

TABLE 2 | Net transport ratios of Danshen phenolic acids at 100 μM final concentration by human and rat hepatic transporters.

Transporter	$Transport_{TC}/Transport_{MC}$ ratio for the SLC transporter or $transport_{ATP}/Transport_{AMP}$ ratio for the ABC transporter							
	Positive substrate	Protocatechuic acid	Tanshinol	Rosmarinic acid	Salvianolic acid D	Salvianolic acid A	Lithospermic acid	Salvianolic acid B
MW (Da)		154	198	360	418	494	538	718
Human hepatic sinusoidal uptake SLC transporters								
OATP1B1	79.5 ± 1.3 (GL)	0.83 ± 0.14	1.04 ± 0.13	4.00 ± 0.43*	5.38 ± 0.83*	1.21 ± 0.33	3.99 ± 0.24*	5.16 ± 1.30*
OATP1B3	33.1 ± 0.5 (GL)	0.75 ± 0.09	0.94 ± 0.21	7.28 ± 0.58*	5.83 ± 0.49*	1.02 ± 0.31	8.02 ± 0.52*	16.2 ± 0.6*
OATP2B1	41.1 ± 1.5 (E_1S)	1.36 ± 0.15	1.45 ± 0.46	1.69 ± 0.71	2.27 ± 1.16	2.45 ± 0.34	1.16 ± 0.27	1.32 ± 0.33
OAT2	70.2 ± 6.6 ($PGF_{2\alpha}$)	417 ± 23*	74.2 ± 13.9*	716 ± 86*	314 ± 44*	2.25 ± 0.47	1.51 ± 0.27	1.04 ± 0.09
OCT1	4.58 ± 0.26 (TEA)	1.09 ± 0.33	0.94 ± 0.11	1.46 ± 0.57	1.04 ± 0.24	1.04 ± 0.32	1.56 ± 0.26	1.03 ± 0.07
OCT3	4.45 ± 0.27 (TEA)	0.94 ± 0.24	0.84 ± 0.32	0.75 ± 0.23	0.94 ± 0.32	1.31 ± 0.09	0.84 ± 0.15	0.75 ± 0.38
NTCP	144 ± 30 (TCA)	1.26 ± 0.15	0.79 ± 0.14	2.76 ± 0.36	2.09 ± 0.36	0.93 ± 0.11	2.44 ± 0.13	2.88 ± 0.21
Human hepatic sinusoidal efflux ABC transporters								
MRP3	6.79 ± 1.49 ($E_2$17βG)	1.25 ± 0.08	1.71 ± 0.41	1.38 ± 0.01	1.35 ± 0.30	1.54 ± 0.23	1.72 ± 0.28	1.47 ± 0.33
MRP4	6.17 ± 0.92 ($E_2$17βG)	1.25 ± 0.14	1.57 ± 0.06	1.99 ± 0.08	5.27 ± 0.51*	1.56 ± 0.05	1.36 ± 0.14	1.99 ± 0.06
Human hepatic canalicular efflux ABC transporters								
MRP2	7.23 ± 1.04 ($E_2$17βG)	0.94 ± 0.31	0.85 ± 0.12	1.13 ± 0.34	1.51 ± 0.73	1.42 ± 0.31	5.02 ± 1.67*	6.21 ± 1.32*
BCRP	4.45 ± 0.67 (MTX)	1.04 ± 0.19	2.55 ± 0.91	1.12 ± 0.55	2.22 ± 0.61	1.12 ± 0.35	1.12 ± 0.31	1.54 ± 0.78
BSEP	4.03 ± 0.89 (TCA)	0.99 ± 0.21	0.93 ± 0.25	1.03 ± 0.09	1.19 ± 0.35	1.32 ± 0.26	0.83 ± 0.20	1.43 ± 0.32
MDR1	5.13 ± 0.87 (GL)	0.93 ± 0.04	1.43 ± 0.27	1.04 ± 0.18	0.92 ± 0.23	1.26 ± 0.05	1.26 ± 0.09	1.66 ± 0.12
Rat hepatic sinusoidal uptake SLC transporters								
Oatp1a1	17.9 ± 2.3 ($E_2$17βG)	1.66 ± 0.77	1.67 ± 0.66	1.45 ± 0.57	2.45 ± 1.88	2.24 ± 0.67	1.41 ± 0.67	1.91 ± 0.42
Oatp1b2	121 ± 2 (GL)	1.32 ± 0.45	1.45 ± 0.32	17.0 ± 2.8*	16.0 ± 0.8*	7.52 ± 1.31*	11.6 ± 0.7*	30.0 ± 0.6*
Oat2	24.3 ± 3.3 ($PGF_{2\alpha}$)	163 ± 30*	17.2 ± 2.8*	334 ± 18*	50.5 ± 10.7*	1.41 ± 0.26	1.36 ± 0.33	0.92 ± 0.22
Oct1	8.16 ± 2.40 (TEA)	1.19 ± 0.41	0.89 ± 0.34	1.56 ± 0.13	1.23 ± 0.54	1.13 ± 0.19	1.18 ± 0.06	0.66 ± 0.17
Oct3	3.90 ± 0.88 (TEA)	0.85 ± 0.11	1.01 ± 0.11	0.74 ± 0.24	0.93 ± 0.15	1.19 ± 0.14	0.81 ± 0.13	0.84 ± 0.31
Octn2	9.85 ± 0.74 (TEA)	0.91 ± 0.17	0.82 ± 0.19	1.14 ± 0.04	1.12 ± 0.22	0.95 ± 0.44	0.95 ± 0.11	1.25 ± 0.21
Ntcp	134 ± 15 (TCA)	1.04 ± 0.27	0.95 ± 0.16	1.68 ± 0.25	1.49 ± 0.23	0.84 ± 0.13	1.71 ± 0.15	1.90 ± 0.02
Rat hepatic sinusoidal efflux ABC transporters								
Mrp4	7.37 ± 1.32 ($E_2$17βG)	1.17 ± 0.06	1.81 ± 0.15	4.79 ± 0.38*	11.1 ± 0.2*	2.09 ± 0.25	1.46 ± 0.01	2.15 ± 0.32
Rat hepatic ABC canalicular efflux ABC transporters								
Mrp2	3.54 ± 0.32 ($E_2$17βG)	0.74 ± 0.13	0.75 ± 0.20	1.24 ± 0.45	2.21 ± 0.89	1.80 ± 0.81	1.83 ± 0.45	4.43 ± 1.12*
Bcrp	20.5 ± 3.2 (MTX)	0.94 ± 0.21	0.83 ± 0.23	1.45 ± 0.32	5.54 ± 1.03*	1.31 ± 0.04	1.27 ± 0.20	1.13 ± 0.14
Bsep	5.14 ± 0.88 (TCA)	1.13 ± 0.17	1.20 ± 0.25	1.39 ± 0.36	1.09 ± 0.23	0.75 ± 0.12	1.69 ± 0.37	1.52 ± 0.67

Values represent the means ± standard deviations (n = 3).

**p < 0.05, indicating a statistically significant difference between $Transport_{TC}$, and $Transport_{MC}$, or between $Transport_{ATP}$, and $Transport_{AMP}$., The final concentrations of positive substrates were 20 μM with incubation time of 10 min.*

protocatechuic acid nor tanshinol was a substrate of Oatp1b2, these two Danshen compounds, together with rosmarinic acid and salvianolic acid D, were substrates of Oat2 (another rat hepatic sinusoidal uptake SLC transporter), with their net transport ratios shown in **Table 2** and associated K_m, V_{max}, and CL_{int} values in **Figure 2** and **Table 3**. In addition, salvianolic acid B was a substrate of rat Mrp2, while rosmarinic acid and salvianolic acid D were substrates of rat Mrp4. Significant interspecies differences were observed for salvianolic acid A, as indicated by this compound being a substrate of Oatp1b2. No other rat hepatic transporter was found to mediate transport of the Danshen compounds.

Transport of Danshen Phenolic Acids by Human and Rat Renal Transporters

Protocatechuic acid (molecular mass, 154 Da), tanshinol (198 Da), rosmarinic acid (360 Da), and salvianolic acid D (418 Da) were found to be substrates of the human OAT1 and OAT2, two renal basolateral uptake SLC transporters. The compounds' net transport ratios for OAT1 are shown in **Table 4**, while such data for OAT2 are shown in **Table 2**. **Figure 3** shows their saturable cellular uptake for OAT1, with K_m, V_{max}, and CL_{int} values in **Table 5**; such data for OAT2 are shown in **Figure 2** and **Table 3**. Recently, Kang et al. (2021) reported that rosmarinic acid was a substrate of human OAT1. In this investigation, we found that both OAT1 and OAT2 were responsible for cellular uptake of rosmarinic acid. Tanshinol and rosmarinic acid were also relatively weak substrates of human OAT4, a renal apical uptake SLC transporter, and OAT3 (tanshinol only), a renal basolateral uptake SLC transporter. The four Danshen phenolic acids were not substrates of other human renal transporters, except for salvianolic acid D being a substrate of renal MRP4. Regarding the other Danshen phenolic acids salvianolic acid A (molecular mass: 494 Da), lithospermic acid (538 Da), and salvianolic acid B (718 Da), no human renal basolateral uptake SLC transporter was found to mediate cellular transport of these compounds, albeit lithospermic acid and salvianolic acid B being substrates of the human renal apical efflux ABC transporter MRP2 (**Table 4**).

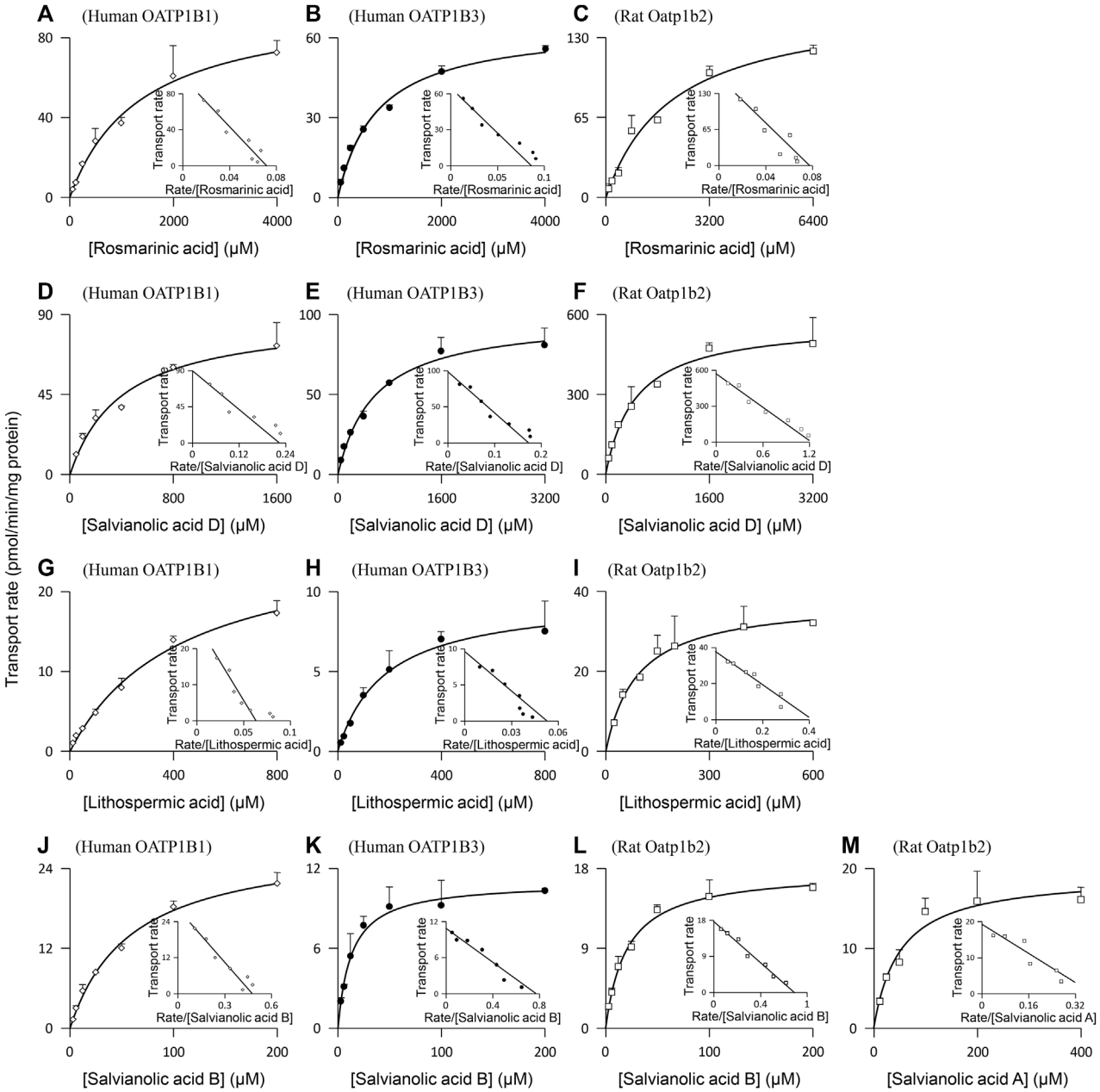

FIGURE 2 | Representative kinetic plots of transport versus substrate concentration for cellular uptake of Danshen phenolic acids [**(A–C)**, rosmarinic acid; **(D–F)**, salvianolic acid D; **(G–I)**, lithospermic acid; **(J–L)**, salvianolic acid B; and **(M)**, salvianolic acid A] mediated by the human and rat hepatic SLC transporters. The K_m, V_{max}, and CL_{int} values are shown in **Table 3**, and they represent the means ± standard deviations ($n = 3$). The final concentrations of the test Danshen compounds in the cellular uptake kinetic study are summarized in **Table 1**.

Similar to the situation for human renal transporters, protocatechuic acid, tanshinol, and rosmarinic acid were substrates of the rat renal basolateral uptake SLC transporters Oat1 and Oat3 (the closest orthologs of human renal OAT1 and OAT3, respectively) (**Table 4**); **Figure 3** shows their saturable cellular uptake with K_m, V_{max}, and CL_{int} values in **Table 5**. Salvianolic acid D was a substrate of only rat Oat1, and not of rat Oat3. Unlike human OAT2 (a renal basolateral uptake SLC transporter), rat Oat2 is a renal apical uptake SLC transporter (Shen et al., 2015). Protocatechuic acid, tanshinol, rosmarinic acid, and salvianolic acid D were substrates of rat Oat2, while salvianolic acid A, lithospermic acid, and salvianolic acid D were not substrates of rat Oat1, Oat3, or Oat2. All the test Danshen compounds were not substrates of other rat renal transporters.

TABLE 3 | Kinetic parameters for transports of Danshen phenolic acids by human and rat hepatic transporters.

Danshen phenolic acid	K_m (μM)	V_{max} (pmol/min/mg protein)	CL_{int} (μL/min/mg protein)
Human hepatic sinusoidal uptake OATP1B1			
Rosmarinic acid	1,371 ± 194	98.1 ± 5.9	0.07
Salvianolic acid D	403 ± 85	89.3 ± 7.4	0.22
Lithospermic acid	428 ± 67	27.0 ± 2.1	0.06
Salvianolic acid B	58.9 ± 6.2	28.1 ± 1.2	0.46
Human hepatic sinusoidal uptake OATP1B3			
Rosmarinic acid	750 ± 101	64.7 ± 3.1	0.09
Salvianolic acid D	570 ± 79	98.5 ± 4.8	0.17
Lithospermic acid	182 ± 26	9.59 ± 0.51	0.05
Salvianolic acid B	13.0 ± 1.6	11.0 ± 0.4	0.85
Human hepatic sinusoidal uptake OAT2			
Protocatechuic acid	185 ± 24	3,822 ± 177	20.7
Tanshinol	1,228 ± 160	7,475 ± 308	6.09
Rosmarinic acid	48.6 ± 4.2	927 ± 22	19.1
Salvianolic acid D	111 ± 13	2,687 ± 114	24.3
Rat hepatic sinusoidal uptake Oatp1b2			
Rosmarinic acid	2049 ± 418	159 ± 14	0.08
Salvianolic acid D	464 ± 62	572 ± 25	1.23
Salvianolic acid A	50.5 ± 12.8	19.2 ± 1.5	0.38
Lithospermic acid	91.3 ± 10.6	37.7 ± 1.4	0.41
Salvianolic acid B	20.5 ± 1.9	17.7 ± 0.5	0.87
Rat hepatic sinusoidal uptake Oat2			
Protocatechuic acid	109 ± 6	1,180 ± 19	10.9
Tanshinol	978 ± 123	1,437 ± 74	1.47
Rosmarinic acid	119 ± 15	620 ± 28	5.20
Salvianolic acid D	60.0 ± 7.2	164 ± 6	2.73

Values represent the means ± standard deviations (n = 3). Error estimates are based on the best fit of the average values obtained at each point to the Michaelis-Menten equation using nonlinear regression analysis.

New Insight Into Hepatobiliary and Renal Excretion in Concert for Elimination of Danshen Phenolic Acids in Humans and Rats

The Danshen phenolic acids protocatechuic acid (molecular mass, 154 Da), tanshinol (198 Da), rosmarinic acid (360 Da), salvianolic acid D (418 Da), salvianolic acid A (494 Da), lithospermic acid (538 Da), and salvianolic acid B (718 Da) are believed to be pharmacologically important for the injection due to their cardiovascular properties (Li et al., 2018; Ren et al., 2019). Because these herbal compounds are of poor or fairly good membrane permeability (Lu et al., 2008), their systemic elimination *via* the liver or kidneys necessitates transporter-mediated hepatic or renal uptake from blood, and this serves as the crucial elimination step. In this investigation, we found both hepatic and renal SLC transporters that could mediate uptake of the Danshen phenolic acids into the hepatocytes and/or renal proximal tubular epithelia, respectively, in a molecular-mass-related manner (**Figure 4**). The relatively high molecular mass compounds lithospermic acid and salvianolic acid B (both >500 Da) underwent systemic elimination, initiated by OATP1B1/OATP1B3-mediated hepatic uptake. Rosmarinic acid and salvianolic acid D (350–450 Da) underwent systemic elimination, initiated by OATP1B1/OATP1B3/OAT2-mediated hepatic uptake and by OAT1/OAT2-mediated renal uptake. The relatively low molecular mass compounds protocatechuic acid and tanshinol (both <200 Da) underwent systemic elimination, initiated by OAT1/OAT2-mediated renal uptake and OAT2-mediated hepatic uptake. However, unlike the preceding Danshen phenolic acids, little is known about how salvianolic acid A (494 Da) was taken up by the two organs. Given its molecular mass being around 500 Da, hepatic uptake of salvianolic acid A might be mediated by an unknown transporter(s). For protocatechuic acid, tanshinol, rosmarinic acid, and salvianolic acid D, the hepatic sinusoidal uptake SLC transporter OAT2 is important, by mediating the hepatic uptake, to facilitate hepatic metabolism (methylation, glucuronidation, and/or sulfation) of these Danshen phenolic acids of relatively low molecular mass (154–418 Da). Regarding the ABC transporters, hepatobiliary excretion of lithospermic acid and salvianolic acid B appeared to be accomplished by MRP2-mediated hepatic efflux into bile. Unlike these two high molecular mass compounds, no ABC transporters was found to mediate efflux of protocatechuic acid, tanshinol, rosmarinic acid, and salvianolic acid D into the bile and/or urine. Our earlier investigation by Tian et al. (2015) indicated that the methylated and sulfated metabolites of tanshinol could be extensively excreted, like the unchanged compound, into the urine. This suggested that involvement of metabolism in the excretion of the Danshen phenolic acids is worth considering. Given that protocatechuic acid and tanshinol have only fairly good membrane permeability and that permeability of rosmarinic

TABLE 4 | Net transport ratios of Danshen phenolic acids at 100 μM final concentration by human and rat renal transporters.

Transporter	$Transport_{TC}/Transport_{MC}$ ratio for the SLC transporter or $transport_{ATP}/Transport_{AMP}$ ratio for the ABC transporter							
	Positive substrate	Protocatechuic acid	Tanshinol	Rosmarinic acid	Salvianolic acid D	Salvianolic acid A	Lithospermic acid	Salvianolic acid B
MW (Da)		154	198	360	418	494	538	718
Human renal basolateral uptake SLC transporters								
OAT1	50.2 ± 8.6 (PAH)	53.1 ± 3.9*	102 ± 26*	46.8 ± 10.9*	11.7 ± 2.4*	1.02 ± 0.14	2.09 ± 0.89	1.21 ± 0.14
OAT2	See OAT2 data in **Table 2**							
OAT3	10.2 ± 1.2 (E_1S)	1.12 ± 0.25	4.54 ± 2.08*	1.56 ± 0.36	1.12 ± 0.56	2.12 ± 0.13	0.96 ± 0.15	1.03 ± 0.24
OCT2	10.0 ± 2.9 (TEA)	0.75 ± 0.35	1.11 ± 0.26	0.85 ± 0.29	0.85 ± 0.26	0.93 ± 0.32	0.89 ± 0.31	0.75 ± 0.23
Human renal apical uptake SLC transporters								
OAT4	7.69 ± 1.74 (E_1S)	1.56 ± 0.46	7.81 ± 1.14*	7.27 ± 0.77*	2.87 ± 0.09	1.56 ± 0.23	2.91 ± 0.17	0.95 ± 0.23
PEPE1	126 ± 31 (GS)	0.93 ± 0.34	1.21 ± 0.51	1.42 ± 0.53	1.06 ± 0.20	1.45 ± 0.27	1.86 ± 0.36	2.05 ± 0.22
PEPT2	360 ± 49 (GS)	1.43 ± 0.32	1.12 ± 0.22	1.12 ± 0.22	1.03 ± 0.11	1.14 ± 0.31	0.74 ± 0.06	1.06 ± 0.12
Human renal apical efflux ABC transporters								
MRP2	See MRP2 data in **Table 2**							
MRP4	See MRP4 data in **Table 2**							
BCRP	See BCRP data in **Table 2**							
Rat renal basolateral uptake SLC transporters								
Oat1	70.5 ± 10.6 (PAH)	104 ± 20*	114 ± 18*	150 ± 46*	11.5 ± 2.9*	1.13 ± 0.64	1.36 ± 0.35	1.56 ± 0.67
Oat3	21.4 ± 6.8 (E_1S)	16.1 ± 2.8*	5.83 ± 1.47*	4.45 ± 1.12*	1.41 ± 0.36	1.09 ± 0.35	0.94 ± 0.23	1.12 ± 0.41
Oct1	See Oct1 data in **Table 2**							
Oct2	7.49 ± 1.62 (TEA)	0.92 ± 0.08	1.09 ± 0.36	0.75 ± 0.32	1.44 ± 0.24	0.94 ± 0.33	1.11 ± 0.32	1.08 ± 0.21
Octn2	See Octn2 data in **Table 2**							
Rat renal apical uptake SLC transporters								
Oat2	See Oat2 data in **Table 2**							
Pept1	90.1 ± 10.4 (GS)	1.37 ± 0.36	1.14 ± 0.32	1.14 ± 0.13	1.43 ± 0.36	1.32 ± 0.13	1.31 ± 0.32	1.21 ± 0.45
Pept2	101 ± 19 (GS)	1.21 ± 0.26	1.19 ± 0.15	0.84 ± 0.17	1.88 ± 0.45	0.84 ± 0.19	0.85 ± 0.14	0.94 ± 0.21
Rat renal ABC apical efflux ABC transporters								
Mrp2	See Mrp2 data in **Table 2**							
Mrp4	See Mrp4 data in **Table 2**							
Bcrp	See Bcrp data in **Table 2**							

Values represent the means ± standard deviations (n = 3).

**p < 0.05, indicating a statistically significant difference between $Transport_{TC}$, and $Transport_{MC}$, or between $Transport_{ATP}$, and $Transport_{AMP}$., The final concentrations of positive substrates were 20 μM with incubation time of 10 min.*

acid and salvianolic acid D is poor, both accumulation of these compounds in the liver and/or kidneys and possibility of new ABC transporters that could mediate the compounds' efflux merit further investigation. Regarding salvianolic acid D, the hepatic canalicular efflux ABC transporter MRP4 was found to be able to mediate the compound's efflux into the blood; this could offset the OATP1B1/1B3-mediated uptake of the compound from the blood and in turn partially contribute the greatest systemic exposure to the compound after dosing DanHong (Li et al., 2015).

Drugs and their metabolites are usually eliminated *via* bile and/or urine. Understanding drug compounds' tendency for excretion into the bile and/or urine is important, because the excretion can be a major factor influencing drugs' therapeutic and toxicological properties. The belief that molecular mass influences the excretion tendency of a drug compound is implied in several early publications (Millburn, 1970; Smith, 1971; Yang et al., 2009). Drugs (particularly anions) highly excreted into bile tend to be of relatively high molecular mass (>500 Da); by contrast, drugs of relatively low molecular mass (<300 Da) tend to be excreted into the urine. Transporters play important roles in hepatobiliary and renal excretion of drugs (Morrissey et al., 2013; Liu and Sahi, 2016). However, little is known about how these transporters respond to drug difference in molecular mass. Our current investigation suggested that the human hepatic and renal uptake SLC transporters act on the Danshen compounds in a compound-molecular-mass-related manner, i.e., OATP1B transporters transporting those with molecular mass ≥360 Da, while OAT transporters transporting those with molecular masses ≤418 Da. A compound with a molecular mass of 360–418 Da could be taken up by both OATP1B and OAT transporters. More compounds of various types merit assessment for more precise setting of the molecular mass cutoffs for substrate preference of these SLC transporters.

For pharmacokinetic research on Chinese herbal medicines (Li, 2017; Zhang et al., 2018; Pintusophon et al., 2019; Lan et al., 2021; Li et al., 2021), rat is an experimental animal that is commonly used in supportive studies of herbal compounds to help understanding their important disposition steps, which are difficult to be measured in humans. To this end, it is important to gain insight into interspecies similarity and differences, before designing supportive animal studies. The hepatobiliary excretion of drugs varies widely among species; empirically, rat is a good biliary excreter for drugs (particularly for anions with molecular mass >320 Da), whereas human is a relatively poor excreter (Millburn et al., 1967; Lin and Lu, 1997). Similar to the human transporters, the rat hepatic and

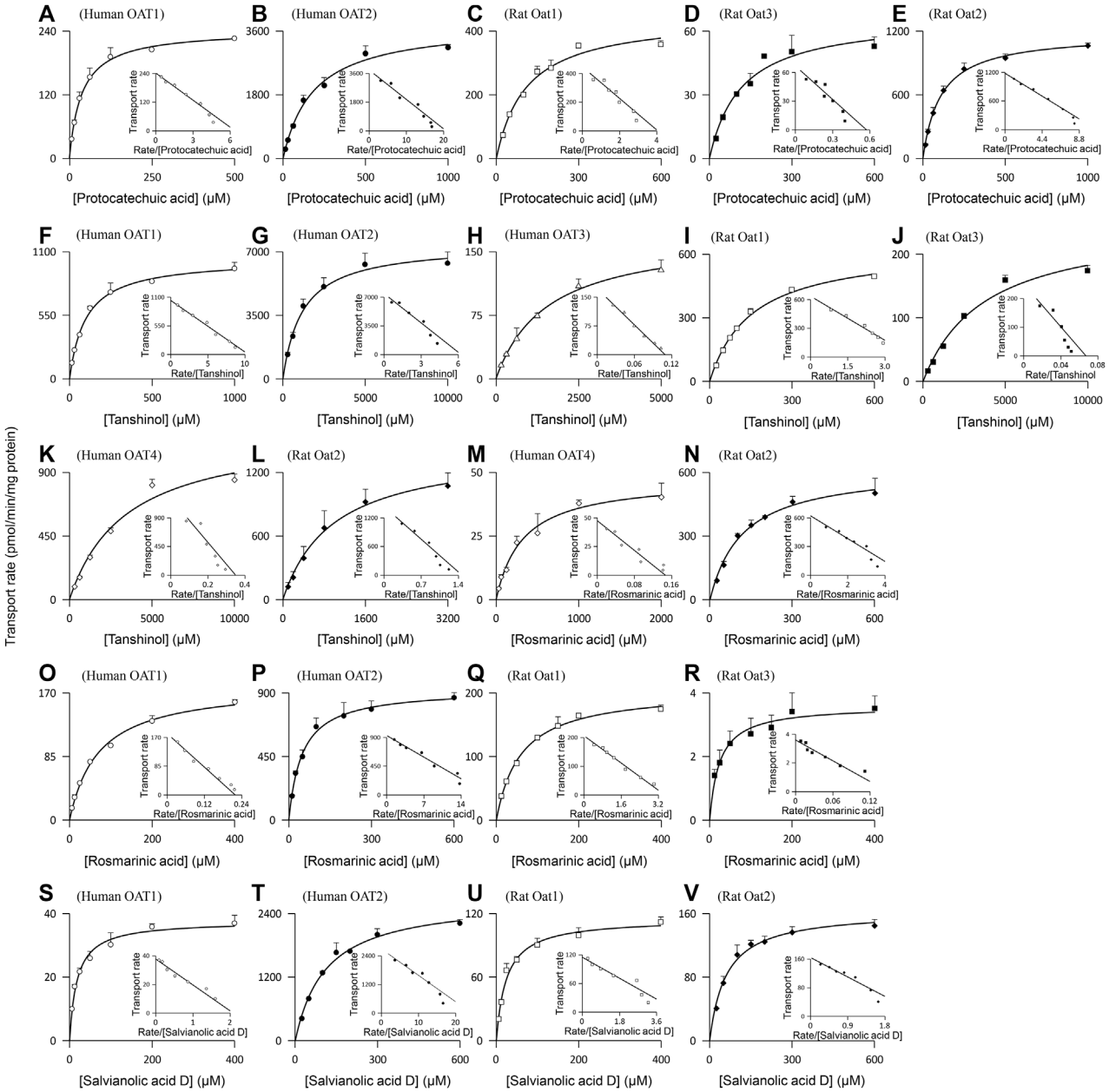

FIGURE 3 | Representative kinetic plots of transport versus substrate concentration for cellular uptake of Danshen phenolic acids [**(A–E)**, protocatechuic acid; **(F–L)**, tanshinol; **(M–R)**, rosmarinic acid; and **(S–V)**, salvianolic acid D] mediated by the human and rat renal SLC transporters. The K_m, V_{max}, and CL_{int} values are shown in **Table 5**, and they represent the means ± standard deviations (n = 3). The final concentrations of the test Danshen compounds in the cellular uptake kinetic study are summarized in **Table 1**.

renal uptake SLC transporters act on the Danshen phenolic acids in a compound-molecular-mass-related manner. For these Danshen compounds, the molecular mass cutoffs for substrate preference of rat hepatic and renal SLC transporters were similar to those of the human transporters. In addition, the K_m values of the rat SLC transporters for the Danshen phenolic acids were generally comparable with those of their respective human orthologs. The observed interspecies difference was rat Oatp1b2 being able to mediate hepatic uptake of salvianolic acid A, whereas no human transporter was found that could do so. Collectively, PK similarities between human and rat, with respect to hepatic and renal disposition of the Danshen phenolic acids, makes the rat a suitable animal model for supportive studies as well as for associated pharmacodynamic studies, safety assessments, and drug-drug interaction (DDI) studies.

TABLE 5 | Kinetic parameters for transports of Danshen phenolic acids by human and rat renal transporters.

Danshen phenolic acid	K_m (μM)	V_{max} (pmol/min/mg protein)	CL_{int} (μL/min/mg protein)
Human renal basolateral uptake OAT1			
Protocatechuic acid	37.6 ± 2.5	242 ± 4	6.43
Tanshinol	98.9 ± 7.1	1,038 ± 22	10.5
Rosmarinic acid	70.8 ± 6.4	181 ± 6	2.55
Salvianolic acid D	18.1 ± 2.3	37.6 ± 1.2	2.08
Human renal basolateral uptake OAT2			
Protocatechuic acid	See OAT2 data in **Table 3**		
Tanshinol	See OAT2 data in **Table 3**		
Rosmarinic acid	See OAT2 data in **Table 3**		
Salvianolic acid D	See OAT2 data in **Table 3**		
Human renal basolateral uptake OAT3			
Tanshinol	1,565 ± 127	171 ± 6	0.11
Human renal apical uptake OAT4			
Tanshinol	3,442 ± 940	1,204 ± 140	0.35
Rosmarinic acid	325 ± 53	47.5 ± 2.6	0.15
Rat renal basolateral uptake Oat1			
Protocatechuic acid	110 ± 19	446 ± 27	4.07
Tanshinol	154 ± 13	636 ± 22	4.13
Rosmarinic acid	59.2 ± 4.7	206 ± 5	3.47
Salvianolic acid D	24.4 ± 3.3	115 ± 4	4.72
Rat renal basolateral uptake Oat3			
Protocatechuic acid	117 ± 27	66.8 ± 5.5	0.57
Tanshinol	3,760 ± 907	252 ± 27	0.07
Rosmarinic acid	24.0 ± 4.2	3.58 ± 0.14	0.15
Rat renal apical uptake Oat2			
Protocatechuic acid	See Oat2 data in **Table 3**		
Tanshinol	See Oat2 data in **Table 3**		
Rosmarinic acid	See Oat2 data in **Table 3**		
Salvianolic acid D	See Oat2 data in **Table 3**		

Values represent the means ± standard deviations (n = 3). Error estimates are based on the best fit of the average values obtained at each point to the Michaelis-Menten equation using nonlinear regression analysis.

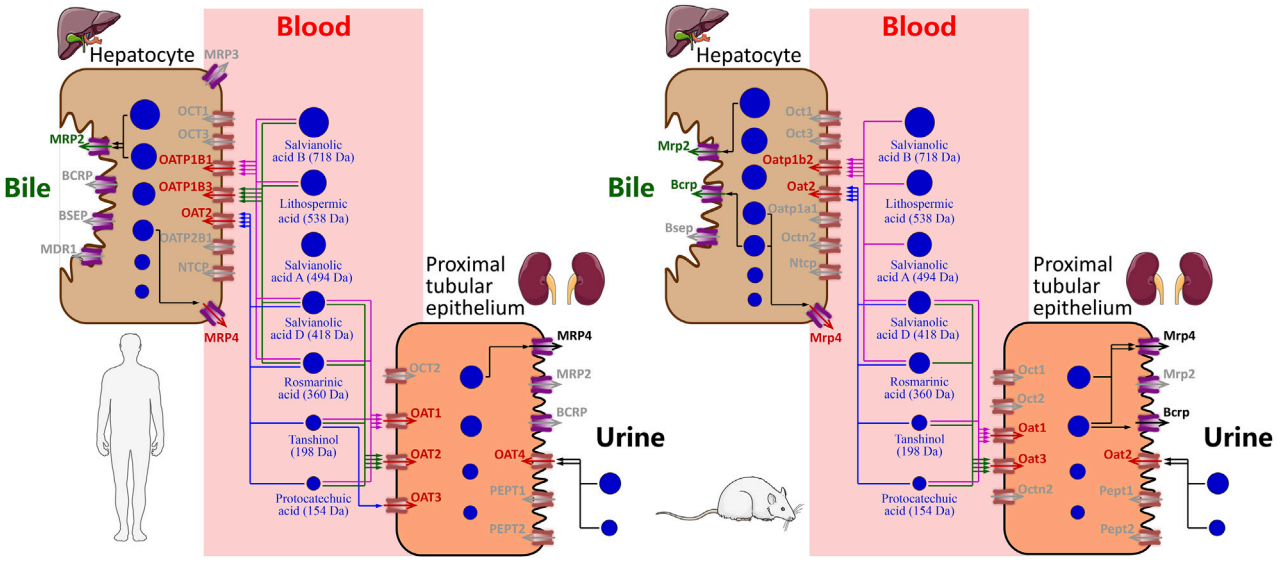

FIGURE 4 | Schematic overview of mechanistic hepatobiliary and renal excretion of Danshen phenolic acids.

Transporters (particularly hepatic and renal uptake transporters) have been found to mediate potential pharmacokinetic DDIs with herbal medicines, comprising the herb-drug interaction (Meng and Liu, 2014; Jiang et al., 2015; Olaleye et al., 2019; Pintusophon et al., 2019) and the drug-herb interaction (Jia et al., 2015; Dong et al., 2018). The *in vitro* transporter kinetic data (**Tables 3** and **5**) indicated that most Danshen phenolic acids had low affinity for the human hepatic and renal uptake transporters with K_m values 38–3,442 μM, suggesting that these herbal compounds from DanHong were unlikely to induce herb-drug interactions by the transporters (DDI index, ≤ 0.02). Here, the DDI indices were estimated based on their $(C_{max} \times f_{u\text{-}plasma})/K_m$ ratios, where the C_{max} and $f_{u\text{-}plasma}$ data were obtained from our earlier human pharmacokinetic study of DanHong (Li et al., 2015). Another investigation indicated that salvianolic acid B had a half maximum inhibitory concentration (IC_{50}) of 38 μM for OATP1B1 (Li et al., 2019); the associated DDI index of 0.001 is still too low to induce DDI with normally dosed DanHong. Regarding the drug-herb interactions associated with the Danshen phenolic acids, our earlier investigation by Jia et al. (2015) indicated that tanshinol could be a victim of such interaction when OAT1/2/3 were inhibited by probenecid. Similarly, pharmacokinetic drug-herb interactions by inhibiting OAT1/2 need to be considered also for protocatechuic acid. Given that there are many dual OATP1B1/1B3 inhibitors in clinical use (Dong et al., 2018), pharmacokinetic drug-herb interactions *via* OATP1B1/1B3 inhibition could occur for lithospermic acid and salvianolic acid B, both of which underwent hepatic uptake but not renal uptake.

CONCLUSION

In this investigation, we identified human transporters responsible for hepatobiliary and renal excretion of Danshen phenolic acids. Lithospermic acid and salvianolic acid B (both >500 Da) underwent systemic elimination, initiated by OATP1B1/OATP1B3-mediated hepatic uptake. Rosmarinic acid and salvianolic acid D (350–450 Da) underwent systemic elimination, initiated by OATP1B1/OATP1B3/OAT2-mediated hepatic uptake and by OAT1/2-mediated renal uptake. Protocatechuic acid and tanshinol (both <200 Da) underwent systemic elimination, initiated by OAT1/OAT2-mediated renal uptake and OAT2-mediated hepatic uptake. A similar scenario was observed with the rat orthologs, including the rat SLC transporters acting on the Danshen compounds, also in a compound-molecular-mass-related manner. The findings of this investigation improve our understanding of disposition of the Danshen phenolic acids and could facilitate pharmacokinetic research on other Danshen-containing injections. Future investigations are planned to elucidate whether any new transporter(s) could mediate hepatic uptake of salvianolic acid A and how efflux of many Danshen phenolic acids from hepatocytes and renal proximal tubular epithelia is achieved after the SLC transporter-mediated hepatic and renal uptake, respectively.

DATA AVAILABILITY STATEMENT

The original contributions presented in the study are included in the article/**Supplementary Materials**, further inquiries can be directed to the corresponding authors.

AUTHOR CONTRIBUTIONS

CL, W-WJ, and J-JD participated in research design. CL, W-WJ, and OO wrote or contributed to the writing of the manuscript. CL, W-WJ, J-JD, and J-LL performed the data analysis. J-JD, W-WJ, J-LL, X-SZ, XZ, J-LY, L-LR, X-YL, F-QW, N-NT, and Y-XZ conducted the experiments.

FUNDING

This work was funded by the grants from the National Key R&D Program of China (2018YFC1704500), Innovation Team and Talents Cultivation Program of National Administration of Traditional Chinese Medicine (ZYYCXTD-C-202009), and the National Natural Science Foundation of China (81673582, 82192912, and 82104700).

SUPPLEMENTARY MATERIAL

The Supplementary Material for this article can be found online at: https://www.frontiersin.org/articles/10.3389/fphar.2022.911982/full#supplementary-material

REFERENCES

Cao, L., Zhou, J., and Wen, J. (2019). Transport of Salvianolic Acid B via the Human Organic Anion Transporter 1B1 in the Liver. *Phytother. Res.* 33, 197–204. doi:10.1002/ptr.6216

Dong, J., Olaleye, O. E., Jiang, R., Li, J., Lu, C., Du, F., et al. (2018). Glycyrrhizin Has a High Likelihood to Be a Victim of Drug-Drug Interactions Mediated by Hepatic Organic Anion-Transporting Polypeptide 1B1/1B3. *Br. J. Pharmacol.* 175, 3486–3503. doi:10.1111/bph.14393

Feng, X., Li, Y., Wang, Y., Li, L., Little, P. J., Xu, S. W., et al. (2019). Danhong Injection in Cardiovascular and Cerebrovascular Diseases: Pharmacological Actions, Molecular Mechanisms, and Therapeutic Potential. *Pharmacol. Res.* 139, 62–75. doi:10.1016/j.phrs.2018.11.006

Jia, W., Du, F., Liu, X., Jiang, R., Xu, F., Yang, J., et al. (2015). Renal Tubular Secretion of Tanshinol: Molecular Mechanisms, Impact on its Systemic Exposure, and Propensity for Dose-Related Nephrotoxicity and for Renal Herb-Drug Interactions. *Drug Metab. Dispos.* 43, 669–678. doi:10.1124/dmd.114.062000

Jiang, R., Dong, J., Li, X., Du, F., Jia, W., Xu, F., et al. (2015). Molecular Mechanisms Governing Different Pharmacokinetics of Ginsenosides and Potential for Ginsenoside-Perpetrated Herb-Drug Interactions on OATP1B3. *Br. J. Pharmacol.* 172, 1059–1073. doi:10.1111/bph.12971

Jiang, R. W., Lau, K. M., Hon, P. M., Mak, T. C., Woo, K. S., and Fung, K. P. (2005). Chemistry and Biological Activities of Caffeic Acid Derivatives from *Salvia miltiorrhiza*. *Curr. Med. Chem.* 12, 237–246. doi:10.2174/0929867053363397

Kang, Y. J., Lee, C. H., Park, S. J., Lee, H. S., Choi, M. K., and Song, I. S. (2021). Involvement of Organic Anion Transporters in the Pharmacokinetics and Drug Interaction of Rosmarinic Acid. *Pharmaceutics* 13 (1), 83. doi:10.3390/pharmaceutics13010083

Lan, X. F., Olaleye, O. E., Lu, J. L., Yang, W., Du, F. F., Yang, J. L., et al. (2021). Pharmacokinetics-Based Identification of Pseudoaldosterogenic Compounds Originating from *Glycyrrhiza uralensis* Roots (Gancao) after Dosing LianhuaQingwen Capsule. *Acta Pharmacol. Sin.* 42, 2155–2172. doi:10.1038/s41401-021-00651-2

Li, C. (2017). Multi-Compound Pharmacokinetic Research on Chinese Herbal Medicines: Approach and Methodology. *China J. Chin. Materia Medica* 42, 607–617. doi:10.19540/j.cnki.cjcmm.2017.0016

Li, C., Cheng, C., Jia, W., Yang, J. L., Olaleye, O. E., and Yu, X. (2021). Multi-Compound Pharmacokinetic Research on Chinese Herbal Medicines: Identifying Potentially Therapeutic Compounds and Characterizing Their Disposition and Pharmacokinetics. *Acta Pharm. Sin.* 56, 2426–2446. doi:10.16438/j.0513-4870.2021-0839

Li, J., Olaleye, O. E., Yu, X., Jia, W., Yang, J., Lu, C., et al. (2019). High Degree of Pharmacokinetic Compatibility Exists between the Five-Herb Medicine Xuebijing and Antibiotics Comedicated in Sepsis Care. *Acta Pharm. Sin. B* 9, 1035–1049. doi:10.1016/j.apsb.2019.06.003

Li, M., Wang, F., Huang, Y., Du, F., Zhong, C., Olaleye, O. E., et al. (2015). Systemic Exposure to and Disposition of Catechols Derived from *Salvia miltiorrhiza* Roots (Danshen) after Intravenous Dosing Danhong Injection in Human Subjects, Rats, and Dogs. *Drug Metab. Dispos.* 43, 679–690. doi:10.1124/dmd.114.061473

Li, Z. M., Xu, S. W., and Liu, P. Q. (2018). *Salvia miltiorrhiza* Burge (Danshen): A Golden Herbal Medicine in Cardiovascular Therapeutics. *Acta Pharmacol. Sin.* 39, 802–824. doi:10.1038/aps.2017.193

Lin, J. H., and Lu, A. Y. (1997). Role of Pharmacokinetics and Metabolism in Drug Discovery and Development. *Pharmacol. Rev.* 49, 403–449.

Liu, H., and Sahi, J. (2016). Role of Hepatic Drug Transporters in Drug Development. *J. Clin. Pharmacol.* 56 (Suppl. 7), S11–S22. doi:10.1002/jcph.703

Liu, J., Li, D. D., Dong, W., Liu, Y. Q., Wu, Y., Tang, D. X., et al. (2021). Detection of an Anti-Angina Therapeutic Module in the Effective Population Treated by a Multi-Target Drug Danhong Injection: A Randomized Trial. *Signal Transduct. Target Ther.* 6, 329. doi:10.1038/s41392-021-00741-x

Lu, T., Yang, J., Gao, X., Chen, P., Du, F., Sun, Y., et al. (2008). Plasma and Urinary Tanshinol from *Salvia miltiorrhiza* (Danshen) Can Be Used as Pharmacokinetic Markers for Cardiotonic Pills, a Cardiovascular Herbal Medicine. *Drug Metab. Dispos.* 36, 1578–1586. doi:10.1124/dmd.108.021592

Meng, Q., and Liu, K. (2014). Pharmacokinetic Interactions between Herbal Medicines and Prescribed Drugs: Focus on Drug Metabolic Enzymes and Transporters. *Curr. Drug Metab.* 15, 791–807. doi:10.2174/1389200216666150223152348

Millburn, P., Smith, R. L., and Williams, R. T. (1967). Biliary Excretion of Foreign Compounds. Biphenyl, Stilboestrol and Phenolphthalein in the Rat: Molecular Weight, Polarity and Metabolism as Factors in Biliary Excretion. *Biochem. J.* 105, 1275–1281. doi:10.1042/bj1051275

Millburn, P. (1970). "Factors in the Biliary Excretion of Organic Compounds," in *Metabolic Conjugation and Metabolic Hydrolysis* (New York: Elsevier), 1–74. doi:10.1016/b978-0-12-257602-7.50008-1

Morrissey, K. M., Stocker, S. L., Wittwer, M. B., Xu, L., and Giacomini, K. M. (2013). Renal Transporters in Drug Development. *Annu. Rev. Pharmacol. Toxicol.* 53, 503–529. doi:10.1146/annurev-pharmtox-011112-140317

Olaleye, O. E., Niu, W., Du, F. F., Wang, F. Q., Xu, F., Pintusophon, S., et al. (2019). Multiple Circulating Saponins from Intravenous Shenmai Inhibit OATP1Bs *in Vitro*: Potential Joint Precipitants of Drug Interactions. *Acta Pharmacol. Sin.* 40, 833–849. doi:10.1038/s41401-018-0173-9

Pintusophon, S., Niu, W., Duan, X. N., Olaleye, O. E., Huang, Y. H., Wang, F. Q., et al. (2019). Intravenous Formulation of Panax Notoginseng Root Extract: Human Pharmacokinetics of Ginsenosides and Potential for Perpetrating Drug Interactions. *Acta Pharmacol. Sin.* 40, 1351–1363. doi:10.1038/s41401-019-0273-1

Ren, J., Fu, L., Nile, S. H., Zhang, J., and Kai, G. (2019). *Salvia miltiorrhiza* in Treating Cardiovascular Diseases: A Review on its Pharmacological and Clinical Applications. *Front. Pharmacol.* 10, 753. doi:10.3389/fphar.2019.00753

Shen, H., Liu, T., Morse, B. L., Zhao, Y., Zhang, Y., Qiu, X., et al. (2015). Characterization of Organic Anion Transporter 2 (Slc22a7): A Highly Efficient Transporter for Creatinine and Species-Dependent Renal Tubular Expression. *Drug Metab. Dispos.* 43, 984–993. doi:10.1124/dmd.114.062364

Smith, R. L. (1971). "Excretion of Drugs in Bile," in *Concepts in Biochemical Pharmacology*. Editors B. B. Brodie, J. R. Gillette, and H. S. Ackerman (Berlin, Heidelberg: Springer), 354–389. doi:10.1007/978-3-642-65052-9_19

Tian, D. D., Jia, W. W., Liu, X. W., Wang, D. D., Liu, J. H., Dong, J. J., et al. (2015). Methylation and its Role in the Disposition of Tanshinol, a Cardiovascular Carboxylic Catechol from *Salvia miltiorrhiza* Roots (Danshen). *Acta Pharmacol. Sin.* 36, 627–643. doi:10.1038/aps.2015.20

Yang, X., Gandhi, Y. A., Duignan, D. B., and Morris, M. E. (2009). Prediction of Biliary Excretion in Rats and Humans Using Molecular Weight and Quantitative Structure-Pharmacokinetic Relationships. *AAPS J.* 11, 511–525. doi:10.1208/s12248-009-9124-1

Zhang, N., Cheng, C., Olaleye, O. E., Sun, Y., Li, L., Huang, Y., et al. (2018). Pharmacokinetics-Based Identification of Potential Therapeutic Phthalides from Xuebijing, a Chinese Herbal Injection Used in Sepsis Management. *Drug Metab. Dispos.* 46, 823–834. doi:10.1124/dmd.117.079673

Conflict of Interest: The authors declare that the research was conducted in the absence of any commercial or financial relationships that could be construed as a potential conflict of interest.

Publisher's Note: All claims expressed in this article are solely those of the authors and do not necessarily represent those of their affiliated organizations, or those of the publisher, the editors and the reviewers. Any product that may be evaluated in this article, or claim that may be made by its manufacturer, is not guaranteed or endorsed by the publisher.

frontiers | Frontiers in Pharmacology

ORIGINAL RESEARCH
published: 08 July 2022
doi: 10.3389/fphar.2022.948678

Pharmacokinetic Differences of Wuji Pill Components in Normal and Chronic Visceral Hypersensitivity Irritable Bowel Syndrome Rats Attributable to Changes in Tight Junction and Transporters

Zipeng Gong[1,2], Qing Yang[2], Yajie Wang[2], Xiaogang Weng[2], Yujie Li[2], Yu Dong[3], Xiaoxin Zhu[2]* and Ying Chen[2]**

[1]State Key Laboratory of Functions and Applications of Medicinal Plants, Guizhou Provincial Key Laboratory of Pharmaceutics, Guizhou Medical University, Guiyang, China, [2]Institute of Chinese Materia Medica, China Academy of Chinese Medical Sciences, Beijing, China, [3]Guang'An Men Hospital, China Academy of Chinese Medical Sciences, Beijing, China

OPEN ACCESS

Edited by:
Guangbo Ge,
Shanghai University of Traditional Chinese Medicine, China

Reviewed by:
Jiangeng Huang,
Huazhong University of Science and Technology, China
Rong Shi,
Shanghai University of Traditional Chinese Medicine, China
Bing-Liang Ma,
Shanghai University of Traditional Chinese Medicine, China

***Correspondence:**
Yu Dong
dongyu250541@sina.com
Xiaoxin Zhu
zhuxx@icmm.ac.cn
Ying Chen
ychen@icmm.ac.cn

Specialty section:
This article was submitted to Ethnopharmacology, a section of the journal Frontiers in Pharmacology

Received: 20 May 2022
Accepted: 15 June 2022
Published: 08 July 2022

Citation:
Gong Z, Yang Q, Wang Y, Weng X, Li Y, Dong Y, Zhu X and Chen Y (2022) Pharmacokinetic Differences of Wuji Pill Components in Normal and Chronic Visceral Hypersensitivity Irritable Bowel Syndrome Rats Attributable to Changes in Tight Junction and Transporters. Front. Pharmacol. 13:948678. doi: 10.3389/fphar.2022.948678

The Wuji pill, also called Wuji Wan (WJW), is an effective traditional medicine for the clinical treatment of irritable bowel syndrome (IBS). It is principally composed of *Rhizoma Coptidis*, *Fructus Evodiae Rutaecarpae*, and *Radix Paeoniae Alba*. There have been no reports on the pharmacokinetics of WJW on IBS. Because it is more meaningful to study pharmacokinetics in relation to specific pathological conditions, our study investigated the pharmacokinetic differences of five representative components (berberine, palmatine, evodiamine, rutaecarpine, and paeoniflorin) in normal rats and chronic visceral hypersensitivity IBS (CVH-IBS) model rats after single dose and multiple doses of WJW using ultra-performance liquid chromatography tandem mass spectrometry (UPLC-MS/MS). Transmission electron microscopy, immunohistochemistry, and immunofluorescence were used to explore mechanisms behind the pharmacokinetic differences in terms of tight junction proteins (Occludin and ZO-1), myosin light chain kinase (MLCK), and transporters including P-glycoprotein (P-gp), multidrug resistance associated protein 1 (MRP1), and multidrug resistance associated protein 2 (MRP2) in rat colons. After a single dose, for all components except rutaecarpine, significant differences were observed between normal and model groups. Compared with normal group, $T_{1/2}$ and $AUC_{0\text{-}t}$ of berberine and palmatine in model group increased significantly (562.5 ± 237.2 vs. 1,384.9 ± 712.4 min, 733.8 ± 67.4 vs. 1,532.4 ± 612.7 min; 5,443.0 ± 1,405.8 vs. 9,930.8 ± 2,304.5 min·ng/ml, 2,365.5 ± 410.6 vs. 3,527.0 ± 717.8 min·ng/ml), while Cl/

Abbreviations: ADME, absorption, distribution, metabolism and excretion; AUC_{0-t}, area under the plasma concentration vs. time curve from zero to last sampling time; CL/F, total body clearance; C_{max}, the peak plasma concentration; CVH-IBS, chronic visceral hypersensitivity irritable bowel syndrome; CYP, cytochrome P450; DMEs, drug-metabolizing enzymes; HE, hematoxylin-eosin; IBS, irritable bowel syndrome; MLCK, myosin light chain kinase; MRP1, multidrug resistance associated protein 1; MRP2, multidrug resistance associated protein 2; P-gp, P-glycoprotein; PTCA, percutaneous transluminal coronary angioplasty; $T_{1/2}$, terminal elimination half-life; TCM, Traditional Chinese medicine; TJ, tight junctions; T_{max}, the time to reach C_{max}; V_d/F, volume of distribution; WJW, Wuji Wan.

F decreased (840.7 ± 250.8 vs. 397.3 ± 142.7 L/h/kg, 427.7 ± 89.4 vs. 288.9 ± 114.4 L/h/kg). C_{max} and AUC_{0-t} of evodiamine in model group increased significantly (1.4 ± 0.6 vs. 2.4 ± 0.7 ng/ml; 573 ± 45.3 vs. 733.9 ± 160.2 min·ng/ml), while $T_{1/2}$, T_{max}, Cl/F, and Vd/F had no significant difference. T_{max} and AUC_{0-t} of paeoniflorin in model group increased significantly (21.0 ± 8.2 vs. 80.0 ± 45.8 min; 15,428.9 ± 5,063.6 vs. 33,140.6 ± 5,613.9 min·ng/ml), while Cl/F decreased (110.5 ± 48.1 vs. 43.3 ± 9.5 L/h/kg). However, after multiple doses, all five components showed significant differences between normal and model groups. Moreover, these differences were related to tight junction damage and the differential expression of transporters in the colon, suggesting that dose adjustment might be required during administration of WJW in the clinical treatment of IBS.

Keywords: Wuji pill, irritable bowel syndrome, pharmacokinetic differences, tight junction, transporters

1 INTRODUCTION

Irritable bowel syndrome (IBS) is a type of intestinal dysfunction with no apparent abnormality in gastrointestinal structure. It is characterized by repeated abdominal pain and changes in intestinal function. Its clinical symptoms include abdominal pain, diarrhea, constipation, or alternating occurrence of constipation, and diarrhea. Previous studies have indicated gastrointestinal motility and sensory disorders resulting from a variety of central and peripheral mechanisms—as the cause of IBS (Kassam et al., 2013; Öhman et al., 2015), but the specific pathogenesis of the disease is still unclear. The involvement of more than one factor is possible. Clinically, colonic dyskinesia and chronic visceral hypersensitivity are the chief manifestations of IBS. As the pathogenesis of IBS is still not clear, treatment is largely targeted at symptoms with limited success. Traditional Chinese medicine (TCM), however, has gained global attention because of its accurate clinical effect.

The Wuji pill, also known as Wuji Wan (WJW), is a classic medicine for the treatment of IBS. It is included in the 1977 edition of Chinese Pharmacopoeia. This medicine has a simple composition (*Rhizoma Coptidis*, *Fructus Evodiae Rutaecarpae*, and *Radix Paeoniae Alba*), and is mainly used to relieve symptoms such as abdominal pain, diarrhea, vomiting and gastric reflux, burning epigastric pain, mouth bitterness, and gastric discomfort. Earlier medical books differ regarding the prescribed ratio of the three herbs in WJW. The Chinese Pharmacopoeia (2020 edition, Volume I) prescribes the following: *Rhizoma Coptidis* 300 g, *Fructus Evodiae Rutaecarpae* 50 g, and *Radix Paeoniae Alba* 300 g (6:1:6) (Chinese Pharmacopoeia Commission, 2020). Recent pharmacological studies have shown that WJW inhibits colon contraction in guinea pigs (Wang et al., 2007), inhibits CYP1A2 enzyme activity (Weng et al., 2010), significantly reduces nitric oxide content in mice infected by *Helicobacter pylori* (Wu et al., 2006), and has anti-colitic (Cho, et al., 1998; Küpeli,et al., 2002; Kuo,et al., 2004; Lee,et al., 2007) and antithrombotic effects (Sheu et al., 2000; Yu, et al., 2009; Jia and Hu, 2010; Yuan,et al., 2011). It is commonly used in the clinical treatment of belching, nausea, vomiting, mouth bitterness, abdominal pain, diarrhea (Chen et al., 2008a), and gastric ulcer (Chen,et al., 2008b). The chemical composition of WJW is well-understood. The main constituents of *Rhizoma Coptidis*, are alkaloids, namely berberine, palmatine, jatrorrhizine, and coptisine, of which berberine is chief active component and the most abundant, in concentrations as much as 10% (Sun,et al., 2006). The *Fructus Evodiae Rutaecarpae* contains predominantly alkaloids, limonoids, and volatile oils, including evodiamine, rutaecarpine, and dehydrorutaecarpine. *Radix Paeoniae Alba* is another drug used in WJW. Its chemical composition includes paeoniflorin, hydroxypaeoniflorin, and albiflorin, of which paeoniflorin is the dominant component (Wang,et al., 2006).

Compared with the many reports on the pharmacology and chemical composition of WJW, some studies have been published on its pharmacokinetics. In the previous study, the absorption, distribution (Zhang, et al., 2014), metabolism and excretion (Wang, et al., 2011) of five representative components including berberine, palmatine, evodiamine, rutaecarpine, and paeoniflorin in WJW were investigated by perfused rat intestine-liver preparation (Wang, et al., 2012), biotransformation of the cytochrome P450 (CYP) enzymes and intestinal flora (Weng, et al., 2010; Men, et al., 2013). Moreover, the pharmacokinetic study of berberine, palmatine, jatrorrhizine, coptisine, evodiamine, rutacarpine, and paeoniflorin in rat by liquid chromatography-tandem mass spectrometry after oral administration of a Chinese medicine WJW were carried out (Yuan, et al., 2012; Chen, et al., 2015). However, the above pharmacokinetic studies on WJW were all conducted in normal animals, and almost none on the pharmacokinetics of this medicine in relation to specific pathological conditions. In recent years, a growing number of studies have shown that the pharmacokinetic characteristics of TCM are influenced by the pathological state of the body. Physiological and pathological changes affect drug-metabolizing enzymes (DMEs), transporters, cell membrane permeability, and microbial flora in the body, thereby altering the ADME of TCM in the body and the pharmacokinetic parameters (Gong et al., 2015). Since TCM is chiefly applied to bodies in the diseased state, it is more meaningful to study its pharmacokinetic parameters in relation to specific pathological conditions rather than in normal body states.

Previous studies on the pharmacokinetics of WJW have all been carried out in normal animals with a single dose of the medicine, and not under specific pathological states. As the pharmacokinetics of a drug is more clinically relevant when studied under a pathological state than under the normal state, it is more meaningful to explore the pharmacokinetics of WJW in a pathological state. Moreover, the number of times a drug is administered also impacts the its pharmacokinetic behavior. Therefore, our study investigated the pharmacokinetic differences of five representative components of WJW (berberine, palmatine, evodiamine, rutaecarpine, and paeoniflorin). We established a chronic visceral hypersensitivity IBS (CVH-IBS) rat model and used ultra-high performance liquid chromatography-tandem mass spectrometry (UPLC/MS-MS) to compare normal rats and model rats after administration of single and multiple WJW doses. We further explored the origin of the pharmacokinetic differences in terms of transporters and tight junctions, with the intention to aid in the adjustment of multiple WJW doses in the ongoing clinical treatment of IBS.

2 MATERIALS AND METHODS

2.1 Animal Subjects

A total of 30 neonatal male SD rats (SPF grade, 5 days old) were purchased from Beijing Vital River Laboratory Animal Technology [Certificate No: SCXK (Beijing) 2012-0001]. They were raised with their mothers under natural lighting conditions and were allowed to feed freely. Weaning took place on day 25, after which they were separated into five rats per cage.

2.2 Experimental Instruments

The following instruments were used in the study: percutaneous transluminal coronary angioplasty (PTCA) balloon dilatation catheter (specification: 3.0 × 20, Cordis); 8F catheter (Beijing Wandong Kuli'aite Medical Products); Finesse 325 manual microtome, Histocentre 3 tissue embedding machine, and Excelsior ES tissue processor (Thermo Scientific); BX51 microscope (Olympus); Varistan Gemini automated slide stainer (Thermo Scientific); Pressure gauge (Shanghai Medical Instruments); TB-215D electronic analytical balance [Denver Instruments (Beijing)]; rat fixing frame (Beijing Huamei Plexiglass Products); Waters ACQUITY Xevo TQ-XS UPLC/MS System with Masslynx v4.1 (Waters, United States); MSU225S-000-DU semi-microelectronic analytical balance (Sartorius, Germany); VX- III multi-tube vortexer (Beijing Tarjin Tech); NA-5L hybrid nitrogen generator (Beijing ZTE Technology Development); Micropipettes and Centrifuge 5424R low-temperature high-speed centrifuge (Eppendorf, Germany); KQ250E ultrasonic cleaner (Kunshan Ultrasonic Instruments); Milli-Q Advantage A10 water purification system (Millipore, United States).

2.3 Reagents and Drugs

2.3.1 Reagents

The following reagents were purchased from Beijing Bioss Biotechnology: *c-fos* rabbit anti-mouse polyclonal antibody, ZO-1 rabbit anti-mouse polyclonal antibody, Occludin rabbit anti-mouse polyclonal antibody, myosin light chain kinase (MLCK) rabbit anti-mouse polyclonal antibody, P-glycoprotein (P-gp) rabbit anti-mouse polyclonal antibody, multidrug resistance associated protein 1 (MRP1) rabbit anti-mouse polyclonal antibody, multidrug resistance associated protein 2 (MRP2) rabbit anti-mouse polyclonal antibody, goat anti-rabbit immunohistochemistry kit, and hematoxylin. Other reagents used were as follows: glacial acetic acid, analytical grade (Beijing Chemical Works, Batch No. 20100603); osmic acid, acetone, embedding media, uranyl acetate stain, and lead citrate stain (supplied by the Experimental Research Center); potassium permanganate, analytical grade (Beijing Chemical Works, Batch No. 820308); toluidine blue, analytical grade (Sinopharm Chemical Reagents, Batch No. WC20050120); anhydrous ethanol, analytical grade (Beijing Chemical Works, Batch No. 20110); xylene, analytical grade (Sinopharm Chemical Reagents, Batch No. 20106); neutral gum (Sinopharm Chemical Reagents, Batch No. 20120320); hematoxylin (Beyotime Biotechnology, Batch No. C0105); ethylenediamine tetraacetic acid (EDTA), analytical grade (Beijing Chemical Works, Batch No. 840529).

2.3.2 Drugs

Berberine hydrochloride (86.7%, Batch No. 110713-201212), palmatine hydrochloride (86.7%, Batch No. 110732-201108), evodiamine (99.9%, Lot 110802-200606), rutaecarpine (99.9%, Lot 110801-201006), paeoniflorin (96.5%, Lot 110736-201136), diphenhydramine hydrochloride (99.9%, Lot 100066-200807: 99.9%), and geniposide (99.9%, Lot 110749-200714) were purchased from the National Institutes for Food and Drug Control, China. Acetonitrile and methanol, chromatographic grade, were purchased from Fisher, United States. Methanoic acid was of chromatographic grade. Water used in the experiment was purified in our laboratory. Other reagents were of analytical grade.

Herbal samples of *Rhizoma Coptidis* were prepared from the dried rhizomes of the plant grown in Sichuan, China, which were identified by Mr. Jinda Hao, a researcher at the Institute of Chinese Materia Medica, China Academy of Chinese Medical Sciences. The berberine content and palmatine content in the samples were 7.93% and 2.29%, respectively. *Rhizoma Coptidis* extract was prepared by the Pharmacy Department of China–Japan Friendship Hospital *via* water extraction and vacuum drying. It was a solid powder with a yield of 19.33%.

Herbal samples of *Fructus Evodiae Rutaecarpae* were prepared from the dried and nearly ripen fruit of the plant grown in Sichuan, China, which were identified by Mr. Jinda Hao, a researcher at the Institute of Chinese Materia Medica, China Academy of Chinese Medical Sciences. The evodiamine content and rutaecarpine content in the samples were 0.49% and 0.37%, respectively. *Fructus Evodiae Rutaecarpae* extract was prepared by the Pharmacy Department of China–Japan Friendship Hospital *via* water extraction and vacuum drying. It was a solid powder with a yield of 17.7%.

Herbal samples of *Radix Paeoniae Alba* were prepared from the dried roots of the plant grown in Anhui, China, which were

identified by Mr. Jinda Hao, a researcher at the Institute of Chinese Materia Medica, China Academy of Chinese Medical Sciences. The paeoniflorin content in the samples was 1.69%. *Radix Paeoniae Alba* extract was prepared by the Pharmacy Department of China–Japan Friendship Hospital *via* water extraction and vacuum drying. It was a solid powder with a yield of 9.37%.

Preparation of WJW was as follows: *Rhizoma Coptidis*, *Fructus Evodiae Rutaecarpae*, and *Radix Paeoniae Alba* in a 6:1:6 ratio was made into a 62.96 mg/ml decoction in purified water using ultrasonic dissolution. The concentration of each herbal component in the decoction was as follows: *Rhizoma Coptidis* extract was 38.4 mg/ml. *Fructus Evodiae Rutaecarpae* extract was 5.88 mg/ml, and *Radix Paeoniae Alba* extract was 18.68 mg/ml.

2.4 Methods

2.4.1 Grouping

A total of 30 neonatal 5-day-old male SD rats were divided into the normal group and the model group after 3 days of adaptation, with 15 rats in each group. They were raised with their mothers and allowed to feed freely at 24°C room temperature under alternating light/dark cycles of 12 h each. They were weaned on day 25. Following that, they were kept at five rats per cage. All studies were performed in accordance with the proposals of the Committee for Research and Ethical Issues of the International Association for the Study of Pain and were approved by the Animal Ethics Committee at the Institute of Chinese Materia Medica, China Academy of Chinese Medical Sciences (approval number: 20142001).

2.4.2 Establishment of Chronic Visceral Hypersensitivity IBS Model

2.4.2.1 Balloon PTCA Stimulation of Neonatal Rat Colons

Using a method as described previously (AlChaer,et al., 2000), the anus of 8-day-old male neonatal rats was wiped with warm saline. PTCA balloon coated with liquid paraffin and connected to the pressure gauge and inflation syringe *via* a three-way valve was inserted. For the model group, colon stimulation took place by injecting air into the balloon until the pressure slowly increased to 60 mm·Hg. This was performed for 2 weeks, twice a day, for 1 min each time, with a 30 min interval in between. After each stimulation, the PTCA balloon was wiped with alcohol and saline. Rats in the normal group were held gently in hands every day and their perinea massaged for 1 min. The experiment started at 8:00 a.m. every day to eliminate the influence of biological cycle differences. The rats were weighed once a week.

2.4.2.2 Behavioral Study: Colorectal Dilation in Adult Rats

At the end of the eighth week, the adult rats underwent 24 h of fasting and were fixed on a customized plexiglass frame (20 cm × 6 cm × 9 cm). A liquid paraffin-coated catheter was inserted from the anus until the end of the balloon was 2 cm from the anus. The catheter was then taped to the root of the rat tail with medical tape. The other end of the balloon was connected to a syringe filled with warm saline (37°C ± 0.5°C). The rats were allowed to adapt to the environment for 30 min before the catheter was filled with saline. The threshold values of abdominal lift (rat lifting its abdomen 0.2 cm from the platform) and pelvic lift (rat lifting its pelvic structure 1 cm from the platform) were noted. Each rat was measured three times, with each measurement lasting 10 s separated by an interval of 30 min. The results were represented as mean values.

2.4.3 Sampling and Sample Treatment

At the end of the eighth week and 1 h after colon dilation, five rats in each group were immediately sacrificed. A small section of the colon was taken immediately and transferred to a 2.5% glutaraldehyde solution. A piece 1 mm^3 in size was cut out for inspection of tight junction morphology under transmission electron microscopy. A section of colon tissue was taken at 2 cm from the anus and another at 2 cm from the ileum–colon junction and fixed in 4% paraformaldehyde solution. The fixed colon tissue went through gradient dehydration with ethanol and was cleared with xylene before paraffin embedding. It was sliced into a thickness of 4 μm and allowed to fully unfold in water at 45°C. The waxed specimens were transferred to the center of the glass slide, remaining water was removed, and the specimens were dried in an oven at 60°C for 30 min. The distal colon specimens were stained with Hematoxylin-eosin (HE) for immunohistochemistry and immunofluorescence studies. The proximal colon specimen was stained with toluidine blue for pathological observation of colon and mast cell counting.

2.4.4 Mast Cell Counting and Colon Inflammation Observation

Mast cells were counted after toluidine blue staining. HE staining was used to observe colon inflammation in the rats.

2.5 Pharmacokinetic Study

After successful model establishment, rats in the model group were used to study the pharmacokinetics after single dose administration and multiple dose administration of WJW. In the single-dose administration, the rats were intragastrically administered 1 ml/100 g of the drug (629.6 mg/kg, which was 4 times the clinical dosage and an equivalence of 88 mg/kg berberine, 21.1 mg/kg palmatine, 0.22 mg/kg evodiamine, 0.28 mg/kg rutaecarpine, and 25.1 mg/kg paeoniflorin). For multiple-dose administration, the drug was given once a day for six consecutive days at the same concentration as the single-dose administration. At 12 h post-administration on day 6, jugular vein cannulation was performed on the rats. 12 h after the operation, the rats were intragastrically administered 1 ml/100 g WJW (629.6 mg/kg, an equivalence of 88 mg/kg berberine, 22.1 mg/kg palmatine, 0.22 mg/kg evodiamine, 0.28 mg/kg rutaecarpine, and 25.1 mg/kg paeoniflorin). Blood samples (200 μL) were taken from the jugular vein pre-administration and at 5 min, 15 min, 30 min, 1 h, 1.5, 2, 3, 4, 6, 8, 10, 12, 24, and 36 h post-administration. Samples were placed in heparin EP tubes, into which 200 μL heparin solution (50 IU/ml) was also added, and the tubes were centrifuged at 3,500 r/min for 15 min. Plasma (100 μL) was withdrawn and kept at −80°C. The amount of berberine, palmatine, evodiamine, rutaecarpine, and paeoniflorin in the rat plasma was determined simultaneously by the UPLC-MS/MS previously developed and validated (Zhang et al., 2014). Briefly, double internal standards including diphenhydramine hydrochloride and geniposide were selected

and the positive and negative ion modes were used for simultaneous monitoring. Quantitation was performed using multiple-reaction monitoring (MRM) of the protonated molecular ion to predominant product ion pair, m/z 335 > 320 for berberine, m/z 352 > 336 for palmatine, m/z 304 > 134 for evodiamine, m/z 288 > 115 for rutaecarpine, m/z 256 > 152 for diphenhydramine hydrochloride detected in positive ion mode, and m/z 525 > 449 for paeoniflorin, m/z 387 > 225 for geniposide in negative ion mode. An aliquot of 100 μL plasma sample was spiked with 20 μL of the mixed internal standard working solution of 5 μg/ml diphenhydramine hydrochloride and 10 μg/ml geniposide and vortexed briefly. Then the mixture was added to 360 μL of acetonitrile to be deproteinized, mixed by vortex for 5 min and centrifuged at 13,000 rpm for 15 min at 4°C. The supernatant was evaporated by a gentle stream of nitrogen gas. The residue was reconstituted in 200 μL of the mobile phase followed by centrifugation at 13,000 rpm for 15 min. The supernatant was transferred into an autosampler vial and an aliquot of 3 μL was subsequently injected into the UPLC-MS/MS system for assay. The lower limit of quantification was established at 0.32 ng/ml for berberine, palmatine, evodiamine, and rutaecarpine, and 0.63 ng/ml for paeoniflorin in plasma.

The pharmacokinetic software WinNonlin 6.3 (Phoenix, Pharsight, United States) was used to plot the mean plasma concentration (ng/ml) vs. time profile for the above drug components. Non-compartmental analysis was performed to find the pharmacokinetic parameters under single-dose and multiple-dose administration, including terminal elimination half-life ($T_{1/2}$), area under the plasma concentration vs. time curve from zero to last sampling time (AUC_{0-t}), volume of distribution (V_d/F), and total body clearance (CL/F). The peak plasma concentration (C_{max}) and the time to reach C_{max} (T_{max}) were read directly from the observed individual plasma concentration-time data. The pharmacokinetic parameters of the representative components of WJW were compared between the normal group and the model group under single high-dose and multiple high-dose scenarios.

After the blood collection at 36 h, the rats were sacrificed. Two colon sections were quickly cut out. One section was fixed in 2.5% glutaraldehyde solution, and the other in 4% paraformaldehyde. Both samples were embedded in paraffin and sliced. The ultrastructure of rat colon epithelial tight junctions was observed under a transmission electron microscope. The expression of tight junction proteins (Occludin and ZO-1), MLCK, and transport proteins (P-gp, MRP1, and MRP2) in the rat colon was detected by immunohistochemistry and immunofluorescence. The mechanism behind the PK difference of the five representative WJW components between the normal rats and CVH-IBS model rats was explored.

2.6 Immunohistochemistry Detection of *c-fos* Expression, Tight Junction Protein (ZO-1 and Occludin), MLCK, and Transporters (P-gp, MRP1, and MRP2) Expression in the Colon

For immunohistochemistry, colon tissue sections were deparaffinized with xylene and rehydrated in a gradient ethanol finishing in phosphate-buffered saline. Endogenous peroxidases were quenched using a few drops of H_2O_2. A citrate buffer solution was used to restore the antigens, and the colon tissues were then blocked with goat serum. After the sections were incubated with the primary antibody (*c-fos* rabbit anti-mouse polyclonal antibody, ZO-1 rabbit anti-mouse polyclonal antibody, Occludin rabbit anti-mouse polyclonal antibody, MLCK rabbit anti-mouse polyclonal antibody, P-gp rabbit anti-mouse polyclonal antibody, MRP1 rabbit anti-mouse polyclonal antibody, and MRP2 rabbit anti-mouse polyclonal antibody) overnight, the secondary antibody was applied. Then, the sections were washed with phosphate-buffered saline, diaminobenzidine was added for color rendering, and counterstaining was completed with hematoxylin. For immunohistochemical staining, the average integrated positive area from nine randomly chosen regions was calculated using Image Pro Plus 5.0 image analysis software. Brown coloration indicated positive expression.

2.7 Immunofluorescence Detection of Tight Junction Protein (ZO-1, Occludin) and MLCK Expression in the Colon

For immunofluorescence, following antigen repair in a 0.01 M citrate buffer, the tissues sections were blocked in goat serum. The tissue slices were incubated for 1 h with primary antibodies (ZO-1 rabbit anti-mouse polyclonal antibody, Occludin rabbit anti-mouse polyclonal antibody, and MLCK rabbit anti-mouse polyclonal antibody) followed by incubation for 1 h with secondary antibodies. The slices were stained with DAPI. Fluorescence was examined under an Olympus FV-1000 laser scanning confocal microscope. Red coloration indicated positive expression.

2.8 Statistical Analysis

All data were expressed as mean ± standard deviation. SPSS 17.0 statistical software was used for one-way analysis of variance and comparison between groups. The least significant difference test was used if homogeneity of variance was assumed for the samples, otherwise Dunnett's T3 test was used. Significant difference was indicated as $p < 0.05$.

3 RESULTS

3.1 Body Mass Change Over Time

The rats in each group were weighed once a week during the course of their growth. There was no significant difference in body weight between the two groups at the corresponding time points. The results are shown in **Figure 1A**.

3.2 Comparison of Abdominal Lifting Threshold and Pelvic Lifting Threshold Between the Two Groups

Compared with the normal group, the abdominal lifting threshold and pelvic lifting threshold in the model group

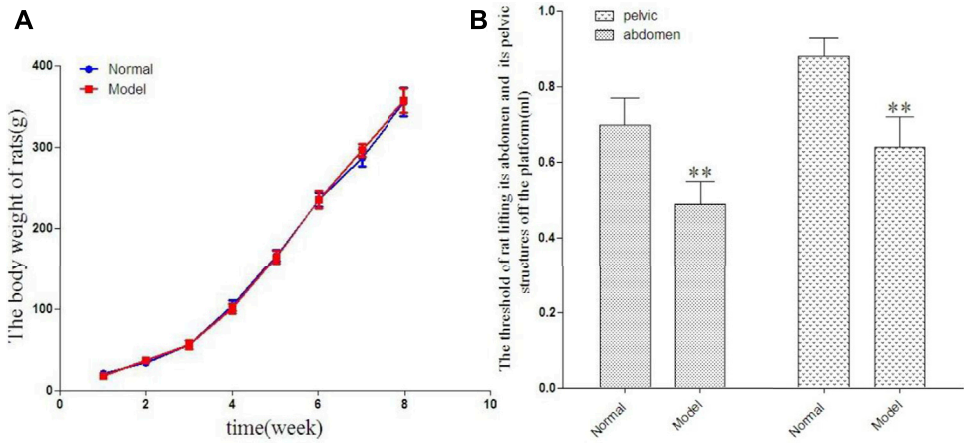

FIGURE 1 | The change of rat in body weight in 8 weeks [**(A)**, g] and the threshold of rat lifting its abdomen off the platform and its pelvic structures off the platform [**(B)**, ml].

showed statistically significant decrease. The results are shown in **Figure 1B**.

3.3 Colon Morphology Change

As shown in **Figure 2A**, the colonic mucosa was complete with intact and continuous epithelium. The crypts were arranged in an orderly manner and their structure was discernable. No anomalies in cell morphology were observed. There was a small number of inflammatory cells infiltrating the lamina propria. There were no obvious inflammatory signs in the normal group or the model group.

3.4 Mast Cell Count in the Proximal Colon

As shown in **Figure 2B**; **Table 1**, mast cells were mainly distributed in the submucosa and muscularis mucosae. They appeared in groups or rows, or were scattered around blood vessels, lymphatic vessels, and peripheral nerves. The cells were round, oval, or irregular, with blue nuclei and purplish red particles randomly distributed in the cytoplasm around the nuclei. Compared with the normal group, a significantly higher number of mast cells was observed in the colonic submucosa of the model group.

3.5 Immunohistochemistry Detection of *c-fos*

The expression of the proto-oncogene *c-fos* in rat colon tissue was quantified by immunohistochemistry. Expression of *c-fos* was significantly higher in the model group than in the normal group. The results are shown in **Figure 2C**; **Table 2**.

3.6 Pharmacokinetic Results

The average plasma concentration profile of the five representative components (berberine, palmatine, evodiamine, rutaecarpine, and paeoniflorin) of WJW after single dose intragastric administration is shown in **Figure 3**, and the pharmacokinetic parameters are presented in **Table 3**. For berberine and palmatine, $T_{1/2}$ and AUC_{0-t} were significantly higher in model rats than in normal rats, while Cl/F was significantly lower. No significant differences were observed in T_{max}, C_{max}, and V_d/F. For evodiamine, C_{max} and AUC_{0-t} were significantly higher in model rats than in normal rats, while no significant differences were observed in $T_{1/2}$, T_{max}, V_d/F, and Cl/F. For rutaecarpine, there was no significant difference in the pharmacokinetic parameters between model rats and normal rats. For paeoniflorin, T_{max} and AUC_{0-t} were significantly higher in model rats than in normal rats, while Cl/F was significantly lower. No significant difference was observed in $T_{1/2}$, C_{max}, and V_d/F.

The average plasma concentration profile of the five representative components of WJW after multiple dose intragastric administration is shown in **Figure 4**, and the pharmacokinetic parameters are given in **Table 4**. The results showed that for berberine, $T_{1/2}$, V_d/F, and Cl/F were significantly higher in model rats than in normal rats, while C_{max} and AUC_{0-t} were significantly lower. No significant difference was observed in T_{max}. For palmatine, $T_{1/2}$, V_d/F, and Cl/F were significantly higher in model rats than in normal rats, while C_{max} and AUC_{0-t} were significantly lower. No significant difference was observed in T_{max}. For evodiamine, C_{max} and AUC_{0-t} were significantly higher in model rats than in normal rats, while $T_{1/2}$, T_{max}, and V_d/F were significantly lower. No significant difference was observed in Cl/F. For rutaecarpine, C_{max} was significantly higher in model rats than in normal rats, while T_{max} was significantly lower. No significant differences were observed in $T_{1/2}$, AUC_{0-t}, V_d/F, and Cl/F. For paeoniflorin, T_{max} was significantly higher in model rats than in normal rats, while no significant difference was observed in $T_{1/2}$, C_{max}, AUC_{0-t}, V_d/F, and Cl/F.

3.7 Electron Microscopy Observation

The ultrastructure of rat colon tissue epithelial tight junctions was observed under transmission electron microscope. The results are shown in **Figure 5**. The epithelial tight junctions of normal rat colon showed a complete structure, featuring compact and well-

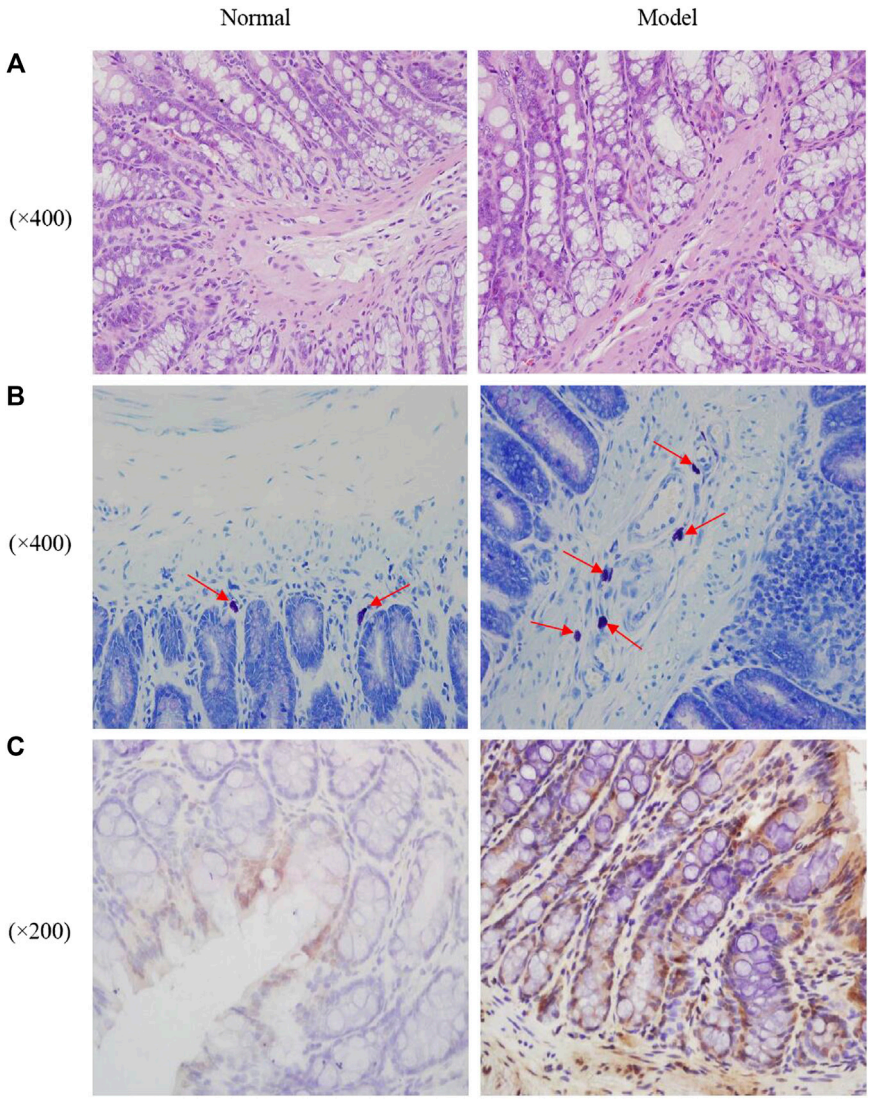

FIGURE 2 | Photomicrographs of distal colons by HE staining **(A)**, mast cell in proximal colons by toluidine blue staining [**(B)**, the red arrows indicated the mast cells] and the expression of *c-fos* in the rats colon **(C)**.

TABLE 1 | The number of the mast cells in proximal colon (mean ± SD, *n* = 5).

Group	Mast cell count (piece)
Normal	2.61 ± 0.86
Model	8.02 ± 1.63**

**p < *0.01 compared with normal group.*

TABLE 2 | The expression of *c-fos* in the rats colon.

Group	AIOD
Normal	843.6 ± 137.5
Model	3,267.0 ± 627.9**

**p < *0.01 compared with normal group.*

sealed junctions. In the model group, the colon epithelial tight junctions appeared damaged. The junctions were loose, and showed wide gaps and reduced junction density. 1 week after WJW administration, the tight junctions of the model group regained their integrity compared with pre-administration time, with re-established junctions.

3.8 Immunohistochemistry Detection of *c-fos*, Tight Junction Protein (ZO-1 and Occludin), MLCK, and Transporters (P-gp, MRP1, and MRP2) Expression in the Colon

Immunohistochemistry results showed that the expression levels of tight junction proteins (Occludin and ZO-1) were significantly lower in the colons of CVH-IBS model rats compared with normal rats. After multiple-dose administration, the expression

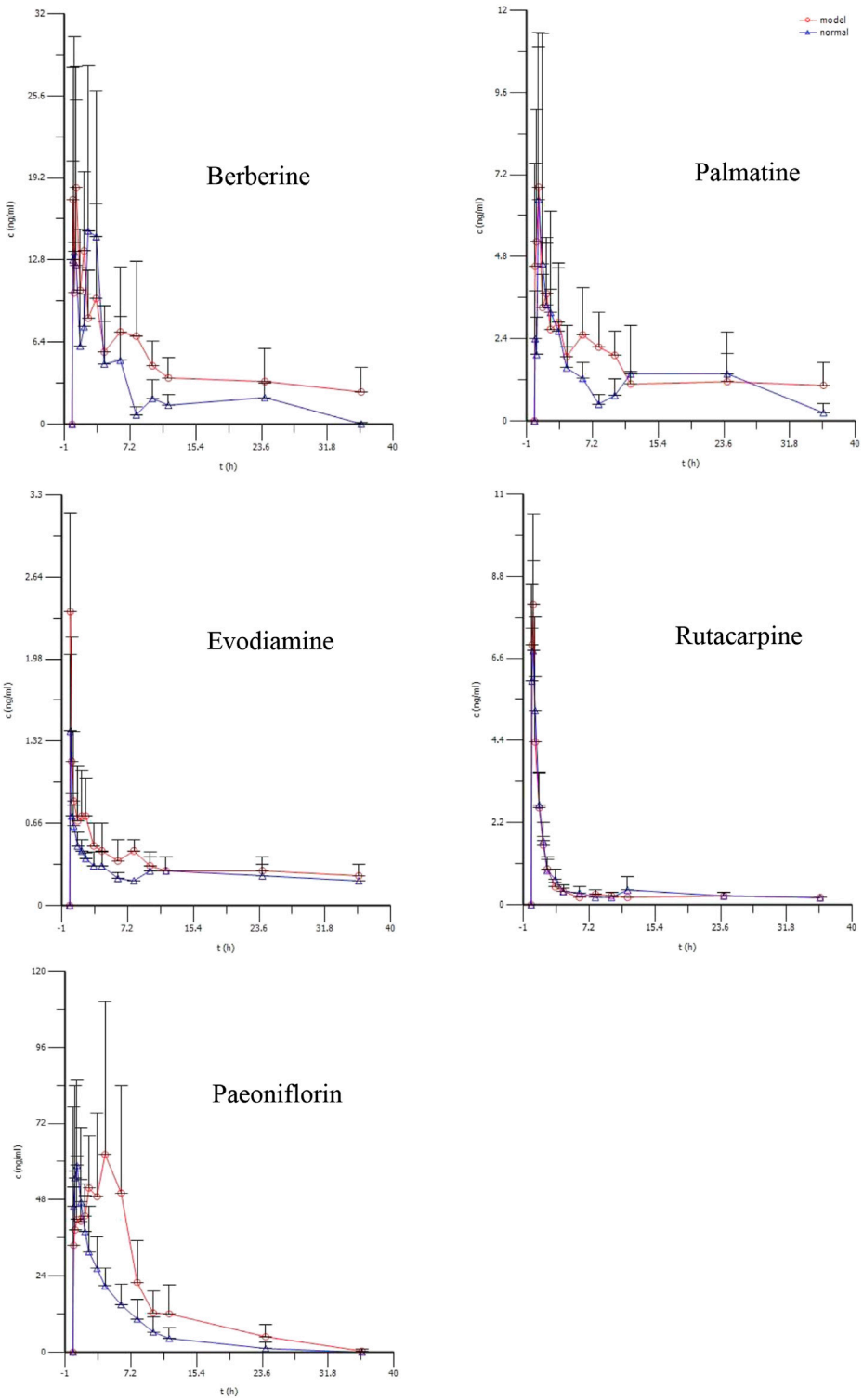

FIGURE 3 | The mean plasma concentration (ng/ml) of berberine, palmatine, Evodiamine, rutacarpine, and paeoniflorin vs. time(h) profiles after single doses of oral administration of WJW Extract (629.6 mg/kg) with the equivalent dose of 88.4 mg/kg, 21.1 mg/kg, 0.22 mg/kg, 0.28 mg/kg, 25.1 mg/kg for berberine, palmatine, evodiamine, rutacarpine, and paeoniflorin respectively in normal and CVH-IBS model rats. Values were expressed as mean ± SD (n = 5).

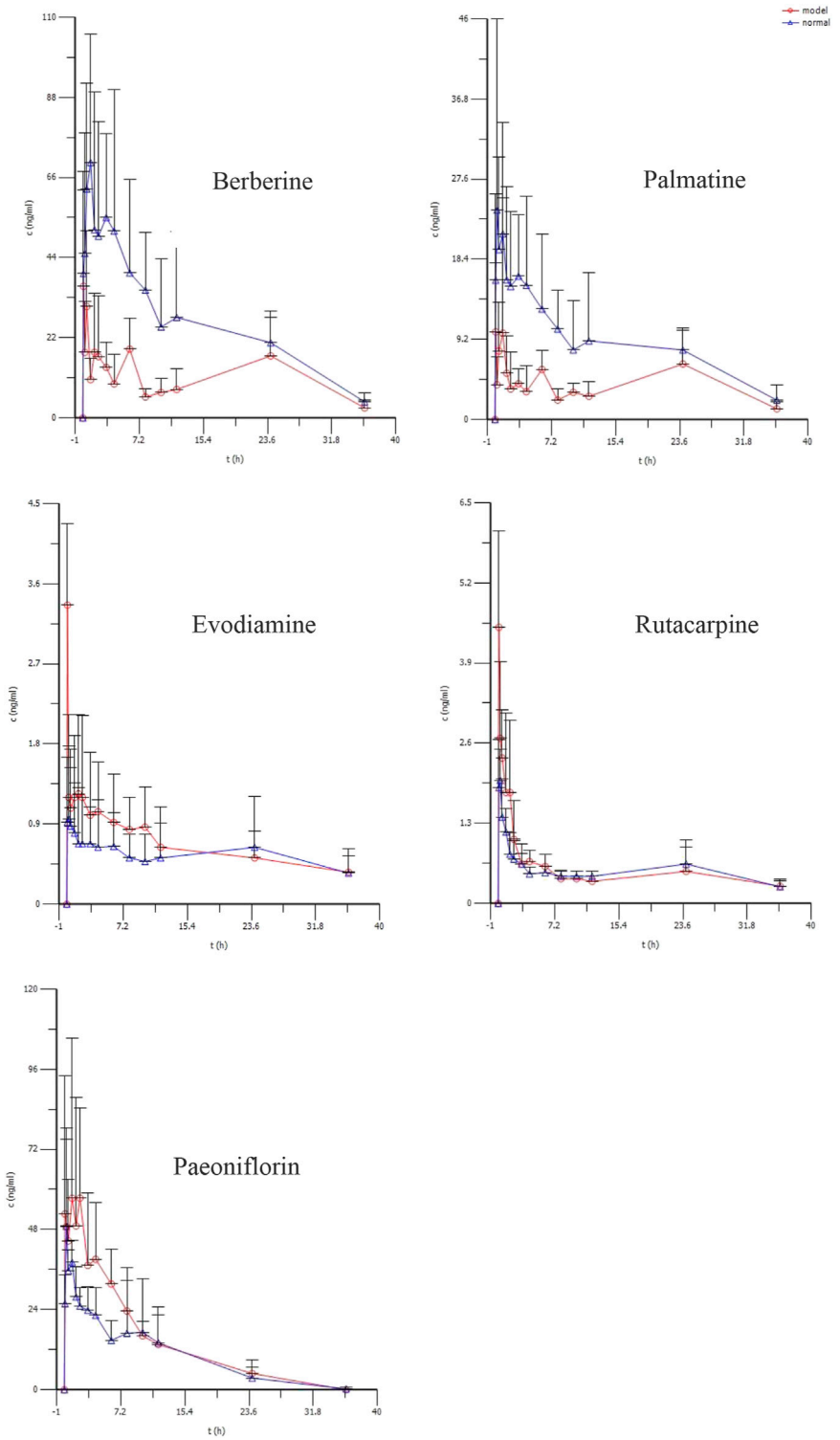

FIGURE 4 | The mean plasma concentration (ng/ml) of berberine, palmatine, Evodiamine, rutacarpine, and paeoniflorin vs. time (h) profiles after multiple doses of oral administration of WJW Extract (629.6 mg/kg) with the equivalent dose of 88.4 mg/kg, 21.1 mg/kg, 0.22 mg/kg, 0.28 mg/kg, 25.1 mg/kg for berberine, palmatine, evodiamine, rutacarpine, and paeoniflorin respectively in normal and CVH-IBS model rats. Values were expressed as mean ± SD (n = 5).

TABLE 3 | Pharmacokinetic parameters of berberine, palmatine, Evodiamine, rutacarpine, and paeoniflorin in rat after single doses of oral administration of WJW Extract (629.6 mg/kg) with the equivalent dose of 88.4 mg/kg, 21.1 mg/kg, 0.22 mg/kg, 0.28 mg/kg, 25.1 mg/kg for berberine, palmatine, evodiamine, rutacarpine, and paeoniflorin, respectively (mean ± SD, $n = 5$).

Parameters	Berberine		Palmatine		Evodiamine		Rutacarpine		Paeoniflorin	
	Normal	Model	Normal	Model	Normal	Model	Normal	Model	Normal	Model
$T_{1/2,\lambda z}$ (min)	562.5 ± 237.2	1,384.9 ± 712.4*	733.8 ± 67.4	1,532.4 ± 612.7*	1,808.4 ± 621.2	1,477.3 ± 341.0	977.5 ± 394.4	774.0 ± 293.5	248.1 ± 101.9	335.2 ± 45.4
T_{max} (min)	36.3 ± 16	30.0 ± 0.0	37.5 ± 15.0	26.3 ± 7.5	5.0 ± 0.0	5.0 ± 0.0	15.0 ± 0.0	15.0 ± 0.0	21.0 ± 8.2	80.0 ± 45.8*
C_{max} (ng/ml)	27.5 ± 10.2	21.8 ± 8.4	8.3 ± 4.3	8.9 ± 3.0	1.4 ± 0.6	2.4 ± 0.7*	7.5 ± 5.1	8.9 ± 6.8	69.4 ± 24.0	85.9 ± 36.7
AUC_{0-t} (min.ng/ml)	5,443.0 ± 1,405.8	9,930.8 ± 2,304.5**	2,365.5 ± 410.6	3,527.0 ± 717.8**	573 ± 45.3	733.9 ± 160.2*	989.9 ± 293.0	894.9 ± 251.4	15,428.9 ± 5,063.6	33,140.6 ± 5,613.9**
$V_d/F_{,\lambda z}$ (L/kg)	9,597.4 ± 1960.5	10,972.4 ± 3,312.9	7,523.3 ± 1,692.1	6,760.2 ± 919.9	513.6 ± 76.7	431.9 ± 145.4	351.5 ± 57.9	332.5 ± 156.5	543.4 ± 213.9	387.5 ± 93.0
Cl/F (L/h/kg)	840.7 ± 250.8	397.3 ± 142.7**	427.7 ± 89.4	288.9 ± 114.4*	12.4 ± 1.9	10.2 ± 3.2	12.7 ± 4.0	13.4 ± 4.9	110.5 ± 48.1	43.3± 9.5**

*p < *0.05 compared with normal group,* **p < *0.01 compared with normal group.*

TABLE 4 | Pharmacokinetic parameters of berberine, palmatine, Evodiamine, rutacarpine, and paeoniflorin in rat after multiple doses of oral administration of WJW Extract (629.6 mg/kg) with the equivalent dose of 88.4 mg/kg, 21.1 mg/kg, 0.22 mg/kg, 0.28 mg/kg, 25.1 mg/kg for berberine, palmatine, evodiamine, rutacarpine, and paeoniflorin, respectively (mean ± SD, $n = 5$).

Parameters	Berberine		Palmatine		Evodiamine		Rutacarpine		Paeoniflorin	
	Normal	Model	Normal	Model	Normal	Model	Normal	Model	Normal	Model
$T_{1/2,\lambda z}$ (min)	559.5 ± 118.8	970.4 ± 211.3**	706.78 ± 249.4	1,376.6 ± 102.4**	1,967.4 ± 499.3	919.3 ± 237.2**	1,370.8 ± 276.1	1,287.2 ± 465.4	386.2 ± 141.2	468.9 ± 156.3
T_{max} (min)	52.5 ± 15.0	5.0 ± 0.0**	20 ± 8.7	13.3 ± 14.4	16.7 ± 11.3	5.0 ± 0.0*	10.0 ± 5.5	5.0 ± 0.0*	18 ± 6.7	105.0 ± 30.0**
C_{max} (ng/ml)	85.6 ± 20.6	48.2 ± 18.2	34.9 ± 14.5	16.8 ± 10.9*	1.1 ± 0.7	3.5 ± 2.5*	2.2 ± 1.2	5.5 ± 2.9*	54.7 ± 16.1	77.8 ± 38.1
AUC_{0-t} (min.ng/ml)	58,252.1 ± 9,131.6	26,206.2 ± 7,505.8**	19,125.1 ± 3,519.3	10,122.9 ± 1,371.9**	857.1 ± 303.9	1,541.3 ± 602.8*	1,153.0 ± 338.5	1,169 ± 348.8	21,785.4 ± 1719.3	26,442.9 ± 6,743.5
$V_d/F_{,\lambda z}$ (L/kg)	1,185.1 ± 360.9	4,189.1 ± 613.2**	1,154.4 ± 335.1	5,545.8 ± 4,148.8*	383.7 ± 147.6	178.3 ± 61.4**	375.7 ± 109.1	323.7 ± 122.5	550.8 ± 128.7	485.9 ± 67.9
Cl/F (L/h/kg)	87.1 ± 13.3	156.9 ± 48.2**	60.2 ± 10.6	162.1 ± 108.9*	11.5 ± 5.8	7.4 ± 2.0	9.6 ± 2.9	10.4 ± 2.7	63.9 ± 11.8	50.6 ± 16.9

*p < *0.05 compared with normal group,* **p < *0.01 compared with normal group.*

in model rats increased significantly compared with pre-administration, but was still lower than that in the normal group. No significant change post-administration was found in normal rats. MLCK expression was significantly higher in the colons of model rats compared with normal rats. After multiple-dose administration, the expression in model rats decreased significantly compared with pre-administration, but was higher than that in the normal group. No significant change post-administration was found in normal rats. The expression of transporters (P-gp, MRP1, and MRP2) did not significantly differ in the colon tissue of model rats compared with normal rats. After multiple-dose administration, their expression in both model rats and normal rats was significantly higher than that before administration. The expression following multiple-dose administration was significantly higher in the model group than in the normal group. The results are shown in **Figures 6**, **7**; **Table 5**.

3.9 Immunofluorescence Detection of Tight Junction Protein (ZO-1 and Occludin) and MLCK-1 Expression in Rat Colon

Immunofluorescence results showed that the expression of tight junction proteins (Occludin and ZO-1) was lower in the colon of model rats compared with normal rats, while the expression of MLCK was higher. After multiple-dose administration, the expression of tight junction proteins in model rats increased significantly compared with pre-administration, while MLCK expression decreased significantly. No significant differences were found in tight junction protein and MLCK expression in normal rats before and after multiple-dose administration. After multiple-dose administration, the expression of tight junction proteins in the model group was lower than that in the normal group, while the expression of MLCK expression was higher. The results are shown in **Figure 8**.

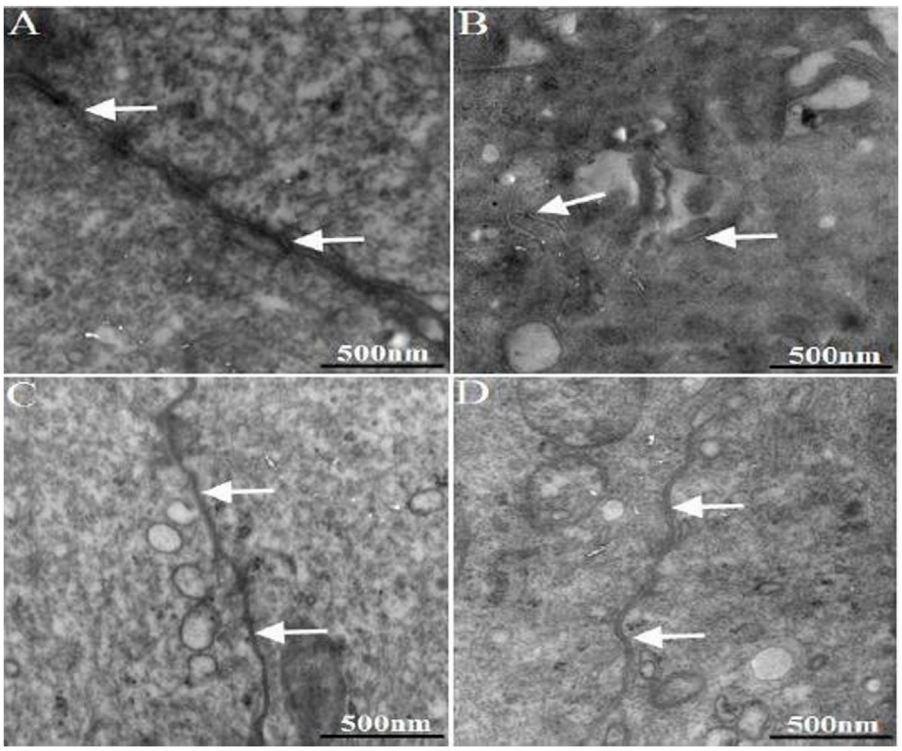

FIGURE 5 | The ultra-structure of TJ in the colonic epithelium of rats. The arrows indicated TJ [**(A)**: normal; **(B)** model; **(C)** multiple dose of WJW in normal; **(D)** multiple dose of WJW in model].

4 DISCUSSION

IBS is a common digestive system condition. Its causes and pathogenesis are not yet well-understood, and effective therapeutic drugs are lacking. In recent years, TCM and its compound prescriptions have been playing an increasingly important role in the treatment of CVH-IBS. An appropriate animal model is indispensable in the screening and evaluation of TCM and its compound prescriptions in the treatment of CVH-IBS. The CVH-IBS rat model established in this study closely simulated the main symptoms of CVH-IBS patients, including the significantly reduced abdominal lifting threshold and pelvic lifting threshold, the lack of apparent colon inflammation, significantly elevated *c-fos* expression, and hypersensitivity towards pain. For these reasons, the established model is applicable as a CVH-IBS rat model for experimental studies.

Following the successful establishment of the CVH-IBS rat model, the pharmacokinetics of WJW in normal rats and model rats after single-dose administration was compared. The results showed that compared with the normal group, the absorption of berberine, palmatine, and paeoniflorin increased in model rats after intragastric administration of the drug, while the elimination of these components slowed. The absorption of evodiamine increased in model rats compared with normal rats, with no significant difference observed in elimination. There was no significant difference in the absorption and elimination of rutaecarpine in model rats compared with normal rats.

The pharmacokinetics of drugs, besides being influenced by physiological state and pathological states, may also be affected by number of doses. Therefore, our study also compared the pharmacokinetics of WJW in normal rats and CVH-IBS rats after 7 days of continued administration. The results showed that the absorption of berberine and palmatine was reduced in model rats compared with normal rats, while the elimination was accelerated. The absorption of evodiamine in model rats increased compared with that in normal rats, with no significant change observed in elimination. No significant difference was found in the absorption and elimination of rutaecarpine and paeoniflorin. These results are in stark contrast to those from single-dose administration.

Hence, pharmacokinetic differences for the representative components of WJW were confirmed between normal rats and CVH-IBS model rats following both single-dose administration and multiple-dose administration. The reason for the differences, however, is still unknown. It is well known that the pharmacokinetic process of drug include absorption, distribution, metabolism, and excretion (ADME). The tight junctions (TJ) between cells and transporters could affect the absorption of drugs. Transporters influence the disposition of drugs within the body by participating in ADME (Klaassen and Aleksunes, 2010), and is one of important mechanisms for

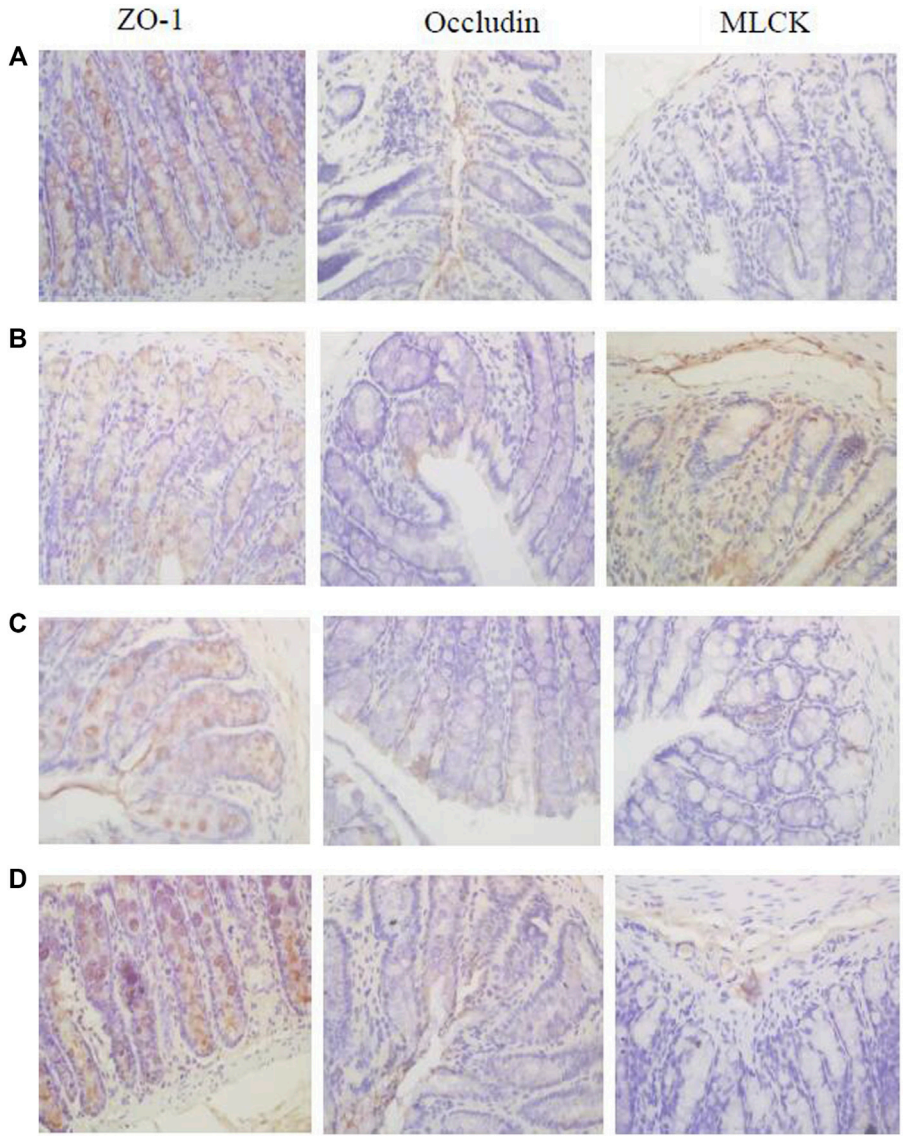

FIGURE 6 | The expression of ZO-1, Occludin, and MLCK in the rats colon [**(A)**: normal; **(B)** model; **(C)** multiple dose of WJW in normal; **(D)** multiple dose of WJW in model].

herb–drug interactions (Choi, et al., 2011). Transporters mainly include influx proteins (organic anion transporters and organic cation transporters, etc.,) and efflux transporters (P-gp, MRP1, and MRP2, etc.). Moreover, the literature reports that berberine is a substrate of P-gp and MRP2 (Pan et al., 2002; Maeng et al., 2002; Qian et al., 2016; Wang et al., 2007). Also, palmatine and paeoniflorin are also substrates of P-gp (Liu et al., 2006; Zhang et al., 2014). In addition, the study of TJ was carried out from the perspective of increasing absorption, so only common efflux transporters (P-gp, MRP1, and MRP2) were selected for transporters, and influx transporters were not involved.

Previous studies have shown that a healthy intestinal mucosal barrier mainly consists of a mechanical, chemical, immunological, and biological barriers, of which the mechanical barrier is the most important (Assimakopoulos,et al., 2011). Under normal physiological conditions, the junction complexes between adjacent cells of intestinal epithelium form a highly selective mechanical barrier, allowing passage of only small-molecular, water-soluble substances such as water and ions *via* passive diffusion, while preventing the entrance of macromolecular antigens through the epithelium to reach the submucosa and incite an immune response (Fernandez-Blanco et al., 2011). A junction complex is made of TJ, gap junctions, adhesion junctions, and desmosomes. TJ are located at the apex of the junction complex and serves as the most important connections between cells. They are a type of dynamic structure consisting of

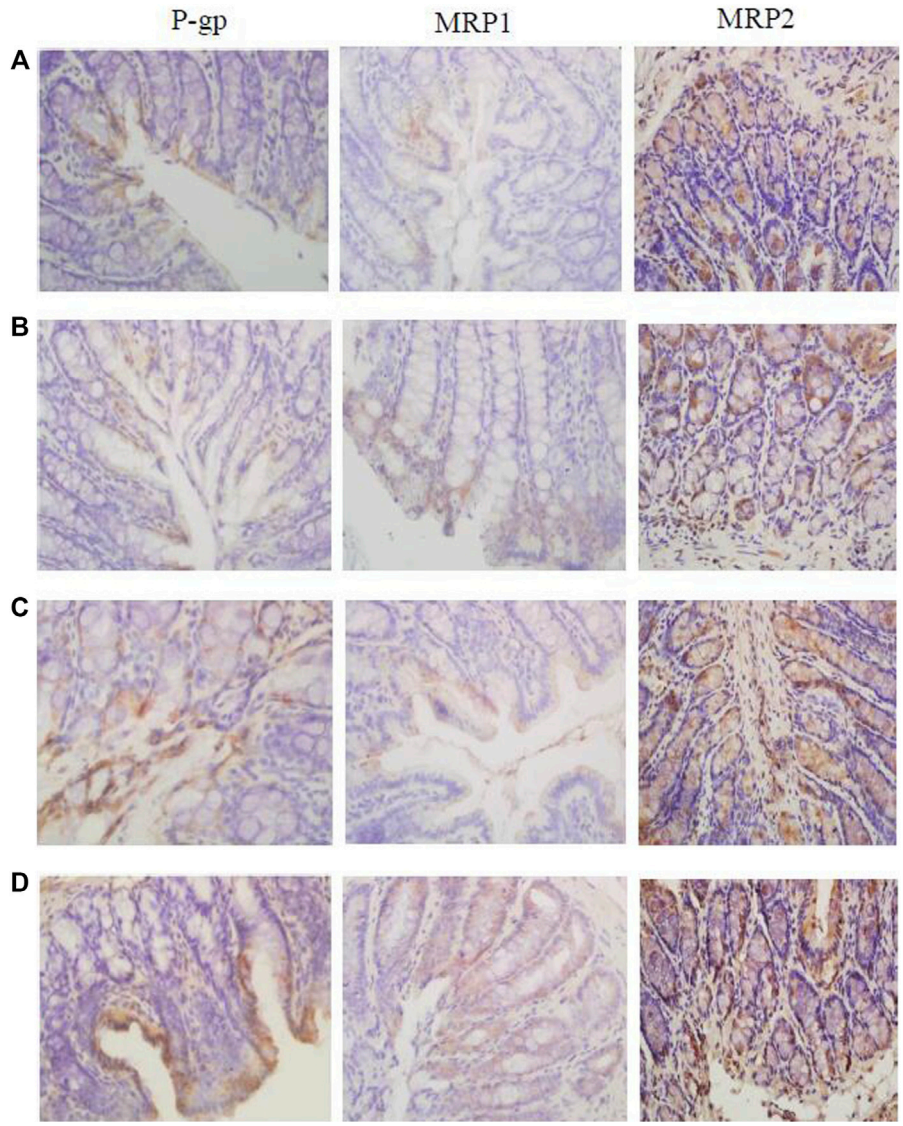

FIGURE 7 | The expression of P-gp, MRP1, and MRP2 in the rats colon [**(A)**: normal; **(B)** model; **(C)** multiple dose of WJW in normal; **(D)** multiple dose of WJW in model].

TABLE 5 | The expression of ZO-1, Occludin, MLCK, P-gp, MRP1, and MRP2 in the rats colon (n = 5, $\bar{x}$ ± s, AIOD).

Group	Normal	Model	Normal + WJW	Model + WJW
ZO-1	6,714.0 ± 396.5	3,371.0 ± 650.7**	6,983.0 ± 702.6	5,614.2 ± 382.5**##△△
Occludin	3,860.6 ± 678.0	1,615.2 ± 447.3**	3,954.4 ± 258.5	2,709.6 ± 252.5**##△△
MLCK	959.8 ± 362.7	4,131.8 ± 500.2**	1,002.6 ± 166.0	2,091.0 ± 492.5**##△△
P-gp	2,927.6 ± 258.2	2,843.8 ± 314.1	5,823.0 ± 800.4**	6,695.0 ± 410.8**##△
MRP1	2,878.4 ± 462.1	2,702.8 ± 429.2	3,905.8 ± 356.4**	4,754.4 ± 467.7**##△△
MRP2	4,551.8 ± 627.1	4,424.6 ± 660.1	6,680.4 ± 509.9**	7,459.4 ± 446.1**##△

**p < *0.01 compared with normal group,* ##p < *0.01 compared with model group,* △p < *0.05, and* △△p < *0.01 compared with normal + WJW group.*

various tight junction proteins, including transmembrane proteins, such as occludin and claudins, junction adhesion molecules, and proteins such as ZOs and 7H6 involved in the assembly of the tight junction at the cytoplasmic surface. Of these, occludin and ZO-1 are key to maintaining the normal structure and function of tight junctions (Wu,et al., 2000).

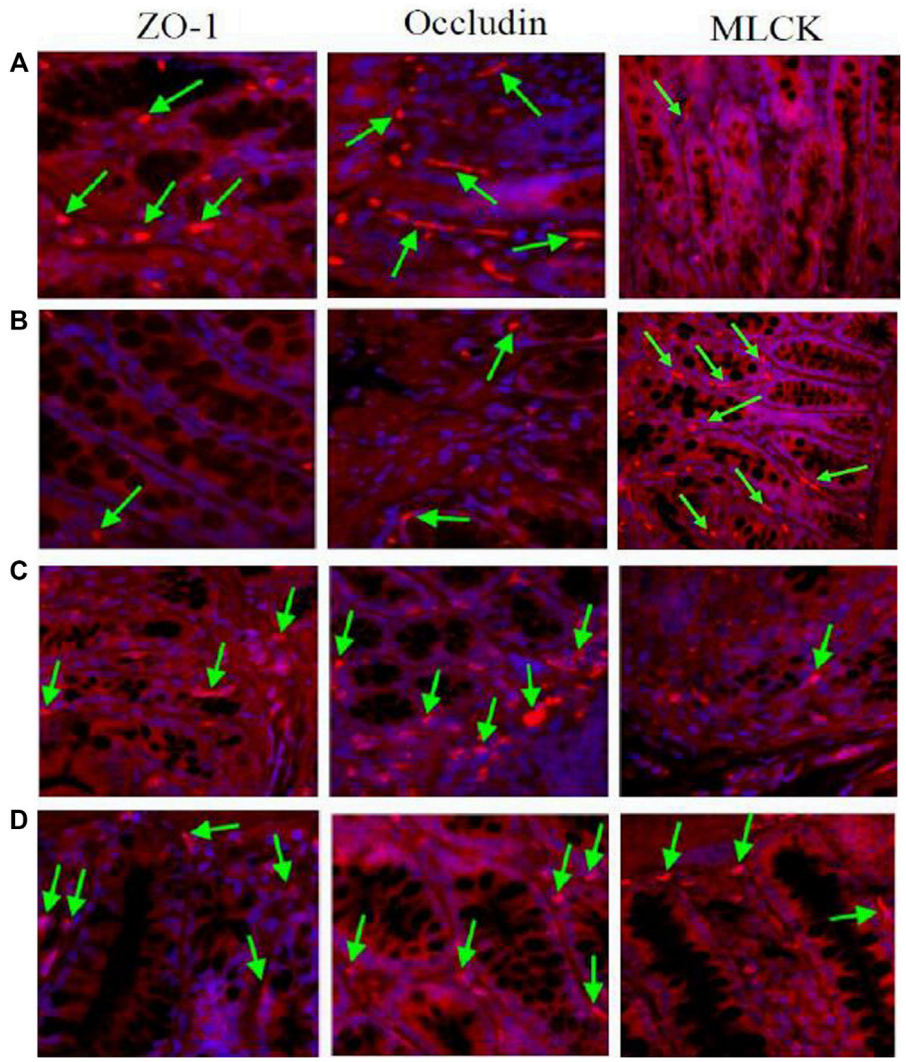

FIGURE 8 | The expression of TJ proteins (Occludin and ZO-1) and MLCK in the rats colon. The arrows indicated the TJ proteins or MLCK [**(A)**: normal; **(B)** model; **(C)** multiple dose of WJW in normal; **(D)** multiple dose of WJW in model].

MLCK is a Ca^{2+}/calmodulin-dependent enzyme located in the cell membrane. It regulates the phosphorylation of myosin light chain, as well as the cytoskeleton (Turner,et al., 1997; Kevin and Jerold, 2012). MLCK has an important function in maintaining the integrity of tight junctions (Shen and Turner, 2006). Because of their compact nature, the destruction of tight junctions inevitably affects the permeability of intestinal mucosa. It has been found that intestinal mucosal permeability is increased (Barbara, 2006; Barbara,et al., 2009), while the expression of Occludin and ZO-1 is decreased in IBS patients compared with healthy individuals (Zeng,et al., 2008). Some studies have suggested the downregulation and redistribution of tight junction proteins as the molecular mechanism behind the intestinal mucosal permeability changes, which affect the absorption of drugs.

In our study, immunohistochemistry results showed that compared with the normal group, the expression of tight junction proteins (Occludin and ZO-1) decreased in the model group, the expression of MLCK increased, and there was no significant difference in the expression of transporters (P-gp, MRP1, and MRP2). Immunofluorescence results also showed that compared with the normal group, the expression of tight junction proteins decreased in the model group, and the expression of MLCK increases, leading to the increased permeability of colon mucosa in the model group and increased drug absorption. This explains to some extent the increased absorption of berberine, palmatine, evodiamine, and paeoniflorin in CVH-IBS rats after the single-dose administration of WJW.

Following the multiple-dose administration of WJW, the expression of tight junction proteins and transport proteins increased significantly in the model group compared with pre-administration, while the expression of MLCK decreased significantly. For the normal group after multiple-dose

administration, no differences were observed in tight junction protein and MLCK expression levels, while the expression of transport proteins significantly increased. This shows the ability of WJW to promote tight junction protein expression and protect the intestinal mucosa. The drug also increased the expression of transporters probably *via* the induction by berberine, palmatine, and paeoniflorin, as they are the substrates of these transporters.

However, comparing the model group and the normal group after multiple-dose administration of WJW, the expression of tight junction proteins (Occludin and ZO-1) was lower in the model, the expression of MLCK was higher, and the expression of transporters (P-gp, MRP1, and MRP2) was significantly higher. These results suggest the removal of berberine and palmatine by the significantly higher level of transporters as a possible reason for the reduced absorption of these two drugs in CVH-IBS model rats compared with normal rats, after the multiple-dose administration of WJW. This effect dominates over the increased absorption by colon mucosa as a result of the permeability change.

It is well known that DMEs and transporters play important roles in the ADME processes. The roles of DMEs in pharmacokinetics have been extensively investigated for years (Zanger and Schwab, 2013). The metabolism of drugs in the body can be mediated by enzymes responsible for phase I (oxidation, reduction, and hydrolysis) and/or phase II (conjugation) biotransformation. Among these, CYP enzymes are well known for their roles in phase I oxidative metabolism (Jabir, et al., 2012; Kumar,et al., 2012; Zhou,et al., 2012); enzymes known for phase II metabolism include N-acetyl transferase, glutathione S-transferase, uridine 50- diphospho-glucuronosyltransferases, and sulfotransferase. Under certain pathological circumstances, the expression and activities of enzymes and transporters can be regulated, thereby leading to an alteration of the pharmacokinetic properties of substrate drugs (Wu and Lin., 2019). In the present study, it is worth mentioning that rutaecarpine differs from other four components after one intake of WJW. However, these results of tight junction and transporters could not explain the phenomenon. The reason for that rutaecarpine differs from other components is unclear. It has been reported P450 1A and 2B might predominantly metabolize rutaecarpine in rat liver microsomes (Lee, et al., 2004). It is still unclear if their quantity and activity change under the pathological state of IBS. Moreover, intestinal microbiome (Gill, et al., 2006; Men et al., 2015) also play a vital part in drug metabolism. Therefore, we propose as the next step in our research to examine the specific mechanisms behind the pharmacokinetic differences of the representative components of WJW between normal rats and IBS rats from the perspectives of intestinal microbiome and CYP enzymes.

DATA AVAILABILITY STATEMENT

The original contributions presented in the study are included in the article/Supplementary Material, further inquiries can be directed to the corresponding authors.

ETHICS STATEMENT

The animal study was reviewed and approved by the Experimental Animal Ethics Committee at the Institute of Chinese Materia Medica, China Academy of Chinese Medical Sciences (approval number: 20142001).

AUTHOR CONTRIBUTIONS

ZG, YD, XZ, and YC conceived and designed the experiments. ZG, QingYang, and YW performed all of the experiments. QY, YW, XW, and YL operated on the rats and contributed reagents/materials/analysis tools. ZG and YC analyzed the data. ZG wrote the paper. YD, XZ, and YC contributed to critical review of the paper.

FUNDING

This research was supported by the National Natural Science Foundation of China (No. 82074103) and Scientific and Technological Innovation Project of China Academy of Chinese Medical Sciences (CI2021A04905, CI2021A04908, and CI2021B015).

REFERENCES

AlChaer, E. D., Kawasaki, M., and Pasricha, P. J. (2000). A New Model of Chronic Visceral Hypersensitivity in Adult Rats Induced by Colon Irritation during Postnatal Development. *Gastroenterology* 119 (5), 1276–1285. doi:10.1053/gast.2000.19576

Assimakopoulos, S. F., Papageorgiou, I., and Charonis, A. (2011). Enterocytes' Tight Junctions: From Molecules to Diseases. *World. J. Gastrointest. Pathophysiol.* 2, 123–137. doi:10.4291/wjgp.v2.i6.123

Barbara, G., Cremon, C., Pallotti, F., De Giorgio, R., Stanghellini, V., and Corinaldesi, R. (2009). Postinfectious Irritable Bowel Syndrome. *J. Pediatr. Gastroenterol. Nutr.* 48, S95–S97. doi:10.1097/MPG.0b013e3181a15e2e

Barbara, G. (2006). Mucosal Barrier Defects in Irritable Bowel Syndrome. Who Left the Door Open? *Am. J. Gastroenterol.* 101 (6), 1295–1298. doi:10.1111/j.1572-0241.2006.00667.x

Chen, J., Wang, F., Liu, J., Lee, F. S., Wang, X., and Yang, H. (2008a). Analysis of Alkaloids in Coptis Chinensis Franch by Accelerated Solvent Extraction Combined with Ultra Performance Liquid Chromatographic Analysis with Photodiode Array and Tandem Mass Spectrometry Detections. *Anal. Chim. Acta.* 613 (2), 184–195. doi:10.1016/j.aca.2008.02.060

Chen, J., Zhao, H., Wang, X., Lee, F. S., Yang, H., and Zheng, L. (2008b). Analysis of Major Alkaloids in Rhizoma Coptidis by Capillary Electrophoresis-Electrospray-Time of Flight Mass Spectrometry with Different Background Electrolytesflight Mass Spectrometry with Different Background Electrolyte. *Electrophoresis* 29 (10), 2135–2147. doi:10.1002/elps.200700797

Chen, Y., Li, Y. J., Wang, Y. J., Yang, Q., Dong, Y., and Weng, X. (2015). Comparative Pharmacokinetics of Active Alkaloids after Oral Administration of Rhizoma Coptidis Extract and Wuji Wan Formulas in Rat Using a UPLC-MS/MS Method. *Eur. J. Drug. Metab. Pharmacokinet.* 40 (1), 67–74. doi:10.1007/s13318-014-0181-1

Chinese Pharmacopoeia Commission (2020). *Pharmacopoeia of the People's Republic of China, Part 1*. Beijing: China Medical Science Press, 810–811.

Cho, J. Y., Park, J., Yoo, E. S., Yoshikawa, K., Baik, K. U., Lee, J., et al. (1998). Inhibitory Effect of Lignans from the Rhizomes of Coptis Japonica Var. Dissecta on Tumor Necrosis Factor-Alpha Production in Lipopolysaccharide-Stimulated RAW264.7 Cells. *Arch. Pharm. Res.* 21 (1), 12–16. doi:10.1007/BF03216746

Choi, Y. H., Chin, Y. W., and Kim, Y. G. (2011). Herb–drug Interactions: Focus on Metabolic Enzymes and Transporters. *Arch. Phar. Res.* 34 (11), 1843–1863. doi:10.1007/s12272-011-1106-z

Fernández-Blanco, J. A., Barbosa, S., Sánchez de Medina, F., Martínez, V., and Vergara, P. (2011). Persistent Epithelial Barrier Alterations in a Rat Model of Postinfectious Gut Dysfunction. *Neurogastroenterol. Motil.* 23 (11), e523–33. doi:10.1111/j.1365-2982.2011.01777.x

Gill, S. R., Pop, M., Deboy, R. T., Eckburg, P. B., Turnbaugh, P. J., Samuel, B. S., et al. (2006). Metagenomic Analysis of the Human Distal Gut Microbiome. *Science* 312 (5778), 1355–1359. doi:10.1126/science.1124234

Gong, Z. P., Chen, Y., Zhang, R. J., Yang, Q., and Zhu, X. X. (2015). Advances on Pharmacokinetics of Traditional Chinese Medicine under Disease States. *Zhongguo Zhong Yao Za Zhi* 40 (02), 169–173. doi:10.4268/cjcmm20150202

Jabir, R. S., Naidu, R., Annuar, M. A., Ho, G. F., Munisamy, M., and Stanslas, J. (2012). Pharmacogenetics of Taxanes: Impact of Gene Polymorphisms of Drug Transporters on Pharmacokinetics and Toxicity. *Pharmacogenomics* 13 (16), 1979–1988. doi:10.2217/pgs.12.165

Jia, S., and Hu, C. (2010). Pharmacological Effects of Rutaecarpine as a Cardiovascular Protective Agent. *Molecules* 15, 1873–1881. doi:10.3390/molecules15031873

Kassam, Z., Collins, S. M., and Moayyedi, P. (2013). Peripheral Mechanisms in Irritable Bowel Syndrome. *N. Engl. J. Med.* 368 (6), 577–578. doi:10.1056/NEJMc1214185

Kevin, E. C., and Jerrold, R. T. (2012). Myosin Light Chain Kinase: Pulling the Strings of Epithelial Tight Junction Function. *Ann. N. Y. Acad. Sci.* 1258 (1), 34–42. doi:10.1111/j.1749-6632.2012.06526.x

Klaassen, C. D., and Aleksunes, L. M. (2010). Xenobiotic, Bile Acid, and Cholesterol Transporters: Function and Regulation. *Pharmacol. Rev.* 62 (1), 1–96. doi:10.1124/pr.109.002014

Kumar, S., Sharma, R., and Roychowdhury, A. (2012). Modulation of Cytochrome-P450 Inhibition (CYP) in Drug Discovery: a Medicinal Chemistry Perspective. *Curr. Med. Chem.* 19 (21), 3605–3621. doi:10.2174/092986712801323180

Kuo, C. L., Chi, C. W., and Liu, T. Y. (2004). The Anti-inflammatory Potential of Berberine *In Vitro* and in Vivo flammatory Potential of Berberine *In Vitro* and *In Vivo*. *Cancer. Lett.* 203 (2), 127–137. doi:10.1016/j.canlet.2003.09.002

Küpeli, E., Koşar, M., Yeşilada, E., Husnu, K., and Baser, C. (2002). A Comparative Study on the Anti-inflammatory, Antinociceptive and Antipyretic Effects of Isoquinoline Alkaloids from the Roots of Turkish Berberis Species. *Life. Sci.* 72 (6), 645–657. doi:10.1016/s0024-3205(02)02200-2

Lee, C. H., Chen, J. C., Hsiang, C. Y., Wu, S. L., Wu, H. C., and Ho, T. Y. (2007). Berberine Suppresses Inflammatory Agents-Induced Interleukin-1beta and Tumor Necrosis Factor-Alpha Productions via the Inhibition of IkappaB Degradation in Human Lung Cellsflammatory Agents-Induced Interleukin-1beta and Tumor Necrosis Factor-Alpha Productions via the Inhibition of IkappaB Degradation in Human Lung Cells. *Pharmacol. Res.* 56 (3), 193–201. doi:10.1016/j.phrs.2007.06.003

Lee, S. K., Kim, N. H., Lee, J., Kim, D. H., Lee, E. S., Choi, H. G., et al. (2004). Induction of Cytochrome P450s by Rutaecarpine and Metabolism of Rutaecarpine by Cytochrome P450s. *Planta. Med.* 70 (8), 753–757. doi:10.1055/s-2004-827207

Liu, Z. H., Liu, L., and Hu, M. (2006). Mechanisms Responsible for Poor Oral Bioavailability of Paeoniflorin: Role of Intestinal Disposition and Interactions with Sinomenine. *Pharm. Res.* 23 (12), 2768–2780. doi:10.1007/s11095-006-9100-8

Maeng, H. J., Yoo, H. J., Kim, I. W., Song, I. S., Chung, S. J., and Shim, C. K. (2002). P-Glycoprotein-Mediated Transport of Berberine Across Caco-2 Cell Monolayers. *J. Pharm. Sci.* 91 (12), 2614–2621. doi:10.1002/jps.10268

Men, W., Chen, Y., Yang, Q., Li, Y. J., Gong, Z. P., Weng, X. G., et al. (2013). Study on Metabolism of Coptis Chinensis Alkaloids from Different Compatibility of Wuji Wan in Human Intestinal Flora. *Zhongguo Zhong Yao Za Zhi* 38 (3), 417–421.

Men, W., Chen, Y., Li, Y. J., Yang, Q., Weng, X. G., Gong, Z. P., et al. (2015). Research Progress of Biotransformation on Effective Ingredients of Chinese Medicine via Intestinal Bacteria. *Chin. J. Expe. Tradi. Med. Formu.* 21 (2), 229–234. doi:10.13422/j.cnki.syfjx.2015020229

Öhman, L., Tornblom, L., and Simren, M. (2015). Crosstalk at the Mucosal Border: Importance of the Gut Microenvironment in IBS. *Nat. Rev. Gastroenterol. Hepatol.* 12 (1), 36–49. doi:10.1038/nrgastro.2014.200

Pan, G. Y., Wang, G. J., Liu, X. D., Fawcett, J. P., and Xie, Y. Y. (2002). The Involvement of P-Glycoprotein in Berberine Absorption. *Pharmacol. Toxicol.* 91 (4), 193–197. doi:10.1034/j.1600-0773.2002.t01-1-910403.x

Qian, Z. Y., Huang, C., Shen, C. L., Meng, X. M., Chen, Z. L., Hu, T. T., et al. (2016). The Permeability Characteristics and Interaction of the Main Components From Zhizi Bopi Decoction in the MDCK Cell Model. *Xenobiotica* 46 (8), 733–742. doi:10.3109/00498254.2015.1113575

Shen, L., and Turner, J. R. (2006). Role of Epithelial Cells in Initiation and Propagation of Intestinal Inflammation. Eliminating the Static: Tight Junction Dynamics Exposed. *Am. J. Physiol. Gastrointest. Liver. Physiol.* 290 (4), G577–G582. doi:10.1152/ajpgi.00439.2005

Sheu, J. R., Hung, W. C., Wu, C. H., Lee, Y. M., and Yen, M. H. (2000). Antithrombotic Effect of Rutaecarpine, an Alkaloid Isolated from Evodia Rutaecarpa, on Platelet Plug Formation in *In Vivo* Experiments. *Br. J. Haematol.* 110 (1), 110–115. doi:10.1046/j.1365-2141.2000.01953.x

Sun, J., Ma, J. S., Jin, J., Wang, H. S., Wen, Q. H., Zhang, H. G., et al. (2006). Qualitative and Quantitative Determination of the Main Components of Huanglianjiedu Decoction by HPLC-UV/MS. *Yao. Xue. Xue. Bao.* 41 (4), 380–384.

Turner, J. R., Rill, B. K., Carlson, S. L., Carnes, D., Kerner, R., Mrsny, R. J., et al. (1997). Physiological Regulation of Epithelial Tight Junctions Is Associated with Myosin Light-Chain Phosphorylation. *Am. J. Physiol.* 273 (4), C1378–C1385. doi:10.1152/ajpcell.1997.273.4.C1378

Wang, Q., Liu, R. X., Guo, H. Z., Zhu, H. N., Bi, K. S., and Guo, D. A. (2006). Study on Influence of Processing Methods on Chemical Constituents in Radix Paeoniae Alba. *Zhongguo Zhong Yao Za Zhi* 31 (17), 1418–1421.

Wang, Y. J., Dong, Y., and Zhu, X. X. (2007). Experimental Studies of Effects of Wujiwan Extracts in Different Compatibilities on Motility of Isolated Colon in guinea Pig. *Zhongguo Zhong Yao Za Zhi* 32 (20), 2161–2165.

Wang, Y. W., Li, Y. J., Wang, Y. L., Yang, W., Chen, Y., Zhnag, D., et al. (2012). Impact on Absorption of Berberine and Palmatine in Different Compatibilities of Wuji Pill. *China. J. Chin. Mat. Med.* 37 (7), 985–990. doi:10.4268/cjcmm2012072

Wang, Y. W., Zhang, Y. F., Li, Y. J., Yang, W. P., Chen, Y., Zhang, D., et al. (2011). Effect of Different Compatibility of Wuji Wan on Bile Excretion of Representative Ingredient. China. *China. J. Chin. Mat. Med.* 36 (23), 3319–3326. doi:10.4268/cjcmm20112322

Weng, X. G., Li, Y. J., Yang, Q., Wang, Y., Liu, X., Han, X., et al. (2010). Effects of Wuji Pill with Different Compatibility on the Activity of Cytochrome P450 CYP31A2 in Rat Liver Microsomes *In Vitro*. *China. J. Chin. Mat. Med.* 35 (9), 1164–1169. doi:10.4268/cjcmm20100918

Wu, C. R., Peng, C., Guo, C. X., Cai, Y., Bai, Y. Q., and Tang, X. M. (2006). Effect of Wuji Pill Decoction on the Content of NO in the Mouse Internal Body Infected by *Helicobacter pylori*. *Guid. J. Tradi. Chin. Med.* 12, 65–66. doi:10.13862/j.cnki.cn43-1446/r.2006.01.036

Wu, K. C., and Lin, C. J. (2019). The Regulation of Drug-Metabolizing Enzymes and Membrane Transporters by Inflammation: Evidences in Inflammatory Diseases and Age-Related Disordersflammation: Evidences in Inflammatory Diseases and Age-Related Disorders. *J. Food. Drug. Anal.* 27 (1), 48–59. doi:10.1016/j.jfda.2018.11.005

Wu, Z., Nybom, P., and Magnusson, K. E. (2000). Distinct Effects of *Vibrio cholerae* Haemagglutinin/protease on the Structure and Localization of the Tight Junction-Associated Proteins Occludin and ZO-1. *Cell. Microbiol.* 2 (1), 11–17. doi:10.1046/j.1462-5822.2000.00025.x

Yu, P. L., Chao, H. L., Wang, S. W., and Wang, P. S. (2009). Effects of Evodiamine and Rutaecarpine on the Secretion of Corticosterone by Zona Fasciculata-Reticularis Cells in Male Rats. *J. Cell. Biochem.* 108 (2), 469–475. doi:10.1002/jcb.22276

Yuan, J., Wang, Y., An, R., Wang, S., Li, J. S., Ma, Y. M., et al. (2012). Simultaneous Determination of Six Alkaloids and One Monoterpene in Rat Plasma by Liquid Chromatography-Tandem Mass Spectrometry and Pharmacokinetic Study after Oral Administration of a Chinese Medicine Wuji Pill. *J. Chromatogr. B. Anal. Technol. Biomed. Life. Sci.* 895-896, 154–161. doi:10.1016/j.jchromb.2012.03.036

Yuan, S. M., Gao, K., Wang, D. M., Quan, X. Z., Liu, J. N., Ma, C. M., et al. (2011). Evodiamine Improves Congnitive Abilities in SAMP8 and APP(swe)/PS1(ΔE9) Transgenic Mouse Models of Alzheimer's Disease. *Acta. Pharmacol. Sin.* 32 (3), 295–302. doi:10.1038/aps.2010.230

Zanger, U. M., and Schwab, M. (2013). Cytochrome P450 Enzymes in Drug Metabolism: Regulation of Gene Expression, Enzyme Activities, and Impact of Genetic Variation. *Pharmacol. Ther.* 138 (1), 103–141. doi:10.1016/j.pharmthera.2012.12.007

Zeng, J., Li, Y. Q., Zuo, X. L., Zhen, Y. B., Yang, J., and Liu, C. H. (2008). Clinical Trial: Effect of Active Lactic Acid Bacteria on Mucosal Barrier Function in Patients with Diarrhoea-Predominant Irritable Bowel Syndrome. *Aliment. Pharmacol. Ther.* 28 (8), 994–1002. doi:10.1111/j.1365-2036.2008.03818.x

Zhang, R. J., Chen, Y., Gong, Z. P., Dong, Y., Zhang, H. X., Yang, Q., et al. (2014). Research on Bioactive Ingredients in Rat Liver after Oral Administration of Different Combinations of Wuji Pill. *Zhongguo Zhong Yao Za Zhi* 39 (09), 1695–1703. doi:10.4268/cjcmm20140930

Zhou, X., Chan, K., and Yeung, J. H. (2012). Herb-drug Interactions with Danshen (Salvia Miltiorrhiza): a Review on the Role of Cytochrome P450 Enzymes. *Drug. Metabol. Drug. Interact.* 27 (1), 9–18. doi:10.1515/dmdi-2011-0038

Conflict of Interest: The authors declare that the research was conducted in the absence of any commercial or financial relationships that could be construed as a potential conflict of interest.

Publisher's Note: All claims expressed in this article are solely those of the authors and do not necessarily represent those of their affiliated organizations, or those of the publisher, the editors and the reviewers. Any product that may be evaluated in this article, or claim that may be made by its manufacturer, is not guaranteed or endorsed by the publisher.

frontiers | Frontiers in Pharmacology

TYPE Original Research
PUBLISHED 09 August 2022
DOI 10.3389/fphar.2022.947978

OPEN ACCESS

EDITED BY
Guangbo Ge,
Shanghai University of Traditional Chinese Medicine, China

REVIEWED BY
Dapeng Chen,
Dalian Medical University, China
Mingmei Zhou,
Shanghai University of Traditional Chinese Medicine, China
Shoude Zhang,
Qinghai University, China

*CORRESPONDENCE
Yu He,
heyu0923@hotmail.com
Haitong Wan,
whtong@126.com

†These authors have contributed equally to this work

SPECIALTY SECTION
This article was submitted to Ethnopharmacology, a section of the journal Frontiers in Pharmacology

RECEIVED 19 May 2022
ACCEPTED 12 July 2022
PUBLISHED 09 August 2022

CITATION
Zhang Y, Yu L, Yang J, Ding Z, He Y and Wan H (2022), Spectrum effect correlation of yangyin tongnao granules on cerebral ischemia-reperfusion injury rats.
Front. Pharmacol. 13:947978.
doi: 10.3389/fphar.2022.947978

Spectrum effect correlation of yangyin tongnao granules on cerebral ischemia-reperfusion injury rats

Yangyang Zhang[1†], Li Yu[2†], Jiehong Yang[1], Zhishan Ding[3], Yu He[4*] and Haitong Wan[2*]

[1]School of Basic Medical Sciences, Zhejiang Chinese Medical University, Hangzhou, China, [2]School of Life Sciences, Zhejiang Chinese Medical University, Hangzhou, China, [3]School of Medical Technology and Information Engineering, Zhejiang Chinese Medical University, Hangzhou, China, [4]School of Pharmaceutical Sciences, Zhejiang Chinese Medical University, Hangzhou, China

Yangyin Tongnao Granules (YYTNG), as traditional Chinese medicine (TCM) compound preparation, have a good curative effect on cerebral ischemia-reperfusion injury. This study aimed to investigate the relationship between the active components of YYTNG in the plasma and the inflammatory response in cerebral ischemia-reperfusion injury rats. High-performance liquid chromatography (HPLC) was conducted to determine the fingerprints at different time points of middle cerebral artery occlusion (MCAO) rats after the administration of YYTNG at different times points. Enzyme-linked immunosorbent assay (ELISA) was performed to detect the levels of interleukin-18 (IL-18) and tumor necrosis factor-α (TNF-α) in the plasma of MCAO rats at different time points. The spectral-effect relationship between the YYTNG fingerprints and inflammatory indexes *in vivo* was established by combining three different mathematical models, grey correlation, multiple linear regression, and partial least-square method. The results revealed that each chromatographic peak in the HPLC of the plasma exhibited a certain correlation with the inflammatory index, in the following order: *P2 >P6 >P5 >P1 >P3 >P4*. Therefore, this study successfully established the spectrum-effect correlation of YYTNG on cerebral ischemia-reperfusion injury rats. The results provide a certain guiding ideology for the analyses of the relationship between fingerprints and the pharmacodynamics of TCM prescriptions.

KEYWORDS

yangyin tongnao granules, cerebral ischemia-reperfusion injury, HPLC fingerprint, mathematical model, spectrum-effect relationship

Abbreviations: CCA, Common Carotid Artery; ECA, External Carotid Artery; ELISA, Enzyme Linked Immunosorbent Assay; HPLC, High-Performance Liquid Chromatography; IL, Interleukin; ICA, Internal Carotid Artery; MCAO, Middle Cerebral Artery Occlusion; OD, Optical Density; SD, Sprague Dawley; SPF, Specific Pathogen Free; TCM, Traditional Chinese Medicine; TNF, Tumor Necrosis Factor; YYTNG, Yangyin Tongnao Granules.

1 Introduction

Since ancient times, stroke has been regarded as critical and severe disease, with ischemic stroke being more common than hemorrhagic stroke. The pathological process of ischemic stroke is quite complex, and its pathogenesis involves energy metabolism disorder, free radical injury, excitatory amino acid toxicity, and inflammatory reaction (Wang and Ma, 2018). As one of the common diseases of the nervous system, ischemic stroke has been associated with high disability and high mortality rates, which causes immense pain to patients and their families.

Several studies on the mechanism of brain injury after ischemia have focused on the inflammatory process after ischemia-reperfusion (Liu et al., 2019; Shi et al., 2019; Liu et al., 2020; Mo et al., 2020). It has been proven that a strong inflammatory response after cerebral ischemia is the causative factor for secondary injury of brain cells (Jayaraj et al., 2019; Seiya et al., 2020). The expression of various inflammatory mediators increases significantly during cerebral ischemia, which is responsible for the dual effects of brain injury and brain protection (Poinsatte et al., 2015).

Yangyin Tongnao granules (YYTNG) are a modern compound preparation of traditional Chinese medicine (TCM). YYTNG is composed of *Rehmannia glutinosa* (Gaertn.) DC [Orobanchaceae], *Pueraria montana var. Lobata* (Willd.) Maesen and S.M.Almeida ex Sanjappa and Predeep [Fabaceae], *Astragalus mongholicus* Bunge [Fabaceae], *Conioselinum anthriscoides 'Chuanxiong'* [Apiaceae], *Dendrobium nobile* Lindl [Orchidaceae], and Hirudo in the ratio of 1:1.2:1:0.67:1:0.2 (Wang et al., 2019). It has also been approved for clinical research (approval number: 2003L00206), and it has completed phase II and phase III clinical trials. According to the TCM theory, YYTNG nourishes Yin and replenishes qi (Wan et al., 2015). In Western medicine, it has been demonstrated to promote blood circulation and improve microcirculation, especially in the treatment of cardiovascular and cerebrovascular diseases (Liang and Su, 2015). Previous studies have shown that YYTNG exerts antioxidant anti-inflammatory effects, inhibits neuronal apoptosis, and improves blood system diseases and other functions (Rong et al., 2017; Rong et al., 2018). The relationship between the spectrum and the effect is often employed to evaluate the potential correlation between the active ingredients of TCM and drug action (Jidan et al., 2019; Zhou et al., 2019). The study of the relationship between the spectrum and the effect has established a representative method to identify the main active ingredients related to the pharmacological effects of the complex TCM formula. Presently, the data processing of the relationship between spectrum and effect mainly includes correlation analysis (Zhou et al., 2021), clustering analysis (Gao et al., 2019), and regression analysis (Liu et al., 2019).

In this study, inflammatory factors (such as tumor necrosis factor-α [TNF-α] and interleukin-18 [IL-18]) were selected to establish the relationship between the high-performance liquid chromatography (HPLC) fingerprint of YYTNG in the middle cerebral artery occlusion (MCAO) rats and inflammatory indexes.

2 Materials and methods

2.1 Experiment animals

Six male Sprague Dawley (SD) rats (weight: 280–300 g; SPF) were provided and raised by the Institutional Animal Care and Use Committee at the Zhejiang Chinese Medical University. The license number of the experimental animals was SYXK (Zhejiang) 2018-0012.

2.2 Chemicals and reagents

YYTNG (product batch number: 170322) was manufactured by Shanxi Buchang Pharmaceutical Co., Ltd. China. Heparin Sodium (product batch number: 1170GR005) was purchased from Shanghai McLin Biochemical Technology Co., Ltd.

Methanol (product batch number: 20105218) and acetonitrile (product batch number: LI70T97) of chromatographic grade were obtained from the Tedia Company. Formic acid (product batch number: 20180709) was provided by Shanghai Aladdin Biochemical Technology Co., Ltd. TNF-α (product batch number: MB-1721A) and IL-18 (product batch number: MB-1735) ELISA kits were purchased from the Jiangsu Enzyme Label Biotechnology Co., Ltd.

2.3 Quality control of yangyin tongnao granules

The preparation technology of YYTNG was based on the existing relevant report of our research group (Wang et al., 2019). Meanwhile, the fingerprints and ingredients of determination were conducted by our research group (Wang et al., 2019; Yu et al., 2021). YYTNG is composed of puerarin, calycosin, formononetin, ferulic acid, daidzein, and other ingredients.

2.4 Instruments and chromatographic conditions

The analysis was performed on the Agilent 1200 Series System (Agilent Technologies, United States) equipped with a diode array detector. Chromatographic separation was achieved on the Eclipse XDB-C_{18} (4.6 × 250 mm, 5 μm)

analytical column at 25°C. A gradient elution program was conducted for chromatographic separation with the mobile phase acetonitrile (A) and 0.5% formic acid aqueous solution (B) as follows: 0–10 min (A: 2%–10%), 10–29 min (A: 10%–12%), 29–35 min (A: 12%–15%), 35–50 min (A: 15%–25%), 50–65 min (A: 25%–60%), 65–70 min (A: 60%–90%), 70–80 min (A: 90%–2%), 80–85 min (A: 2%). The flow rate was set to 1.0 ml/min. Then, 10 μL of the sample was injected automatically.

2.5 Middle cerebral artery occlusion models establishment

The rats were anesthetized via intraperitoneal injection with 3% (w/v) sodium pentobarbital (45 mg/kg). The MCAO model was established according to the modified Zea Longa method (Longa et al., 1989; Yu et al., 2018). Briefly, the right common carotid artery (CCA), internal carotid artery (ICA), and external carotid artery (ECA) were separated. A small cut was made on the CCA with ophthalmic scissors. Nylon thread was gently pushed into the ICA from this small cut on the CCA. The black mark of the nylon thread stopped when it reached the trigeminal orifice. After 1 h of ischemia, the nylon thread was pulled out and the incision was sutured before reperfusion. The rats with Horner's syndrome in the right eye, long and short legs in the left forelimb when lifting the tail, and hemiplegic behavior when walking freely were selected for the subsequent analyses.

2.6 Reagent preparation and dosage

Heparin sodium powder (0.1722 g) was precisely weighed and added to a centrifuge tube, to which 4 ml of normal saline was added. The heparin sodium powder was then fully dissolved via ultrasound. The resultant heparin sodium solution was stored in a refrigerator at 4°C until further use.

After MCAO modeling, the rats were administered with YYTNG orally 1 h after reperfusion. Based on the clinical conversion dose, adult dose/60 kg × 6.3 (adult dose: 16.5 g), the drug dose for a rat was determined to be 3 times that of the adult dose, that is, 5.20 g/kg.

2.7 Preparation of drug-containing plasma

The blood samples were collected from the mandibular vein of MCAO/R rats at 2, 4, 6, 8, 12, 24, 48, and 72 h after the first dose (immediately administered with the same amount of YYTNG as the first dose after the blood sampling at 24 and 48 h). The plasma was placed in a centrifuge tube containing 20 μL of the heparin sodium solution, shaken up and down gently, and then fully mixed. Then, the mixture was placed at room temperature for 30 min and centrifuged at 4,500 rpm for 15 min. The supernatant was used as the medicated plasma. The samples were placed in the refrigerator at −20°C overnight, and then transferred to a refrigerator at −80°C for storage until further use.

2.8 Sample pretreatment

The medicated plasma (100 μL) was precisely aspirated, to which 3 times the amount of methanol was added to remove the protein, and centrifuged at 12,000 rpm for 12 min at 4°C. Then, the supernatant was aspirated, and subjected to nitrogen blowing for concentration and enrichment. Finally, 100 μL of 50% methanol was added to reconstitute the sample.

2.9 Preparation of the blank plasma

Normal SD rats were fasted (no water deprivation) for 12 h, and their blood was sampled and processed according to the aforementioned sample pretreatment methods to obtain the corresponding blank plasma.

2.10 Establishment of fingerprints of yangyin tongnao granules at different time points in middle cerebral artery occlusion rats

The reconstituted plasma samples were centrifuged at the speed of 12,000 rpm at 4°C for 12 min, followed by aspiration of the supernatant for HPLC detection. The plasmas of each rat at different time points were analyzed by the established HPLC method. The HPLC charts of each time point were subsequently obtained. After importing the HPLC charts at each timepoint into the Chinese medicine chromatographic fingerprint similarity evaluation system (version 2012A), the fingerprint of the rat medicated plasma was automatically generated.

2.11 Detection of the inflammatory indexes in middle cerebral artery occlusion rats

We took appropriate amounts of the medicated plasma at different time points and detected the changes in the levels of inflammatory factors (i.e., IL-18 and TNF-α) in accordance with the instructions of the ELISA kit. Then, the microplate reader was used to determine the OD value at the wavelength of 450 nm.

2.12 Evaluation of the spectrum-effect relationship between the fingerprint of yangyin tongnao granules and inflammatory indexes of cerebral ischemia-reperfusion injury

2.12.1 Data normalization processing for inflammation indicators

Both IL-18 and TNF-α were indicators of inflammation, they shared some inherent correlation. Accordingly, the entropy weight method was applied to weigh these two indicators, after which they were normalized to obtain the comprehensive evaluation value of the drug effect. The calculation of the entropy weight method was performed using the following steps:

1) Data standardization

$$r_{ij} = \frac{x_{ij} - \min(x_j)}{\max(x_j) - \min(x_j)} \quad (1)$$

$$r_{ij} = \frac{\max(x_j) - x_{ij}}{\max(x_j) - \min(x_j)} \quad (2)$$

where Eq. 1 presents a positive data standardization, while Eq. 2 presents a negative data standardization. $\min(x_j)$ is the minimum value of column jth data; $\max(x_j)$ is the maximum value of column jth data; $\min(x_j)$ is the minimum value of column jth data; and $\max(x_j)$ is the maximum value of column jth data.

2) Calculation of the information entropy E_j of each index

$$E_j = -\frac{1}{\ln(n)} \times \sum_{i=1}^{n} p_{ij} ln p_{ij} \quad (3)$$

where, $p_{ij} = r_{ij} / \sum_{i=1}^{n} r_{ij}$, and n is the number of experiments.

3) Determination of the weight of each indicator

$$W_j = \frac{1 - E_j}{k - \sum_{j=1}^{k} E_j} \quad (4)$$

where k is the number of evaluation indexes.

2.12.2 Grey correlation analysis

Grey correlation analysis (Sarraf and Nejad, 2020) refers to the method of applying a grey correlation degree to analyze the grey systems with partly known and partly unknown information. Most of the chromatographic peaks in the fingerprint are unknown compounds, and the efficacy of these compounds in animals is unknown. Therefore, the area of six common peaks was used as the independent variable, and the values of pharmacodynamic comprehensive evaluation acted as a dependent variable for grey correlation analyses. The gray correlation analysis steps are described below:

1) The establishment of the original matrix x_i of the related indicators

$$x_i = x_i(1), x_i(2), \cdots x_i(k),$$

where $x_i(k)$ represents the original data of the ith peak at the kth time point.

2) Using the average value $x_i(1)$ of each peak area at each time as the mother sequence, the solution of the initial value transformation matrix $x_i^{'}$

$$x_i^{'} = (x_i(1)/x_i(1), x_i(2)/x_i(1), \cdots x_i(k)/x_i(1),) = \left(x_i^{'}(1), x_i^{'}(2), \cdots x_i^{'}(k)\right) \quad (5)$$

3) Difference sequence $\Delta_{0i}(k)$

$$\Delta_{0i}(k) = \left|x_0^i(k) - x_i^{'}(k)\right| = (\Delta_{0i}(1), \Delta_{0i}(2), \cdots \Delta_{0i}(k)) \quad (6)$$

4) Calculation of the correlation coefficient $\delta_{0i}(k)$

$$\delta_{0i}(k) = \frac{\min \min \Delta_{0i}(k) + \varphi \times \max \max \Delta_{0i}(k)}{\Delta_{0i}(k) + \varphi \times \max \max \Delta_{0i}(k)} \quad (7)$$

where, φ is the resolution coefficient, which can increase the significance of the difference between the correlation coefficient $\delta_{0i}(k)$, $\varphi \in (0, 1)$, generally 0.5.

5) Calculation of the correlation degree r_i

$$r_i = \frac{1}{n-1} \sum_{k=1}^{n} \delta_i(k) \quad (8)$$

The more the r_i value tends to 1, the better the correlation between the two. $r_i > 0.6$, which indicates a certain correlation between the chemical components represented by the chromatographic peak and the values of pharmacodynamic comprehensive evaluation. $r_i > 0.8$ indicates a better correlation between the chemical components represented by the chromatographic peak and the values of pharmacodynamic comprehensive evaluation. $r_i > 0.9$, indicates an excellent correlation between the chemical components represented by the chromatographic peak and the values of pharmacodynamic comprehensive evaluation.

2.12.3 Multiple linear regression

The analysis of the fingerprints of YYTNG in MCAO rats demonstrated six common peaks in the HPLC chart of the medicated plasma at different time points. Moreover, the structure and name of the chemical ingredients represented by these six chromatographic peaks are unknown.

Meanwhile, the relationship between the ingredients and the efficacy was relatively vague. Therefore, the data were subjected to a correlation analysis using the calculation formula shown in Eq. 9:

$$r(X,Y) = \frac{Cov(X,Y)}{\sqrt{Var(X) \times Var(Y)}} \quad (9)$$

2.12.4 Partial least-square method

The partial least-square method is a mathematical optimization technique that combines multiple linear regression analysis, canonical correlation analysis, and principal component analysis (Yu, 2014). This method optimizes the best matching function between the independent and dependent variables by minimizing the error sum of squares. The calculation step of the partial least-square method is depicted below:

1) Data standardization

The obtained peak area and the normalized comprehensive score were standardized according to Eqs.1, 2

2) The principal component extraction of the two variable groups was performed to maximize the correlation

The corresponding formula is depicted in Eqs 10, 11.

$$t_1 = w_{11}x_1 + w_{12}x_2 + \cdots + w_{1m}x_m \quad (10)$$

$$u_1 = v_{11}y_1 + v_{12}y_2 + \cdots + v_{1p}y_p \quad (11)$$

where t_1 is the first principal component of the independent variable, and u_1 is the first principal component of a dependent variable.

3) The establishment of regression between $y_1, y_2, \cdots, y_p$ and t_1

$$y_p = r_{1p}t_1 + r_{2p}t_2 + \cdots + r_{kp}t_k \quad (12)$$

where k is the number of principal components extracted from the independent variable.

4) The establishment of a partial least-squares regression equation between the independent variable (x) and the dependent variable (y)

$$y_p = r_{1p}(w_{11}x_1 + w_{12}x_2 + \cdots + w_{1m}x_m) + r_{2p}(w_{21}x_1 + w_{22}x_2 + \cdots + w_{2m}x_m) + \cdots + r_{kp}(w_{k1}x_1 + w_{k2}x_2 + \cdots + w_{km}x_m) \quad (13)$$

The functional relationship between the peak area of six common peaks and the values of the pharmacodynamic comprehensive evaluation was established through the partial least square analysis method using the MATLAB R2018 b software.

3 Results

3.1 High-performance liquid chromatography fingerprints of yangyin tongnao granules in rats with cerebral ischemia-reperfusion

The HPLC fingerprint of YYTNG in rats with cerebral ischemia reperfusion demonstrated that the blank plasma of the rat was shown in Figure 1A. The six common peaks occurred in the medicated plasma of rats, represented as 1-6 in Figure 1B. The fingerprints of medicated plasma of rats at different time points are shown in Figure 1C. The area of each peak in the medicated plasma at different time points is shown in Table 1. The six common peaks were represented as P1-P6.

3.2 Effect of yangyin tongnao granules on inflammatory factors at different time points in rats with cerebral ischemia-reperfusion

As shown in Figure 2, after the SD rats were modeled by MCAO and orally administered YYTNG, the levels of TNF-α and IL-18 in the plasma of the rats with cerebral ischemia-reperfusion at different time points revealed a downward trend. The levels of TNF-α and IL-18 reached the lowest point at 8 h, followed by a gradual increase.

3.3 Analysis of the results of spectrum-effect correlation

3.3.1 The results of normalization of inflammatory indexes

The entropy weight method was applied to assign values to each inflammation indicator. First, all raw data were standardized according to Eqs 1, 2. Second, according to Eq. 3, the information entropies IL-18 and TNF-α were 0.896 and 0.937, respectively. Finally, according to Eq. 4, the calculated weights of IL-18 and TNF-α were 0.621 and 0.379, respectively. Therefore, the formula used to obtain the pharmacodynamic comprehensive evaluation values was: $Y = 0.621 \times Y1 + 0.379 \times Y2$, where, Y represented the values of a pharmacodynamic comprehensive evaluation, $Y1$ represented the level of IL-18 inflammatory factor, and $Y2$ represented the level of TNF-α inflammatory factor.

The peak areas and pharmacodynamic comprehensive evaluation values (Y) of the six common peaks ($P1$-$P6$) at different time points were obtained. The results are depicted in Table 2.

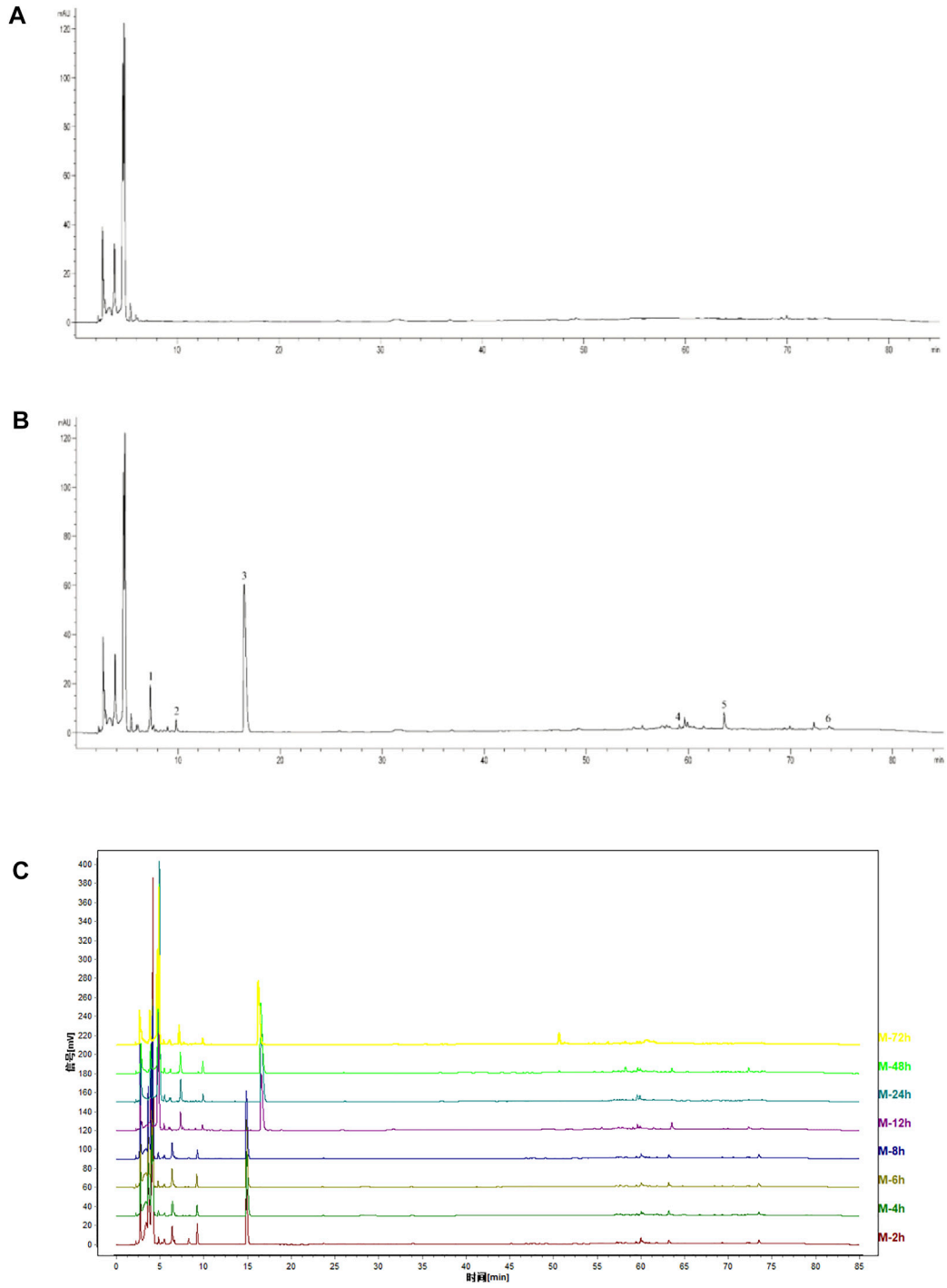

FIGURE 1
HPLC chromatograms of YYTNG in MCAO rats. **(A)** Blank plasma; **(B)** Medicated plasma of 2 h after administration; **(C)** Fingerprints at different time points.

3.3.2 Results of gray correlation analysis

The results calculated according to Eq. 8 are shown in Table 3. The correlation between the peak areas of the six common peaks and the pharmacodynamic comprehensive evaluation values were all >0.6, indicating the presence of a certain correlation between the compounds corresponding to

TABLE 1 The peak areas in the rat plasma at different time points ($\bar{x}$ ±s, n = 6).

	2 h	4 h	6 h	8 h	12 h	24 h	48 h	72 h
P1	181.5 ± 57	184.1 ± 30.2	171.8 ± 18.2	172.1 ± 18.2	141.2 ± 20.4	183.8 ± 47.3	176 ± 22.4	159.9 ± 33
P2	107.1 ± 23	82.1 ± 3.3	85.6 ± 9.5	59.4 ± 9.5	41.5 ± 2.5	48.8 ± 7.8	94.2 ± 3	53.7 ± 6.1
P3	921.8 ± 293.4	1050.2 ± 173.2	907.6 ± 38.2	892.8 ± 38.2	949.5 ± 103.3	1266.5 ± 297.6	1158.8 ± 142	1003.1 ± 83.3
P4	12.3 ± 1.4	11.6 ± 1.5	11.2 ± 0.9	28.4 ± 0.9	15.7 ± 4.6	21.1 ± 6.3	33.3 ± 13.5	45.7 ± 23
P5	36 ± 5.4	40.1 ± 9.6	33.5 ± 5.5	86.9 ± 5.5	66.7 ± 0.1	28.6 ± 24	57.1 ± 36.7	72.6 ± 49.4
P6	27.7 ± 7.4	31 ± 1.6	31.3 ± 1.6	18.7 ± 1.6	12.2 ± 0.2	16.3 ± 3.7	15.4 ± 1.4	13.6 ± 1.1

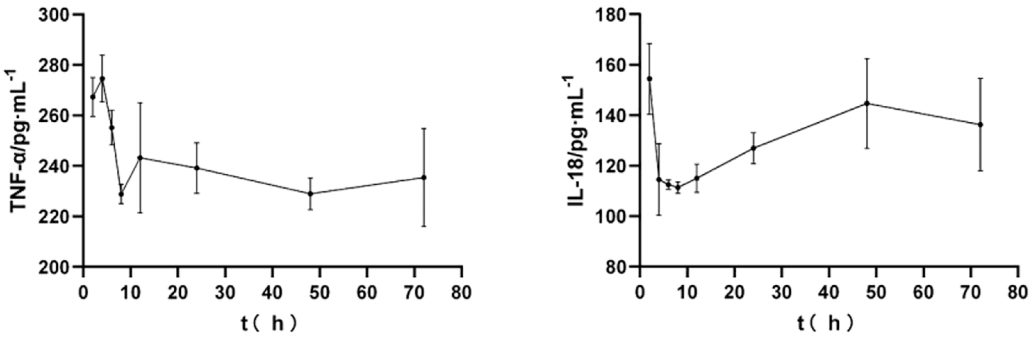

FIGURE 2
Effect of YYTNG on the inflammatory factors at different time points in MCAO rats ($\bar{x}$ ±s, n = 6)

TABLE 2 Peak areas and pharmacodynamic comprehensive evaluation value at different time points ($\bar{x}$ ±s, n = 6).

	2 h	4 h	6 h	8 h	12 h	24 h	48 h	72 h
P1	181.5	184.1	171.8	172.1	141.2	183.8	176	159.9
P2	107.1	82.1	85.6	59.4	41.5	48.8	94.2	53.7
P3	921.8	1050.2	907.6	892.8	949.5	1266.5	1158.8	1003.1
P4	12.3	11.6	11.2	28.4	15.7	21.1	33.3	45.7
P5	36.0	40.1	33.5	86.9	66.7	28.6	57.1	72.6
P6	27.7	31	31.3	18.7	12.2	16.3	15.4	13.6
Y	197.3	175.2	166.6	155.9	163.7	169.5	176.7	173.9

TABLE 3 Gray correlation value between the ingredients and the comprehensive evaluation value of efficacy.

	P1	*P2*	*P3*	*P4*	*P5*	*P6*
Y	0.921	0.825	0.931	0.743	0.720	0.788

these six peaks and the inflammation indicators. Among these, the correlation degree between the *P2* peak and the pharmacodynamic comprehensive evaluation value was >0.8, suggesting that the correlation between the compound corresponding to the *P2* peak and the inflammation indicators are better. The correlation degree between the *P1* and *P3* peaks and the pharmacodynamic comprehensive evaluation value was >0.9, implying that the correlation between the compound corresponding to these two peaks and the inflammation indicators are in an excellent state.

3.3.3 Results of multiple linear regression analysis

The relationship between the pharmacodynamic comprehensive evaluation value and the area of each chromatographic peak was calculated using multiple linear regression analysis, as shown in Eq. 14.

$$Y = 151.257 - 0.014P1 + 0.232P2 + 0.001P3 + 0.302P4 - 0.100P5 + 0.206P6 \quad (14)$$

3.3.4 Results of partial least-square analysis

After standardizing the data, the principal components of the two variable groups were extracted according to Eqs 10, 11, and two principal components were extracted from the independent variables. The relationship between the two principal components and each peak area (standardized data) was as follows:

TABLE 4 The predicted value, actual value, and D-value of pharmacodynamic comprehensive evaluation value (Y).

Y (actual value)	*Y* (predicted value)[1]	Difference[1]	*Y* (predicted value)[2]	Difference[2]
197.252	184.314	12.938	182.135	15.117
175.222	176.053	4.931	177.225	6.356
166.639	176.720	10.081	176.683	10.044
155.926	167.122	11.196	170.749	14.823
163.653	159.542	8.839	162.883	7.880
169.499	167.385	5.137	167.613	4.416
176.693	178.419	8.342	173.402	10.756
173.881	169.208	13.555	168.073	12.628

Note: predicted value [1] was calculated by using a multiple linear regression model. The predicted value [2] was calculated by using a partial least squares regression model.

$$t_1 = -0.538P_1 - 0.411P_2 - 0.319P_3 - 0.184P_4 - 0.386P_5 - 0.508P_6,$$

$$t_2 = 0.343P_1 - 0.585P_2 + 0.295P_3 - 0.070P_4 + 0.438P_5 - 0.510P_6.$$

According to Eq. 12, the regression coefficients between *Y* and the two principal components were −0.293 and −0.210, respectively.

The relationship between the pharmacodynamic comprehensive evaluation value (actual value) and the peak area of each chromatographic peak (actual value) was obtained according to Eq. 13. The result is shown in Eq. 15.

$$y = 143.460 + 0.038P1 + 0.118P2 + 0.002P3 + 0.064P4 + 0.009P5 + 0.412P6 \quad (15)$$

3.3.5 Comparison of the two mathematical models

The predicted value of the pharmacodynamic comprehensive evaluation value *Y* was calculated using Eqs 14, 15. The results are shown in Table 4.

As shown in Table 4, the prediction results of the two mathematical models were similar. The total error between the predicted and actual values of the pharmacodynamic comprehensive evaluation value as per multiple linear regression was 225.057. However, the total error between the predicted and actual values of the pharmacodynamic comprehensive evaluation value according to the partial least-squares method was 246.059. Based on these results, it can be seen that the predicted value calculated using multiple linear regression was closer to the actual value. Therefore, this method was used in this experiment to establish the correlation between the peak areas of the six chromatographic peaks and the pharmacodynamic comprehensive evaluation value. The correlation coefficients between each chromatographic peak area and those between the peak area and the comprehensive evaluation value of pharmacodynamics in the medicated plasma were calculated. The results are shown in Table 5.

TABLE 5 The correlation coefficients between the individual chromatographic peak area and between the peak area and the comprehensive evaluation value of pharmacodynamics.

	P1	*P2*	*P3*	*P4*	*P5*	*P6*	*Y*
P1	1.000	0.345	0.504	−0.078	−0.341	0.239	0.221
P2	0.345	1.000	−0.187	−0.229	−0.375	0.636	0.556
P3	0.504	−0.187	1.000	0.005	−0.280	−0.208	−0.055
P4	−0.078	−0.229	0.005	1.000	0.637	−0.495	0.010
P5	−0.341	−0.375	−0.280	0.637	1.000	−0.659	−0.276
P6	0.239	0.636	−0.208	−0.495	−0.659	1.000	0.410
Y	0.221	0.556	−0.055	0.010	−0.276	0.410	1.000

Y represents the correlation coefficient between the peak area and the comprehensive evaluation value of pharmacodynamics.

As shown in Table 5, the correlation coefficients between the areas of the chromatographic peaks were all <0.7. The correlations between the ingredients were small, which signified that most of the ingredients were independent of each other. According to the absolute value of the correlation coefficient, the correlation between the chemical ingredients represented by the chromatographic peak and the pharmacodynamic comprehensive evaluation values was ranked as follows: *P2* > *P6* > *P5* > *P1* > *P3* >*P4*.

4 Discussion

TCM compounds are composed of two or more types of TCMs, and their efficacy is closely related to their chemical composition. However, the chemical components in TCM compounds are quite complex, with multiple components acting synergistically, and their pharmacological effects being chiefly exerted on the blood components (Wang et al., 2017). Therefore, it is extremely important to study the relationship between the chemical

components of TCMs and their efficacy as well as to examine the prototype components and metabolites in the plasma samples. For example, past studies have demonstrated that the "Qi-invigorating" and "blood-activating" components in Qishen Yiqi Fang can confer protection against cerebral ischemia injury by regulating the inflammatory response and autophagy (Wang et al., 2022). Moreover, the spectrum-effect correlation can be applied to determine and describe the intrinsic relationship between the chemical constituents in TCM compounds and their efficacy (Luo et al., 2019; Zhang et al., 2019). Therefore, this study attempted to identify the chemical constituents in the YYTNG plasma samples that were highly correlated with inflammatory indicators by establishing the spectral-effect correlation between the HPLC fingerprint of YYTNG in MCAO rat plasma samples and inflammatory indicators.

TNF-α is the earliest and the most important inflammatory response marker (Dinarello, 2000) that can activate neutrophils and lymphocytes and enhance cell permeability (Cattani-Cavalieri et al., 2019). Excess TNF-α could promote the synthesis and the release of other inflammatory factors as well as aggravate the inflammatory injury. IL-18 is an important inflammatory factor in the IL-1 family, which is predominantly secreted by epithelial cells, dendritic cells, and macrophages (Dinarello, 2002). IL-18 is the main cytokine downstream of NLRP3 inflammasome that can be released by inflammasome at the time of inflammation (Zhang et al., 2021). As the downstream indicators of the JAK2/STAT3 signaling pathway (Raible et al., 2014; Qin et al., 2019; Sun et al., 2020), IL-18 and TNF-α are the key factors in the inflammatory response (Zhou et al., 2016; Li et al., 2018). Previous research has shown that YYTNG could significantly improve the inflammatory reaction in MCAO rats by reducing the levels of IL-18 and TNF-α in the plasma. The exogenous rCX3CL1 could significantly inhibit the activation of NLRP3 and NF-κB and reduce the expression of IL-1β and IL-18 (Ge et al., 2022). The death-associated protein kinase (DAPK) family is one of the important families of serine/threonine kinases involved in regulating certain biological functions in human cells. Past studies have demonstrated the inhibition of TNF-α and IL-1β expression via modulation of DAPK1 signaling in stroke (Noori et al., 2022). Therefore, TNF-α and IL-18 were selected in this experiment to explore the spectrum-effect relationship of YYTNG in MCAO rats. The results of our research revealed that the levels of inflammatory factors in the plasma of rats decreased with time. Thus, YYTNG can reduce the levels of related inflammatory factors in the plasma of MCAO rats, thereby significantly alleviating the inflammatory injury. The findings indicated that the levels of inflammatory factors decreased with time, implying that YYTNG could reduce the levels of the related inflammatory factors in the plasma of MCAO rats, thereby significantly improving the inflammatory injury.

Mathematical models are often used to evaluate the relationship between the fingerprints of TCM compounds and their efficacy as well as to determine the chromatographic peaks closely related to pharmacodynamics from the fingerprints (Feng et al., 2020; Bai et al., 2021). We had previously investigated the *in vitro* spectrum-activity relationship of YYTNG (Yu et al., 2021). However, the *in vitro* chemical fingerprints could not accurately assess the relationship between TCM components and their efficacy (Dan-dan Wang et al., 2014; Wei et al., 2018). Medicated plasma is more consistent with what is actually happening within the human body (Lin et al., 2016) as it can retain more TCM components (He et al., 2005). Therefore, the medicated plasma was selected for determination via HPLC in this experiment. Six common peaks with good resolution ($R > 1.5$) and high peak area were detected in the HPLC fingerprints of the YYTNG plasma samples. The results demonstrated that the peak area of *P3* was large, which indicated the presence of a correspondingly high amount of chemical ingredients in the medicated plasma. The chemical ingredients in the plasma changed with time, and the areas of most of the peaks decreased with time; however, the peak areas increased after 24 h owing to repeated oral administration. Although HPLC can determine the common peak areas in the plasma, it cannot discern the chemical structure of the ingredients represented by these peaks. Therefore, this experiment provides a strong basis for further investigations on the changes in the constituents of YYTNG in the plasma of MCAO rats.

Different mathematical models could be used to obtain varying results. Therefore, this study established the spectrum-effect relationship between YYTNG fingerprints and inflammatory factors in the plasma of MCAO rats via three mathematical models, namely gray correlation, multiple linear regression, and partial least squares. To eliminate possible multicollinearity among multiple independent variables (Franke, 2010), common peaks in the *in vivo* drug-containing plasma were denoted as P1-P6. Y represents the comprehensive evaluation value of the plasma pharmacodynamics in the MCAO rats. The results of gray correlation analysis showed that the correlations between the six chromatographic peaks and the comprehensive evaluation value of pharmacodynamics were all >0.6, thus signifying that the six components in the YYTNG fingerprint had a certain correlation with the inflammatory indicators. SPSS Statistics 25 software and Matlab R2018b software were used to select the six chromatographic peaks for correlation analysis using multiple linear regression and the partial least-square method. The comprehensive evaluation value of pharmacodynamics was predicted using a regression equation. The results indicated that the predicted values were not very different from the actual values. Furthermore, the error between the predicted value and the actual value calculated using multiple linear regression was small. Therefore, the multiple linear regression analysis was employed to analyze the correlation between the six chromatographic peaks and the comprehensive evaluation value of pharmacodynamics. As shown in Table 5, the absolute correlation coefficients between the peak areas of *P2*, *P6*, *P5*, and *P1* and the comprehensive evaluation value of pharmacodynamics were all ≥0.2. These results alluded that the chemical constituents corresponding to these peaks were

significantly associated with the inflammatory factors. Although no highly correlated chromatographic peaks were identified in this experiment, these compounds can be isolated and analyzed in the future.

This experiment established the spectrum-effect relationship between the HPLC fingerprint of YYTNG in the plasma of MCAO rats and the inflammatory indicators. The present findings have laid the foundation for the further determination of the main anti-inflammatory injury components of YYTNG in MCAO rats. The limitation of this study is that it failed to identify several chromatographic peaks with a high correlation. In future research, we intend to identify these chromatographic peaks with a high anti-inflammatory correlation to analyze the YYTNG plasma prototype components and the metabolite components related to anti-inflammatory injury in plasma samples.

5 Conclusion

In this experiment, mathematical models were used to analyze the correlation between HPLC fingerprints and inflammatory indicators in MCAO rats. The results revealed a relatively large correlation between six chromatographic peaks in rat plasma and inflammatory indicators, albeit the results were inadequate. This could be because the six chromatographic peaks have not been identified. Therefore, in subsequent experiments, we plan to combine various experimental techniques to isolate and identify these six components and further verify the relationship between them and inflammatory indicators through cell experiments. This study lays a preliminary experimental foundation for the separation and structural identification of the chemical components represented by the six common peaks in the later period, thereby providing an idea for the establishment of *in vivo* fingerprints of traditional Chinese medicine compounds and drug metabolism research. The combination of mathematical models and *in vitro* and *in vivo* experiments is expected to provide certain guiding significance for clinical rational drug use and safety evaluation.

Data availability statement

The original contributions presented in the study are included in the article/Supplementary Material, further inquiries can be directed to the corresponding authors.

Ethics statement

The animal study was reviewed and approved by Animal welfare and experimental procedures were strictly in accordance with the Regulation for the Administration of Affairs Concerning Experimental Animals (State Science and Technology Commission, 1988) and approved by the Animal Subjects Review Board of the Zhejiang Chinese Medical University.

Author contributions

LY: Conceptualization. LY and YZ: Methodology, Data Curation, Writing—Original Draft. ZD: Project administration. LY, ZD, HW, and JY: Funding acquisition. YH and HW: Writing—Review and Editing. All authors read and approved the final manuscript.

Acknowledgments

This study was supported by the National Natural Science Foundation of China Nos. 81904083, and 81630105, National Key R&D Program of China 2019YFC1708600, 2019YFC1708604, Key Laboratory of TCM Encephalopathy of Zhejiang Province No. 2020E10012.

Conflict of interest

The authors declare that the research was conducted in the absence of any commercial or financial relationships that could be construed as a potential conflict of interest.

Publisher's note

All claims expressed in this article are solely those of the authors and do not necessarily represent those of their affiliated organizations, or those of the publisher, the editors, and the reviewers. Any product that may be evaluated in this article, or claim that may be made by its manufacturer, is not guaranteed or endorsed by the publisher.

References

Bai, X., Liu, L., Zhang, J., Chen, L., Wu, T., Aisa, H. A., et al. (2021). Spectrum–effect relationship between GC-QTOF-MS fingerprint and antioxidant, anti-inflammatory activities of Schizonepeta tenuifolia essential oil. *Biomed. Chromatogr.* 35, e5106. doi:10.1002/bmc.5106

Cattani-Cavalieri, I., Valenca, S. S., Lanzetti, M., Carvalho, G., Zin, W. A., Monte-Alto-Costa, A., et al. (2019). Acute exposure to diesel-biodiesel particulate matter promotes murine lung oxidative stress by Nrf2/HO-1 and inflammation through the NF-kB/TNF-α pathways. *Inflammation* 42 (2), 526–537. doi:10.1007/s10753-018-0910-8

Dan-dan Wang, J. L., Yang, W-Z., Hou, J-J., Yang, M., Da, J., Wang, Y., et al. (2014). HPLC/qTOF-MS-oriented characteristic components data set and chemometric analysis for the holistic quality control of complex TCM preparations: niuhuang Shangqing pill as an example. *J. Pharm. Biomed. Anal.* 89, 130–141. doi:10.1016/j.jpba.2013.10.042

Dinarello, C. A. (2000). Proinflammatory cytokines. *Chest* 118, 503–508. doi:10.1378/chest.118.2.503

Dinarello, C. A. (2002). The IL-1 family and inflammatory diseases. *Clin. Exp. Rheumatol.* 20, S1–S13.

Feng, Y., Teng, L., Wang, Y., Gao, Y., Ma, Y., Zhou, H., et al. (2020). Using spectrum-effect relationships coupled with LC–TOF–MS to screen anti-arrhythmic components of the total flavonoids in hypericum attenuatum extracts. *J. Chromatogr. Sci.* 59, 246–261. doi:10.1093/chromsci/bmaa101

Franke, G. R. (2010). "Multicollinearity," in *Wiley international encyclopedia of marketing*. Atlanta: American Cancer Society.

Gao, S., Chen, H., and Zhou, X. (2019). Study on the spectrum-effect relationship of the xanthine oxidase inhibitory activity of Ligustrum lucidum. *J. Sep. Sci.* 42, 3281–3292. doi:10.1002/jssc.201900531

Ge, Y., Wang, L., Wang, C., Chen, J., Dai, M., Yao, S., et al. (2022). CX3CL1 inhibits NLRP3 inflammasome-induced microglial pyroptosis and improves neuronal function in mice with experimentally-induced ischemic stroke. *Life Sci.* 300, 120564. doi:10.1016/j.lfs.2022.120564

He, S. L., Ge, J. W., He, R., and Mei, Z. G. (2005). Doubt the validity of serum pharmacology, emphasize the exvivo experiments on multiple levels. *Chin. Pharmacol. Bull.* 21, 277–279. doi:10.3321/j.issn:1001-1978.2005.03.006

Jayaraj, R. L., Azimullah, S., Beiram, R., Jalal, F. Y., and Rosenberg, G. A. (2019). Neuroinflammation: friend and foe for ischemic stroke. *J. Neuroinflammation* 16, 142. doi:10.1186/s12974-019-1516-2

Jidan, Z., Tong, C., Haiyu, R., Liang, W., Wang, H., Wang, W., et al. (2019). Screening active ingredients of rosemary based on spectrum-effect relationships between UPLC fingerprint and vasorelaxant activity using three chemometrics. *J. Chromatogr. B Anal. Technol. Biomed. Life Sci.* 1134-1135, 121854. doi:10.1016/j.jchromb.2019.121854

Li, M., Zhang, X., Wang, B., Xu, X., Wu, X., Guo, M., et al. (2018). Effect of JAK2/STAT3 signaling pathway on liver injury associated with severe acute pancreatitis in rats. *Exp. Ther. Med.* 16 (3), 2013–2021. doi:10.3892/etm.2018.6433

Liang, L. F., and Su, Q. H. (2015). Clinical observation of Yang Yin Tong Nao granule in the treatment of 30 cases of stroke recovery(deficiency of both qi and yin, blood stasis syndrome). *Chin. community Dr.* 31, 72–73. doi:10.3969/j.issn.1007-614x.2015.20.46

Lin, Z. M., Zhong, J. X., and Li, Q. N. (2016). Progress in the application of serum pharmacology and plasma pharmacology of Chinese medicine. *Asia-Pacific Tradit. Med.* 12, 62–64. doi:10.11954/ytctyy.201612025

Liu, H., Zhu, S., Liu, Q., and Zhang, Y. (2019a). Spectrum–effect relationship study between HPLC fingerprints and antioxidant of honeysuckle extract. *Biomed. Chromatogr.* 33, e4583. doi:10.1002/bmc.4583

Liu, M., Xu, Z., Wang, L., Zhang, L., Ma, Y., Cao, J., et al. (2020). Cottonseed oil alleviates ischemic stroke injury by inhibiting the inflammatory activation of microglia and astrocyte. *J. Neuroinflammation* 17, 270. doi:10.1186/s12974-020-01946-7

Liu, Z., Ran, Y., Qie, S., Gong, W., Xi, J., Ding, Z. T., et al. (2019b). Melatonin protects against ischemic stroke by modulating microglia/macrophage polarization toward anti-inflammatory phenotype through STAT3 pathway. *CNS Neurosci. Ther.* 25, 1353–1362. doi:10.1111/cns.13261

Longa, E. Z., Weinstein, P. R., Carlson, S., and Cummins, R. (1989). Reversible middle cerebral artery occlusion without craniectomy in rats. *Stroke* 20 (1), 84–91. doi:10.1161/01.str.20.1.84

Luo, C., Yi, F., Xia, Y., Huang, Z., Zhou, X., Jin, X., et al. (2019). Comprehensive quality evaluation of the lateral root of Aconitum carmichaelii debx. (Fuzi): simultaneous determination of nine alkaloids and chemical fingerprinting coupled with chemometric analysis. *J. Sep. Sci.* 42, 980–990. doi:10.1002/jssc.201800937

Mo, Y., Sun, Y. Y., and Liu, K. Y. (2020). Autophagy and inflammation in ischemic stroke. *Neural Regen. Res.* 15, 1388–1396. doi:10.4103/1673-5374.274331

Noori, T., Shirooie, S., Sureda, A., Sobarzo-Sanchez, E., Dehpour, A., Saldías, M., et al. (2022). Regulation of DAPK1 by natural products: an important target in treatment of stroke. *Neurochem. Res.* (online). doi:10.1007/s11064-022-03628-7

Poinsatte, K., Selvaraj, U. M., Ortega, S. B., Plautz, E. J., Kong, X., Gidday, J. M., et al. (2015). Quantification of neurovascular protection following repetitive hypoxic preconditioning and transient middle cerebral artery occlusion in mice. *J. Vis. Exp.* 99, e52675. doi:10.3791/52675

Qin, M-Z., Qin, M-B., Liang, Z-H., and Tang, G-D. (2019). Effect of SOCS3 on lung injury in rats with severe acute pancreatitis through regulating JAK2/STAT3 signaling pathway. *Eur. Rev. Med. Pharmacol. Sci.* 23, 10123–10131. doi:10.26355/eurrev_201911_19582

Raible, D. J., Frey, L. C., and Brooks-Kayal, A. R. (2014). Effects of JAK2-STAT3 signaling after cerebral insults. *JAK-STAT* 3, e29510. doi:10.4161/jkst.29510

Rong, Y., He, Y., Cheng, L., Wang, H., Yu, L., Yang, J., et al. (2018). Study on the protective mechanism of Yangyintongnao granules in combination with active ingredients on cerebral ischemia-reperfusion injury in rats. *Chin. J. Pharm.* 53, 199–204.

Rong, Y., Zhang, Y., Yang, J., He, Y., Fu, N., Cheng, L., et al. (2017). Effects of Yangyin Tongnao Granule on endoplasmic reticulum stress in hippocampus of rats with cerebral ischemia-reperfusion injury. *J. Traditional Chin. Med.* 58, 405–409. doi:10.13288/j.11-2166/r.2017.05.013

Sarraf, F., and Nejad, S. H. (2020). Improving performance evaluation based on balanced scorecard with grey relational analysis and data envelopment analysis approaches: case study in water and wastewater companies. *Eval. Program Plan.* 79, 101762. doi:10.1016/j.evalprogplan.2019.101762

Seiya, T., Harutoshi, S., Takahiro, M., Shotaro, O., Kazuki, N., Norimatsu, K., et al. (2020). Disruption of Midkine gene reduces traumatic brain injury through the modulation of neuroinflammation. *J. Neuroinflammation* 17, 40. doi:10.1186/s12974-020-1709-8

Shi, K., Tian, D. C., Li, Z. G., Ducruet, A. F., and Shi, F. D. (2019). Global brain inflammation in stroke. *Lancet. Neurol.* 18, 1058–1066. doi:10.1016/S1474-4422(19)30078-X

Sun, Y., Cheng, M., Liang, X., Chen, S., Wang, M., Zhang, X. u., et al. (2020). JAK2/STAT3 involves oxidative stress-induced cell injury in N2a cells and a rat MCAO model. *Int. J. Neurosci.* 130, 1142–1150. doi:10.1080/00207454.2020.1730829

Wan, H., Bie, X., Yao, Z., Xu, B., Liu, H., Yang, J., et al. (2015). Observation on the curative effect of Yangyin Yiqi Huoxue Recipe in the treatment of ischemic stroke with Qi and Yin deficiency syndrome and blood stasis blocking collaterals syndrome. *Chin. J. Integr. Med.* 35, 281–286. doi:10.7661/CJIM.2015.03.0281

Wang, A. Y., Shen, Y., Chen, W. X., Wang, X., Hua, Y. Q., Wang, W., et al. (2017). Scientific thinking on key mode of action of Chinese medicine. *World Sci. Technoloyg/Modernizationg Traditional Chin. Med. Materia Medica* 019, 1692–1701. doi:10.11842/wst.2017.10.018

Wang, L., and Ma, Q. (2018). Clinical benefits and pharmacology of scutellarin: a comprehensive review pharmacology & therapeutics. *Pharmacol. Ther.* 190, 105–127. doi:10.1016/j.pharmthera.2018.05.006

Wang, Y., Liu, X., Zhang, W., He, S., Zhang, Y., Orgah, J., et al. (2022). Synergy of "Yiqi" and "Huoxue" components of QishenYiqi formula in ischemic stroke protection via lysosomal/inflammatory mechanisms. *J. Ethnopharmacol.* 293, 115301. doi:10.1016/j.jep.2022.115301

Wang, Y., Yang, J., Du, H., Zhang, H., Wan, H., and He, Y. (2019). Yangyin Tongnao granules enhance neurogenesis in the peri-infarct area and upregulate brain-derived neurotrophic factor and vascular endothelial growth factor after focal cerebral ischemic infarction in rats. *Mol. Biol. Rep.* 46, 3817–3826. doi:10.1007/s11033-019-04824-5

Wei, S., Cai, Z., Zhao, D., Wang, L., and Li, H. (2018). Discovery of hepatotoxic equivalent combinatorial markers from Dioscorea bulbifera tuber by fingerprint-toxicity relationship modeling. *Sci. Rep.* 8, 462. doi:10.1038/s41598-017-18929-z

Yu, L., Wan, H. F., Li, C., Yang, J. H., Zhou, H. F., Wan, H. T., et al. (2018). Pharmacokinetics of active components from guhong injection in normal and pathological rat models of cerebral ischemia: A comparative study. *Front. Pharmacol.* 9, 493. doi:10.3389/fphar.2018.00493

Yu, L., Zhang, Y., Zhao, X., He, Y., Wan, H., Wan, H., et al. (2021). Spectrum-effect relationship between HPLC fingerprints and antioxidant activity of Yangyin Tongnao prescription. *J. Anal. Methods Chem.* 2021, 6650366. doi:10.1155/2021/6650366

Yu, Z. P. (2014). *Structural identification and biological activity study of egg white-derived active peptides*. Changchun: Jilin University.

Zhang, X., Liu, J., Gao, S., Chen, R., Qi, Y., Zhang, B., et al. (2019). Research methods and application progress of spectrum-effect relationship of traditional Chinese medicine. *Chin. J. Traditional Chin. Med.* 44, 4405–4411. doi:10.19540/j.cnki.cjcmm.20190429.201

Zhang, Y., Kuang, W., Li, D., Li, Y., Feng, Y., Lyu, X., et al. (2021). Natural killer-like B cells secreting interleukin-18 induces a proinflammatory response in periodontitis. *Front. Immunol.* 12, 641562. doi:10.3389/fimmu.2021.641562

Zhou, G. Y., Yi, Y. X., Jin, L. X., Lin, W., Pan, C. W., Lin, X. Z., et al. (2016). The protective effect of juglanin on fructose-induced hepatitis by inhibiting inflammation and apoptosis through TLR4 and JAK2/STAT3 signaling pathways in fructose-fed rats. *Biomed. Pharmacother.Biomedecine Pharmacother.* 81, 318–328. doi:10.1016/j.biopha.2016.04.013

Zhou, X., Li, Y., Zhang, M., Hao, J., Li, G., Liu, H., et al. (2019). Spectrum-effect relationship between UPLC fingerprints and antilung cancer effect of Si jun zi tang. *Evid. Based. Complement. Altern. Med.* 2019, 7282681. doi:10.1155/2019/7282681

Zhou, X., Liu, H., Zhang, M., Li, C., and Li, G. (2021). Spectrum-effect relationship between UPLC fingerprints and anti-lung cancer effect of Panax ginseng. *Phytochem. Anal.* 32, 339–346. doi:10.1002/pca.2980

frontiers | Frontiers in Pharmacology

TYPE Original Research
PUBLISHED 22 August 2022
DOI 10.3389/fphar.2022.951613

OPEN ACCESS

EDITED BY
Wei-Wei Jia,
Shanghai Institute of Materia Medica (CAS), China

REVIEWED BY
Junling Yang,
Shanghai Institute of Materia Medica (CAS), China
Yanxu Chang,
Tianjin University of Traditional Chinese Medicine, China

*CORRESPONDENCE
Guang-Ping Zhang,
gpzhang@icmm.ac.cn
Ying-Fei Li,
yfli@icmm.ac.cn
Zu-Guang Ye,
zgye@icmm.ac.cn

SPECIALTY SECTION
This article was submitted to Ethnopharmacology, a section of the journal Frontiers in Pharmacology

RECEIVED 24 May 2022
ACCEPTED 15 July 2022
PUBLISHED 22 August 2022

CITATION
Chen T-F, Song L, Gao Y-H, Li H, Li J-L, Hou H-P, Peng B, Wang H-Y, Cheng W-H, Ye Z-G, Li Y-F and Zhang G-P (2022), Pharmacokinetics of baicalin and oroxyloside in plasma and different tissues of rats after transnasal aerosol inhalation and intravenous injection of Tanreqing.
Front. Pharmacol. 13:951613.
doi: 10.3389/fphar.2022.951613

Pharmacokinetics of baicalin and oroxyloside in plasma and different tissues of rats after transnasal aerosol inhalation and intravenous injection of Tanreqing

Teng-Fei Chen[1], Ling Song[1], Yun-Hang Gao[1], Han Li[1], Jian-Liang Li[1], Hong-Ping Hou[1], Bo Peng[1], Hui-Ying Wang[1], Wen-Hao Cheng[2], Zu-Guang Ye[1]*, Ying-Fei Li[1]* and Guang-Ping Zhang[1]*

[1]Institute of Chinese Materia Medica, China Academy of Chinese Medical Science, Beijing, China, [2]School of Chinese Pharmacy, Beijing University of Chinese Medicine, Beijing, China

To avoid adverse drug reactions associated with injection, off-label nebulization of Tanreqing (TRQ) injection is often used in China to treat respiratory diseases. However, the aerodynamic properties and lung availability of TRQ aerosols remain largely uninvestigated. This study aimed to investigate the size distribution of TRQ aerosols and to compare the pharmacokinetics and tissue distribution of two compounds from TRQ (baicalin and oroxyloside) after transnasal aerosol inhalation and intravenous administration. Furthermore, this study aimed to evaluate the efficacy of TRQ against lipopolysaccharide-induced lung inflammation. The Dv(50) and transmission of TRQ aerosols were 2.512 μm and 74.867%, respectively. The C_{max} of baicalin and oroxyloside in rat plasma after inhalation was lower than that after intravenous injection. After inhalation, the area under the curve (AUC) of baicalin and oroxyloside in tissues (lung, bronchoalveolar lavage fluid, and trachea) was 7.9–115.3 and 9.5–16.0 times that observed after intravenous administration, respectively. Baicalin and oroxyloside maintained high concentrations 4 h after inhalation, but only 1 h after intravenous injection. The mean lung-to-plasma concentration ratios of baicalin and oroxyloside were 287.6 and 49.9 times higher than with intravenous administration. Inhaled TRQ achieved the same effect against lipopolysaccharide-induced lung inflammation in mice at doses of only 1/16–1/8 of those administered intravenously. The results indicate that

Abbreviations: AUC, area under the curve; BAI, baicalin; BALF, bronchoalveolar lavage fluid; HQ, huang qin; IS, internal standard; IV, intravenous; JYH, jin yin hua; LPS, lipopolysaccharide; LQ, lian qiao; MRT, mean residence time; ORO, oroxyloside; PAE, paeoniflorin; RSD, relative standard deviation; SYJ, shan yang jiao; TRQ, tanreqing; TI, transnasal aerosol inhalation; XD, xiong dan.

TRQ inhalation is a promising alternative to intravenous injections for the treatment of respiratory infection.

KEYWORDS

baicalin, lung, oroxyloside, pharmacokinetics, Tanreqing, transnasal aerosol inhalation

Introduction

Tanreqing (TRQ) injection is a Chinese medicinal preparation derived from five traditional Chinese medicines, namely, *Scutellaria baicalensis* Georgi [Lamiaceae; Scutellariae Radix; Huang Qin in Chinese, HQ; 23.6%], *Selenaretos thibetanus* Cuvier [Ursidae; Ursi Fellis Pulvis; Xiong Dan in Chinese, XD; 3.8%], *Naemorhedus goral* Hardwicke [Bovidae; Caprae Hircus Cornu; Shan Yang Jiao in Chinese, SYJ; 1.9%], *Lonicera japonica* Thunb. [Caprifoliaceae; Lonicerae Japonicae Flos; Jin Yin Hua in Chinese, JYH; 23.6%], and *Forsythia suspensa* (Thunb.) Vahl [Oleaceae; Forsythiae Fructus; Lian Qiao in Chinese, LQ; 47.1%] (Rivera et al., 2014; He et al., 2021). The botanical drugs were extracted by water extraction (HQ, JYH, and LQ) and were purified by alcohol sedimentation, hyperfiltration (HQ), saponification (XD), and acid hydrolysis (SYJ), respectively (Mu, 2011). The chemical composition of TRQ includes flavonoids, iridoids, phenolic acids, amino acids, phenethyl alcohol glycosides, lignans, and steroids (Li C et al., 2019; Xie et al., 2021). TRQ possesses anti-inflammatory, antibacterial, antiviral, antitumor, and other pharmacological effects. Furthermore, TRQ can inhibit inflammatory exudation and interstitial pulmonary edema, reduce inflammatory cell infiltration, and prevent acute inflammatory injury to the alveolar epithelium (Zhong et al., 2010; Liu H et al., 2020; Liu W et al., 2020). TRQ was approved by the China Food and Drug Administration in 2003 and has been widely used clinically in the treatment of acute exacerbations of chronic obstructive pulmonary disease, acute upper respiratory tract infections, pneumonia, and other lung diseases (Li et al., 2010; Wang et al., 2011; Wang et al., 2016). However, its clinical applications are limited by the increasing incidence of adverse reactions, including anaphylactic shock (Wang et al., 2018; Li X X et al., 2019).

Compared to intravenous (IV) administration, inhalation does not cause pain and can increase patients' comfort and compliance, improving the effectiveness of treatment of respiratory diseases. Aerosol inhalation in traditional Chinese medicine has been widely used to clinically treat respiratory diseases, especially the medicine with heat-clearing and detoxifying effects. Lung and respiratory diseases, such as pneumonia, respiratory infections, tracheitis, and bronchitis, can be treated by single or combined aerosolization (Han et al., 2016), demonstrating that traditional Chinese medicines have great potential to treat respiratory diseases. In recent years, numerous studies have reported that TRQ can be clinically used to treat respiratory diseases by aerosol inhalation. Deng and Lei (2017) retrieved 24 related reports involving 1,348 children in domestic and foreign medical databases using TRQ injection, aerosol inhalation, respiratory infections, and pediatric patients as keywords. The results showed that aerosol inhalation of TRQ was found to be safe and effective, with a total clinical efficacy rate >85% and an extremely low incidence of adverse reactions. Through literature analysis and research, Sun et al. (2013) found that TRQ aerosol inhalation was mainly used to treat and prevent respiratory infections in children and the elderly, with significant curative effects and low adverse reactions.

The clinical aerosolization application of TRQ is beyond that indicated on the package insert. Nonetheless, the particle size of the TRQ nebulized aerosols has not been systematically studied, and the absorption and metabolism of multiple components in the lungs after aerosolization are not clear. Based on the chemical composition of TRQ, seven analytes were selected to conduct a preliminary study on pharmacokinetics (PK) after transnasal aerosol inhalation (TI). These analytes include baicalin (BAI) and oroxyloside (ORO, both from HQ), chlorogenic acid (from JYH), forsythoside D and forsythoside E (both from LQ), and ursodeoxycholic acid and chenodeoxycholic acid (both from XD). The preliminary study showed that BAI, ORO, ursodeoxycholic acid, and chenodeoxycholic acid could be detected in rat plasma after TI of TRQ. Ursodeoxycholic acid and chenodeoxycholic acid are endogenous components and have high blood concentrations. The concentration changes of the two compounds after TI administration were difficult to distinguish from the blank. Therefore, BAI and ORO from HQ were selected as the target compounds in the current study. This study evaluated the particle size distribution of TRQ aerosols generated by a nebulizer. The pharmacokinetic characteristics of BAI and ORO were compared in plasma and tissues, including the lung and trachea after TI and IV administration, and the anti-inflammatory effects were investigated in mice lungs.

Materials and methods

Reagents and chemicals

BAI (CAS No. 21967-41-9, Lot No. 110715-201117, and 91.7% purity) was purchased from the National Institutes for Food and Drug Control (Beijing, China). ORO (CAS No. 36948-76-2, Lot No. SS20190628, and 98.0% purity) was purchased from Chengdu SinoStandards BioTech Co., Ltd. (Chengdu,

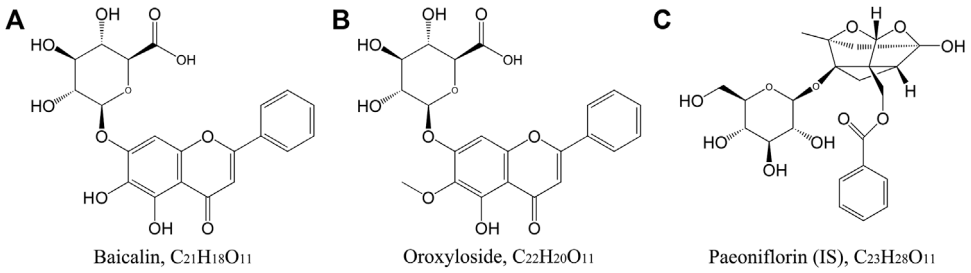

FIGURE 1
Chemical structure of BAI **(A)**, ORO **(B)**, and PAE (**(C)**, IS).

China). Paeoniflorin [PAE, internal standard (IS), CAS No. 23180-57-6, Lot No. C10833465, and 98.0% purity] was obtained from Shanghai Macklin Biochemical Co. Ltd. (Shanghai, China). The chemical structures of the two analytes and IS are shown in Figure 1. TRQ (Lot No. 2006103) was provided by Shanghai Kaibao Pharmaceutical Co., Ltd. (Shanghai, China). Dexamethasone sodium phosphate (Lot No. 19110802A) was purchased from Guizhou Tiandi Pharmaceutical Co., Ltd. (Guizhou, China). Lipopolysaccharide (LPS, Lot No. 0000114329) was obtained from Sigma-Aldrich Co. (Darmstadt, Germany). Radio immunoprecipitation assay (RIPA) lysis buffer (Lot No. 01408/60527) was purchased from Beijing ComWin Biotech Co., Ltd. (Beijing, China). Mouse interleukin (IL)-6 enzyme-linked immunosorbent assay (ELISA) kit (96T, Lot No. 20211014) was obtained from Beijing Solarbio Science and Technology Co., Ltd. (Beijing, China). Chromatographic methanol and acetonitrile were provided by Merck (Darmstadt, Germany), and chromatographic formic acid was provided by ROE SCIENTIFIC (Newark, United States). Other reagents were commercially available and were analytically and chromatographically pure.

Animals

The animal procurement and experiments were approved by the Animal Ethics Committee of the Institute of Chinese Materia Medica, China Academy of Chinese Medical Sciences (approval No. 2020B036). Specific pathogen-free (SPF) Sprague–Dawley (SD) rats (200–240 g) and SPF ICR mice (20–24 g) were purchased from the Beijing Vital River Laboratory Animal Technology Co., Ltd. (Beijing, China). All animals were maintained on a 12/12 h light/dark cycle in an environmentally controlled SPF room (temperature 23°C ± 1°C; relative humidity 50% ± 15%). The animals were acclimated to the laboratory for at least 5 days and were unfed 12 h before the experiment, but with free access to water.

Instrument and analytical conditions

A high-performance liquid chromatography-mass spectrometry (HPLC-MS/MS) system (AB SCIEX, Toronto, Canada) equipped with an ExionLC HPLC tandem with a Qtrap 5500 mass spectrometer was used for analysis and determination. The Shimadzu Shim-pack Velox SP-C18 LC column (100 × 2.1 mm, 2.7 μm) was used as the chromatographic column at a temperature of 40°C. The autosampler temperature was 6°C. After 5 μl injection, mobile phases A (water) and B (methanol: acetonitrile = 1:1) containing 0.05% formic acid were used for elution at a flow rate of 0.3 ml/min according to the following procedure: 0–0.5 min, 95% A; 0.5–0.6 min, 95%–60% A; 0.6–2.0 min, 60% A; 2.0–2.5 min, 60%–5% A; 2.5–3.0 min, 5% A; 3.0–3.1 min, 5%–95% A; 3.1–6.0 min, 95% A.

In the positive ion mode of the electrospray ionization (ESI) source, multiple reaction monitoring scans were used to detect the analytes and IS. The ion spray voltage and curtain gas pressure were maintained at 5500 V and 35 psi, respectively. The collision gas was set at 6 psi, the turbo spray temperature was maintained at 500°C, and the nebulizer (gas 1) and heater gases (gas 2) were set at 45 psi using nitrogen. The precursor/product pairs of BAI, ORO, and IS were *m/z* 447.3→271.0, m/*z* 461.2→284.9, and *m/z* 498.2→179.2, respectively. The declustering potential (DP) of BAI, ORO, and IS was 53.1, 91.9, and 147.0 V, respectively. The collision energy (CE) of BAI, ORO, and IS was 26.9, 26.1, and 23.0 V, respectively. The dwell time and collision exit potential (CXP) for all compounds were 100 ms and 15 V, respectively.

Blank matrix samples and sample preparation

After anesthesia, blood samples of six rats were collected from the abdominal aorta into heparinized tubes. Plasma was harvested by centrifuging blood samples at 10,000 rpm for 2 min

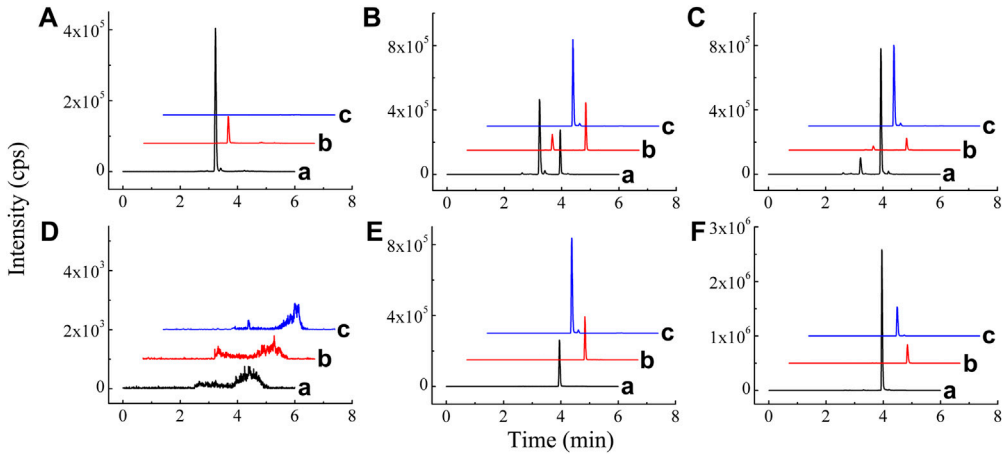

FIGURE 2
Chromatograms of BAI **(A)**, ORO **(B)**, and IS **(C)** in blank plasma **(A)**; blank plasma spiked with BAI, ORO, and IS **(B)**; plasma sample 20 min after TI of TRQ **(C)**; blank lung homogenate sample **(D)**; blank lung homogenate spiked with BAI, ORO, and IS **(E)**; and lung homogenate sample 10 min after TI of TRQ **(F)**.

at 4°C. The lung, trachea, and brain were dissected rapidly and harvested. The tissues were rinsed thoroughly, weighed, and processed by homogenization with cold saline in a 1:4, 1:9, and 1:4 (w/v) radio for the lung, trachea, and brain, respectively. Blank plasma and tissue homogenates were stored at −80°C until use.

Biological samples were pre-treated via protein precipitation as follows: 50 μl biological samples were vortex-mixed with 400 μl IS working solution (the plasma samples needed to add 2 μl formic acid first) for 1 min, ultrasound for 2 min, and centrifuged at 14,000 rpm for 5 min at 4°C. The supernatant (400 μl) was centrifuged and concentrated at 1,700 rpm at 47°C until it becomes dry. The residue was redissolved in 100 μl of 70% methanol (0.05% formic acid) followed by a 1 min vortex and a 2 min ultrasound. The supernatant was injected into the HPLC-MS/MS system for analysis after centrifuging at 14,000 rpm for 5 min at 4°C.

For the preparation of working and sample solution, and method validation of HPLC-MS/MS, refer to Supplementary Material.

Size distribution of TRQ aerosols

TRQ was nebulized using a TurboBoy nebulizer with a red nozzle from PARI Pharma GmbH (Starnberg, Germany). A Spraytec laser diffractometer (Malvern Panalytical Ltd., United Kingdom) was used to evaluate the size distribution of TRQ aerosols generated by the nebulizer at a flow rate of 15 L/min. The experiments were carried out by placing 2 ml of the TRQ solution into the nebulizer cup. The nebulizer cup was then connected to the laser diffractometer and measured. The aerosol transmission volume and particle size distribution were recorded in real-time. The experiment was repeated three times.

Dose and method of TI

The actual aerosol inhalation dose was calculated using the following equation:

$$W = C \times T \times f \times TV, \quad (1)$$

where C is the aerosol concentration at dynamic equilibrium, T is the time of aerosol inhalation, f is the respiratory rate, and TV is the average tidal volume (Zhang et al., 2021). The experimental animals were atomized using the FinePointe oral and nasal exposure system (DSI Buxco, Delaware, United States), which ensured equal concentrations for each animal. The TI groups were nebulized with TRQ for 5, 10, and 20 min. The actual doses calculated according to the formula were 0.03, 0.06, and 0.12 ml/kg for the pharmacokinetic experiment in rats and 0.08, 0.16, and 0.32 ml/kg for the anti-inflammatory experiment in mice.

Pharmacokinetics of BAI and ORO in rats after TI and IV of TRQ

For the pharmacokinetic experiment, SD rats were randomly divided into four groups (0.03 ml/kg), a low dose group of TI (0.03 ml/kg), a medium dose group of TI (0.06 ml/kg), and a high dose group of TI (0.12 ml/kg), each group consisted of six rats. The animals in each group underwent a jugular vein

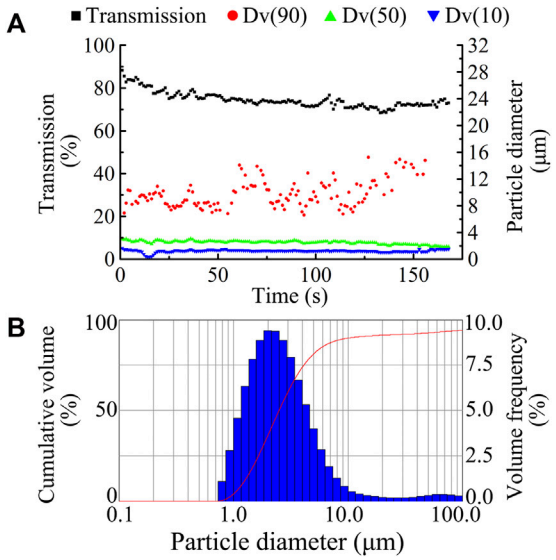

FIGURE 3
Dynamic changes in aerosol size and transmission ((**A**), ■ transmission, ● Dv90, ▲ Dv50, and ▼ Dv10) and typical aerosol size distribution (**B**) by using a red nozzle of PARI TurboBoy N nebulizer for the nebulization of TRQ.

catheterization the day before the experiment. They were unfed overnight but had free access to water. For the IV group, rats were intravenously injected with TRQ through the tail vein. For the three TI groups, rats were placed in the FinePointe oral and nasal exposure system. A TurboBoy N nebulizer with a red nozzle was used to nebulize TRQ for 5, 10, and 20 min. A photometer was used to record aerosol concentrations at dynamic equilibrium. Before administration and 0.083, 0.167, 0.333, 0.5, 0.75, 1, 2, 4, 6, 8, 10, and 24 h after administration, approximately 0.15 ml of blood was collected from the jugular vein into a 1.5 ml centrifuge tube with heparin anticoagulation followed by centrifuging at 10,000 rpm for 2 min at 4°C. After blood collection at each treatment time, an equal volume of 0.9% saline was added through the jugular vein catheterization to the rat. The 2 μl of formic acid was added to a 50 μl plasma sample and stored at −80°C until analysis. All rats were euthanized with carbon dioxide after sample collection.

Tissue distribution of BAI and ORO in rats after TI and IV of TRQ

For the tissue distribution experiment, 60 SD rats were randomly divided into the IV group (0.12 ml/kg, intravenously injected through the tail vein) and the TI group (0.12 ml/kg, transnasal aerosol inhalation for 20 min). The inhalation system was the same as that used in the pharmacokinetic experiments. Six rats for each treatment time

TABLE 1 Particle size distribution of TRQ aerosols after nebulization using the PARI TurboBoy N nebulizer with red nozzle (n = 3).

Spraytec testing	Mean ± SD
Dv (50) (μm)	2.512 ± 0.017
Transmission (%)	74.867 ± 0.551
Span	3.504 ± 0.247
Nebulized time (s)	177.333 ± 9.452

were anesthetized at 0.083, 0.333, 1, 4, and 8 h after administration, respectively. Blood samples were collected from the abdominal aorta into heparinized tubes. The right lung was clamped, and the left lung was lavaged with 1.5 ml cold saline twice to collect bronchoalveolar lavage fluid (BALF). Subsequently, the right lung, trachea, and brain were dissected rapidly and harvested, and homogenized according to "2.4."

Anti-inflammatory effect of TRQ in mice after TI and IV

Seventy male ICR mice were randomized and divided into the normal, model, positive, IV, and low-, medium-, and high-dose groups of TI. There were 10 mice in each group. Except for the normal group, mice in the other six groups were placed in an inhalogic NIES inhalation tower (Melton Lab, Shanghai, China). A 4 mg/ml LPS solution was nebulized for 30 min using a TurboBoy N nebulizer with a red nozzle for modeling. The first intervention was immediately initiated in each group after modeling, and the second intervention was initiated 15 h thereafter. The normal and model groups were nebulized with saline for 20 min. The positive and IV groups were injected with 5.2 mg/kg dexamethasone sodium phosphate and 2.6 ml/kg TRQ (according to the ratio of body surface area of humans and mice, which was calculated from the clinical dose of TRQ, which was 0.29 ml/kg) through the tail vein, respectively. The TI groups were nebulized with TRQ for 5, 10, and 20 min through the inhalation tower. One hour after the last administration, mice in each group were sacrificed. The lungs were dissected rapidly and harvested, and rinsed thoroughly with cold saline. Subsequently, 100 mg of lung tissue was weighed and homogenized in an ice bath after adding 20× (by weight) RIPA lysis buffer. The homogenate was centrifuged at 12,000 rpm for 15 min at 4°C. The level of IL-6 in the lung homogenate was determined by using a mouse IL-6 ELISA kit with a Spectramax i3x reader (Molecular Devices, United States) at 450 nm.

Data analysis

Data acquisition and analysis for the concentration of BAI and ORO were performed using Analyst 1.7 software (AB SCIEX,

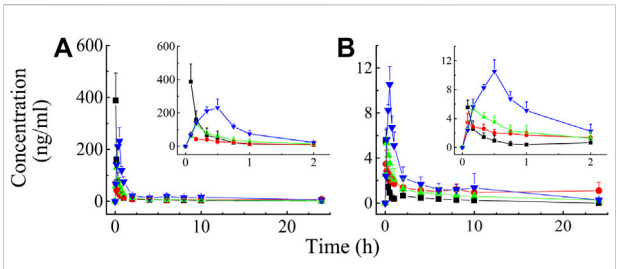

FIGURE 4
Mean rat plasma concentration-time profiles of BAI **(A)** and ORO **(B)** after IV injection at the dose of 0.03 ml/kg (—■—) and TI at the dose of 0.03 (—●—), 0.06 (—▲—), and 0.12 (—▼—) ml/kg of TRQ (n = 6). Bars represent standard deviation.

Toronto, Canada). Plasma and tissue homogenate concentrations of BAI and ORO were determined using the calibration curve of each analysis batch. Pharmacokinetic parameters were calculated using a noncompartment model with the MaS Studio 1.5.2.14 stable software (Shanghai BioGuider Medicinal Technology Co., Ltd., Shanghai, China). C_{max} and T_{max} were obtained directly from the experimental process.

Data were expressed as mean ± standard deviation (SD), with relative standard deviation (RSD). Multiple data sets were subjected to independent t-tests. $p < 0.05$ was considered to be statistically significant.

Results

Method optimization and validation

Mass spectrometry parameters of BAI, ORO, and PAE (IS) were optimized by using 100 ng/ml methanol solution of the three compounds. In the positive ion mode, the two analytes and IS were more sensitive, which made them suitable for detection in the ESI (+) mode. In ESI (+) mode, DP, CE, CXP, gas 1, gas 2, spray voltage, and curtain gas were optimized to determine the precursor ions and product ions of the three compounds. The optimized chromatographic column was a Shimadzu Shim-pack Velox SP-C18 LC column. The chromatographic separation was performed using water-methanol-acetonitrile containing 0.05% formic acid as the mobile phase system. Representative chromatograms of BAI, ORO, and IS in plasma and lung homogenates are shown in Figure 2. Under the optimized analysis conditions, the retention times of BAI, ORO, and IS were 3.93, 4.13, and 2.99 min, respectively. There were no endogenous and exogenous peaks for the same retention time of analytes and IS in the blank plasma (Figure 2A) and lung homogenate samples (Figure 2D). These results indicated that this method had good specificity and selectivity. This analytical method revealed BAI and ORO in plasma and homogenate samples had a good linear relationship. The linear range of BAI and ORO in the two matrices using $1/X^2$ weighting was 2–200 ng/ml and 1–100 ng/ml, respectively. The lower limit of quantification (LLOQ) of BAI and ORO in the two matrices was 2 ng/ml and 1 ng/ml, respectively. The intra-day and inter-day precision (RSD) and accuracy (RE) in plasma and lung homogenate samples of BAI ranged from 0.47% to 6.25% and 92.23%–114.4%, respectively. The intra-day and inter-day precision and accuracy in plasma and lung homogenate samples of ORO ranged from 0.34% to 7.63% and 90.41%–107.50%, respectively. The dilution procedure showed excellent precision (RSD < 3.74%) and accuracy (RE: 95.80–103.85%). The RSD of relative matrix effects for all analytes ranged from 1.38% to 13.07%, and the average extraction recovery was 37.81%–48.14%. The RSD values ranged from 0.79% to 10.42%, and the deviation values ranged from −13.53% to 6.78%, indicating that BAI and ORO were stable in the autosampler at 6°C for 24 h, at room temperature (25°C) for 1 h, after three freeze/thaw cycles from −80°C to room temperature, and in long-term storage at −80°C for 30 days in plasma and lung samples from rats. The detailed results of the method validation are shown in Supplementary Tables S1–S5.

TRQ aerosol characteristics

The Spraytec laser diffraction system (Malvern) was used to study changes in particle size and percentage transmission of TRQ aerosols nebulized by the PARI TurboBoy N nebulizer with a red nozzle over time, where Dv(10) and Dv(50) remained stable for 3 min, as shown in Figure 3A. The results showed that the red nozzle nebulizer produced aerosols with a uniform particle size (Figure 3B). The mean Dv(50) of the aerosols was 2.512 μm, and the percentage transmittance was 74.867% (Table 1).

Pharmacokinetics study of BAI and ORO in rats

Validated analytical methods were used to determine the rat plasma concentration of BAI and ORO after IV (0.03 ml/kg) and TI (0.03, 0.06, and 0.12 ml/kg) of TRQ. The plasma concentrations of BAI and ORO at different times after administration are shown in Supplementary Tables S6, S7, respectively. The mean plasma concentration-time profiles are shown in Figure 4.

After IV of TRQ, BAI and ORO were rapidly distributed in 20 min and slowly eliminated (Figure 4). After low, medium, and high dose TI of TRQ, BAI, and ORO were rapidly absorbed. At low, medium, and high doses, BAI and ORO reached C_{max} at 5, 10, and 30 min and were slowly eliminated (Figure 4). Plasma pharmacokinetic parameters of BAI and ORO were calculated using the noncompartment model and are shown in Table 2.

TABLE 2 PK parameters of BAI and ORO in rat plasma after IV at the dose of 0.03 ml/kg and TI at the dose of 0.03, 0.06, and 0.12 ml/kg of TRQ (n = 6, Mean ± SD).

Analytes	PK parameters	IV (ml/kg)	TI (ml/kg)		
		0.03	0.03	0.06	0.12
BAI	$T_{1/2}$ (h)	4.662 ± 0.801	7.978 ± 3.567	5.170 ± 0.657	5.492 ± 0.714
	T_{max} (h)	——	0.083 ± 0.000	0.167 ± 0.00	0.444 ± 0.086
	C_{max} (ng/ml)	387.821 ± 106.256	69.817 ± 14.582	130.466 ± 43.830	244.107 ± 47.932
	AUC_{0-t} (h·ng/mL)	230.879 ± 22.456	167.610 ± 57.845	203.747 ± 74.149	475.421 ± 70.913
	$AUC_{0-\infty}$ (h·ng/mL)	251.293 ± 19.107	257.171 ± 98.169	226.565 ± 84.421	521.204 ± 70.184
	MRT_{0-t} (h)	4.510 ± 1.271	8.118 ± 3.613	6.228 ± 0.857	6.197 ± 0.451
	$MRT_{0-\infty}$ (h)	6.638 ± 2.552	15.992 ± 7.556	8.683 ± 1.461	8.493 ± 1.480
ORO	$T_{1/2}$ (h)	4.057 ± 2.788	9.164 ± 4.043	5.441 ± 1.820	4.886 ± 1.280
	T_{max} (h)	——	0.102 ± 0.033	0.176 ± 0.00	0.500 ± 0.000
	C_{max} (ng/ml)	5.513 ± 1.016	3.512 ± 1.223	5.318 ± 0.937	10.527 ± 1.603
	AUC_{0-t} (h·ng/mL)	5.490 ± 1.307	23.287 ± 10.882	17.172 ± 7.528	32.414 ± 15.338
	$AUC_{0-\infty}$ (h·ng/mL)	7.382 ± 2.864	25.680 ± 3.547	19.217 ± 8.453	34.748 ± 15.386
	MRT_{0-t} (h)	3.031 ± 1.089	6.732 ± 2.980	6.310 ± 1.956	5.694 ± 1.613
	$MRT_{0-\infty}$ (h)	6.001 ± 5.197	14.619 ± 6.077	8.767 ± 3.040	7.299 ± 1.943

After IV injection, $T_{1/2}$ of BAI and ORO was 4.66 h and 4.06 h, and the mean residence time (MRT_{0-t}) was 4.51 h and 3.03 h, respectively. The $T_{1/2}$ of BAI (5.17–7.98 h) and ORO (4.89–9.16 h), and the MRT_{0-t} of BAI (6.20–8.12 h) and ORO (5.69–6.73 h) after TI administration were longer than after IV administration. The C_{max} of BAI (69.817, 130.466, and 244.107 ng/ml), and C_{max} of ORO (3.512, 5.318, and 10.527 ng/ml) in plasma after low, medium, and high doses TI of TRQ increased with increasing dose (Figures 5A,C). The mean area under the curve ($AUC_{0-\infty}$) of BAI (226.565 h·ng/ml) after medium dose TI of TRQ was slightly lower than that after low dose TI (257.171 h·ng/ml), but the $AUC_{0-\infty}$ showed an increasing trend with the increase of TI doses in the range of 0.03-0.12 ml/kg (Figure 5B). The mean $AUC_{0-\infty}$ of ORO (25.680, 19.217, and 34.748 h·ng/ml) in plasma after TI did not increase with increasing dose (Figure 5D). The linear relationship between pharmacokinetic parameters and dose was evaluated using confidence intervals (Wang et al., 2008). The correlation between C_{max} of BAI and ORO with doses of TI was positive, but the linear relationship was uncertain. The $AUC_{0-\infty}$ of BAI was positively correlated with doses of TI, but the relationship was nonlinear. There was no clear correlation between $AUC_{0-\infty}$ of ORO with increasing doses of TI (Table 3).

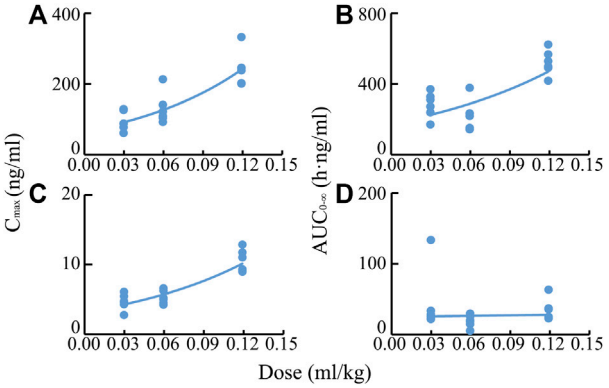

FIGURE 5
Correlations of C_{max} values of BAI **(A)** and ORO **(C)**, and $AUC_{0-\infty}$ values of BAI **(B)** and ORO **(D)** in plasma with TI doses of TRQ (0.03, 0.06, and 0.12 ml/kg).

Tissue distribution study of BAI and ORO in rats

The distribution of BAI and ORO in rat lung tissue, BALF, trachea, plasma, and brain after TI and IV administration of TRQ (0.12 ml/kg) were studied. Concentrations of BAI and ORO for biological samples at different sampling times are shown in Supplementary Tables S8, S9, respectively. The mean concentration-time profiles of BAI and ORO in the lung, BALF, trachea, and plasma are shown in Figure 6, and those of the brain are shown in Supplementary Figure S1. The exposure of BAI and ORO in rat tissue and plasma after TI and IV administration of TRQ is listed in Table 4. The pharmacokinetic parameters of BAI and ORO in the lung, BALF, trachea, plasma, and brain, calculated by noncompartmental analysis, are listed in Supplementary Table S10.

As shown in Figure 6, after TI of TRQ, BAI, and ORO are rapidly distributed to the lungs, respiratory mucus, and trachea. As the inhalation procedure was carried out, the

TABLE 3 Relationship between dose of TRQ and system exposure levels (C_{max} and $AUC_{0-\infty}$) of BAI and ORO in rats after TI (n = 6).

Analytes	PK parameters	r^2	*p value*	Slope (95%CI)	Conclusion[a]
BAI	C_{max}	0.709	1.170×10^{-5}	0.694 (0.458–0.929)	Positive correlation with dose. Uncertainty of linear relationship
	$AUC_{0-\infty}$	0.692	1.868×10^{-5}	0.600 (0.388–0.812)	Positive correlation with dose. Nonlinear correlation
ORO	C_{max}	0.341	0.011	0.459 (0.121–0.797)	Positive correlation with dose. Uncertainty of linear relationship
	$AUC_{0-\infty}$	0.002	0.864	−0.047 (−0.617–0.523)	No clear correlation with dose

[a]Dose, C_{max}, and $AUC_{0-\infty}$ were logarithmic for regression analysis. If the 95% confidence interval (95% CI) of the slope of C_{max} and $AUC_{0-\infty}$ was completely within the range of judgment interval (C_{max} 0.74–1.26, $AUC_{0-\infty}$ 0.84–1.16), C_{max} and $AUC_{0-\infty}$ were linearly correlated within the range of dose (0.03–0.12 ml/kg). If the 95% CI fell completely outside the range of the judgment interval, the correlation was nonlinear. If the 95% CI overlapped with the judgment interval, the linear relationship was uncertain.

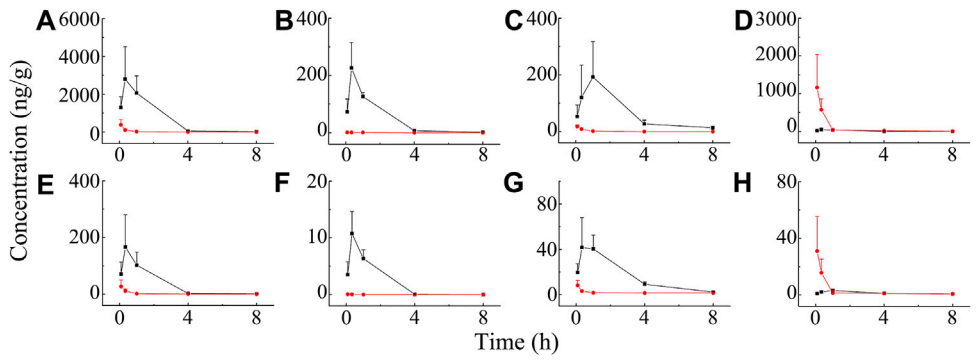

FIGURE 6
Mean concentration-time profiles of BAI in rat lung **(A)**, BALF **(B)**, trachea **(C)**, plasma **(D)**, and ORO in rat lung **(E)**; BALF **(F)**, trachea **(G)**, and plasma **(H)** after TI (—■—) and IV (—●—) of TRQ both at the dose of 0.12 ml/kg (n = 6). Bars represent standard deviation.

drug concentration gradually increased. At the end of the inhalation (20 min), the concentration slowly decreased. BAI and ORO in the lungs, BALF, and trachea were maintained at high concentrations for 4 h. However, after 4 h, the concentrations were lower than those at 0.083 h. After inhalation, the concentration of BAI in the lung (Figure 6A) was the highest. Concentrations in BALF (Figure 6B) and trachea (Figure 6C) were almost equivalent and lower than those in lung tissue. The concentration of ORO in the lung (Figure 6E) was the highest, followed by that in the trachea (Figure 6G), and was the lowest in the BALF (Figure 6F). After IV administration of TRQ, BAI, and ORO were quickly distributed to the lungs and trachea with the T_{max} of 5 min (Supplementary Table S10). Subsequently, the concentrations gradually decreased, and their concentrations were significantly lower than those after TI throughout the entire observation period (0–8 h). Only trace amounts of BAI and ORO were detected in BALF after IV administration (Figures 6B,F). It was found that after TI and IV, the two components quickly entered the brain tissue at a low concentration (Supplementary Figure S1; Supplementary Table S10). This study also investigated the permeability of BAI and ORO in the lungs after TI and IV administration of TRQ (Figure 7). The lung-to-plasma drug concentration ratio of BAI ranged from 15.5 to 102.9 at 20 min and 1 h after TI of TRQ, which was approximately 76.4–518.8 times that of the ratio (0.1–1.6) after IV administration at the same dose. The ratio of ORO ranged from 18.1 to 125.4 at 20 min and 1 h after TI of TRQ, which was approximately 6.4–165.8 times that of the ratio (0.40–2.8) after IV administration at the same dose.

Anti-inflammatory effects of TRQ

A mouse pneumonia model was established by aerosol inhalation of LPS at 4 mg/ml. The level of IL-6 in lung homogenates was used as an index to evaluate the model and the anti-inflammatory effect of TRQ (Liu et al., 2016; Rao et al., 2022). Compared to the normal group, the level of IL-6 in the lung homogenate of the model group increased significantly ($p < 0.001$). After administration of dexamethasone, the content of IL-6 in mouse lung homogenate decreased significantly ($p < 0.001$). These results indicated that LPS-induced mice models experienced acute lung injury. Compared to the model group, the content of IL-6 in the IV group (2.6 ml/kg), and in the medium and high dose groups of TI (inhalation for 10 and 20 min, respectively) decreased significantly ($p < 0.01$), as shown in Figure 8.

TABLE 4 Exposure of BAI and ORO in rat lung, BALF, trachea, brain, and plasma after TI and IV of TRQ both at the dose of 0.12 ml/kg (n = 6).

Analytes	Biological matrix	PK parameters	TI (0.12 ml/kg)[a]	IV (0.12 ml/kg)
BAI	Lung	C_{max} (ng/ml)	2796.486 (7.379) [52.468]	378.988 [0.326]
		AUC_{0-t} (h·ng/ml)	5502.070 (29.230) [37.142]	188.232 [0.296]
		$AUC_{0-\infty}$ (h·ng/ml)	5532.702 (27.970) [32.257]	197.806 [0.303]
	BALF	C_{max} (ng/ml)	226.175 (177.300) [4.243]	1.276 [0.001]
		AUC_{0-t} (h·ng/ml)	375.607 (115.318) [2.536]	3.257 [0.005]
		$AUC_{0-\infty}$ (h·ng/ml)	378.552 (91.341) [2.207]	4.144 [0.006]
	Trachea	C_{max} (ng/ml)	192.134 (10.876) [3.605]	17.666 [0.015]
		AUC_{0-t} (h·ng/ml)	535.834 (73.062) [3.617]	7.334 [0.012]
		$AUC_{0-\infty}$ (h·ng/ml)	571.582 (72.450) [3.332]	7.889 [0.012]
	Brain	C_{max} (ng/ml)	7.928 (1.078) [0.149]	7.353 [0.006]
		AUC_{0-t} (h·ng/ml)	27.86 (1.202) [0.188]	23.187 [0.037]
		$AUC_{0-\infty}$ (h·ng/ml)	57.383 (1.025) [0.335]	55.995 [0.086]
	Plasma	C_{max} (ng/ml)	53.299 (0.046)	1163.122
		AUC_{0-t} (h·ng/ml)	148.135 (0.233)	635.230
		$AUC_{0-\infty}$ (h·ng/ml)	171.518 (0.262)	653.895
ORO	Lung	C_{max} (ng/ml)	166.717 (6.112) [51.332]	27.278 [0.879]
		AUC_{0-t} (h·ng/ml)	286.940 (16.970) [22.426]	16.908 [0.821]
		$AUC_{0-\infty}$ (h·ng/ml)	288.773 (15.771) [17.345]	18.310 [0.807]
	BALF	C_{max} (ng/ml)	10.763 (166.224) [3.314]	0.065 [0.002]
		AUC_{0-t} (h·ng/ml)	17.270 (1060.761) [1.35]	0.016 [0.001]
		$AUC_{0-\infty}$ (h·ng/ml)	17.306 (1062.989) [1.04]	0.016 [0.001]
	Trachea	C_{max} (ng/ml)	41.609 (5.103) [12.811]	8.154 [0.263]
		AUC_{0-t} (h·ng/ml)	133.312 (9.552) [10.419]	13.956 [0.678]
		$AUC_{0-\infty}$ (h·ng/ml)	139.142 (5.720) [8.358]	24.327 [1.072]
	Brain	C_{max} (ng/ml)	0.641 (0.703) [0.197]	0.912 [0.029]
		AUC_{0-t} (h·ng/ml)	3.472 (0.937) [0.271]	3.704 [0.180]
		$AUC_{0-\infty}$ (h·ng/ml)	8.627 (1.604) [0.518]	5.379 [0.237]
	Plasma	C_{max} (ng/ml)	3.248 (0.105)	31.045
		AUC_{0-t} (h·ng/ml)	12.795 (0.622)	20.587
		$AUC_{0-\infty}$ (h·ng/ml)	16.648 (0.734)	22.692

[a]The values in round brackets "( )" are the ratios of the PK parameters of TI to IV. The values in square brackets "[ ]" are the ratios of the PK parameters of different tissues to those of plasma.

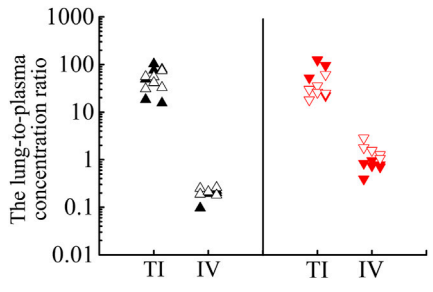

FIGURE 7
Lung-to-plasma concentration ratios of BAI at 20 min (▲) and 1 h (△), ORO at 20 min (▼) and 1 h (▽) after TI and IV of TRQ at the dose of 0.12 ml/kg.

Discussion

The TRQ injection extracted and processed from five botanical drugs has been reported to achieve curative effects in the clinical treatment of acute bronchitis, acute pneumonia, chronic obstructive pulmonary disease, and other respiratory infections. In recent years, numerous respiratory diseases have been treated by aerosol inhalation. Although aerosol inhalation administration of TRQ can reduce adverse reactions caused by IV administration, it is still an off-label drug use. For more efficient and safer clinical use, it is necessary to systematically study its inhalable properties, including component analysis, preparation process, pharmacological effects, safety evaluation,

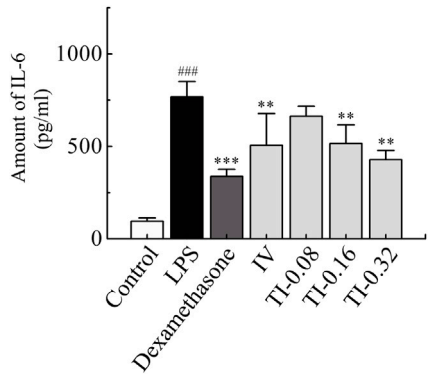

FIGURE 8
Amount of IL-6 in lung homogenate after TI (5, 10, 20 min) and IV (2.6 ml/kg) of TRQ on LPS-induced mice lung inflammation model (n = 10, mean ± SD). $^{###}p < 0.001$ vs. Control group, $^{**}p < 0.01$ and $^{***}p < 0.001$ vs. LPS group.

pharmacokinetics, and tissue distribution. This study focused on the characteristics of TRQ aerosols, the pharmacokinetics and tissue distribution, and anti-inflammatory effects after TI administration of TRQ.

Based on our preliminary experimental results, the representative flavonoids BAI and ORO in TRQ were selected as the target compounds. BAI, ORO, and IS standard solutions were used to optimize the respective precursor ions and product ions. The analytical conditions of HPLC-MS/MS for BAI and ORO were optimized. This established method has high specificity and sensitivity and can be used for the quantitative analysis of BAI and ORO in biological samples from rats.

Compared to oral administration, TI can avoid the liver first-pass effect and increase drug concentration in the bronchi and alveoli. After delivery to lung tissue, the target organ of respiratory diseases, drug ingredients are absorbed into the blood through the air–blood barrier in the lung alveoli. Subsequently, the active ingredients are distributed to various organs and tissues through blood circulation. The concentration of ingredients entering the systemic circulation after TI is markedly reduced, thus avoiding adverse reactions caused by IV administration.

The size and distribution of aerosol particles are key parameters that influence the nebulization process and the therapeutic effect. Due to the particularity of the respiratory system, aerosol particles of different sizes are deposited at different positions. Moreover, only aerosol particles with a size of 1–5 μm can enter and deposit in the bronchi and alveoli (Chrystyn, 2001; Ibrahim et al., 2015). In addition, commercial nebulizers exhibit significant differences in particle size distribution. Therefore, it is necessary to analyze the particle size and aerodynamic characteristics of aerosols generated by the nebulizer (Loffert et al., 1994; Chang et al., 2020). In this study, the mean Dv(50) of TRQ aerosol was 2.512 μm, which can facilitate the deposition of aerosol particles in the lower respiratory tract, such as the pulmonary alveoli, with good inhalable properties (Reychler et al., 2014).

Systemic adverse reactions are directly related to high systemic exposure, and adverse drug reactions can be reduced with a decrease in C_{max} (China National Medical Products Administration, 2009). After low, medium, and high doses TI of TRQ, the C_{max} of BAI in plasma was lower than that of low dose IV. After low and medium doses TI of TRQ, the C_{max} of ORO in plasma was lower than that of low dose IV. After high-dose TI, the C_{max} of ORO was higher than that of low dose IV. These results may be due to the fact that the drug ingredients after aerosol inhalation need to be absorbed by lung tissues first before entering the systemic blood circulation. It has been reported (Chen et al., 2021) that after intratracheal administration of Shuang-Huang-Lian, the C_{max} of chlorogenic acid, forsythiaside A, and BAI in rats was significantly lower than those following IV administration. After intratracheal administration lasted about 60 min, the plasma concentration decreased, similar to that observed following IV administration. Our previous studies showed that the plasma concentration of the target ingredient after TI was significantly lower than after IV administration (Zhang et al., 2019; Ding et al., 2020).

The local curative effect on respiratory diseases is directly related to the concentration of drugs in the respiratory tissues. Aerosol inhalation can target drug delivery to the lungs. Therefore, administration via inhalation has unique advantages over other routes, such as oral and IV administration, as it avoids the liver first-pass effect and allows the drug to accumulate in the lung or trachea. It compensates for the low concentration of drug components in lung tissue after oral and intravenous administration (Patton and Byron, 2007). After TI of TRQ, the exposure (C_{max} and AUC) of BAI and ORO in rat lung, BALF, and trachea (Table 4) was higher than those achieved after IV at the same dose (BAI, 7.379–177.300 times; ORO, 6.112–1062.989 times). Plasma C_{max} and AUC after TI (Table 4) were lower than those after IV (BAI, 0.046–0.262 times; ORO, 0.105–0.734 times). These results were consistent with the pharmacokinetic results. The lung absorption rate after TI was almost equivalent to that after IV, but there was a significant difference in the distribution *in vivo* after absorption. The high distribution of drug ingredients in the lungs indicated that TI administration has better lung availability than IV administration. Compounds with small molecules can be rapidly absorbed into the lung and their absorption rate depends on the lipophilicity of the drug. The T_{max} of hydrophilic compounds is within 30 min (Patton et al., 2004). The permeability of the drug in lung tissue is

expressed as the ratio of the lung drug concentration to the plasma drug concentration. The larger the ratio, the easier it is for the drug to penetrate the lungs. In contrast, the smaller the ratio, the more difficult it is for the drug to enter the lung parenchyma (Goldstein et al., 2002). As shown in Figure 7, BAI and ORO showed good lung permeability. In the anti-inflammatory study, medium and high doses TI of TRQ were approximately 1/16 and 1/8 of those achieved following IV, respectively.

Conclusion

This study showed that TRQ aerosols produced by the jet nebulizer have good aerodynamic characteristics, which is beneficial for lung deposition. Compared to IV administration, drug exposure in the rat lungs, BALF, and trachea was increased significantly and the local anti-inflammatory efficacy was better after TI administration. In conclusion, according to the analysis of pharmacokinetics, tissue distribution, and anti-inflammatory effects in animals, transnasal aerosol inhalation administration of TRQ has advantages over intravenous administration in the treatment of respiratory diseases. Further clinical studies are needed to confirm the prospects of TRQ inhalation administration.

Data availability statement

The original contributions presented in the study are included in the article/Supplementary Material; further inquiries can be directed to the corresponding authors.

Ethics statement

The animal study was reviewed and approved by the Animal Ethics Committee of the Institute of Chinese Materia Medica, China Academy of Chinese Medical Sciences.

Author contributions

T-FC, Y-HG, HL, and J-LL contributed to the experimental procedures. T-FC and LS analyzed the data, prepared all the figures, and wrote the manuscript. G-PZ, Y-FL, Z-GY, and T-FC contributed to the conception and design of the study. H-PH, BP, H-YW, and W-HC participated in the animal experiment of this study. All authors contributed to the article revision and approved the submitted version.

Funding

This research was funded by the Fundamental Research Funds for the Central Public Welfare Research Institutes (ZZ13-YQ-058 and ZXKT18004), the National Natural Science Foundation of China (82104502), and the Scientific and Technological Innovation Project of China Academy of Chinese Medical Sciences (CI2021A04615).

Conflict of interest

The authors declare that the research was conducted in the absence of any commercial or financial relationships that could be construed as a potential conflict of interest.

Publisher's note

All claims expressed in this article are solely those of the authors and do not necessarily represent those of their affiliated organizations, or those of the publisher, the editors, and the reviewers. Any product that may be evaluated in this article, or claim that may be made by its manufacturer, is not guaranteed or endorsed by the publisher.

Supplementary material

The Supplementary Material for this article can be found online at: https://www.frontiersin.org/articles/10.3389/fphar.2022.951613/full#supplementary-material

References

Chang, K. H., Moon, S. H., Yoo, S. K., Park, B. J., and Nam, K. C. (2020). Aerosol delivery of dornase alfa generated by jet and mesh nebulizers. *Pharmaceutics* 12, E721. doi:10.3390/pharmaceutics12080721

Chen, W. Y., Yang, F. F., Li, C. B., Li, W. H., Hu, J. C., Liao, Y. H., et al. (2021). Comparison of plasma and pulmonary availability of chlorogenic acid, forsythiaside A and baicalin after intratracheal and intravenous administration of shuang-huang-lian injection. *J. Ethnopharmacol.* 274, 114082. doi:10.1016/j.jep.2021.114082

China National Medical Products Administration. (2009). Adverse drug reaction information bulletin (No. 23). Available at: http://www.nmpa.gov.cn/WS04/CL2155/318838.html.

Chrystyn, H. (2001). Methods to identify drug deposition in the lungs following inhalation. *Br. J. Clin. Pharmacol.* 51, 289–299. doi:10.1046/j.1365-2125.2001.01304.x

Deng, H., and Lei, Z. B. (2017). Clinical efficacy and safety evaluation of tanreqing injection for aerosol inhalation in 1348 children with respiratory diseases. *Anti. Infect. Pharm.* 14, 750–752. doi:10.13493/j.issn.1672-7878.2017.04-009

Ding, H., Wu, S. Y., Dai, X. H., Gao, Y., Niu, Y., Fang, N., et al. (2020). Pharmacokinetic behavior of peramivir in the plasma and lungs of rats after trans-nasal aerosol inhalation and intravenous injection. *Biomed. Pharmacother.* 129, 110464. doi:10.1016/j.biopha.2020.110464

Goldstein, I., Wallet, F., Robert, J., Becquemin, M. H., Marquette, C. H., Rouby, J. J., et al. (2002). Lung tissue concentrations of nebulized amikacin during mechanical ventilation in piglets with healthy lungs. *Am. J. Respir. Crit. Care Med.* 165, 171–175. doi:10.1164/ajrccm.165.2.2107025

Han, F., Yan, L., Zhu, D. Z., Yang, S. W., Hou, J. H., Wei, X. X., et al. (2016). Research progress in clinical application of aerosol inhalation. *Chin. Hosp. Pharm. J.* 36, 2218–2222. doi:10.13286/j.cnki.chinhosppharmacyj.2016.24.21

He, Y. Q., Zhou, C. C., Deng, J. L., Wang, L., and Chen, W. S. (2021). Tanreqing inhibits LPS-induced acute lung injury *in vivo* and *in vitro* through downregulating STING signaling pathway. *Front. Pharmacol.* 12, 746964. doi:10.3389/fphar.2021.746964

Ibrahim, M., Verma, R., and Garcia-Contreras, L. (2015). Inhalation drug delivery Devices: Technology update. *Med. Devices (Auckl)* 8, 131–139. doi:10.2147/MDER.S48888

Li, C., Zang, C., Nie, Q. X., Yang, B., Zhang, B. X., Duan, S. F., et al. (2019). Simultaneous determination of seven flavonoids, two phenolic acids and two cholesterines in Tanreqing injection by UHPLC-MS/MS. *J. Pharm. Biomed. Anal.* 163, 105–112. doi:10.1016/j.jpba.2018.08.058

Li, W., Mao, B., Wang, G., Wang, L., Chang, J., Zhang, Y., et al. (2010). Effect of tanreqing injection on treatment of acute exacerbation of chronic obstructive pulmonary disease with Chinese medicine syndrome of retention of phlegm and heat in fei. *Chin. J. Integr. Med.* 16, 131–137. doi:10.1007/s11655-010-0131-y

Li, X. X., Zhuo, L., Zhang, Y., Yang, Y. H., Zhang, H., Zhan, S. Y., et al. (2019). The incidence and risk factors for adverse drug reactions related to tanreqing injection: A large population-based study in China. *Front. Pharmacol.* 10, 1523. doi:10.3389/fphar.2019.01523

Liu, H., Ding, X. F., Guo, R., Zhao, M. F., Deng, D., Hao, Y., et al. (2020). Effects and safety of tanreqing injection on viral pneumonia: A protocol for systematic review and meta-analysis. *Med. Baltim.* 99, e21808. doi:10.1097/MD.0000000000021808

Liu, W., Jiang, H. L., Cai, L. L., Yan, M., Dong, S. J., Mao, B., et al. (2016). Tanreqing injection attenuates lipopolysaccharide-induced airway inflammation through MAPK/NF-κB signaling pathways in rats model. *Evid. Based. Complement. Altern. Med.* 2016, 5292346. doi:10.1155/2016/5292346

Liu, W., Zhang, X. W., Mao, B., and Jiang, H. L. (2020). Systems pharmacology-based study of tanreqing injection in airway mucus hypersecretion. *J. Ethnopharmacol.* 249, 112425. doi:10.1016/j.jep.2019.112425

Loffert, D. T., Ikle, D., and Nelson, H. S. (1994). A comparison of commercial jet nebulizers. *Chest* 106, 1788–1792. doi:10.1378/chest.106.6.1788

Mu, L. A. (2011). *A kind of phlegm removing and heat clearing agent and preparation method thereof. China patent No ZL 2005 1 0030554.7*. (Beijing: China National Intellectural Property Administration).

Patton, J. S., and Byron, P. R. (2007). Inhaling medicines: Delivering drugs to the body through the lungs. *Nat. Rev. Drug Discov.* 6, 67–74. doi:10.1038/nrd2153

Patton, J. S., Fishburn, C. S., and Weers, J. G. (2004). The lungs as A portal of entry for systemic drug delivery. *Proc. Am. Thorac. Soc.* 1, 338–344. doi:10.1513/pats.200409-049TA

Rao, Z. L., Li, X. Y., Zhang, X., Zeng, J. S., Wang, B. J., Yang, R. C., et al. (2022). Fengreqing oral liquid exerts anti-inflammatory effects by promoting apoptosis and inhibiting PI3K/AKT and NF-κB signaling pathways. *Front. Pharmacol.* 13, 824579. doi:10.3389/fphar.2022.824579

Reychler, G., Aubriot, A. S., Depoortere, V., Jamar, F., and Liistro, G. (2014). Effect of drug targeting nebulization on lung deposition: A randomized crossover scintigraphic comparison between central and peripheral delivery. *Respir. Care* 59, 1501–1507. doi:10.4187/respcare.03068

Rivera, D., Allkin, R., Obón, C., Alcaraz, F., Verpoorte, R., Heinrich, M., et al. (2014). What is in a name? The need for accurate scientific nomenclature for plants. *J. Ethnopharmacol.* 152, 393–402. doi:10.1016/j.jep.2013.12.022

Sun, H. Q., Zheng, X. Q., and Wang, X. P. (2013). Bibliometric analysis of publications about aerosol inhalation of tanreqing injection. *Chin. J. Clin. Ration. Drug Use.* 6, 20–22. doi:10.15887/j.cnki.13-1389/r.2013.05.020

Wang, C., Chen, L., and Yang, J. (2008). Application of confidence interval in the assessment of dose proportionality. *J. China Pharm. Univ.* 39, 534–537. doi:10.1007/s11401-007-0162-7

Wang, P., Liao, X., Xie, Y. M., Chai, Y., and Li, L. H. (2016). Tanreqing injection for acute bronchitis disease: A systematic review and meta-analysis of randomized controlled trials. *Complement. Ther. Med.* 25, 143–158. doi:10.1016/j.ctim.2016.02.008

Wang, Y., Fan, L. P., Song, J., Cai, Y. P., Jiang, T. T., Wang, Y. G., et al. (2018). Retrospective analysis and discussion on 74 cases of adverse reactions of traditional Chinese medicine injection. *Chin. J. Chin. Mat. Med.* 43, 4347–4351. doi:10.19540/j.cnki.cjcmm.20180815.004

Wang, Y., Wang, T., Hu, J. J., Ren, C. Y., Lei, H. T., Hou, Y. M., et al. (2011). Anti-biofilm activity of TanReQing, A traditional Chinese medicine used for the treatment of acute pneumonia. *J. Ethnopharmacol.* 134, 165–170. doi:10.1016/j.jep.2010.11.066

Xie, L. K., Wang, Y. Y., Yin, H., Li, J. J., Xu, Z., Sun, Z. L., et al. (2021). Identification of the absorbed ingredients and metabolites in rats after an intravenous administration of tanreqing injection using high-performance liquid chromatography coupled with quadrupole time-of-flight mass spectrometry. *J. Sep. Sci.* 44, 2097–2112. doi:10.1002/jssc.202000898

Zhang, G. P., Li, Y. F., Chen, T. F., Gao, Y. H., Sun, J., Yang, W., et al. (2019). Comparative study of the efficacy and pharmacokinetics of reduning injection and atomization inhalation. *Biomed. Pharmacother.* 118, 109226. doi:10.1016/j.biopha.2019.109226

Zhang, T. Y., Liu, M. J., Gao, Y. H., Li, H., Song, L., Hou, H. P., et al. (2021). Salvianolic acid B inhalation solution enhances antifibrotic and anticoagulant effects in a rat model of pulmonary fibrosis. *Biomed. Pharmacother.* 138, 111475. doi:10.1016/j.biopha.2021.111475

Zhong, Y. Q., Mao, B., Wang, G., Fan, T., Liu, X. M., Diao, X., et al. (2010). Tanreqing injection combined with conventional western medicine for acute exacerbations of chronic obstructive pulmonary disease: A systematic review. *J. Altern. Complement. Med.* 16, 1309–1319. doi:10.1089/acm.2009.0686

frontiers | Frontiers in Pharmacology

TYPE Original Research
PUBLISHED 29 August 2022
DOI 10.3389/fphar.2022.974578

OPEN ACCESS

EDITED BY
Michael Heinrich,
University College London,
United Kingdom

REVIEWED BY
Xin Wang,
East China Normal University, China
Ying-yuan Lu,
Peking University, China

*CORRESPONDENCE
Guangbo Ge,
geguangbo@shutcm.edu.cn
Wei Liu,
lwhzayl@shutcm.edu.cn
Yan Han,
hanyan@shutcm.edu.cn

SPECIALTY SECTION
This article was submitted to Ethnopharmacology, a section of the journal Frontiers in Pharmacology

RECEIVED 21 June 2022
ACCEPTED 28 July 2022
PUBLISHED 29 August 2022

CITATION
Zhang F, Zhang T, Gong J, Fang Q, Qi S, Li M, Han Y, Liu W and Ge G (2022), The Chinese herb Styrax triggers pharmacokinetic herb-drug interactions via inhibiting intestinal CYP3A.
Front. Pharmacol. 13:974578.
doi: 10.3389/fphar.2022.974578

The Chinese herb Styrax triggers pharmacokinetic herb-drug interactions *via* inhibiting intestinal CYP3A

Feng Zhang[1,2], Tiantian Zhang[3], Jiahao Gong[2], Qinqin Fang[4], Shenglan Qi[1,4], Mengting Li[1], Yan Han[1]*, Wei Liu[4]* and Guangbo Ge[2]*

[1]Department of Neurology, Yueyang Hospital of Integrated Traditional Chinese and Western Medicine, Shanghai University of Traditional Chinese Medicine, Shanghai, China, [2]Shanghai Frontiers Science Center of TCM Chemical Biology, Institute of Interdisciplinary Integrative Medicine Research, Shanghai University of Traditional Chinese Medicine, Shanghai, China, [3]School of Pharmacy, Zunyi Medical University, Zunyi, China, [4]Key Laboratory of Liver and Kidney Diseases (Ministry of Education), Institute of Liver Diseases, Shanghai Key Laboratory of Traditional Chinese Clinical Medicine, Shuguang Hospital Affiliated to Shanghai University of Traditional Chinese Medicine, Shanghai, China

Human cytochrome P450 3A4 (hCYP3A4) is a predominant enzyme to trigger clinically relevant drug/herb-drug interactions (DDIs or HDIs). Although a number of herbal medicines have been found with strong anti-hCYP3A4 effects *in vitro*, the *in vivo* modulatory effects of herbal medicines on hCYP3A4 and their potential risks to trigger HDIs are rarely investigated. Herein, we demonstrate a case study to efficiently find the herbal medicine(s) with potent hCYP3A4 inhibition *in vitro* and to accurately assess the potential HDIs risk *in vivo*. Following screening over 100 herbal medicines, the Chinese herb Styrax was found with the most potent hCYP3A4 inhibition in HLMs. *In vitro* assays demonstrated that Styrax could potently inhibit mammalian CYP3A in liver and intestinal microsomes from both humans and rats. *In vivo* pharmacokinetic assays showed that Styrax (i.g., 100 mg/kg) significantly elevated the plasma exposure of two CYP3A-substrate drugs (midazolam and felodipine) when midazolam or felodipine was administered orally. By contrast, the plasma exposure of either midazolam or felodipine was hardly affected by Styrax (i.g.) when the victim drug was administered intravenously. Further investigations demonstrated that seven pentacyclic triterpenoid acids (PTAs) in Styrax were key substances responsible for CYP3A inhibition, while these PTAs could be exposed to intestinal tract at relatively high exposure levels but their exposure levels in rat plasma and liver were

Abbreviations: AUC, area under the plasma concentration; CMC-Na, sodium carboxymethyl cellulose; CYPs/P450s, cytochrome P450 enzymes; DDIs, drug-drug interactions; DMEs, drug-metabolizing enzymes; ESI, electrospray ionization; G-6-P, D-Glucose-6-phosphate; G-6-PDH, glucose-6-phosphate dehydrogenase; HDIs, herb-drug interactions; hCYP3A4, human cytochrome P450 3A4; HIMs, human intestine microsomes; HLMs, human liver microsomes; IC50, half maximal inhibition concentration; IS, internal standard; i.v., intravenous; i.g., intragastrical; MRM, multiple reaction monitoring; NEN, N-ethyl-1,8-naphthalimide; NEHN, N-ethyl-4-hydroxyl-1,8-naphthalimide; PBS, potassium phosphate buffer; PTAs, pentacyclic triterpenoid acids; RIMs, rat intestine microsomes; RLMs, rat liver microsomes; SHUTCM, Shanghai University of Traditional Chinese Medicine; $t_{1/2}$, half-life; TICs, total ion chromatograms.

extremely low. These findings well explained why Styrax (i.g.) could elevate the plasma exposure of victim drugs only when these agents were orally administrated. Collectively, our findings demonstrate that Styrax can modulate the pharmacokinetic behavior of CYP3A-substrate drugs *via* inhibiting intestinal CYP3A, which is very helpful for the clinical pharmacologists to better assess the HDIs triggered by Styrax or Styrax-related herbal products.

KEYWORDS

herb-drug interactions (HDIs), styrax, pentacyclic triterpenoid acids (PTAs), intestinal CYP3A, CYP3A-substrate drugs

Introduction

The concomitant use of herbal medicines and Western medicines is widely used in clinical settings for curing various diseases including digestive diseases, cardiovascular and cerebrovascular diseases, infectious diseases, especially in China and other Asia countries (Zhang and Xu, 2012; Su and Geng, 2016; Xu et al., 2017; Qiu et al., 2020). However, the herb-drug interactions (HDIs) caused by the concomitant use of herbal medicines and Western medicines cannot be ignored (Gouws et al., 2012; Fasinu et al., 2015; Gallo et al., 2019; Parvez and Rishi, 2019). A number of studies have shown that cytochrome P450 3A4 (CYP3A4, mainly expressed in liver and small intestine, Supplementary Figure S1, https://www.proteinatlas.org/search/CYP3A4) plays a crucial role in the metabolism and detoxification of a wide range of Western medicines *in vivo*, thus acts as a key mediator in herb-drug interactions (HDIs) and drug-drug interactions (DDIs) (Galetin et al., 2007; Zhou, 2008; Tian and Hu, 2014). It has been reported that a wide range of herbal medicines can regulate the pharmacokinetic behavior of some important CYP3A-substrate drugs (especially for those drugs with very narrow therapeutic windows) by inhibiting or inactivating CYP3A, which may trigger clinically significant HDIs and adverse drug reactions (Zhou et al., 2019; Zhang F. et al., 2021; Zhang F. et al., 2022). Therefore, it is urgent and necessary to accurately assess the inhibitory effects of herbal medicines against human CYP3A, and to precisely evaluate the potential risks of herbal medicines to trigger clinically relevant HDIs when they are concomitantly used with CYP3A-substrate drugs.

Recently, our group and colleagues developed a novel fluorescence-based high-throughput assay for assessing the inhibitory effects of compounds/herbal extracts on human CYP3A4, which offers a powerful platform for investigating CYP3A4-related HDIs or DDIs (Ning et al., 2019; Wu et al., 2021; Jin et al., 2022; Tu et al., 2022). With the help of fluorescence-based high-throughput CYP3A4 inhibition assays, the inhibitory effects of more than 100 herbal medicines against hCYP3A4 were assessed in human liver preparations. The results clearly showed that the Chinese herb Styrax (a herbal medicine used for treating

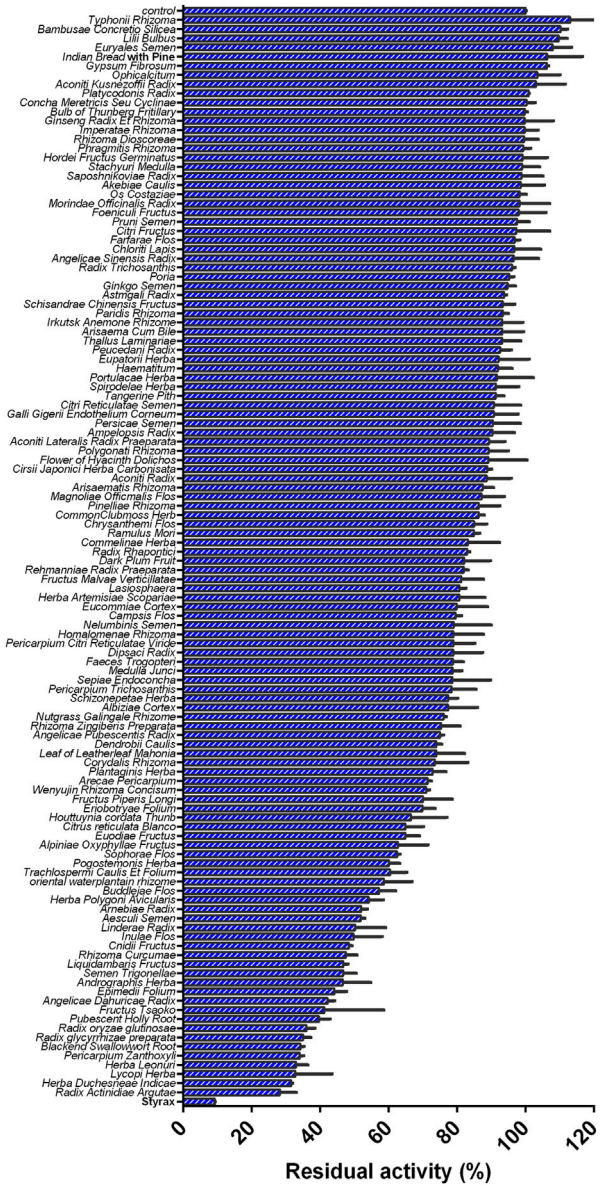

FIGURE 1
Inhibition effects of 119 Chinese medicine granules/Chinese medicines (100 μg/ml, final concentration) against CYP3A4-catalyzed NEN 4-hydroxylation in HLMs.

cardiovascular diseases) displayed the most potent inhibitory effect against hCYP3A4 (Figure 1). Notably, Styrax is often used as a key material for preparing some marketed herbal products (such as Suhexiang Pill, Shexiang Baoxin Pill, Subing Dropping Pill, Guanxin Suhe Pill, Shixiang fansheng Pill), owing to the high safety profiles and beneficial effects of this herb in preventing and treating cardiovascular diseases (Bian and Zhang, 2016; Guo et al., 2021). In Asia countries, Styrax and Styrax-related herbal products are frequently used in combination with a panel of marketed cardiovascular drugs (such as warfarin, digoxin and simvastatin) to treat cardiovascular diseases (Zhu, 2009; Tao et al., 2016; Yang et al., 2021). As an important ester spice, Styrax is also used for making a variety of foods (Yu, 2021). Since Styrax is widely used as a key material for making Chinese medicines or foods, the HDIs between this herb and co-administrated Western drugs should be carefully investigated.

The major constituents in Styrax have been reported, in which cinnamic acids, phenylpropanoids and pentacyclic triterpenoid acids (PTAs) are major constituents in this herb, while the PTAs in Styrax are reported as naturally occurring CYP3A inhibitors (Zhang et al., 2020). However, the oral bioavailabilities and plasma exposure of PTAs are extremely low (Wang et al., 2020; Ban et al., 2021; Zhang Y. W. et al., 2021; Ren et al., 2021), and it is not clear whether oral administration of Styrax can inhibit intestinal CYP3A or hepatic CYP3A in living systems and then modulate the pharmacokinetic behavior of CYP3A-substrate drugs *in vivo*. Therefore, this study aims to solve two key questions: 1) Can Styrax change the pharmacokinetic behavior of co-administrated CYP3A-substrate drugs and trigger HDIs *in vivo*; 2) Styrax triggers clinically relevant HDIs *via* inhibiting either hepatic CYP3A4 or intestinal CYP3A4 or both.

To better solve these two questions, two CYP3A-substrate drugs (midazolam and felodipine) were selected as victim drugs in this work, while two administrated ways (oral and intravenous) were used to study the pharmacokinetic interactions between Styrax and two CYP3A-substrate drugs (midazolam and felodipine). Briefly, the inhibitory effects of Styrax against CYP3A-catalyzed midazolam 1′-hydroxylation were carefully assessed in liver and intestinal microsomes from both humans and rats. After then, the pharmacokinetic interactions between Styrax (oral) and CYP3A-substrate drugs (midazolam and felodipine) by two administrated ways (oral and intravenous) were assessed in rats. Furthermore, the inhibitory effects of the PTAs in Styrax on CYP3A were assessed, while the tissue distributions of seven major PTAs in Styrax (the key substances responsible for CYP3A inhibition) were investigated carefully.

Materials and methods

Chemicals and reagents

The standard extract of Styrax was acquired by Shanghai Hutchison Pharmaceuticals (Shanghai, China). More than 100 herbal medicines granules were provided by Jiangyin Tianjiang Pharmaceutical Co., Ltd. (Wuxi, Jiangsu, China). Lansoprazole was provided by Hairong (Dujiangyan, Sichuan, China). D-glucose-6-phosphate (G-6-P), glucose-6-phosphate dehydrogenase (G-6-PDH) and β-$NADP^+$ were purchased from Sigma-Aldrich (St. Louis, MO, United States). $MgCl_2$, 0.9% NaCl, and sodium carboxymethyl cellulose (CMC-Na) were provided by Sinopharm Chemical Reagent (Shanghai, China). The soybean oil was supplied by COFCO Fulinmen Food Marketing Co., Ltd. (China). Midazolam was from J&K Scientific (Shanghai, China). 1′-Hydroxymidazolam was provided by Shanghai Macklin Biochemical Co., Ltd. (Shanghai, China). Felodipine was purchased from Shanghai Yuanye Biotechnology Co., Ltd. (Shanghai, China). Osalmide was ordered from Meilun Bio. Tech (Dalian, China). N-ethyl-1,8-naphthalimide (NEN) and N-ethyl-4-hydroxyl-1,8-naphthalimide (NEHN) were synthesized by using the previously reported protocol (Ning et al., 2019). Betulinic acid, epibetulinic acid, betulonic acid, oleanonic acid, oleanolic acid, maslinic acid and corosolic acid were supplied by Shanghai Standard Technology Co., Ltd. (Shanghai, China). The pooled HLMs (Lot No. H0610), pooled HIMs (Lot No. H0610.I), pooled RIMs (Lot No. R1000.I) were obtained from XenoTech (United States). The pooled RLMs (Lot No. LM-DS-02M) was ordered from Research Institute for Liver Diseases (RILD, Shanghai, China). BCA Protein Quantification Kit was acquired by Thermo Fisher Scientific Co., Ltd. Ultrapure water purified by Milli-Q® Integral Water Purification System (Millipore, United States) was used throughout. LC grade methanol, acetonitrile and formic acid were supplied by Fisher Scientific Co., Ltd. (Fair Lawn, NJ, United States). Other reagents were of the highest grade commercially available. The purities of all compounds used in this study were greater than 98%.

CYP3A inhibition assays

Inhibition of CYP3A4-catalyzed NEN 4-hydroxylation by herbal medicines or natural constituents

The inhibitory effects of more than 100 herbal medicines against CYP3A4 were assayed by using a previously reported fluorescence-based biochemical assay (Ning et al., 2019; Tu et al., 2022). In brief, PBS (pH 7.4, 100 mM), herbal medicines (100 μg/ml, final concentration)/PTAs/solvent, NEN, G-6-P, G-6-PDH, $MgCl_2$, and HLMs were added to the 96-well plate in turn, then the samples were vortexed and pre-incubated for 3 min at 37 °C.

The oxidative reactions were initiated by adding β-NADP$^+$ to yield a final volume of 200 μl, then the formation rates of NEHN (hydroxylated metabolite of NEN) were continuously monitored for 30 min at 37 °C using a 96-well fluorescence microplate reader (SpectraMax® iD3, Molecular Devices, Austria). The percentage of organic solvent in all incubation is not over 1%. Please refer to the supplementary material (Supplementary Table S1) for detailed experimental conditions.

Inhibition of CYP3A-catalyzed midazolam 1′-hydroxylation by Styrax or its constituents

The inhibitory effects of Styrax or its constituents against CYP3A were assayed by using midazolam as the substrate (Lee et al., 2013; Dunkoksung et al., 2019; Fang et al., 2020; Tu et al., 2020). Briefly, PBS (pH 7.4, 100 mM), Styrax/PTAs/solvent, midazolam, G-6-P, G-6-PDH, $MgCl_2$, and enzyme sources (HLMs/RLMs/HIMs/RIMs, 0.1 mg/ml, final concentrations) were added to the EP tube in turn and vortexed, then the samples were pre-incubated for 3 min at 37 °C. Next, the reactions were initiated by adding β-NADP$^+$ to yield a final volume of 200 μl. Following incubation for 30 min at 37 °C, and 200 μl ice-cold acetonitrile containing internal standard (IS, 90 ng/ml) was subsequently added to quench the oxidative reaction. The mixture was then centrifuged at 20,000 ×g, 4 °C for 20 min, and the supernatant was quantified by LC-MS/MS analysis as described in Supplementary Table S2.

Pharmacokinetic studies

Sprague-Dawley rats (weighing 200–220 g) were purchased from Shanghai Xipuer-Bikai Experimental Animal Co., Ltd. (Shanghai, China, Permit Number: SCXK (Hu) 2018-0006). The animal experiments were carried out in Experimental Animal Center of Shanghai University of Traditional Chinese Medicine (Approval Number: PZSHUTCM210709016) and conducted in accordance with the State Committee of Science and Technology of China. In brief, forty male rats were housed under controlled environmental conditions (22 ± 2°C; 40%–80% relative humidity; 12 h light/dark cycle) for 1 week with free access to food and water. The rats were fasted overnight before dosing but were free to drink water, and provided food after finishing the study. Styrax was suspended in soybean oil. Oral midazolam/felodipine was suspended in 0.5% CMC-Na, and intravenous midazolam/felodipine was suspended in 0.9% NaCl. Styrax or soybean oil was administered orally at a dose of 100 mg/kg. The oral dose of midazolam is 20 mg/kg and the intravenous dose is 5 mg/kg. The oral dose of felodipine is 10 mg/kg and the intravenous dose is 2 mg/kg. The dose of Styrax in rats was referred to the daily recommended oral dose in humans. The dose of midazolam and felodipine in rats was referred to the doses in published literature (Lundahl et al., 1997; Kotegawa et al., 2002; Li et al., 2010; Surya Sandeep et al., 2014). Forty rats were randomly divided into eight groups.

group 1: Styrax + midazolam (oral);
group 2: soybean oil + midazolam (oral);
group 3: Styrax + midazolam (intravenous);
group 4: soybean oil + midazolam (intravenous);
group 5: Styrax + felodipine (oral);
group 6: soybean oil + felodipine (oral);
group 7: Styrax + felodipine (intravenous);
group 8: soybean oil + felodipine (intravenous);

Styrax (100 mg/kg, experiment group) or soybean oil (100 mg/kg, control group) was administered orally. After 30 min, midazolam/felodipine was administered orally and intravenously. For oral midazolam groups, blood samples were collected at 5, 10, 20, 30, 60 min, 2, 3, 4, 6, 9 h. For intravenous midazolam groups, blood samples were collected at 2, 5, 10, 20, 30, 60 min, 2, 3, 4, 6, 9 h. For oral felodipine groups, blood samples were collected at 10, 30, 60 min, 3, 4, 6, 8, 10, 24 h. For intravenous felodipine groups, blood samples were collected at 2, 5, 10, 15, 30, 45, 60 min, 4, 6, 10 h. Then blood samples were centrifuged at 8,000 rpm, 4 °C for 10 min, the supernatant was stored at −80 °C until analysis (Li et al., 2010; Xue et al., 2011; Kallem et al., 2013; Xiang et al., 2017). 50 μl plasma was mixed with 50 μl ultrapure water and 300 μl acetonitrile (containing 50 ng/ml IS). The mixture was vortexed for 1 min and then centrifuged at 10,000 × g, 4 °C for 10 min. The supernatant (320 μl) was dried by nitrogen and dissolved with 80 μl of 10% acetonitrile. The supernatant (5 μl) was injected for UHPLC-Q-Orbitrap HRMS analysis (Mass spectrometry parameters were described in Supplementary Figure S2,S3 & Supplementary Table S3,S4). Both midazolam and felodipine were quantified within the linear range of their calibration curves. The pharmacokinetic parameters of midazolam, felodipine were fitted by standard noncompartmental analyses using PKSolver.

Tissue distribution of PTAs of Styrax in rats

Animal handling and sampling

Nine Male Sprague-Dawley rats (250–300 g) were purchased from Shanghai Sippe-Bk Lab Animal Co., Ltd. (Shanghai, China) and were fed in Experimental Animal Center of SHUTCM. All animals were housed under controlled environmental conditions (22 ± 2°C; 40%–80% relative humidity; 12 h light/dark cycle) for 1 week with free access to food and water. The rats were fasted overnight before dosing but were free to drink water. Nine rats were randomly divided into three groups (1, 2, and 4 h). Styrax (100 mg/kg) was administered orally, then nine rats were anesthetized by pentobarbital after administrating 1, 2, and 4 h, respectively. Blood samples were collected from the abdominal aorta, and the

tissues (including the liver, duodenum, jejunum, ileum and colon) were removed rapidly and placed on ice. After then, the blood samples were centrifuged at 8,000 rpm, 4 °C for 10 min, and the supernatant was stored at −80 °C until analysis.

Determination of PTAs in rat tissues

Firstly, each tissue (such as liver, duodenum, jejunum, ileum, colon) was accurately weighed after sucking the water on tissue surface. Each tissue was put into an EP tube and then cut (3-5 times) by a scissor. After then, PBS (pH 7.4) and magnetic beads were added into EP tube, grind the tissue by a tissue grinder. The tissue grinding fluid was centrifuged at 9,000 g, 4 °C for 20 min. 50 μl tissue supernatant was diluted by adding 250 μl LC grade acetonitrile. The protein was precipitated by centrifuging at 20,000 ×g, 4 °C for 30 min and the supernatant was collected to determine the protein concentration by a BCA Protein Quantification Kit. After then, the concentrations of seven PTAs were determined by using UHPLC-Q-Orbitrap HRMS analysis. Mass spectrometry parameters were described in Supplementary Figure S4 & Supplementary Table S5.

Data analysis

The dose-inhibition curves of Styrax/PTAs against CYP3A were depicted by using different dosages of Styrax/PTAs, while the half maximal inhibition concentration (IC_{50}) was determined as the concentration of Styrax/PTAs at the catalytic activity of CYP3A was inhibited by 50% compared to the negative control (solvent only). In this study, all assays were tested in triplicate, while the data were shown as mean ± standard deviation (SD). IC_{50} values were fitted by GraphPad Prism 6.0 (GraphPad Software, Inc., La Jolla, United States). Meanwhile, the following formula was used to calculate the residual activities of CYP3A:

The residual activity (%) = (the Peak Area or Fluorescence value of the metabolite in the presence of inhibitor)/the Peak Area or Fluorescence value of the metabolite in negative control (solvent only) × 100%.

Results

Screening of the herbal medicines with potent CYP3A4 inhibition

Firstly, with the help of fluorescence-based high-throughput CYP3A4 inhibition assay, the inhibitory potentials of more than 100 herbal medicines against CYP3A4-catalyzed NEN 4-hydroxylation were assayed in HLMs by using a single dose (100 μg/ml, final concentration). As shown in Figure 1 and Supplementary Table S6, all tested herbal medicines showed different inhibitory effects on CYP3A4-catalyzed NEN 4-hydroxylation in HLMs. Among all the tested herbal medicines, the Chinese herb Styrax was found with the most potent hCYP3A4 inhibition in HLMs. At the dose of 100 μg/ml, Styrax inhibited CYP3A4-catalyzed NEN 4-hydroxylation near completely, with the residual activity of 9.25%. By contrast, other herbal medicines displayed relatively weak inhibitory effects on hCYP3A4 at the same dose. These findings clearly demonstrate that the Chinese herb Styrax displays strong CYP3A4 inhibition potency, which may interact with CYP3A4-substrate drugs to trigger HDIs in living systems.

Inhibitory effects of Styrax against midazolam 1′-hydroxylation

Next, the inhibitory effects of Styrax against mammalian CYP3A were validated by using a substrate-drug (midazolam) in different tissue preparations. To this end, the inhibitory effects of Styrax against CYP3A-catalyzed midazolam 1′-hydroxylation were carefully investigated in different enzyme sources including HLMs, HIMs, RLMs, and RIMs. As shown in Figure 2 and Supplementary Table S7, Styrax could potently inhibit CYP3A-catalyzed midazolam 1′-hydroxylation, with IC_{50} values of 3.72 μg/ml, 2.84 μg/ml, 2.90 μg/ml and 1.67 μg/ml, for HLMs, HIMs, RLMs, RIMs, respectively. These findings demonstrated that Styrax could potently inhibit mammalian CYP3A in liver and intestinal microsomes from both human and rat *in vitro*, with similar inhibition tendency and potency. However, it is still unclear that Styrax can inhibit hepatic CYP3A or intestinal CYP3A *in vivo*. Therefore, the *in vivo* pharmacokinetic interactions between Styrax and midazolam were carefully investigated by using two administrated ways (i.v. and i.g.).

Pharmacokinetic interactions between Styrax and midazolam by i.v. and i.g.

Next, the *in vivo* effects of Styrax on the pharmacokinetics of midazolam (i.v. and i.g.) were carefully investigated in rats, by using soybean oil (without Styrax) as control groups. The blood concentration-time profiles of midazolam with two administrated ways (oral and intravenous) were shown in Figure 3 and the pharmacokinetic parameters were detailed in Table 1. Interestingly, the plasma exposure of midazolam was hardly affected by Styrax when midazolam was administered intravenously in combination with Styrax (i.g.) to rats. By contrast, when midazolam (i.g.) was co-administered orally with Styrax (i.g.) to rats, the pharmacokinetic behavior of midazolam was significantly changed compared with the control group (soybean oil instead of Styrax). The $AUC_{(0\text{-inf})}$ of midazolam (i.g.) was increased 2.04-fold (from 211.23 ng/mL·h

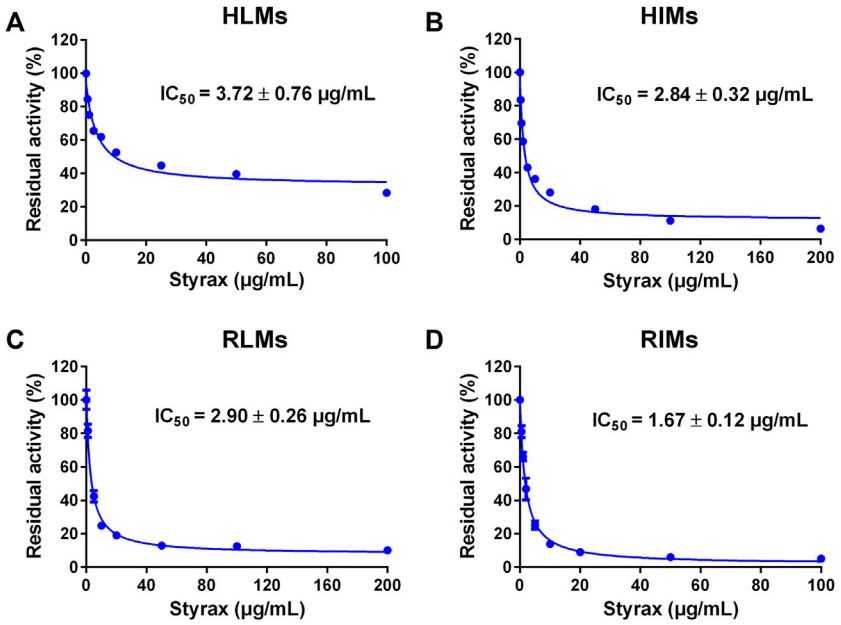

FIGURE 2
(A) Dose-inhibition curve of Styrax extract towards midazolam 1′-hydroxylation in HLMs. **(B)** Dose-inhibition curve of Styrax extract towards midazolam 1′-hydroxylation in HIMs. **(C)** Dose-inhibition curve of Styrax extract towards midazolam 1′-hydroxylation in RLMs. **(D)** Dose-inhibition curve of Styrax extract towards midazolam 1′-hydroxylation in RIMs. Data are expressed as mean ± SD.

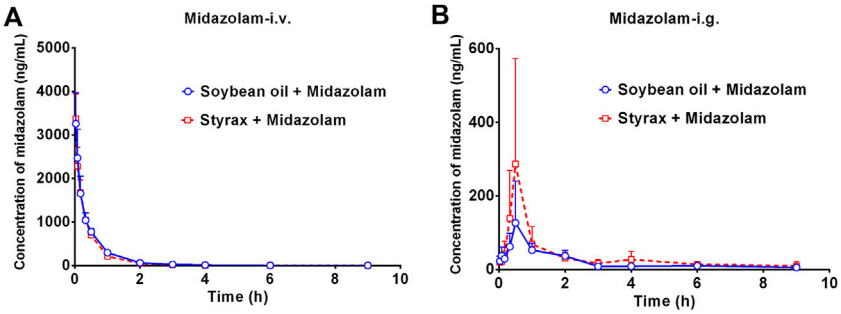

FIGURE 3
(A) The mean plasma concentration-time curves of midazolam after intravenous administration of midazolam (5 mg/kg) in rats pretreated with Soybean oil (blue) or Styrax (i.g. 100 mg/kg, red). **(B)** The mean plasma concentration-time curves of midazolam after intragastric administration of midazolam (20 mg/kg) in rats pretreated with (blue) or Styrax (i.g. 100 mg/kg, red). Data are expressed as the mean ± SD.

to 431.20 ng/mL·h), while the C_{max} value of midazolam (i.g.) in rats plasma was increased 2.28-fold (from 129.16 ng/ml to 294.05 ng/ml). Moreover, the metabolic half-life ($t_{1/2}$) of midazolam (i.g.) was prolonged 2.11-fold (from 2.14 to 4.52 h). These findings clearly suggested that Styrax strongly elevated the plasma exposure of midazolam when midazolam was co-administered orally. Considering that both intestinal CYP3A and hepatic CYP3A participate in midazolam metabolism when this agent is administrated orally, while Styrax (i.g.) cannot influence hepatic metabolism of midazolam, suggesting that Styrax may modulate the *in vivo* pharmacokinetic behavior of midazolam (i.g.) *via* inhibiting intestinal CYP3A but not hepatic CYP3A.

Pharmacokinetic interactions between Styrax and felodipine by i.v. and i.g.

To further confirm that Styrax could influence the pharmacokinetic behavior of orally administrated agent, felodipine

TABLE 1 Pharmacokinetic parameters of midazolam after administrating midazolam (i.v., 5 mg/kg; i.g., 20 mg/kg) in rats pretreated with Soybean oil, Styrax (100 mg/kg). Data are the mean ± SD.

Route of administration	Group	$AUC_{(0\text{-}inf)}$ (ng/mL·h)	C_{max} (ng/ml)	$t_{1/2}$ (h)	T_{max} (h)
Midazolam (i.v.)	Soybean oil + midazolam	1324.24 ± 130.11	3258.43 ± 708.33	0.88 ± 0.28	0.03 ± 0.00
	Styrax + midazolam	1201.37 ± 114.05	3371.29 ± 569.54	0.52 ± 0.14	0.03 ± 0.00
	Ratio	0.91	1.03	0.59	1.00
Midazolam (i.g.)	Soybean oil + midazolam	211.23 ± 87.21	129.16 ± 110.80	2.14 ± 0.28	0.63 ± 0.25
	Styrax + midazolam	431.20 ± 217.14	294.05 ± 277.47	4.52 ± 3.96	0.63 ± 0.25
	Ratio	2.04	2.28	2.11	1.00

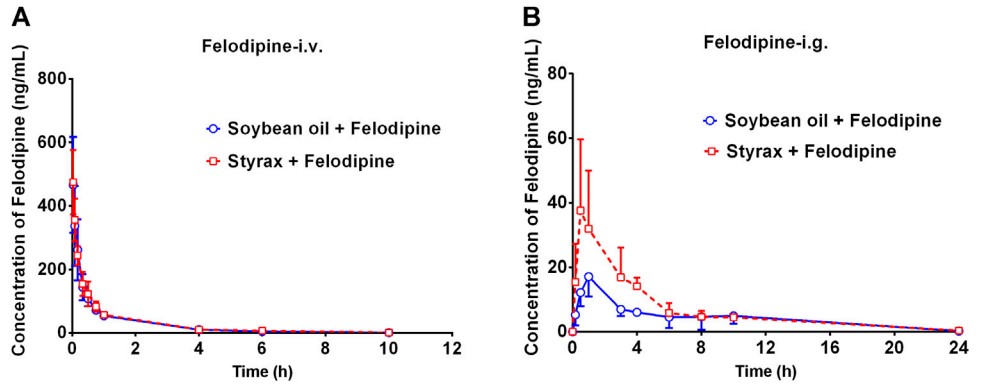

FIGURE 4
(A) The mean plasma concentration-time curves of felodipine after intravenous administration of felodipine (2 mg/kg) in rats pretreated with Soybean oil (blue) or Styrax (i.g. 100 mg/kg, red). **(B)** The mean plasma concentration-time curves of felodipine after intragastric administration of felodipine (10 mg/kg) in rats pretreated with (blue) or Styrax (i.g. 100 mg/kg, red). Data are expressed as the mean ± SD.

TABLE 2 Pharmacokinetic parameters of felodipine after administrating felodipine (i.v., 2 mg/kg; i.g., 10 mg/kg) in rats pretreated with Soybean oil, Styrax (100 mg/kg). Data are the mean ± SD.

Route of administration	Group	$AUC_{(0\text{-}inf)}$ (ng/mL·h)	C_{max} (ng/ml)	$t_{1/2}$ (h)	T_{max} (h)
Felodipine (i.v.)	Soybean oil + felodipine	274.51 ± 51.21	466.24 ± 151.20	1.41 ± 0.41	0.03 ± 0.00
	Styrax + felodipine	294.99 ± 34.21	474.57 ± 101.10	1.44 ± 0.31	0.03 ± 0.00
	Ratio	1.07	1.02	1.02	1.00
Felodipine (i.g.)	Soybean oil + felodipine	111.72 ± 18.92	17.40 ± 5.86	4.83 ± 3.05	1.30 ± 0.97
	Styrax + felodipine	156.98 ± 44.70	37.58 ± 22.16	3.81 ± 1.99	0.50 ± 0.00
	Ratio	1.41	2.16	0.79	0.38

(an orally administrated CYP3A-substrate drug) was used as a victim drug to assess the pharmacokinetic interactions between Styrax (i.g., 100 mg/kg) and felodipine *via* two administrated ways (i.v. and i.g.). As shown in Figure 4A and Table 2, when felodipine was administered intravenously in rats, Styrax displayed negligible effect on the pharmacokinetic parameters of felodipine. Notably, as shown in Figure 4B and Table 2, compared with the control group (soybean oil instead of Styrax), Styrax significantly increased the values of $AUC_{(0\text{-}inf)}$ (1.41-fold, from 111.72 ng/mL·h to 156.98 ng/mL·h) and C_{max} (2.16-fold, from 17.40 ng/ml to 37.58 ng/ml) of felodipine when felodipine was administered orally in combination with Styrax (i.g.) in rats. These findings further suggest that Styrax

TABLE 3 Inhibitory effects of pentacyclic triterpenoid acids on CYP3A in HLMs. Data are the mean ± SD.

Probe reaction	Compounds	Target enzyme	IC_{50} (μM)
Midazolam 1′-hydroxylation	maslinic acid	HLMs	19.39 ± 3.04
	corosolic acid	HLMs	32.20 ± 5.63
	oleanolic acid	HLMs	14.83 ± 2.34
	betulinic acid	HLMs	7.74 ± 0.95
	epibetulinic acid	HLMs	0.64 ± 0.10
	betulonic acid	HLMs	2.51 ± 0.34
	oleanonic acid	HLMs	0.99 ± 0.09
NEN 4-hydroxylation	maslinic acid	HLMs	3.44 ± 0.77
	corosolic acid	HLMs	41.93 ± 11.69
	oleanolic acid	HLMs	1.10 ± 0.27
	betulinic acid	HLMs	4.11 ± 0.80
	epibetulinic acid	HLMs	0.47 ± 0.08
	betulonic acid	HLMs	0.96 ± 0.14
	oleanonic acid	HLMs	0.80 ± 0.06

can modulate the pharmacokinetic behavior of orally administrated CYP3A-substrate drugs (midazolam and felodipine) by inhibiting intestinal CYP3A but not hepatic CYP3A *in vivo*.

Chemical profiling of Styrax

Next, the chemical constituents in Styrax were analyzed by using UHPLC-Q-Exactive Orbitrap HRMS. The total ion chromatograms (TICs) of Styrax were shown in Supplementary Figure S5. A total of 21 chemical constituents were identified in Styrax by comparing the retention times, MS fragmentation behavior, literature information and the MS/MS databases of natural products. The major constituents in Styrax are cinnamic acids, phenylpropanoids and PTAs. The mass spectrometry data of the identified constituents in Styrax were summarized in Supplementary Table S8.

The inhibitory effects of seven PTAs on CYP3A

A previous study revealed that the PTAs in Styrax displayed potent inhibition on CYP3A-catalyzed testosterone 6β-hydroxylation (Zhang et al., 2020). In this study, the inhibitory effects of these PTAs on CYP3A were assessed in HLMs by using a CYP3A-substrate drug (midazolam) and a newly reported CYP3A4 fluorescent substrate (NEN). As shown in Figures 5, 6 and Table 3, as well as Supplementary Figure S6, S7, the PTAs inhibited CYP3A-catalyzed midazolam 1′-hydroxylation in a dose-dependent manner, showing the IC_{50} values of 19.39, 32.20, 14.83, 7.74, 0.64, 2.51, and 0.99 μM, for maslinic acid, corosolic acid, oleanolic acid, betulinic acid, epibetulinic acid, betulonic acid and oleanonic acid, respectively. Meanwhile, all tested PTAs dose-dependently inhibited CYP3A4-catalyzed NEN 4-hydroxylation, with the IC_{50} values of 3.44, 41.93, 1.10, 4.11, 0.47, 0.96, and 0.80 μM, for maslinic acid, corosolic acid, oleanolic acid, betulinic acid, epibetulinic acid, betulonic acid and oleanonic acid, respectively. These results suggest that the PTAs in Styrax are key substances responsible for CYP3A inhibition, while epibetulinic acid, betulonic acid and oleanonic acid display potent CYP3A inhibitory effects.

Tissue distribution of seven PTAs from Styrax in rats

Next, the tissue distribution (in plasma, liver, duodenum, jejunum, ileum and colon) of seven PTAs from Styrax was determined in rats after single oral dose of Styrax (100 mg/kg). As shown in Figure 7, Supplementary Figure S8, and Supplementary Tables S9–S12, maslinic acid, corosolic acid and betulinic acid could not be detected (lower the detection limit) in rat plasma and rat liver, while very low exposure levels of epibetulinic acid, betulonic acid, oleanonic acid, oleanolic acid were detected in rat plasma and rat liver. By contrast, these PTAs could be easily detected from the intestinal tract (especially in jejunum, ileum and colon) in rats. Notably, the local exposure of oleanonic acid to rat jejunum could reach 745.69 nM/mg tissue protein (1 h), which was near to the IC_{50} value of oleanonic acid against CYP3A4. These results suggested that the major PTAs in Styrax could be distributed in intestinal tract at relatively high exposure levels but their plasma and liver exposure in rats was extremely low. These

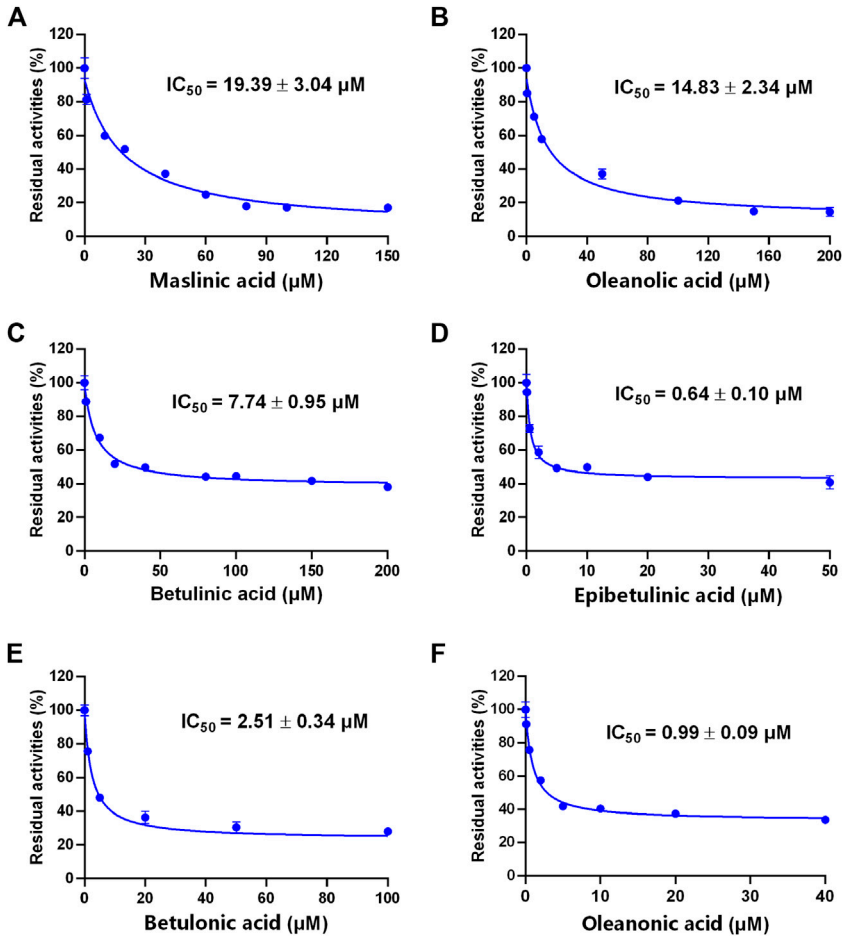

FIGURE 5
The inhibitory effects of the pentacyclic triterpenoid acids (maslinic acid **(A)**, oleanolic acid **(B)**, betulinic acid **(C)**, epibetulinic acid **(D)**, betulonic acid **(E)** and oleanonic acid **(F)**) against midazolam 1′-hydroxylation in HLMs. Data are expressed as mean ± SD.

findings well explain why Styrax (i.g.) significantly elevates the plasma exposure of CYP3A-substrate drugs only when these agents are orally administrated, and why Styrax cannot modulate the pharmacokinetic behavior of CYP3A-substrate drugs when these agents administered intravenously.

Discussion

Over the past few decades, the concomitant use of Chinese medicines and Western medicines has widely been used to cure a range of human diseases, such as digestive diseases, cardiovascular diseases, infectious diseases and various types of cancer (Klotz, 2009; Cong et al., 2015; Mair et al., 2020). In most cases, the concomitant use of Chinese medicines and Western medicines can bring better therapeutic effects *via* acting on various therapeutic targets or prolonging the half-lives of active compounds in either Chinese medicines or Western medicines (Wu et al., 2011; Shao et al., 2021; Zhang T. et al., 2022). However, in some cases, the concomitant use of Chinese medicines and Western medicines (especially for those agents with very narrow therapeutic windows) has a high risk of triggering potential HDIs (Meijerman et al., 2006; Han et al., 2020). It is well-known that most herbal medicines are administered orally, while Western medicines are administered in various ways including oral administration and injection. Oral drugs are generally absorbed through the mesentery, through the portal vein to the liver, and then enter into the blood circulation system. Thus, it should be clarified whether herbal medicines can modulate the pharmacokinetic behavior of Western medicine(s) by inhibiting/inactivating intestinal or hepatic drug-metabolizing enzymes *in vivo*.

As one of the most abundant drug-metabolizing enzymes (DMEs) in human liver and intestine, CYP3A4 plays a crucial role in the metabolic clearance and detoxification of a wide range of Western medicines *in vivo*, thus acts as a key

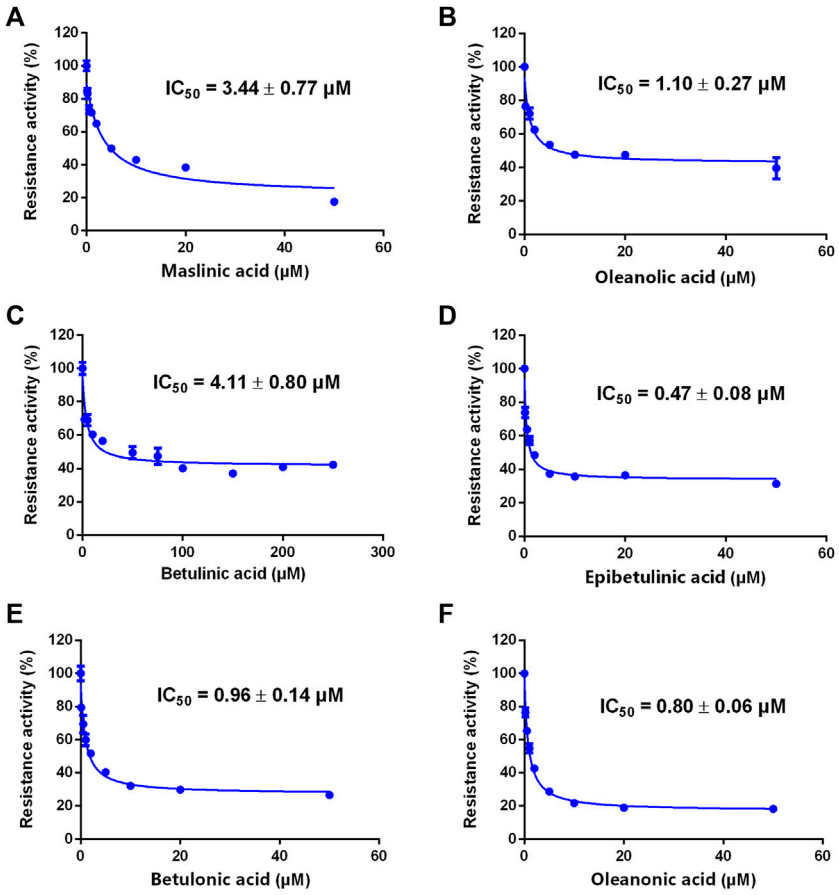

FIGURE 6
The inhibitory effects of the pentacyclic triterpenoid acids (maslinic acid **(A)**, oleanolic acid **(B)**, betulinic acid **(C)**, epibetulinic acid **(D)**, betulonic acid **(E)** and oleanonic acid **(F)**) against NEN-hydroxylation in HLMs. Data are expressed as mean ± SD.

mediator in HDIs and DDIs (Galetin et al., 2007; Zhou, 2008; Tian and Hu, 2014). In this study, following screening more than 100 kinds of clinical commonly used Chinese medicines, Styrax is found with the most potent CYP3A4 inhibitory effect (almost completely inhibit CYP3A4 at 100 μg/ml). Considering that Styrax and Styrax-related herbal products are frequently used in combination with a panel of marketed cardiovascular drugs (such as warfarin, digoxin and simvastatin) to treat cardiovascular diseases (Zhu, 2009; Tao et al., 2016; Yang et al., 2021). It is well-known that Styrax/Styrax-related herbal products are often taken orally for the treatment of human diseases, while a number of studies have reported that the local distribution of herbal constituents in the intestine is much higher than that in the liver (Lai et al., 2009; Wang et al., 2018). In these cases, it is necessary to clarify whether Styrax can trigger HDIs *in vivo* and to reveal the key organ(s) and molecular mechanisms involved in the pharmacokinetic HDIs triggered by Styrax.

The small intestine is the key organ for absorption, metabolism, and excretion of orally administered drugs in mammals (Yamashita et al., 2021). Many oral drugs can be metabolized by mammalian CYPs, while intestinal CYP3A4 makes a significant contribution to the metabolism of drugs (Galetin et al., 2007). In this study, *in vitro* assays demonstrated that Styrax and its major constituents (seven PTAs) potently inhibited CYP3A-catalyzed oxidative metabolism of various substrates. *In vivo* assays showed that Styrax only affected the pharmacokinetic behavior of oral victim CYP3A-substrate drugs (midazolam and felodipine), which prompted us to carefully evaluate the tissue distribution of Styrax/its active constituents (seven PTAs) after oral administration of this herbal extract in rats. These results clearly showed that seven PTAs from Styrax could be exposed to the intestinal tract (especially in jejunum, ileum and colon) at relatively high levels in rats after single oral dose of Styrax (100 mg/kg), but these PTAs were hardly exposed to the liver. The extremely low exposure of these PTAs from Styrax to

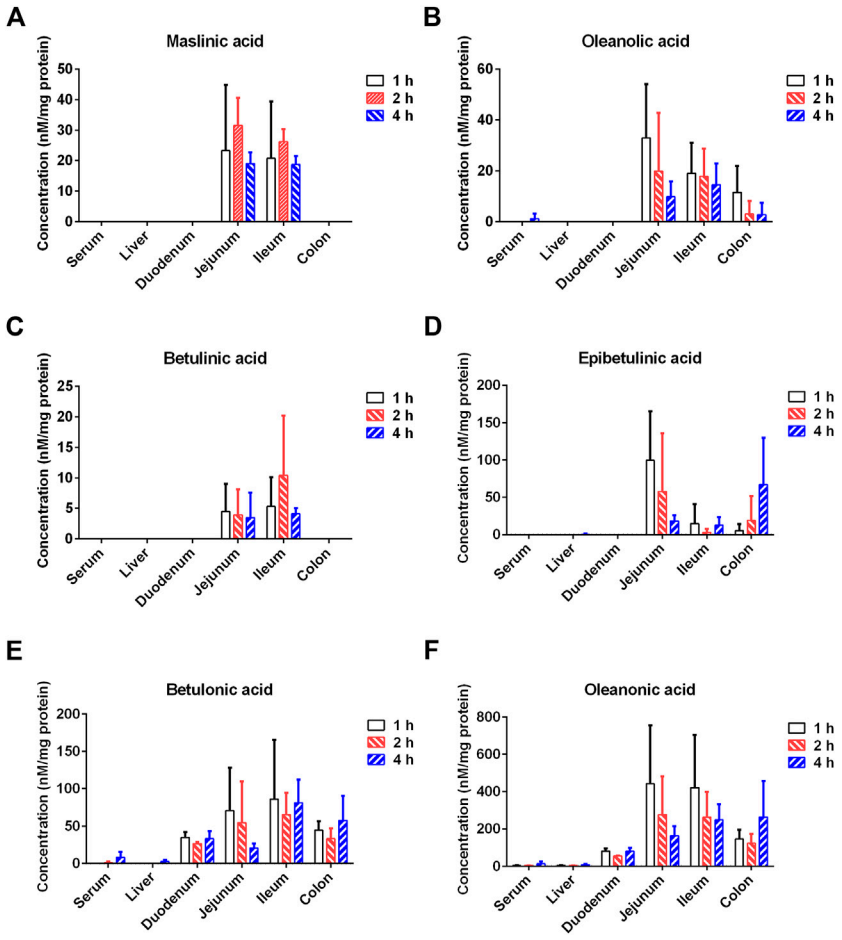

FIGURE 7
Tissue distribution of the major constituents of Styrax (maslinic acid **(A)**, oleanolic acid **(B)**, betulinic acid **(C)**, epibetulinic acid **(D)**, betulonic acid **(E)**, and oleanonic acid **(F)**) after a single oral dose of Styrax (100 mg/kg) to rats.

mammal liver could be attributed to the poor oral bioavailability and the first-pass metabolism of PTAs (Zhang et al., 2019; Yin et al., 2022). The high local exposure of PTAs in the intestinal tract indicated that intestinal CYP3A could be significantly inhibited by these natural compounds in Styrax, while the extremely low exposure of PTAs to mammal liver well-explained why Styrax hardly modulated the *in vivo* pharmacokinetic behaviors of the CYP3A-substrate drugs administrated by intravenous injection.

It should be noted that some CYP3A4 potent inhibitors (such as ritonavir) have been approved by FDA in combination with CYP3A4-substrate drugs to slow down the metabolic clearance of some important CYP3A4-substrate drugs *in vivo*, such as Aluvia/Kaletra (lopinavir and ritonavir) and paxlovid (nirmatrelvir and ritonavir) (Hurst and Faulds, 2000; Agarwal and Agarwal, 2021; Eng et al., 2022; Lamb, 2022). Thus, the potent CYP3A4 inhibitors with improved safety profiles could be developed as oral agents for improving the systemic exposure of CYP3A4-substrate drugs *in vivo*. Considering that hepatic CYP3A plays an important role in endogenous metabolism (such as bile acids and hormones) and the metabolic clearance of toxins, potent inhibition of hepatic CYP3A may lead to serious consequences (such as drug-induced liver injury and imbalance of hormone metabolism) (Li et al., 1995; Burk and Wojnowski, 2004; Banankhah et al., 2016; Qin et al., 2021). In this study, our findings show that the PTAs in Styrax are difficult to enter into the circulation system after oral administration of Styrax, Styrax or its main constituents (PTAs) can be intentionally used in combination with some CYP3A-substrate drugs with low oral bioavailability, aiming to improve its oral bioavailability without affecting the function of hepatic CYP3A. In future, the naturally occurring PTAs in Styrax could be used as promising lead compounds to develop more efficacious CYP3A inhibitors with strong anti-CYP3A effects, improved cell membrane permeability and high safety profiles.

Conclusion

In summary, we demonstrate a case study to efficiently find the herbal medicine(s) with potent hCYP3A4 inhibitory effect *in vitro* and to accurately assess the potential HDIs risk *in vivo*. With the help of fluorescence-based high-throughput hCYP3A4 inhibition assay, the Chinese herb Styrax was found with the most potent hCYP3A4 inhibition in HLMs. *In vivo* pharmacokinetic assays demonstrated that Styrax (i.g., 100 mg/kg) only affected the pharmacokinetic behavior of orally administrated CYP3A-substrate drugs (midazolam and felodipine). Further investigations demonstrated that seven PTAs in Styrax were key substances responsible for CYP3A inhibition, while these PTAs could be exposed to intestinal tract at relatively high exposure levels but the exposure levels of these PTAs in rat plasma and liver were extremely low. Collectively, our findings showed that the Chinese herb Styrax (i.g.) could significantly elevate the plasma exposure of orally administrated CYP3A-substrate drugs but hardly modulated the pharmacokinetic profiles of intravenously administrated CYP3A-substrate drugs, which could be attributed to the high exposure levels of the PTAs in Styrax in intestinal tract and the extremely low exposure levels in rat liver. All these findings clearly suggest that the tissue exposure of some key constituents in herbal medicines strongly affect their *in vivo* inhibitory effects on CYP3A4, which are very helpful for the clinical pharmacologists to better understand the pharmacokinetic HDIs triggered by herbal products that contains naturally occurring CYP3A4 inhibitors.

Data availability statement

The raw data supporting the conclusions of this article will be made available by the authors, without undue reservation.

Ethics statement

The animal study was reviewed and approved by Animal experiment was carried out in Experimental Animal Center of SHUTCM (Approval Number: PZSHUTCM210709016) and conducted in accordance with the State Committee of Science and Technology of China.

Author contributions

GG, YH, and WL designed the study. FZ, TZ, and JG performed the experiments. GG, YH, ML, QF, and SQ analyzed the data. GG, WL, and FZ wrote the paper. YH critically revised the manuscript.

Funding

This work was supported by the National Key Research and Development Program of China (2017YFC1700200, 2017YFC1702000), the NSF of China (81922070, 81973286, 82141203), Shanghai Science and Technology Innovation Action Plans (20S21901500, 20S21900900) supported by Shanghai Science and Technology Committee, Innovation Team and Talents Cultivation Program of National Administration of Traditional Chinese Medicine (ZYYCXTDD-202004), Three-year Action Plan for Shanghai TCM Development and Inheritance Program [ZY(2021-2023)-0401], and Clinical Research Plan of SHDC (SHDC2020CR 2046B).

Conflict of interest

The authors declare that the research was conducted in the absence of any commercial or financial relationships that could be construed as a potential conflict of interest.

Publisher's note

All claims expressed in this article are solely those of the authors and do not necessarily represent those of their affiliated organizations, or those of the publisher, the editors and the reviewers. Any product that may be evaluated in this article, or claim that may be made by its manufacturer, is not guaranteed or endorsed by the publisher.

Supplementary material

The Supplementary Material for this article can be found online at: https://www.frontiersin.org/articles/10.3389/fphar.2022.974578/full#supplementary-material

References

Agarwal, S., and Agarwal, S. K. (2021). Lopinavir-ritonavir in SARS-CoV-2 infection and drug-drug interactions with cardioactive medications. *Cardiovasc. Drugs Ther.* 35 (3), 427–440. doi:10.1007/s10557-020-07070-1

Ban, Y. J., Chen, R., Zhang, Y., Zhang, L., Liu, W. X., Zhu, G. F., et al. (2021). Research progress on oral absorption and metabolism of pentacyclic triterpenoids. *Chem. Reagents* 43 (07), 906–916. doi:10.13822/j.cnki.hxsj.2021008033

Banankhah, P. S., Garnick, K. A., and Greenblatt, D. J. (2016). Ketoconazole-associated liver injury in drug-drug interaction studies in healthy volunteers. *J. Clin. Pharmacol.* 56 (10), 1196–1202. doi:10.1002/jcph.711

Bian, J., and Zhang, H. Y. (2016). A preliminary study on the ancient and modern application of Suhexiang pills. *Clin. J. Traditional Chin. Med.* 28 (06), 875–878. doi:10.16448/j.cjtcm.2016.0310

Burk, O., and Wojnowski, L. (2004). Cytochrome P450 3A and their regulation. *Naunyn. Schmiedeb. Arch. Pharmacol.* 369 (1), 105–124. doi:10.1007/s00210-003-0815-3

Cong, Y., Sun, K., He, X., Li, J., Dong, Y., Zheng, B., et al. (2015). A traditional Chinese medicine xiao-ai-tong suppresses pain through modulation of cytokines and prevents adverse reactions of morphine treatment in bone cancer pain patients. *Mediat. Inflamm.* 2015, 961635. doi:10.1155/2015/961635

Dunkoksung, W., Vardhanabhuti, N., Siripong, P., and Jianmongkol, S. (2019). Rhinacanthin-C mediated herb-drug interactions with drug transporters and phase I drug-metabolizing enzymes. *Drug Metab. Dispos.* 47 (10), 1040–1049. doi:10.1124/dmd.118.085647

Eng, H., Dantonio, A. L., Kadar, E. P., Obach, R. S., Di, L., Lin, J., et al. (2022). Disposition of nirmatrelvir, an orally bioavailable inhibitor of SARS-CoV-2 3C-like protease, across animals and humans. *Drug Metab. Dispos.* 50 (5), 576–590. doi:10.1124/dmd.121.000801

Fang, S. Q., Huang, J., Zhang, F., Ni, H. M., Chen, Q. L., Zhu, J. R., et al. (2020). Pharmacokinetic interaction between a Chinese herbal formula Huosu Yangwei oral liquid and apatinib *in vitro* and *in vivo*. *J. Pharm. Pharmacol.* 72 (7), 979–989. doi:10.1111/jphp.13268

Fasinu, P. S., Gurley, B. J., and Walker, L. A. (2015). Clinically relevant pharmacokinetic herb-drug interactions in antiretroviral therapy. *Curr. Drug Metab.* 17 (1), 52–64. doi:10.2174/1389200216666151103115053

Galetin, A., Hinton, L. K., Burt, H., Obach, R. S., and Houston, J. B. (2007). Maximal inhibition of intestinal first-pass metabolism as a pragmatic indicator of intestinal contribution to the drug-drug interactions for CYP3A4 cleared drugs. *Curr. Drug Metab.* 8 (7), 685–693. doi:10.2174/138920007782109805

Gallo, P., De Vincentis, A., Pedone, C., Nobili, A., Tettamanti, M., Gentilucci, U. V., et al. (2019). Drug-drug interactions involving CYP3A4 and p-glycoprotein in hospitalized elderly patients. *Eur. J. Intern. Med.* 65, 51–57. doi:10.1016/j.ejim.2019.05.002

Gouws, C., Steyn, D., Du Plessis, L., Steenekamp, J., and Hamman, J. H. (2012). Combination therapy of western drugs and herbal medicines: Recent advances in understanding interactions involving metabolism and efflux. *Expert Opin. Drug Metab. Toxicol.* 8 (8), 973–984. doi:10.1517/17425255.2012.691966

Guo, J., Qin, Z., He, Q., Fong, T. L., Lau, N. C., Cho, W. C. S., et al. (2021). Shexiang Baoxin Pill for acute myocardial infarction: Clinical evidence and molecular mechanism of antioxidative stress. *Oxid. Med. Cell. Longev.* 2021, 7644648. doi:10.1155/2021/7644648

Han, M. Z., Li, S. S., Li, J., Li, X. C., Gao, L. L., Lu, Y., et al. (2020). Qingfei Paidu Decoction causes hyperkalemia in patients with novel coronavirus pneumonia. *J. Adverse Drug React.* 22 (06), 375–376.

Hurst, M., and Faulds, D. (2000). Lopinavir. *Drugs* 60 (6), 1371–1379. discussion 1380-1. doi:10.2165/00003495-200060060-00009

Jin, Q., Wu, J., Wu, Y., Li, H., Finel, M., Wang, D., et al. (2022). Optical substrates for drug-metabolizing enzymes: Recent advances and future perspectives. *Acta Pharm. Sin. B* 12 (3), 1068–1099. doi:10.1016/j.apsb.2022.01.009

Kallem, R. R., Ramesh, M., and Seshagirirao, J. V. (2013). Validated LC-ESI-MS/MS method for simultaneous quantitation of felodipine and metoprolol in rat plasma: Application to a pharmacokinetic study in rats. *Biomed. Chromatogr.* 27 (6), 784–791. doi:10.1002/bmc.2861

Klotz, U. (2009). Pharmacokinetics and drug metabolism in the elderly. *Drug Metab. Rev.* 41 (2), 67–76. doi:10.1080/03602530902722679

Kotegawa, T., Laurijssens, B. E., Von Moltke, L. L., Cotreau, M. M., Perloff, M. D., Venkatakrishnan, K., et al. (2002). *In vitro*, pharmacokinetic, and pharmacodynamic interactions of ketoconazole and midazolam in the rat. *J. Pharmacol. Exp. Ther.* 302 (3), 1228–1237. doi:10.1124/jpet.102.035972

Lai, L., Hao, H., Wang, Q., Zheng, C., Zhou, F., Liu, Y., et al. (2009). Effects of short-term and long-term pretreatment of Schisandra lignans on regulating hepatic and intestinal CYP3A in rats. *Drug Metab. Dispos.* 37 (12), 2399–2407. doi:10.1124/dmd.109.027433

Lamb, Y. N. (2022). Nirmatrelvir plus ritonavir: First approval. *Drugs* 82 (5), 585–591. doi:10.1007/s40265-022-01692-5

Lee, S. Y., Lee, J. Y., Kang, W., Kwon, K. I., Park, S. K., Oh, S. J., et al. (2013). Cytochrome P450-mediated herb-drug interaction potential of Galgeun-tang. *Food Chem. Toxicol.* 51, 343–349. doi:10.1016/j.fct.2012.10.012

Li, A. P., Kaminski, D. L., and Rasmussen, A. (1995). Substrates of human hepatic cytochrome P450 3A4. *Toxicology* 104 (1-3), 1–8. doi:10.1016/0300-483x(95)03155-9

Li, H. Y., Xu, W., Su, J., Zhang, X., Hu, L. W., and Zhang, W. D. (2010). *In vitro* and *in vivo* inhibitory effects of glycyrrhetinic acid on cytochrome P450 3A activity. *Pharmacology* 86 (5-6), 287–292. doi:10.1159/000320956

Lundahl, J., Regårdh, C. G., Edgar, B., and Johnsson, G. (1997). Effects of grapefruit juice ingestion-pharmacokinetics and haemodynamics of intravenously and orally administered felodipine in healthy men. *Eur. J. Clin. Pharmacol.* 52 (2), 139–145. doi:10.1007/s002280050263

Mair, A., Wilson, M., and Dreischulte, T. (2020). Addressing the challenge of polypharmacy. *Annu. Rev. Pharmacol. Toxicol.* 60, 661–681. doi:10.1146/annurev-pharmtox-010919-023508

Meijerman, I., Beijnen, J. H., and Schellens, J. H. (2006). Herb-drug interactions in oncology: Focus on mechanisms of induction. *Oncologist* 11 (7), 742–752. doi:10.1634/theoncologist.11-7-742

Ning, J., Wang, W., Ge, G., Chu, P., Long, F., Yang, Y., et al. (2019). Target enzyme-activated two-photon fluorescent probes: A case study of CYP3A4 using a two-dimensional design strategy. *Angew. Chem. Int. Ed. Engl.* 58 (29), 9959–9963. doi:10.1002/anie.201903683

Parvez, M. K., and Rishi, V. (2019). Herb-drug interactions and hepatotoxicity. *Curr. Drug Metab.* 20 (4), 275–282. doi:10.2174/1389200220666190325141422

Qin, X., Zhang, Y., Lu, J., Huang, S., Liu, Z., and Wang, X. (2021). CYP3A deficiency alters bile acid homeostasis and leads to changes in hepatic susceptibility in rats. *Toxicol. Appl. Pharmacol.* 429, 115703. doi:10.1016/j.taap.2021.115703

Qiu, R., Zhao, C., Liang, T., Hao, X., Huang, Y., Zhang, X., et al. (2020). Core outcome set for clinical trials of COVID-19 based on traditional Chinese and western medicine. *Front. Pharmacol.* 11, 781. doi:10.3389/fphar.2020.00781

Ren, C., Kong, D., Ning, C., Xing, H., Cheng, Y., Zhang, Y., et al. (2021). Improved pharmacokinetic characteristics of ursolic acid in rats following intratracheal instillation and nose-only inhalation exposure. *J. Pharm. Sci.* 110 (2), 905–913. doi:10.1016/j.xphs.2020.10.006

Shao, H., He, X., Zhang, L., Du, S., Yi, X., Cui, X., et al. (2021). Efficacy of ligustrazine injection as adjunctive therapy in treating acute cerebral infarction: A systematic review and meta-analysis. *Front. Pharmacol.* 12, 761722. doi:10.3389/fphar.2021.761722

Su, J. L., and Geng, N. Z. (2016). Observation on the efficacy of traditional Chinese medicine Yiqi Tongmai Decoction combined with conventional Western medicine in the treatment of angina pectoris after myocardial infarction in the elderly. *Clin. Res. Traditional Chin. Med.* 8 (27), 11–12.

Surya Sandeep, M., Sridhar, V., Puneeth, Y., Ravindra Babu, P., and Naveen Babu, K. (2014). Enhanced oral bioavailability of felodipine by naringenin in Wistar rats and inhibition of P-glycoprotein in everted rat gut sacs *in vitro*. *Drug Dev. Ind. Pharm.* 40 (10), 1371–1377. doi:10.3109/03639045.2013.819885

Tao, J., Jiang, P., Peng, C., Li, M., Liu, R., and Zhang, W. (2016). The pharmacokinetic characters of simvastatin after co-administration with Shexiang Baoxin Pill in healthy volunteers' plasma. *J. Chromatogr. B Anal. Technol. Biomed. Life Sci.* 1026, 162–167. doi:10.1016/j.jchromb.2016.01.018

Tian, D., and Hu, Z. (2014). CYP3A4-mediated pharmacokinetic interactions in cancer therapy. *Curr. Drug Metab.* 15 (8), 808–817. doi:10.2174/1389200216666150223152627

Tu, D., Ning, J., Zou, L., Wang, P., Zhang, Y., Tian, X., et al. (2022). Unique oxidative metabolism of bufalin generates two reactive metabolites that strongly inactivate human cytochrome P450 3A. *J. Med. Chem.* 65 (5), 4018–4029. doi:10.1021/acs.jmedchem.1c01875

Tu, D. Z., Mao, X., Zhang, F., He, R. J., Wu, J. J., Wu, Y., et al. (2020). Reversible and irreversible inhibition of cytochrome P450 enzymes by methylophiopogonanone A. *Drug Metab. Dispos.* 49 (6), 459–469. doi:10.1124/dmd.120.000325

Wang, M., Xu, Z. Q., Li, Z. X., and Liu, Y. L. (2020). Effects of intestinal network barrier on the absorption mechanism of pentacyclic triterpenoid saponins from Pulsatilla chinensis. *Jiangxi Tradit. Chin. Med.* 51 (01), 69–71.

Wang, Z., You, L., Cheng, Y., Hu, K., Wang, Z., Cheng, Y., et al. (2018). Investigation of pharmacokinetics, tissue distribution and excretion of schisandrin B in rats by HPLC-MS/MS. *Biomed. Chromatogr.* 32 (2), e4069. doi:10.1002/bmc.4069

Wu, B., Zhao, S., Wang, X., Dong, Q., and Zheng, G. (2011). Mechanism of traditional Chinese medicine on animal model of Parkinson's disease. *Zhongguo Zhong Yao Za Zhi* 36 (18), 2588–2591.

Wu, J. J., Guan, X. Q., Dai, Z. R., He, R. J., Ding, X. X., Yang, L., et al. (2021). Molecular probes for human cytochrome P450 enzymes: Recent progress and

future perspectives. *Coord. Chem. Rev.* 427, 213600. doi:10.1016/j.ccr.2020.213600

Xiang, Q., Li, C., Zhao, X., and Cui, Y. M. (2017). The influence of CYP3A5*3 and BCRPC421A genetic polymorphisms on the pharmacokinetics of felodipine in healthy Chinese volunteers. *J. Clin. Pharm. Ther.* 42 (3), 345–349. doi:10.1111/jcpt.12505

Xu, Z. L., Zhang, Y., Tao, X. J., Zhang, M. B., Dou, D. Q., and Kang, T. G. (2017). Interaction of synergism and detoxification in the combined use of traditional Chinese medicine and anti-infective Western medicine. *Shizhen Tradit. Chin. Med.* 28 (01), 202–204.

Xue, X., Huang, M., Xiao, H., Qin, X., Huang, L., Zhong, G., et al. (2011). Rapid and simultaneous measurement of midazolam, 1'-hydroxymidazolam and digoxin by liquid chromatography/tandem mass spectrometry: Application to an *in vivo* study to simultaneously measure P-glycoprotein and cytochrome P450 3A activity. *J. Pharm. Biomed. Anal.* 28 (551), 187–193. doi:10.1016/j.jpba.2011.01.018

Yamashita, T., Inui, T., Yokota, J., Kawakami, K., Morinaga, G., Takatani, M., et al. (2021). Monolayer platform using human biopsy-derived duodenal organoids for pharmaceutical research. *Mol. Ther. Methods Clin. Dev.* 22, 263–278. doi:10.1016/j.omtm.2021.05.005

Yang, Y., Gao, S., Fang, Q., and Zhu, M. (2021). Efficacy and safety of Shexiang Baoxin Pill combined with western medicine in the treatment of acute myocardial infarction: A single-center, double-blind, randomized controlled trial. *Med. Baltim.* 100 (3), e24246. doi:10.1097/MD.0000000000024246

Yin, Y., Sheng, L., Zhang, J., Zhang, L., Liu, J., Wen, X., et al. (2022). Synthesis and *in vitro*/*in vivo* anticancer evaluation of pentacyclic triterpenoid derivatives linked with l-phenylalanine or l-proline. *Bioorg. Chem.* 126, 105865. doi:10.1016/j.bioorg.2022.105865

Yu, Q. (2021). A brief analysis of the application of styraxine series spices in the food field. *Food Saf. Guide* (12), 181–182. doi:10.16043/j.cnki.cfs.2021.12.101

Zhang, B., Lu, Y., Li, P., Wen, X., and Yang, J. (2019). Study on the absorption of corosolic acid in the gastrointestinal tract and its metabolites in rats. *Toxicol. Appl. Pharmacol.* 378, 114600. doi:10.1016/j.taap.2019.114600

Zhang, F., Huang, J., He, R. J., Wang, L., Huo, P. C., Guan, X. Q., et al. (2020). Herb-drug interaction between Styrax and warfarin: Molecular basis and mechanism. *Phytomedicine.* 77, 153287. doi:10.1016/j.phymed.2020.153287

Zhang, F., Huang, J., Liu, W., Wang, C. R., Liu, Y. F., Tu, D. Z., et al. (2021). Inhibition of drug-metabolizing enzymes by Qingfei Paidu decoction: Implication of herb-drug interactions in COVID-19 pharmacotherapy. *Food Chem. Toxicol.* 149, 111998. doi:10.1016/j.fct.2021.111998

Zhang, F., Liu, W., Huang, J., Chen, Q. L., Wang, D. D., Zou, L. W., et al. (2022). Inhibition of drug-metabolizing enzymes by jingyin granules: Implications of herb-drug interactions in antiviral therapy. *Acta Pharmacol. Sin.* 43 (4), 1072–1081. doi:10.1038/s41401-021-00697-2

Zhang, L. G., and Xu, X. S. (2012). 30 cases of peptic ulcer treated with Western medicine combined with traditional Chinese medicine Xiaokuiping decoction. *Chin. Ethn. Folk. Med.* 21 (23), 101.

Zhang, T., Li, X., Chen, Y., Zhao, L., Tian, J., and Zhang, J. (2022). Evidence mapping of 23 systematic reviews of traditional Chinese medicine combined with western medicine approaches for COVID-19. *Front. Pharmacol.* 12, 807491. doi:10.3389/fphar.2021.807491

Zhang, Y. W., Tu, L. L., Zhang, Y., Pan, J. C., Zheng, G. L., and Yin, L. N. (2021). Liver-targeted delivery of asiatic acid nanostructured lipid carrier for the treatment of liver fibrosis. *Drug Deliv.* 28 (1), 2534–2547. doi:10.1080/10717544.2021.2008054

Zhou, Q. H., Zhu, Y. D., Zhang, F., Song, Y. Q., Jia, S. N., Zhu, L., et al. (2019). Interactions of drug-metabolizing enzymes with the Chinese herb Psoraleae Fructus. *Chin. J. Nat. Med.* 17 (11), 858–870. doi:10.1016/S1875-5364(19)30103-7

Zhou, S. F. (2008). Drugs behave as substrates, inhibitors and inducers of human cytochrome P450 3A4. *Curr. Drug Metab.* 9 (4), 310–322. doi:10.2174/138920008784220664

Zhu, S. Z. (2009). Digoxin, Shexiang Baoxin Pill and aspirin combined treatment of 30 cases of chronic fast ventricular atrial fibrillation. *Contemp. Med.* 15 (12), 149–150.

frontiers | Frontiers in Pharmacology

TYPE Original Research
PUBLISHED 19 September 2022
DOI 10.3389/fphar.2022.981112

OPEN ACCESS

EDITED BY
Guangbo Ge,
Shanghai University of Traditional Chinese Medicine, China

REVIEWED BY
Jingjing Wu,
Dalian Medical University, China
Wei Liu,
Shanghai University of Traditional Chinese Medicine, China
Wei Dong Chen,
Anhui University of Chinese Medicine, China

*CORRESPONDENCE
Yi Chen,
chenyi_19890319@126.com
Zipeng Gong,
gzp4012607@126.com

†These authors have contributed equally to this work

SPECIALTY SECTION
This article was submitted to Ethnopharmacology, a section of the journal Frontiers in Pharmacology

RECEIVED 29 June 2022
ACCEPTED 08 August 2022
PUBLISHED 19 September 2022

CITATION
Huang J, Chen R, Zhou J, Zhang Q, Xue C, Li Y, Zheng L, Huang Y, Wang Q, Chen Y and Gong Z (2022), Comparative pharmacokinetic study of the five anti-inflammatory active ingredients of Inula cappa in a normal and an LPS-induced inflammatory cell model. *Front. Pharmacol.* 13:981112. doi: 10.3389/fphar.2022.981112

Comparative pharmacokinetic study of the five anti-inflammatory active ingredients of *Inula cappa* in a normal and an LPS-induced inflammatory cell model

Jing Huang[1†], Ruixing Chen[1†], Jie Zhou[1†], Qing Zhang[1†], Cun Xue[1], Yueting Li[1], Lin Zheng[1], Yong Huang[1], Qun Wang[2], Yi Chen[1*] and Zipeng Gong[1,3*]

[1]State Key Laboratory of Functions and Applications of Medicinal Plants, Guizhou Provincial Key Laboratory of Pharmaceutics, School of Pharmacy, Guizhou Medical University, Guiyang, China, [2]Guizhou University of Traditional Chinese Medicine, Guiyang, China, [3]Guizhou Provincial Engineering Research Center for the Development and Application of Ethnic Medicine and TCM, Guizhou Medical University, Guiyang, China

Inula cappa is a commonly used medicine in the Miao area of Guizhou Province in China. We established an *in vitro* inflammatory model of mouse macrophage RAW264.7 cells to study the different pharmacokinetics of five anti-inflammatory active ingredients in the *I. cappa* extract namely luteolin (LUT), chlorogenic acid (CA), cryptochlorogenic acid (CCA), 3,4-dicaffeoylquinic acid (3,4-DCQA) and 4,5-dicaffeoylquinic acid (4,5-DCQA), in a normal and an inflammatory cell model. First, RAW264.7 cells were treated *in vitro* with l μg/mL lipopolysaccharide (LPS) for 24 h to establish an inflammatory cell model. Then, the pharmacokinetic characteristics of the five ingredients were compared in normal and inflammatory cells after treatment with 200 μg/ml and 800 μg/ml of *I. cappa* extracts. After treatment with 1 μg/ml LPS for 24 h, the volume of RAW264.7 cells was increased, the morphology was changed, the antennae were obvious, and the secretion of inflammatory factors nitric oxide and TNF-α was increased. The pharmacokinetics results showed that the five ingredients in normal and inflammatory cells exhibited an increase in C_{max} and AUC values with increasing doses, and the C_{max} and AUC values of five ingredients were positively correlated with the extract concentration. Each of these five ingredients presented nonlinear pharmacokinetic characteristics. After treatment with 200 μg/ml of *I. cappa* extract, the uptake of five ingredients increased in inflammatory cells, T_{max} was prolonged, MRT and $t_{1/2}$ were

Abbreviations: LUT, Luteolin; CA, chlorogenic acid; CCA, cryptochlorogenic acid; 3,4-DCQA, 3,4-dicaffeoylquinic acid; 4,5-DCQA, 4,5-dicaffeoylquinic acid; LPS, lipopolysaccharide; NO, nitric oxide; TNF-α, tumor necrosis factor-α; CYP, cytochrome P450; DMEs, drug-metabolizing enzymes; $T_{1/2}$, terminal elimination half-life; AUC_{0-t}, area under the concentration vs. time curve from zero to last sampling time; V_d/F, volume of distribution; CL/F, total body clearance; C_{max}, the peak concentration; T_{max}, the time to reach C_{max}.

prolonged, and CL_F and Vz_F were decreased, while after treatment with 800 μg/ml of *I. cappa* extract, the uptake of five ingredients decreased, T_{max} was prolonged, absorption was faster, and MRT and $t_{1/2}$ were prolonged. The five analyzed components in *I. cappa* extract exerted different effects on normal cells and LPS-induced inflammatory cells. Compared to normal cells, the uptake of five ingredients in inflammatory cells was faster and the AUC and C_{max} values increased with increasing doses, showing a dose-dependent nonlinear pharmacokinetic profile. These results indicate that the pharmacokinetic effects of the five analyzed ingredients in *I. cappa* extract are changed in the inflammatory state.

KEYWORDS

***Inula cappa*, cellular pharmacokinetics, UPLC-MS/MS, RAW264.7 cells, inflammatory model**

1 Introduction

Inula cappa (Buch.-Ham. ex D. Don) DC. is a member of the Asteraceae family whose dried whole herb or root is used as a traditional Chinese medicine. It is also called BaiNiudan, DaLiwang, or YeXiabai. *I. cappa* is distributed in Guizhou, Yunnan, Guangxi, and Hunan Province in China. Its properties and functions are described in the Provincial Quality Standards for Medicinal Materials (Guangxi Zhuang Autonomous Region, Department of Health, 1992; Guizhou Province Drug Administration, 2003; Yunnan Food and Drug Administration, 2007; Hunan Food and Drug Administration, 2010). As a commonly used medicine in the Miao region of Guizhou Province, *I. cappa* has the function of dispersing wind-heat, detumescence, and detoxification. It is used for the treatment of cold and fever, swelling and pain of the throat, rheumatism arthralgia pain, ulcerative carbuncle, and furunculosis, among others (Qiu and Du, 2005). Among the Dai people, *I. cappa* also known as "Nahan", is the main medicine of the famous Dai medical prescription "Ya Hutton San", which is included in the 2020 edition of the Chinese Pharmacopoeia. *I. cappa* has the effect of clearing away heat and toxic materials, analgesia, and hemostasis, and it is used in the treatment of cold and fever, pharyngitis, thoracoabdominal pain, palpitation, deficiency, irregular menstruation, and postpartum bleeding (Chinese Pharmacopoeia Commission, 2020). *I. cappa* is mainly composed of terpenoids, flavonoids, phenols, organic acids, and volatile oil (Xie, et al., 2007; Yao and Liang, 2008; Wu, et al., 2010; Hu and He, 2012; Guan, et al., 2014; Wu, et al., 2017; Yao, 2017; Zhou, et al., 2017). Modern pharmacological studies have indicated that *I. cappa* has many biological activities and exerts anti-inflammatory, analgesic, antibacterial, antitumor, antioxidant, and immunomodulatory effects (Liu et al., 2009; Liu, et al., 2010; Jiraporn, et al., 2011; Xie, et al., 2012; Dong, et al., 2015; Li, 2017). Compared with the many studies on the pharmacological properties and chemical composition of *I. cappa*, there are few pharmacokinetic studies on its active ingredients, and cellular pharmacokinetic studies on its active ingredients are still lacking. In fact, classical pharmacokinetic studies based on the determination of plasma drug concentrations may not be sufficient to predict pharmacological response *in vivo*. Many drugs must pass through multiple biological barriers before they reach the intracellular target. There is a pressing need to expand classic pharmacokinetics from macroscopic plasma concentrations of drugs to the cellular or subcellular levels. In this context, cellular pharmacokinetics came into being.

Cellular pharmacokinetics is focused on the quantitative study of the kinetic processes of absorption, distribution, metabolism, and excretion of drugs in cells, which could elucidate the disposition pattern of drugs in cells and evaluate the efficacy of drugs by establishing mathematical models (Ni, et al., 2014; Liu, et al., 2021). It is worth noting that studies have shown that at least one-third of drug targets are currently located in cells, including DNA, nuclear receptors, various kinases, and metabolic enzymes. The representative drugs include antibiotics (azithromycin, moxifloxacin), antimalarial drugs (chloroquine), anticancer drugs (doxorubicin, paclitaxel, topotecan) and antidiabetic drugs (berberine). Drugs with these targets located in cells must penetrate multiple biological barriers and bind to intracellular targets to exert their efficacy. The process of intracellular drug disposal and the binding of the drug to the target are the determinants of drug therapy efficacy. For drugs whose targets are located in cells, it may be more important to study the time course of the drug concentration in cells/subcellular organelles than to study the plasma drug concentration. Therefore, from the perspective of cellular pharmacokinetics, this study regards cells as a microscopic organic whole, quantitatively studies the kinetic process of drugs in cells, then clarifies the laws of drug disposal in cells, and scientifically evaluates the drug efficacy.

For some traditional Chinese medicines whose targets are located in cells, the free drug concentration in the target cells is related to pharmacology, that is, the target that produces the drug's effect may also exist in the cell; so, the intracellular free drug concentration affects the target inside the cell

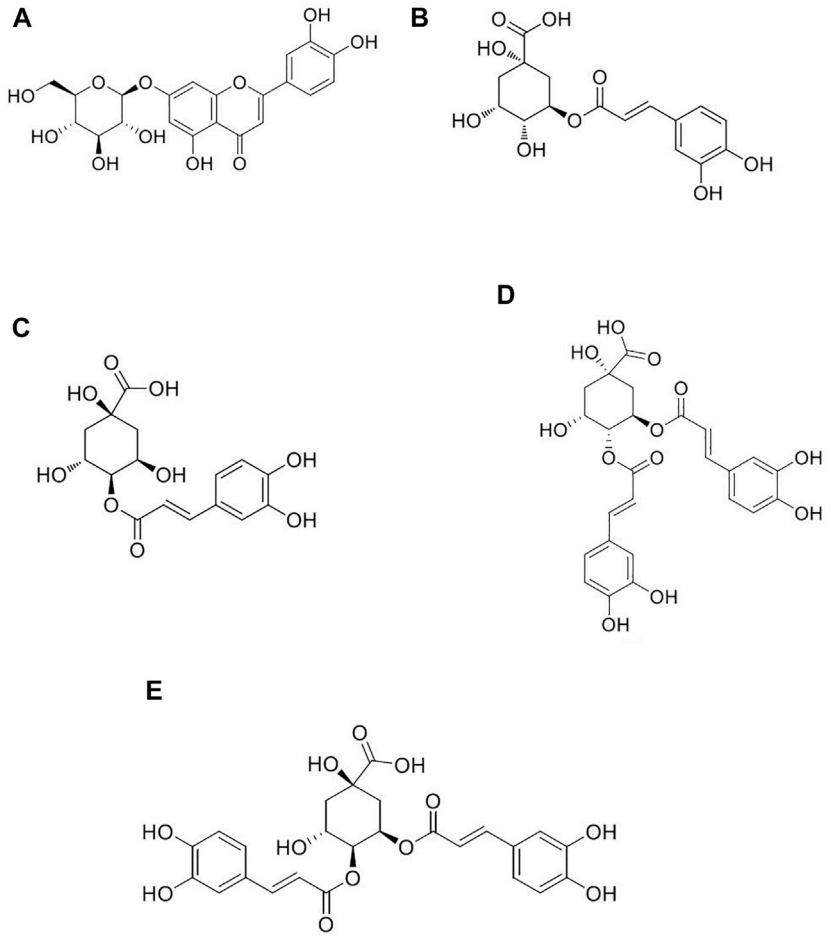

FIGURE 1
Chemical structures of luteolin **(A)**, chlorogenic acid **(B)**, cryptochlorogenic acid **(C)**, 3,4-dicaffeoylquinic acid **(D)**, and 4,5-dicaffeoylquinic acid **(E)**.

(Mateus, et al., 2013). Therefore, it is particularly important to measure the free concentration of the drug in target cells. Moreover, the analysis of the pharmacokinetic processes of drugs inside cells is closely related to its production efficacy. In inflammatory states, the presence of inflammatory factors affects the kinetic disposition of drugs in the body, which leads to the pharmacokinetic parameters of the drugs in the body being different from that of organisms in the normal state. Therefore, it is more relevant to study the pharmacokinetic characteristics of drugs in the inflammatory state than in the normal state (Gao, et al., 2011).

Our previous study completed the fingerprint and chemical composition identification of the extract of *I. cappa* (Gong, et al., 2017b; Zhang, et al., 2019). Moreover, we revealed that the 60% ethanol fraction of *I. cappa* has shown good anti-inflammatory effects *in vitro* and *in vivo* (Gong, et al., 2017a; Wang, et al., 2018). The active ingredients of the 60% ethanol fraction included caffeic acid compounds, phenylpropanoids, and flavonoids, and the main ingredients showing anti-inflammatory activity entering the blood circulation are luteolin (LUT), chlorogenic acid (CA), cryptochlorogenic acid (CCA), 3,4-dicaffeoylquinic acid (3,4-DCQA) and 4,5-dicaffeoylquinic acid (4,5-DCQA) (Gong, et al., 2017c). In addition, our previous study evaluated the absorption and transport properties of active ingredients from *I. cappa* extract using a Caco-2 cell model and showed that the uptake and transport of five active ingredients in Caco-2 cells exhibited a first-order kinetic process (Xue, et al., 2020). Therefore, in the present study, the five ingredients, namely LUT, CA, CCA, 3,4-DCQA, and 4,5-DCQA were used as indicators to study cellular pharmacokinetics of *I. cappa* extracts, and Figure 1 shows the chemical structures of the five ingredients. Firstly, the drug concentrations of the five active components were determined in normal and LPS-induced RAW264.7 cells after treatment with

200 μg/ml and 800 μg/ml of *I. cappa* extracts. Then, the pharmacokinetic parameters were calculated with WinNonLin software to reveal the changes of the five active ingredients over time. Finally, the effects of inflammation on the cellular pharmacokinetics of the active ingredients of *I. cappa* were investigated by comparing the pharmacokinetic parameters of the five active ingredients at different concentrations between the normal and inflammatory states.

2 Materials and methods

2.1 Instruments

The following instruments were used: UPLC Xevo TQ-S Ultra Performance Liquid Triple Quadrupole Mass Spectrometer (ACQUITY UPLC I-Class System, MassLynx Mass Spectrometry Workstation, Waters Corporation, United States); CO_2 incubator, ultra-low temperature refrigerator (Thermo Fisher Scientific, United States); Model 680 Enzyme Labeler (Burroughs Life Medical Products Co., Ltd.); TS-100 F inverted microscope (Nikon Corporation, Japan); Ultra Clean Bench; Allegra 32 R Benchtop Refrigerated Centrifuge; Allegra X-30 R low-temperature high-speed centrifuge (Beckman, United States); VX-III multi-tube vortex oscillator (Fujikin (Beijing) Pharmaceutical Technology Co., Ltd.); XYN-15LP nitrogen blowing instrument nitrogen generator (Shanghai Analytical Instruments Co., Ltd.); Water purifier (Sichuan Water Treatment Equipment Co., Ltd.).

2.2 Reagents and drugs

The following agents were purchased: puerarin (China Institute of Food and Drug Administration, Lot No. 110752-201514, purity ≥95.5%); CA (Chengdu Efa Biotechnology Co., Ltd., Lot No. AF8112791, purity ≥98%); CCA (Chengdu Efa Biotechnology Co., Ltd., Lot No. AF20032707, purity ≥98%); LUT (Sichuan Vickers Biotechnology Co., Ltd., Lot No. wkq20031803, purity ≥98%); 3,4-DCQA (Chengdu Efa Biotechnology Co., Ltd., Lot No. AF9060515, purity ≥98%); 4,5- DCQA (Chengdu Efa Biotechnology Co., Ltd., Lot No. AF0011701, purity ≥98%).

The mouse mononuclear macrophage RAW264.7 cell line used in this experiment was purchased from Wuhan Puno Life Sciences Co. (No. CL-0910). Australian fetal bovine serum (FBS) (2206991CP), DMEM (8120518), double antibody (15140-122), and Tryptic digest (25200-056) were all purchased from Gibco, United States. LPS (L8880) and the BCA protein quantification kit were purchased from Beijing Solai Bao Technology Co.; the NO one-step kit (A013-2-1) was purchased from Nanjing Jiancheng Institute of Biological Engineering; the TNF-α ELISA kit (KE10002) was purchased from Wuhan Sanying Biotechnology Co.

I. cappa was identified by associate Professor Chunhua Liu, School of Pharmacy of Guizhou Medical University. *I. cappa* extract was prepared as described in our previous study. The contents of LUT, CA, CCA, 3,4-DCQA, and 4,5-DCQA in the *I. cappa* extract were 0.18%, 0.26%, 0.30%, 4.52%, and 4.36%, respectively.

2.3 Methods

2.3.1 Solution preparation

2.3.1.1 Preparation of internal standard solution

We precisely weighed 5.7 mg of puerarin, placed into a 5 ml brown volumetric flask and added methanol to obtain a stock solution of 2.74 mmol/L, which was prepared to the proper concentration and stored at −20°C.

2.3.1.2 Preparation of control solution

We accurately weighed 5.7 mg of luteolin, 10.13 mg of chlorogenic acid, 10.28 mg of cryptochlorogenic acid, 15.21 mg of 3,4-dicaffeoylquinic acid, and 15.17 mg of 4,5-dicaffeoylquinic acid. The corresponding concentrations of 2.25, 5.67, 5.79, 5.85, and 5.83 mmol/L were obtained by adding methanol to 5 ml of standard stock solution and stored at −20 °C; the stock solution was diluted to mixed standard solutions before use (LUT, CA, CCA, 3, 4-DCQA, and 4, 5-DCQA were 0.14, 0.35, 0.35, 0.95, and 0.96 μmol/L, respectively). Finally, as shown in Table 1, we diluted the standard solutions by multiples to the series concentrations.

2.3.1.3 Preparation of LPS solution

We dissolved 10 mg of LPS in 10 ml of PBS to obtain LPS stock solution at a concentration of 1 mg/ml. The solution was filtered through a 0.22-μm microporous membrane and stored at −20°C. The solution was diluted with complete medium to the desired concentration before use.

2.3.1.4 Preparation of MTS solution

The appropriate amount of MTS was dissolved in DMEM culture solution at a ratio of 1:20, avoiding light.

2.3.1.5 *I. cappa* extract stock solution for cells

First, 5 g of *I. cappa* extract was dissolved in DMSO by ultrasonication. PBS was added to a final volume of 25 ml to obtain a concentration of 200 mg/ml. The extract was filtered through a 0.22-μm microporous membrane and stored in aliquots at −20°C. Stock solution was diluted to the desired concentration with complete medium before use.

TABLE 1 The standard series concentration of five ingredients including LUT, CA, CCA, 3,4-DCQA, and 4,5-DCQA (μmol/L).

Ingredients	The number of standard series concentration							
	1	2	3	4	5	6	7	8
LUT	0.14	0.069	0.034	0.017	0.0086	0.0043	0.0022	0.0011
CA	0.35	0.18	0.088	0.044	0.022	0.011	0.0055	0.0028
CCA	0.35	0.18	0.088	0.044	0.022	0.011	0.0055	0.0028
3,4-DCQA	0.95	0.48	0.24	0.12	0.059	0.030	0.015	0.0075
4,5- DCQA	0.96	0.48	0.24	0.12	0.060	0.030	0.015	0.0075

2.3.2 Establishment of inflammatory cell model

2.3.2.1 Safe concentration range of LPS in RAW 264.7 cells

RAW264.7 cells were cultured in DMEM with 10% FBS at 37 °C and 5% CO_2 for 36–48 h with 1:6 passaging. When the cells grew to 90% confluency, we digested them with 0.25% trypsin, adjusted the cell density to 1×10^5 cells/mL, inoculated them in 96-well culture plates (100 μL per well), and incubated them at 37°C for 24 h. The following groups were set up: the normal control group (100 μL of DMEM with 10% FBS in each well) and the model group (100 μL of DMEM with 10% FBS containing 0.1, 0.2, 0.5, 1, or 2 μg/ml LPS in each well). After 24 h of incubation, cell activity was measured by the MTS method. The experiment was performed in six parallel wells per concentration and repeated three times. Cell viability was calculated as follows:

$$\text{Cell viability}\,(\%) = \frac{\text{OD}\,(\text{experimental group})}{\text{OD}\,(\text{blank group})} \times 100\%$$

2.3.2.2 Screening of LPS concentration and incubation time in RAW 264.7 cells

Cells at the logarithmic growth stage were selected for counting. The cell suspension was adjusted to 1×10^5 cells/well, and cells were inoculated in 6-well plates (2 ml of cell suspension per well). The following groups were set up: the normal control group (DMEM with 10% FBS in each well) and the model group (DMEM with 10% FBS containing 0.1, 0.2, 0.5, 1, or 2 μg/ml LPS). The supernatant was collected after 6, 12, and 24 h of incubation, and nitric oxide (NO) and tumor necrosis factor-α (TNF-α) levels were measured using commercial kits.

2.3.2.3 Safe concentration range of *I. cappa* extract in RAW 264.7 cells

Cells at the logarithmic growth stage were trypsinized, and the cell suspension was adjusted to 1×10^5 cells/well. Cells were inoculated in a 96-well plate (100 μL per well) and incubated for 24 h. The medium was discarded, the cells were washed twice with PBS buffer, and 100 μL of DMEM containing 10% FBS and different concentrations of *I. cappa* extract (0, 100, 200, 400, 600, 800, 1000, 2000, and 4000 μg/ml) was added.

Six replicate wells were set up and incubated for 24 h. The medium was discarded, and the cells were washed three times with PBS buffer and then incubated for 2–4 h with ready-made MTS solution. We measured the OD value at 490 nm and calculated the cell survival rate according to the above equation.

2.3.3 Cellular pharmacokinetic experiments of five active ingredients after treatment with 200 μg/ml and 800 μg/ml of *I. cappa* extracts

Cells at the logarithmic growth stage were trypsinized, and the cell suspension was adjusted to 1×10^5 cells/well. Cells were inoculated in 6-well plates (2 ml of cell suspension per plate). The following groups were set up: the normal group (no LPS and zero, 200 μg/ml, and 800 μg/ml *I. cappa* extract concentrations) and the model group (LPS and zero, 200 μg/ml, and 800 μg/ml *I. cappa* extract concentrations). After 24 h, the medium was discarded. We added 2 ml of DMEM containing 10% FBS per well to the normal group and 2 ml of DMEM containing 10% FBS and 1 μg/ml LPS per well to the model group. Both groups were incubated for 24 h, the medium was discarded, and the cells were washed twice with PBS. The dosing settings were as follows: DMEM containing 10% FBS in the normal groups; DMEM containing 10% FBS and 200 μg/ml of *I. cappa* extract (an equivalence of 0.80 mmol/L LUT, 1.47 mmol/L CA, 1.69 mmol/L CCA, 17.5 mmol/L 3,4-DCQA, and 16.88 mmol/L 4,5-DCQA); and DMEM containing 10% FBS and 800 μg/ml of *I. cappa* extract (an equivalence of 3.20 mmol/L LUT, 5.88 mmol/L CA, 6.76 mmol/L CCA, 70.00 mmol/L 3,4-DCQA, and 67.52 mmol/L 4,5-DCQA). Cells were collected at 0, 5, 15, 30, 45 min, 1, 2, 4, 6, 8, 12, and 24 h. Cells were washed twice quickly with 2 ml of pre-chilled PBS, and 2 ml of ultrapure water was added to each well. The cells were frozen and thawed at −80°C three times before collecting the dissociated cells from the 6-well plates into centrifuge tubes for cellular pharmacokinetic studies.

A previously established UPLC-MS/MS analytical method was applied to determine the intracellular concentrations of the five ingredients in *I. cappa* extract (Zhou, et al., 2022). Briefly, puerarin was selected as an internal standard and the

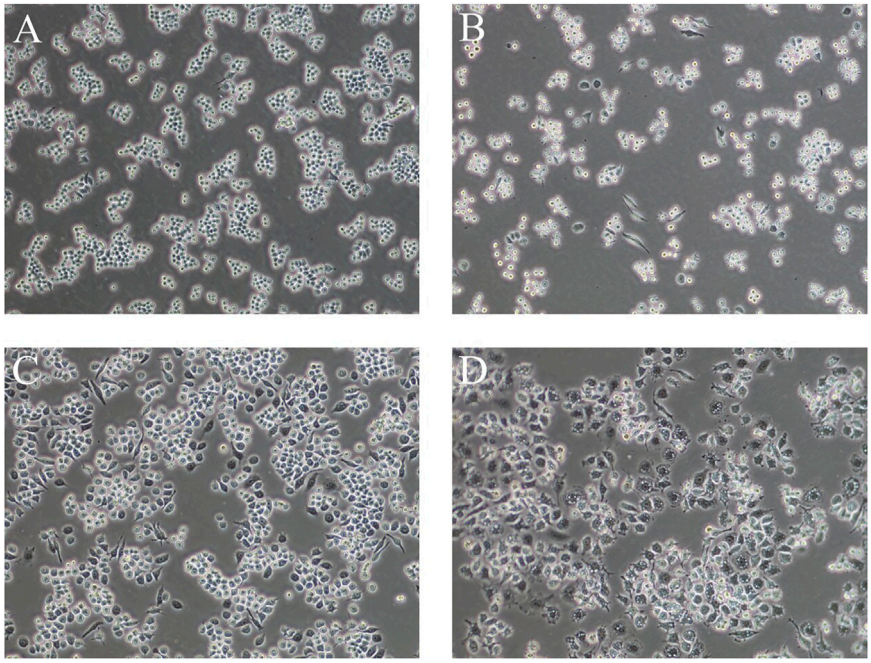

FIGURE 2
Cell morphology of LPS-induced RAW264.7 cells at different times **(A)**: normal cells, **(B)** 1 μg/ml LPS-induced cells at 6 h, **(C)** 1 μg/ml LPS-induced cells at 12 h, **(D)** 1 μg/ml LPS-induced cells at 24 h) (100×).

positive and negative ion modes were used for simultaneous monitoring. Quantitation was performed using multiple-reaction monitoring of the protonated molecular ion to the predominant product ion pair (m/z 449.2 > 287.1 for LUT and m/z 417.0 > 267.0 for puerarin detected in the positive ion mode; m/z 353.1 > 191.1 for CA, m/z 353.2 > 172.9 for CCA, m/z 515.1 > 353.1 for 3,4-DCQA, and m/z 515.1 > 353.1 for 4,5-DCQA in the negative ion mode). An aliquot of 800 μL cell suspension after three freeze–thaw cycles was spiked with 50 μL of the internal standard solution containing 0.036 μmol/L puerarin and vortexed briefly. Then, the mixture was added to 160 μL of aqueous 20% formic acid and 800 μL of methanol, followed by 5 min of vortexing and 10 min of sonication. The supernatant was centrifuged at 12,000 rpm for 10 min at 4°C and blown dry using a nitrogen blower. Next, 150 μL of 50% methanol was added to the residue, and samples were vortexed for 5 min, sonicated for 10 min, and centrifuged at 14,000 rpm for 10 min at 4°C. The supernatant was transferred into an autosampler vial, and an aliquot of 3 μL was subsequently injected into the UPLC-MS/MS system for assay. The lower limit of quantification was established at 0.0011 μmol/L for LUT, 0.0027 μmol/L for CA and CCA, and 0.0074 μmol/L for 3,4-DCQA and 4,5-DCQA in cell suspension.

2.3.4 BCA protein quantification

We used BCA kits to determine protein concentrations.

2.3.5 Data analysis

SPSS18.0 statistical software was used for data analysis, and experimental results were expressed as mean ± standard deviation. We used the independent samples *t*-test for comparisons between groups, and $p < 0.05$ was considered statistically different. Pharmacokinetic parameters were processed with WinNonLin 8.3 data processing software.

3 Results

3.1 *In vitro* inflammation model validation

3.1.1 Cell morphology

As shown in Figure 2, the control RAW264.7 cells were small, round, and translucent, showed low differentiation, and had no pseudopods. Upon LPS induction, the morphology of the cells changed significantly: the cells were larger, the intracellular vacuoles were obvious, the pseudopods were longer and more extended, and the cells were irregularly spindle-shaped and polygonal. This change in morphology became larger with longer induction times.

3.1.2 Survival rate of cells treated with different concentrations of LPS after 24 h

Cells were treated with different concentrations of LPS. As shown in Figure 3A, after 24 h, the cell survival rate was not significantly affected.

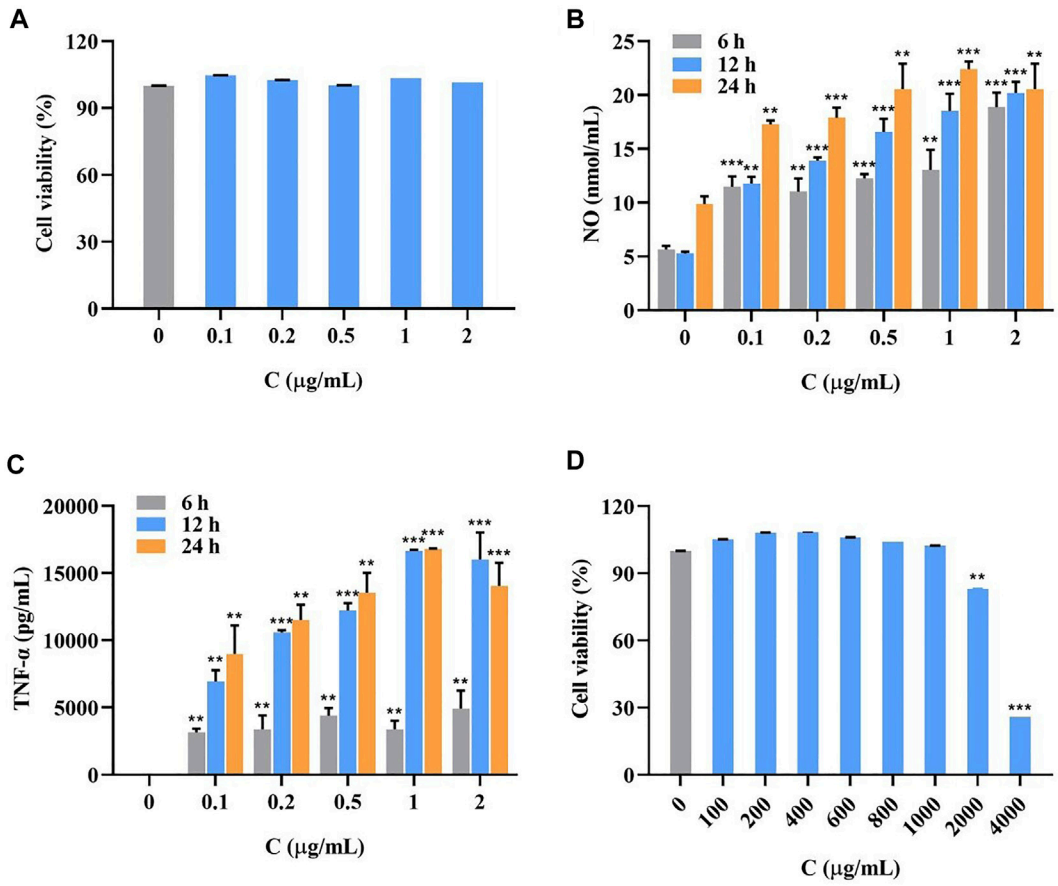

FIGURE 3
Survival rate of LPS-induced RAW264.7 cells at LPS different concentrations for 24 h **(A)**, the accumulation of NO **(B)** and TNF-α **(C)** in LPS-induced RAW264.7 cells at different concentrations for 6, 12 and 24 h ($\bar{x}\pm$ SD, n = 3, nmol/mL), and survival rate of RAW264.7 cells after the addition of *I. cappa* extract **(D)**. Compared with the blank group, $^{*}p < 0.05$, $^{**}p < 0.01$, $^{***}p < 0.001$.

3.1.3 Measurement of inflammatory factor secretion

As shown in Figure 3, the secretion of inflammatory factors NO (Figure 3B) and TNF-α (Figure 3C) significantly increased with longer LPS treatment and higher concentrations. The secretion was most pronounced at an induction time of 24 h and a concentration of 1 μg/ml. The data of all groups were significantly different compared with the blank group.

3.1.4 Safe concentration range of *I. cappa* in RAW264.7 cells

As shown in Figure 3D, the cell survival rate was above 90% at *I. cappa* extract concentrations of 0–1000 μg/ml, indicating that the drug was not significantly toxic to the cells. Considering this safe range and the detectability of trace amounts of drug entering cells, the concentrations of 200 and 800 μg/ml were chosen for the pharmacokinetic study.

3.2 Pharmacokinetic results

After calculating the measured intracellular concentrations of the five ingredients in *I. cappa* extract, the pharmacokinetic software WinNonlin 8.3 (Phoenix, Pharsight, United States) was used to plot the mean cell concentration (ng/mg) versus time profile for the above drug components. Non-compartmental analysis was performed to find the pharmacokinetic parameters after treatment with 200 μg/ml and 800 μg/ml of *I. cappa* extracts, including terminal elimination half-life ($T_{1/2}$), area under the concentration versus time curve from zero to last sampling time (AUC_{0-t}), volume of distribution (V_d/F), and total body clearance (CL/F). The peak concentration (C_{max}) and the time to reach C_{max} (T_{max}) were read directly from the individual concentration-time data. The pharmacokinetic parameters of the five representative ingredients of *I. cappa* were compared and analyzed between the normal and the model groups at low and high concentrations to illustrate the kinetic process of the drug in the cells.

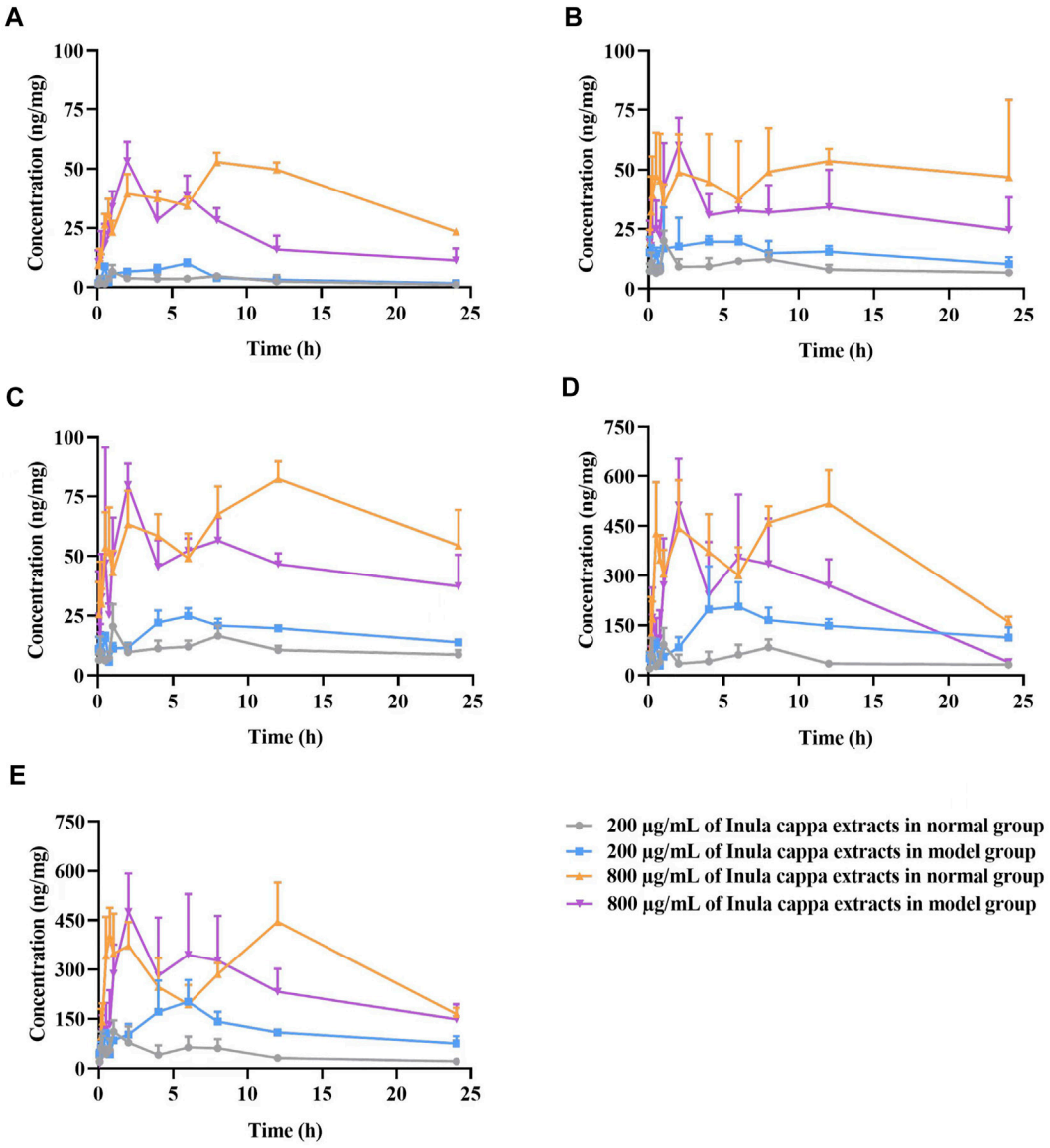

FIGURE 4
The mean concentration (ng/mg) of luteolin **(A)**, chlorogenic acid **(B)**, cryptochlorogenic acid **(C)**, 3,4-dicaffeoylquinic acid **(D)**, and 4,5-dicaffeoylquinic acid **(E)** versus time profiles in RAW264.7 cells after treatment with 200 μg/ml and 800 μg/ml of *I. cappa* extracts ($\bar{x} \pm$ SD, n = 6).

For LUT, as shown in Figure 4A and Table 2, the $AUC_{0\text{-}t}$ and C_{max} values of the main pharmacokinetic parameters of LUT in normal and inflammatory RAW264.7 cells after administration of *I. cappa* extract showed a dose-dependent effect. With increasing doses, C_{max} and AUC also tended to increase, reflecting a dose-dependent pharmacokinetic profile. However, there were differences in their T_{max}, CL_F, Vz_F, and $MRT_{0\text{-}t}$ values among them. After treatment with 200 μg/ml of *I. cappa* extracts, in normal cells, the $AUC_{(0\text{-}t)}$, T_{max}, and CL_F values were 66.85 ± 25.23 h*ng/mL, 1.20 ± 0.45 h, and 8.64 ± 2.64 ml/h, respectively, while in inflammatory cells, the parameters were 99.66 ± 21.24 h*ng/mL, 6.00 ± 0.00 h, and 5.73 ± 0.96 ml/h, respectively. The results showed that the uptake of LUT in inflammatory cells was faster at low concentrations, but T_{max} lagged and uptake of LUT was slower than in the normal group, and CL_F and Vz_F were also lower than in the normal group. After treatment with 800 μg/ml of *I. cappa* extracts, in normal cells, the $AUC_{0\text{-}t}$, T_{max}, Vz_F, and CL_F values were 931.01 ± 14.06 h*ng/mL, 10.00 ± 2.19 h, 36.76 ± 2.76 ml, and 2.09 ± 0.06 ml/h, respectively, while in inflammatory cells, the corresponding parameters were 528.65 ± 82.74 h*ng/mL, 2.00 ± 0.00 h, 61.50 ± 12.67 ml, and 4.10 ± 1.49 ml/h, respectively. The

TABLE 2 The pharmacokinetic parameters of luteolin in RAW264.7 cells after treatment with 200 μg/ml and 800 μg/ml of *I. cappa* extracts ($\bar{x} \pm$ SD, n = 6).

Parameters	unit	200 μg/ml		800 μg/ml	
		Normal group	Model group	Normal group	Model group
AUC_{0-t}	h*ng/mL	66.85 ± 25.23	99.66 ± 21.24*	931.01 ± 14.06	528.65 ± 82.74***
$AUC_{0-\infty}$	h*ng/mL	86.61 ± 23.13	125.30 ± 22.12*	1343.24 ± 36.14	736.26 ± 175.54***
MRT_{0-t}	h	9.05 ± 0.48	8.57 ± 0.41	11.01 ± 0.28	8.82 ± 0.91**
$MRT_{0-\infty}$	h	16.73 ± 4.70	14.86 ± 2.67	20.44 ± 1.18	17.54 ± 5.13
$t_{1/2}$	h	10.85 ± 3.07	10.09 ± 1.83	12.24 ± 1.21	11.50 ± 3.95
T_{max}	h	1.20 ± 0.45	6.00 ± 0.00***	10.00 ± 2.19	2.00 ± 0.00***
CL_F	mL/h	8.64 ± 2.64	5.73 ± 0.96*	2.09 ± 0.06	4.10 ± 1.49*
Vz_F	mL	134.94 ± 48.39	83.95 ± 21.53	36.76 ± 2.76	61.50 ± 12.67**
C_{max}	ng/mL	8.11 ± 1.42	10.14 ± 1.55*	54.19 ± 2.37	53.16 ± 8.22
R^2	-	0.70 ± 0.09	0.90 ± 0.04	0.96 ± 0.02	0.90 ± 0.13

Compared with normal group, *$p < 0.05$, **$p < 0.01$, ***$p < 0.001$.

TABLE 3 The pharmacokinetic parameters of chlorogenic acid in RAW264.7 cells after treatment with 200 μg/ml and 800 μg/ml of *I. cappa* extracts ($\bar{x} \pm$ SD, n = 6).

Parameters	unit	200 μg/ml		800 μg/ml	
		Normal group	Model group	Normal group	Model group
AUC_{0-t}	h*ng/mL	219.14 ± 19.64	405.87 ± 153.61*	1151.63 ± 260.90	715.66 ± 160.49**
$AUC_{0-\infty}$	h*ng/mL	419.19 ± 77.98	695.12 ± 215.82*	1881.18 ± 846.92	1377.31 ± 610.95
MRT_{0-t}	h	10.63 ± 0.60	10.74 ± 0.97	11.95 ± 1.87	10.22 ± 0.96
$MRT_{0-\infty}$	h	30.81 ± 7.04	27.99 ± 10.99	22.75 ± 4.28	30.26 ± 9.96
$t_{1/2}$	h	20.12 ± 4.79	18.56 ± 6.82	12.62 ± 1.99	20.57 ± 6.79*
T_{max}	h	1.00 ± 0.00	3.40 ± 1.95**	13.00 ± 9.44	2.00 ± 0.00*
CL_F	mL/h	2.56 ± 0.46	1.62 ± 0.48**	2.48 ± 0.75	3.47 ± 1.30
Vz_F	mL	72.09 ± 8.62	41.55 ± 11.87**	45.10 ± 14.67	93.61 ± 16.19***
C_{max}	ng/mL	20.08 ± 4.17	33.62 ± 14.14*	53.46 ± 18.86	60.10 ± 11.63
R^2	-	0.67 ± 0.23	0.77 ± 0.14	0.80 ± 0.23	0.78 ± 0.15

Compared with normal group, *$p < 0.05$, **$p < 0.01$, ***$p < 0.001$.

results show that after treatment with 800 μg/ml of *I. cappa* extracts, the uptake of LUT in inflammatory cells was slower, but T_{max} was prolonged, absorption was faster, $t_{1/2}$ was shorter, metabolism was prolonged, and CL_F was increased. The pharmacokinetic parameters of LUT at each concentration differed significantly between the normal and inflammatory states.

For CA, as shown in Figure 4B and Table 3, in normal and inflammatory RAW264.7 cells, the AUC_{0-t} and C_{max} values of CA after administration of *I. cappa* extract showed a dose-dependent effect. The C_{max} and AUC values tended to increase with increasing concentrations. After treatment with 200 μg/ml of *I. cappa* extracts, in control cells, the AUC_{0-t}, T_{max}, C_{max}, CL_F, and Vz_F values were 219.14 ± 19.64 h*ng/mL, 1.00 ± 0.00 h, 20.08 ± 4.17 ng/ml, 2.56 ± 0.46 ml/h, and 72.09 ± 8.62 ml, respectively, while in inflammatory cells, the corresponding parameters were 405.87 ± 153.61 h*ng/mL, 3.40 ± 1.95 h, 33.62 ± 14.14 ng/ml, 1.62 ± 0.48 ml/h, and 41.55 ± 11.87 ml, respectively. The results showed that CA uptake in inflammatory cells was faster after treatment with 200 μg/ml of *I. cappa* extracts, but T_{max} lagged and CA uptake was slower than in the normal group, and CL_F and Vz_F were also lower than in the normal group. The AUC_{0-t}, T_{max}, $t_{1/2}$, and Vz_F values of CA in normal cells After treatment with 800 μg/ml of *I. cappa* extracts were 1151.63 ± 260.90 h*ng/mL, 13.00 ± 9.44 h, 12.62 ± 1.99 h, and 45.10 ± 14.67 ml, respectively, and the corresponding parameters in inflammatory cells were 715.66 ± 160.49 h*ng/mL, 2.00 ± 0.00 h, 20.57 ± 6.79 h, and 93.61 ±

TABLE 4 The pharmacokinetic parameters of cryptochlorogenic acid in RAW264.7 cells after treatment with 200 μg/ml and 800 μg/ml of *I. cappa* extracts ($\bar{x} \pm SD$, n = 6).

Parameters	unit	200 μg/ml		800 μg/ml	
		Normal group	Model group	Normal group	Model group
AUC_{0-t}	h*ng/mL	265.24 ± 31.31	427.29 ± 32.92***	1559.95 ± 139.88	1138.24 ± 70.46***
$AUC_{0-\infty}$	h*ng/mL	495.91 ± 92.60	928.16 ± 168.41***	2823.69 ± 669.23	2420.18 ± 1003.94
MRT_{0-t}	h	11.04 ± 0.74	11.42 ± 0.42	11.91 ± 0.72	10.91 ± 0.87
$MRT_{0-\infty}$	h	30.25 ± 8.70	37.64 ± 9.46	38.74 ± 23.85	37.01 ± 23.93
$t_{1/2}$	h	19.39 ± 6.15	24.89 ± 6.53	18.10 ± 5.71	23.76 ± 18.54
T_{max}	h	1.00 ± 0.00	6.33 ± 0.82***	11.33 ± 1.63	1.75 ± 0.61***
CL_F	mL/h	2.49 ± 0.50	1.32 ± 0.23**	1.56 ± 0.59	2.29 ± 0.98
Vz_F	mL	70.37 ± 16.71	45.98 ± 6.16**	43.99 ± 3.28	59.93 ± 26.43
C_{max}	ng/mL	21.90 ± 7.29	25.32 ± 3.26	84.79 ± 5.92	89.04 ± 26.15
R^2	-	0.84 ± 0.31	0.69 ± 0.05	0.74 ± 0.19	0.94 ± 0.05

Compared with normal group, *$p < 0.05$, **$p < 0.01$, ***$p < 0.001$.

16.19 ml, respectively. The results showed that after treatment with 800 μg/ml of *I. cappa* extracts, CA uptake in inflammatory cells was slower than that in normal cells, but T_{max} was prolonged, uptake was faster, $t_{1/2}$ was prolonged, metabolism was slower, and CL_F and Vz_F increased. The pharmacokinetic parameters of CA at each concentration differed significantly between normal and inflammatory states.

For CCA, as shown in Figure 4C and Table 4, the AUC_{0-t} and C_{max} values of CCA in normal and inflammatory RAW264.7 cells after administration of *I. cappa* extract showed a dose-dependent effect. The C_{max} and AUC values tended to increase with increasing concentrations. After treatment with 200 μg/ml of *I. cappa* extracts, the AUC_{0-t}, T_{max}, CL_F, and Vz_F values in normal cells were 265.24 ± 31.31 h*ng/mL, 1.00 ± 0.00 h, 2.49 ± 0.50 ml/h, and 70.37 ± 16.71 ml, respectively, while in inflammatory cells, the corresponding parameters were 427.29 ± 32.92 h*ng/mL, 6.33 ± 0.82 h, 1.32 ± 0.23 ml/h, and 45.98 ± 6.16 ml, respectively. The results showed that after treatment with 200 μg/ml of *I. cappa* extracts, CCA uptake in inflammatory cells increased, but T_{max} lagged and the uptake of CCA in the inflammatory cell group was slower than that in the normal group, and CL_F and Vz_F were also lower than in the normal group. After treatment with 800 μg/ml of *I. cappa* extracts, the AUC_{0-t} and T_{max} values in normal cells were 1559.95 ± 139.88 h*ng/mL and 11.33 ± 1.63 h, respectively, while the corresponding parameters in inflammatory cells were 1138.24 ± 70.46 h*ng/mL and 1.75 ± 0.61 h, respectively. The results showed that after treatment with 800 μg/ml of *I. cappa* extracts, CCA uptake in inflammatory cells was reduced, T_{max} was prolonged, the uptake of CCA was faster, $t_{1/2}$ was prolonged, metabolism was slowed down, and Vz_F and CL_F were increased. The pharmacokinetic parameters of CCA differed significantly between normal and inflammatory states at each concentration.

For 3,4-DCQA, as shown in Figure 4D and Table 5, the AUC_{0-t} and C_{max} values of 3,4-DCQA in cells after the administration of *I. cappa* extract to normal and inflammatory RAW 264.7 cells showed a dose-dependent effect. The C_{max} and AUC values tended to increase with increasing concentrations. After treatment with 200 μg/ml of *I. cappa* extracts, in normal cells, the AUC_{0-t}, T_{max}, C_{max}, MRT_{0-t}, $t_{1/2}$, CL_F, and Vz_F values were 1168.85 ± 240.66 h*ng/mL, 1.00 ± 0.00 h, 136.24 ± 70.99 ng/ml, 10.40 ± 0.74 h, 13.32 ± 2.70 h, 10.59 ± 2.30 ml/h, and 201.47 ± 52.06 ml, respectively, while in inflammatory cells, the corresponding parameters were 3499.51 ± 536.34 h*ng/mL, 6.00 ± 3.10 h, 255.49 ± 79.43 ng/ml, 11.49 ± 0.90 h, 20.32 ± 4.09 h, 2.77 ± 0.68 ml/h, and 77.99 ± 10.00 ml, respectively. The results showed that after treatment with 200 μg/ml of *I. cappa* extracts, 3, 4-DCQA uptake was increased in inflammatory cells, but T_{max} lagged, its uptake was slower compared to the normal group, $t_{1/2}$ was prolonged, metabolism was slowed down, and CL_F and Vz_F were reduced. After treatment with 800 μg/ml of *I. cappa* extracts, in normal cells, the AUC_{0-t}, T_{max}, $t_{1/2}$, Vz_F, and $MRT_{0-\infty}$ values of 3,4-DCQA were 8916.50 ± 1010.81 h*ng/mL, 9.00 ± 4.69 h, 8.41 ± 2.10 h, 80.82 ± 18.46 ml, and 15.11 ± 1.69 h, respectively, and the corresponding parameters in inflammatory cells were 6426.51 ± 1438.14 h*ng/mL, 2.50 ± 1.76 h, 16.30 ± 6.63 h, 147.13 ± 20.73 ml, and 24.50 ± 9.39 h, respectively. The results showed that after treatment with 800 μg/ml of *I. cappa* extracts, 3,4-DCQA uptake in inflammatory cells was reduced, T_{max} was advanced, absorption was faster, $t_{1/2}$ was prolonged, metabolism was slowed, and Vz_F was increased.

TABLE 5 The pharmacokinetic parameters of 3,4-dicaffeoylquinic acid in RAW264.7 cells after treatment with 200 μg/ml and 800 μg/ml of *I. cappa* extracts ($\bar{x} \pm SD$, n = 6).

Parameters	unit	200 μg/ml		800 μg/ml	
		Normal group	Model group	Normal group	Model group
AUC_{0-t}	h*ng/mL	1168.85 ± 240.66	3499.51 ± 536.34***	8916.50 ± 1010.81	6426.51 ± 1438.14**
$AUC_{0-\infty}$	h*ng/mL	1776.35 ± 384.24	6926.13 ± 1912.52***	10884.10 ± 1066.05	11408.00 ± 3813.22
MRT_{0-t}	h	10.40 ± 0.74	11.49 ± 0.90*	10.33 ± 0.44	10.54 ± 1.02
$MRT_{0-\infty}$	h	21.69 ± 4.31	31.85 ± 6.76*	15.11 ± 1.69	24.50 ± 9.39*
$t_{1/2}$	h	13.32 ± 2.70	20.32 ± 4.09**	8.41 ± 2.10	16.30 ± 6.63*
T_{max}	h	1.00 ± 0.00	6.00 ± 3.10**	9.00 ± 4.69	2.50 ± 1.76**
CL_F	mL/h	10.59 ± 2.30	2.77 ± 0.68***	6.70 ± 0.66	6.87 ± 2.04
Vz_F	mL	201.47 ± 52.06	77.99 ± 10.00***	80.82 ± 18.46	147.13 ± 20.73***
C_{max}	ng/mL	136.24 ± 70.99	255.49 ± 79.43*	579.51 ± 100.02	612.61 ± 147.92
R^2	-	0.91 ± 0.38	0.67 ± 0.36	0.93 ± 0.09	0.86 ± 0.12

Compared with normal group, *$p < 0.05$, **$p < 0.01$, ***$p < 0.001$.

Significant differences were observed in the pharmacokinetic parameters of 3, 4-DCQA at various concentrations between normal and inflammatory states.

For 4,5-DCQA, as shown in Figure 4E and Table 6, the AUC_{0-t} and C_{max} values of 4,5-DCQA in normal and inflammatory RAW264.7 cells after administration of *I. cappa* extract showed a dose-dependent effect. The C_{max} and AUC values tended to increase with increasing concentrations. After treatment with 200 μg/ml of *I. cappa* extracts, the AUC_{0-t}, T_{max}, MRT_{0-t}, $t_{1/2}$, CL_F, and Vz_F values in normal cells were 1032.84 ± 280.12 h*ng/mL, 0.96 ± 0.60 h, 10.44 ± 2.39 h, 8.86 ± 0.76 h, 13.98 ± 4.51 ml/h, and 201.17 ± 42.85 ml, respectively, while in inflammatory cells, the corresponding parameters were 2817.10 ± 572.08 h*ng/mL, 5.67 ± 1.51 h, 10.43 ± 0.41 h, 15.05 ± 1.10 h, 4.08 ± 0.87 ml/h, and 88.80 ± 20.50 ml, respectively. The results showed that after treatment with 200 μg/ml of *I. cappa* extracts, 4,5-DCQA uptake was increased in inflammatory cells, but its T_{max} was lagged, uptake was slower than in the normal group, $t_{1/2}$ and MRT were prolonged, metabolism was slowed, and CL_F and Vz_F were also reduced. After treatment with 800 μg/ml of *I. cappa* extracts, the AUC_{0-t}, T_{max}, $t_{1/2}$, and Vz_F values of 4,5-DCQA in normal cells were 7475.39 ± 996.99 h*ng/mL, 7.00 ± 5.48 h, 9.09 ± 2.69 h, and 94.80 ± 24.43 ml, respectively, and the corresponding parameters in inflammatory cells were 5955.63 ± 1217.95 h*ng/mL, 2.50 ± 1.76 h, 12.25 ± 3.62 h, and 136.49 ± 18.20 ml, respectively. The results showed that 4,5-DCQA uptake in inflammatory cells was reduced, T_{max} was prolonged, its uptake was faster, $t_{1/2}$ was prolonged, metabolism was slowed down, and Vz_F and CL_F were increased after treatment with 800 μg/ml of *I. cappa* extracts. Significant differences were observed in the pharmacokinetic parameters of 4,5-DCQA at various concentrations between normal and inflammatory states.

4 Discussion

The LPS-induced *in vitro* inflammation model is a commonly used research tool for natural drug screening. This cell model is relatively simple, rapid, sensitive, and efficient and requires only small amounts of sample. We observed that after modeling, cells were larger, the intracellular vacuole was obvious, the pseudopods were longer and more extended, and the cells were more irregularly spindle-shaped and polygonal. According to the literature, RAW264.7 cells in this form are in a state of inflammation (Zhou, et al., 2019; Zhang, et al., 2020), and this morphological change was more significant with increasing induction time. The secretion of NO and TNF-α increased with the increase of LPS induction time and concentration. Based on our results and the literature, we chose an induction time of 24 h and a concentration of 1 μg/ml for the establishment of the *in vitro* inflammation model.

The cellular pharmacokinetic results showed that the uptake of five ingredients (LUT, CA, CCA, 3,4-DCQA, and 4,5-DCQA) by RAW264.7 cells is a nonlinear pharmacokinetic process. Their pharmacokinetic parameters changed with concentration; C_{max} and AUC kinetics were not proportional to the concentration, and $t_{1/2}$ was prolonged with increasing concentrations. For LUT and CCA, their C_{max} and AUC values increased with increasing concentrations and were not proportional in both normal and model cells, which indicates that the cellular uptake of the two ingredients was concentration-dependent. The differences in C_{max} and AUC of CA were not significant after treatment with 200 μg/ml of *I. cappa* extracts, even in inflammatory cells, where both C_{max} and AUC increased substantially after treatment with 800 μg/ml of *I. cappa* extracts. In normal cells 3,4-DCQA and 4,5-DCQA showed a concentration-dependent increase. Overall, the AUC values of the five components at different concentrations were not proportional to the

TABLE 6 The pharmacokinetic parameters of 4,5-dicaffeoylquinic acid in RAW264.7 cells after treatment with 200 μg/ml and 800 μg/ml of *I. cappa* extracts ($\bar{x} \pm SD$, n = 6).

Parameters	unit	200 μg/ml		800 μg/ml	
		Normal group	Model group	Normal group	Model group
AUC_{0-t}	h*ng/mL	1032.84 ± 280.12	2817.10 ± 572.08***	7475.39 ± 996.99	5955.63 ± 1217.95*
$AUC_{0-\infty}$	h*ng/mL	1361.08 ± 417.72	4448.02 ± 989.58***	9672.25 ± 983.10	8967.64 ± 2062.61
MRT_{0-t}	h	8.86 ± 0.76	10.43 ± 0.41*	10.62 ± 0.68	10.19 ± 1.41
$MRT_{0-\infty}$	h	16.03 ± 2.59	23.27 ± 1.68***	16.84 ± 3.27	18.74 ± 4.75
$t_{1/2}$	h	10.44 ± 2.39	15.05 ± 1.10**	9.09 ± 2.69	12.25 ± 3.62*
T_{max}	h	0.96 ± 0.60	5.67 ± 1.51**	7.00 ± 5.48	2.50 ± 1.76*
CL_F	mL/h	13.98 ± 4.51	4.08 ± 0.87***	7.28 ± 0.71	8.11 ± 1.80
Vz_F	mL	201.17 ± 42.85	88.80 ± 20.50***	94.80 ± 24.43	136.49 ± 18.20**
C_{max}	ng/mL	153.88 ± 59.85	224.23 ± 60.39	575.66 ± 159.23	589.11 ± 148.35
R^2	-	0.90 ± 0.12	0.66 ± 0.15	1.00 ± 0.00	0.92 ± 0.08

Compared with normal group, *$p < 0.05$, **$p < 0.01$, ***$p < 0.001$.

administered concentrations and exhibited a nonlinear pharmacokinetic process.

In normal cells, $t_{1/2}$ of LUT was prolonged with increasing concentrations, but there was no significant difference. The $t_{1/2}$ values of CA and CCA were shorter with increasing concentrations, and the $t_{1/2}$ values of 3,4-DCQA and 4,5-DCQA remained essentially unchanged with increasing concentrations. In inflammatory cells, the $t_{1/2}$ values of the remaining four components were prolonged with increasing concentrations, except for LUT, whose $t_{1/2}$ became shorter and metabolism accelerated with an increasing concentration. Moreover, T_{max} of the five ingredients in inflammatory cells was prolonged after treatment with 200 μg/ml of *I. cappa* extracts, showing that the uptake was slower than in the normal group, and the T_{max} values of each component in normal and inflammatory cells were inconsistent. However, $t_{1/2}$ was prolonged, metabolism slowed down, and both CL_F and Vz_F decreased significantly. After treatment with 800 μg/ml of *I. cappa* extracts, compared to the normal cell group, T_{max} of the components was prolonged and absorption became faster in the model group. This indicates that the morphology and internal microenvironment of the cells are altered, except in the inflammatory state. This leads to differences in the entry of the drug into the body, and we speculate that this difference may result from the increase in concentration.

We previously determined that the plasma protein binding abilities of LUT, CA, CCA, 3,4-DCQA, and 4,5-DCQA in human and rat plasma were in the range of 81.25 ± 0.038% to 97.46 ± 0.013% by equilibrium dialysis (Bao, et al., 2019). This indicates that all five components have strong protein binding abilities. For this type of drug, at increasing drug doses, plasma protein binding is decreased, the free drug concentration is increased, and absorption distribution and pharmacological action are altered (Feng, et al., 2019). In addition, FBS contains a large number of proteins, and it has been shown that polyphenolic compounds, like bovine serum albumin and globulin, can interact with each other (Mai, et al., 2021). According to the nonlinear pharmacokinetic characteristics, the metabolic pathways and elimination processes were facilitated and the half-life was decreased when we increased the dose of components with strong plasma protein binding ability. This could explain why there was a difference in $t_{1/2}$, CL_F, and other values for each component between different concentrations.

Drug absorption is related to drug physicochemical properties, cell membrane permeability, and drug transporters. Biological membrane permeation is a key factor for the cellular uptake of free drugs. The cell membrane is selectively permeable and has a bilayer lipid structure. Thus, selectively absorbed ions and small molecules and lipid-soluble drugs can easily pass through the cell membrane. Generally, some drugs with low lipid solubility, large molecular weight, and polar groups enter cells by endocytosis (Xie, et al., 2004). CA is a caffeic acid with high polarity, and macrophages may take up the drug into the cells by endocytosis. The change of cell permeability is an important pathological process in a variety of diseases such as inflammatory responses, tissue hypoxia, and impaired cellular metabolism (Zhang, et al., 2018). Cellular modeling causes an increase in permeability, which is presumed to be associated with increased p38 MAPK pathway and PI3K/Akt pathway activity during LPS-induced production of inflammatory factors, according to the relevant literature (Chang and Qi, 2020). Macrophages are immune cells that rely on their phagocytosis and clearance ability to participate in the immune process. They have a variety of receptors on their surface that are involved in cytophagy or cytokinesis. During LPS treatment, LPS combines with Toll-like receptor 4 proteins on the cell surface, actin

aggregates, the cytoskeleton contracts, and pseudopods are extended. At this time, the phagocytic capacity of RAW264.7 cells is greatly enhanced (Wang, et al., 2001), which causes the cells to swallow particles from the external environment into the cells, increasing drug uptake.

In general, the differences in the pharmacokinetic parameters of different concentration compounds between the normal and model groups were inconsistent. After treatment with 200 μg/ml of *I. cappa* extracts, the AUC_{0-t}, MRT_{0-t}, T_{max}, and C_{max} values of the five compounds in the model group were higher than those in the normal group, while the CL_F and Vz_F values in the model group were lower than those in the normal group; After treatment with 800 μg/ml of *I. cappa* extracts, their AUC_{0-t}, MRT_{0-t}, T_{max}, and C_{max} values in the model group were lower than those in the normal group, while CL_F and Vz_F values in the model group were higher than those in the normal group. These results indicated that compared with the normal group, the five compounds in the model group had increased absorption and slowed elimination after treatment with 200 μg/ml of *I. cappa* extracts, while the absorption decreased and elimination accelerated in the model group after treatment with 800 μg/ml of *I. cappa* extracts. The main reason for this phenomenon is that the permeability of the cell membrane increases in the inflammatory state. Therefore, after treatment with 200 μg/ml of *I. cappa* extracts, the absorption of the drug in the model group was increased. However, after treatment with 800 μg/ml of *I. cappa* extracts, the AUC values of five ingredients were reduced in the model group compared with the normal group. We hypothesize that this might be explained as follows. First, drug toxicity may play a role. The composition of *I. cappa* extract is complex. With the increase in drug concentration, the concentrations of toxic ingredients also increased. This may have resulted in a decreased survival rate of RAW264.7 cells in the original inflammatory state. Second, the substance enters the cell through membrane dynamic transport and attaches to the cell with the help of certain specific proteins. Compared to the normal cell group, the intracellular drug concentration becomes higher and the toxicity increases, leading to a decrease in affinity and intracellular AUC. Finally, membrane permeability at high concentrations is limited, and when cells are damaged in the inflammatory state, some functional transporter proteins and drug metabolism enzymes (DMEs) on the surface of the cell membrane are altered accordingly, which causes a decrease in the intracellular accumulation of drugs.

When the administered dose and drug concentration exceed a certain limit, the enzyme catalytic capacity and carrier transport capacity are saturated, and its pharmacokinetics show a clear dose dependence. Nonlinear pharmacokinetic processes are subject to metabolic enzyme saturation, where enzyme metabolism is saturated, which will cause drug accumulation with an exponential increase in AUC, C_{max}, and $T_{1/2}$ (Ye, et al., 2020). In the body, the metabolic enzymes of some drugs have a limited capacity to metabolize them, and the administration of larger doses leads to a saturable metabolic process of the corresponding substrate drug. The blood concentration and the dose are not proportional at this time, which also leads to a significant increase in the body's drug concentration and causes clinical effects and toxic side effects (Liu, 2016).

Moreover, carrier protein saturation has an effect on pharmacokinetic processes. Drug transport is influenced by transport proteins in the cell membrane, which can be divided into uptake proteins and efflux proteins. Nonlinear pharmacokinetics are regulated by uptake proteins and efflux proteins, resulting in nonlinear phenomena in the *in vivo* dynamics of the drug. As a result of saturation of absorbed proteins, the C_{max} or AUC does not increase proportionally with increasing doses, while the saturation of exocytosis proteins causes a decrease in exocytosis of secreted drugs and an increase in the AUC value with increasing concentrations. In the present research, the nonlinear kinetics are induced by the saturation of exocytosis proteins through AUC values/doses. In addition, drug efflux proteins, such as P-glycoprotein, are widely distributed on the cell surface. They are able to regulate the permeability of cell membranes and the intracellular concentrations of certain drugs. The involvement of efflux proteins may further decrease the intracellular drug concentration, and drug redistribution may also occur in subcellular organelles after cellular uptake (Zhang, et al., 2018; Liu, et al., 2019; Zhou, et al., 2020).

In addition, enzyme saturation has an effect on pharmacokinetic processes. There are two forms of intracellular elimination of drugs: cellular elimination and conversion by enzymatic regulation. The metabolism of most drugs is associated with cytochrome P450 (CYP) enzymes. The metabolic capacity of CYP enzymes is complex, and the profile of DMEs may change in pathological states, which may affect drug metabolism, as well as the body state, which may also affect drug distribution and elimination. It was found that macrophages attacked by LPS secrete large amounts of the inflammatory factor NO. Excessive NO reduces the affinity of cytochrome *c* for oxygen, which inhibits mitochondrial respiratory chain function, and NO combines with peroxides to form peroxynitrite anion ($ONOO^-$), which can affect the function of glycolytic and respiratory enzymes and interfere with cellular energy metabolism (Ma et al., 2019). Clinical studies have shown that in some pathological states, such as inflammation, DME expression and activity can be reduced, resulting in a decrease of 20–70% in drug clearance (Bissery et al., 1996), which may also be responsible for the large individual differences in pharmacokinetic parameters of patients. Current reports suggest that acute inflammation may alter the pharmacokinetics of non-steroidal anti-inflammatory analgesics (Projean, et al., 2005; Uno, et al., 2008) and that such differences may arise from inflammation and fluctuations in CYP enzyme activity during drug administration (Gong et al., 2014). Our previous study found that *I. cappa* may inhibit this enzyme activity when combined

with drugs metabolized via CYP3A, CYP2C9, CYP2C19, and CYP1A2 (Song et al., 2019). It is speculated that the five components may inhibit the activity of their own DMEs, thus causing slowed metabolism, decreased clearance, a prolonged half-life, and increased blood concentrations and AUC values. In the present study, five components showed a decrease in clearance with increasing concentrations. There was an increase or decrease in normal and inflammatory cells, suggesting that the expression of metabolic enzymes in cells may be different between components of *I. cappa* in the inflammatory state.

Changes in pharmacokinetic behavior and pharmacokinetic parameters are not determined by a single factor but may be the complex result of multiple factors. Cell permeability, cell surface transporters, and saturation of DMEs are altered in the inflammatory state, and these factors are key determinants of drug entry into target cells, intracellular metabolism, and the corresponding drug efficacy (Zhou, et al., 2011; Patrick, et al., 2016). The specific mechanisms underlying the differences in the pharmacokinetic processes of the five anti-inflammatory active ingredients in *I. cappa* are subject to further study.

Data availability statement

The original contributions presented in the study are included in the article/supplementary material, further inquiries can be directed to the corresponding authors.

Author contributions

JH, YC, and ZG conceived and designed the experiments. JH, CX, RC, JZ and QZ performed all of the experiments. YL, LZ, YH, QW operated on the cells and contributed reagents/materials/analysis tools. JH and CX analyzed the data. JH, RC and JZ wrote the paper. QZ contributed greatly to the improvement of the quality of the figures. YC and ZG contributed to critical review of the paper.

Funding

This research was supported by the National Natural Science Foundation of China (No. 81860734), the Excellent Young Talents Plan of Guizhou Medical University (No. 2022-104, 2021-103), National University Student Innovation and Entrepreneurship Project (No. 20195200132), University Student Innovation and Entrepreneurship Project of Guizhou Province (No. S202110660046) and Guizhou Science and Technology Department (GCC[2022]031-1).

Conflict of interest

The authors declare that the research was conducted in the absence of any commercial or financial relationships that could be construed as a potential conflict of interest.

Publisher's note

All claims expressed in this article are solely those of the authors and do not necessarily represent those of their affiliated organizations, or those of the publisher, the editors and the reviewers. Any product that may be evaluated in this article, or claim that may be made by its manufacturer, is not guaranteed or endorsed by the publisher.

References

Bao, H. S., Hou, J. Y., Hu, H. J., Li, Y. T., Zheng, L., Huang, Y., et al. (2019). Determination of plasma protein binding rate of nine compounds *Inula cappa* extraction based on method of equilibrium dialysis. *China. J. Chin. Mat. Med.* 44 (07), 1475–1484. doi:10.19540/j.cnki.cjcmm.20190116.007

Bissery, M. C., Vrignaud, P., Lavelle, F., and Chabot, G. G. (1996). Experimental antitumor activity and pharmacokinetics of the camptothecin analog irinotecan (CPT-11) in mice. *Anticancer. Drugs* 7 (4), 437–460. doi:10.1097/00001813-199606000-00010

Chang, L. L., and Qi, W. J. (2020). Research progress of Chinese medicine monomer to improve endothelial cell permeability. *Beijing Tradit. Chin. Med.* 39 (12), 1331–1334. doi:10.16025/j.1674-1307.2020.12.030

Chinese Pharmacopoeia Commission (2020). *Pharmacopoeia of the people's Republic of China, Part 1*. Beijing: China Medical Science Press, 1715.

Dong, M., Hiwasa, T., and Cong, B. (2015). Protein kinase Cα-mediated cytotoxic activity of ineupatorolide B from Inula cappa DC HeLa cells. *Int. J. Oncol.* 47 (5), 1839–1844. doi:10.3892/ijo.2015.3172

Feng, X. Y., Liu, C. D., Zhang, Y. M., Kang, Z., Jiang, Z. T., and Yu, H. (2019). Determination of plasma protein binding rate of gardenia glycosides, peony glycosides and naringin in gastritis ling granules by equilibrium dialysis. *Int. J. Traditional Chin. Med.* 41 (06), 608–613. doi:10.3760/cma.j.issn.1673-4246.2019.06.014

Gao, L. C., Zhang, W., Fan, L., and Zhou, H. H. (2011). Inflammation affects the expression and activity of drug transporters. *Chin. Pharmacol. Bul.* 27 (01), 7.

Gong, Z. P., Chen, T. T., Hou, J. Y., Wu, L. L., Li, M., Li, Y. T., et al. (2017a). Analysis of components in plasma from effective fractions of Inula cappa based on UHPLC/Q-TOF/MS. *Chin. Pharmacol. Bul.* 33 (11), 1605–1610. doi:10.3969/j.issn.1001-1978.2017.11.025

Gong, Z. P., Chen, Y., Zhang, R. J., Wang, Y. H., Guo, Y., Yang, Q., et al. (2014). Pharmacokinetic comparison of berberine in rat plasma after oral administration of berberine hydrochloride in normal and post inflammation irritable bowel syndrome rats. *Int. J. Mol. Sci.* 15 (1), 456–467. doi:10.3390/ijms15010456

Gong, Z. P., Li, M., Xiong, D. F. F., Wu, L. L., Liu, T., Lan, Y. Y., et al. (2017b). Evaluation of anti-inflammatory activity of *Inula Cappa* extract based on inflammation model *in vitro* and *in vivo*. *Nat. Prod. Res. Dev.* 29 (12), 2050–2055.

Gong, Z. P., Xiong, D. F. F., Li, M., Wu, L. L., Chen, T. T., Li, Y. T., et al. (2017c). Analysis of chemical constituents of effective components of Inula cappa. *J. Anhui. Agri.Sci.* 45 (29), 131–133. doi:10.13989/j.cnki.0517-6611.2017.29.041

Guan, H. Y., Lan, Y. Y., Liao, S. G., Liu, J. H., Han, Y., Zheng, L., et al. (2014). Caffeoylquinic acid derivatives in. *Inula cappa Nat. Prod. Res. Dev.* 26 (12), 1948–1952. doi:10.16333/j.1001-6880.2014.12.010

Guangxi Zhuang Autonomous Region, Department of Health (1992). in *Guangxi herbal medicine standard* (Nanning: Guangxi Science and Technology Press), 49.

Guizhou Province Drug Administration (2003). *Quality standards for Chinese herbal medicines and ethnic medicines in Guizhou Province*. Beijing: China Medical Science and Technology Press, 176.

Hu, L., and He, Z. S. (2012). Advances in chemical composition and pharmacological activity of *Inula cappa*. *Chin. J. Mod. Appl. Pharm.* 29 (10), 889–894. doi:10.13748/j.cnki.issn1007-7693.2012.10.008

Hunan Food and Drug Administration (2010). *Standard for Chinese herbal medicines in Hunan Province (2009 edition)*. Changsha: Hunan Science and Technology Publishing House, 340.

Jiraporn, N., Puttinan, M., and Yingmanee, T. (2011). Inhibition of Inula cappa(Ham.ex D.Don) DC.extracts on herpes simplex virus infection *in vitro*. *Afri. J. Microbiol. Res.* 5 (24), 4049–4058. doi:10.5897/AJMR10.387

Li, F. L. (2017). Anti-inflammatory effect and mechanism of aqueous extract of *Inula cappa* on rats with severe pneumonia caused by Klebsiella pneumonia. *World. Chin. Med.* 12 (10), 2438–2442. doi:10.3969/j.issn.1673-7202.2017.10.041

Liu, D. C., Zhou, F., Zhang, J. W., and Wang, G. J. (2021). New insight and new methodology for herb-drug interactions based on cellular pharmacokinetics. *J. Nanjing. Univ. Tradit. Chin. Med.* 37 (03), 325–330. doi:10.14148/j.issn.1672-0482.2021.0325

Liu, J. P. (2016). *Biopharmacology and pharmacokinetics*. Beijing: People's Health Publishing House, 245.

Liu, J. Y., Geng, T., Duan, K., Gao, X., Huang, C. J., Wang, J. J., et al. (2019). Cellular pharmacokinetics and pharmacodynamics mechanisms of ginkgo diterpene lactone and its modulation of P-glycoprotein expression in human SH-SY5Y cells. *Biomed. Chromatogr.* 33 (12), 4692–4706. doi:10.1002/bmc.4692

Liu, S. G., Hu, X., Liu, X., and Deng, L. (2009). Study on the chemical composition of volatile oil and its role in scavenging free radicals of Inula Cappa. *J. Anhui. Agri.Sci.* 37 (26), 12536–12537. doi:10.13989/j.cnki.0517-6611.2009.26.148

Liu, W. J., Ge, T., Liu, S. G., and Liu, X. R. (2010). Extraction and antibacterial effects of flavonoids from Inula Cappa. *Hubei Agric. Sci.* 49 (02), 426–429. doi:10.14088/j.cnki.issn0439-8114.2010.02.072

Ma, Q., Zhang, X. L., Wang, C. Y., Guo, L., Zhao, Y. J., Hou, Y. L., et al. (2019). Ginsenoside Rb1 regulates cerebral microvascular NOS/NO to improve brain cell membrane permeability. *Prog. Mod. Biomed.* 19 (08), 1430–1435. doi:10.13241/j.cnki.pmb.2019.08.007

Mai, Q. Y., Fan, Y. W., Deng, Z. Y., and Zhang, B. (2021). Mechanism of non-covalent interaction between fetal bovine serum and centaureidin-3-glucoside and its effect on antioxidant activity. *Food Sci.* 42 (05), 1–8. doi:10.7506/spkx1002-6630-20200108-096

Mateus, André., Matsson, Pär., and Artursson, Per. (2013). Rapid measurement of intracellular unbound drug concentrations. *Mol. Pharm.* 10 (6), 2467–2478. doi:10.1021/mp4000822

Ni, P., Zhang, J. W., Liu, J. L., Chen, Q. Y., Wang, G. J., and Zhou, F. (2014). Research progress in cellular pharmacokinetic. *Prog. Pharm. Sci.* 38 (12), 881–885.

Patrick, P., Frank, J., and Burczynski, S. H. (2016). The role of extracellular binding proteins in the cellular uptake of drugs: Impact on quantitative *in vitro* -to-*in vivo* extrapolations of toxicity and efficacy in physiologically based pharmacokinetic-pharmacodynamic research. *J. Pharm. Sci.* 105 (2), 497–508. doi:10.1002/jps.24571

Projean, D., Dautrey, S., Vu, H. K., Groblewski, T., Brazier, J. L., and Ducharme, J. (2005). Selective downregulation of hepatic cytochrome P450 expression and activity in a rat model of inflammatory pain. *Pharm. Res.* 22 (1), 62–70. doi:10.1007/s11095-004-9010-6

Qiu, D. W., and Du, J. (2005). *Chinese materia medica: Miao medicine volume. Guiyang*. Guiyang: Guizhou Science and Technology Publishing House, 273–274.

Song, F., Yang, J., Wang, C., Wang, X., Li, W. W., Pan, J., et al. (2019). Effect of Inula cappa on CYP450 enzyme in rats by cocktail probe drugs. *Chin. J. Expe. Tradi. Med. Formu.* 25 (02), 60–67. doi:10.13422/j.cnki.syfjx.20181905

Uno, S., Fujii, A., Komura, H., Kawase, A., and Iwaki, M. (2008). Prediction of metabolic clearance of diclofenac in adjuvant-induced arthritis rats using a substrate depletion assay. *Xenobiotica* 38 (5), 482–495. doi:10.1080/00498250801935982

Wang, A. M., Li, M., Sun, J., Xiong, D. F. F., Chen, T. T., Wu, L. L., et al. (2018). Study on the antibacterial and anti-inflammatory activities of extracts of *Inula cappa*. *LiShiZhen.Med. Mater. Medica. Res.* 29 (07), 1580–1584.

Wang, L. H., Feng, Y., Zhong, S., Zhu, Y. P., Lou, Y. H., Jiao, B. H., et al. (2001). Toll-like receptor antibodies inhibit phagocytic activity of lipopolysaccharide-activated macrophages. *Adv. Biochem. Biophysics* (03), 367–371. doi:10.3321/j.issn:1000-3282.2001.03.022

Wu, J. W., Tang, C. P., Cai, Y. Y., Ke, C. Q., Lin, L. G., Yao, S., et al. (2017). Cytotoxic germacrane-type sesquiterpene lactones from the whole plant of Inula cappa. *Chin. Chem. Lett.* 28 (5), 927–930. doi:10.1016/j.cclet.2016.11.011

Wu, Z. J., Lei, S., Lu, M., Shen, Y. H., Tang, J., and Zhang, W. D. (2010). Chemical constituents from *Inula cappa*. *Chem. Nat. Compd.* 46 (2), 298–300. doi:10.1007/s10600-010-9595-4

Xie, H. G., Zhang, H. W., Zhang, J., Xu, L. Z., and Zhou, Z. M. (2007). The chemical composition of. *Inula cappa Chin. Nat. Med.* (03), 193–196. doi:10.3321/j.issn:0513-4870.1999.03.012

Xie, H. T., Wang, G. J., Zhao, X. C., and Sun, J. G. (2004). Uptake and metabolism of ginsenoside Rg3 by Caco-2 cells. *Chin. J. Clin. Pharmacol. Ther.* 9 (3), 257–260. doi:10.3969/j.issn.1009-2501.2004.03.005

Xie, H. T., Wang, J., Chen, Z. D., Yuan, G. Q., Li, Q. Q., and Lin, W. (2012). Analysis of antimicrobial substances and their antibacterial properties of *Inula cappa*. *Nat. Prod. Res. Dev.* 24 (11), 1534–1537. doi:10.16333/j.1001-6880.2012.11.021

Xue, C., Hu, H. J., Xiao, H. Q., Hou, J. Y., Zhang, Q., Wang, G. C., et al. (2020). Uptake and transport of the nine active components from Inula cappa extract in caco-2 cell model. *Lat. Am. J. Pharm.* 39 (8), 1579–1587.

Yao, B., and Liang, X. Y. (2008). Study on the volatile oil composition of Inula cappa. *J. Yunnan Univ. Traditional Chin. Med.* 31 (06), 27–29. doi:10.3969/j.issn.1000-2723.2008.06.010

Yao, L. C. (2017). *Research on chemical composition and quality standard of Inula cappa*. Chengdu: Chengdu University of Traditional Chinese Medicine.

Ye, M., Zhu, Z., Fu, Q., Shen, K., and Li, D. K. (2020). Nonlinear pharmacokinetic study of paclitaxel in patients treated with chemotherapy for ovarian cancer. *Chin. Pharm. J.* (09), 28–30. doi:10.3321/j.issn:1001-2494.2000.09.011

Yunnan Food and Drug Administration (2007). *Yunnan provincial standard for Chinese materia medica (2005 edition), book 2 Yi medicine*, 57. Kunming: Yunnan Science and Technology Publishing House.

Zhang, Q., Cong, D. H., An, D. C., Liu, Q., et al. (2018). Determination of oroxylin A and oroxylin A 7- O-d-glucuronide in HepG2 cell lysate and subcellular fractions with SPE-UPLC–MS/MS: Cellular pharmacokinetic study to indicate anti-cancer mechanisms. *J. Pharm. Biomed. Anal.* 154, 364–372. doi:10.1016/j.jpba.2018.03.019

Zhang, X. M., An, D. W., Zhang, H., Yang, N. H., and Guligena, S. (2020). Effect and mechanism of Ziziphora clinopodioides Favonoids on secretion of inflammatory factors from Lipopolysaccharide Induced RAW264.7 cells. *Liaoning. J.Traditional. Chin. Med.* 47 (02), 158–161. doi:10.13192/j.issn.1000-1719.2020.02.049

Zhang, Y., and Jiang, R. Z. (2018). Research progress on the relationship between HIF2α and cell permeability. *J. Med.Res.* 47 (01), 13–15. doi:10.11969/j.issn.1673-548X.2018.01.004

Zhang, Z. Y., Hu, H. J., Xiong, D. F. F., Li, Y. T., Huang, Y., Zheng, L., et al. (2019). Study on quality control of Miao medicine Inula cappa based on anti-inflammatory active ingredients. *Chin. Traditional.erb. Drugs.* 50 (22), 5571–5576. doi:10.7501/j.issn.0253-2670.2019.22.027

Zhou, F., Zhang, J. W., Li, P., Wu, X. L., Wang, G. J., et al. (2011). Toward a new age of cellular pharmacokinetics in drug discovery. *Drug Metab. Rev.* 43 (3), 335–345. doi:10.3109/03602532.2011.560607

Zhou, F., Zhang, Y. B., Zheng, X., and Lin, H. Y. (2019). Effect of white tea extract on LPS-induced inflammation in RAW264.7 cells. *Tea. Lett.* 46 (04), 455–462.

Zhou, H., Zheng, L. T., Lin, A. H., and Liu, Y. M. (2020). Determination of the pharmacokinetics of mangostin in INS-1 cells by LC-MS/MS. *Chin. Pharmacol. Bul.* 36 (07), 1024–1029. doi:10.3969/j.issn.1001-1978.2020.07.024

Zhou, J., Xue, C., Zhang, Q., Chen, S. Y., Chen, Y., Huang, J., et al. (2022). Establishment of a method determining the contents of seven anti-inflammatory active components of the Miao medicine Inula cappa in Raw 264.7 cells. *J. Jiangsu Univ. Ed.* 32 (6). doi:10.13312/j.issn.1671-7783.y220071

Zhou, W., Wang, X., Fu, S. H., Sun, X., Chen, S. Y., Lan, Y. Y., et al. (2017). Chemical constituents of Inula cappa. *Chin. Pharm. J.* 52 (01), 25–30. doi:10.1002/cbdv.200690041

Frontiers in Pharmacology

Explores the interactions between chemicals and living beings The most cited journal in its field, which advances access to pharmacological discoveries to prevent and treat human disease.

Discover the latest Research Topics

See more →

Frontiers

Avenue du Tribunal-Fédéral 34
1005 Lausanne, Switzerland
frontiersin.org

Contact us

+41 (0)21 510 17 00
frontiersin.org/about/contact